



Consiglio Nazionale
delle Ricerche

20th ISEC

 INTERNATIONAL STIRLING
ENGINE CONFERENCE

Neaples, 25th-27th June 2024

editor

Francesco Saverio Marra

PROCEEDINGS

20th ISEC

 INTERNATIONAL STIRLING
ENGINE CONFERENCE

Neaples, 25th-27th June 2024

editor

Francesco Saverio Marra

ORGANIZERS

SIA – Stirling International Association



CO-ORGANIZERS

CNR – Istituto di Scienze e Tecnologie per l'Energia e la Mobilità Sostenibili
Università di Napoli Federico II



© Cnr Edizioni, 2025

P.le Aldo Moro 7, 00185 Roma

www.edizioni.cnr.it

ISBN 978 88 8080 641 7

DOI <https://doi.org/10.48221/ISEC20-2024>



This work is licensed under [CC BY-SA 4.0](https://creativecommons.org/licenses/by-sa/4.0/)

Un ringraziamento a Cinzia Napolitano (STEMS-CNR) per il contributo nella revisione dei testi.

Sviluppo grafico a cura di Fulvia Ciurlia, Istituto di Fisica Applicata “Nello Carrara” (IFAC-CNR)

Impaginazione a cura di Patrizia Andronico, Istituto di Informatica e Telematica (IIT-CNR)

CHAIRS

Francesco Saverio MARRA (Chair), Amedeo AMORESANO (Co-Chair)

EXECUTIVE COMMITTEE OF SIA

Chin-Hsiang CHENG (President), Luc BAUWENS, Hans-Detlev KÜHL, Francesco Saverio MARRA, Khamid MAHKAMOV, Luca CIOCCOLANTI (Secretary General)

PROGRAM COMMITTEE

Javier ARANCETA (Spain), Carlo Maria BARTOLINI (Italy), Luc BAUWENS (Canada), Tetsushi Biwa (Japan), Chin-Hsiang CHENG (Taiwan), Luca CIOCCOLANTI (Italy), Don Murray CLUCAS (New Zealand), Juan Auñón HIDALGO (Spain), Jian-Ying HU (China), Jhen-Syuan HUANG (Taiwan), Carmen INIESTA BARBERÀ (Spain), Hans-Detlev KÜHL (Germany), François LANZETTA (France), Ercang LUO (China), Khamid MAHKAMOV (United Kingdom), Vincenzo NASO (Italy), Toshio OTAKA (Japan), K. Srinivas REDDY (India), Pascal STOUFFS (France), Hang-Suin YANG (Taiwan)

LOCAL HOST COMMITTEE

Francesco Saverio Marra, Luigi Muriello, Antonio Rossi, Martina Rossi, Cinzia Napoletano, Antonio Albano, CNR – STEMS, Italy

CONFERENCE SECRETARIAT

M.C.M. Congressi



20 th ISEC – Technical Program	7
Introduction	10
Progress on Some Fundamental Problems and Key Technologies of Thermoacoustic and Stirling Machines	12
Stirling engines prototype development and testing	16
Speed Control Mechanism of Stirling Engine.	
Towards Invention of the Mechanical Governor for Stirling Engine	17
Evaluation of Liquid-piston Stirling Engine integrated with Self-rectifying Impulse Turbine	29
Design Methodology for a Looped-Tube Thermoacoustic Engine Incorporating a Flywheel	40
Development and Testing of a Free Liquid Piston Ericsson Engine	48
Numerical and Experimental Investigation of a Combustor-coupled Thermoacoustic Stirling Generator	66
An Integration Model and Performance Measurement of a Stirling Generation System	84
On Operating Frequency of Three-Stage Double-Acting Fluidyne Stirling Oscillators	96
Field test of a diesel powered 300 We free-piston Stirling electric generator	109
Experimental Confirmation of Numerical Design of Slot-Spaced Permanent Magnet Linear Alternator	125
Stirling refrigerators and cryocoolers	140
Measurement of Minor Loss at T-junction tube	141
Influence of Displacement Phase Angle on the Performance of Rotary Stirling Cryocooler	150
Development of a Miniature Free Piston Stirling Cryocooler for HOT Infrared Detector	158
Third-Order Modelling and Comparison of a Thermal Compressor Versus a Mechanical Compressor in a Heat-actuated Stirling Refrigerator	175
Thermodynamic Analysis of a β -Type Stirling Cryocooler at Low Charged Pressures	192
Fluent simulation of a beta Stirling engine for very low temperatures	206
Thermodynamic modelling and CFD simulation	218
New Analytical Method for Stirling Engine Thermodynamic Cycle Calculation Using Simplified Adiabatic Model	219
Performance of β -type Stirling Engine Under Various Kinematic-drive Mechanisms	231

β Stirling-engine for Laboratory and Educational Applications in Heat Engine and Cooling Mode	250
Quantifying Hysteresis Loss in a Stirling Refrigerator using Sage	269
Simple Prediction method of Gas Temperature for Stirling Engine	284
Artificial Intelligence Applications for Stirling Engines Development: a mini-review	299
Heat transfer / fluid flow analysis	318
A Straight-tube Type Thermoacoustic Engine designed as a Heat Transfer Device	319
Study on Internal Cooling of a High-temperature Linear Alternator for Free-piston Stirling Generators	331
Novel designs of drive mechanisms and configurations	349
A Novel Cam-Drive Mechanism for Non-Sinusoidal Motion in a Stirling Engine	350
Direct Generation of Compressed Air by Cascaded Overdriven Free Displacer Thermocompressors	366
Study on Stable Operation of Displacer with Low Damping	385
Stirling heat pumps	400
Experimental Study of an Efficient Low-temperature Free-piston Stirling Heat Pump	401
Numerical Investigation on Ultra-High- Temperature Thermoacoustic Stirling eat Pump	420
Stress analysis/noise and vibration	434
Vibration Analysis of a V6 Double-acting Gamma Stirling Heat Pump	435
Regenerator and porous medium	448
Determination of the Regenerator Loss in a Stirling Engine by Gas Temperature Measurements	449
Thermal receivers, combustors and heat exchangers	466
Cyclone Nozzle Structure Optimization for Combustor Performance Enhancement in a Stirling Engine fueled by Reformed Gas and Diesel Fuel	467
Renewable applications of Stirling engines	494
Optimization of Hybrid Solar-Syngas Power System Using Response Surface Methodology	495
Authors index	509

20th ISEC – Technical Program

Tuesday, June 25 th , 2024		
8.30-10:00	Welcome Breakfast	
10:00-10:30	Opening Ceremony (Aula Barsanti e Matteucci)	
10:30-11:35	Plenary Lecture Recent Progress on Some Fundamental and Technical Issues of Thermoacoustic and Stirling Machines Prof. Ercang Luo (University of Chinese Academy of Sciences, China) Chairs: T. Biwa and Hang-Suin Yang	
11:35-11:45	Break (transition to morning sessions)	
	Aula Barsanti e Matteucci	Aula Ferretti
Topics	Stirling engines prototype development and testing I Chair: Carmen Iniesta Barbera	Stirling refrigerators and cryocoolers I Chair: Chin-Hsiang Cheng
11:45-12:10	Speed Control Mechanism for Stirling Engine (#22) Tatsuro Kitahara, Tomoaki Sato	Measurement of Minor Loss at T-junction tube (#35) Y. Kurai, S. Sekimoto, Y. Ueda
12:10-12:35	Evaluation of liquid-piston Stirling engine integrated with self-rectifying turbine (#23) J. Tomihira, E. Shoji, T. Biwa, P. Murti, M. Takao, S. Okuhara	Influence of Displacement Phase Angle on the Performance of Rotary Stirling Cryocooler (#34) Jhen-Syuan Huang
12:35- 13:00	Design Methodology for a Looped-Tube Thermoacoustic Engine Incorporating a Flywheel (#40) Keita Tetsuka, Eita Shoji, and Tetsushi Biwa	Development of a Miniature Free Piston Stirling Cryocooler for HOT Infrared Detector (#12) Zhongli Xi, Xing Xiao, Xiaoqing Zhang
13:00-14:30	Lunch	
Topics	Stirling refrigerators and cryocoolers II Chair: Jhen-Syuan Huang	Thermodynamic modelling and CFD simulation I Chair: Francesco Saverio Marra
14:30-14:55	Third-order modelling and comparison of a thermal compressor versus a mechanical compressor in a heat-actuated Stirling refrigerator (#33) Zindh Waleed, Michael Gschwendtner, Danielle Yang	New Analytical Method for Stirling Engine Thermodynamic Cycle Calculation Using Simplified Adiabatic Model (#05) S. P. Stolyarov, A. S. Stolyarov, Ye Maung
14:55-15:20	Thermodynamic Analysis of a β -Type Stirling Cryocooler at Low Charged Pressures (#36) Duc-Thuan Phung, Chin-Hsiang Cheng, Stefan Popesku	Performance of β -type Stirling Engine Under Various Kinematic-drive Mechanisms (#43) A. Abuelyamen, R. Ben-Mansour
15:20-15:45	Fluent simulation of a beta Stirling engine for very low temperatures (#47) J.A. Auñón Hidalgo, D. Núñez Gevorkian	β -Stirling-engine for laboratory and educational applications in heat engine and cooling mode (#48) Norbert Lümmen, Arne Høeg
15:45-16:15	Coffee Break & Posters	
Topics	Stirling engines prototype development and testing II Chair: Hans-Detlev Kühl	Heat transfer / fluid flow analysis Chair: Tetsushi Biwa
16:15-16:40	Development and testing of a free liquid piston Ericsson engine (#53) R. Chouder, P. Stouffs	A Straight-tube Type Thermoacoustic Engine designed as a heat transfer device (#32) Akitsugu Watanabe, Kazuyuki Yoshioka, Yuki Ueda
16:40-17:05	A 100 kW Free-piston Thermoacoustic-Stirling Alternator (#31) Jianying Hu, Limin Zhang, Yanyan Chen, Zhanghua Wu, Yanlei Sun, Xiaotao Wang, Ercang Luo	Study on Internal Cooling of High-temperature Linear Alternator for Free-piston Stirling Generators (#06) Jing Luo, Yanlei Sun, Yanyan Chen, Qingyue Jin, Xinyu Zhu, Limin Zhang, Jianying Hu, Ercang Luo
17:05-17:30	Numerical and experimental investigation of a combustor-coupled thermoacoustic Stirling generator (#15) Qingyue Jin, Jing Luo, Haojie Sun, Jianhua Xue, Ying Ma, Zhuang Ma, Guoyao Yu, Ercang Luo	Numerical Analysis of the Fundamental Heat Transfer Characteristics of the Free-Piston Stirling Engine (#13) Xinyu Zhu, Yanyan Chen, Jing Luo, Yanlei Sun, Guoyao Yu, Ercang Luo

Wednesday, June 26 th , 2024		
	Aula Barsanti e Matteucci	Aula Ferretti
Topics	Novel designs of drive mechanisms and configurations Chair: Hang-Suin Yang	
9:00-9:25	A Novel Cam-Drive Mechanism for Non-Sinusoidal Piston and Displacer Motion in a Stirling Engine (#07) Wong HM	
9:25-9:50	Direct Generation of Compressed Air by Cascaded Overdriven Free Displacer Thermocompressors (#38) H.-D. Kühl, F. Fischer	
9:50-10:15	Study on Stable Operation of Displacer with Low Damping (#10) Yuanhang Chen, Yanyan Chen, Guoyao Yu, Yiwei Hu, Jing Luo, Yanlei Sun, Ercang Luo	
10:15-10:45	Coffee Break & Posters	
Topics	Stirling engines prototype development and testing III Chair: Pascal Stouffs	Stirling heat pumps Chair: Amedeo Amoresano
10:45-11:10	An Integration Model and Performance Measurement of a Stirling Generation System (#29) Yuan-Chun Cheng, Cai-Shuo Yin, Hang-Suin Yang	Experimental Study of an Efficient Low-Temperature Free-piston Stirling Heat Pump (#68) Riyang Wang, Jianying Hu, Zhanghua Wu, Ercang Luo, Yanlei Sun
11:10-11:35	On Operating Frequency of Three-Stage Double-Acting Fluidyne Stirling Oscillators (#09) A.R. Tavakolpour-Saleh, M. H. Sangdani	Numerical Investigation on Ultra-High-Temperature Thermoacoustic Stirling Heat Pump (#42) K.Q. Luo, L.R. Dai, Y.L. Sun, Z.H. Wu, J.Y. Hu, Y. Huang, E.C. Luo
11:35-12:00	Field test of a diesel powered 300 We free-piston Stirling electric generator (#11) Wang Xiao, Guoyao Yu, Ying Ma, Zhuang Ma, Yangbin Cheng, Shuibing Jiang, Ercang Luo	Study on operating characteristics of high temperature free-piston Stirling heat pump suitable for 120~180 °C (#19) Longran Dai, Kaiqi Luo, Yanlei Sun, Jianying Hu, Xinglin Zhao, Ercang Luo
12:00-12:10	Break	
Topics	Stress analysis/noise and vibration & Thermal receivers, combustors and heat exchangers Chair: Luc Bauwens	Regenerator and porous medium & Waste heat recovery systems Chair: Juan Antonio Auión Hidalgo
12:10-12:35	Vibration analysis of a V6 double-acting gamma Stirling heat pump (#45) Arne Høeg, Sindre Abrahamsen, Gunnar Vartdal, Tobias Dahl, Norbert Lümmen	Determination of the Regenerator Loss in a Stirling Engine by Gas Temperature Measurements (#39) S. Peveling, F. Kusche, H.-D. Kühl
12:35-13:00	Cyclone Nozzle Structure Optimization for Combustor Performance Enhancement in a Stirling Engine fueled by Reformed Gas and Diesel Fuel (#26) J. Lan, X. Liang, T. Lyu, G.T. Lin, X. Yang, G.X. Gu, D. Han	Optimization of a Hybrid Solar-Syngas Power System Using Response Surface Methodology (#28) Shang-Ting Huang, Chin-Hsiang Cheng
13:00-14:30	Lunch	
Excursion & Banquet		

Thursday, June 27 th , 2024		
9:00-10:50	Meeting of the SIA	
10:50-11:20	Coffee Break & Posters	
	Aula Barsanti e Matteucci	Aula Ferretti
Topics	Renewable applications of Stirling engines & Stirling engines in hybrid co-generation systems Chair: Luca Cioccolanti	Thermodynamic modelling and CFD simulation II Chair: Juan Antonio Auñón Hidalgo
11:20-11:45	Experimental Confirmation of Numerical Design of Slot-Spaced Permanent Magnet Linear Alternator (#27) Surender Dhanasekaran, Chin-Hsiang Cheng	Quantifying Hysteresis Loss in a Stirling Refrigerator using Sage (#37) Danielle Yang, Michael Gschwendtner, Aishath Zindh Waleed, Michael Protheroe
11:45-12:10	Why cryogenics is able to help recovering fatal heats, cleaning smokes and gases, and then producing energies (solar or geothermal) in a big quantity (#44) Vernet Jean Philippe	Simple Prediction Method of Gas Temperature for Stirling Engine (#54) Fujio Toda, Mari Matsubara, Takasi Ishijima
12:10-12:35		Artificial Intelligence Applications for Stirling Engines Development: a mini-review (#03) Francesco Saverio Marra, Luigi Acampora
Farewell Party		

Posters Session

Thermal Machine of the STIRLING - FRANCHOT type With Cylindrical Pistons (#55)

Thierry Raballand, Antonio Treilhou

Introduction

The 20th edition of the International Stirling Engine Conference was held in Naples, Italy for the first time. It was a significant honor and privilege to host the conference at the recently established STEMS Institute of the National Research Council of Italy. The Institute of Science and Technology for Sustainable Energy and Mobility focuses on research activities for the development of solutions for clean energy, which aligns with the objectives of most Stirling Engine applications.

The resurgence of interest in this relatively old technology, which was invented more than 200 years ago, may be considered unexpected. However, this phenomenon is not uncommon. Frequently, the significance and utility of a novel technology can only be recognized when subsidiary technologies have progressed sufficiently to enable widespread, economically viable, and environmentally advantageous implementation of the technology, which may have previously been regarded merely as an intriguing curiosity. This has been observed, for instance, in the case of concentrated solar energy, likely invented over 2000 years ago by Archimedes as a weapon, but now, due to advancements in optical technology and energy transformation, represents a viable and one of the most environmentally sustainable methods of energy production. Similarly, this occurred for other technologies, such as the steam engine, first observed nearly 2000 years ago as the “Aeolipile,” which subsequently became central to the industrial transformation, or the electrical battery, invented by Volta in 1799, which now serve as essential components in numerous electric and electronic devices and, more recently, have become crucial for developing energy and mobility systems. Another exemplar is the bicycle, which was considered primarily a device for sporting activities 200 years ago, while now serving as the primary mode of transportation in many countries. Currently, when coupled with compact and powerful electrical motors and batteries, it is experiencing a renewed proliferation in urban mobility applications.

Stirling engine technology has undergone similar advancements. Despite being overshadowed by competitive engine technologies that were developed shortly after its invention, primarily the internal combustion engine, it has gradually garnered renewed interest due to several of its distinctive characteristics. The foremost among these is the absence of direct emissions during operation. Additional notable features include high theoretical efficiency in the conversion of thermal to mechanical energy, minimal noise production, potential for miniaturization, adaptability to various primary energy sources, capability to operate in reverse cycles, and minimal maintenance requirements. These attributes render this engine suitable for diverse applications, encompassing small-scale clean energy production, cryocoolers, submarine propulsion, scientific instruments, and space exploration.

The current development of the technology progresses along multiple trajectories, as evidenced by these proceedings, which compile the extended papers of the majority of contributions presented during the conference. Fundamental theoretical advancements remain necessary to address phenomena that are not yet fully comprehended, and to develop models for novel configurations. Technological developments are becoming increasingly sophisticated and encompass not only the core of the Stirling engine cycle but also the components essential for practical applications, such as electric generators or control systems. It is anticipated that this conference series, now spanning more than four decades, will continue to expand and incorporate expertise from numerous other disciplines.

It is necessary to acknowledge the numerous individuals who contributed to the realization of this conference. Foremost among these are the former members of the SIA board of directors, particularly Vincenzo Naso and Carlo Maria Bartolini, whose commitment has facilitated the continuation of the Stirling International Association's activities, along with the assistance of Luca Cioccolanti, who has consistently provided expertise in various aspects of the SIA's operations. The support and confidence of the current Board of Directors, comprising Luc Bauwens, Hans-Detlev Kühl, Khamid Mahkamov, and chaired by Chin-Hsiang Cheng, of which I am privileged to be a member, has established the foundation for the conference's success in terms of participation and global recognition.

The high quality of scientific contributions and associated discussions was fundamentally ensured through the efforts of all program committee members, who reviewed all submissions and chaired the program sections.

So much support has been provided also from the Director of the CNR-STEMS Institute, Bianca Maria Vaglieco, and my colleagues Luigi Muriello, Antonio Rossi, Martina Rossi, Cinzia Napolitano and Antonio Albano, who helped in so many practical aspects. I am also very grateful to the personnel of MCM Congressi, Stefania Acanfora and Lucia Melchiorre, which were very professional in siding me in the management of the conference secretariat and practical organization.

Acknowledgment is also due to the Editorial Office of the CNR, under the leadership of Sara Di Marcello, for recognizing the significance of this volume, which serves as a valuable and publicly accessible source of information for individuals interested in the multifaceted aspects of contemporary Stirling engine technology. Particular gratitude is extended to Patrizia Andronico for her diligent efforts in compiling the volume.

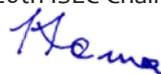
In conclusion, I extend my gratitude to all conference participants, marking the first in-person gathering following the COVID-19 pandemic, for their exemplary presentations and contributions. The conference facilitated an exceptional exchange of knowledge through discussions, consistently maintaining an atmosphere of international collegiality—a particularly valuable aspect during this challenging period for the global community.

In anticipation of increasing success for future editions of the ISEC, I encourage readers to contribute to the effort of establishing the Stirling engine as a valuable technology for a more environmentally sustainable world.

Napoli, January 20, 2025

Francesco Saverio Marra

20th ISEC Chair



Progress on Some Fundamental Problems and Key Technologies of Thermoacoustic and Stirling Machines

Ercang Luo^{1,2}

1. University of Chinese Academy of Sciences, Beijing, China

2. Technical Institute of Physics and Chemistry, Beijing, China

Email: ecluo@mail.ipc.ac.cn

Abstract

The Stirling heat engine prototype for power generation was first proposed and developed by Robert Stirling in 1816. More than 200 years has already gone, and numerous different configurations and prototypes originating from that oldest Stirling heat engine have been developed. Due to the very complicated heat transfer, flowing and thermodynamic process, some fundamental problems have not been well understood yet. Consequently, key techniques for achieving high capacity, high reliability and low cost have not been solved and developed. In recent years, the requirement of decarbonization and carbon neutrality of energy is revitalizing this old heat engine technology because of its many intrinsic advantages. Important progresses on some fundamentals and key technologies have been made, leading to an exciting future of this technology and its close relatives, thermoacoustic technology. In this plenary talk, I would like to deliver my contents focusing on the following three aspects:

I. Theoretical aspect

a) Novel perspectives and understanding on thermodynamic processes and thermodynamic cycle

All thermoacoustic and previously so-called Stirling machines operate on complex interaction between compressible oscillating gas and solid regenerator and heat exchangers. Traditionally, these regenerative machines have been thought to undergo Stirling cycle which mainly incorporate two isothermal processes and two isovolumic processes. However, the advance of thermoacoustics in recent decades has demonstrated a totally different micro/macro-scale thermodynamic processes for the regenerative machines. Hereby, a detailed study on the thermodynamic processes of micro-scale single gas parcels and macro-scale all gas envelope has been implemented in the past decades. As a result of the study, a quite novel and fundamental perspective on thermodynamic cycle on the regenerative machines has been proposed, in which a micro-scale gas parcel in the so-called regenerator undergoes Lorentz-like thermodynamic cycle, while the envelope of all gas parcels forms Ericsson-like cycle. Effects of non-ideal heat transfer and viscous flowing only add some little shaping effect on the unique

thermodynamic cycle. In other word, each gas parcel finishes its own thermodynamic cycle under different temperature level and in different locations, etc. The regenerator is not only regenerative heat exchanger, but it is really a micro-scale heat-to-power convertor. Several examples for the kinematic Stirling configuration, free-piston Stirling and some thermoacoustically-driven heat engine and refrigerator are given for supporting the novel viewpoint. Furthermore, a 3D description and characterization for such unique thermodynamic cycle, e.g., P-v-x and T-s-x diagrams, is proposed and reported in this talk for the first time.

This work has led to a novel LEC thermodynamic cycle theory for deeply understanding Stirling-type and thermoacoustic-type prime movers and refrigerators.

b) In-depth physical understanding of thermoacoustic effect and advanced weakly nonlinear thermoacoustic model

Historically, there have been several quantification mathematical-physical models for explaining and quantifying the Stirling and the like regenerative machines. Sometimes, they are called zeroth-order, first-order, second-order, and third-order. However, all most of these models have not clearly shown the fundamental physical essence of the complex interaction of oscillating gas and solid nearby. In the recent past decades, thermoacoustics really reveal the physical fact, leading to a very clear physical picture of the regenerative thermoacoustic and Stirling machines' operation. However, in the beginning period and even up to now, many researchers have no correct understanding for dynamic and time-averaged thermoacoustic effects. Thus, a so-called linear thermoacoustic model has been developed and used for quantifying various thermodynamic parameters and performance under linear acoustic approximation. Based on the misleading understanding, two fundamental questions have been puzzled for a long time. Hereby, an in-depth viewpoint on how to understand various thermoacoustic effects including dynamic and time-averaged thermoacoustic effects has been proposed. As a result, an advanced thermoacoustic models and equations has been proposed. With the help of the novel perspective and theory, two classic puzzled questions have been successfully solved. In addition, the advanced theory has provided a powerful guidance for us to design numerous high-performance thermoacoustic and Stirling prototypes and commercial products. This work has been summarized to form a weakly nonlinear locally-analytical thermoacoustic models and theory for qualitatively

understanding thermoacoustic effect and quantitatively predicting thermodynamic performance of the Stirling-like and thermoacoustic-like machines.

c) Time-domain dynamic evolution process and non-linear thermoacoustic network models for thermally self-exciting thermoacoustic and Stirling machines

There are two kinds of thermally-driven mechanical power generator, one is non-resonant system and the other is resonant system. The kinematic Stirling heat engine is actually a kind of non-resonant mechanical power system, while the free-piston Stirling and thermoacoustic systems are basically belong to resonant thermal-mechanical system. For the later type, the onset temperature and resonant frequency are very important parameters to evaluate its basic feature. In particular, the dynamic evolution process from the onset moment to saturation state (e.g., steady periodic oscillation) is critical and valuable to understand the operating state and global thermodynamic performance. There are several mathematical-physical ways to answer the question. In this part, we introduce a nonlinear electrical-like network way to solve the above-mentioned issue. First, the network models based on lumped-parameter are derived for different thermodynamic and mechanical components such as regenerator, heat exchangers, free-piston displacer, linear motor, etc. Then, several representative systems such as free-piston Stirling heat engine, thermoacoustically-driven heat engine and refrigerators are modeled to show their dynamic evolution processes including the dynamic pressure amplification and limit cycle, etc. This nonlinear network method is very straightforward and effective to evaluate the dynamic and steady performance of thermally-driven Stirling and thermoacoustic systems.

II. Technical aspect

The kinematic Stirling machines has long development history, but they have very limited application so far. The obstacle of hindering wide and large-scale commercial application may exist various reasons, among which the low reliability and lifetime, due to serious mechanical friction of kinematic piston-cylinder pair, is one of the most serious problems. Therefore, free-piston type and thermoacoustic type of systems have been studied intensively in the past and recent decades. Inside these systems, free solid piston, liquid piston, and gas resonator, etc., have been adopted to ease or eliminate the kinematic crank-shaft connection problem. In this part, several key technical progresses

on free-piston Stirling power generator including our 100kWe-class prototype, our commercialized high-frequency liner-motor driven pulse tube cryocoolers, and thermoacoustically-driven high-efficiency air-conditioning prototype with a COP being better than other thermally-driven systems like adsorption and absorption refrigeration systems.

III. Application aspect

Because recent important progress and huge potential of several improved Stirling configurations and newly-proposed thermoacoustic systems, this old yet dynamic technology is welcoming to a huge development opportunity. Firstly, these systems typically have used environment-friendly working substance such as helium gas and nitrogen gas, intrinsically having low-carbon advantage. Secondly, many future markets for decarbonization are opening a huge opportunity for this regenerative technology which has a good potential to realize high efficiency for larger temperature span lifting. In this regard, various kinds of thermoacoustic and Stirling heat pumps for achieving lower cooling temperature range, or achieving high even ultra-high temperature heating ranging from 100 °C up to 800 °C, can be developed. Not only industrial water steam generation can be realized based on this technology, but also the high temperature heating over 600 °C for future hydrogen iron-making industrial process can be used, too. Thirdly, for the ultimate utilization of human being energy resource such as solar energy, the distributed high-performance free-Stirling generator would be a critical solution to produce clean electricity.

All in a word, significant progress including scientific and technical work have been made in the past decades. The development trend of decarbonization and electrification of energy exploration and utilization provide a huge opportunity for the Stirling and thermoacoustic technology. Certainly, the wonderful dream of those exciting application scenes still needs a huge effort and innovative researches from the Stirling community worldwide. Let's work together!

Stirling engines prototype development and testing

Speed Control Mechanism of Stirling Engine. Towards Invention of the Mechanical Governor for Stirling Engine

Tatsuro Kitahara^{a,*}, Tomoaki Sato^b

a Department of Engineering, Shonan Institute of Technology, 1-1-25, Tsujido Nishikaigan, Fujisawa City, Kanagawa, Japan

b Department of Engineering, Kanagawa Institute of Technology, 1030 Shimohagino, Atsugi City, Kanagawa, Japan

Corresponding author: kitahara@md.shonan-it.ac.jp

Keywords: Governor, Speed control, Power output control, Engineering education

Abstract

This research aims to invent a mechanical governor for the Stirling Engine. From cost-effectiveness, safety, and educational application perspectives, we tried to develop a speed control mechanism that utilizes the basic engine operating principles without employing electrically controlled mechanisms such as a gear reducer or electrical generator. It is difficult for Stirling engines to perform rapid power output control, unlike the throttle of an internal combustion engine. Therefore, the operation often involves auxiliary control mechanisms such as variable-ratio gears or frictional resistance.

In this study, we have developed a speed control device that regulates the pressure of the engine's internal working gas. By branching off the connecting tube between the high-temperature and low-temperature cylinders and further linking a third control cylinder and piston, we devised a mechanism in which the stroke of the control piston could be adjusted and kept free. When the Stirling engine operates in this state, a portion of the working gas flows into the third cylinder during the heat exchange. As the control piston is free, it reciprocates synchronously with the operational cycle of the Stirling engine within its stroke range as desired. Increasing the stroke range lowers the output while reducing the stroke range can increase the output. We measured the rotation speed, internal pressure, and output of an α -type Stirling engine equipped with this control device. In addition, the correlation between changes in pressure and volume was examined based on the Schmidt analysis. We found the possibility that these research results could become the fundamental principle of the mechanical governor for the Stirling engine.

Power Output Control of Stirling Engine

One of the problems of Stirling engines is the power output control. Unlike the throttle of internal combustion engines, it is difficult for the Stirling engine to respond quickly and perform phase control well. It is also challenging to maintain a constant power output. The reason is that the Stirling engine utilizes the temperature differences between two chambers to create movement. However, changing the heat input takes time to

generate a temperature differential in the working gas, resulting in considerable time delays and challenging rapid output control. Thus, current Stirling engines often rely on auxiliary control mechanisms such as variable-ratio gears or frictional resistance.

There are several control systems for power regulation in the Stirling engine. The first example is utilizing the valves, where the working gas flow is regulated and moves between the hot and cold spaces. By restraining the volume flow of the connecting pipe between cylinders, gas friction increases, thereby reducing the power output. The small model engine based on this idea is commercially available. Its rotational speed varies from approximately 2000 rpm (maximum) to 300 rpm (minimum) by closing the valves. This structurally simple method is widely used but requires a delicate adjustment.

Another model of output control mechanism is the “Variable Phase Angle Stirling Engine” developed by Hirata et al. This mechanism controls output power by changing the volume per unit of time of the cylinders in an alpha-type Stirling engine. The phase angle differences can be varied even during Stirling engine operation by connecting the main shaft through a differential driven by bevel gears attached to each piston’s connecting rod. Hirata et al. reported successful experimental determination of the optimal output against variations in the heat source and the ability to adjust to any speed as desired. However, the controllable range was limited to a phase angle of 90 to 150 degrees, and the rotational speed varied from 750 to 1300 rpm. Additionally, it has been reported that this mechanism may not be suitable for high-output engines due to the mechanical losses.

There have been further attempts to control the temperature difference of the heat source. Katayama et al. [3] presented a device to control the engine’s internal temperature differences and power output by equipping a Stirling engine with a radiator to adjust the cooling medium’s temperature and switch the cooling path. This method utilizes the fundamental principles of Stirling engines and is considered an efficient control mechanism as it does not contribute to mechanical losses. However, there remains a challenge regarding response speed under control as temperature change requires a certain amount of time to affect the operation. To wit, various forms of output control for Stirling engines have been devised, each with its advantages and limitations.

Output Power Control by Variable Pressure of Working Gas

In this study, we developed a speed control device to control the pressure of the internal working gas of the engine (Figure 1, 2). A model Stirling engine was prepared, and a connecting pipe branching off between the hot-side and cool-side cylinders was set up. Then, we prepared the third cylinder and piston and connected them. In addition, the adjusting screw was equipped to control the stroke volume of this piston. The piston position was kept free, not fixed.

As a result, the stroke of the control piston also changes according to the increase and decrease in internal engine pressure. When the engine is operated by heating, some of the working gas flows into the additional control cylinder. The control piston opens in synchronization with the increase in internal pressure. Conversely, during heat exchange and pressure decrease, the control piston closes. Additionally, when the stroke of the control piston is fixed, the overall engine volume increases regardless of the internal engine pressure. This study conducted a comparative analysis of the free and fixed status of the control piston stroke.

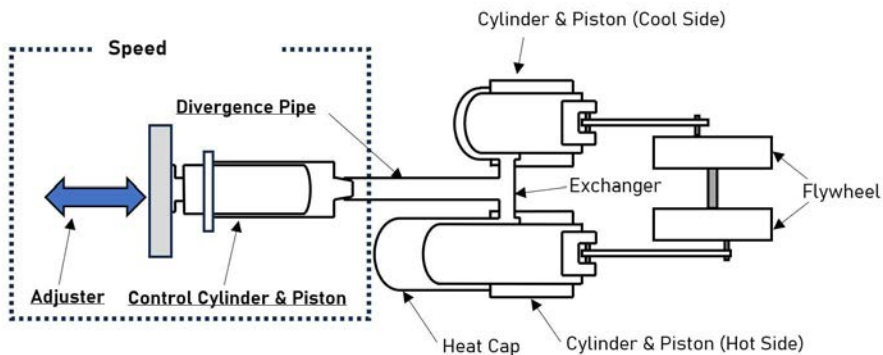


Figure 1. Speed Controllable α -Type Stirling Engine (Diagram).

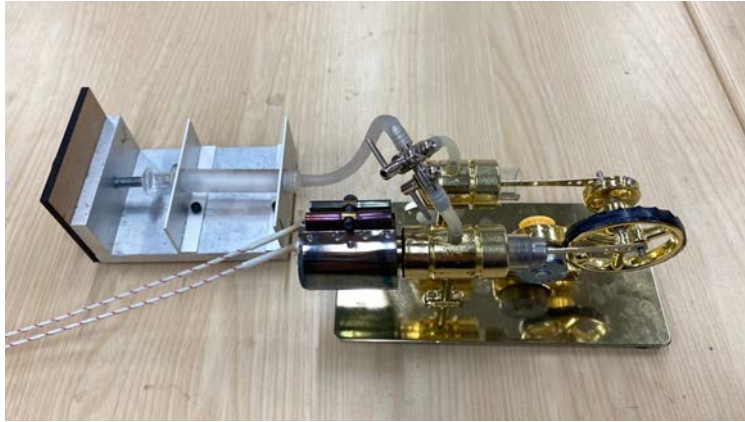


Figure 2. Speed Controllable α -Type Stirling Engine (Photo).

Preliminary Study Based on Schmidt Theory

We measured the Stirling engine equipped with this power output control mechanism. Initially, we equipped the small-sized α -Type Stirling Engine with control piston, and conducted simulation based on the Schmidt Theory. The results of this analysis would be used as the reference values and compared with data derived from subsequent experiments to verify the effectiveness of this control mechanism. Table 1 shows the details of the model engine used for measurements.

Table 1. Volume of Each Engine Component.

The cross-sectional area of the expansion piston (E_m)	124.69	(mm^2)
The cross-sectional area of the compression piston (C_m)	124.69	(mm^2)
Control sectional area of compression piston (A_m)	80.00	(mm^2)
Max. instantaneous volume of expansion space ($V_{E\text{max}}$)	1745.66	(mm^3)
Max. instantaneous volume of compression space ($V_{C\text{max}}$)	1745.66	(mm^3)
Max. instantaneous volume of compression space ($V_{A\text{max}}$) (Control piston stroke set as 10 mm)	800.77	(mm^3)
The stroke volume of the expansion piston (v_e)	1745.66	(mm^3)
Instantaneous volume of expansion space (V_E)	255.65	(mm^3)
The stroke volume of the compression piston (v_c)	1745.66	(mm^3)
Instantaneous volume of compression space (V_C)	255.65	(mm^3)

The stroke volume of the compression piston (v_a)	Depending on the control stroke setting	(mm^3)
The instantaneous volume of compression space (V_A)	Depending on the control stroke setting	(mm^3)
Volume of heat exchanger pipe (V_R)	259.00	(mm^3)
The instantaneous volume of the internal engine (V)	$1035.76 + V_A$	(mm^3)
Dead volume of expansion space (V_{de})	132.73	(mm^3)
The dead volume of compression space (V_{dc})	132.73	(mm^3)
Total dead volume	524.46	(mm^3)
The volume of the internal engine (V_{min})	1035.76	(mm^3)
Volume of internal engine (V_{max})	$3504.49 + V_A$	(mm^3)

Figures 3 and 4 illustrate the timing of pressure changes within the engine and the volume changes of each cylinder. In the figures, the stroke of the control piston is set to 8 mm. We prepared two different types of the control pistons; one is free, and the other is fixed. When the control piston is fixed, the total volume of the engine increases by the amount of control piston strokes (Figure 3). We set the phase angle difference between the heating and cooling pistons of the model Stirling engine to a typical angle of 90 degrees. The precise phase angle difference is hard to detect. Thus, we assumed that the volume of the control cylinder reaches its minimum when the sum of the volumes of the heating and cooling cylinders is maximum, and vice versa. We thought that the movement of the control piston would illustrate the sine wave (Figure 4).

We calculate the pressure using the Schmidt Theory and create P-V diagrams based on this cycle. These graphs are shown in Figures 5 and 6. Multiple graphs illustrate that the control piston's operating stroke increased in 2 mm increments. When the control piston is fixed, the engine volume expands, shifting the graphs to the right. Additionally, as the stroke of the control piston increases, a decrease in pressure is observed. When the control piston is free, the maximum volume of the internal engine remains constant, while only the minimum volume changes. This change causes a decrease in maximum pressure. It should be noted that fluid friction and volume expansion of the rubber tubes and branching joints connecting the cylinders are not considered in this measurement. Additionally, our calculation does not consider the volume and inertial force of the control piston nor the friction caused by the control piston and the cylinder.

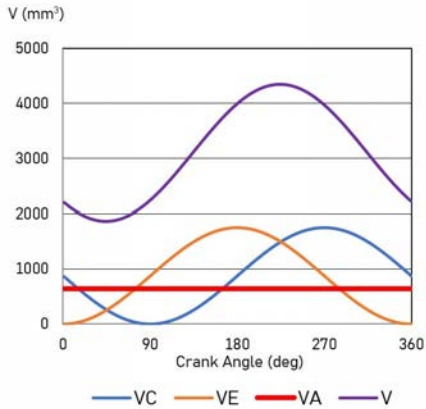


Figure 3. V-θ Diagram.

(The Control Piston in a Fixed State)

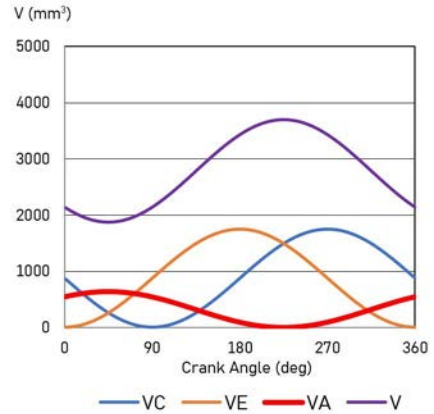


Figure 4. V-θ Diagram.

(The Control Piston in a Free State)

P (Pa)

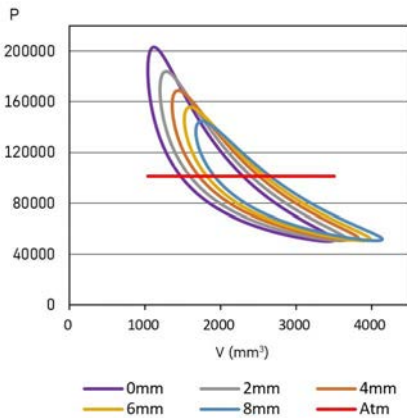


Figure 5. Shmidt Analysis P-V Diagram.

(The Control Piston in a Fixed State)

P (Pa)

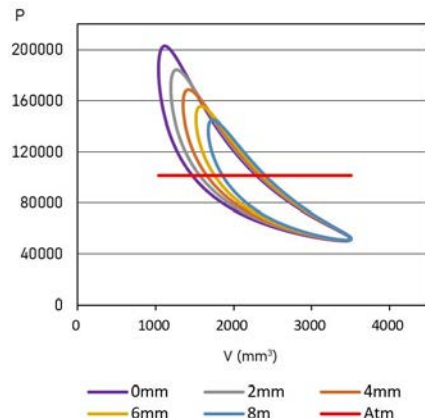


Figure 6. Shmidt Analysis P-V Diagram.

(The Control Piston in a Free State)

Measurement of Engine Power Output with Control Mechanism

Performance measurements were conducted on the model Stirling engine equipped with the control device by varying the stroke of the control piston. The parameters measured include the transition of rotational speed under no-load conditions, the output transition, and the internal pressure transition. A comparison was made between the fixed and free states of the control piston.

A cylindrical band heater (100V/100W) was attached to the engine's heating section. A transformer adjusted the input voltage to maintain a constant temperature of 400 °C in the heating section. The ambient temperature was maintained at 23 °C. Figure 7 illustrates the measurement method used.

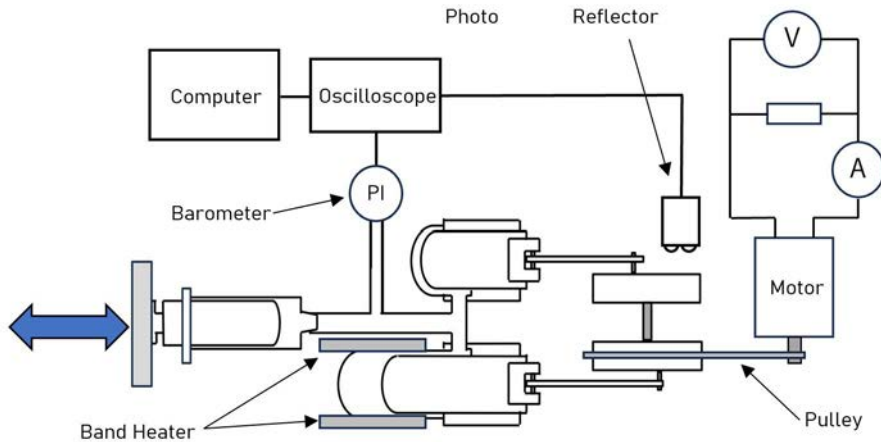


Figure 7. Illustration of the Measurement Process.

First, we measured the rotational speed and power output. Rotational speed was tested under no-load conditions by a non-contact tachometer after steady-state operation. For power output measurement, a mini generator motor was connected to the engine crankshaft via a pulley, and the generated power was calculated. The stroke of the control piston was increased in 0.25 mm increments, and values were measured at each point. The results are presented below (Figures 8 and 9).

When the stroke of the control piston was fixed, there was little change in rotational speed and power output, indicating a slight decrease in each value. When the control piston was kept free, on the other hand, the rotational speed varied from 1650 to 150 rpm, and it was possible to maintain any desired rotational speed. The rotational speed change was significant in the high to medium-speed range, with the rate decreasing as it entered the low-speed range. When the stroke of the control piston exceeded 10 mm, the operation became rapidly unstable in both free and fixed states, resulting in engine shutdown.

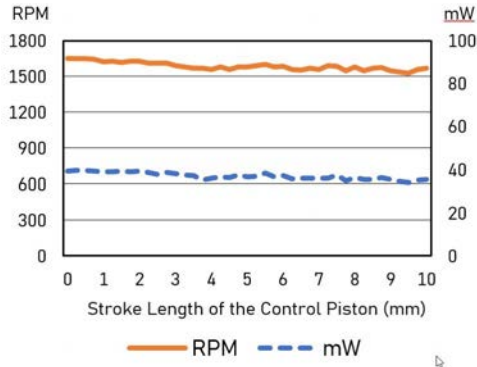


Figure 8. Power Output & Rotational Speed.
(The Control Piston in a Fixed State)

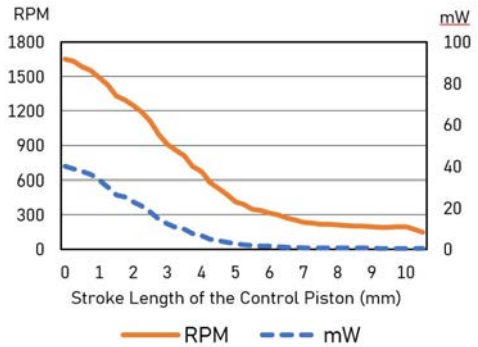


Figure 9. Power Output & Rotational Speed.
(The Control Piston in a Free State)

Measurement of the Pressure of the Internal Engine with Control Mechanism

The change in the internal pressure of the engine equipped with a control mechanism was measured. The connecting tube between the heating and cooling cylinders was branched with an air tube and connected to a barometer. Using a Bosch BME280 pressure sensor, numerical values were sampled at a rate of 3 msec by a data logger. The angle of the flywheel was set to 0 degrees when the heating side piston reached the top dead center. A white mark was placed at the 0-degree position, obtained by a photo reflector. Then, we checked one cycle of engine movement. Each stroke of the control piston was measured for 10 seconds, increasing in 2 mm increments. From the obtained data, ten cycles of noise-free values were randomly selected, and the P-V diagram was created from their average values. Graphs overlaying the change in control stroke and individual graphs are shown below. (Figures 10 and 11)

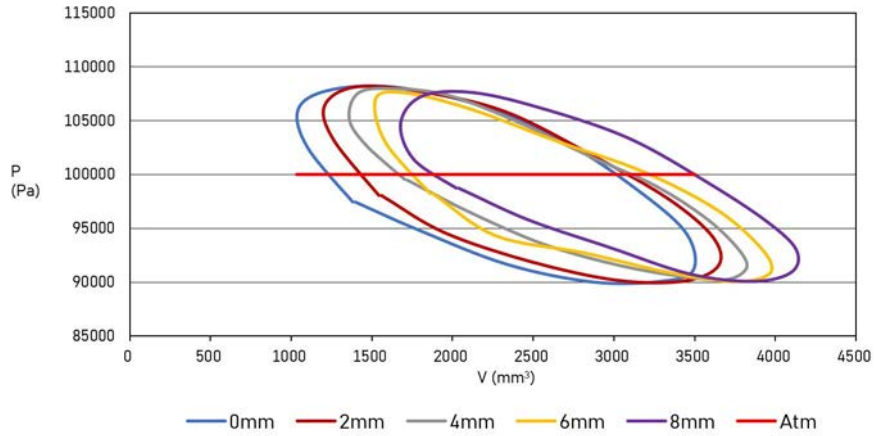


Figure 10. P-V Diagram (The Control Piston in a Fixed State).

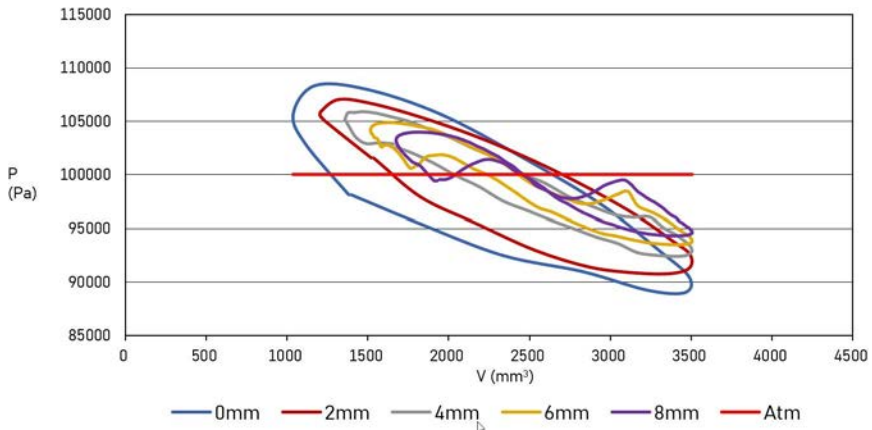


Figure 11. P-V Diagram (The Control Piston in a Free State).

Discussion and Challenges

Control Piston in Free State

The experiments show that the relationship between rotational speed and power output varies significantly depending on the stroke volume. Furthermore, the internal pressure

of the engine also changes with the phase fluctuation in the controlled space volume since the power output decreases along with rotational speed.

This change in the P-V diagram makes the graph's shape thinner with increased stroke volume, indicating a visible reduction in pressure difference. A remarkable point is a momentary increase or decrease in pressure just before the internal engine volume reaches its maximum or minimum. This differs significantly from the hypothetical graph based on the Schmidt cycle simulation.

From this cycle point, the pressure decreases before the internal engine volume becomes small and the internal pressure reaches its maximum. On the contrary, before the internal engine volume increases and the internal pressure reaches its minimum, there is an increase in pressure. These points probably indicate the moments when the control piston opens or closes. Therefore, we assume that the variation in the control piston stroke does not occur as the phase in Figure 4 (sine wave), but rather, it occurs suddenly at a particular phase angle, as shown in Figure 12. .

To sum up, the control piston in the free state lowers the maximum compression ratio of the engine before its reach and the minimum compression ratio before its reach, serving as a kind of governor function.

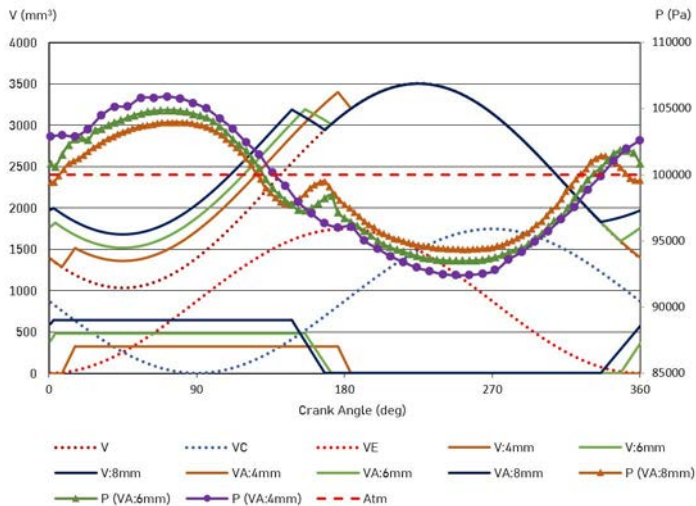


Figure 12. Engine Displacement V-θ Diagram (The Control Piston in a Free State).

Control Piston in Fixed State

When the stroke volume of the control piston was fixed, a slight decrease was observed in both rotational speed and output. However, there was no significant variation even with increased stroke volume. The engine suddenly stopped when it exceeded a specific stroke volume. The common understanding of Stirling engines is that the larger the dead volume, the lower the power output. However, from this experiment, the gradual expansion of the dead volume during operation did not lead to a significant decrease in power output. The P-V diagram also supports this.

Even when the control piston stroke was expanded to approximately 8 mm, no significant differences were observed in the shape or area of the cycle curve. We assumed the working gas did not move in and out to the dead volume generated by the control piston. The reason could be explained that the dead volume is dead-end, preventing the working gas from entering.

Thus, we can say that it is essential to synchronize the movement cycle of the internal working gas and the strokes of the control piston. However, it should be noted that the research finding was obtained by the preliminary experiments, which calls for further detailed data and analysis.

Conclusion and Future Applications

This study demonstrated that the engine output could be controlled with an extremely simple structure by connecting the control piston to the cylinder. Furthermore, the results of the experiments showed the potential utilization of this control mechanism as a governor for Stirling engines. The stroke volume requires manual adjustment at the current stage, making it somewhat of a semi-automatic governor. In the future, however, the fully automated speed control mechanism would provide Stirling engines to be applied in wide-ranging fields, such as automobiles, vessels, and electric generators, and possibly as engineering education materials. We would like to continue developing a fully automatic Stirling engine governor in the future.

References

- [1] Toda F. Development of Low Temperature Difference Stirling Engine. In: 6th International Stirling Engine Conference, 417-476 (1993).

- [2] Bengs Modellbau. Stirling engine Rainer with centrifugal governor material kit. <https://www.bengs-modellbau.com/Stirling-engine-Rainer-with-centrifugal-governor-materialkit/2280> (Accessed 29 March 2024)
- [3] Hirata K, Kawada M, Yokokawa Y, Yamashita I. Performance of a Variable Phase Angle Stirling Engine with Changing of Heat Input. In: 8th Stirling Cycle Symposium Proceedings, the Japan Society of Mechanical Engineers, 63-64 (2004).
- [4] Katayama M, Tatsuno M, Komori S. Power output control mechanism of Stirling engine (International Application Number: 2013506649). Toyota Motor Corporation. https://jglobal.jst.go.jp/en/detail?JGLOBAL_ID=201403015609411336
- [5] Okada K, Sugaya S. A Development of Stirling Engine Design Calculation Support Software. In: Annual Bulletin, Institute of Technologists, 15-22 (2015).
- [6] Partlow W. Power Control Systems in Beyond Discovery. <https://www.beyonddiscovery.org/stirling-engines/power-control-systems.html> (Accessed 29 March 2024)

Evaluation of Liquid-piston Stirling Engine integrated with Self-rectifying Impulse Turbine

J. Tomihira ^{a,*}, E. Shoji ^a, T. Biwa ^a, P. Murti ^b, M. Takao ^c, S. Okuhara ^d

a Department of Mechanical Systems Engineering, Tohoku University, 6-6, Aramaki, Aoba-ku, Sendai, 980-8579, Japan

b Department of Mechanical and Industrial Engineering, Faculty of Engineering, Universitas Gadjah Mada, Jl. Grafika No. 2, Yogyakarta 55281, Indonesia

c Department of Mechanical Engineering, National Institute of Technology, Matsue College, 14-4, Nishiikuma-cho, Matsue 690-8518, Japan

d Support Center for Practical Education, National Institute of Technology, Matsue College, 14-4, Nishiikuma-cho, Matsue 690-8518, Japan

Corresponding author: jidai.tomihira.p3@dc.tohoku.ac.jp

Keywords: Thermoacoustic engine, Liquid piston, Stirling engine, Self-rectifying turbine, Thermo-electric generator

Abstract

The liquid piston Stirling engine has a simple structure and highly available working fluids such as air and water. To convert the liquid piston Stirling engine into a generator using a self-rectifying impulse turbine, this study tested the power consumption by the turbine, which had a similar load characteristic to the orifice plate. From the experiments using orifice plates with various aperture ratios, the one with the aperture ratio of 0.4 maximized the power consumption by the orifice plate, suggesting that the equivalent turbine should be employed to maximize the input power to the turbine. Furthermore, the efficiency of converting thermal power to input power to the turbine under various conditions revealed that the efficiency reached a maximum of 7.7% when two orifices were placed in adjacent liquid columns and when four orifices were placed.

Introduction

A multi-cylinder type liquid piston Stirling engine is a kind of double-acting Stirling engines, which was introduced by C.D. West [1]. It is constructed of interconnected U-shaped pipes forming a ring structure. Even with a temperature difference of less than 60 K at both sides of the regenerator, the working fluids of air and water at ambient pressure oscillate spontaneously with the natural frequency of the engine. The simplicity of the engine structure and highly available materials make it cost effective for manufacturing and repairing.

Various studies about liquid piston Stirling engines have been reported. An equivalent dynamical model provided the natural frequencies and oscillation modes of the system

based on the pipe dimensions and thermal properties of the working fluids [2]. This model has demonstrated that the gas in the regenerator undergoes a thermoacoustic cycle similar to that executed in a Stirling engine, in line with the experimental observation of pressure and velocity oscillations of the working gas [3]. The numerical analysis using Design Environment Low-Amplitude Thermoacoustic Energy Conversion (DeltaEC) developed by Los Alamos laboratory [4] has reported that a maximum thermal efficiency can reach about 51% when the hot temperature is 1500 K [5]. Moreover, the application of a thermally driven refrigerator has been reported using a liquid piston Stirling engine [6, 7]. However, the application of an electrical generator has not been reported.

The objective of this study is to convert the liquid piston Stirling engine into an electrical generator using a self-rectifying impulse turbine, capable of rotating in one direction regardless of the flow direction in oscillating flow [8]. Our group has already succeeded in running the turbine by installing it in the liquid column of the engine. Besides, we found that the turbine reduced the oscillation amplitude of the liquid column, suggesting that the engine may cease oscillation in extreme cases. This result indicates that an optimum turbine characteristic should be clarified to improve the system efficiency. However, many design parameters of the turbine make it difficult to identify the optimum turbine design by experiment. In this study, we focus on how much power can be transferred to the turbine. For this purpose, orifice plates, having the load characteristics equivalent to the turbine [9, 10], were used in place of the turbine, to examine the power input to the turbine at a given temperature difference. The impact of the number of orifice plates and the orifice aperture ratio was evaluated by numerical calculation.

Experiment setup and method

Experiment setup

Fig. 1 illustrates a schematic of the engine used in the present study. The engine consists of four interconnected unit sections forming a ring structure. Each unit has a gas column and a liquid column constructed by cylindrical pipes with inner diameter of 41 mm. The working fluids are air and water at ambient pressure. The total length of the centerline of each unit is 3.0 m and the ratio of liquid column length to the unit length is 0.56. The cylindrical floats, made of ultra-high-molecular-weight polyethylene, is installed on both side of liquid columns to suppress the Rayleigh-Taylor instability at the free surface of

water [11]. The regenerator, a cylindrical catalyst support with numerous square pores measuring $0.68 \times 0.68 \text{ mm}^2$, is installed in each gas column. The hot heat exchanger (HHX) is a cylindrical block with 37 holes, each of which has an inner diameter of 3.5 mm and length of 70 mm. The HHX block is heated by an electrical heater. The ambient heat exchanger (AHX) has 37 tubes with an inner diameter of 3.5 mm, and length of 100 mm. These tubes are water cooled.

Fig. 2(a) depicts the schematic view of the self-rectifying impulse turbine. The rotor is forced to rotate in one direction regardless of the direction of water flow because of the impact of the guide vanes at the top and bottom of the rotor. Fig. 2(b) presents detailed information of the turbine. The turbine geometry is based on the suitable cascade geometry in Wave Power Generation field [8,13]. However, for manufacturing reasons, the numbers of rotor blades and guide vanes are each half of the preferred values.

Fig. 2(c) shows the schematic of the orifice plates, each having a thickness of 2 mm. A geometrical variable of orifice plates is aperture ratio m given the cross-sectional ratio of pipe A_{pipe} and orifice hole A_{ori} , equal to the ratio of squares of diameter of pipe d_{pipe} and that of hole d_{ori} .

$$m = \left(\frac{A_{\text{ori}}}{A_{\text{pipe}}} \right) = \left(\frac{d_{\text{ori}}}{d_{\text{pipe}}} \right)^2$$

In this experiment, we use orifice plates with the aperture ratio of $m = 0.1, 0.15, 0.2, 0.4, 0.6, 0.8$. Either the turbine or the orifice plate was installed in one of the units in the experiment.

Experiment method

During the engine operation, the HHX was heated by a heating wire, whereas the AHX was cooled by circulating water at a temperature of $23 \text{ }^\circ\text{C}$. These temperatures were monitored by thermocouples, the locations of which are shown in Fig. 1 (b). Once the hot side temperature reached a stable state under steady heat input, we measured the pressure at the top and bottom of the turbine or orifice plate using pressure transducers (PD104, JTEKT). The displacement of liquid columns was measured by a high-speed camera (Fastcam AX50, Photron) and the velocity of liquid columns was calculated from the temporal change of the displacement.

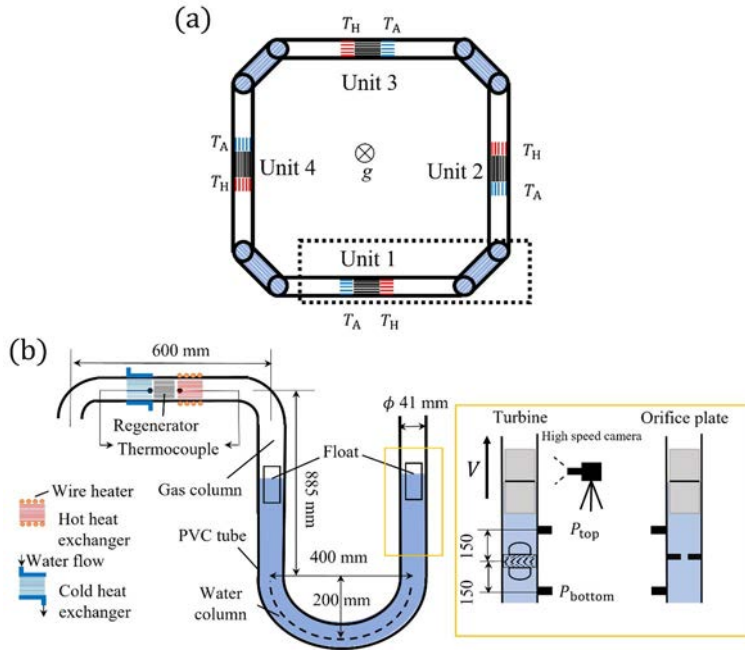


Figure 1. The schematic of liquid piston Stirling engine and the experimental method.

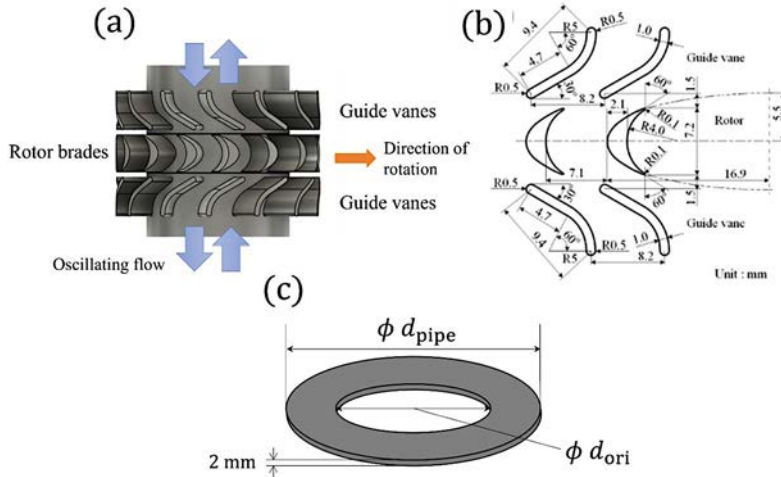


Figure 2. The schematic of the self-rectifying impulse turbine (a) and the details (b). The schematic of the orifice plate is shown in (c).

Result

Comparison of Orifice and Turbine

We present here the similarity in the load characteristics between the turbine and orifice plate. The impedance Z of the duct containing the self-rectifying turbine or orifice plate is given by

$$Z = -\frac{\Delta P}{V} \quad (1)$$

with

$$\Delta P = P_{\text{bottom}} - P_{\text{top}} \quad (2)$$

where V is the complex amplitude of liquid column volume velocity; P_{bottom} and P_{top} denote the complex amplitude of pressures at 0.15 m above and below the turbine, respectively. The real part of impedance means the resistance and the imaginary part means the product of inertance and angular frequency of the oscillation. The real part of impedance, $\text{Re}[Z]$, is shown against $|V|$ in Fig. 3. Dots are the experimental values and lines are the results of linear fitting. From Fig. 3, it is found that $\text{Re}[Z]$ increases proportionally with $|V|$ in both the cases with orifice plate and turbine. The slope of the line increases as the aperture ratio decreases, meaning the greater load to the engine. Furthermore, we can see that the orifice plates with $m = 0.15$ is equivalent to the present turbine.

Optimum orifice

The power consumed by the impedance Z can be evaluated from

$$\Delta W = \frac{1}{2} \frac{\text{Re}[Z]}{|V|} |V|^3. \quad (3)$$

Although this represents the power consumption in the case of the orifice plate, it corresponds to the power delivered from the engine to the turbine, which is used to derive the shaft power once the orifice plate is replaced with the turbine. Fig. 4 shows that the relation between ΔW and hot side temperature T_{H} . The markers depict the experimental results and the line in graph shows the results of DeltaEC calculation, where the orifice plate was modeled by a volume-velocity dependent resistance using

original RPN command, consistently with Fig. 3. In the results, the optimum aperture ratio of the orifice plate was found to be 0.4 when ΔW reached a maximum in the T_H region exceeding 110°C . The calculation results shows that the orifice plate with aperture ratio of 0.4 maximized ΔW for T_H greater than 140°C , which is similar to experimental results. Therefore, to maximize the input power to the turbine, one should choose the one equivalent to the orifice plate with $m = 0.4$.

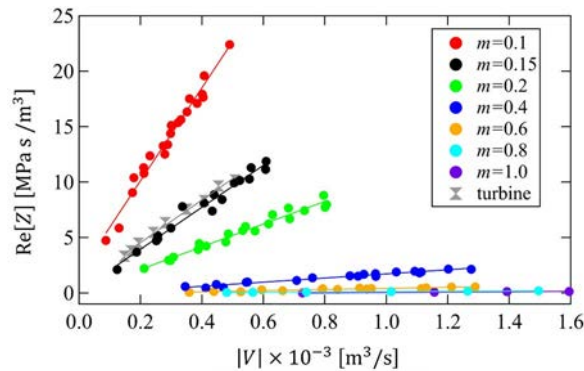


Figure 3. The load characteristic of the turbine and orifice plate.

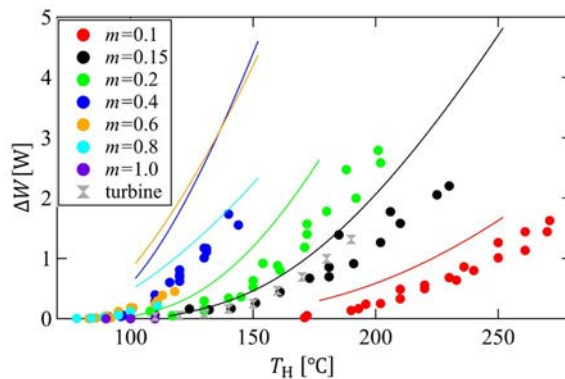


Figure 4. The relation between the power consumption at the orifice plate and hot side temperature.

Numerical calculation

Having confirmed the validity of DeltaEC, we numerically searched for optimal load under the conditions with various numbers of orifice plates and load characteristic of

orifice plate using DeltaEC. We calculated the total power consumption by the orifice plates and the efficiency, defined by the ratio relative to the thermal input power. The calculations were conducted for the geometries shown in Fig. 5, where the gray box represents the liquid column with the orifice plate.

Fig. 6 depicts (a) the total power consumption by the orifice plates and (b) the efficiency. Here the horizontal axis denotes the slope of the real part of impedance when it is plotted against the volume velocity as shown in Fig. 3. In the calculation, 500 K of hot side temperatures was assumed. The vertical dotted lines in Fig. 6 present the slope values of the representative orifice plates with $m = 0.4, 0.6$ and 0.8 . Fig. 6 (a) shows the total power consumption reached 20 W in type 2 and 5 when the aperture ratio of orifice is close to 0.6. Fig. 6 (b) shows the efficiency reached 7.7 % in type 2 and 5 when $m = 0.4$ and 0.6. Therefore, type 2 or 5 should be employed for maximizing the output power and efficiency.

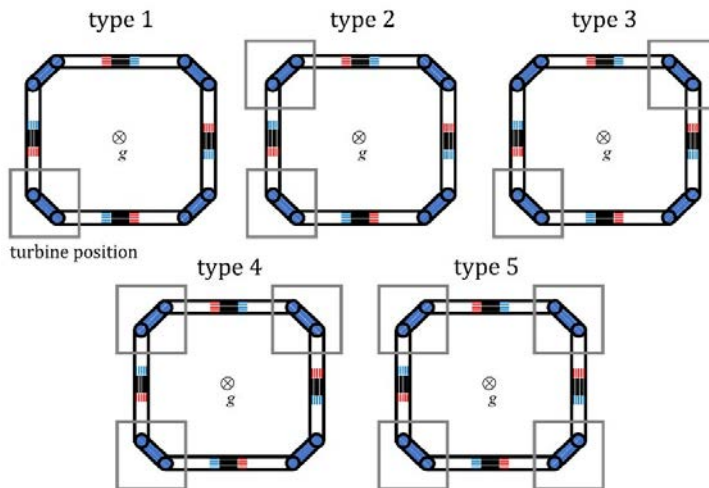


Figure 5. Types 1–5 of integrated turbine and engine system. The gray box represents the orifice plate position.

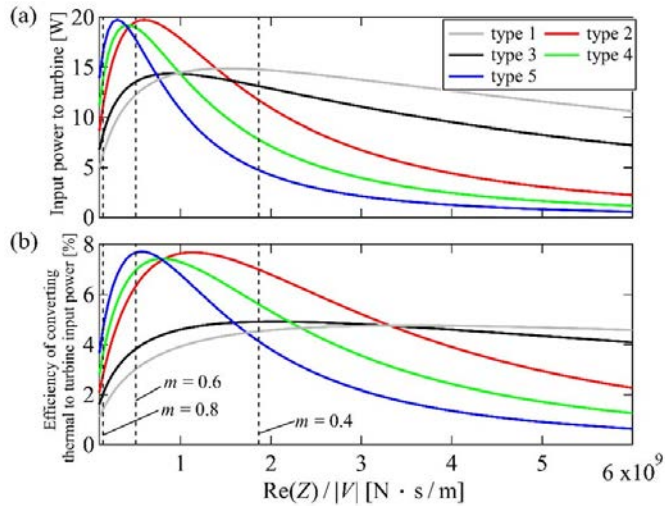


Figure 6. The input power to turbine and the efficiency of converting thermal to turbine input power when $T_H=500$ K.

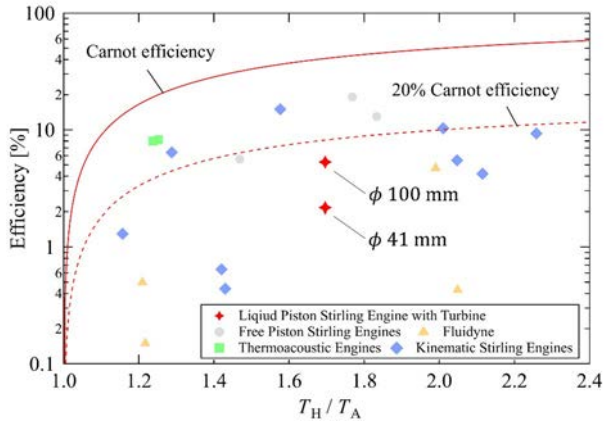


Figure 7. The thermal efficiency of various Stirling-cycle devices [12].

Discussion

We compare the thermal-electric efficiency of the Stirling-cycle devices such as free piston Stirling engines, Fluidyne, thermoacoustic engines, and kinematic Stirling engines [12]. Fig. 7 illustrates the thermal-electric efficiency of the relevant devices and the liquid

piston Stirling engine used in this study. Assuming that the efficiency of the turbine converting input power to shaft power is 35% [13], and efficiency of the alternator is 80%, we determined the thermal-electric efficiency when hot side temperature is 500 K. For simple performance improvement, the calculations were performed with an enlarged diameter. The thermo-electric efficiency is 2.2% when the pipe diameter is ϕ 41 mm and efficiency is 5.3% when the pipe diameter is ϕ 100 mm. The curve represents the Carnot efficiency with heat source temperatures of 500 K and 300 K. Because some of the engines operate with different ambient temperatures (288 K – 313 K), the curve serves as a rough reference for comparing the engines operating with various hot side temperatures. The dotted line means the 20 % of the Carnot efficiency determined in the same manner. Although the present liquid piston Stirling engine with the turbine has relatively low efficiency, it is important to note that the engine operates with air and water at ambient pressure. The optimization of liquid piston Stirling engine in terms of engine geometry and working fluid is planned to improve efficiency.

Conclusion

The goal of this research is to convert the liquid piston Stirling engine into an electrical generator using a self-rectifying impulse turbine. As the initial phase, the turbine load was evaluated by the impedance measurement, which was found to have the same volume velocity dependence as the orifice plate. The power consumption by the orifice plates with various aperture ratios was experimentally evaluated to identify the optimum load to maximize the input energy to the turbine at a given temperature difference.

DeltaEC was used to predict the losses and efficiency when the orifices were installed in multiple liquid columns. The results showed that the power and efficiency could be increased to 20 W and 7.7% when two turbines were installed next to each other and when four turbines were installed. At this time, the turbine loads were equivalent to orifice plates with aperture ratios of between 0.4 and 0.6.

Assuming that the efficiency of converting turbine input power to shaft power is 35%, and the efficiency of a typical generator is 80%, we find the thermal-electric efficiency is 2.2% with the pipe diameter ϕ 41 mm and the efficiency is 5.3% with the pipe diameter ϕ 100 mm. We intend to investigate the efficiency experimentally in future studies.

References

- [1] C. D. West, *Liquid Piston Stirling Engines*. New York: Van Nostrand Reinhold Company, 1983.
- [2] H. Hyodo, S. Tamura, and T. Biwa., 'A looped-tube traveling-wave engine with liquid pistons', *Journal of Applied Physics*, 122(11), 114902, 2017.
- [3] S. Tamura, H. Hyodo, and T. Biwa., 'Experimental and numerical analysis of a liquid-piston Stirling engine with multiple unit sections', *Japanese Journal of Applied Physics*, 58(1), 017001, 2019.
- [4] John P. Clark, William C. Ward, and Gregory W. Swift, 'Design environment for low-amplitude thermoacoustic energy conversion (DeltaEC)', *Journal of the Acoustic Society of America*, 122, 3014, 2007.
- [5] S. Zhang, E. Luo, 'The Thermodynamic Performance of a Double-Acting Traveling-Wave Thermoacoustic Engine with Liquid-Water Piston', *International Journal of Green Energy*, 12(3), 198–206, 2015.
- [6] P. Murti, E. Shoji, and T. Biwa, 'Analysis of multi-cylinder type liquid piston Stirling cooler', *Applied Thermal Engineering*, 219, 119403, 2023.
- [7] L. Xiao, J. Xu, K. Luo, G. Chen, and E. Luo, 'Numerical study of a heat-driven thermoacoustic refrigerator based on a time-domain lumped acoustic–electrical analogy model', *Energy Conversion and Management*, 268(10), 115982, 2022.
- [8] M. Takao, S. Fukuma, S. Okuhara, M. M. A. Alam, and Y. Kinoue, 'A comparative study of bi-directional airflow turbines', *International Journal of Fluid Machinery and Systems*, 12(3), 228–234, 2019.
- [9] J. C. C. Portillo, J. C. C. Henriques, L. M. C. Gato, and A. F. O. Falcão, 'Model tests on a floating coaxial-duct OWC wave energy converter with focus on the spring-like air compressibility effect', *Energy*, 263, 125549, 2023.
- [10] A. F. O. Falcão and J. C. C. Henriques, 'Model-prototype similarity of oscillating-water-column wave energy converters', *International Journal of Marine Energy*, 6, 18–34, 2014.
- [11] P. Murti, H. Hyodo, and T. Biwa, 'Suppression of liquid surface instability induced by finite-amplitude oscillation in liquid piston Stirling engine', *Journal of Applied Physics*, 127(15), 154901, 2020.

- [12] K. Wang, S. R. Sanders, S. Dubey, F. H. Choo, and F. Duan, 'Stirling cycle engines for recovering low and moderate temperature heat: A review', *Renewable and Sustainable Energy Reviews*, 62, 89–108, 2016.
- [13] T. Setoguchi, M. Takao, S. Santhakumar, and K. Kaneko, 'Study of an impulse turbine for wave power conversion: Effects of Reynolds number and hub-to-tip ratio on performance', *Journal of Offshore Mechanics and Arctic Engineering*, 126(2), 137–140, 2004.

Design Methodology for a Looped-Tube Thermoacoustic Engine Incorporating a Flywheel

Keita Tetsuka^{a,*}, Eita Shoji^a, and Tetsushi Biwa^a

a Department of Mechanical Systems Engineering, Tohoku University Aramaki, Aoba-ku, Sendai, 980-8579, Japan

*Corresponding author: tetsuka.keita.r7@dc.tohoku.ac.jp

Keywords: Thermoacoustic engines, Acoustic impedance, Equivalent circuit model

Abstract

We report a design methodology of a thermoacoustic looped-tube engine having a piston-crank-flywheel assembly by using the analogy between acoustic and electrical systems. Through the analysis of circuit equations, we derived the acoustic impedance of the looped tube engine, which is proportional to the output power of the engine. It was found from the analysis that the volume of the main tube, along with the volume ratio of the thermal buffer tube and main tube, and the volume ratio of the branch tube and main tube, were the crucial parameters influencing the impedance. This finding was verified from the experiments conducted on looped-tube engines with four different parameter sets. The experimental results supported the effectiveness of our design methodology.

Introduction

Stirling engines inherently have high thermal efficiency, due to their operating principle based on a reversible thermodynamic cycle. Simplifying the mechanical structure of Stirling engines has been a significant goal for many years to broaden their application fields. The development of free-piston Stirling engines demonstrated a potential to remove the link mechanism, which was previously considered essential in traditional kinematic Stirling engines. Another example is a traveling-wave thermoacoustic engine, which utilizes a self-sustained acoustical traveling wave that is thermally induced in a looped tube [1]. In that engine, the acoustic oscillations of the working gas execute the Stirling thermodynamic cycle [2] and thereby replace a solid piston in a free-piston Stirling engine. Indeed, Backhaus et al. attached a branch resonator to the looped tube engine and constructed the acoustical counterpart of the mechanical Stirling engine, which achieved a thermal efficiency of 30% [3], corresponding to 42% of the Carnot efficiency. Recently, a looped-tube engine was demonstrated to operate with a piston-crank-

flywheel assembly [4]. While this engine can be classified as a kinematic Stirling engine, it notably lacks the displacer piston. Unlike thermoacoustic engines that integrate linear alternators as electro-acoustic transducers, this engine enables the use of conventional rotary generators to produce electricity from shaft power. This feature may open up new application fields for Stirling engine technology.

This study aims to show the methodology to develop the looped-tube engine with a flywheel, using a simplified equivalent circuit model based on the analogy between acoustic and electrical systems. In this model, the pressure and velocity of the working gas are assumed to be harmonic oscillations at a specified frequency. The frequency is subsequently determined through the energy balance between the power supply from the engine loop and the energy loss in the piston-flywheel system. Crucial design parameters of the looped-tube engine are deduced from the acoustic impedance, contributing to the improvement of power output to the piston.

Equivalent Circuit Model of a Looped-Tube Engine

Figure 1(a) shows a schematic illustration of the looped-tube thermoacoustic engine incorporating a flywheel. The working gas of the engine is air at ambient temperature and pressure, whereas other gases such as pressurized helium gas can be assumed. The engine consists of two subsystems: an engine subsystem and a load subsystem. The engine subsystem is composed of the feedback tube, main tube, heat exchangers, regenerator, thermal buffer tube, and branch tube. Due to the low oscillation frequency of the engine [4], the acoustic wavelength, estimated from the sound speed and oscillation frequency of the working gas, is much longer than the loop length. Consequently, we can assume a lumped parameter circuit, which simplifies the analysis of the engine subsystem.

Figure 1(b) shows an equivalent circuit model of the engine subsystem. In this model, the acoustic pressure and volume velocity correspond to voltage and current, respectively. The feedback tube is represented by an impedance Z_1 , while the main tube, thermal buffer tube, and branch tube are depicted by an admittance Y_j , where $j = 1, 2,$ and 3 denote the main tube, thermal buffer tube, and branch tube, respectively. Additionally, the regenerator is represented by a resistance R_r and a current source. Whereas the resistance accounts for the viscous interaction between the gas and the regenerator flow channel walls, the current source represents the impact of the temperature difference

at the ends of the regenerator, where the volume velocity is amplified by a factor of temperature ratio $\tau=T_H/T_C$.

The impedance Z_L and admittance Y_j are expressed as

$$Z_L = i\omega L, Y_j = i\omega C_j \quad (1)$$

where i represents the imaginary unit, and ω represents the angular frequency of the gas oscillation in the loop. Inertance L , compliance C_j and resistance R_r are circuit constants reflecting the physical properties of the working gas and size of the tube sections. From the results of the thermoacoustic theory, L, C_j, R_r are expressed as

$$L = \frac{\rho_m l_L}{S_L}, C_j = \frac{S_j l_j}{\gamma P_m}, R_r = \frac{\rho_m l_r}{S_r} \frac{4}{\tau_v} \quad (2)$$

where ρ_m is the mean density of the working gas, l_L is the length and S_L is the cross-sectional area of the feedback tube, S_j is the cross-sectional area, l_j is the length of the main tube, thermal buffer tube and branch tube, γ is the specific heat ratio and P_m is the mean pressure of the working gas. l_r is the length, S_r is the flow channel cross-section area of the regenerator and τ_v is the viscous relaxation time of the working gas at the regenerator.

The acoustic power emitted from the loop W_{loop} is expressed by using the real part of the impedance Z as

$$W_{loop} = \frac{1}{2} \text{Re}[Z] |U|^2. \quad (3)$$

The flywheel rotates at the frequency when W_{loop} coincides with the power dissipation in the load subsystem W_{loss} consisting of the piston and flywheel. As W_{loss} increases with the frequency, the engine needs the greater W_{loop} in the higher frequencies. Therefore, we specifically consider the impedance Z in section 3 to ascertain the engine potential.

Circuit Equations

Using pressures P, P_C and volume velocities U, U_L, U_R shown in Figure 1(b), circuit equations can be written as

$$\begin{cases} Z_L U_L + R_r U_R = 0 \\ P - P_C = Z_L U_L \\ \tau U_R - (Y_2 + Y_3)P = U + U_L \\ U_L - U_R = Y_1 P_C \end{cases} \quad (4)$$

Equations (4) can be solved analytically to obtain the impedance Z at the connecting point of two subsystems:

$$Z = \frac{1}{Y} = \frac{1}{A\omega C_1 - i\{B + (C_2 + C_3)/C_1\}} \quad (5)$$

where A and B are constants defined by

$$A = (\tau - 1) \frac{a}{1 + a^2}, \quad (6)$$

$$B = (\tau - 1) \frac{a^2}{1 + a^2} + 1, \quad (7)$$

$$a = \frac{\omega L}{R_r}. \quad (8)$$

From equation (5), $\text{Re}[Z]$ is expressed as

$$\text{Re}[Z] = \frac{A}{\omega C_1 A^2 + \{B + (C_2 + C_3)/C_1\}^2}. \quad (9)$$

Compliances C_1, C_2, C_3 are proportional to the volume of the main tube, thermal buffer tube and branch tube respectively. Hence, W_{loop} increases by making C_1 and $(C_2 + C_3)/C_1$ small. In the following section, we report the experimental result when C_1 and $(C_2 + C_3)/C_1$ are varied.

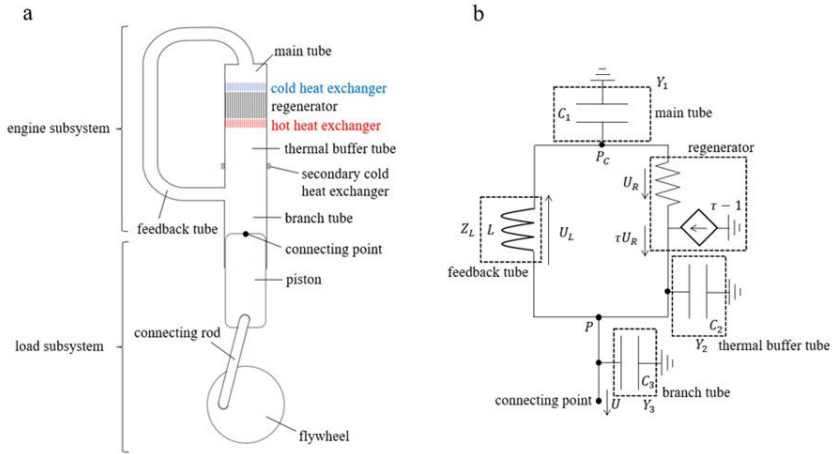


Figure 1. Schematic of (a) the looped-tube thermoacoustic engine incorporating a flywheel, (b) equivalent circuit model of the engine subsystem.

Experiment

We constructed Type 1-4 looped-tube engines with different lengths of the main tubes, the thermal buffer tubes, and the branch tubes, but with the same tube diameters (20 mm). The length of each component is shown in Table 1. For all types, the same regenerator and heat exchangers were used. The feedback tube length was kept at around 420 mm but was changed in response to the lengths of the main tube, thermal buffer tube, and branch tube. The tube diameter of the feedback was kept at 6 mm.

The 20-mm long regenerator was made by stacking stainless steel mesh screens (#40, wire diameter was 0.18 mm). The heat exchangers were parallel plates with a spacing of 1 mm, and the plate thickness was 0.5 mm. The length of the cold heat exchanger was 10 mm, and the hot heat exchanger was 15 mm. The cold heat exchanger was cooled by circulating water at room temperature. The hot heat exchanger was heated by applying a DC electrical current to a heater wire wound around the heat exchanger. A pair of sheathed thermocouples were placed on the tube axis of the regenerator and at the boundary with the heat exchangers, and the temperature difference between the two ends of the regenerator was monitored by a data logger.

The working gas pressure was measured with a pressure transducer (DD104, JTEKT) attached to the branch tube. The pressure signal was amplified by a DC amplifier (AA6210,

JTEKT, gain 1000). The analog voltage of the pressure was sampled by a multi-channel AD converter (DS-3000, Ono Sokki). The measurements were conducted when the engine was in the steady rotation state that was achieved after an external excitation was applied by hand.

Table 1. Lengths of each component of Type 1-4 engines.

	Type 1	Type 2	Type 3	Type 4
feedback tube	437	417	422	402
main tube	50	30	50	30
regenerator length (mm)	20	20	20	20
thermal buffer tube	105	105	90	90
branch tube	90	90	15	15

Results and discussion

The rotational frequency of the flywheel was determined from the frequency of the measured pressure of the working gas. Figure 2 shows a relation of the rotational frequency of the flywheel f and the temperature difference between the ends of the regenerator ΔT when the crank radius was set to $r=10$ mm. The curves were predicted from the energy balance between W_{loop} and W_{loss} , where W_{loss} was determined experimentally in our past study [5]. From the experiment, we find that Type 3 engine has the highest rotational frequency $f = 18.6$ Hz at $\Delta T = 280.9$ K. The same tendency was obtained also by the energy balance analysis. Although there is a quantitative difference between the predicted curves and experimental points, the experimental result supports the equivalent circuit model. Optimization based on this approach will lead to the thermoacoustic engine with flywheel with higher performance.

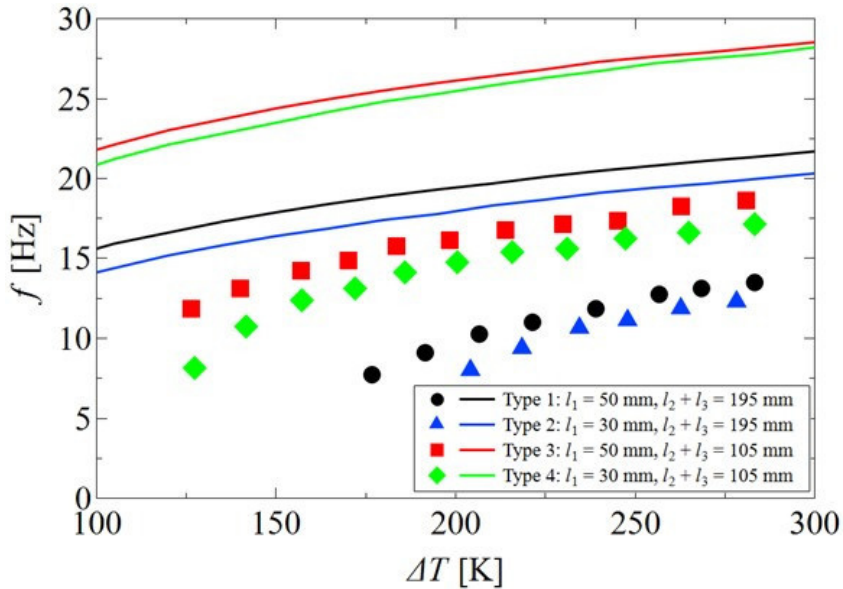


Figure 2. A relation of the rotational frequency of the flywheel f and the temperature difference between the two ends of the regenerator ΔT . The crank radius was set to $r = 10$ mm.

Summary

We presented the design methodology of the loop-tube engine from the equivalent circuit model of looped-tube engine. From the circuit equations, we derived the analytical expression for the acoustic impedance of the looped tube engine and found that the volume of the main tube, as well as the volume ratio of the thermal buffer tube and main tube, and the volume ratio of the branch tube and main tube, served as the important parameters for the output power of the looped-tube engine. We constructed four types of engines with different geometrical parameters and tested them through the relation between the rotation frequency and the temperature difference. The experimental results showed that T engine with a 50-mm main tube, 105-mm thermal buffer tube and branch tube had the best performance, consistent with the analysis.

Reference

- [1] Ceperley, P. H. A pistonless Stirling engine — The traveling wave heat engine. *J Acoust Soc Am* 66, 1508-1513 (1979).

- [2] Yazaki, T., Iwata, A., Maekawa, T. & Tominaga, A. Traveling wave thermoacoustic engine in a looped tube. *Phys Rev Lett* 81, 3128-3131 (1998).
- [3] Backhaus, S. & Swift, G. W. A thermoacoustic-Stirling heat engine: Detailed study. *J Acoust Soc Am* 107, 3148-3166 (2000).
- [4] Biwa, T., Watanabe, T. & Penelet, G. Flywheel-based traveling-wave thermoacoustic engine. *Appl Phys Lett* 117, 243902 (2020).
- [5] Watanabe, T., Shoji, E., Biwa, T. & Penelet, G. Rotational Dynamics of a Looped-Tube Thermoacoustic Engine with a Flywheel. *Phys Rev Appl* 18, 044079 (2022).

Development and Testing of a Free Liquid Piston Ericsson Engine

R. Chouder^a, P. Stouffs^{a,*}

a Université de Pau et des Pays de l'Adour, E2S UPPA, LaTEP, Pau, France

*Corresponding author: pascal.stouffs@univ-pau.fr

Keywords: Free piston engine, Ericsson engine, Liquid piston, Experimental results

Abstract

The family of hot air engines has the following characteristics: separate reciprocating compression and expansion cylinders, external heat supply, regenerator or heat recovery exchanger, monophasic gaseous working fluid. This family of thermal engines is proving to be a relevant technological solution for the conversion of thermal energy such as solar energy, the energy recovery of hot gaseous effluents or the combustion of biomass, in order to produce low power mechanical or electrical energy. The hot air engines family is subdivided into two sub-families: Stirling engines, which have no valves, and Ericsson engines, which have valves around the cylinders. These valves add complexity to the ingenious design simplicity of the Stirling engine. But they also provide a number of advantages. These include the fact that the heat exchangers are not dead volumes and can therefore be sized solely on heat transfer considerations, while the designer of a Stirling engine is always faced with the difficult compromise between maximizing heat exchange surfaces and minimizing dead volumes.

Liquid piston machines are particularly interesting because they ensure a perfect seal between the piston and the cylinder, while drastically reducing frictional forces. In addition, they can considerably improve heat transfer with the working fluid, for example to approach isothermal compression.

Free piston engines do not require a crank-connecting rod arrangement to transform reciprocating motion into rotary motion. Mechanical losses are therefore lower and the cost of the engine is reduced. Free piston engines are often coupled with linear generators in order to extract the useful energy produced. One of the great difficulties of free piston engines is to ensure stable and regular periodic movement.

In this paper, a totally new engine configuration combining the advantages of Ericsson engines, liquid piston machines and free piston engines is studied. Dynamic simulation results of this engine have shown that it is possible to design a free liquid piston Ericsson engine (FLPEE) which, combined with a judicious choice of operational parameters, allows stable operation with interesting energy performance. In particular, the FLPEE has a much better energy performance than the Fluidyne, which is the most similar configuration.

An experimental bench was developed to validate the theoretical results. This bench is described and the first tests results are presented. These results confirm what the theoretical modelling had predicted, namely that it is possible to obtain a set of values of the operational parameters of the system leading to a stable operation of the free-piston system..

Introduction

There is a significant need for low-power energy systems (a few hundred watts to a few dozen kilowatts) that can efficiently convert heat at medium temperature (200 °C...400 °C) into electricity. Power plants based on turbomachinery (Steam Rankine cycles, Organic Rankine Cycles, Gas Turbines with hot source heat exchanger) are better suited for much higher powers. For low-power thermal energy conversion systems, power plants based on positive displacement machines are more appropriate. Among volumetric machines, reciprocating piston-cylinder machines are still proving very effective. These power plants can use either a two-phase working fluid (Steam engines) or a monophasic working fluid (Hot Air engines). The family of Hot Air engines [1] has the following characteristics: separate reciprocating compression and expansion cylinders, external heat supply, regenerator or heat recovery exchanger, monophasic gaseous working fluid [2]. This family of thermal engines is proving to be a relevant technological solution for the conversion of low-power thermal energy such as solar energy, energy recovery of hot gaseous effluents or the combustion of biomass, in order to produce mechanical or electrical energy. The hot air engines family is subdivided into two sub-families: Stirling engines, invented in 1816, which have no valves, and Ericsson engines, invented in 1833, which have valves around the cylinders (Figure 1). Each sub-family has its own advantages and disadvantages. In this paper, the intellectual approach that led to the development of a Free Liquid Piston Ericsson Engine concept is detailed and some preliminary experimental results are presented.

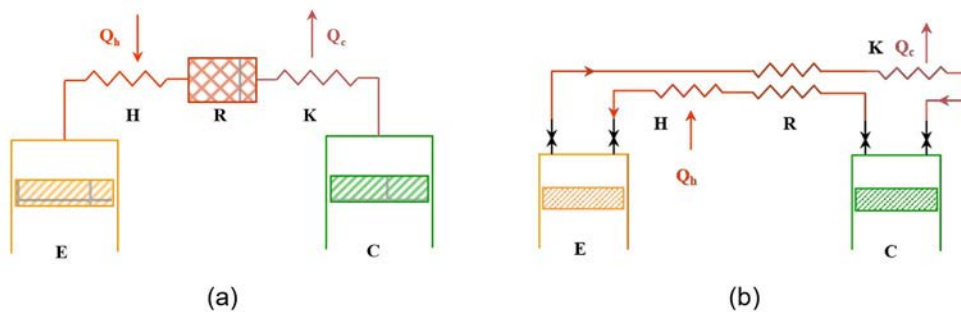


Figure 1. Schematic diagram of a Stirling engine (a) and an Ericsson engine (b).

The design handicap of Stirling engines

Both types of Hot Air Engines have known commercial success during the XIXth century [3], but, since the beginning of the XXth century, they have been discarded and replaced by internal combustion engines or electric motors. Since the pioneer work of the Philips Company, around the Second World War, the attention has been drawn again on Stirling engines [4] and lots of research and developments have been carried out.

These works have rapidly led to very nice and efficient engines designed for high temperature hot sources like fossil fuel combustion or concentrated solar energy [5]. On the other hand, very interesting low temperature differential engines have also been studied and designed [6], but these engines are not intended for useful power production.

Not many Stirling engines have been developed for efficient thermal energy conversion in the range of intermediate hot source temperature (200 °C... 400 °C). A ST05G Viebach Stirling engine [7] has been tested in our Lab [8]. It is a quite simple and interesting gamma-type engine with air as the working fluid. The maximum pressure is 1 MPa. The cylinder has a bore of 80 mm and the working piston has a stroke of 75 mm. The rated speed is 600 rpm. This engine can supply mechanical shaft power of 500 W. Instantaneous temperature measurements have been realized at the heater-regenerator interface and at the regenerator-cooler interface of the engine (Figure 2).

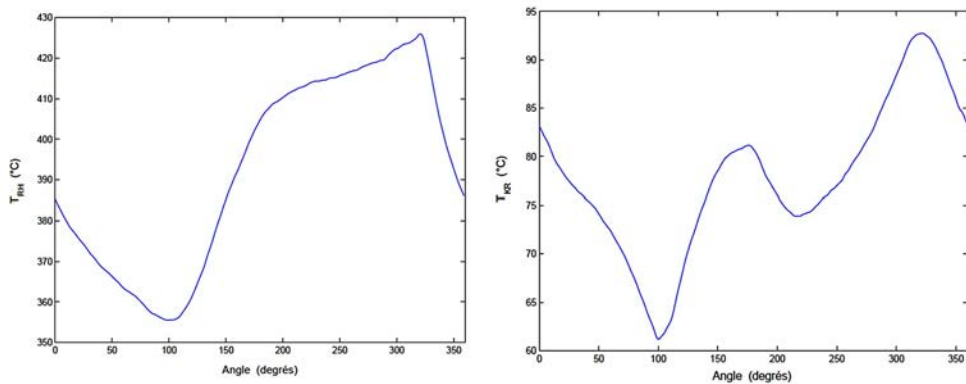


Figure 2. Instantaneous temperature at the heater-regenerator (left) and regenerator-cooler (right) interface of a ST05G Stirling engine.

Figure 2 shows that the instantaneous temperature of the working fluid at each end of the regenerator is far to be constant as assumed by the usual simple Stirling engine models. Temperature variations of around 70 °C at the hot end and 30 °C at the cold end of the regenerator are observed. But most of all, Figure 2 highlights that the average temperature of the working fluid at the hot end of the regenerator is lower than 400 °C whereas the wall temperature of the heater is higher than 550 °C. In the same way, the average temperature of the working fluid at the cold end of the regenerator is about 75 °C whereas the temperature of the cooling water in the cooler is around 15 °C. So very high irreversibilities between the heat sources and the working fluid severely degrades the performance of the tested Stirling engine, due to the low heat transfer coefficient between the working fluid and the wall of the heater and cooler, and the limited heat transfer area. In the case of high temperature differential Stirling engines, these irreversibilities can be accepted. In the case of medium temperature Stirling engines, they are hard to tolerate. Are they avoidable? Actually, not really. Indeed, the designer of a Stirling engine is always faced with the difficult compromise between maximizing heat exchange surfaces and minimizing dead volumes.

The advantages of Ericsson engines

The Ericsson engine can be carried out either by a closed cycle (Fig. 1, b) with a cooler (in this case the system can run at high pressure and can use working fluids such as helium or hydrogen), or by an open cycle with or without heat recovery exchanger. In this case, the working fluid is air that can be expanded down to the atmospheric pressure.

Unfairly, Ericsson engines have not enjoyed the same revival as Stirling engines. Up to now, not many studies are dedicated to Ericsson engines. Yet they have many advantages too.

The major advantage of Ericsson engine is that compression and expansion enclosures are isolated from heat exchangers when working; this means that the heat exchangers volume is not to be considered as dead (unswept) volume which is detrimental to specific power and, to a lesser degree, efficiency; there is no compromise to find between (dead) heat exchangers volume to minimize and heat transfer exchangers area to maximize; this balance is difficult to obtain in the case of the Stirling engine design.

Ericsson engines have other advantages:

- The fluid circuit is a loop; the flow is one-directional whereas it is oscillating in the Stirling engine; the thermodynamic behaviour of one-directional flow can be modelled accurately; the internal heat exchanger can be a simple counter flow heat exchanger inducing lower pressure losses than the equivalent regenerator in the Stirling configuration.
- The loop circuit of the Ericsson configuration suppresses the aberration of the Stirling configuration: in the Stirling configuration (Fig. 1, a) the working fluid flows through both the heater and the cooler in each fluid flow direction, whereas it would be preferable that the fluid bypasses the heater H when flowing from the expansion space E to the compression space C and conversely, it would be preferable that it bypasses the cooler K when flowing from the compression space C to the expansion space E.
- The kind of pistons motion used for the kinematic mechanism has no influence on the engine performance in the Ericsson engine, whereas it is of significant importance in Stirling engine; simple and efficient mechanism can thus be used for Ericsson engine.
- The valves of Ericsson engines could be used to control the engine.

On the other hand, these advantages are offset by a number of disadvantages, due to the presence of the valves:

- The valves of Ericsson engines lead to supplementary pressure losses and mechanical energy consumption with reference to the equivalent Stirling engine.
- The valves could be noisy.
- The valves could reduce the reliability of the Ericsson engine compared to the Stirling engine.
- The valves increase the engine complexity.

Efficient, reliable and silent valves have been designed in the field of internal combustion engines. However, it should be noted that in the case of a 4-stroke internal combustion engines, a valve has to be opened during a full stroke from one dead center to the other. In the case of an Ericsson engine, the exhaust valve of the compression cylinder and the inlet valve of the expansion cylinder have to be opened in a small fraction of the stroke only. Even if Ericsson engines can operate at much lower rotation speed as internal combustion engine, this makes the design of efficient valves particularly complex in the case of Ericsson engines.

Despite these difficulties, it has been chosen to rely on the Ericsson engine configuration for thermal energy conversion in the range of intermediate hot source temperature.

Liquid piston machines

Liquid piston technology is very interesting because it allows the working fluid to be perfectly sealed from the environment, while maintaining mechanical losses due to piston friction on the cylinder walls at much lower levels than those observed with solid pistons. This technology is therefore receiving a great deal of attention and different liquid piston engines have been designed [9].

So, a liquid piston Ericsson engine configuration has been chosen for our medium temperature energy conversion application. Apart from the perfect sealing and low friction losses interest, this configuration has the advantage of being very simple from a mechanical point of view, as the pistons of the compression and expansion cylinders are made up of the same quantity of liquid oscillating in a U-tube (Figure 3) [10]. The use of large liquid piston limits the engine's operating frequency to around 3 Hz in order to keep correct liquid/working fluid interfaces. This is an advantage for the valves, which do not have to be operated at too high a frequency. But on the other hand, this leads to larger engines. In our case, this was not considered to be a major drawback, given the simplicity of the system.

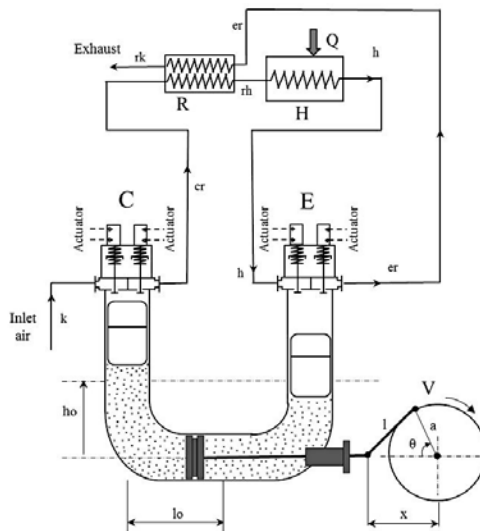


Figure 3. The single U-tube liquid piston Ericsson engine configuration.

Free piston engines

In the configuration of Figure 3, the mechanical energy is extracted from the engine by means of a solid piston located in the lower part of the U-tube. In order to keep the low friction losses advantage of the liquid piston configuration, a small annular gap has been created between the solid piston and the U-tube wall. This allows for small leaks around the solid piston. Now, pressure changes during a cycle are not symmetrical, which leads to a progressive imbalance between the water columns on either side of the solid piston. The concept of a solid piston to extract mechanical energy from the engine has therefore been abandoned for our application.

If the solid piston is removed, the liquid column is free to move, and a free liquid piston configuration is obtained. Free piston engines have long been considered a very interesting technology [11], both in the field of internal combustion engines and in that of engines with external heat input, such as Stirling engines (FPSE, Free Piston Stirling Engines). The free piston configuration results in a lightweight engine of modest size, with very few moving parts, at the cost of difficulty in achieving stable piston movement. In the case of a Free Liquid Piston Ericsson Engine (FLPEE), there are various ways of extracting the mechanical energy from the oscillating liquid column [10]. The approach adopted for our medium-temperature thermal energy conversion application involves treating the FLPEE as a compressed air generator and expanding this compressed air in an external expansion machine. This configuration is similar to the one of the historical Pescara free piston engine [12].

The chosen configuration

Figure 4 shows the configuration chosen for our medium-temperature thermal energy conversion application. The new engine is composed of a compression cylinder (C), and an expansion cylinder (E), consisting of a U-shaped tube partially filled with liquid (water) in its lower part. The cylinders are closed by a cylinder head in their upper part. Traditional automatic valves isolate the compression cylinder of the engine, while the expansion cylinder uses controlled valves. The engine also has a heater (H) to supply thermal power from the heat source to the working fluid. A recovery counter-current heat exchanger (R) is also considered for low-pressure ratios only, i.e. when the temperature at the exit of the expansion space is higher than the temperature at the exit of the compression space.

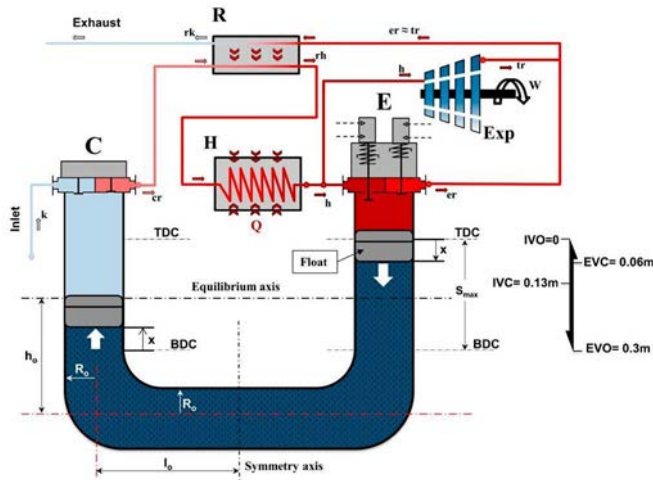


Figure 4. Schematic diagram of the Free Liquid Piston Ericsson Engine considered in this study.

The results of dynamic modelling of the FLPEE have shown that it is possible to find sets of engine operating parameters that lead to stable operation, with expected energy performance well above that of Fluidyne-type Stirling engines [13].

The test bench

Figure 5 shows the schematic diagram of the test bench, while figure 6 shows an overview of the experimental set-up. In order for the system to be tested in 'motored engine' mode, the device (Figure 5) is supplied with compressed air from the lab network (1). The compressed air from the external air compressor first passes through a pressure regulator (2) which allows the bench supply pressure to be adjusted, and then passes through a safety valve (3) which limits the downstream pressure to 3 bar, in order to avoid any risk of bursting the Pyrex tube (11). The valve (4) allows the compressed air in the test rig to be drained. A T-connection allows the expansion cylinder to be supplied from both the external compressor and the compression chamber of the liquid piston engine.

When the valves (1) and (5) are open, the compressed air from the external compressor pressurises the entire high-pressure branch of the device, including the two buffer tanks (8) and (15). The pressure line of the compression cylinder is pressurised and the engine

can be started by opening the inlet valve of the expansion cylinder and introducing external compressed air.

When the valve (5) is closed, no more compressed air is introduced from the external compressor. A fluidic circuit is established which allows the bench to operate in "engine mode", i.e. the compressed air leaving the compression cylinder is divided into two flows: one part passes into the cold buffer (8), then through the heating cartridge (14) and the hot buffer tank (15) to be admitted into the expansion cylinder (11), and the other part passes into a back-pressure regulator (7) which makes it possible to keep the upstream pressure constant. The flow of air delivered by this back-pressure regulator can be measured by the float flow meter (6). This measurement allows the available air flow to be assessed for practical applications of the engine, such as the production of compressed air or mechanical power by adding an external expander.

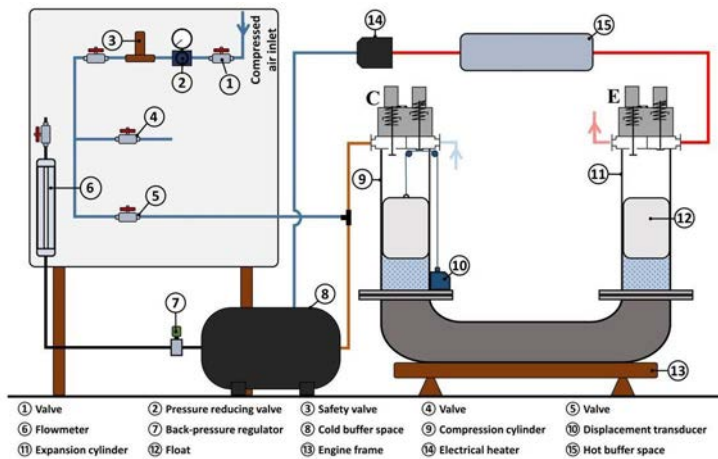


Figure 5. Schematic diagram of the test bench.

The lower part of the liquid piston system is made from commercial high-strength PN 10 pressure PVC pipe. The compression cylinder is made of stainless steel, while the expansion cylinder is made of Pyrex pipe with an external diameter of 180 mm, thickness of 8 mm, length of 500 mm. Two floats, with an external diameter of 156 mm and a length of 250 mm, are inserted in the cylinders. The length of the floats has been chosen to be at least equal to the maximum amplitude of movement of the liquid piston, so that

water never licks portions of the wall of the expansion cylinder that would have been in contact with hot air. This reduces the evaporation of water from the liquid piston, as the nominal temperature of introduction of air into the expansion cylinder is 360°C. Commercial YAMAHA XT500 motorbike engine heads are used to close the compression and expansion cylinders. The valves in these heads are operated by Festo 3/2-way quick-acting 1/4" valves, model MHE4-MS1H3/2G14K, and single-acting pneumatic cylinders, model AEN-40-8APA-S6, also from Festo. These valves are supplied with compressed air from the external air compressor.

The compressed air is heated before it enters the expansion workspace by an electric heating cartridge (item (14) in Figure 5), Osram Sylvania model SureHeat JET 074719, with a maximum power of 8 kW. A control box allows the supply temperature of the expansion cylinder to be set.

The test bench is equipped with K-type thermocouple temperature sensors with a measuring uncertainty of ± 1.5 °C, Keller-Druk PR23S and 23SY pressure sensors which have been calibrated beforehand and have a measuring uncertainty of ± 0.025 bar, and a micro-Epsilon WDS-300-P60-SR-I displacement sensor with a measuring uncertainty of ± 0.25 %. This sensor (item (10) in Figure 5) is connected by a pulley system to the float of the compression cylinder. The measurement of the instantaneous pressure in each compression and expansion space is obtained by means of pressure sensors connected to the original location of the spark plugs in the cylinder heads. The sensors are connected to a National Instrument NI cDAQ 9172 modular chassis data logger controlled by Labview. The sampling rate is 1 kHz. A control box operates the solenoid valves on the valve cylinders based on a comparison between the setpoints and the float position measured by the taut wire sensor.



Figure 6. Overview of the experimental set-up.

First experimental results

The first tests did not allow the system to operate autonomously [14], for reasons that will be explained later. The results presented here are therefore all related to a 'motored engine' mode, i.e. with consumption of compressed air from the network. In addition, according to the theoretical results, the displacement amplitude of the free liquid piston increases with the intake pressure of the expansion cylinder. However, in the current version of the test bench, the amplitude is limited by the length of the tubes and the length of the floats. Therefore, the tests that have been carried out are limited to low pressure ratios. On the other hand, the frequency also depends on the inlet pressure of the expansion cylinder. Experience shows that above a frequency of about 3 Hz, the liquid-air interface no longer behaves satisfactorily. Due to its inertia, the float 'lifts off' from the liquid column and the interface breaks up into a multitude of droplets. For these reasons, the tests are limited to an absolute pressure of 1.6 bar at the inlet of the expansion cylinder.

Valves setting

The position of the liquid piston is denoted by x . The position $x = 0$ corresponds to the lowest bottom dead centre possible in the expansion cylinder (float on the bottom

stop of the cylinder) and the highest top dead centre (TDC) possible in the compression cylinder (float in contact with the top stop of the cylinder). The position $x = 0.3$ m corresponds to the lowest bottom dead centre (BDC) possible in the compression cylinder (float on the bottom stop of the cylinder) and the highest top dead centre possible in the expansion cylinder (float in contact with the top stop of the cylinder). The compression cylinder valves are supposed to simulate automatic valves, whereas the expansion cylinder valves are actuated valves whose opening and closing are governed by the values of the position of the liquid piston and its direction of movement.

The valves are actuated as follows:

- The inlet valve of the compression cylinder is open when the liquid piston moves downward and the in-cylinder pressure is lower than the atmospheric pressure.
- The outlet valve of the compression cylinder is open when the liquid piston moves upward and the in-cylinder pressure is higher than the pressure in the exhaust pipe.
- The inlet valve of the expansion cylinder is open when the liquid piston moves upward and $x > IVO$ or when the liquid piston moves downward and $x > IVC$.
- The exhaust valve of the expansion cylinder is open when the liquid piston moves downward and $x < EVO$ or when the liquid piston moves upward and $x > IVC$.

Figure 7 presents the valves setting of the expansion cylinder. Unless otherwise specified, the results presented here correspond to the following expansion cylinder valves setting :

- $IVO = 0.16$ m
- $IVC = 0.1$ m
- $EVO = 0.03$ m
- $EVC = 0.16$ m

Theoretically, with this valve setting, there should be an expansion process of the working fluid, since all valves are closed when the liquid piston moves downward from $IVC = 0.1$ m to $EVO = 0.03$ m, but there should be no re-compression of the dead space volume since the inlet valve opens at the same time as the exhaust valve closes: $EVC = IVO$.

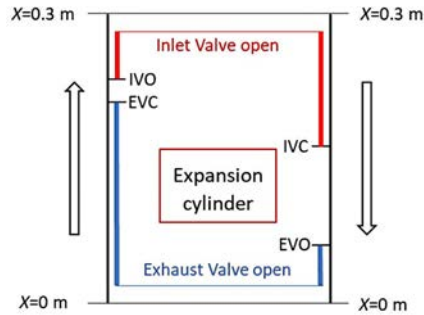


Figure 7. Valves setting for the expansion cylinder.

Unfortunately, in the current version of the test bench, there is a delay of a few milliseconds between the measurement of the float position and the valve actuation, which affects the experimental results. This problem will be corrected in a new version of the experimental rig.

Cold tests

Figure 8 shows the theoretical and experimental liquid piston displacement as a function of time, for a test duration of 20 s with a time step of 10^{-3} s. The expansion cylinder inlet pressure is set to 1.3 bar. There is good agreement between the theoretical and experimental data, both in term of frequency (about 2.2 Hz for the experimental and theoretical results) and stroke (about 124 mm for the theoretical results and 105 mm for the experimental ones, that is less than half the maximum possible travel between the stops).

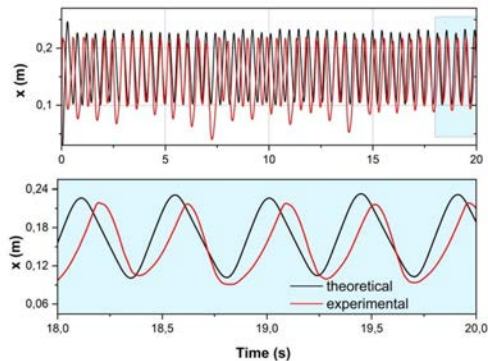


Figure 8. Liquid piston displacement as a function of time.

Figure 9 presents the frequency and the stroke as a function of the expansion cylinder inlet pressure. As the modelling has shown, it is not possible to vary the expansion cylinder inlet pressure without adjusting the valves setting. The experimental results shown in figure 9 are obtained by varying the pressure of the air admitted into the expansion cylinder from 1.15 to 1.5 bar. For the theoretical results, the model has been re-run, with the experimentally imposed pressure and valves setting, to allow comparison between the experimental and theoretical data. It can be seen that the theoretical frequency and stroke increases nearly linearly with the expansion cylinder inlet pressure. The experimental values are in fairly good agreement with the theoretical values, and the differences can be attributed largely to the fact that the experimental instantaneous pressure in the expansion cylinder is far from the theoretical pressure, due to pressure losses in the intake line, as will be shown below. The same applies to the compression cylinder, where the exhaust valve generates large pressure losses.

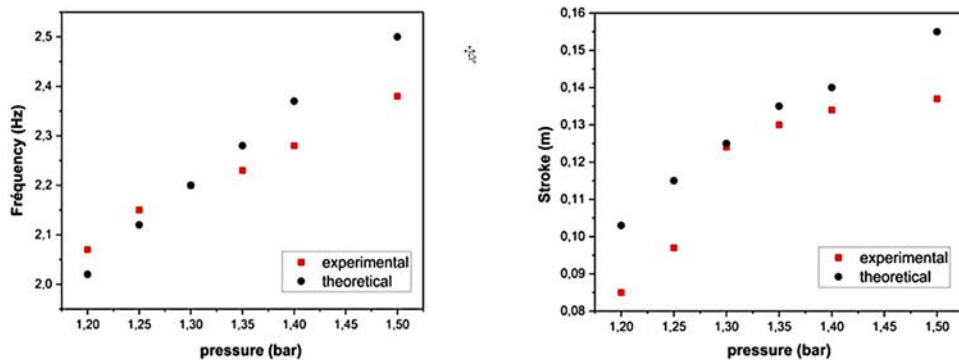


Figure 9. Frequency and stroke as a function of the expansion cylinder inlet pressure.

Figure 10 presents the instantaneous pressures measured at the expansion cylinder inlet (p_{admE}), in the compression cylinder (p_C), at the compression cylinder outlet (p_{echC}), in the expansion cylinder (p_E) and at the heater cartridge inlet (p_{Cart}), as a function of time.

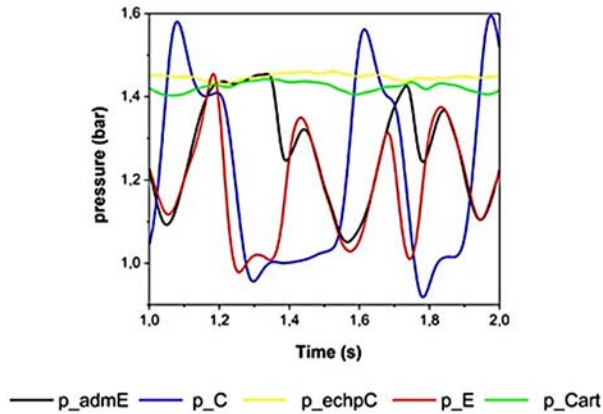


Figure 10. Instantaneous pressures as a function of time.

It can be seen in figure 10 that the pressures at the inlet of the heater cartridge p_{Cart} and at the outlet of the compression cylinder p_{echpC} are almost constant, and almost identical, the pressure at the inlet of the cartridge being slightly lower due to the greater pressure drop in the connecting pipe. In contrast, the expansion cylinder inlet pressure p_{admE} , which is supposed to be constant in the model, varies greatly when the inlet valve opens and closes. This is due to the high pressure drop generated by the pipe that connects the hot buffer tank to the expansion cylinder head. This line 'deflates' when the inlet valve opens and 're-inflates' to the cartridge inlet pressure when the inlet valve closes. The higher the pressure imposed by the compressed air in the high-pressure branch, the more pronounced this phenomenon becomes. This high pressure drop is the main reason why the engine has not yet been able to operate autonomously, without energy supply from the compressed air network. During the opening phases of the expansion cylinder intake valve, the pressure p_{E} in the cylinder is almost identical to the pressure in the intake pipe p_{admE} , proving that the pressure losses in the intake valve are negligible. However, these pressures are far from being equal to the constant pressure p_{Cart} as assumed in the model.

As far as the compression cylinder p_{C} is concerned, it can be seen that when the free liquid piston moves up towards its top dead centre, the pressure in the cylinder p_{C} exceeds the pressure in the exhaust pipe p_{echpC} even though the exhaust valve is open, which

indicates that the pressure losses generated by this valve are too high under these operating conditions.

Hot tests

Different tests were carried out at hot temperatures, up to 200 °C. The results of the experimental tests showed that the temperature does not affect the frequency or the stroke of the free liquid piston, as shown in figure 11, which represents the temporal evolution of the liquid piston displacement for different air inlet temperatures in the expansion cylinder, at the same inlet pressure of 1.3 bar. It can be seen that for the different temperature levels, the amplitude is almost the same. If, for example, we take the displacement for a temperature of 20 °C and 190 °C, we notice that it is almost the same stroke that is covered by the liquid piston, with the same cycle frequency, as predicted by the theoretical model.

The hot tests were carried out in a completely satisfactory manner, without any technical problems. At most, some fogging was observed on the wall of the Pyrex tube, due to the weak evaporation-condensation phenomena of the water in the liquid piston at high temperatures of the air admitted into the expansion cylinder.

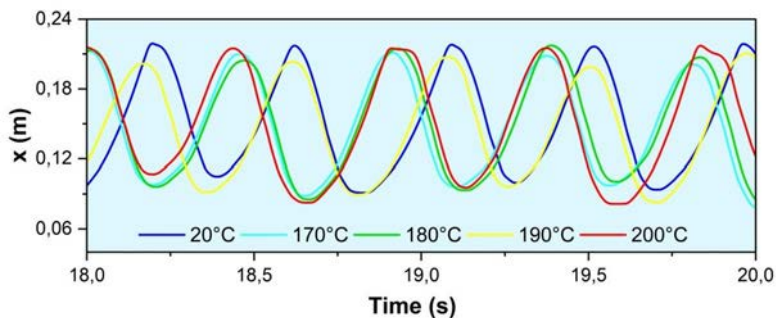


Figure 11. Liquid piston displacement for different inlet temperatures of the expansion cylinder.

Conclusion

The intellectual approach that led to develop a Free Liquid Piston Ericsson engine for medium thermal energy conversion has been presented. The test bench has been described and first experimental results are shown. In its current configuration, the

test bench did not allow for 'engine' operation. Tests in 'motored engine' mode using an external compressed air supply showed that it is possible to obtain stable engine operation, provided that the operational parameters (supply pressure, valve opening/closing settings) are carefully chosen. The oscillation frequency of the free piston and its stroke are in good agreement with the results of the theoretical model. The hot tests also demonstrated the good operation of the engine at high temperatures without encountering any technical problems. The examination of the experimental results highlighted the improvements to be made to the test bench.

References

- [1] Finkelstein Th, Organ AJ. Air engines. Professional Engineering Publishing Ltd, London (2001).
- [2] Stouffs P, Hot Air Engines, Journal of Applied Fluid Mechanics, 4-2: 1-8 (2011).
- [3] Kolin I. Stirling Motor. Zagreb Univ. Publications Ltd, Zagreb (1991).
- [4] Reader GT, Hooper C. Stirling engines. E. & F. N. Spon, London (1983).
- [5] Stine WB, Diver RB, A Compendium of Solar Dish/Stirling Technology. Rapport SAND93-7026 UC-236, Sandia National Laboratories, Albuquerque (1994).
- [6] Senft J. An Introduction to Low Temperature Differential Stirling Engines. Moriya Pr (1996).
- [7] <https://www.oocities.org/viebachstirling/> (Accessed March 29, 2024).
- [8] Bonnet S, Alaphilippe M, Stouffs P, Instantaneous temperature field in a small Stirling engine: a comparison between experiments and modeling results, in: Proceedings of ECOS 2003, 1185-1191, Copenhagen (2003).
- [9] Gupta A, Sharma S, Narayan S. Liquid piston engines. Wiley (2017).
- [10] Chouder R, Stouffs P, Benabdesselam A. A variant of the Fluidyne: the liquid piston ERICSSON engine. In: International Stirling Engine Conference, ISEC 2021, Sep 2021, Rome, Italy. pp.04001

- [11] Mikalsen R, Roskilly AP. A review of free-piston engine history and applications. *Appl Therm Eng* 27(14–15):2339–2352 (2007).
- [12] Pescara RP. Motor compressor of the free piston type. Patent, N 2 241 957 (1941).
- [13] Chouder R, Benabdesselam A, Stouffs P. Modeling results of a new high performance free liquid piston engine. *Energy*, Volume 263, Part D, 125960 (2023).
- [14] Chouder R. Étude théorique et expérimentale d'un moteur Ericsson à piston liquide libre de configuration originale. Thèse de l'Université de Pau et des Pays de l'Adour (2023). <https://theses.hal.science/tel-04473770>

Numerical and Experimental Investigation of a Combustor-coupled Thermoacoustic Stirling Generator

Qingyue Jin^{a,b,c}, Jing Luo^{a,b,c}, Haojie Sun^{a,b,c}, Jianhua Xue^{a,d}, Ying Ma^{a,d}, Zhuang Ma^{a,d}, Guoyao Yu^{a,b,d,*}, Ercang Luo^{a,b,c}

a Key Laboratory of Cryogenics, Technical Institute of Physics and Chemistry, Chinese Academy of Sciences, 29 Zhong Guan Cun East Road, Haidian District, Beijing, China

b Key Laboratory of Cryogenic Science and Technology, 29 Zhong Guan Cun East Road, Haidian District, Beijing, China

c University of Chinese Academy of Sciences, 80 Zhong Guan Cun East Road, Haidian District, Beijing, China

d Institute of Optical Physics and Engineering Technology, 1001 Ke Chuang Road, Gaoxin District, Jinan, China

* Corresponding author: gyyu@mail.ipc.ac.cn

Keywords: Free-piston, Stirling generator, Novel gas combustor, Multiple nozzles, Numerical simulation, Experimental validation

Abstract

A distributed Combined Heat and Power (CHP) system, positioned as a promising complement to traditional centralized electric generation technologies, plays a vital role in integrating renewable energy sources and mitigating carbon emissions. The Free-Piston Stirling Generator (FPSG), operating as a hybrid thermoacoustic heat engine, has garnered substantial attention for micro- and small-scale applications due to its commendable attributes such as high efficiency, reliability, and an extended lifespan. This paper introduces an innovative multi-nozzle gas combustor designed to interface with an FPSG for distributed power applications. Due to the unique construction of the combustor and the intrinsic external combustion characteristics of the FPSG, the system promises remarkable fuel adaptability, accommodating butane, natural gas, and liquefied petroleum (LPG). To elucidate the heat transfer characteristics of external combustion with internal oscillating flow, a comprehensive numerical and experimental investigation was conducted. The study initiated with a detailed analysis of the effects of nozzle and tubular high-temperature heat exchanger (HHX) arrangements, as well as the impact of tubular HHX with or without external spiral fins on the flow field, temperature distribution, and heat flux density within the combustor. Meticulous experimental investigations were then undertaken to evaluate the system performance as well as the energy distribution. In the final stage, a comprehensive analysis scrutinized the system's performance, energy flow distribution of each component under rated operating conditions. Numerical calculations reveal that, optimal heat accepted by the HHX and temperature uniformity is achieved when employing 36 fuel nozzles, each directed towards an individual heater tube. Operating at a fuel flow rate of 0.55 Nm³/h and an air-fuel ratio of 18, the HHX absorbs 6.67 kW of heat, with 34% radiative heat. The integration of spiral fins improves both the heat accepted capacity and coefficient of heat transfer of the HHX by 14.63% and 22.29%, respectively. Additionally, experimental results demonstrate that,

under a fuel flow rate of 0.54 Nm³/h and an external resistance of 20 Ω , the system achieved an output electric power of 1.53 kW, corresponding to fuel-to-electricity efficiency and net thermal-to-electric efficiency of 9.8% and 32.4%, respectively.

Introduction

The free-piston Stirling generator [1,2] (FPSG) is an externally combusted closed dynamic thermoelectric converter based on the Stirling cycle, categorized within the domain of generalized thermoacoustic heat engines. Its distinctive feature, stemming from external combustion, facilitates the exploitation of a diverse spectrum of heat sources, encompassing new energy sources like solar, nuclear, and biomass, alongside the harnessing of low-grade energy sources such as industrial waste heat and residual thermal energy. The generator forsakes conventional mechanical transmission in favor of key technological advancements such as clearance sealing, gas bearings, and linear reciprocating motion. Consequently, it owns a suite of advantages including heightened efficiency, enhanced reliability, and environmental friendliness. Positioned as a promising candidate for the sustainable utilization of clean energy resources, including solar power generation [3], micro-cogeneration [4], and waste heat recovery [5], it holds significant potential in reshaping the energy landscape.

The fuel diversity of Combustor-coupled FPSGs is extensive, encompassing options such as fuel oil, natural gas, coal-fired sources, and biomass fuel. During the operation of the power generation system, fuel and air are continuously mixed and diffusion combustion in the chamber after passing through the ignition device in the combustor. The resulting flames and high-temperature flue gases are then exchanged through convective and radiative heat transfer with high-pressure helium gas in a high-temperature heat exchanger (HHX), ensuring efficient heat transfer from external combustion to internal oscillating flow for stable operational performance. The helium gas within the HHX absorbs heat from the combustor to achieve isothermal expansion. The majority of the generated acoustic power in the compression space is transferred to the linear alternator, where it is converted into electrical power. The residual acoustic power is directed to the ambient-temperature heat exchanger and then amplified by the regenerator where thermoacoustic cycle ensues.

While significant attention has been dedicated to studying the overall performance of FPSGs utilizing electrical heating, there exists a notable scarcity of research on

combustor-coupled FPSGs. Specifically, there is limited research on the fluid dynamics at the interface between the combustor and the HHX, as well as in evaluating the experimental performance of the entire system. In 2012, A. Parente et al. [6] presented a simulation and experimental study on a flameless combustor equipped with a Stirling engine, focusing on the impact of hydrogen-enriched fuels. The results showed that the addition of hydrogen to methane affects the flame structure within the combustor, and detailed kinetic schemes facilitates obtaining a close-to-realistic temperature field distribution and pollutant emissions. In 2014, Evelyn Cardozo et al. [7,8] conducted an experimental study of 1 kW Stirling generator coupled to 20 kW wood pellet combustor, and found that the distance between the combustor and HHX significantly impacted the temperature of HHX, with a mere 5 cm variation inducing a 100 °C change. Subsequently, the effect of biomass fuel type on system performance was evaluated. Experiments results indicated similar temperature of HHX for both fuels, but bagasse pellets exhibited lower CO emissions compared to wood pellets, albeit with higher levels of NOx and accumulated ash. The cogeneration efficiency of bagasse pellets remained above 83% after three operational cycles, while that of wood pellets remained above 90%. In 2018, Songgang Qiu et al. [9,10] conducted a numerical analysis of the flow of flame and flue gas within a combustor. The study revealed that the incorporation of combustion flow guides enhanced the velocity distribution of the flue gas at the top of the tubular HHX, and the use of diffuser plates further improved the heat transfer between the flue gas and helium. Building upon this research, subsequent simulations in 2019 investigated a cogeneration system employing additive manufacturing for fabricating essential components such as the pressure vessel, heat exchangers, and new foil type regenerator, which can provide 1 kW of electrical power output and 1.1 kW of heating at 80 °C with a fuel-electric efficiency of nearly 38%. In 2022, Dong-Jun Kim et al. [11] focused on the impact of displacer spring stiffness on the dynamics and performance of a 2.5 kW class FPSG and constructed an engine testbed for LNG combustion heating. The test results showed that the average electrical output was measured to be 2.46 kW under the conditions of a flue gas temperature of 1110 °C and a cooling water temperature of 21 °C. This paper presents a novel gas combustor designed for FPSGs, featuring multiple nozzles and flue gas top discharge, focusing on simulating the heat transfer characteristics of external combustion and internal oscillating flow, as well as conducting performance

tests of the combustor-coupled FPSG system. Initially, detailed analyses were carried out to investigate the effects of nozzle and tubular HHX arrangements, along with the impact of tubular HHX with or without spiral fins, on the flow field, temperature distribution, and heat flux density within the combustor. Subsequently, the experimental setup for the coupled system was constructed, and a series of experiments were conducted to assess the performance and energy flow of the system. Finally, a conclusion was drawn.

Numerical simulation

Numerical model

The novel gas combustor-coupled FPSG system is illustrated in Figure 1, comprising primarily of a gas combustor and a 1.5 kW class FPSG. The combustor includes a combustion chamber, fuel nozzle, HHX, and other essential components. Unlike traditional single-nozzle structures, this paper proposes a novel design with distributed multiple nozzles, releasing flue gas from the upper part of the HHX (as shown in figure 1). The rationale behind the multi-nozzle is to ensure temperature uniformity within the HHX. The discharge of flue gas from the upper of the HHX facilitates enhanced flame and flue gas scouring effects on the HHX, thereby improving system heat transfer efficiency. Notably, the HHX is of a 36-tube bundle structure, adopting the novel spiral fins design to increase heat exchange area and reduce processing difficulty and cost.

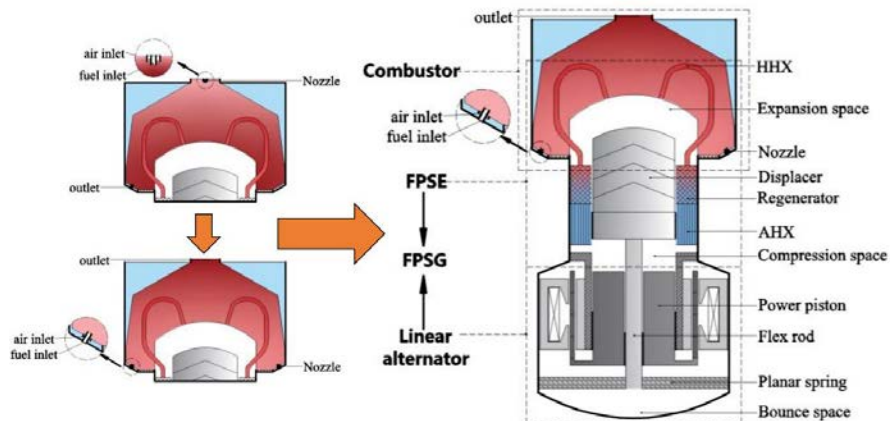


Figure 1. Schematic diagram of a combustor-coupled FPSG prototype.

The primary constituent of the fuel is liquefied petroleum gas (LPG), comprising a molar fraction of 66.5% n-butane and 28.5% propane. The fuel, operating at a flow rate of 0.55 Nm³/h and a temperature of 328 K, is mixed and diffused with air at a temperature of 300 K within the combustor, with the resulting flame and flue gases engaging in heat exchange with the HHX. The wall surface of HHX is assigned with convective heat transfer boundary conditions, encompassing a heat transfer coefficient (h) of 2067.46 W/(m²·K) and a free stream temperature (T_{He}) of 810.57 K, derived from a one-dimensional thermodynamic computational model of a 1.5 kW FPSG. The comparison of four combustor structures evaluates the impact of fuel nozzle design and tubular HHX arrangement on the external combustion characteristics of FPSG, with Figure 2 illustrating the computed fluid domain for these models. Models 1 and 2 share a common feature: 36 fuel nozzles evenly distributed along the circumference at the bottom of the combustor, matching the number of heater tubes of the tubular HHX, with alternating arrangement with the air nozzles. The fuel nozzles of Model 1 are oriented towards the gap between adjacent heater tubes, while the fuel nozzles of Model 2 are directed towards each individual heater tube. Models 3 and 4 feature 12 and 9 fuel nozzles, respectively, at the bottom of the combustor, with one fuel nozzle equipped with 2 air nozzles on both sides. For all four combustors, 2 mm inner diameter fuel nozzles and 5 mm inner diameter air nozzles are adopted.

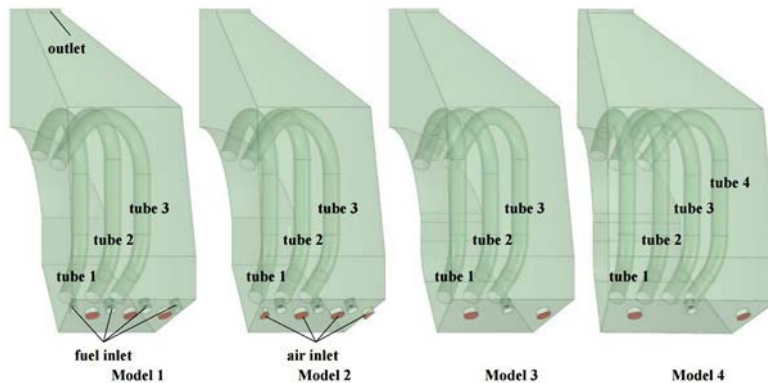


Figure 2. Computed fluid domain.

The models encompass a variety of components, such as turbulence model, chemical reaction model, radiation model and so on. Specifically, the standard k- ϵ model is

employed to simulate the intricate flow field generated post-fuel combustion, thereby ensuring reasonable computational accuracy within a limited computational fluid domain. The Eddy Dissipation Model (EDM), utilized for simulating LPG combustion, is capable of addressing one-step or two-step global kinetic mechanisms, with the chemical reaction equations shown in Eq. (1). The Discrete Ordinates Radiation Model (DO) and the Weighted Sum of Gray Gases Model (WSGGM), both suitable for all optical depths and offering high computational accuracy, are employed to solve the radiative transfer equations. The emissivity of the wall surface of HHX is set to be 0.75, while the remaining walls are designated as adiabatic no-slip boundaries with an emissivity of 1.



Simulation results and discussions

Nozzle and tubular high-temperature heat exchanger (HHX) arrangements

The air-fuel ratio determines both combustion completeness and flue gas temperature, consequently influencing heat transfer. Illustrated in Figure 3 are the results of varying air-fuel ratios on the heat accepted of HHX (Q_r) and the extent of combustion incompleteness (Ψ), observed at a fuel flow rate of 0.55 Nm³/h across four distinct combustor structures. The extent of combustion incompleteness is quantified as the ratio of the combined mass flow rates of n-butane and propane at the outlet to those at the fuel nozzle. Figure 3(a) demonstrates that the heat accepted by HHX initially rises before subsequently declining in response to variations in the air-fuel ratio. As the air flow rate increases, the temperatures of both the flame and flue gas rise owing to the more complete combustion, consequently augmenting the heat accepted of HHX. As the air flow rate continues to increase, a significant volume of lower temperature (328 K) air into the combustor, where it mixes with the high-temperature flue gas, resulting in a reduction of the flue gas temperature. The heat accepted by HHX decreases due to the reduced temperature difference for heat exchange between the HHX wall surface and the flue gas. Therefore, there is an optimal accepted heat of HHX for various combustor structures, corresponding to an optimal air-fuel ratio, achieved through a synergistic interaction between combustion completeness and lower temperature air.

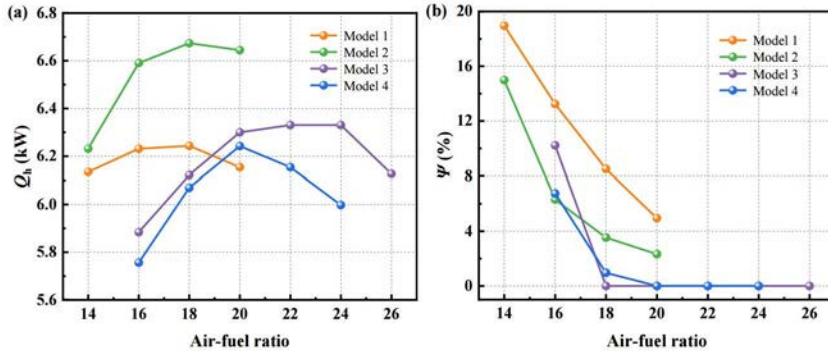


Figure 3. (a) The heat accepted, (b) Combustion incompleteness with varying air-fuel ratio.

Figure 4 illustrates the optimal accepted heat of HHX for four combustor structures alongside the extent of combustion incompleteness. Model 2 exhibits the largest optimal heat accepted of 6.67 kW for the tubular HHX, under conditions of a fuel flow rate of 0.55 Nm³/h and an air-fuel ratio of 18, with 66% attributed to convective heat transfer and 34% to radiative heat transfer. However, there is still an extent of combustion incompleteness of 3.53% in the scenario where Model 2 achieves optimal accepted heat of HHX. Model 3 obtains the optimal accepted heat of 6.33 kW at a fuel flow rate of 0.55 Nm³/h and an air-fuel ratio of 24, with complete combustion. Compared to Model 2, Model 3 minimizes the production of incomplete combustion pollutants, enhances fuel utilization efficiency, and offers simpler manufacturing and processing methods, while meeting the design accepted heat of HHX requirements of the FPSG.

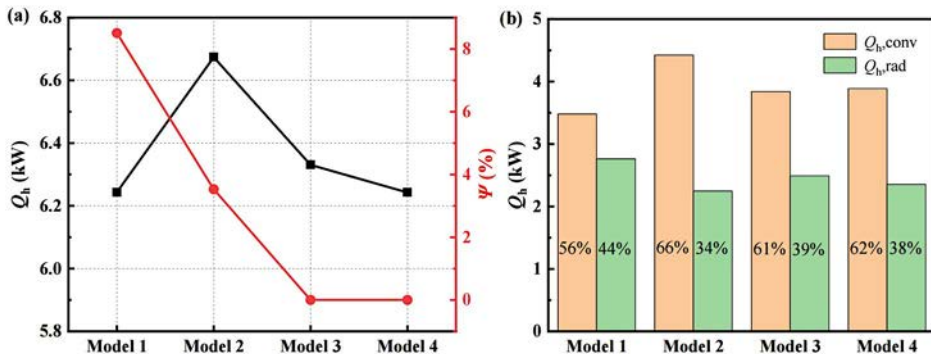


Figure 4. (a) The heat accepted, (b) Combustion incompleteness across four combustor structures.

The temperature distributions of the fuel nozzle cross-section and HHX cross-section for the four combustor structures under the optimal accepted heat of HHX conditions are illustrated in figure 5. As the number of fuel nozzles decreases sequentially from 36 (Model 1 and Model 2), 12 (Model 3), to 9 (Model 4), the fuel flow rate of each individual fuel nozzle increases accordingly, resulting in higher fuel injection velocity and causing a gradual shift inflame concentration area towards the outlet of combustor. The relatively low fuel injection velocity of the individual nozzles in Models 1 and 2 means that the lower temperature (300 K) fuel is not directly in contact with the wall surface of HHX, and therefore there is no "reverse heat transfer" phenomenon hindering the HHX from absorbing heat from the flue gas, which is the heat transfer from the HHX to the fuel. Since Model 1 features an air nozzle orientation towards the heater tube compared to Model 2, this arrangement causes the tail end of the air jet with lower temperature (328 K) to make direct contact with the wall surface of HHX, leading to a reversed heat transfer from the heater tube to the air. Models 3 and 4 are characterized by higher fuel and air velocities compared to Models 1 and 2, resulting in longer jet lengths within the combustion chamber. Even the vortex zones formed at the upper of the fuel nozzles due to the excessive fuel injection velocity in Model 4 resulted the deviation of the fuel jet's trajectory towards the upper of the fuel nozzle. This inevitably increases the area of direct contact between the fuel, air, and the wall surface of HHX, thus affecting the accepted heat of the HHX. This influence persists even though both the fuel nozzle and the air nozzle of Model 4 are poised at the gaps of two adjacent heater tubes.

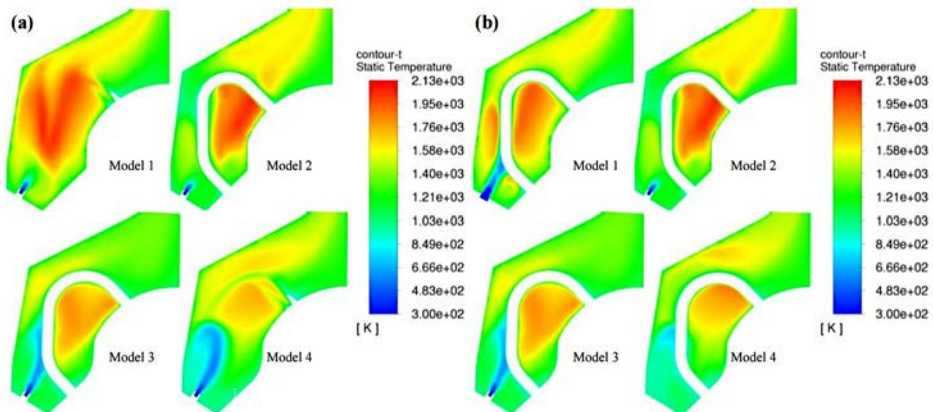


Figure 5. The temperature distributions of (a) fuel nozzle cross-section, (b) HHX cross-section.

Figure 6 illustrates the surface heat flux distribution on the wall surface of HHX. Table 1 shows the heat accepted and average surface heat flux (q) per heater tube. The tubular HHXs of Models 1 and 2 exhibit the notably uniform surface heat flux in the circumferential direction. The difference in heat accepted per heater tube is calculated to be 1.35 W and 4.22 W in models 1 and 2, respectively, and 12.59 W in model 3. The uniformity in surface heat flux in the circumferential direction is primarily influenced by the number of fuel nozzles. Specifically, the arrangement of one fuel nozzle per heater tube promotes uniform combustion within the combustor's circumferential direction, consequently enhancing circumferential surface heat flux uniformity. Additionally, concerning the surface heat flux uniformity of individual heater tubes, Model 2 demonstrates greater uniformity, whereas Model 4 exhibits the least uniformity. Except for Model 2, the other combustor structures display visible reverse surface heat flux (total surface heat flux greater than zero) from the HHX to the surrounding flue gas, which leads to a diminished overall heat transfer capacity of the HHX. The occurrence of reverse surface heat flux is primarily correlated with the number of fuel nozzles and the orientation of the air nozzles. Higher fuel nozzle counts result in reduced fuel velocity of the individual fuel nozzle, diminishing the area of lower temperature fuel in direct contact with the wall surface of HHX and thereby minimizing reverse heat transfer. In models with the highest number of fuel nozzles, such as Model 1 and Model 2, reverse heat transfer is further mitigated when air nozzles are directed towards the gap between the two heater tubes. Compared to the fuel flow rate, the air flow rate will be higher. When the air nozzles are directed towards the gap between the two heater tubes, it can reduce the direct contact area between the fuel, air, and the wall surface of HHX, thus decreasing reverse heat transfer. The region of reverse surface heat flux depicted in figure 6 corresponds to the location illustrated in figure 5, where the tail end of the fuel and air jet is in direct contact with the surface of the HHX. Lastly, the presence of the highest point of surface heat flux at the lower side of the upper section of the heater tubes for the four combustor structures coincides with the elevated flue gas temperatures depicted in figure 5, near the lower side of the upper section of the heater tubes.

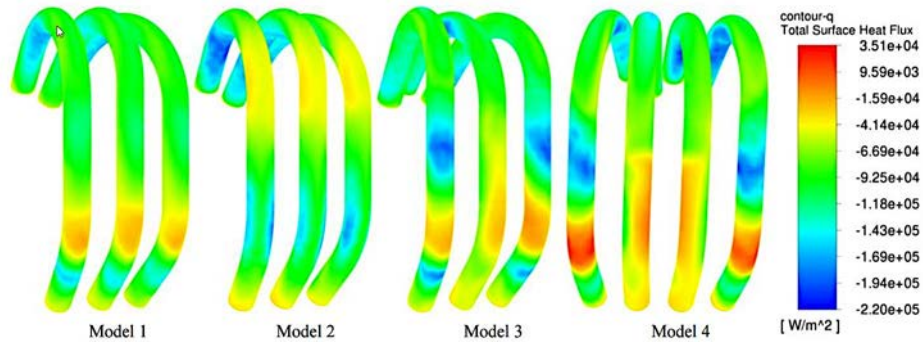


Figure 6. Surface heat flux distribution on the wall surface of HHX.

Table 1. The heat accepted and average surface heat flux per heater tube.

	Model 1			Model 2			
	tube 1	tube 2	tube 3	tube 1	tube 2	tube 3	
Q_h (W)	-172.76	-173.45	-174.11	-183.52	-187.74	-184.88	
q (W/m ²)	-87684.87	-88179.94	-88360.87	-93145.43	-95445.02	-93823.17	
	Model 3			Model 4			
	tube 1	tube 2	tube 3	tube 1	tube 2	tube 3	tube 4
Q_h (W)	-177.08	-168.93	-181.52	-188.66	-163.57	-161.85	-179.53
q (W/m ²)	-90088.56	-85850.46	-92363.16	-95766.51	-82898.73	-82165.03	-90965.78

The temperature distribution across the wall surface of HHX is illustrated in figure 7. Models 1 and 2 manifest the highest degree of circumferential temperature uniformity across the wall surface of HHX. Following closely in terms of temperature uniformity is Model 3, Model 4 exhibits the least desirable temperature uniformity among the examined models. Table 2 illustrates the maximum (T_{max}), minimum (T_{min}), average temperatures (T_{ave}), and maximum temperature difference (T_{diff}) per heater tube in the axial direction across four combustor structures. A progressive increase in the maximum difference in average temperature per heater tube in the circumferential direction is observed as the number of fuel nozzles decreases. The maximum difference in average temperature per heater tube for models 1 and 2 stands at 0.32 K and 1.12 K, while models 3 and 4 exhibit more substantial variations with 3.22 K and 6.54 K, respectively. Furthermore, regarding the axial temperature uniformity across the wall surface of HHX,

it is observed that Model 1 showcases a commendable level of temperature uniformity among its heater tubes. For Model 1 and Model 2, the temperature difference between the highest and lowest temperatures falls within the range of 69.39 K to 79.67 K and 79.64 K to 91.48 K, respectively. In contrast, for Models 3 and 4, this temperature disparity widens, spanning ranges of 81.41 K to 95.96 K and 105.89 K to 114.84 K, respectively. In contrast to Model 2, although Model 1 demonstrates superior circumferential and axial temperature uniformity across the wall surface of HHX, its overall heat absorption is somewhat diminished by a minor occurrence of reverse surface heat flux from the HHX to the air. As a result, Model 2 emerges as the preferable choice, excelling in both the heat accepted, surface heat flux uniformity, and temperature uniformity across the wall surface of HHX.

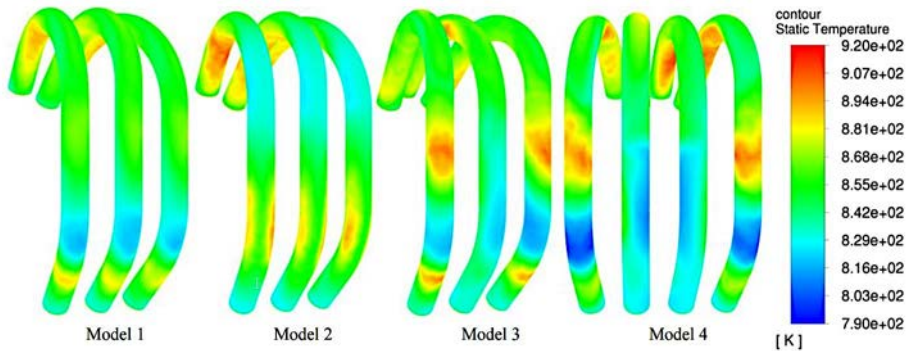


Figure 7. Temperature distribution across the wall surface of HHX.

Table 2. Maximum, minimum, average temperatures, and maximum temperature difference per heater tube.

	Model 1			Model 2			
	tube 1	tube 2	tube 3	tube 1	tube 2	tube 3	
T_{min} (K)	813.52	818.54	818.75	825.73	826.22	826.73	
T_{max} (K)	893.19	895.08	888.14	917.20	917.38	906.37	
T_{ave} (K)	852.47	852.71	852.79	856.01	857.13	856.34	
T_{diff} (K)	79.67	76.55	69.39	91.48	91.15	79.64	
	Model 3			Model 4			
	tube 1	tube 2	tube 3	tube 1	tube 2	tube 3	tube 4
T_{min} (K)	816.68	819.90	813.78	792.40	809.52	814.34	799.05
T_{max} (K)	907.42	901.31	909.74	907.24	915.41	922.02	910.19
T_{ave} (K)	854.25	852.16	855.38	854.60	850.31	850.67	856.85
T_{diff} (K)	90.73	81.41	95.96	114.84	105.89	107.68	111.14

Tubular HHX with or without fins

To bolster the heat transfer efficiency between the flame, flue gas and HHX, this paper proposes novel spiral fins. Inspired by principles in heat transfer enhancement using fins in various applications, this approach aims to magnify the heat transfer effect by increasing the effective heat transfer area of the external wall surface of HHX. Unlike conventional fin structures, which often involve intricate manufacturing processes and higher costs, the proposed spiral fins offer a more straightforward fabrication method and is more cost-effective. Given the constraints imposed by limited computational resources and the practical considerations of combustor manufacturing and processing, this paper opts to focus on tube 2 of Model 3 for evaluating the efficacy of the novel spiral fins in enhancing the heat transfer capacity of the HHX. As indicated in Table 1, the discrepancy between total accepted heat calculated by aggregating accepted heat of the three heater tubes and the total accepted heat calculated based solely on the accepted heat of tube 2 amounts to a negligible 3.93%. Consequently, in this section, the heat accepted of tube 2 in Model 3, multiplied by 36 (the number of tubes), is employed to compute the total heat accepted of the HHX to ensure accuracy and reliability in evaluating.

Table 3 shows the energy balance within the combustor and the heat transfer characteristics of the HHX with and without fins. Note that the system is deemed to be in energy balance when the disparity between the inlet and outlet energy is less than 1% of the total inlet energy. At a fuel flow rate of 0.55 Nm³/h, fins indeed increase the heat accepted and coefficient of heat transfer (h) of the HHX from 6.08 kW and 173.69 W/m²·K to 6.97 kW and 212.41 W/m²·K, which is an increase of 14.63% and 22.29%, respectively. The proportions of convective heat transfer ($Q_{h,conv}/Q_h$) and radiative heat transfer ($Q_{h,rad}/Q_h$) remain nearly unchanged. Without fins, 37.55% of the energy entering the combustor is absorbed by the high-pressure helium inside the HHX, while 62.72% exits the combustor through the outlet as high-temperature flue gas. With fins, 42.82% of the energy is absorbed by the high-pressure helium, while 58.24% of the energy leaves the combustor in the form of high-temperature flue gas through the outlet.

Table 3. Energy balance and heat transfer characteristics at the HHX with and without fins.

	H_{in} (W)	Q_h (W)	H_{out} (W)	Q_{LPG} (W)	Sum	
Without fins	249.89	-6081.61	-10158.29	15947.06	-42.95	
With fins	246.66	-6971.58	-9482.44	16034.95	-172.41	
	Q_h (kW)	$Q_{h,conv}/Q_h$	$Q_{h,rad}/Q_h$	q (kW/m ²)	T_{HHX} (K)	h (W/(m ² •K))
Without fins	-6.08	59.50%	40.50%	-85.85	852.16	-173.69
With fins	-6.97	62.25%	37.75%	-76.02	847.34	-212.41

Figure 8 presents a comparison of the temperature and heat flux distribution of the wall surface of the HHX with or without fins. Spiral fins serve to enhance the heat transfer efficiency of the HHX, particularly notable in the lower section of the upper tube. The spiral fins result in an expansion of the heat transfer area, thereby augmenting total accepted heat of the HHX. Simultaneously, spiral fins can enhance the curvature of the HHX surface, causing the fins to face the flue gas and flame from all directions at an increased angle, thus ensuring that heat becomes more concentrated within the larger curvature of the fins. Consequently, the fins on the lower section of the upper tube experience a noticeable increase in both heat flux and temperature.

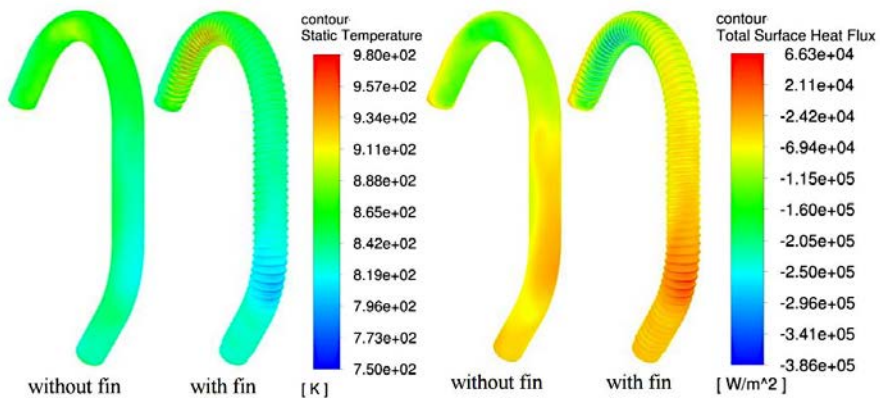


Figure 8. Temperature and heat flux distribution of HHX with or without fins.

Experiments and discussion

Experimental setup

Given the challenges in processing and manufacturing, this paper opted for Model 3 as the arrangement for the fuel nozzle and tubular HHX, serving as the combustor structure for preliminary experimental tests, meanwhile HHX with spiral fins was adopted. The photograph in Figure 9 depicts the lab-developed combustor-coupled FPSG. The combustor side. The FPSG side encompasses measurement such as pressure, piston acceleration, and cooling water flow rate. Two PT100 platinum resistance thermometers and a turbine flow meter are installed at the inlet and outlet of the cooling water circuit to determine the heat rejected by the system. An accelerometer and a PCB dynamic pressure sensor are mounted to capture the acoustic power from the FPSE to the linear alternator. Additionally, an ammeter and a voltmeter are employed to gauge the current and voltage of the external resistance, enabling the calculation of the system's output electrical power. On the combustor side, several sets of K-type thermocouples are installed within the combustor to analyze the energy distribution. Two K-type thermocouples are deployed at the air inlet and combustor outlet, while twelve additional thermocouples are evenly distributed circumferentially on the inner wall surfaces of the combustor, as well as at the top and center of the HHX. Additionally, a gas Roots flow meter and a fan voltage sensor are utilized to measure fuel flow and air flow.

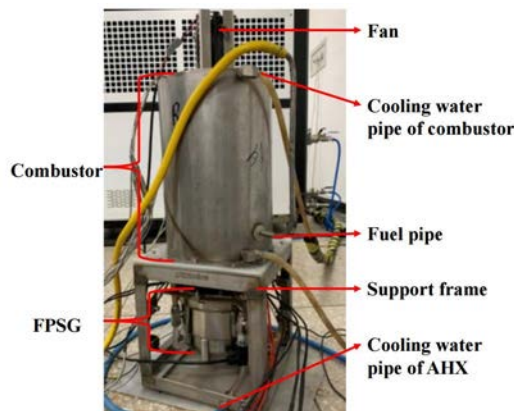


Figure 9. Photograph of a combustor-coupled FPSG prototype.

Experimental results

The performance under rated operating conditions was initially examined. Due to the inability to directly measure the heat accepted by helium in the tubular HHX, this paper considered the sum of the heat rejected (Q_c) by the ambient-temperature heat exchanger (AHX) and the linear alternator, along with the output electric power, as the heat accepted by the HHX. The experimental results were obtained under rated operating conditions with an LPG flow rate of 0.54 Nm³/h and an external resistance of 20 Ω . Fix a fuel flow rate, adjust the fan voltage to obtain the optimal output electrical power. The generator's charge pressure was set at 4.6 MPa, and the operating conditions for the cooling water circulation in the AHX were maintained at 0.45 m³/h at 25 °C. Table 4 presents the fundamental performance of the system under rated operating conditions. The temperature of HHX (T_{HHX}) wall surface of is 884 K, the heat accepted by the HHX is 4.74 kW, and the output electrical power (W_e) is 1.53 kW.

Table 4. Performance of the system under rated operating conditions.

f (Hz)	X_{pis} (mm)	T_{HHX} (K)	Q_h (kW)	Q_c (kW)	W_e (kW)	η_{-e}
83.61	5.30	884	4.74	3.20	1.53	32.4%

Figure 10 illustrates the energy flow distribution within combustor-coupled FPSG system under rated operating conditions. Approximately 68.1% of the energy entering the system exits the combustor in the form of high temperature flue gas about 1147 K, wall heat loss, and incomplete combustion of the fuel, while only 30.1% of the energy (4.74 kW) is absorbed by the FPSG and utilized for power generation. This broadly corresponds to the findings from the simulations with fins as listed in Table 3. Some of the heat accepted by the FPSE is converted into acoustic power, amounting to 1.85 kW, while the remaining heat is rejected through cooling water circulation via the AHX and the linear alternator. The output electrical power of the linear alternator is 1.53 kW with an acoustic-to-electric efficiency of 82.9%. Correspondingly, the fuel-to-electricity efficiency and thermal-to-electric efficiency are 9.8% and 32.4%, respectively. The predominant factor contributing to the system's unsatisfactory fuel-to-electric efficiency during the conversion and transfer of energy lies in the low heat absorption efficiency of combustor. In the next phase, embracing Model 2's configuration of nozzles and tubular HHX holds promise for enhancing the combustor's heat absorption efficiency. Additionally, by repurposing the

high-temperature flue gases—whether for preheating inhaled air, for heating supply, or for heat storage—it presents an opportunity to elevate fuel-to-electricity efficiency up to 30% or achieve an energy utilization efficiency beyond 90%.

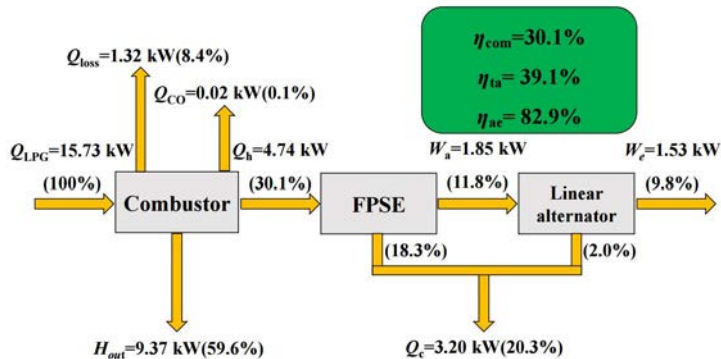


Figure 10. Temperature and heat flux distribution of HHX with or without fins.

Conclusion

This paper presented a novel gas combustor design characterized by distributed multiple nozzles and top-discharged flue gas, and an extensive series of simulation and experimental studies were undertaken to evaluate the performance of the novel gas combustor-coupled 1.5 kW FPSC system. Simulations were conducted to meticulously examine the effects of nozzle and tubular HHX arrangement, as well as tubular HHX with or without fins, on the flow field, temperature distribution, and heat flux within the combustor. Concurrently, experimental analyses were carried out to evaluate the system's performance and energy flow. The primary conclusions drawn from these investigations are outlined as follows:

- (1) For each nozzle and tubular HHX arrangement, the heat accepted by the HHX peaks at a specific air-fuel ratio. Model 2 outperforms other arrangements in terms of the heat accepted of HHX, temperature uniformity, and heat flux uniformity. At a fuel flow rate of $0.55 \text{ Nm}^3/\text{h}$ and an air-fuel ratio of 18, the HHX absorbs 6.67 kW of heat, with convection contributing 66% and radiation 34%.
- (2) Spiral fins boost the heat accepted and coefficient of heat transfer of the HHX notably, from 6.08 kW and $173.69 \text{ W/m}^2\cdot\text{K}$ to 6.97 kW and $212.41 \text{ W/m}^2\cdot\text{K}$, showing increases of

14.63% and 22.29%, respectively. This enhancement is due to the combined effects of expanded heat transfer area and surface curvature.

(3) The experiments reveal that the system generates 1.53 kW of output electrical power with an LPG flow rate of 0.54 Nm³/h and an external resistance of 20 Ω, corresponding to fuel-to-electricity efficiency and thermal-to-electric efficiency of 9.8% and 32.4%, respectively. About 68.1% of the energy entering the combustor exits without being utilized, while only 30.1% is absorbed by the FPSC for power generation.

Acknowledgements

This work was financially supported by National Natural Science Foundation of China (Grant No. 51876214) and the National Key Research and Development Program of China (No. 2021YFC28026003).

References

- [1] Jia Z, Wang R, Hu J, Zhang L, Wu Z, Chen Y, et al. Study on the coupling between engine and alternator in a free-piston Stirling generator. *Applied Thermal Engineering* 2022;217:119222.
- [2] Jiang Z, Xu J, Yu G, Yang R, Wu Z, Hu J, et al. A Stirling generator with multiple bypass expansion for variable-temperature waste heat recovery. *Applied Energy* 2023;329:120242.
- [3] Gu L, Li Y, Wen X, Zhong S, Shen R, Zheng R, et al. Research on a new type of solar dish Stirling cogeneration system based on adjustable receiver and control strategy. *Energy Conversion and Management* 2021;249:114836.
- [4] Zhu S, Yu G, Liang K, Dai W, Luo E. A review of Stirling-engine-based combined heat and power technology. *Applied Energy* 2021;294:116965.
- [5] Yun J, Kim I, Kim D. Hybrid energy harvesting system based on Stirling engine towards next-generation heat recovery system in industrial fields. *Nano Energy* 2021;90:106508.
- [6] Parente A, Galletti C, Riccardi J, Schiavetti M, Tognotti L. Experimental and numerical investigation of a micro-CHP flameless unit. *Applied Energy* 2012;89:203–14.
- [7] Cardozo E, Erlich C, Malmquist A, Alejo L. Integration of a woodpellet burner and a Stirling engine to produce residential heat and power. *Applied Thermal Engineering* 2014;73:671–80.

- [8] Cardozo E, Malmquist A. Performance comparison between the use of wood and sugarcane bagasse pellets in a Stirling engine micro-CHP system. *Applied Thermal Engineering* 2019;159:113945.
- [9] Solomon L, Qiu S. Computational analysis of external heat transfer for a tubular Stirling converter. *Applied Thermal Engineering* 2018;137:134–41.
- [10] Qiu S, Gao Y, Rinker G, Yanaga K. Development of an advanced free-piston Stirling engine for micro combined heating and power application. *Applied Energy* 2019;235:987–1000.
- [11] Kim D-J, Park J-S, Sim K. Development and performance measurements of a 2.5 kW-class free-piston Stirling converter with detailed design and fabrication processes. *Energy Reports* 2022;8:15011–26.

An Integration Model and Performance Measurement of a Stirling Generation System

Yuan-Chun Cheng^{a,*}, Cai-Shuo Yin^a, Hang-Suin Yang^a

a Department of Mechanical Engineering, Institution of National Chung Cheng University No.168, Sec. 1, University Rd., Minhsiung, Chiayi, Taiwan 621301, R.O.C.

*Corresponding author: ethano882@gmail.com

Keywords: Beta type, Stirling engine, Generator, Integration model, Performance measurement

Abstract

This study proposes a Stirling generation system and simulates the operation of a beta-type Stirling engine with a generator. The behavior and performance of the system are evaluated through numerical simulations of torque, voltage, and current, which are then compared with experimental results. The investigation includes different working temperatures, charged pressures, and various external electrical loads to explore the shaft power of the engine and the electrical power of the generator.

The experimental setup is divided into two systems, namely the engine and the generator. The engine was halted gradually by a hysteresis brake, and the torque and speed during this process were recorded. The results indicate that the torques decreases as the engine speed increased. The torques exerted on the generator under different electric loads and rotating speed were measured as shown in Fig. 1. The intersection points of the torque curves for the engine and generator at the same speed represent the stable operating points of the generation system. Then the shaft power and electrical power of the system at the stable operating conditions can be obtained from these points as shown in Fig. 2. The numerical model proposed in this paper is established by measuring the relationship between the torque of generator, the rotor current, and the rotating speed. The simulated torque, voltage, and current are validated with experimental data. The shaft power and electrical power of the overall system under various loads, heating temperatures, and charged pressures can be predicted using the proposed model.

The results reveal that the torque of generator increases with rotating speed before 2800 rpm, then decreases as the speed higher than that value. The decrement in torque is caused by the decrement in the rotor current for preventing overload. The generator exhibits a maximum torque of $5.6 \text{ N}\cdot\text{m}$ at 2800 rpm with an external electrical load of 25 ohms. The numerical results reveal that the maximum shaft and electrical power of the system can reach 664 W and 545 W, respectively, under a heating temperature of 1073 K and a charged pressure of 10 bar.

Introduction

With the vigorous development of technology, the electricity demand has surged rapidly with the vigorous development of technology that resulted in a great of emissions of

carbon dioxide, global warming, and climate change. Therefore, carbon reduction has become an important issue in recent years. For these reasons, people searched the renewable energies, such as solar power, wind power, and hydropower.

The Stirling power generation system is a remarkable technology that offers numerous advantages. It has the highest thermal efficiency than other thermal cycles, thus making it a more efficient method to generate electricity. Another benefit is that it can be operated using various heat sources, such as geothermal energy, waste heat, or solar thermal energy. Therefore, the Stirling technology has been applied in many fields.

When evaluating the performance of a power generation system, it's essential to consider both the engine and generator systems. Therefore, the experimental setup is divided into two systems, namely the engine and the generator. The compatibility and stability between these components within a given operating range are important. To obtain the capabilities of the power generation systems and the optimal environment for operating the systems, the testing of the system under different charged pressures, heating temperatures, electric loading, and generator operation conditions.

For this purpose, we established a general numerical model of a beta-type Stirling engine with a rhombic drive mechanism based on a modified non-ideal adiabatic model [2]. To delve deeply into the stable operating region of Stirling generation systems, a numerical model for the generator was built based on the experimental data. With the help of the proposed model, the electrical power of the Stirling generation system under varying external electrical loads can be predicted.

Theoretical model and experimental apparatus

Experimental apparatus

To validate the proposed theoretical model, an engine testing platform and a power generation measurement platform were built. The testing platform is equipped with a beta-type Stirling engine that uses a rhombic-drive mechanism. The engine serves as the power source for the generator. The basic specifications of the proposed engine are provided in Table 1. Figure 1 illustrates the schematic of the testing platform which includes a gearbox, a starter motor, a torque-speed transducer, and two hysteresis brakes. The gearbox and starter motor are used to start the engine. After the engine running steadily, the brake torque was exerted gradually by the hysteresis brakes. The torque and speed were recorded simultaneously by the torque-speed sensor.

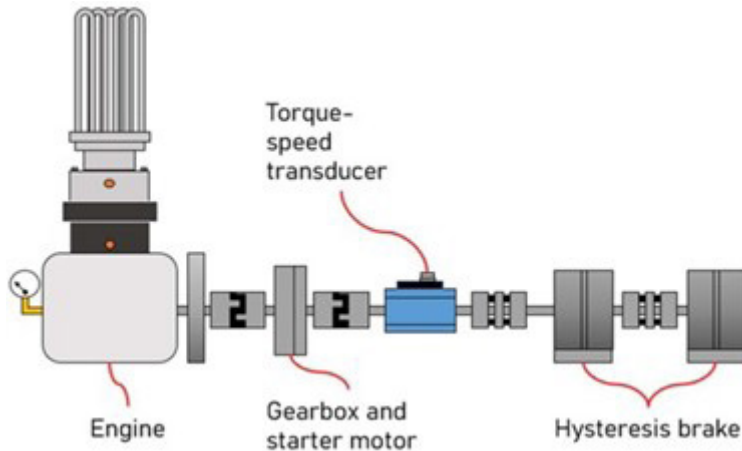


Figure 1. Schematic of the engine testing platform.

Table 2. Basic specifications of the proposed engine.

Power capacity (W)	200~1500
Working fluid	Helium
Charged pressure (bar)	2~15
Heater type	Tube heat exchanger
Cooler type	Finned heat exchanger
Regenerator type	Wire mesh
Heating temperature (K)	873~1073
Cooling temperature (K)	300

To obtain the comprehensive performance of the generator, the testing platform was established as illustrated in figure 2. The platform is composed of a starter motor, an electronic loading, and a torque-speed transducer which is utilized to measure the torque, speed, and electrical power of the generator. In this study, a single-phase AC generator was used. The basic specifications are listed in Table 2. The starter motor is used to drive the generator. The torque, current, and voltage of the generator under different speeds and electrical loading were recorded.

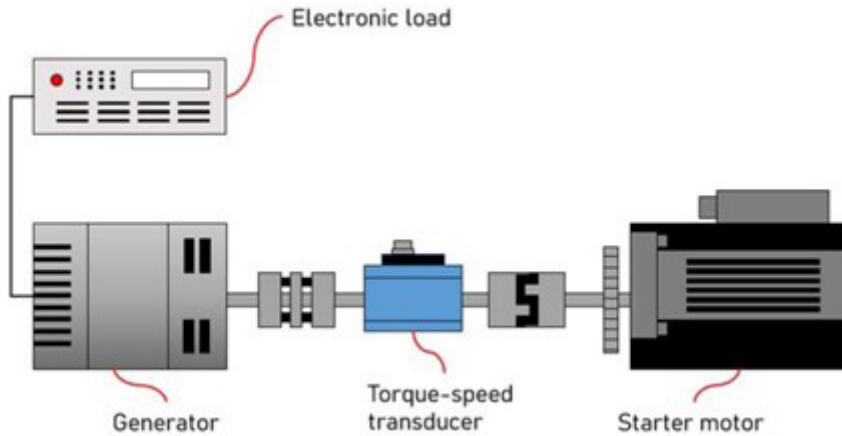


Figure 2. Schematic of the generator testing platform.

Table 2. Basic specifications of the generator.

Stator inner diameter (m)	0.12
Stator outer diameter (m)	0.19
Rotor outer diameter (m)	0.117
Stator length (m)	0.125
Rotor length (m)	0.13
Stator winding turns	560
Rotor winding turns	1200
Stator resistance (ohms)	18
Rotor resistance (ohms)	10

It is important to establish the relationship between the engine and generator in practical situations which is to identify the stable operating point. Figure 3 shows the performance curves of the engine and generator. The results reveal that both of them exist cross point. In the low-speed region, the torque produced by the engine exceeds the torque consumed by the generator which increases operating speed. On the contract, in the high-speed region, the operating speed decreases because the torque produced by the engine is lower than the torque consumed by the generator. Eventually, the operating

speed will approach the cross point. This point is called the stable operating point. The electrical and shaft power output of the generation system under various input and loading conditions can be determined.

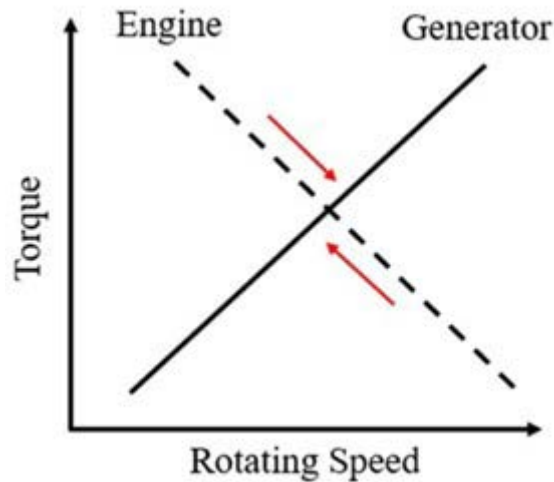


Figure 3. Schematic of the stable operating point.

Theoretical model

This study utilized an engine model that drew from the thermodynamic and dynamic models developed by Yang's research [2]. To analyze the generation system, the electric and magnetic models were combined with the engine model.

The generator used in this study is composed of a rotor and a stator. The rotor was excited by a given current which is used to generate magnetic flux, and the derivative electromotive force can be evaluated using Ampère's law. The induction electromotive force in the stator generated by the rotor can be predicted by Faraday's law. The current and voltage in the stator can be obtained using Kirchhoff's laws. Then the generator's performance can be obtained.

Through the experimental measurements, the correlation between the generator torque and rotor current can be established. It was observed that the torque varied with different rotor speeds and rotor currents. To build their relationship, the rotor current was segregated into two regions: the low-speed region ranging from 1500 to 2800 rpm,

and the high-speed region spanning from 2800 to 3600 rpm. The formula for the rotor current is shown below.

$$i_r = \begin{cases} a\omega^2 + b\omega + c & , 1500 \leq \omega \leq 2800 \text{ rpm} \\ i_f + (i_i - i_f) \exp(-d(\omega - \omega_{\max})) & , 2800 < \omega \leq 3600 \text{ rpm} \end{cases} \quad (1)$$

In this equation, ω represents the rotational speed, i_i denotes the current magnitude at 2800 rpm, and i_f represents the current magnitude at 3600 rpm.

Using the above equation, the rotor current magnitude can be simulated at different rotational speeds. Then the rotor torque can be obtained as follows:

$$\tau_{rot} = \frac{i_r^2 R_r}{\omega} \quad (2)$$

The electrical power and shaft power can be obtained separately through Eqs. (1) and (2). The shaft power can be calculated by:

$$\dot{W}_{shaft} = \tau_{rot} \omega \quad (3)$$

The power consumed by the rotor can be calculated by:

$$\dot{W}_{ele,load} = 4R_{load} i_s^2 \quad (4)$$

Result and Discussion

In this study, the torques exerted on the rotor of the generator under different electrical loads and rotational speeds were measured to determine the rotor current. The torque of the rotor is shown in Fig. 4. The results indicate that torque increases with rotating speed until 2800 rpm, then it decreases with rotating speed. The decrement in the torque is caused by the reduction in the magnitude of the rotor current which is used to prevent the overloading in the generator. To compare the torque at the same rotating speed, it can be found that the torque decreases with an increasing external electrical load. Ohm's law indicates that the current decreases as the external electrical load increases under a certain voltage of the generator.

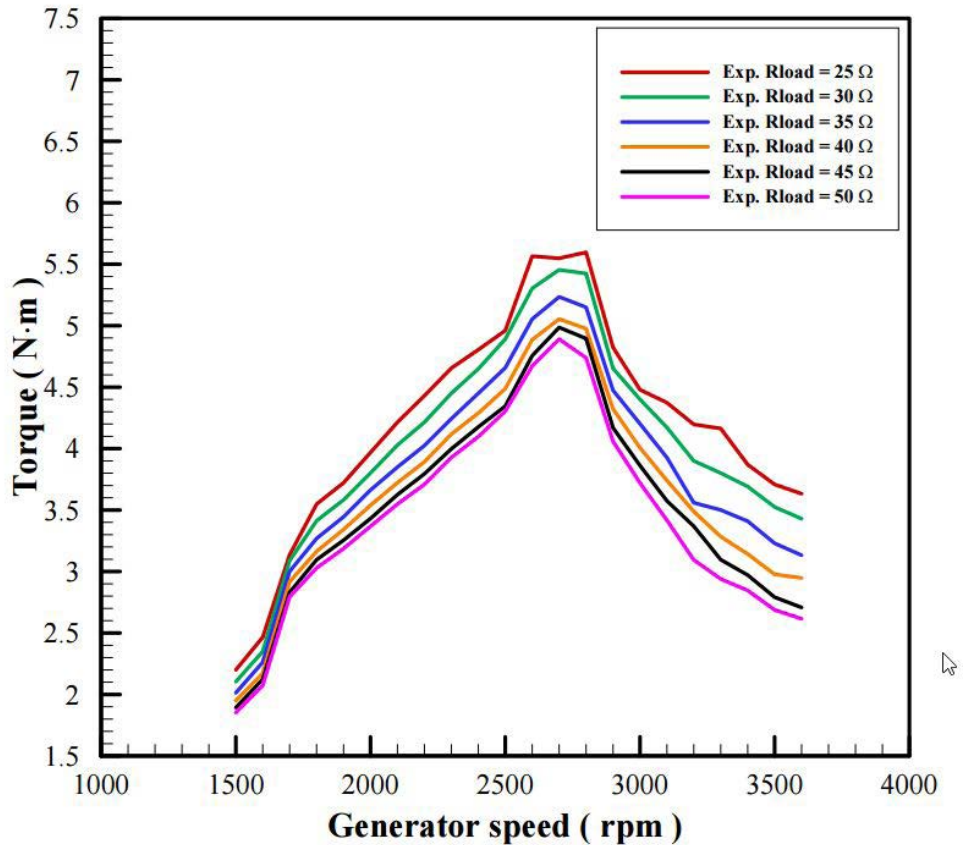


Figure 4. The torque under different rotating speeds and electrical loads.

The rotor current of the generator can be predicted numerically according to the torque. The results of the numerical simulation for rotor current are displayed in Fig. 5. The tendency of the rotor current at different rotating speeds and electrical loads is similar to torque. The current decreases with an increased electrical load.

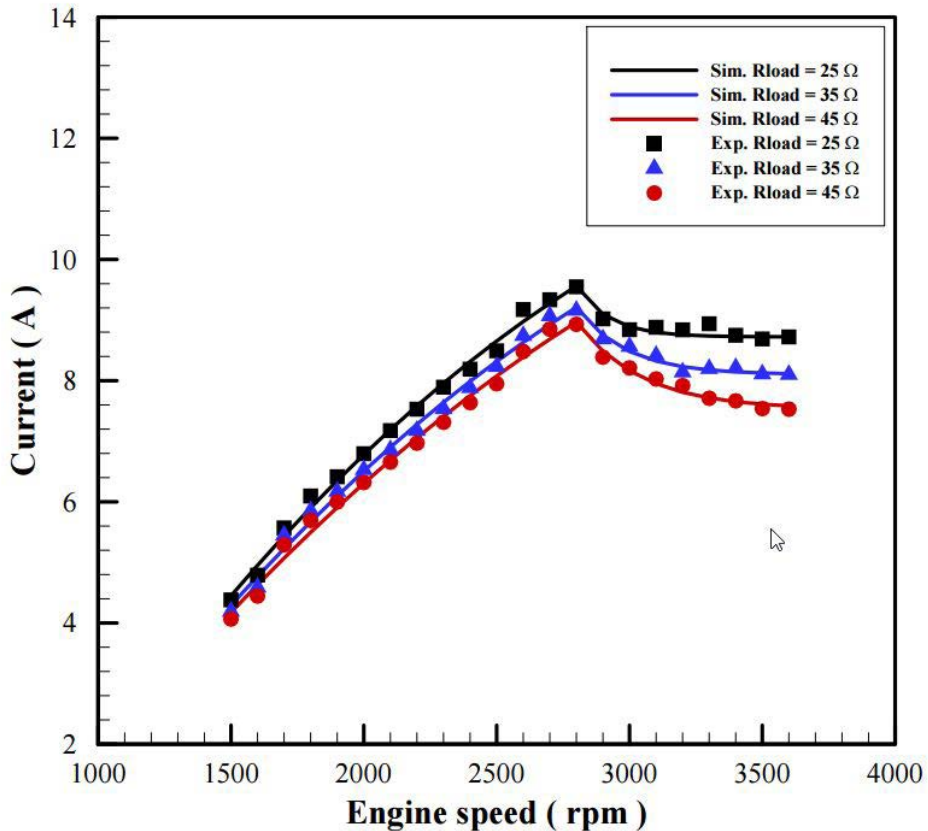


Figure 5. The rotor current under different rotating speeds and electrical loads.

Figure 6 illustrates the torque curves of the engine simulation and generator experimental result, in which the engine speed is increased to match the generator speed using a 1:2 gear ratio. The results reveal that the output torque of the engine decreases with engine speed. As depicted in Fig. 3, the intersection points denote the stable operating points. After obtaining the stable operating points of the generator and the engine, the shaft power can be calculated using Eq. (3), and which results are shown in Fig. 7. Figure 7 illustrates the shaft power under different rotating speeds, charged pressures, and heating temperatures. The results indicate that the maximum shaft power can achieve

664 W at a charged pressure of 10 bar and a heating temperature of 1073 K.

Figure 8 illustrates the electrical power under different rotating speeds, charged pressures, and heating temperatures. The results indicate that the maximum electrical power can approach 500 W at a charging pressure of 10 bar and a working temperature of 1073 K. It can be observed that the power output approaches a maximum value with charged pressure. Because the engine operates at a higher charging pressure requires higher performance of heat exchangers.

Figure 9 illustrates the trend of electrical power under different electrical loads. It can be observed that the electrical power decreases with electrical load. This phenomenon is caused by the reduction in the current as the electrical load increases. Consequently, the overall electrical power declines.

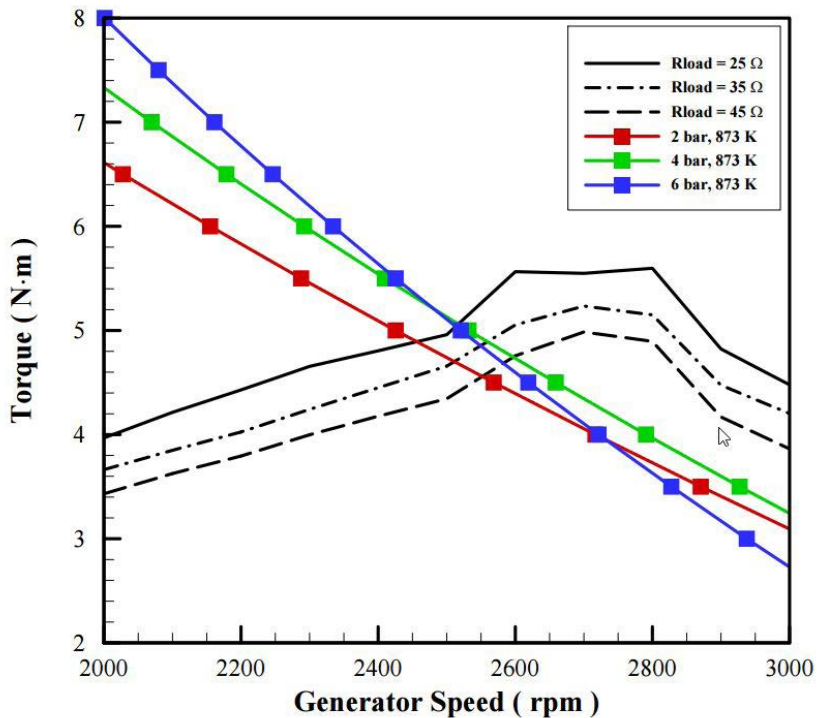


Figure 6. The torque curve of the engine and generator.

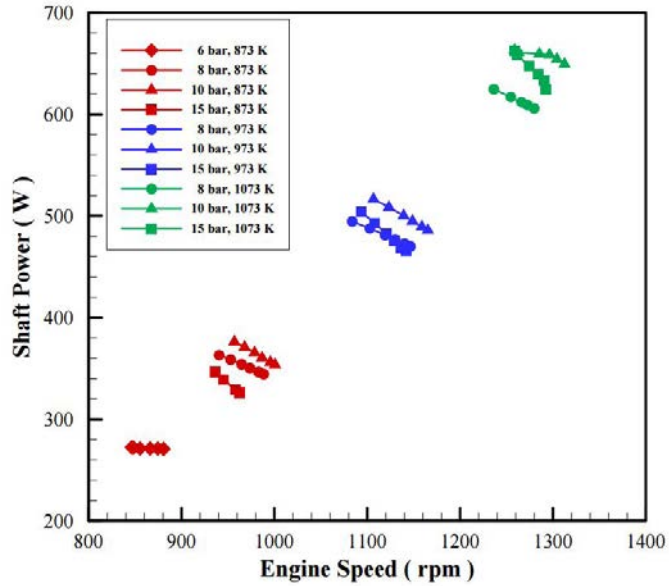


Figure 7. Shaft power of the Stirling generator system.

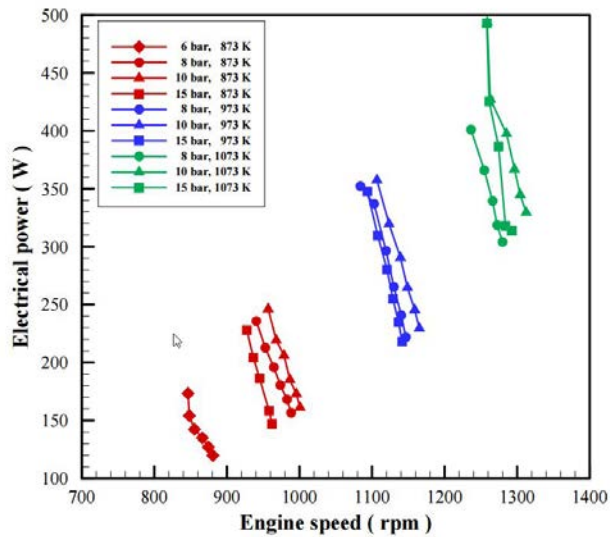


Figure 8. Electrical power of the Stirling generator system.

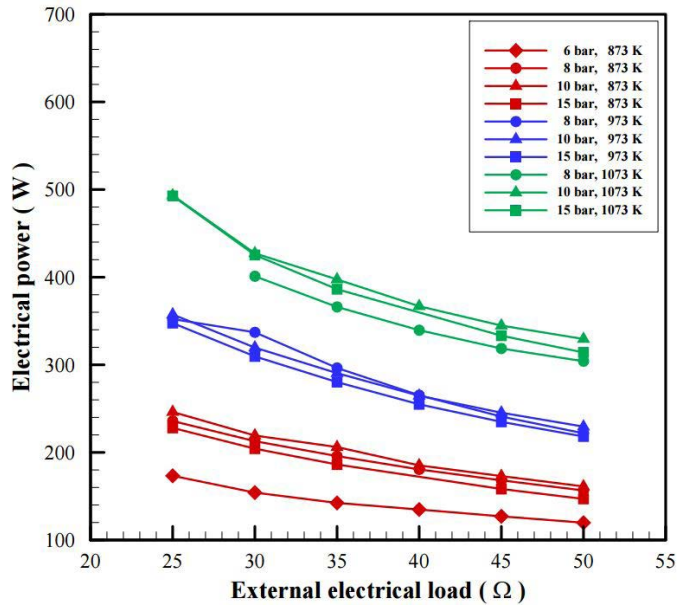


Figure 9. Electrical power versus external electrical load.

Conclusion

The conclusions drawn from this study are as follows.

1. The torque of the generator increases with rotating speed before 2800 rpm, then decreases as the speed is higher than that value. The decrement in torque is caused by the decrement in the rotor current for preventing overload.
2. The generator exhibits a maximum torque of 5.6 N·m at 2800 rpm with an external electrical loading of 25 ohms. However, the torque decreases as the external electrical loading increases which may be caused by the decrease in the current of the rotor.
3. The simulation results indicate that the electrical power produced by the system increases with charged pressure. But the electrical power decreases as the charged pressure exceeds 10 bar.
4. The electrical power and shaft power decreased as the external electrical load increased. The maximum shaft and electrical power of the system can reach 664 W and 545 W, respectively, under a heating temperature of 1073 K and a charged pressure of 10 bar.

Acknowledgements

Authors would like to thank the National Science and Technology Council, Taiwan, for the financial support under grant NSTC 112-2221-E-194-010-MY3.

References

- [1] Uday Raj Singh, Anil Kumar. Review on Solar Stirling Engine. Development and Performance. Thermal Science and Engineering Progress 8 (2018).
- [2] HS Yang, CH Cheng, S Huang. A complete model for dynamic simulation of a 1- Kw class b-type stirling engine with rhombic-drive mechanism. Energy 161: 892-906 (2018).

On Operating Frequency of Three-Stage Double-Acting Fluidyne Stirling Oscillators

A.R. Tavakolpour-Saleh^{a,*}, M. H. Sangdani^a

a Department of Mechanical Engineering, Shiraz University of Technology, Modares BLVD, Shiraz, Iran

***Corresponding author:** tavakolpour@sutech.ac.ir

Keywords: Fluidyne Stirling oscillator, Three-stage, Double-acting, Operating frequency

Abstract

In this work, a prototype three-stage double-acting Fluidyne Stirling oscillator (TDFS0) is developed and tested. Indeed, one of the crucial design parameters affecting the overall performance of such a Stirling system is the engine frequency. Hence, this work is conducted to present an in-depth investigation of the engine frequency and its influencing parameters. First, a dynamic model of the Stirling oscillator is given and then, the effect of temperature difference and dimensions of water column resonators on the engine frequency is studied. Next, the impact of mismatched dimensions of one water column compared to the others on the overall operating frequency of the TDFS0 is assessed. Finally, an experimental TDFS0 is developed and experimentally evaluated to verify the obtained results. Accordingly, the frequency changes of the TDFS0 corresponding to the inconsistency among the water columns' lengths are experimented. It is found that the operating frequency of the TDFS0 is considerably higher than the resonant frequency of the water columns. Besides, the TDFS0 can operate within an allowable range of dimensions of the water columns and the best performance of the system is found once the dimensions of all water columns are matched.

Introduction

In recent years, there has been a growing focus on environmental impact and energy efficiency in energy production. Modern internal combustion engines rely heavily on non-renewable resources such as gasoline and coal, leading to significant air pollution that poses ecological harm and long-term sustainability challenges. Thermoacoustic heat engines offer a promising alternative as external combustion engines with adaptable heating temperatures, making them suitable for harnessing low-grade heat sources like industrial waste heat or solar energy. These engines use eco-friendly working gases such as helium or nitrogen and boast increased durability due to their lack of moving parts. The Three-Stage Double-Acting Fluidyne Stirling Oscillators present an opportunity to further enhance thermoacoustic conversion efficiency, resulting in greater compactness

and improved load matching compared to traditional thermoacoustic engines. By employing gas-liquid coupling vibrations [1], it significantly boosts pressure amplitude and effectively lowers the resonant frequency. Each unit of the heat engine in the looped, double-acting system operates without the need for a phase-adjusting device and can function within an ideal acoustic field [2].

The frequency of systems with a liquid piston is lower than that of systems with a solid piston due to the larger acoustic velocity. These systems also exhibit larger pressure amplitudes, making them desirable for certain applications such as utilization in thermoacoustic engines to drive pulse tube refrigerators [1]. Li et al. [3] introduced a gas-liquid, double-acting traveling-wave thermoacoustic heat engine and conducted both numerical and experimental investigations. To address the challenge of unstable water surfaces under high-frequency large-amplitude oscillations, they devised cylinder floats made of plastic rods that float on the water surface. However, this modification disrupted the self-start mechanism of the engine. To overcome this issue, they utilized an oil-lubricated compressor operating at a frequency of 17 Hz to initiate engine oscillation. Zhang and Luo [4] undertake another numerical investigation on a double-acting traveling-wave thermoacoustic engine with a liquid-water piston using the DeltaEC program. They examine various parameters such as mean pressure, water piston mass, and heating temperature on the system's performance in cases both with and without acoustical load. Their findings indicate that the frequency increases with the mean pressure of the system and decreases with the increase of water piston mass. Li et al. investigate the influence of mean pressure on the frequency of system for different operating gas and they report that system has higher frequency with helium as the operating gas. Li et al. [5] investigate the influence of mean pressure on the frequency of the system for different operating gases, reporting that the system exhibits a higher frequency with helium as the operating gas.

According to a wide range of applications of TDFSO in thermoacoustic electrical generators, thermoacoustic pumps, thermoacoustic cryocoolers etc. this work has been focused on such advanced Stirling converters. The main purpose of this study is to investigate the effect of design parameters on the frequency of a three-stage double-acting Fluidyne Stirling engine. Both simulation and experiment are considered in this work to support the claims. First, a numerical model of system is obtained and then, the

effect of temperature difference, water column length, and mismatched water column length on the system frequency is checked via root locus technique. Another issue that will be examined in this study is the comparison between the working frequency of the engine and the natural frequency of the U-tubes. At the end, a three-phase experimental double-acting thermoacoustic Stirling engine, equipped with water column resonators, is fabricated and tested to validate the outcomes anticipated by the proposed analytical model.

Three-stage double-acting Fluidyne Stirling oscillator

The system in Figure 1 is a new type of engine that uses sound waves and heat. It has three identical sections, each containing a hot heat exchanger (HHX), a main cold heat exchanger (MCHX), a secondary cold heat exchanger (SCHX), a thermal buffer tube (PT), a U-shaped resonator, a regenerator (REG) and a linear alternator. It's valuable to note that the thermal buffer tube and the secondary cold heat exchanger serve to shield the expansion piston of the alternator from the high-temperature environment, thereby enhancing the reliability of the alternator, because the alternator has an important role and the useful work is extracted from this part. The key innovation is that the U-shaped tubes are filled with water, which acts like pistons or resonators in the engine. Interestingly, the way these water columns move is similar to how solid pistons move in a different type of engine called a double-acting free-piston Stirling engine.

In a three-phase, double-acting Stirling engine (see Figure 1), each cylinder has only one piston. This unique piston performs both compression and expansion duties simultaneously. One advantage of this type of thermoacoustic engine (TAE) is its ability to efficiently transfer heat from one stage to the next due to its looped design. This contributes to its high overall efficiency. The movement of each water column naturally has a 120-degree phase difference compared to its two neighboring columns.

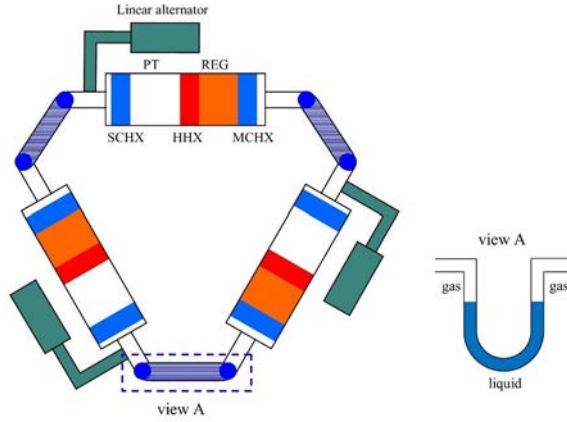


Figure 1. Schematic of the TDFS0.

Mathematical scheme

In this section, an appropriate mechanical model is acquired for TDFS0. Initially, the dynamic equation of a single U-tube is introduced, followed by the derivation of the overall dynamics of the TDFS0, which integrates the dynamics of the U-tube in accordance with Schmidt's theory.

Based on Figure 2 and according to the Newton's second law of motion (Equation 1), the dynamic equation of a single U-tube is obtained as Equation 2.

$$\ddot{h} + \frac{32\mu}{\rho d^2} \dot{h} + \frac{2g}{L} h = \frac{1}{\rho L} (P - P_0) \quad (1)$$

ρ is the density of the liquid and μ is viscosity of the liquid, d is diameter of pipe, L is total length of U-tube in one stage, m is total mass of liquid in one U-tube, P is pressure and P_0 is initial pressure of working gas.

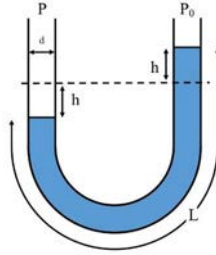


Figure 2. A U-tube with pressure difference at both ends.

As said before the dynamic equations of TDFS0 is obtained based on Schmidt's theory. So, based on this theory and Figure 3 the dynamic equations of TDFS0 are acquired as follows.

□

$$\ddot{h}_1 + \frac{32\mu}{\rho d^2} \dot{h}_1 + \frac{2g}{L_1} h_1 = \frac{1}{\rho L_1} (P_1 - P_2) \quad (2)$$

$$\ddot{h}_2 + \frac{32\mu}{\rho d^2} \dot{h}_2 + \frac{2g}{L_2} h_2 = \frac{1}{\rho L_2} (P_2 - P_3) \quad (3)$$

$$\ddot{h}_3 + \frac{32\mu}{\rho d^2} \dot{h}_3 + \frac{2g}{L_3} h_3 = \frac{1}{\rho L_3} (P_3 - P_1) \quad (4)$$

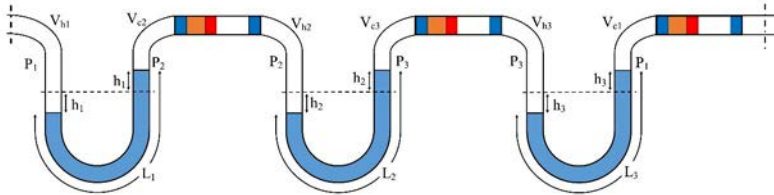


Figure 3. A schematic of the TDFS0 with the corresponding parameters.

The Schmidt's theory and the ideal gas law ($PV = mRT$) can be combined to determine the instantaneous pressure of the working gas within the engine [6].

]

$$\hat{P}_1 = m_1 \left(\frac{V_{h1}}{RT_h} + \frac{V_{c1}}{RT_c} \right)^{-1} \quad (5)$$

407 °C on the engine frequency was studied once the water column length was 0.36 m corresponding to two column diameters of 0.019 m and 0.025 m.

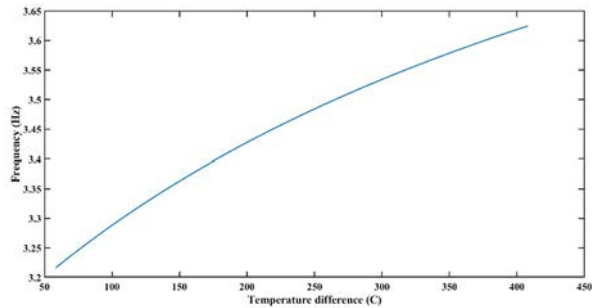


Figure 4. Frequency versus temperature difference within the range 57 C – 407 C for water column of 0.36 m and U-tube diameter of 0.019 m ($T_c = 20$ °C).

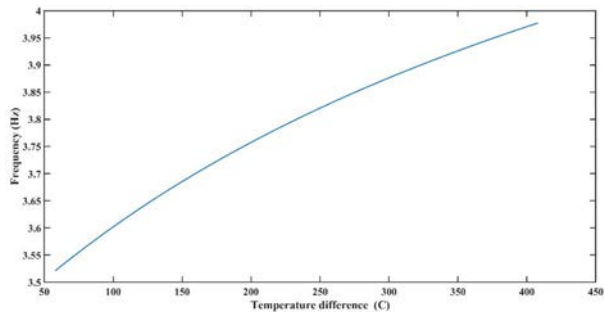


Figure 5. Frequency versus onset temperature difference within the range 57 C – 407 C for water column of 0.36 m and U-tube diameter of 0.025 m ($T_c = 20$ °C).

As seen in Figures 4 and 5, increasing the temperature difference results in an increase in the oscillator frequency from 3.52 Hz to 3.97 Hz in the startup moment meaning that the engine frequency is not so sensitive to the temperature difference.

Effect of water column length on the oscillator frequency

In this section, an exploration is undertaken on how changes in the length of the water column (ranging from 0.36 m to 0.8 m at diameters of 0.019 m and 0.025 m) affect the engine frequency, while ensuring consistency in the water column lengths across all U-tube resonators (referred to as matched water columns). Effect of water column length on the frequency is depicted in figures 6 and 7 based on the numerical simulation.

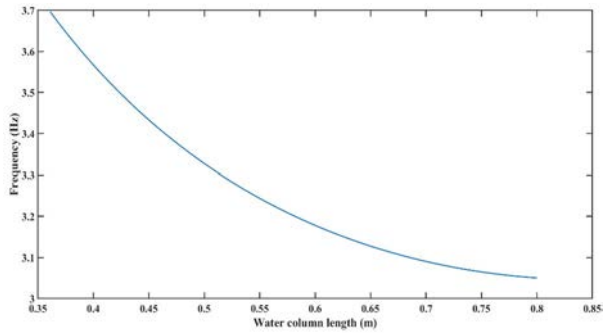


Figure 6. Frequency versus water column length for U-tube diameter of 0.019 m.

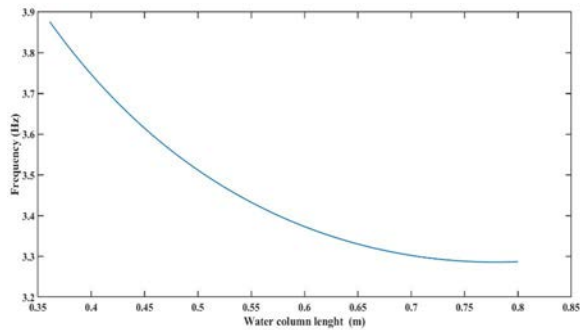


Figure 7. Frequency versus water column length for U-tube diameter of 0.025 m.

As can be seen, the frequency is decreased by increasing the water column length while increasing the diameter results in increasing the engine frequency in the startup moment. It is important to note that this conclusion is valid over the considered range of diameter variations.

Effect of mismatched water column length on the oscillator frequency

In order to investigate this issue, the length of water columns remains constant at 0.48 m in two of the U-tubes, while in the third, the length of the water column varies from 0.34 m to 0.8 m. This study considers two water column diameters of 0.019 m and 0.025 m, respectively. The results are shown in figures 8 and 9.

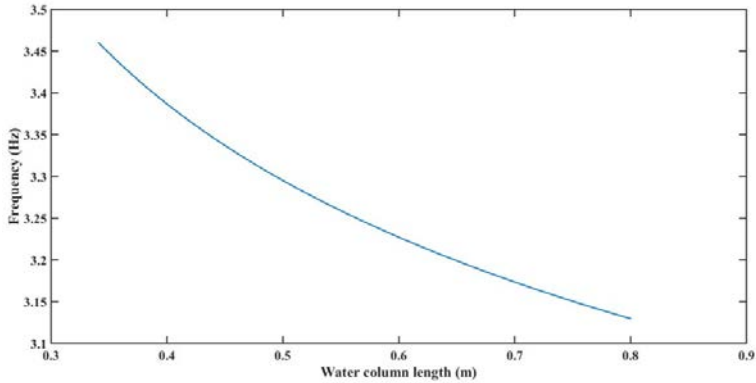


Figure 8. Frequency versus mismatched water column length in one U-tube (diameter = 0.019m).

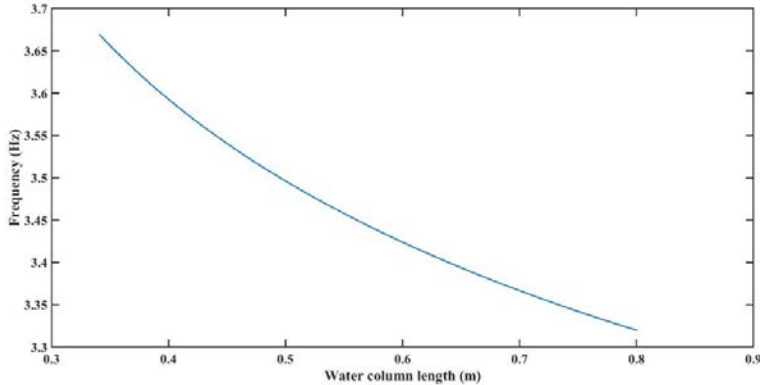


Figure 9. Frequency versus mismatched water column length in one U-tube (diameter = 0.025 m).

The figures show that increasing the water column length decreases the frequency of the system.

Experimental study

In this section, a prototype of the TDFSO with water column resonators (figure 10) is constructed and tested to validate the obtained results of previous section. An MPXV7002 pressure module is utilized to measure working gas pressure and system frequency (based on fast Fourier transform (FFT) of the pressure signal). An NI-USB6009 data acquisition system with 14-bit resolution (for analog input channels) is employed to log the measured data. In the following, the effect of water column length and mismatch

water column length on the operating frequency of the Stirling oscillator is investigated experimentally.

Effect of matched water columns lengths on oscillator frequency

The frequency of the system is calculated through the FFT of the pressure signal. The frequency is obtained for three water column length of 0.019 m. The results and comparison with simulation outcomes are shown in Table 1. As can be seen, the frequency is diminished as the water column length is augmented.



Figure 10. The developed three-stage double-acting Fluidyne Stirling oscillator.

Table 1. Comparison of experimental and simulation operating frequency of the Stirling oscillator corresponding to various water column lengths.

Water column length (m)	Working frequency of the engine (Hz) (experiment)	Working frequency of the engine (Hz) (simulation)
0.52	3.14	3.29
0.44	3.34	3.45
0.36	3.55	3.7

Now, an important question may arise about the consistency of the overall operating frequency with that of a single water column within the U-tube. In order to peruse this issue, the natural frequency of a single water column possessing the lengths considered in Table 1 is obtained (see Table 2). Comparing the experimental results of Tables 1 and 2 reveals that the overall operating frequency of the Stirling oscillator is considerably higher than natural frequency of a single water column within a U-tube. This latest finding can be attributed to the fact that the working gas trapped between the two adjacent water columns behave as a gas spring with significant stiffness. Consequently, such a significant stiffness affects the overall operating frequency of the oscillator rather than the mass and dimensions of water columns in the U-tubes.

Table 2. Natural frequency of a U-tube for various water column lengths.

Water column length (m)	Natural frequency of water columns (Hz)
0.52	0.81
0.44	1
0.36	1.1

Effects of mismatched water columns lengths on oscillator frequency

To experimentally explore the impact of mismatched lengths of water columns in the U-tube resonators on system frequency, the lengths of water columns in two of the U-tube resonators are maintained at a constant value of 0.48 m, while the length of the water column in only one of the U-tubes is altered. The experiment is done for 0.019 m of U-tube diameter considering the water column length between 0.4 m and 0.56 m. The results can be seen in Table 3.

Table 3. Comparison of experimental and simulation operating frequency of the TDFSO with a mismatched water column length.

Water column length of mismatched resonator (m)	Operating frequency (Hz) (experiment)	Operating frequency (Hz) (simulation)
0.40	3.28	3.38
0.44	3.24	3.34
0.48*	3.23	3.31
0.52	3.19	3.28
0.56	3.19	3.25

*Matched water column length

It is worth noting that reducing the water column length in only one U-tube lower than the matched length (i.e., 0.48 m) increases the overall operating frequency of the Stirling oscillator; whereas, increasing the water column length beyond the matched length decreases the operating frequency.

Conclusion

This work focused on analyzing the frequency of a three-stage double-acting Fluidyne Stirling engine under various situations. Initially, a mechanical model was proposed for the system in the state-space and the applicability of the proposed model to predict operating frequency of the Fluidyne Stirling oscillator was evaluated. The results indicated that increasing the temperature differences resulted in a smooth increase of the engine frequency meaning that the system frequency is not considerably affected by the temperature changes (above the onset temperature). It implied that the proposed Fluidyne Stirling oscillator was operated within a limit cycle which was robust to parameter changes. Hence, a further nonlinear analysis is recommended. It was found that the frequency increased from 3.2 Hz to 3.6 Hz when the temperature differences got higher from 57 °C to 407 °C for water column diameters of 0.019 m. Similarly, for the same range of temperature differences but with water column diameter of 0.025 m, the frequency increased from 3.5 Hz to 3.95 Hz. The influence of water column length on the frequency was another parameter that was investigated. The outcomes demonstrated that increasing the matched water columns lengths decreased the overall frequency of the system. The analysis was conducted for both U-tube diameters of 0.019 m and 0.025

m. Accordingly, the frequency decreased from 3.7 Hz to 3.1 Hz for a diameter of 0.019 m and from 3.9 Hz to 3.3 Hz for a diameter of 0.025 m when the water column length increased from 0.36 m to 0.8 m. Finally, the influence of mismatched water column lengths on the overall frequency of the system was studied. To address this issue, a water column length of 0.48 m was considered constant in two U-tubes, while in the third U-tube, the length of the water column varied from 0.34 m to 0.8 m. The results indicated that increasing the water column length in one mismatched U-tube caused the overall frequency to be decreased. A significant finding of this study was to show the discrepancy between the overall operating frequency of the engine and the resonant frequency of the U-shaped resonators which was affirmed experimentally.

References

1. Tang, K., et al., A standing-wave thermoacoustic engine with gas-liquid coupling oscillation. *Applied Physics Letters*, 2009. 94(25).
2. Swift, G.W., *Thermoacoustics: A unifying perspective for some engines and refrigerators*. 2003, Acoustical society of America.
3. Li, D.H., et al., Numerical simulation and experimental investigation of a gas-liquid, double-acting traveling-wave thermoacoustic heat engine. *International journal of energy research*, 2013. 37(15): p. 1963-1970.
4. Zhang, S. and E. Luo, The thermodynamic performance of a double-acting traveling-wave thermoacoustic engine with liquid-water piston. *International Journal of Green Energy*, 2015. 12(3): p. 198-206.
5. Li, D.-H., et al., Study of a liquid-piston traveling-wave thermoacoustic heat engine with different working gases. *Energy*, 2014. 74: p. 158-163.
6. Yang, H.-S., Numerical model for predicting the performance and transient behavior of a gamma-type free piston Stirling engine. *Applied Thermal Engineering*, 2021. 185: p. 116375.

Field test of a diesel powered 300 We free-piston Stirling electric generator

Wang Xiao^{a,b,c}, Guoyao Yu^{a,b,d,*}, Ying Ma^a, Zhuang Ma^a, Yangbin Cheng^a, Shuibing Jiang^e, Ercang Luo^{a,b,c}

a Key Laboratory of Cryogenics, Technical Institute of Physics and Chemistry, Chinese Academy of Sciences, Beijing 100190, China

b Key Laboratory of Cryogenic Science and Technology, Beijing 100190, China

c University of Chinese Academy of Sciences, Beijing 100049, China

d Institute of Optical Physics and Engineering Technology, Qilu Zhongke, Jinan 251000, China
e Beijing Zhongke Thermoacoustic New Energy Technology Co., Ltd., Beijing 100005, China

*Corresponding author: gyyu@mail.ipc.ac.cn

Keywords: Field test, Diesel powered, Free-piston Stirling generator, Computational fluid dynamics, Ultra-high frequency

Abstract

Free Piston Stirling Generators (FPSGs) are renowned for their quiet operation, compact design, and efficiency, making them highly regarded for portable power applications. Their external-combustion attributes not only facilitate extended range but also offer exceptional adaptability to various fuels. Crucially, the combustion process of FPSGs is stable, continuous, and more manageable compared to internal-combustion engines. This endows a distinct competitive edge, particularly in challenging environments where internal-combustion engines falter, such as harsh field with rarefied air or extremely low temperatures.

In this study, we developed a 300 We-class portable power using an ultra-high-frequency FPSG driven by a Porous Media Evaporative Combustor (PMEC). The FPSG's design and optimization leveraged a quasi-one-dimensional thermoacoustic analysis method, while a three-dimensional Computational Fluid Dynamics (CFD) approach elucidated the comprehensive combustion process, encompassing diesel fuel combustion, and gas-solid heat transfer. Notably, we scrutinized the impact of thin and low-temperature fresh air on the combustion process. Comprehensive performance parameters, including solid temperatures of the hot-end heat exchanger, cooling water temperatures, output electrical power, voltage, current, PMEC exhaust gas temperatures, and key flue gas constituents such as CO, O₂, CO₂, NO/NO_x, were meticulously measured. Our findings underscore the FPSG's robust adaptability, especially in high-altitude and low-temperature settings.

Experimental results revealed that the system operates at an ultra-high frequency of up to 135 Hz, resulting in a peak electrical power output of 415 W with a diesel mass flow rate of 245 g/h. The fuel-electricity efficiency, calculated based on the low heating value of the diesel fuel, stands at 13.9%. Moreover, the stand-alone generator body achieves a specific power of 112 W/kg. The enhancement of air supply has led to improved combustion efficiency across all tested air supply parameters at varying altitudes. Specifically, the output power of the FPSG tends to increase with higher air supply at elevated locations, while conversely, the output power decreases at lower altitudes due to increased flue gas heat loss. Impressively, at an altitude of 2800 m, the output electric power

at the same fuel-air parameters decreases by approximately 30 W compared to 20 m altitudes, and the total system efficiency drops by about 1.3 percentage points. Even at altitudes of 4,600 m and temperatures plunging to -13 °C, coupled with a reduced oxygen content of 13.18%, although the combustion adequacy deteriorates significantly for the same fuel-air parameters, the decrease in power generation diminishes gradually. These challenges can be mitigated by further increasing the air supply, demonstrating its exceptional adaptability to extreme environments.

Introduction

The emergence of complex and diverse outdoor power usage scenarios, such as outdoor exploration and emergency rescue, arouses the enthusiasm of portable power sources in the hundreds of watts range [1]. In response to these surging demands, researchers have proposed various paths of portable power technology, whereas most of them in vain due to insufficient power density, poor environment adaptability, high noise levels, low intelligence, and high lifetime cost [2–5]. The silent, compact, and efficient characteristics of the free-piston Stirling generator (FPSG) align well with the performance characteristics of portable power sources. Akin to the kinematic Stirling heat engine, the external combustion feature ensures a stable and controllable combustion heating process, with a wide range of fuel options and the ability to achieve extended operation by adding fuel at any time [6,7]. However, as a dynamic thermoelectric generator but hermetically sealed, its energy conversion capability is rather robust compared with kinematic Stirling engines.

The Palm Power project initiated by the U.S. Department of Defense in 2003 marked the debut of portable power systems based on mesoscale combustion energy driven FPSG. The project pioneered the development of a 35 W electric-spray catalytic combustor (ECC) driven FPSG using JP-8 fuel, achieving specific power densities of 64 W/kg for the stand-alone FPSG and 16.4 W/kg for the system [8,9]. The system's adaptability to gaseous fuels such as propylene, propane, and hydrogen was also validated. Preliminary verifications were conducted on the system's environmental temperature, humidity, and placement angle effects [10]. Subsequently, a dual-opposed FPSG system based on an 80 W FPSG was developed. With hot and cold end temperatures of 850°C/90°C respectively, the single FPSG unit achieved a high thermoelectric conversion efficiency of 38% and a specific power density of approximately 90 W/kg. The system's dual-opposed configuration involved linear alternator back-to-back deployment, with each

engine independently heated by combustion from both sides. After including auxiliary components such as the system controller, the system's specific power density reached 18.4 W/kg [11,12].

Although the aforementioned research has showcased the viability, detailed results are lacking. It is evident that operating environmental parameters such as the oxygen content and ambient temperature impose a significant impact on such highly thermally-coupled systems, necessitating the study on its environment adaptivity.

This study integrates a porous media evaporative combustor (PMEC) into a high specific power portable power supply system based on ultra-high frequency (UHF) FPSG. The UHF FPSG is designed using the quasi-1D thermoacoustic analysis method of the SAGE program, and the novel helical tube hot-end heat exchanger ensures its high heat transfer efficiency. The PMEC combustor is designed based on 3D CFD combustion heat transfer numerical simulations, and the M-shaped corrugated plate recuperator recovers a large amount of flue gas waste heat to preheat fresh air, thus improving the efficiency of the combustor. The effects of different air densities and temperatures on combustion and heat transfer due to high altitude are compared in detail. Comprehensive performance parameters, including solid temperatures of the HHX, cooling water temperatures, output electrical power, voltage, current, PMEC exhaust gas temperatures, and key flue gas constituents such as CO, O₂, CO₂, NO/NO_x, were meticulously measured. The results of numerical simulations and experiments underscore the FPSG's high specific power and robust adaptability, especially in high-altitude and low-temperature settings.

System configuration

The power generation system contains a PMEC, a UHF-FPSG, a cooling water subsystem, an electrical load subsystem, and a signal acquisition and control subsystem. Detailed components are labeled in figure 1.

Regarding the rudimentary operating mechanism, local #0 diesel is used as the fuel, delivered to the PM evaporator by a pulse pump ready for gasification, subsequently after the initial ignition aided by an electric cartridge, the ample heat in the high-temperature combustion chamber ensures continuous self-sustaining evaporation of diesel, which is then mixed and burned with fresh air preheated by high-temperature exhaust gas in the recuperator. Through thermal radiation and convection, the heat absorbed by the FPSG

is converted into mechanical energy in the form of acoustic power by the free-piston Stirling engine (FPSE), which in turn drives the power piston in the linear alternator (LA) to convert the mechanical energy into electric power. It is worth noting that for the sake of demagnetization suppression, the recirculating cooling water first flows through the water jacket of the LA before entering the AHX of the FPSE.

The component parameters of the FPSG are listed in Table 1. Its distinctive ultra-high frequency of approximately 130 Hz is the primary reason why the FPSG exhibits outstanding specific power, as shown in the performance results presented in Table 2, while it's filled by helium with working pressure of 6 MPa.

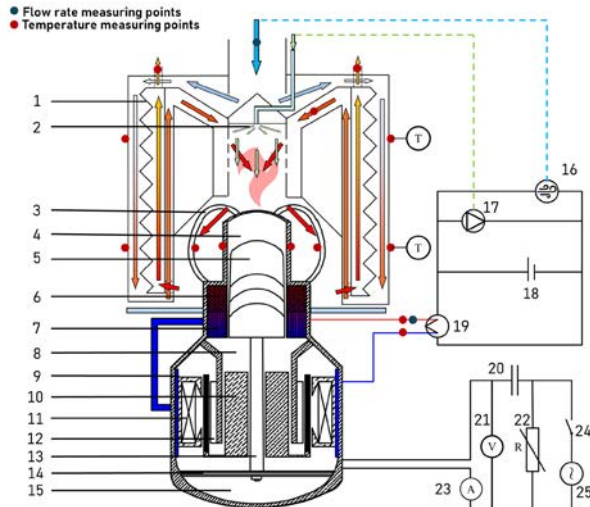


Figure 1. Schematic diagram of the test system. (1-recuperator, 2-PM evaporator, 3-spiral tube HHX, 4-expansion chamber, 5-displacer, 6-regenerator, 7-AHX, 8-compression chamber, 9-cooling water in LA, 10-power piston, 11-coil, 12-stator, 13-rod, 14-planer spring, 15-back chamber, 16-air supply, 17-fuel pump, 18-12V DC power supply, 19-cooler, 20-capacitor, 21-voltmeter, 22-resistance, 23-ammeter, 24-excitation switch, 25-excitation signal).

Table 1. Critical dimension of the main components of the FPSG.

Components	Critical dimension	
EC	Volume (mL)	9.8
AHX	Type	Shell and tube
	Axial length (mm)	31
	Inner diameter (mm)	1
	Tube numbers	120
REG	Type	Stainless steel fiber
	Wire diameter (μm)	16
	Porosity	0.878
HHX	Type	Tube
	Axial length (mm)	71
	Inner diameter (mm)	2
	Tube numbers	24
DIS	Diameter (mm)	40
	Diameter of connecting rod (mm)	12
	Moving mass (kg)	0.16
	Equivalent mechanical damping (N/s)	10
	Spring stiffness (kN/m)	120
CC	Volume (mL)	10
LA	Moving mass (kg)	0.43
	Diameter (mm)	40
	BL (N/A)	15.5
	Spring stiffness (kN/m)	38
	Coil internal resistance (Ω)	0.4

Table 2. System output characteristic.

parameter	value	Unit
Working frequency	123.4	Hz
Heating power	1769	W
Hot-end Temperature	550	$^{\circ}\text{C}$
Cold-end Temperature	20	$^{\circ}\text{C}$
Output electrical power	412.7	W
Power piston displacement	5@0	mm@degree

Displacer displacement	3.96@58.68	mm@degree
Acoustic power of FPSE	649.1	W
FPSE efficiency	35.6	%
LA efficiency	67.6	%
Relative Carnot efficiency	54.8	%
FPSG efficiency	23.3	%

Akin to internal combustion heat engine, low oxygen content and low temperature of the fresh air caused by high altitudes have adverse effects on the external combustion process. Therefore, we conducted comprehensive tests on the power output performance and the exhaust gas emission levels at three distinct test fields with altitudes of 19.4 m, 2784.3 m, and 4596.6 m, respectively, as shown in Table 3, to explore the system's adaptability to harsh environmental conditions.

Table 3. Environmental parameters of the test fields.

Test field	Altitude/m	Barometric pressure/kPa	Temperature/°C	Oxygen content/%
1	19.4	101.3	18	20.90
2	2784.3	70.9	-6	16.07
3	4596.6	56.7	-13	13.18

Prior to the field experimental test, we first performed a three-dimensional numerical simulation of the combustion of diesel fuel and its resulting high-temperature flue gas heat exchange process with HHX by using ANSYS Fluent [13] according to the above environmental parameters. The combustion process of diesel is simplified into a two-step reaction as shown in Eq. (1) and (2). This simplification of the complex combustion process offers a substantial reduction in computational cost without compromising the accuracy of heat transfer results at the outlet. Considering the CO component is beneficial for assessing the completeness of combustion. Moreover, in the experiment, a close agreement between the flame front in experiment and the interface of CO content at the 1000 ppm enables a more precise analysis of flame morphology.



Figure 2 shows photographs depicting the field test of the power generation system. Additionally, Figure 3 illustrates the size of each major component, while Table 4 provides details regarding their respective weights within the complete power generation system. The FPSG weight is as low as 3.7 kg, and the total weight of the system is 15 kg.

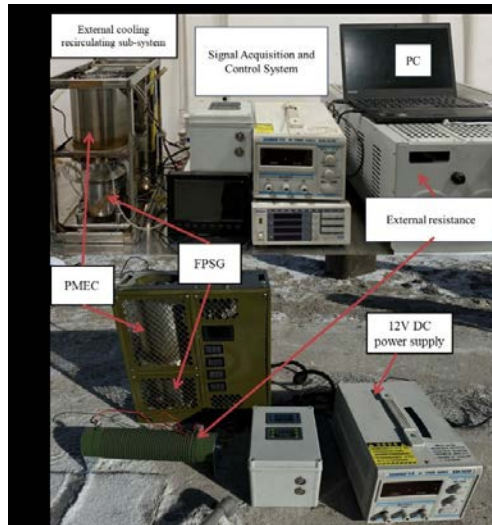


Figure 2. Photo of the test system. (a) Laboratory test Field with an altitude of 19.4 m, (b) Field test Field with an altitude of 4596.6 m.

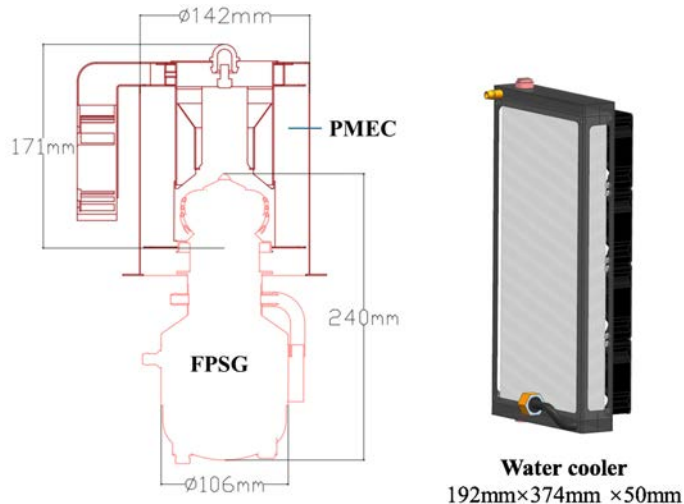


Figure 3. Schematic diagram of FPSG, PMEC and water cooler.

Table 4. Size and weight of system components.

Components	Size	Weight (kg)
FPSG	Φ 106mm×240mm	3.7
PMEC	Φ 142mm×171mm	2.5
Fuel pump	/	0.1645
Water pump	/	0.1885
Water cooler	192mm×374mm×50mm	1.6626
Controller	/	2.7
System case	192mm×374mm×370mm	4.1
Total	192mm×374mm×370mm	15

Results and discussion

Benchmark laboratory results

During preliminary laboratory tests, the power generation system was connected to an external industrial water chiller operating at a constant temperature of 20 °C with a flow rate set at 0.5 m³/h. The dependence of generated power and heating temperature on external resistance at different fuel flow rates are shown in figure 4 and figure 5, respectively. The maximum output electric power of the system at a fuel flow rate of 245 g/h is 415 W, the efficiency in terms of the lower heating value of local #0 diesel (43.9MJ/kg) is 13.9%, and the measured heating temperatures are 766/692 °C, respectively.

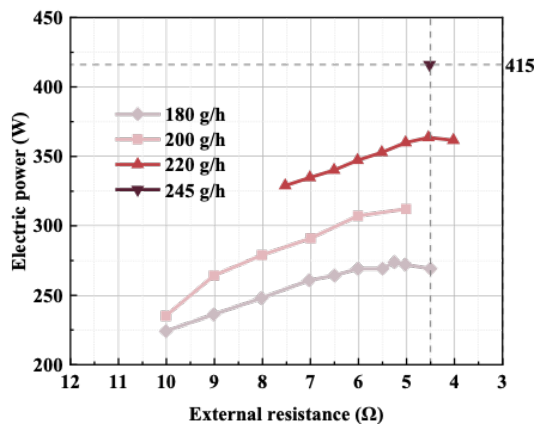


Figure 4. Dependence of output electric power on load resistance at different fuel flow rates.

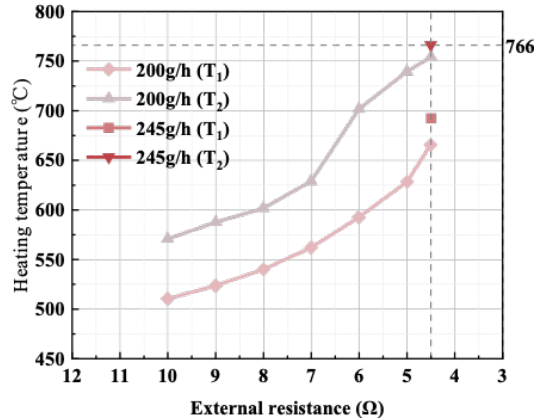


Figure 5. Dependence of heating temperature on load resistance at different fuel flow rates.

Field test

Before continuing with the field test, a series of 3D coupled combustion and heat transfer numerical simulations were carried out in terms of the contents of O_2 at different altitudes with a diesel flow rate of 218 g/h. It is worth noting that air density decreases significantly in high-altitude environments, and the total mass of oxygen in the same volume of fresh air decreases. Whereas, if the same mass flow rate of air is provided to ensure the total mass of oxygen, it leads to a greatly increased air flow rate. Therefore, numerical simulations were conducted to analyze the air parameters in Field 2 and 3, employing an identical volume flow rate as that in Field 1. This facilitated the acquisition of insights into combustion and heat transfer characteristics within high-altitude environments. The aggregate depicted in the bar chart of figure 6 represents the heat of combustion in the combustion chamber, a value that diminishes notably with decreasing oxygen content. This reduction consequently results in a significant decrease in radiative and convective heat transfer. Figure 7 illustrates the distribution of average temperature, average molar fraction of CO, and average mass fraction of $C_{10}H_{22}$ along the axial direction of the combustor. When oxygen is abundant, combustion reactions proceed more rapidly and intensely, with the highest temperatures located in the upper part of the combustion chamber. Conversely, in oxygen-deficient conditions, the high-temperature region shifts noticeably downwards, with significant high-temperature

combustion reactions still occurring near the HHX of FPSG. This is also the primary reason why convective heat transfer in Field 1 is lower than that in Field 2 and 3. With a reduction in oxygen content, there is a tangible decrease in combustion and a significantly decline in the peak molar fraction of CO. Additionally, the concentration of in the heat transfer region rises, indicating a decrease in the reaction completeness within the combustion chamber.

Figure 8 depicts the influence of ambient temperature on combustion and heat exchange. By utilizing the recuperator to preheat fresh air to temperatures exceeding 500 °C, comparisons were made among fresh air of -20/0/20 °C preheated to 510/530/550°C. While maintaining consistent air flow rates and oxygen levels, the heat generated by combustion reactions remains relatively stable. However, the variance in air temperature leads to discrepancies within the combustion chamber, affecting the heat transfer between the flue gas and the heat exchanger. Generally, lower air temperatures marginally reduce the heat absorption of the FPSG. Conversely, a greater portion of combustion heat is utilized to heat the air and is subsequently emitted with exhaust gases. This underscores the significance of efficient waste heat recovery.

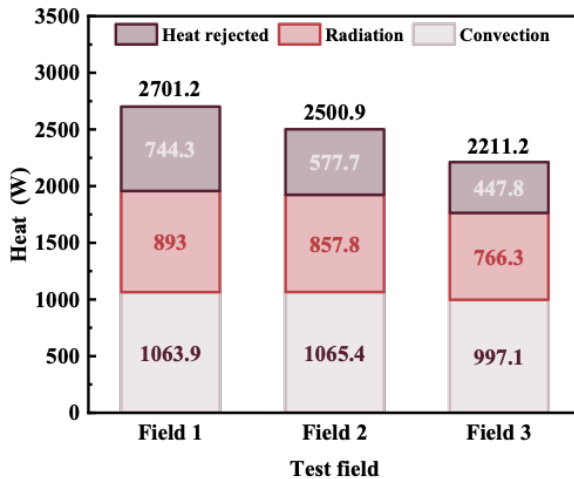


Figure 6. Variation of heat of reaction and heat transfer with oxygen content in the combustion chamber.

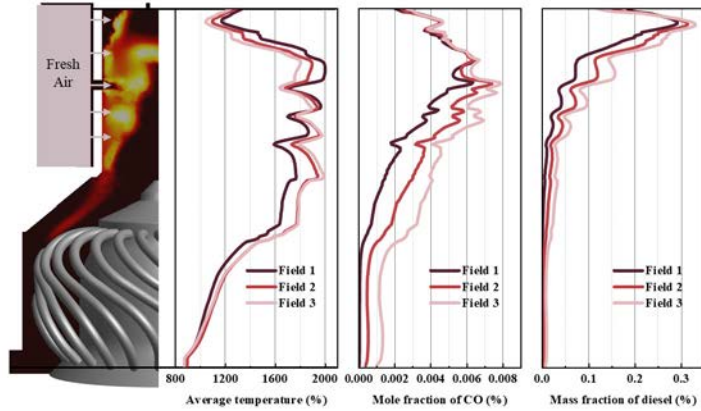


Figure 7. Distribution of average temperature, average mole fraction of CO, and average mass fraction of diesel in the axial direction of the combustion chamber.

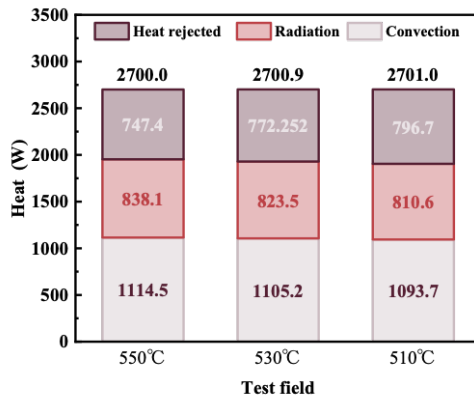


Figure 8. Variation of combustion heat and heat transfer with fresh air temperature in the combustion chamber.

During the field test, the system's built-in water-cooler is used for heat rejection, while the power generated by the system is consumed through a series-connected 6Ω external resistance. The output power of the system, as well as the CO, O₂ and NO_x content of the exhaust gas outlet, were measured for various fuel levels and fan duty cycles in different test Fields, as presented in figure 9. Specifically, the experimental results for diesel flow rates of 190 g/h and 218 g/h are depicted in figure 9 (a)-(d) and figure

9 (e)-(h), respectively. It is evident that the output power significantly decreases with increasing altitude. The results from different experimental Fields exhibit a consistent trend with changes in airflow. In Field 1, as the airflow increases, the power decreases significantly, whereas in Fields 2 and 3, the output power increases with higher airflow, and this increasing trend is amplified with higher altitudes. The CO content in figure 9 (b) and (f) suggests that the combustion situation is better in Field 1, especially at lower fuel levels where the CO content in the exhaust gas is below 50 ppm. Field 2 demonstrates an improvement in combustion completeness with increased airflow. However, for Field 3, the extremely low oxygen content due to high altitude results in CO content in the exhaust gas exceeding 10000 ppm within the test range, indicating an extremely poor combustion state. The limitation of the instrument range also leads to incomplete exhaust gas testing at this experimental Field. Furthermore, the O₂ content in Figure 9 (c) and (g) demonstrates that under more complete combustion conditions, the O₂ content in the exhaust gas generally exceeds 8%, which serves as a valuable indicator of combustion completeness.

Regarding NO_x, its generation is significantly influenced by both combustion completeness and combustion temperature. As observed in figure 9 (d) and (h), the NO_x content in Fields 1 and 2 decreases with increasing airflow, while in Field 3, the NO_x content increases with airflow but remains notably lower than in Fields 1 and 2. This phenomenon occurs because when oxygen supply is sufficient, excess air can dilute and cool the combustion process. However, In Field 3, where oxygen supply is severely inadequate and the ambient temperature is low, leading to lower combustion temperatures. Increased airflow exacerbates combustion, significantly raising the combustion chamber temperature and increasing the content of thermal type NO_x.

In summary, the combination of low oxygen content and low temperature in high-altitude regions profoundly affect the combustion process. Compared to Field 1 at an altitude of 19.4 m, Field 3 witnesses a decrease in output power of nearly 30 W, accounting for approximately 10% under the same air-fuel parameters. While it's foreseeable that a larger airflow supply could potentially mitigate this issue, it is hampered by the extremely harsh testing environment and the power limitations of the fan in this experiment. To address these challenges, more extensive testing and analysis will be undertaken in future endeavors.

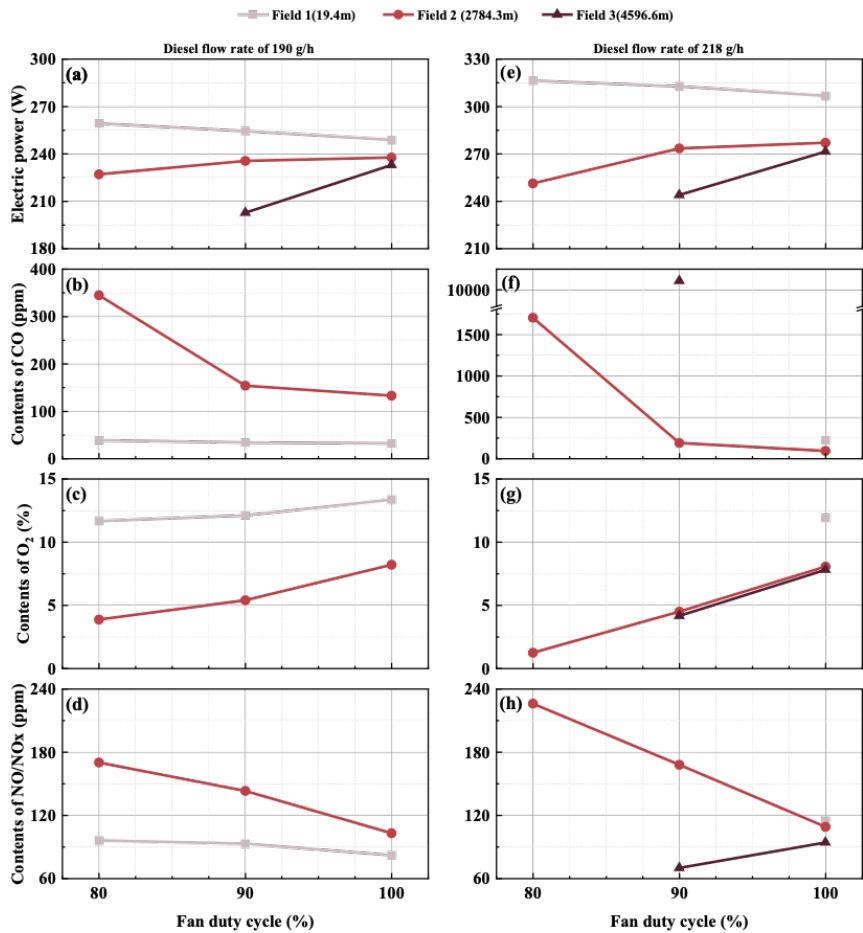


Figure 9. Variation of electric power and contents of CO/O₂/NO_x with fan duty cycle at different test fields.

Comparison and Prospects

The primary objectives of the portable power source driven by PMEC proposed in this study encompass high specific power, high efficiency, and cost-effectiveness. High specific power aims to provide copious power supply while ensuring portability, offering substantial benefits in short-term portable power scenarios. In long-term portable power applications, fuel consumption becomes more critical than specific power, highlighting

the importance of improved energy conversion efficiency. Additionally, cost-effectiveness plays a pivotal role in fostering the widespread adoption of this technology.

Analysis from Table 5 reveals that the attempt of ultra-high frequency, approximately 140 Hz, bestows upon this system remarkably high specific power to this system. However, the employment of cost-effective materials results in a certain disparity in conversion efficiency compared to previous studies. Nonetheless, the system exhibits outstanding competitiveness in providing portable power supply within a period of 10 days. However, as the duration approaches 10 days, its effectiveness diminishes. Future efforts will focus on quantifying losses at ultra-high frequencies and in turn improving efficiency in future works.

Table 5. System output characteristic.

	Palm power [9]	Palm power [12]	This project
FPSG Type	EE-35	ASC	TSC-231
Combustor	ECC	ECC	PMEC
Fuel	JP-8	JP-8	o# diesel
Output power (We)	42.5	160	415
FPSG weight (kg)	0.66	2.5	3.7
FPSG specific power (W/kg)	64.4	64	112.2
Hot-end Temperature (°C)	550	550	550
Cold-end Temperature (°C)	70	70	20
Operating frequency (Hz)	105	102	135
FPSG efficiency (%)	32	38	23.3
System efficiency (%)	21	N/A	13.9
System weight (kg)	2.1	9.8	15
System specific power, (dry, W/kg)	16.4	16.3	27.7
System specific energy (wet, 3 days operation, W h/kg)	800	/	916
System specific energy (wet, 10 days operation, W h/kg)	1505	/	1350

Conclusion

An FPSG based power generate system operates at an ultra-high frequency of up to 135 Hz, yielding a peak electrical power output of 415 W with a diesel mass flow rate of 245 g/h. The fuel-electricity efficiency, calculated based on the low heating value of the

diesel fuel, is measured at 13.9%. Furthermore, the stand-alone FPSG achieves a specific power of 112.2 W/kg, while the system-level specific power reaches 27.7W/kg. The system maintains a stable output even in high altitude, cold and rarefied air environments.

Acknowledgements

This work was financially supported by National Natural Science Foundation of China (Grant No. 51876214) and the National Key Research and Development Program of China (No. 2021YFC28026003).

References

- [1] Podlesak, T. Stirling Engine Research at the Army Research Laboratory. In 5th International Energy Conversion Engineering Conference and Exhibit (IECEC), p. 4702.
- [2] Cho, J H, Lin, C S, Richards, C D, Richards, R F, Ahn, J, Ronney, P D. Demonstration of an external combustion micro-heat engine. Proceedings of the combustion institute, 32(2), 3099-3105 (2009).
- [3] Dunn-Rankin, D, Leal, E M, Walther, D C. Personal power systems. Progress in energy and combustion science, 31(5-6), 422-465 (2005).
- [4] Zhang, K., Chou, S. K., & Ang, S. S. MEMS-based solid propellant microthruster design, simulation, fabrication, and testing. Journal of microelectromechanical systems, 13(2), 165-175 (2004).
- [5] Fernandez-Pello, A. C. Micropower generation using combustion: Issues and approaches. Proceedings of the combustion institute, 29(1), 883-899 (2002).
- [6] Jin Q, Luo J, Sun H, Xue J, Ma Y, Ma Z, et al. Numerical and experimental investigation of a combustor-coupled free-piston Stirling electric generator. Energy Conversion and Management, 299, 117805 (2024).
- [7] Luo J, Zhang L, Sun Y, Chen Y, Yu G, Hu J, et al. Operational characteristics of a free-piston Stirling generator with resonant self-circulating heat exchangers. Applied Thermal Engineering; 229:120534 (2023).
- [8] Huth J, Collins J. Diesel Fuel-to-Electric Energy Conversion Using Compact, Portable, Stirling Engine-Based Systems. In 13th International Stirling Engine Conference. (2007).

- [9] Gomez, A, Berry, J J, Roychoudhury, S, Coriton, B, & Huth, J. From jet fuel to electric power using a mesoscale, efficient Stirling cycle. Proceedings of the Combustion Institute, 31(2), 3251-3259. (2007).
- [10] Huth J, Gomez A, Roychoudhury S. Progress toward a Wearable 35 We Free-Piston Stirling Engine-Based Soldier Power Source. In 4th International Energy Conversion Engineering Conference and Exhibit (IECEC), p. 4016 (2006).
- [11] Hendrickson M, Podlesak T, Huth J, Brandhorst H, Rose F. Stirling Engines for Military Applications. 3rd International Energy Conversion Engineering Conference, San Francisco, California: American Institute of Aeronautics and Astronautics, p. 5519 (2015).
- [12] Hendrickson M, Podlesak T, Huth J, Roychoudhury S, Brandhorst H, Kirby R, et al. 160 W Dual Opposed Stirling Engine Power Source for Military Applications. 4th International Energy Conversion Engineering Conference and Exhibit (IECEC), San Diego, California: American Institute of Aeronautics and Astronautics, p.4039 (2006).
- [13] Baker TJ. Fluent User's Guide (2021).

Experimental Confirmation of Numerical Design of Slot-Spaced Permanent Magnet Linear Alternator

Surender Dhanasekaran^{a, *}, Chin-Hsiang Cheng^b

a International Doctoral Degree Program on Energy Engineering, National Cheng Kung University, Taiwan (R.O.C)

b Institution of Aeronautics and Astronautics, National Cheng Kung University, Taiwan (R.O.C)

* Corresponding author: surenderdhanasekaran@gmail.com

Keywords: Free-Piston Stirling engines, Linear Alternator, Experimental validation, Clean energy, and Renewable energy

Abstract

In contemporary Free-Piston Stirling Engine (FPSE) applications, linear alternators are pivotal, serving as the primary mechanism for power production with minimal mechanical to electrical energy conversion losses. A notable advancement in this field is the development of a slot-spaced permanent magnet linear alternator. This indigenous innovation represents a significant leap in tubular linear alternator design, specifically engineered for seamless integration with FPSEs to facilitate clean power production.

The design of the Permanent Magnet Linear Alternator (PMLA) is characterized by its tubular stator, which incorporates strategically positioned slot-spaces between each coil. This novel structural configuration enhances the power density of the alternator, setting it apart from conventional PMLA models. The assembly process of this alternator is meticulously designed, featuring a toroidal wound coil that is expertly encased within the stator. A specialized stacking technique is employed during this process, ensuring optimal positioning and stability of the coil.

The translator component of the PMLA comprises neodymium magnets, arranged in a Quasihallbach configuration. This arrangement is particularly effective in exploiting the strengths of both strong and weak magnetic fields. The use of neodymium magnets not only contributes to the overall efficiency of the alternator but also underscores the commitment to utilizing high-quality materials in its construction.

The parametric analysis through numerical simulations of the model achieves an optimal rating of 100W for a baseline scenario, characterized by a 5 mm stroke operating at a frequency of 60 Hz. Under peak operating conditions, the PMLA can deliver a maximum power output of 1 KW. A notable challenge in the design is the cogging force, an undesired phenomenon that impedes the smooth movement of the translator. To mitigate this issue, various strategies have been implemented in the experimental setup, aiming to minimize this opposing force effectively.

An experimental model with no-load condition of the PMLA has been established and rigorously tested under the baseline parameters. However, the maximal operational frequency has been restricted to 20 Hz, primarily due to the limitations posed by the linear bearings utilized in the design. The performance of the machine has been extensively evaluated across a range of strokes - 5, 10, 15, and 18mm - and at various frequencies. These experimental conditions have been tailored to align with the specifications of our in-house FPSE.

The comparison between the experimental results and the simulation data reveals a commendable degree of congruence, indicating that the real-world performance of the PMLA closely mirrors the outcomes predicted by the simulations. This alignment not only validates the accuracy of the simulation models but also underscores the reliability of the PMLA design under varied operational conditions. This assessment is crucial in refining the design and enhancing the efficiency of the PMLA, thereby contributing to the advancement of linear alternator technologies.

Introduction

The persistent rise of global warming and its direct consequences on our planet have become central topics of concern and discussion in recent years. It is widely acknowledged that if no immediate and effective actions are taken, the continuous increase in global temperatures could lead to catastrophic disasters with irreversible outcomes. The collective aim should be to limit global warming to within 1.5 °C to mitigate these risks, promoting sustainable growth while addressing the escalating demand for global energy. This requires a balanced approach to power production and a significant reduction in greenhouse gas emissions, ideally by 2030, to avoid dire consequences [1]. The threat of climate change is further exemplified by projections of unprecedented climatic events and the potential for significant sea-level rises, threatening coastal areas and ecosystems worldwide. The Paris Agreement underscores the urgency of limiting global warming to 1.5–2.0 °C to prevent catastrophic environmental changes, such as the loss of the Greenland ice sheets and the flooding of the Amazon rainforests. These changes not only endanger biodiversity but also pose a risk to human settlements through the flooding of global rivers and impacts on the marine ecosystem due to elevated thermal ranges [2].

To meet the imminent requirement for a substantial increase in clean energy production, an eight-fold change is necessary to completely transition by 2050 [3]. With the nearest prediction indicating that global clean energy production could reach 33% by 2024, it is clear that rigorous developments and continuous advancements in green energy are vital. Notably, innovations such as free-piston Stirling engines, which are crankless, offer advantages including reduced noise and vibrations, longevity, low maintenance, and self-operating capabilities, presenting a promising direction for clean energy production [4].

A linear alternator integrates seamlessly with the Free Piston Stirling Engine (FPSE) to convert linear motion into electrical power without any significant power loss.

Linear alternators offer a distinct advantage due to their minimal moving parts [5]. The prototype developed features an innovative design with a stator that has spaced slots [6]. The model presented in this study is an enhanced version of the traditional tubular Permanent Magnet Linear Alternator (PMLA). The current design of the PMLA is efficient in its use of materials, and the stator is designed to be more compact, reducing the overall weight and increasing power density. By introducing a slot space within the tooth's area, the design effectively extends the tooth's width, contributing to the alternator's improved performance.

This study focuses on validating the results from the simulation phase of this model's development. The performance of the PMLA can be adjusted through various design and material selections. In operating the machine, the PMLA has only two adjustable parameters: the operating frequency and the stroke length. Throughout the design development, the machine's performance was evaluated at frequencies ranging from 10 to 100 Hz in increments of 10, and at stroke lengths from 5 to 25 mm in increments of 5. The stroke length is constrained by the design's limits and the maximum distance the translator can move, while the frequency limit is determined by the maximum operational conditions of the current FPSEs. The simulation of the presented model was carried out in JMag Designer V.18.0. The experimental results were obtained and compared with the simulation data to assess the real-world effectiveness of this stator design and to fine-tune it for specific applications.

Design and baseline condition

The design of the Permanent Magnet Linear Alternator (PMLA) adopts a tubular topology, which enhances rigidity and ensures that structural integrity is preserved without deformation. The permanent magnets are arranged in a Quasi-Halbach pattern to effectively exploit the magnets' strong and weak sections. N48H is the selected material for the magnets due to its high resistance to heat and its ability to retain magnetization under high-temperature conditions. These magnets are encased within a rod of SUS304 grade stainless steel. The coil, situated within the stator, is placed between the teeth, with a slot space introduced to accommodate it. Figure 1 illustrates the cut-section view of the PMLA, emphasizing the slot spacing on the stator. The coil is toroidally wound in both clockwise and counterclockwise configurations. The stator is made from 35CS350

material, chosen for its effectiveness, with a stacking factor of 96%. The machine's geometrical parameters are detailed in Table 1.

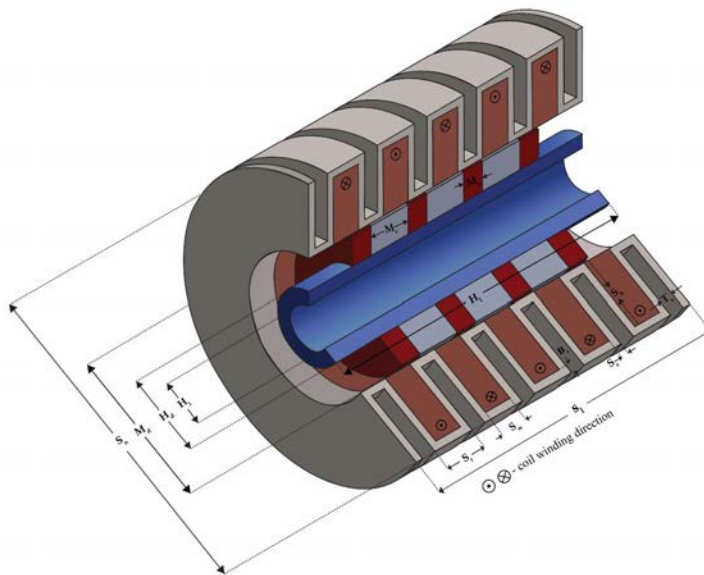


Figure 1. Cross-sectional view of the linear alternator.

The baseline conditions for the PMLA were established for various parameters following a parametric analysis of the model [6]. Modifications to the original model were made in light of this analysis, with changes to the structure of the stator, magnet, and other aspects related to the machine's overall geometry in simulation scenarios. These modifications were guided by a study focused on reducing cogging force [7]. This study significantly decreased the cogging force exerted on the translator, aligning the force profile more closely with a perfectly sinusoidal displacement curve. A comparison of induced voltage, cogging force on the translator, and displacement with a stroke of 5mm at a frequency of 60 Hz is presented in Figure 2. The choice to maintain the frequency at 60 Hz is deliberate, as the global standard for domestic power supply is either 50 or 60 Hz, ensuring the machine's performance is evaluated within a relevant operational range.

Table 1. Geometrical parameters of the presented PMLA for simulation and prototype.

Stator outer diameter, S_o	100	mm
Slot Width, S_w	10	mm
Tooth thickness, S_t	5	mm
Tooth Width, T_w	10	mm
QH(Radial) Magnet thickness, M_r	15	mm
Slot height, S_h	23.5	mm
Shaft Inner Diameter, H_i	25	mm
Air gap, g	4	mm
Back Iron Thickness, B_t	2.5	mm
Coil Inner Diameter, C_i	48	mm
Coil Outer Diameter, C_o	95	mm
Tooth slot thickness, S_s	2.5	mm
Shaft Stack Length, H_l	15	mm
QH(Axial) Magnet thickness, M_a	7.5	mm
Tooth slot gap, T_s	5	mm
Magnet Outer Diameter, M_d	40	mm
Stator Stack Length, S_l	110	mm

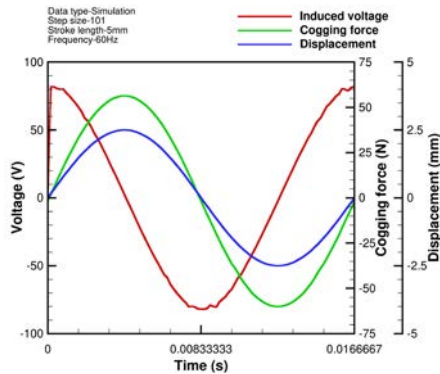


Figure 2. Transient variation of induced emf, cogging force, and displacement in baseline condition.

Experimental arrangement

The experimental setup is designed to assess the prototype's endurance and repeatability. The machine's operational capability is evaluated under two conditions: when connected to a purely resistive load and when unloaded. For comparability with simulation results, the experimental procedure employs a purely resistive load of 100Ω , rated at 100W , mirroring the simulation's parameters. To gauge the machine's performance under natural conditions, a no-load state is primarily considered in this study, focusing on two operational variables: stroke length and frequency. These factors are central to evaluating the machine's performance.

The prototype is linked to a rotating motor, which, through an off-centered rotor hub, converts rotary motion into linear motion. This hub prompts the translator to oscillate at the desired frequency. The motor used is a high-power unit capable of reaching up to 6000 rotations per minute (RPM). However, due to the linear bearing that aligns and secures the translator being limited to a maximum operating frequency of 20 Hz, the experimental results presented are confined to this frequency range, as no commercially available solutions could exceed this limit. The prototype is encased to secure the stator firmly and prevent any movement caused by vibration from cogging forces. The conversion of rotational to linear motion dictates the frequency, with measurements ranging from 5, 10, 15, to 20 Hz, corresponding to RPMs of 300, 600, 900, and 1200, respectively. Stroke adjustments are made by switching the drive mechanism, following stroke analyses from previous studies, set at 5, 10, 15, and 18 mm. The choice to substitute a 20 mm stroke with an 18 mm one aligns with the internal stroke requirements of the in-house Free Piston Stirling Engine (FPSE), facilitating preliminary tests before integrating the FPSE with the PMLA. Figure 3 provides a clear illustration of the test bed setup for the prototype testing.

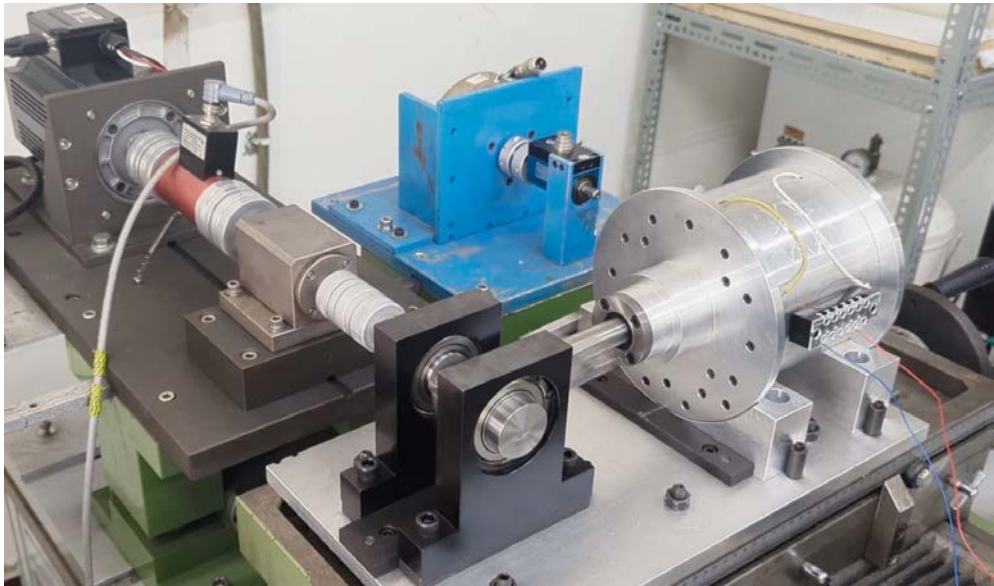


Figure 3. Experimental test bed of the prototype.

Conditions and assumptions

The data acquisition in the experiment is governed by specific conditions, detailed as follows:

1. Data collection is conducted using the NI CDAQ system, ensuring precise measurements. To maintain uniform accuracy throughout the study, the sampling rate is consistently held at 2.5 KHz.
2. The frequency of linear motion, derived from rotational motion, cannot be kept constant during the experimental phase due to the influence of cogging forces. Therefore, the frequency values will be represented by their Root Mean Square (RMS) moving forward.
3. From this point onward, the voltage values presented are the RMS of one cycle, applicable to both experimental and simulation data.
4. Occasional spikes observed in the continuous data representation fall within the acceptable tolerance range.

Results and discussions

The impact of translational motion on induced voltage varies with frequency and stroke length, indicating that the machine exhibits optimal performance within a specific

range. The maximum achievable voltage and power output are contingent upon its operational conditions. The design of the machine ensures that after an initial increase, the induced voltage reaches a saturation point, typically around 60 Hz. However, current experimental capabilities limit testing to 20 Hz, with simulation data similarly constrained. Consequently, the anticipated voltage in simulations mirrors findings from previous studies. To elucidate the gathered data, Figure-4 depicts the results obtained for an 18mm stroke at 20 Hz, representing the machine's current peak performance, where the peak voltage achieved was precisely 160 V. The significant effect of cogging force is observable through torque reversal in the motor. This opposing force generates a negative torque, causing the frequency to exhibit oscillatory behavior.

To juxtapose the peak operational experimental condition with its simulated counterpart, Figure 5 presents a comparison of the profiles for both scenarios. The 18mm stroke exceeds the optimal stroke, while the 20 Hz frequency falls below the optimal frequency. This discrepancy is evident in the simulation's profile; however, the experimental curve closely resembles a sinusoidal shape. Furthermore, the experimental setup recorded a voltage of 109.59 V, compared to 113.98 V in the simulation. This 4% variance falls comfortably within the acceptable range, given the significant stroke length involved. This comparative analysis serves as a precursor for discussions on various other cases. The mismatch in profiles can be attributed to the fluctuating operational conditions experienced in real-time, which diverge from the idealized conditions assumed in simulations.

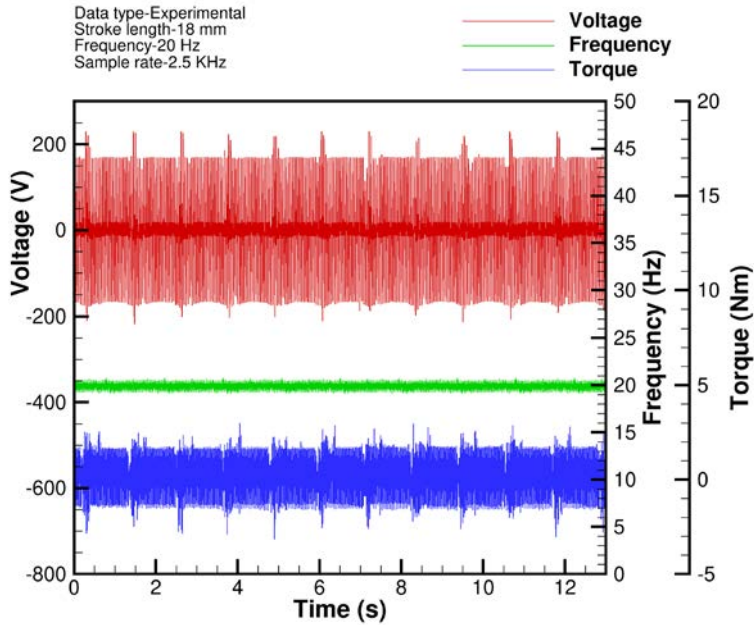


Figure 4. Experimental data obtained from an 18 mm stroke at 20 Hz.

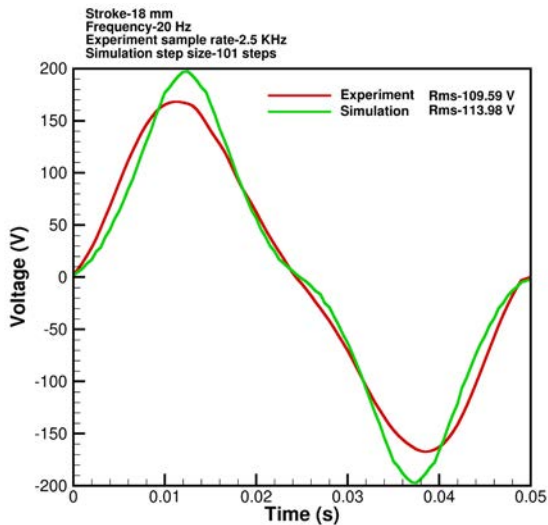


Figure 5. Profile comparison of experimental and simulation induced voltage for an 18 mm stroke at 20 Hz.

Comparison of simulation and experimental no-load voltage

At 5 Hz, the lowest operational condition feasible in both simulation and experimental setups, the translator's instantaneous torque required to counteract cogging force and align with the stator is significantly high, a condition that persists even during continuous operation. Despite the ideal conditions assumed in simulations, this challenge remains evident. Figure-6 demonstrates the translator's behavior, where the induced EMF is low due to the incomplete rotational motion, resulting in a stop-and-go motion across various stroke lengths. Consequently, an inconsistent sinusoidal profile is observed. Notably, at a 5 mm stroke, the output is merely 5 V, yet the voltage profile appears more sinusoidal compared to the 18mm stroke, which suffers from greater cogging force. The experimental setup showcases a smoother transition in induced voltage compared to the simulation. In both simulation and experimental cases, the 5 Hz frequency leads to inconsistent results.

Increasing the frequency to 10 Hz stabilizes the operation. The 600 RPM aligning with the natural frequency of the rotary motor in use. At the lowest stroke of 5 mm, the voltage difference between the experimental and simulation voltage is 7.18 V, whereas increasing the stroke to 10 mm results in a 9.16 V difference, observable at both 5 Hz and 10 Hz frequencies. The 10 mm stroke exhibits unusual behavior in both the 5 Hz and 10 Hz scenarios, a pattern consistent in both simulation and experimental settings. As anticipated, the experimental voltage at an 18 mm stroke closely matches the simulation results, with a difference of 4.53 V, highlighting this as a noteworthy observation. The curve trends for both simulation and experimental results now closely align, marking a significant difference from the 5 Hz scenario. The standard deviation in the 10 Hz case shows considerable improvement over the 5 Hz case for both simulated and experimental values. Figure 7 displays this trend, highlighting a noteworthy distinction when compared to the 5 Hz case.

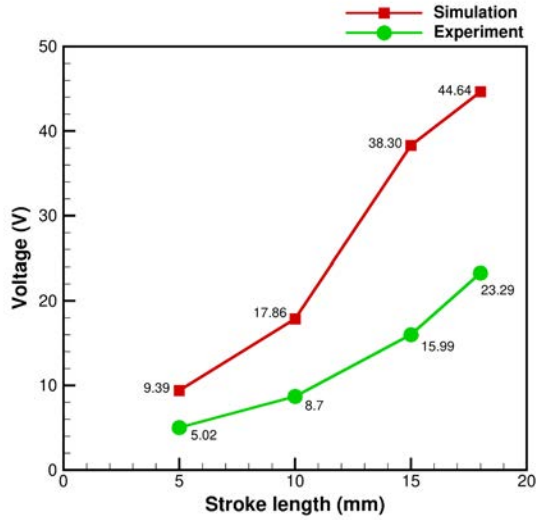


Figure 6. Comparison of simulation and experimental no-load voltage for 5 Hz.

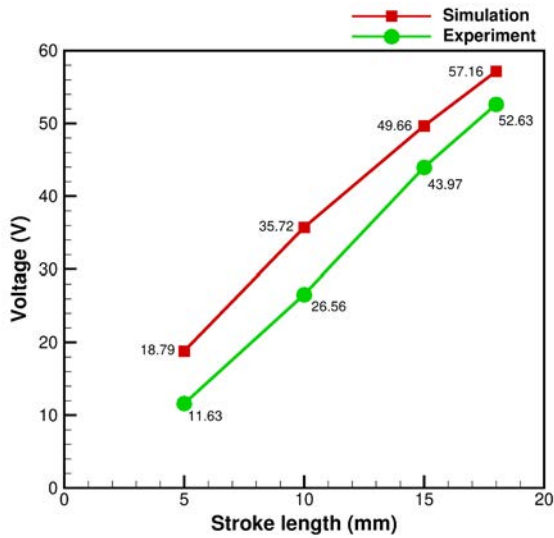


Figure 7. Comparison of simulation and experimental no-load voltage for 10 Hz.

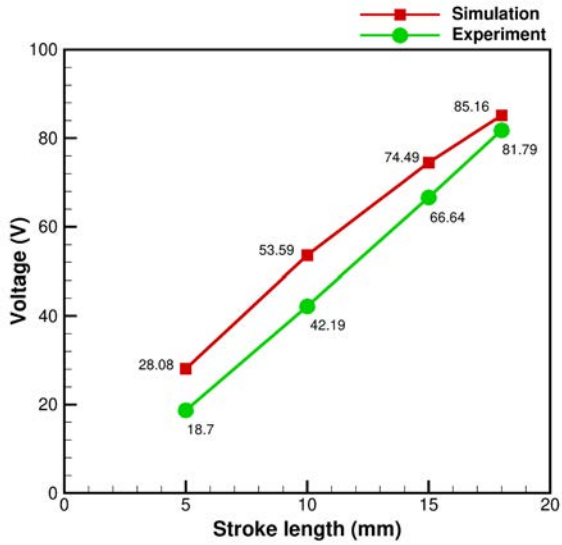


Figure 8. Comparison of simulation and experimental no-load voltage for 15 Hz.

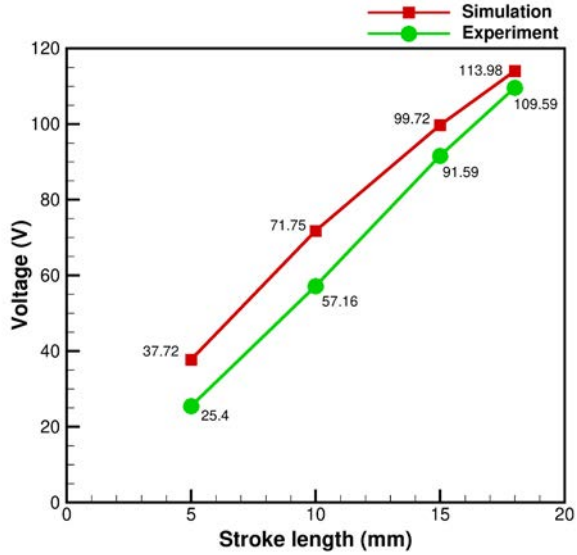


Figure 9. Comparison of simulation and experimental no-load voltage for 20 Hz.

In the 15 and 20Hz scenarios, there's a notable convergence in the trends of the curves, illustrating a similarity in their behavior. As stroke length increases, the simulation shows a tendency towards saturation in induced voltage, unlike the experimental values which exhibit a continuous linear increase without reaching saturation. For both scenarios, the difference between simulation and experimental values at a 5mm stroke is substantial. This disparity grows even larger at a 10mm stroke, mirroring the patterns observed in the 5 and 10Hz cases. However, as we approach a 15 mm stroke, this difference diminishes, with the 18 mm stroke showcasing the closest alignment between simulation and experimental outcomes. This indicates that, across all simulation scenarios, the largest stroke in the experimental setup tends to align closely with the simulated results. Moreover, the curve demonstrates a linear increase in correspondence with the stroke length. Figure-8 and 9 illustrates the comparison of simulation and experimental results across the 15 and 20Hz cases respectively.

Figure 10 intriguingly compares experimental values, yielding several significant insights:

1. The induced voltage from an 18mm stroke at 5Hz is lower than that from a 5mm stroke at 20Hz. This highlights the critical role of frequency in the machine's performance, a finding corroborated by our study [6]. Although saturation levels are attained later with increasing stroke length, frequency impacts the induced voltage right from the baseline case, resulting in higher initial values. This conclusion is supported by experimental comparisons across different frequencies.
2. As frequencies increase, the voltage curve trends toward linearity, attributed to the diminishing effect of cogging forces and the challenges of instantaneous alignment. At lower frequencies and strokes, these forces impose a more significant barrier, causing notable spikes in the voltage curve. However, at higher frequencies, the force required to overcome these obstacles is markedly less, leading to a smoother, more sinusoidal curve.
3. While the difference in induced voltage at lower strokes across varied frequencies is minor, it becomes substantially more pronounced at higher strokes. Importantly, this difference does not remain constant but escalates with frequency. This nonlinear relationship suggests that the system's response is intricately affected by factors beyond simple proportionality, such as resonance, damping, or system inertia, indicating a complex dynamic behavior.

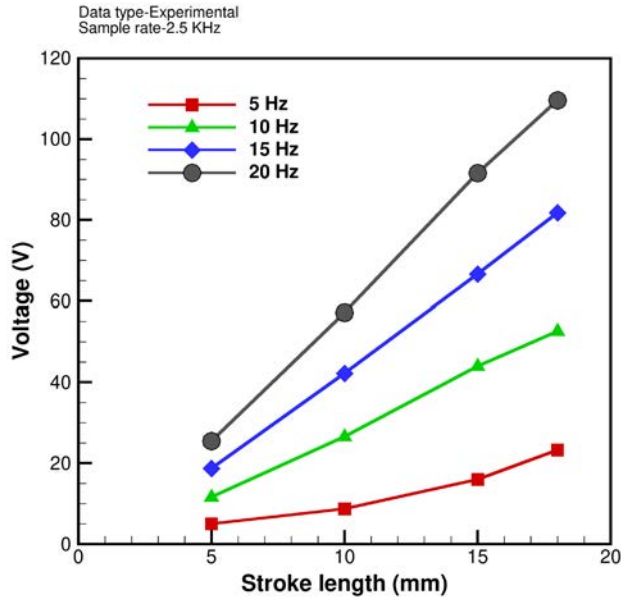


Figure 10. Comparison of experimental induced voltage across 5, 10, 15, and 18mm stroke length upon 5, 10, 15, and 20 Hz operational frequency.

Conclusion

The developed prototype of the Permanent Magnet Linear Alternator (PMLA) has delivered outcomes consistent with its numerical simulations. This achievement aligns with our modified design, which incorporates further adjustments to diminish the cogging force, notably reducing the original outer diameter of the magnets by 3mm and enlarging the air gap to 4 mm. The experimental no-load voltage aligns with our expectations, as underscored by the comparisons mentioned previously. However, the prototype's performance is constrained by the 20Hz operating frequency limit, highlighting the significance of frequency over stroke length in affecting the machine's operational efficiency. Higher strokes demonstrate a closer alignment with the simulation outcomes, revealing a linear trend as frequency increases. These insights are crucial in understanding the prototype's dynamic behavior under various operating conditions, providing a valuable foundation for future enhancements and applications.

References

- [1] Wunderling N, Winkelmann R, Rockström J, Loriani S, Armstrong McKay DI, Ritchie PD, Sakschewski B, Donges JF. Global warming overshoots increase risks of climate tipping cascades in a network model. *Nature Climate Change*. 13(1):75-82 (2023).
- [2] Zhang S, Zhou L, Zhang L, Yang Y, Wei Z, Zhou S, Yang D, Yang X, Wu X, Zhang Y, Li X. Reconciling disagreement on global river flood changes in a warming climate. *Nature Climate Change*. 12(12):1160-7 (2022).
- [3] Holechek JL, Geli HM, Sawalhah MN, Valdez R. A global assessment: can renewable energy replace fossil fuels by 2050?. *Sustainability*. 14(8):4792 (2022).
- [4] Durcansky P, Nosek R, Jandacka J. Use of stirling engine for waste heat recovery. *Energies*. 13(16):4133 (2020).
- [5] Cawthorne WR, Famouri P, Chen J, Clark NN, McDaniel TI, Atkinson RJ, Nandkumar S, Atkinson CM, Petreanu S. Development of a linear alternator-engine for hybrid electric vehicle applications. *IEEE transactions on vehicular technology*. 48(6):1797-802 (1999).
- [6] Cheng CH, Dhanasekaran S. Design of a Slot-Spaced Permanent Magnet Linear Alternator Based on Numerical Analysis. *Energies*. 15(13):4523 (2022).
- [7] Cheng CH, Dhanasekaran S. Cogging Force Reduction and Profile Smoothing Methods for a Slot-Spaced Permanent Magnet Linear Alternator. *Energies*. 16(15):5827 (2023).

Stirling refrigerators and cryocoolers

Measurement of Minor Loss at T-junction tube

Y. Kurai^{a,*}, S. Sekimoto^b, Y. Ueda^c

a Graduate School of Bio-Applications and Systems Engineering, Tokyo University of Agriculture and Technology, 2-24-16 Nakamachi, Koganeishi, Japan

b Graduate School of Engineering, Tokyo University of Agriculture and Technology, 2-24-16 Nakamachi, Koganeishi, Japan

c Graduate School of Engineering, Tokyo University of Agriculture and Technology, 2-24-16 Nakamachi, Koganeishi, Japan

***Corresponding author:** s229705x@st.go.tuat.ac.jp

Keywords: Thermoacoustic refrigerators, T-junction tube, Viscous dissipation, Minor loss

Abstract

Thermoacoustic refrigerators have the advantages of low cost and high maintainability because they have simple construction. To improve the performance of thermoacoustic refrigerators, it is necessary to reduce acoustic power loss called "minor loss". However, minor loss at the T-junction tube (one of the components of thermoacoustic refrigerators) has not yet been investigated. The aim of this paper is to measure the minor loss at the T-junction tube, and to investigate factors affecting it. In this paper, the effects of "the direction of acoustic wave input to T-junction tube" and "the shape of the T-junction tube" on the minor loss are investigated. As a results, the minor loss could be reduced 17% when the direction of acoustic wave input to the T-junction tube was changed. On the other hand, the minor loss could be reduced 78% when the shape of the T-junction tube was changed.

Introduction

Conventional refrigerators, like vapor-compression and adsorption refrigerators, need complex mechanical parts, such as pistons, and valves, to produce work. However, thermoacoustic refrigerators have simple construction and their only mechanical element is an acoustic generator. Thermoacoustic refrigerators use an acoustic wave to generate refrigeration. When the acoustic wave propagates in a narrow tube, a temperature gradient in the direction of wave propagation is created. This phenomenon is used as the cooling principle for thermoacoustic refrigerators.

Thermoacoustic refrigerators are composed of an acoustic driver (Liner motor), waveguides (tubes) and a regenerator sandwiched by two heat exchangers. Standing wave thermoacoustic refrigerators (SWTR), which is mainly investigated in the 1990s,

is shown in Fig.1(A). They have low efficiency, because the phase angle between pressure and velocity oscillation in a regenerator is about 90° , resulting in the use of irreversible thermal process in a regenerator. The breakthrough in the development of thermoacoustic refrigerators was realized by Swift et al. in 1999 [1] and they realized an efficient traveling-wave thermoacoustic refrigerators (TWTR). The key point of the breakthrough is the use of a looped waveguide: the looped waveguide has a regenerator and is connected to the straight waveguide via T-junction tube (as shown in Fig.1(B)). Because of the use of the looped waveguide, the phase angle in a regenerator becomes 0° , which allows us to use reversible thermal process in a regenerator.

Although the efficiency of the TWTR is enough high, there are points to be improved. One of them is the reduction of nonlinear viscous dissipation, called minor loss [2], occurring at the T-junction tube which connected the looped waveguide and the straight waveguide. Swift et al. constructed the efficient traveling-wave thermoacoustic engine and estimated that 20% of the acoustic output power of the engine was lost as the minor loss [3]. As just described above, the reduction of the minor loss is very important to improve the performance of thermoacoustic systems. However, minor loss at the T-junction tube has not been investigated yet. Furthermore, the effects of minor loss occurring in a certain component on the overall refrigerator is unidentified.

The aim of this paper is to measure the minor loss at the T-junction tube, and to investigate factors affecting it.

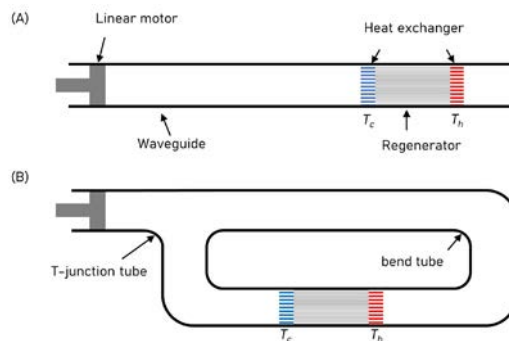


Figure 1. Drawings of the experimental device for the minor loss.

Theory

In this section, calculation methods of the waveguide and the minor loss are described.

Waveguides

Based on the linear acoustic theory, the momentum and continuity equations [3], [4] for a circular tube can be expressed as,

$$\frac{dP}{dx} = -\frac{i\omega\rho_m}{1-\chi_v} U, \quad (1)$$

$$\frac{dU}{dx} = -\frac{i\omega[1+(\gamma-1)\chi_\alpha]}{\gamma P_m} P + \frac{\chi_\alpha - \chi_v}{(1-\chi_v)(1-\sigma)} \frac{1}{T_m} \frac{dT_m}{dx} U, \quad (2)$$

where P is the pressure and U is the velocity of the gas in the tube (both of them are complex numbers). ρ_m , γ , P_m , and i are the average density of the working gas, specific heat ratio, mean pressure, and imaginary number, respectively. χ_v and χ_α are viscous and thermal thermoacoustic functions [5]. This model is defined as

$$\chi_v = \frac{2J_1[(i-1)\sqrt{\omega\tau_v}]}{(i-1)\sqrt{\omega\tau_v} J_0[(i-1)\sqrt{\omega\tau_v}]} \quad (3)$$

$$\chi_\alpha = \frac{2J_1[(i-1)\sqrt{\omega\tau_\alpha}]}{(i-1)\sqrt{\omega\tau_\alpha} J_0[(i-1)\sqrt{\omega\tau_\alpha}]} \quad (4)$$

where J_0 is primary Bessel function and J_1 is secondary Bessel function. τ_v is viscous relaxation time, and τ_α is thermal relaxation time. τ_v and τ_α are defined as

$$\tau_v = \frac{r^2}{2\nu} \quad (5)$$

$$\tau_\alpha = \frac{r^2}{2\alpha} \quad (6)$$

where r is radius of the waveguides. In this paper, it is assumed that no temperature gradient exists in the waveguides. Therefore, since $(dT_m)/dx=0$, the second term on the right side of equation (2) is zero. If T_m is a constant, the values of χ_α and ρ_m , which depend on T_m , are determined. Therefore, a double differential equation that is a combination of Eqs. (1) and (2) is expressed as

$$[1+(\gamma-1)\chi_\alpha]P + \gamma \frac{P_m}{\omega^2} \frac{d}{dx} \frac{1-\chi_v}{\rho_m} \left(\frac{dP}{dx}\right) = 0, \quad (7)$$

and obtained as

$$\frac{d^2 P}{dx^2} = -\frac{\omega^2}{a_0^2} \frac{1 + (\gamma - 1)\chi_\alpha}{1 - \chi_v} P, \quad (8)$$

where a_0 is adiabatic speed of sound. Furthermore, the complex wave number d required to solve Eq. (8) is defined as [6],

$$d \equiv -\frac{\omega}{a_0} \sqrt{\frac{1 + (\gamma - 1)\chi_\alpha}{1 - \chi_v}}. \quad (9)$$

By solving Eq. (8) using d , the pressure amplitude $P(x_2)$ and the velocity amplitude $U(x_2)$ can be obtained from the information of $P(x_1)$ and $U(x_1)$ as,

$$P(x_2) = P(x_1) \cos d(x_2 - x_1) - \frac{i\omega\rho_m}{d(1 - \chi_v)} U(x_1) \sin d(x_2 - x_1), \quad (10)$$

$$U(x_2) = \frac{d(1 - \chi_v)}{i\omega\rho_m} P(x_1) \sin d(x_2 - x_1) + U(x_1) \cos d(x_2 - x_1). \quad (11)$$

Where x_1 and x_2 are two axial points of the waveguides.

By modifying Eqs. (10) and (11), we can express $P(x_2)$ and $U(x_2)$ by two adjacent segments in a matrix form as

$$\begin{pmatrix} P(x_2) \\ U(x_2) \end{pmatrix} = M_{\text{waveguide}} \begin{pmatrix} P(x_1) \\ U(x_1) \end{pmatrix} \quad (12)$$

$$M_{\text{waveguide}} \equiv \begin{bmatrix} \cos d(x_2 - x_1) & -\frac{i\omega\rho_m}{d(1 - \chi_v)} \sin d(x_2 - x_1) \\ \frac{d(1 - \chi_v)}{i\omega\rho_m} \sin d(x_2 - x_1) & \cos d(x_2 - x_1) \end{bmatrix}. \quad (13)$$

Acoustic power flow $W(x)$ can be expressed by $P(x)$ and $U(x)$.

$$W(x) = \frac{1}{2} A(x) \text{Re} [P(x) \overline{U(x)}] \quad (14)$$

where $A(x)$ is the cross-sectional area of waveguides.

Minor loss

A minor loss occurs when oscillating gas flows across geometrical irregularities. Wakeland and Keolian [2] proposed an equation for the acoustic minor loss. The equation

is expressed as

$$\Delta W_{loss} = \frac{2}{3\pi} \rho_m A K |U|^3 \quad (15)$$

where ΔW_{loss} is the acoustic minor loss, A is the cross-sectional area of the waveguides at minor loss occurs, $|U|$ is the amplitude of the velocity at the waveguides, and K is the coefficient of the minor loss.

Hence, the value of minor loss can be calculated if the minor-loss coefficient K is known. The mainstream thermoacoustic refrigerators have three components causing minor loss: the tapered tube, the T-junction tube, and the bend tubes. The coefficients of minor loss for the tapered tube and the bend tube are reported by Ueda et al. [7] and Xiachen et al. [8], respectively. The preliminary experiments indicated that the minor loss at the bend tubes is negligible, so K of the bend tube is determined to be zero. The coefficient of minor loss at T-junction tube is not known, so the measurement is needed.

Investigation of the relationship between the direction of acoustic wave input to T-junction tube and the magnitude of the minor loss.

Set up

The schematic of the experimental device is illustrated in Fig.2. One or two loudspeaker unit(s)(FW168HS, Fostex Co. Ltd.), the tapered tube($\theta_{taper}=20.0^\circ$), three waveguides, the T-junction tube, and closed ends are used. The radius of the waveguides r_{tube} , the length of the waveguide X (between tapered tube and T-junction tube) L_x , and the length of the waveguides Y (between T-junction tube and closed end) L_y are 20.0 mm, 0.445 m, and 0.450 m, respectively. The bending radius R of the T-junction tube is 0 mm. To investigate the effect of the direction of the acoustic wave, three experimental conditions are tested: (A) the speaker including the tapered tube is connected to the left end of waveguide X, (B) one of two speakers is connected to the left end and the other is done to the bottom end, and (C) one speaker is connected to the left end and the other is connected to the right end.

All experiments are performed at room temperature ($T_m=292\pm 1$ K) and atmospheric pressure. In the experiments, the two-sensor method [9], in which two pressure sensors are used to measure the velocity amplitude and acoustic power in the waveguide, is used. All experiments are performed at the resonance frequency (the frequency under

the condition (A), $f(A)$ is 76.8 Hz, $f(B)=106.5$ Hz, and $f(C)$ is 107.5 Hz) of the experimental device. According to the previous research [10], the velocity amplitude in the waveguide A is used as the representative value.

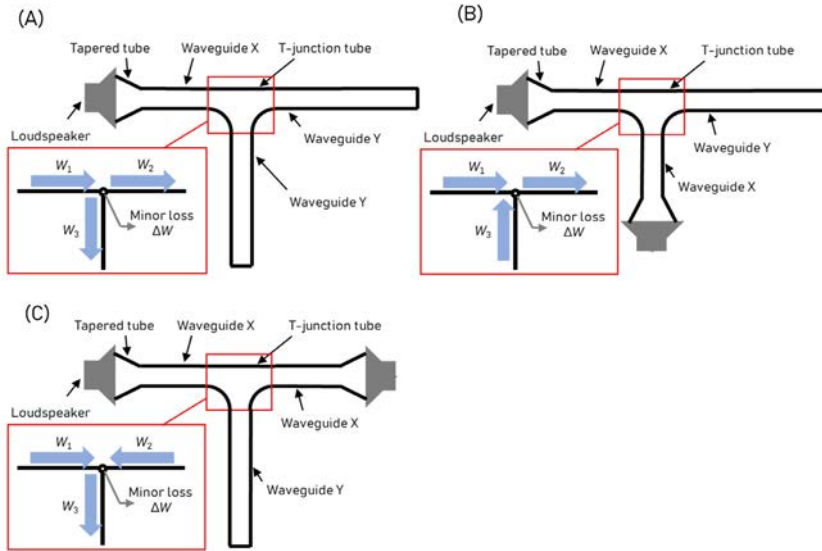


Figure 2. Drawings of the experimental device for the minor loss.

The magnitude of minor losses ΔW_{loss} is calculated from the loss of acoustic power around the T-junction tube. ΔW_{loss} for the conditions (A), (B), and (C) are defined as

$$\Delta W_{\text{loss}} = W_1 - (W_2 + W_3), \quad (16A)$$

$$\Delta W_{\text{loss}} = (W_1 + W_3) - W_2, \quad (16B)$$

$$\Delta W_{\text{loss}} = (W_1 + W_2) - W_3, \quad (16C)$$

where W_1 , W_2 , W_3 are the acoustic power on the left, right, and bottom sides of the T-junction tube, respectively. (See the insets of Fig. 2)

Results

In Fig. 3, the measured ΔW_{loss} is depicted as a function of $|U_3|$. The black squares, red triangles, and blue circles show the experimental results for conditions (A), (B), and (C), respectively. Figure 3 shows that the value of ΔW_{loss} linearly increases with the increase in

$|U|_3$. When $|U|_3=4.0 \times 10^4 \text{ m}^3/\text{s}^3$, ΔW_{loss} of condition (A), (B), and (C) are 15.6 W, 13.0 W, and 15.2 W, respectively.

As previously mentioned, the measured ΔW_{loss} is proportional to $|U|_3$; hence, we can use Eq. (15), as suggested by Swift [3] and Wakeland and Keolian [2]. Using the least squares method, the gradient of g of the obtained data at condition (A), (B), and (C) are calculated to be $3.91 \times 10^{-4} \text{ kg/m}$, $3.25 \times 10^{-4} \text{ kg/m}$, and $3.80 \times 10^{-4} \text{ kg/m}$, respectively. From Eq. (15), g can be related to the coefficient of the minor loss K as,

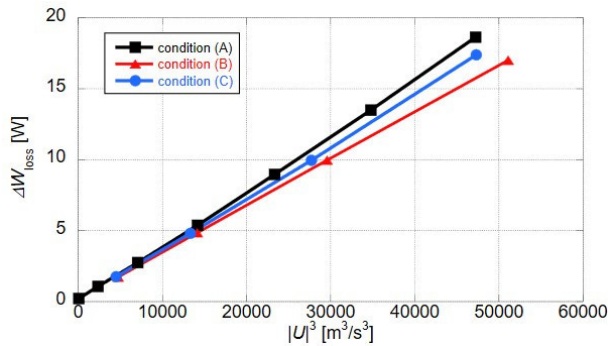


Figure 3. Direction of acoustic wave dependence of the minor loss.

$$K = \frac{3\pi}{2A\rho_m} g. \quad (17)$$

Hence, K of condition (A), (B), and (C) are 1.23, 1.02, and 1.19, respectively. According to these results, it was found that the relative error between condition (A) and condition (B) was 17%, and also between condition (A) and condition (C) was 3%.

Investigation of the relationship between the shape of the T-junction tube and the magnitude of the minor loss

Set up

To investigate the effect of the shape of the T-junction tube, we measure minor loss by varying the bending radiuses R of the T-junction tubes; the values of R are set to 0 mm, and 40 mm. The schematic of the experimental device is illustrated in Fig.2(A). The structure and the conditions of the experimental device are same as condition (A) in the previous section.

Results

In Fig. 4, the measured ΔW_{loss} is depicted as a function of $|U|_3$. The black square shows the experimental results for $R=0$ mm, and the red triangle shows the results for $R=40$ mm. Figure 4 shows that the value of ΔW_{loss} linearly increases with the increase in $|U|_3$. When $|U|_3=4.0 \times 10^4 \text{ m}^3/\text{s}^3$, ΔW_{loss} with $R=0$ mm and $R=40$ mm are 15.6 W and 3.42 W, respectively. From Eq. (15), K of $R=0$ mm and $R=40$ mm is 1.23 and 0.27, respectively. According to these results, the minor loss can be reduced 78% by increasing R of the T-junction tube to the same value as the radius of the waveguide.

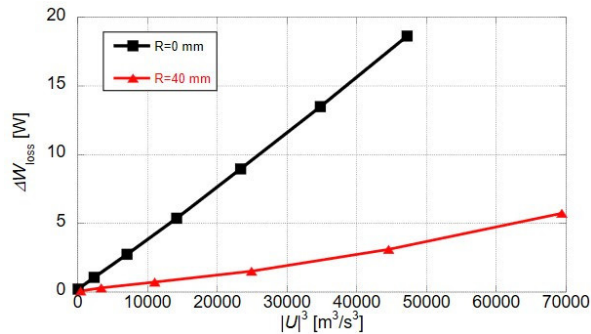


Figure 4. Measured minor loss at the T-junction tube.

Conclusion

The aim of this paper is to measure the minor loss occurring at T-junction tube in the waveguide and to investigate factors affecting it. On investigation, the minor loss occurring at the T-junction tube was experimentally shown to be proportional to the cube of the representative velocity. Furthermore, we found that the effect of the direction of acoustic wave input to the T-junction tube is sufficiently small compared to the effect of the shape of it.

References

- [1] Swift, G. W., Gardner, D. L., and Backhaus, S. "Acoustic recovery of lost power in pulse tube refrigerators." *The Journal of the Acoustical Society of America* 105.2 (1999): 711-724.

- [2] Wakeland, R. S., and Keolian, R. M. "Influence of velocity profile nonuniformity on minor losses for flow exiting thermoacoustic heat exchangers (L)." *The Journal of the Acoustical Society of America* 112.4 (2002): 1249-1252.
- [3] Swift, G. W., "Thermoacoustics: A unifying perspective for some engines and refrigerators." Springer, 2017.
- [4] Rott, G., "Damped and thermally driven acoustic oscillations," *Z. Angew. Math. Phys.* 20 (1969): 230–243.
- [5] Tominaga, A. "Thermodynamic aspects of thermoacoustic theory." *Cryogenics* 35.7 (1995): 427-440.
- [6] Yazaki, T., Tashiro, Y., and Biwa, T. "Measurements of sound propagation in narrow tubes." *Proceedings of the Royal Society A: Mathematical, Physical and Engineering Sciences* 463.2087 (2007): 2855-2862.
- [7] Ueda, Y., et al. "Measurement and empirical evaluation of acoustic loss in tube with abrupt area change." *The Journal of the Acoustical Society of America* 147.1 (2020): 364-370.
- [8] Ding, X., et al. "Research on the effects of resonance tube bending in loop thermoacoustic refrigeration system." *Applied Thermal Engineering* (2024): 122985.
- [9] Biwa, T., et al. "Acoustic intensity measurement in a narrow duct by a two-sensor method." *Review of scientific instruments* 78.8 (2007).
- [10] Idelchik, I. E., Steinberg, M. O., and Martynenko, O. G., "Handbook of hydraulic resistance. Vol. 2." New York: Hemisphere publishing corporation, 1986.

Influence of Displacement Phase Angle on the Performance of Rotary Stirling Cryocooler

Jhen-Syuan Huang

Department of Mechanical and Computer-Aided Engineering, Feng Chia University, No. 100, Wenhua Road, Xitun District, Taichung City, Taiwan

*Corresponding author: jhenshuang@fcu.edu.tw

Keywords: Stirling cryocooler, displacement phase angle, Thermodynamic model, Heat load

Abstract

Stirling cryocooler is a miniature cooling system that is operated as a closed-loop gas cycle. Gases such as air, nitrogen, or helium can be utilized as the working fluid in Stirling cryocooler, avoiding greenhouse gas emissions. This type of cryocooler finds widespread applications in high-end cooling systems, including infrared thermal sensing devices, superconductors, and low-temperature cold chains. Stirling cryocooler typically consists of two moving components, a displacer and a piston. In addition, their displacement should be designed with appropriate phase angle so that working gas can absorb and release heat efficiently. Rotary integral configuration of Stirling cryocooler offers advantages such as compact volume and precise design parameters. In this study, effect of displacement phase angle between displacer and piston on the performance of rotary-integral Stirling cryocooler is investigated via a thermodynamic model. The phase angle is altered by increasing or decreasing the angle between axes of cylinders. Operational parameters in present study are charged pressure of 30 bar and rotation speed of 3000 rpm, respectively. With the present methodology, it is concluded that the optimal phase angle for the lowest cold head temperature is 67° - 70° based on the model.

Introduction

Stirling cryocooler is compact cooling device that can be miniaturized to meet crucial applications such as optical sensor and unmanned aerial vehicle. Among mature mechanical cryocoolers, Stirling type is demonstrated with better efficiency [1]. It is basically constituted of two moving parts which are called displacer and piston. For the purpose of compressing and expanding working gas, piston can be driven by rotary or linear motor. Based on the reverse Stirling cycle principle, displacer and piston are actuated periodically with a phase angle that is 90 degrees in theory [2]. Cylinders of displacer and piston can be integrated in one base or connected with a pipe, which are commonly termed integral type and split type, respectively. Due to its low mass

and simple mechanism, rotary integral has been a favorable configuration in Stirling cryocooler. In the existing rotary integral design, displacer and piston cylinders are arranged in L-shape, which results in a precise displacement phase angle of 90 degrees. Thermodynamic model with logical assumptions is a means to analyze transient variation and predict performance of Stirling cryocooler. Walker et al. [3] built a first order simulation in which compression and expansion chamber were regarded as isothermal. Li and Grosu [4] furtherly considered possible heat losses and temperature variation in the regenerator. In order to obtain detail thermal fluid field, Garg et al. [5] accomplished a complicated numerical simulation with axisymmetric domain. Huang and Cheng [6] had also presented a theoretical model of rotary integral Stirling cryocooler by taking thermo-physical properties of working gas and geometrical evaluation of wire mesh into account. Moreover, a prototype was constructed to validate the model. At charged pressure of 30 bar and rotation speed of 3000 rpm, cold head temperature was 98.6 K by theoretical model and 103.4 K by experimental measurement. As a result, the model is adopted to investigate the circumstance that displacer cylinder and piston cylinder are not perpendicular in this research. Purpose of this paper is to find the optimal phase angle that leads to lowest cooling temperature.

Methodology

Figure 1 shows the studied rotary integral Stirling cryocooler in which a cylinder angle (ε) is introduced as a variable in this study. As ε is changed, displacement phase angle between displacer and piston is followed. The working space is divided into compression, tube, regenerator and expansion chambers. Volumes of compression and expansion are determined by piston and displacer, respectively. Hence, cylinder angle (ε) simultaneously stands for displacement phase angle that displacer leads piston and volume phase angle that expansion chamber leads compression chamber as the crank is rotated counterclockwise. According to geometrical relation, kinematic equations describing displacer and piston can be written as

$$y_d = r_o \cos(\pi - \varepsilon - \theta) + \left(l_d^2 - r_o^2 \sin^2(\pi - \varepsilon - \theta) \right)^{1/2} \quad (1)$$

$$y_p = -r_o \cos \theta + \left(l_p^2 - r_o^2 \sin^2 \theta \right)^{1/2} \quad (2)$$

Dimensions of r_o , l_p and l_d are 1 mm, 15 mm and 14 mm. In addition, the charged working fluid considered in present analysis is 30-bar helium.

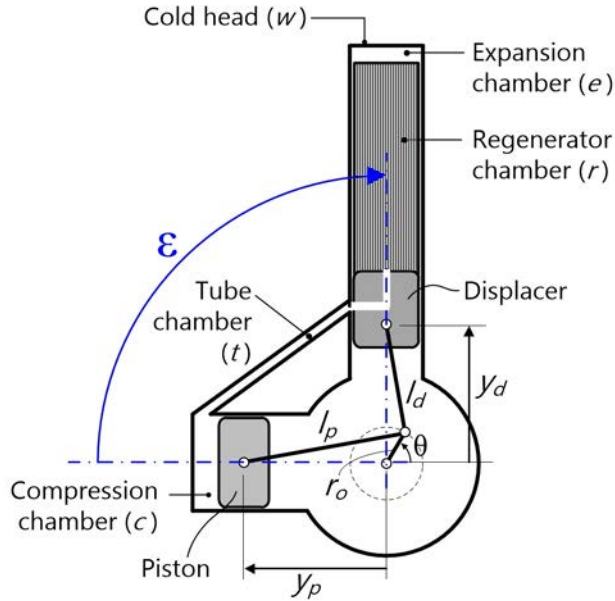


Figure 1. Schematic of rotary integral Stirling cryocooler with variable cylinder angle.

In the thermodynamic model, volumes of compression and expansion chamber are firstly calculated. Average pressure is then obtained according to ideal gas law as

$$P_{avg} = \frac{MR}{\frac{V_c}{T_c} + \frac{V_t}{T_t} + \sum_{i=1}^{n_r} \frac{V_{r,i}}{T_{r,i}} + \frac{V_e}{T_e}} \quad (3)$$

where M is the total mass filled in the cryocooler, R is the gas constant. n_r is the number of sub-volumes in the regenerator that can be used to acquire temperature gradient along regenerator. Pressure change, mass change and mass flow rate are then evaluated. Stacked wire mesh is used as regenerator, and the friction factor can be expressed as [7]

$$f = \frac{129}{Re} + 2.91Re^{-0.103} \quad (4)$$

The mesh number and wire diameter used are 400 in-1 and 0.025 mm.

Finally, temperature in each chamber is updated by energy equation of working gas

$$\frac{d(m c_p T)_j}{dt} = \dot{Q}_j - \frac{P_j dV_j}{dt} + \dot{m}_{in,j} c_p T_{in,j} - \dot{m}_{out,j} c_p T_{out,j} + \dot{Q}_{loss} \quad , \quad j = c, t, r, e \quad (5)$$

\dot{Q}_{loss} is the thermodynamic losses that result from movement of displacer. In present model, shuttle loss and pump loss are incorporated. On the other hand, cold head temperature is calculated by considering associated heat transfer

$$\frac{d(m_w c_w T_w)}{dt} = -\dot{Q}_e + \dot{Q}_{cy} + \dot{Q}_{load} \quad (6)$$

\dot{Q}_{cy} is heat conduction through the cold head cylinder. \dot{Q}_{load} is heat load exerted on the cold head. Furthermore, dependence of thermo-physical properties of working gas on pressure and temperature is considered in present model.

Results and discussion

Figure 2 shows a prototype of rotary integral Stirling cryocooler that has been manufactured. It is designed with typical configuration so that displacement phase angle is 90° . Stroke lengths of both piston and displacer are 2 mm. The prototype is equipped with a brushless DC motor rated by 30 W. During operation, temperature of cold head shown in Figure 2 is detected by a silicon diode sensor. As for heat load, polyimide film heater is adopted to provide thermal energy. In case of 30-bar charged pressure and 3000-rpm rotation speed, it is validated that cold head reaches 103.4 K, 107.9 K and 113.6 K under 0 W, 0.1 W and 0.2 W heat load, respectively.

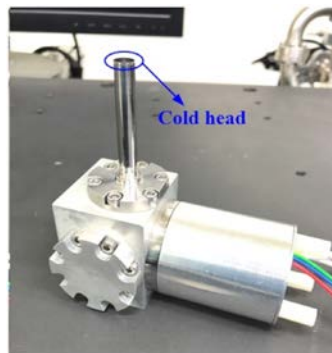


Figure 2. Prototype of rotary integral Stirling cryocooler with phase angle of 90° .

Displacements of displacer and piston during two rotations are displayed in Figure 3. Piston axis is fixed horizontally so that position of piston versus crank angle is unchanged. On the other hand, trajectory of displacer will be shifted as ϵ is varied between 50° and 110° . Since the volume of expansion chamber is governed by displacer, total volume of the working gas in Stirling cryocooler is also altered. As a result, dimensionless parameter compression ratio will not be the same with different phase angle. Values of compression ratio in studied range are listed in Table 1. It can be seen that compression ratio is increased as phase angle is decreased because the instants of maximum expansion volume and compression value approach.

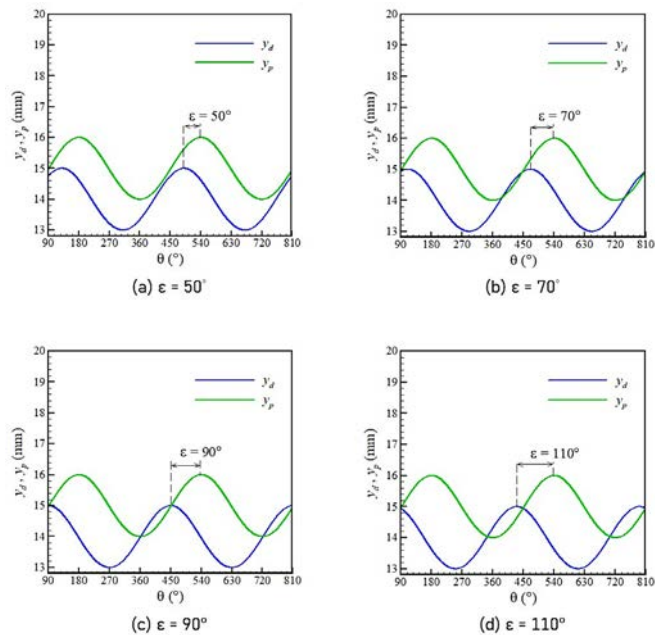


Figure 3. Displacement versus crank angle.

Table 1. Compression ratio with different phase angles.

Phase angle	Compression ratio
50°	1.619
70°	1.578
90°	1.529
110°	1.480

With the help of present thermodynamic model, parametric analysis of displacement phase angle is conducted. Figure 4 displays no-load cold head temperature with phase angle of 50° , 70° , 90° , and 110° . It can be seen that cold head temperatures of 96.5 K, 93.2 K, 98.6 K and 111.3 K are obtained, respectively. Among the four cases, the lowest temperature takes place at $\epsilon = 70^\circ$. Hence a complete sweep is carried out by resolution of 1° and the results are shown in Figure 5. Blue curve stands for the case of zero heat load while green and pink curves depict cold head temperature under heat load of 0.1 W and 0.2 W. From the numerical results, optimal displacement phase angle is 67° without heat load. As the heat load is applied by 0.1 W and 0.2 W, optimal values are slightly increased to 68° and 70° . Furthermore, experimental values measured from the mentioned prototype are also marked in the figure in which phase angle of 90° is designed. There are deviations of rough 5 K between thermodynamic model and experiment. However, this study proposed a concept of variable displacement phase angle of rotary integral Stirling cryocooler by altering axis of displacer cylinder. It is still possible to be implemented by modifying the basecase of prototype in the future despite of high cost.

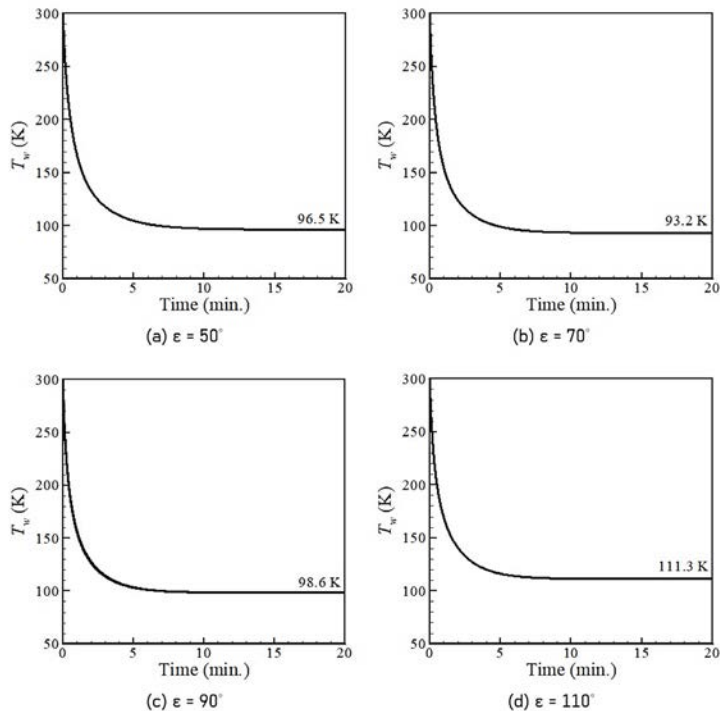


Figure 4. No-load temperature with different phase angle.

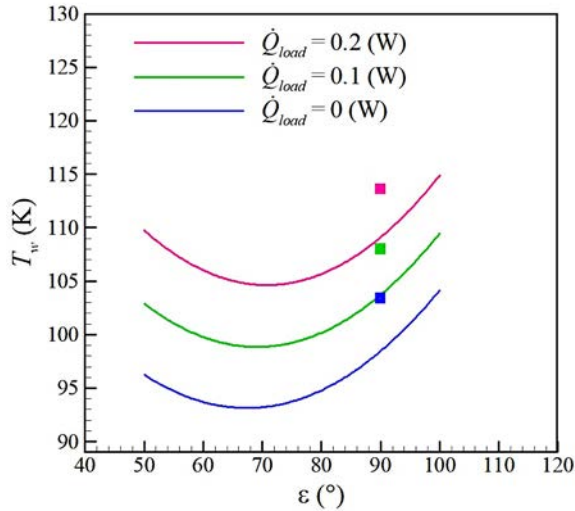


Figure 5. Cold head temperature versus displacement phase angle with heat loads.

Summary

In this work, a miniature Stirling cryocooler designed with the rotary integral configuration is studied by thermodynamic model. A prototype had been demonstrated to validate the model. The cryocooler showed no-load cooling temperature of 98.6 K and 103.4 K by simulation and experiment, respectively. In the original structure, piston and displacer cylinder are arranged with vertical orientation, which results in a 90° displacement phase angle. However, cylinder angle is treated as a variable in this paper so that cooling performance under different phase angle can be obtained. From the results, it is concluded that optimal phase angle lies in 67°-70° in conditions of 0-0.2 W heat load.

Acknowledgment

The author would like to thank the National Science and Technology Council, Taiwan, for the financial support under Grant NSTC 112-2221-E-035-038-MY2.

References

- [1] Chakravarthy, V. S., Shah, R. K., & Venkatarathnam, G. (2011). A review of refrigeration methods in the temperature range 4–300 K. *ASME. Journal of Thermal Science and Engineering Applications*, 3(2), 020801.

- [2] Organ, A. J. (1999). The miniature, reversed Stirling cycle cryo-cooler: integrated simulation of performance. *Cryogenics*, 39(3), 253-266.
- [3] Walker, G., Weiss, M., Fauvel, R., & Reader, G. (1989). Microcomputer simulation of Stirling cryocoolers. *Cryogenics*, 29(8), 846-849.
- [4] Li, R., & Grosu, L. (2017). Parameter effect analysis for a Stirling cryocooler. *International Journal of Refrigeration*, 80, 92-105.
- [5] Garg, S. K., Premachandran, B., & Singh, M. (2019). Numerical study of the regenerator for a miniature Stirling cryocooler using the local thermal equilibrium (LTE) and the local thermal nonequilibrium (LTNE) models. *Thermal Science and Engineering Progress*, 11, 150-161.
- [6] Huang, J. S., & Cheng, C. H. (2023). An efficient theoretical model of rotary-integral Stirling cryocooler validated by experimental testing. *Thermal Science and Engineering Progress*, 43, 101996.
- [7] Gedeon, D., & Wood, J. G. (1996). Oscillating-flow regenerator test rig: hardware and theory with derived correlations for screens and felts (No. E-10076).

Development of a Miniature Free Piston Stirling Cryocooler for HOT Infrared Detector

Zhongli Xi, Xing Xiao, Xiaoqing Zhang*

Department of Refrigeration & Cryogenics, Huazhong University of Science and Technology, 1037 Luoyu Road, Wuhan, China

*Corresponding author: zhangxq@mail.hust.edu.cn

Keywords: Free piston Stirling, Miniature cryocooler, Thermo-dynamic network model, Experimental prototype, HOT infrared detector

Abstract

With the development of infrared chip technology, the demand for miniature cryocoolers in the 150K operating temperature range has become increasingly prominent for High Operating Temperature (HOT) infrared detector. Split-type free-piston Stirling cryocoolers, characterized by low vibration, small size, and light weight, have found its unique advantage in this HOT infrared detector applications. However, the complex operating mechanism of free-piston Stirling cryocoolers, influenced by factors such as linear compressor, miniature regenerator, and the pneumatic displacer, poses design challenges due to their intercoupled effects. Application requirements, in such scenarios of limiting the optical axis length and weight dimensions, further challenge their design and development. This study addresses these challenges by utilizing a thermo-dynamics network model, considering the active nature of the Stirling regenerator, thermal and dynamic characteristics and nonlinear effects in various chambers of the Stirling cryocooler. In comparison with traditional thermoacoustic network models, besides considering the active nature of the Stirling regenerator, the present thermo-dynamic network model for the miniature Stirling cryocooler more emphasizes the coupling analysis between thermodynamics and dynamics in actual operating conditions, and takes into account some corrections to nonlinear effects through network transmission parameters. The present model is verified by the experiments with good accuracy. Subsequently, a miniature free-piston Stirling cryocooler was fabricated, which comprises three main assemblies: the miniature compressor with opposed dual linear motor, an expander, and a split connection tube. The miniature Stirling cryocooler is tested by an experimental system, and necessary data are collected for analyses, including the displacements of the compressor piston and the displacer piston, pressure waves at the outlet of compressor chamber, cooling temperature and cooling capacity at the expander's cold end, and input electrical power to the compressor as well. The testing results demonstrate a good overall performance: cooling capacities of 1.35 W at 150 K with a power consumption of 10WAC in a 23 °C ambient temperature and the relative Carnot efficiency at 150 K exceeds 13.5%. The total weight of the miniature cryocooler is less than 210 g and the maximum input electrical power is 20 WAC.

Introduction

As we know, in 1985, C. T. Elliott et al. first proposed the concept of using non-equilibrium mode to improve the working temperature of the photon detector, that is, high operation temperature (HOT) infrared photonic device [1]. In 1999, Donald et al. proposed that the third-generation infrared focal plane detector should have the characteristics of high performance and low cost, and the operating temperature of the device should be increased to 180 K [2]. In recent ten years, with the development of infrared semiconductor technology, the optimized operating temperature of low-temperature refrigeration infrared detectors has been increased to the temperature range of 150K~160K. In addition, the pixel spacing also decreases, which greatly reduces the demand for the cooling capacity of the infrared detector chip in this temperature zone, providing new opportunities for a wider range of applications [3, 4]. At the same time, it also puts forward new requirements for the size, weight, power consumption, cost and reliability of the cryocooler [5-6].

Table 1 lists the performances of miniature Stirling cryocoolers used in HOT detector from some companies in recent years, mainly the rotary Stirling and linear free piston Stirling cryocooler (FPSC) structure [7-11]. Rotary Stirling cryocooler usually has high thermal efficiency, but its internal structure is complex, making its miniaturization a certain challenge, and the friction pair has a large side force, the machine vibration is large, affecting the reliability. On the contrary, the free piston Stirling cryocooler driven by linear motor has become the best choice, because of its simple structure, low vibration and high reliability, for the cooling of infrared detector chips in the temperature zone of 150K and above.

Table 1. Miniature Stirling cryocoolers from different company for HOT infrared detectors.

Company	Ricor	Ricor	Thales Cryogenics	AIM-IR	Cobham	FLIR
Model	K580	K588	UP8197	SX020	LC1076	FL-100
Motor	Rotary	Linear	Linear	Linear	Linear	Linear
Configuration	Rotary	Dual	Dual	Single	Dual	Dual
Cooling capacity* (W)	< 1	< 1	0.9	0.65	0.5	1.45
Max power consumption (WAC)	< 10	< 12	20	20	15	15

Compressor size						
(mm×mm)	54.8×48.2	Φ26×52	Φ30×62	Φ27.5×62	Φ28.2×53.6	Φ31×67.6
Expander length (mm)	57.5	47	58.4	57.6	40	52.7
Cooler weight (g)	190	190	250	220	226	262

*Cooling capacity is @150K@23 °C, 10WAC Input

At present, most of free piston Stirling cryocoolers adopt the pneumatic expander structure driven by the split-type linear compressor. As known, the operating principle of this kind of structure of cryocoolers involves the strong coupling of thermal, acoustic, mechanic-electromagnetic multiple physical fields, and its characteristic analysis and performance prediction need to solve the coupling basic equations to achieve, which makes the design process more complicated. The thermo-dynamic network analysis method, which combines classical thermoacoustic theory and dynamics modeling of Stirling cycle machine, provides an effective solution for analysis and design [12]. Based on the thermoacoustic theory and considering the dynamic characteristics of each moving part of the free-piston Stirling cryocooler and the actual heat transfer process in each chamber, as well as the axial temperature distribution and active characteristic of the expander regenerator, this study adopted a two-port network to describe the transmission process of pressure wave and volume flow rate in each component of the cryocooler, and established a thermal-dynamic active network analysis model. The performance of the cryocooler is also predicted. A prototype of free piston Stirling cryocooler was developed with weighing only 200 grams and excellent overall performance. It was driven by a moving magnetic linear compressor with dual motor opposed structure. The model predicted performance is in good agreement with measured performance.

Thermo-dynamic network model of FPSC

Physical model of miniature Stirling cryocooler

Fig. 1 is a schematic diagram of the physical model for the miniature split-type free piston Stirling cryocooler. The linear compressor is driven by a moving magnetic opposing double linear motor, and the compression piston is fixed on the mover of linear motor

with spring to form a compression piston resonance system and does reciprocating motion under AC drive. The expander uses a regenerator built into the displacer structure to reduce size and axial heat conduction. The thermal end of the displacer piston is fixed to the spring to form the resonant system of the displacer piston, and the reciprocating movement is produced under the aerodynamic driving force caused by pressure difference across the displacer. A suitable operating phase difference is maintained between the movement of the compression piston and the displacer piston. The detector chip is bonded on the end face of the expansion chamber to be cooled through heat conduction, which is called the cold finger of the cryocooler.

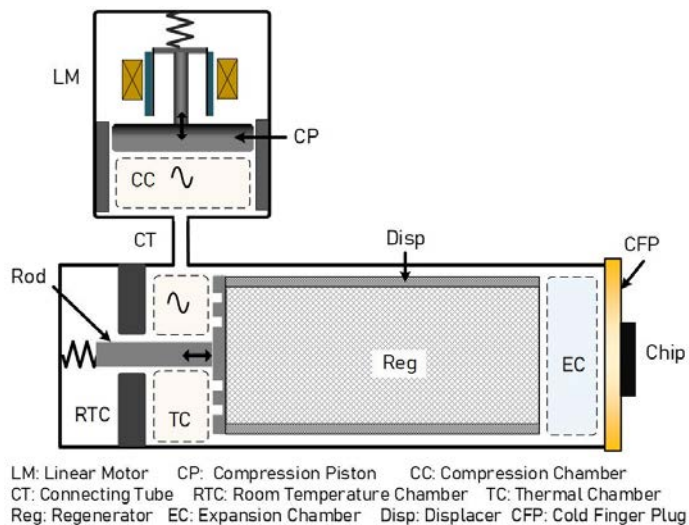


Figure 1. Physical Model diagram of the miniature FPSC.

2.2 Basic assumptions and governing equations

According to the actual operating characteristics of the miniature Stirling cryocooler, reasonable assumptions are made: the working fluid helium is an ideal gas; the long wave approximation is assumed, and the pressure wave is regarded as a one-dimensional plane wave. The acoustic wave variables are treated as one-dimensional linear quantities; The nonlinear effects caused by internal DC, jet and higher order harmonics are ignored; In addition, the parameters of the working fluid are evenly distributed in the compression

chamber, the thermal chamber and the expansion chamber of Stirling cryocooler. In the oscillating flow, the time-invariable quantity of the pressure is regarded as uniform at each position of the system, that is, equal to the charging pressure; The volume of room temperature chamber is usually much larger than that of thermal chamber and expansion chamber, and the influence of pressure change in room temperature chamber on the dynamics of expander is ignored.

Under the above assumptions and in frequency domain form, the basic control equations of Stirling cryocooler are given by Eq. (1) through (5) [12].

$$j\omega\tilde{p}(x, j\omega) - \frac{P_m}{T_m(x)} \left(j\omega\tilde{T}(x, j\omega) + u(x, j\omega) \frac{\partial T_m(x)}{\partial x} \right) + \frac{P_m}{A_f} \frac{\partial \tilde{v}(x, j\omega)}{\partial x} = 0 \quad (1)$$

$$j\omega \frac{P_m}{R_g T_m(x) A_f} \tilde{v}(x, j\omega) + \frac{\partial \tilde{p}(x, j\omega)}{\partial x} + \frac{\alpha P_m}{R_g T_m(x) A_f} \tilde{v}(x, j\omega) = 0 \quad (2)$$

$$j\omega\tilde{T}(x, j\omega) + \frac{\dot{v}(x, t)}{A_f} \frac{dT_m(x)}{dx} - \frac{j\omega}{\rho c_p} \tilde{p} + \frac{hA_{HX}}{\rho c_p v} (T(x, j\omega) - T_w(x, j\omega)) - \frac{N_s \lambda}{\rho c_p} \frac{\partial^2 T_m(x)}{\partial x^2} = 0 \quad (3)$$

$$j\omega \rho_s c_s v_s \tilde{T}_s(x, j\omega) = -hA_{HX} (T_w(x, j\omega) - T(x, j\omega)) - f_s \lambda_s v_s \frac{\partial^2 T_{sm}(x)}{\partial x^2} \quad (4)$$

$$u_E = \psi_E \dot{x}_p + i_E R_E + L_E \frac{di_E}{dt} \quad (5)$$

where, $\alpha = f_D \mu_{\max} / 2d_h$, is the resulting friction factor used to linearize the viscous shear stress of the momentum equation, f_D is the Darcy friction factor, and d_h is the hydraulic diameter of the flow channel [13]. N_λ is the enhancement coefficient of axial thermal conduction of the fluid, T_s is the average temperature of the solid, λ_s is the thermal conductivity of the solid, A_{se} is the effective thermal conduction area of the solid, that is, $A_{se} = f_s A_s$, where f_s is the distortion coefficient of the cross-section of the solid, and $f_s = 1$ for solid solids. By applying the basic equations to each chamber or component of the cryocooler as shown in Fig. 1, the corresponding two-port network equation of component can be established, and then the thermo-dynamic network model of the entire Stirling cryocooler can be obtained.

Thermo-dynamic network model

Network transmission equation of variable volume chamber

(a) Method of coupling thermodynamics of variable volume chamber and dynamics

In this paper, the chamber, whose volume changes greatly due to the reciprocating motion of compression piston or displacer piston, is called variable volume chamber. By the variable volume chamber, thermodynamics is coupled with the dynamics of the cryocooler, and mass and energy transfer and conversion are carried out with the outside world. Fig. 1 shows that there are three typical variable-volume chambers in a free-piston Stirling cryocooler: compression chamber, thermal chamber and expansion chamber. Among them, the force schematic diagram of compression piston and displacer piston is shown in Fig. 2 (a) and (b), respectively.

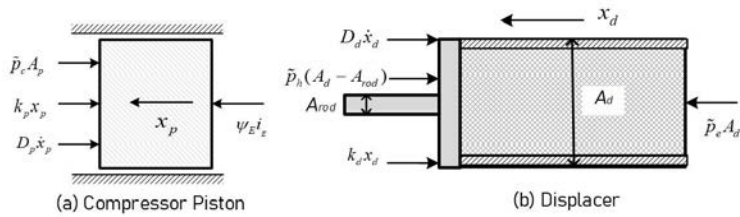


Figure 2. Force diagrams of the moving parts of compressor and displacer.

The corresponding dynamic equations are given by

$$m_p \ddot{x}_p(t) + D_p \dot{x}_p(t) + k_p x_p(t) + \tilde{p}_c(t) A_p - \psi_E i_E(t) = 0 \quad (6)$$

$$m_d \ddot{x}_d(t) + D_d \dot{x}_d(t) + k_d x_d(t) = A_d (\tilde{p}_h(t) - \tilde{p}_e(t)) + A_{rod} \tilde{p}_h(t) \quad (7)$$

Eq. (5) is rearranged and the two-port network transmission equation is obtained by

$$\begin{bmatrix} u_E(j\omega) \\ i_E(j\omega) \end{bmatrix} = \begin{bmatrix} R_E + j\omega L_E & j\omega \psi_E \\ 1 & 0 \end{bmatrix} \begin{bmatrix} i_E(j\omega) \\ x_p(j\omega) \end{bmatrix} \quad (8)$$

(b) Coupling thermodynamic process of the compression chamber with the dynamics of the compression piston

The compressor generally runs at a higher working frequency, the wall of the compression chamber is usually stainless-steel thick wall, and the thermal conductivity is poor, so the thermal process in the chamber can be considered as an adiabatic compression process, and the pressure is regarded as uniform, and then the inlet and outlet pressure are the

same, that is, $\tilde{p}_c = \tilde{p}_{ci} = \tilde{p}_{co}$, thus the network transmission equation of the compression chamber is given by

$$\begin{bmatrix} \tilde{p}_{co}(j\omega) \\ \tilde{v}_{co}(j\omega) \end{bmatrix} = \begin{bmatrix} 0 \\ \dot{v}_c(j\omega) \end{bmatrix} + \begin{bmatrix} 1 & 0 \\ -j\omega \frac{v_{cm} - A_p x_p(j\omega)}{\gamma p_m} & 1 \end{bmatrix} \begin{bmatrix} \tilde{p}_{ci}(j\omega) \\ 0 \end{bmatrix} \quad (9)$$

For a practical cryocooler, the driving voltage or current is usually used as the known input, and the acoustic impedance determines the amplitude and phase of the piston displacement, as well as the required input power. Therefore, with the drive current i_e as the known input parameter and the piston displacement x_p as the design parameter, combined with Eq. (6), Eq. (8) and Eq. (9), the two-port network transmission equation of the compression chamber is given by

$$\begin{bmatrix} \tilde{p}_{co}(j\omega) \\ \tilde{v}_{co}(j\omega) \end{bmatrix} = \begin{bmatrix} \psi_E / A_p & -M_c / A_p \\ Z_c & Y_c \end{bmatrix} \begin{bmatrix} i_E(j\omega) \\ x_p(j\omega) \end{bmatrix} \quad (10)$$

where, $M_c = -m_p \omega^2 + j\omega D_p + k_p$, is the mechanical harmonic oscillator of compression motor; $Z_c = (j\omega / \gamma p_m) \psi_E (x_p(j\omega) - X_p)$, $Y_c = (j\omega / \gamma p_m) (\gamma p_m A_p + M_c X_p - M_c x_p(j\omega))$, and X_p is design maximum displacement of compression piston.

(c) *Coupling the thermodynamic process of the thermal chamber with the dynamics of the displacer piston of expander*

Similar to the compression chamber, the thermal chamber wall of the expander is usually stainless-steel thick wall with poor thermal conductivity, and the thermal process in the thermal chamber can be regarded as adiabatic process. The volume change of the thermal chamber is caused by the reciprocating movement of the displacer piston. Let the movement displacement of the displacer piston be x_d . According to the mass conservation equation, there are Eq. (11).

$$\tilde{v}_{ho} = \tilde{v}_{hi} - \dot{x}_d (A_d - A_{rod}) - \frac{v_{hm} + x_d (A_d - A_{rod})}{\gamma p_m} \tilde{p}_{hi} \quad (11)$$

According to the assumption that the pressure in the thermal chamber is uniform, that is, the inlet and outlet pressure are the same, having $\tilde{p}_h = \tilde{p}_{hi} = \tilde{p}_{ho}$, and then the network

$$\begin{bmatrix} \tilde{p}_{ho}(j\omega) \\ \tilde{v}_{ho}(j\omega) \end{bmatrix} = \begin{bmatrix} 0 \\ -j\omega x_d(A_d - A_{rod}) \end{bmatrix} + \begin{bmatrix} 1 & 0 \\ -\frac{v_{hm} + x_d(A_d - A_{rod})}{\gamma p_m} & 1 \end{bmatrix} \begin{bmatrix} \tilde{p}_{hi}(j\omega) \\ \tilde{v}_{hi}(j\omega) \end{bmatrix} \quad (12)$$

(d) Coupling the thermodynamic process in the cold chamber of expander with the dynamics of the displacer piston

As shown in Fig. 1, the cold finger of an expander is generally a thin-walled structure, encapsulated in a vacuum Dewar, and the circumferential thin wall of the expansion chamber can be considered as an adiabatic wall surface, while the cold finger end face is a good thermal conductivity surface, which can be regarded as an isothermal process. Then the two-port network transmission equation of the expansion chamber is given by

$$\begin{bmatrix} \tilde{p}_{eo}(j\omega) \\ \tilde{v}_{eo}(j\omega) \end{bmatrix} = \begin{bmatrix} 0 \\ j\omega x_d A_d \end{bmatrix} + \begin{bmatrix} 1 & 0 \\ -\frac{v_{em} - x_d A_d}{p_m} & 1 \end{bmatrix} \begin{bmatrix} \tilde{p}_{ei}(j\omega) \\ \tilde{v}_{ei}(j\omega) \end{bmatrix} \quad (13)$$

where, the outlet of the expansion chamber is the closed heat exchange surface and then the outlet flow rate $\tilde{v}_{eo} = 0$. Let the volume change rate of the expansion chamber be $\dot{v}_e(j\omega) = j\omega A_d x_d(j\omega)$, and substituting Eq. (7), the network transmission equation of displacer piston is given by

$$(j\omega L_d + R_d - j\frac{1}{\omega C_d})\dot{v}_d(j\omega) = (1 - \frac{A_{rod}}{A_d})\tilde{p}_h(j\omega) - \tilde{p}_e(j\omega) \quad (14)$$

where, $L_d = m_d / A_d^2$, $R_d = D_d / A_d^2$, $C_d = A_d^2 / k_d$.

Thermo-dynamic network equations of fluid channel components

In this study, the component of Stirling cryocooler, whose volume does not change, is referred to as fluid channel component, such as regenerator and split metal connecting tube between compressor and expander. Considering the different internal flow path structure and whether there exists a temperature gradient, different resulting friction factor α is used in momentum equation Eq. (2) and the influence of temperature gradient is considered in energy equation Eq. (3).

Stirling cryocooler regenerator adopts high-density stainless steel wire mesh. In this study, regenerator is regarded not only as a heat exchanger for gas and solid packing

to achieve heat exchange, but also as an active component for thermo-acoustic conversion. Here, two important parameters defined in literature [12], heat capacity ratio Φ and characteristic heat transfer angular frequency Ω_H , are used in simplification derivation. Considering thermoacoustic theory, the two-port network transmission equation of regenerator, with pressure and volume flow rate as transmission variable, can be obtained by

$$\begin{bmatrix} \tilde{p}_{ro}(x, j\omega) \\ \tilde{v}_{ro}(x, j\omega) \end{bmatrix} = \begin{bmatrix} \frac{r_2 e^{r_1 x} - r_1 e^{r_2 x}}{r_2 - r_1} & \frac{e^{r_1 x} - e^{r_2 x}}{r_2 - r_1} Z \\ -\frac{r_1 r_2 (e^{r_1 x} - e^{r_2 x})}{r_2 - r_1} \frac{1}{Z} & -\frac{r_1 e^{r_1 x} - r_2 e^{r_2 x}}{r_2 - r_1} \end{bmatrix} \begin{bmatrix} \tilde{p}_{ri}(x, j\omega) \\ \tilde{v}_{ri}(x, j\omega) \end{bmatrix} \quad (15)$$

where, $r_1, r_2 = (g_r \pm \sqrt{g_r^2 + 4Z_r Y_r}) / 2$, is the propagation constant per unit length of the channel, characterizing the flow features of the fluid in channel. $Z_r = p_m (j\omega + \alpha) / (R_g T_m(x) A_f)$, $Y_r = (j\omega A_f / \gamma p_m) [1 + (\gamma - 1) f_{WT}]$, and $g_r = (dT_m(x) / dx) f_{WT} / T_m(x)$ is flow impedance, flow admittance and fluid source due to temperature difference in the regenerator, respectively. $f_{WT} = (1 - \Phi) \Omega_H / (j\omega \Phi (1 - \Phi) + \Omega_H)$ is a heat-work conversion factor per unit length, the specific derivation process can be referred to [12].

Considering that the split metal connecting tube in Stirling cryocooler is an isothermal part with regular flow path, that is, the coefficient f_{WT} and temperature difference term g_r of Eq. (15) are 0 [14-15], the resulting friction factor f_v is the viscous distribution function of the flow path cross section. Therefore, the two-port network transmission equation of the connecting tube can be obtained by

$$\begin{bmatrix} \tilde{p}_{cto}(x, j\omega) \\ \tilde{v}_{cto}(x, j\omega) \end{bmatrix} = \begin{bmatrix} \frac{r_2 e^{r_1 x} - r_1 e^{r_2 x}}{r_2 - r_1} & \frac{e^{r_1 x} - e^{r_2 x}}{r_2 - r_1} Z_{ct} \\ -\frac{r_1 r_2 (e^{r_1 x} - e^{r_2 x})}{r_2 - r_1} \frac{1}{Z_{ct}} & -\frac{r_1 e^{r_1 x} - r_2 e^{r_2 x}}{r_2 - r_1} \end{bmatrix} \begin{bmatrix} \tilde{p}_{cti}(x, j\omega) \\ \tilde{v}_{cti}(x, j\omega) \end{bmatrix} \quad (16)$$

where, $r_1, r_2 = \pm \sqrt{Z_{ct} Y_{ct}}$, $Z_{ct} = j\omega p_m / (R_g T_m (1 - f_v) A)$, and $Y_{ct} = j\omega A / p_m$.

The thermo-dynamic network model of the whole cryocooler

According to the two-port transmission equation of each component and chamber of the cryocooler, the thermo-dynamic network model of the whole cryocooler can be obtained, as shown in Fig. 3.

The performance of cryocooler, such as cooling capacity and COP, can be predicted using

the network analysis model. It should be noted that when calculating acoustic power of expansion chamber (where the acoustic power has taken into account the pressure drop loss Q_{fr} caused by the flow resistance of the cryocooler), it is necessary to subtract the non-ideal heat transfer loss H_{reg} of the regenerator, the axial heat conduction loss Q_{cond} across the displacer, and the shuttle and pump gas loss Q_{sp} in the inner surface gaps of the piston cylinder and the cold finger as well, resulting from the reciprocating motion of the piston and displacer.

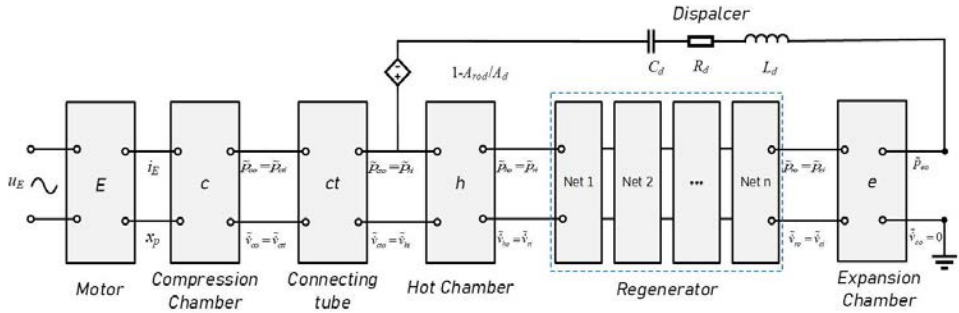


Figure 3. Thermo-dynamic network model of the miniature FPSC.

Therefore, the actual cooling capacity of the refrigerator is given by

$$Q_c = W_e - H_{reg} - Q_{cond} - Q_{sp} \quad (17)$$

Because the cold finger plug in the expansion chamber is a heat-conducting solid, there is a temperature difference between the cold finger plug and the fluid in expansion chamber, and the fluid temperature is lower than the cooling temperature measured by the cold end thermometer. Due to the polytropic process in the expansion chamber, the actual temperature of the fluid in the expansion chamber is unknown. In this paper, the actual temperature of the fluid in the expansion chamber is obtained by an iterative calculation process coupling energy equation.

Development of cryocooler prototype

Design of miniature linear compressor

It can be seen from Table 1 that the linear compressor usually accounts for more than 80% of the total weight of cryocooler. By comparing the advantages and disadvantages of moving coil and moving magnetic linear motor, this study adopts moving magnetic structure as linear motor for high efficiency and compactness, which makes it more potential for lightweight and miniaturization. Fig. 4 shows the single-phase cylindrical moving magnetic linear motor scheme used.

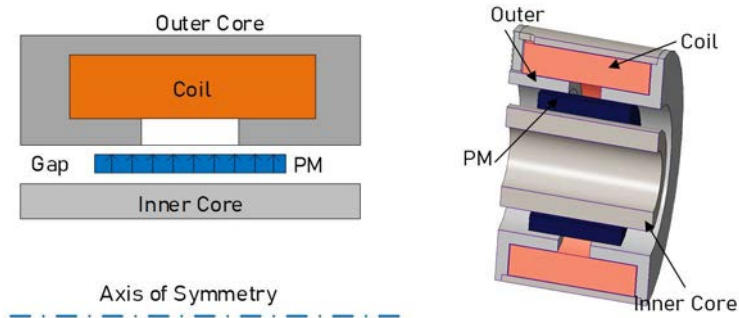


Figure 4. Cutaway view of the linear motor.

The inner core and the outer stator are both composed of ferrite material, the outer stator is a C-type structure, the coil is wrapped in it, and the surface of the coil copper wire is coated with polyimide high temperature insulation material. The permanent magnet is a radially magnetized multi-tile structure composed of Nd-Fe-B alloy material. The design requires the movement of the permanent magnet in the air gap between the outer stator and the inner core within the magnetic field range of the design stroke. Its advantage is that it is not sensitive to external magnetic field interference, and the magnetic radial force is small, which is beneficial to reduce the wear of the compression piston.

In the miniaturization process of motor, the design margin is relatively small, and it is possible for the motor to run in the limit state, so finite element analysis is needed to ensure the reliability. Fig. 5 shows the magnetic field strength of the actuator at different positions for different driving current using the finite element method.

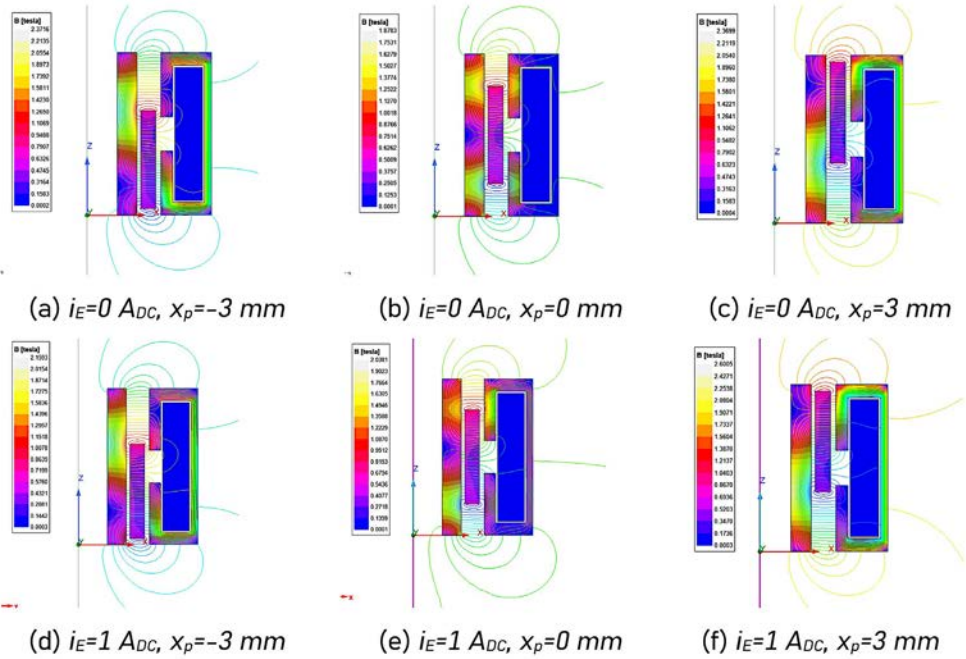
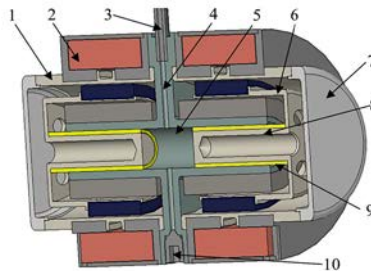


Figure 5. FEA simulation of the moving magnet linear motor.

Fig. 6 shows the structural profile of the linear compressor. The compressor adopts dual motor opposition layout to suppress axial vibration. The axial length of the compressor prototype is 56 mm, the outer diameter is 28.4 mm, and the weight is 170 g.



1 coil frame, 2 coils, 3 metal connection tubes, 4 main frame, 5 compression chamber, 6 permanent magnet bracket, 7 compressor end cover, 8 compression piston, 9 piston wear-resistant bushing, 10 setting screws

Figure 6. Cutaway view of the linear compressor.

Experimental performance test and model validation

FIG. 7 shows the prototype of the miniature free piston Stirling cryocooler, which weighs 200 g, has a maximum input power of $20 W_{AC}$ and a designed operating temperature of 150 K. The pressure sensor is installed in the middle of the metal connection pipe and is used to collect the pressure wave signal at the compressor outlet. The cryocooler is driven by AC power supply, and can collect driving voltage, current, input power and other parameters at the same time. The cold finger of the expander is packaged in the metal test dewar, and the cold end of the dewar is equipped with a temperature sensor and a resistance heater, which can collect the cooling temperature and cooling capacity data of the cryocooler. The cooling capacity of the cold end can be adjusted by changing the input power of the cryocooler.



Figure 7. Prototype photos of the miniature free piston Stirling cryocooler.

Main operating and structural parameters of the cryocooler are listed in Table 2.

Table 2. Main operating and structural parameters of miniature FPSC prototype.

Main conditions	Charging Pressure P_{ch}	3	MPa
	Frequency f_{eq}	110	Hz
Linear motor	Resistance, R_E	0.6	Ω
	Inductance, L_E	7.5	mH
	Thrust force constant, ψ_E	4.5	N/A

Compressor	Mass of the moving part, m_p	10	g
	Spring stiffness, k_p	800	N/m
	Cross-sectional of compression piston, A_p	19.6	mm ²
Displacer	Mass of the moving displacer, m_d	2.8	g
	Spring stiffness, k_d	1050	N/m
	Cross-sectional area of displacer, A_d	27.9	mm ²
	Cross-sectional area of driving rod, A_{rod}	3.14	mm ²
Regenerator	Length of the matrix, L_r	23	mm
	Cross-sectional area of matrix, A_r	15.9	mm ²
	Volume porosity, ϵ	0.68	
	Wire mesh diameter, d_w	0.0254	mm

Fig. 8 shows the variation of the cooling capacity of the cryocooler with the input electric power when the cooling temperature is 150 K, and the comparison of the network model with the experimental results.

Both simulation and experiment show that the cooling capacity increases with the increase of electric power, but the cooling capacity increases slowly when the input power exceeds 12 W_{AC}. The calculated value of the network model is about 12% larger than the experimental data, mainly because the gap leakage between the compression piston and the cylinder is not considered in the network model, and also the influence of coil heating of the experimental prototype caused by the increase of motor loss during high-power operation is not taken account in the modelling.

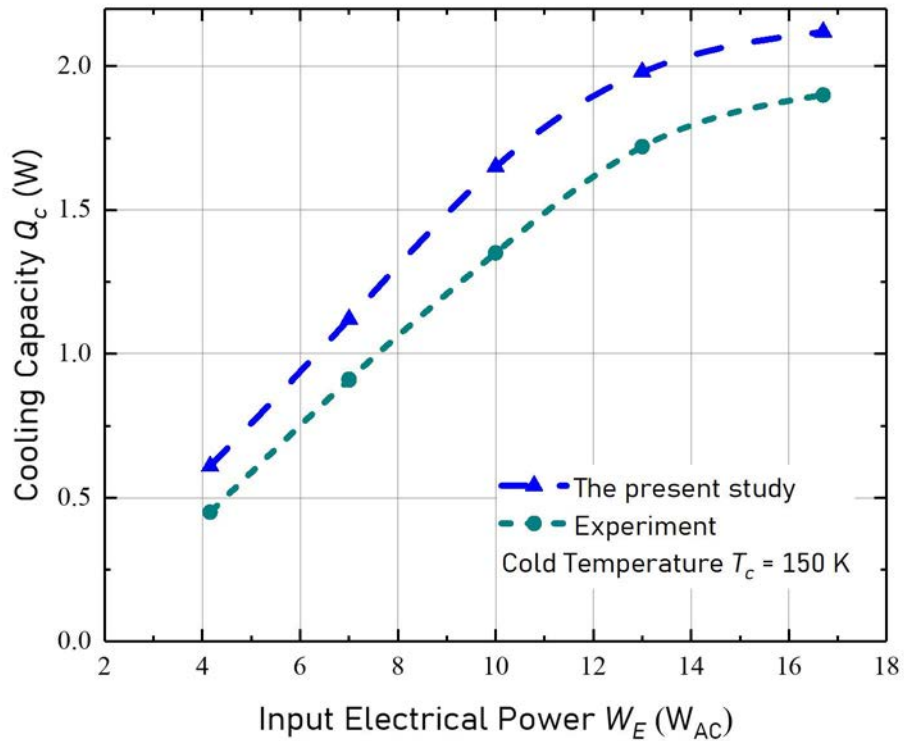


Figure 8. Variation of the cooling capacity of the cryocooler with the input electric power, at the cooling temperature of 150 K, for the simulation and experiment.

Conclusion

By coupling the thermoacoustic theory with the dynamics of the free-piston Stirling cryocooler, and considering the active properties of the regenerator, especially the actual heat transfer process in the expansion chamber, a thermo-dynamic network analysis model was established for a miniature free piston Stirling cryocooler. The experimental prototype was developed and the model was verified with reasonable accuracy. The developed prototype has excellent comprehensive performance: at the input power of 10 W_{AC}, the cooling capacity of 1.35W@150 K can be obtained, the relative Carnot efficiency of the cryocooler is 13.5%, and the weight of the prototype is only 200g.

Acknowledgements

This work was supported by the National Natural Science Foundation of China (NSFC) (Grant No. 51976066).

References

- [1] Ashley T, Elliott C T. Nonequilibrium devices for infrared detection. *Electronics Letters*, 21: 451-452 (1985).
- [2] Donald A R, Stuart B H, James C Jr, et al. Third-generation imaging sensor system concepts. *Proceedings of SPIE*, 3701: 108-117 (1999).
- [3] Rogalski A. *Infrared Detectors*. Boca Raton: CRC Press (2000).
- [4] Veprik A, Tavori A, Raviv Z, Zehctzer S, Refaeli R, Wise A. Low cost cryogenic coolers for commercial infrared imagers. *Infrared Technology and Applications XLV, Proc of SPIE Vol 110022019* (2019).
- [5] Philip K, Olga K, Steve G, et al. High Operating Temperature X_{Bn}-InAsSb Bariode detectors. *Proc. of SPIE*, 8268: 82680U (2012).
- [6] Lutz H., Breiter R., Eich D., et al. Ultra-compact high-performance MCT MWIR engine. *Proc. of SPIE*, 10177: 101771A-1 (2017).
- [7] Filis A, Carmiel M, Nachman I, Fulop GF, Kimata M, Zheng L, et al. Ricor's advanced rotary and linear miniature cryocoolers for HOT IR detectors. *Proc. SPIE 12107, Infrared Technology and Applications XLVIII, 121070K* (2022).
- [8] Willems D, Arts R, de Jonge G, Mullie J, Benschop T. Miniature Stirling Cryocoolers at Thales Cryogenics Qualification Results and Integration Solutions. *Cryocoolers 19*, 85-93 (2016).
- [9] Mai M, Rosenhagen C, Ruehlich I. Development of Single Piston Moving Magnet Cryocooler SX020. *Cryocoolers 18*, 65-71 (2014).
- [10] Squires M. Cobham Microcooler for High Temperature Applications - Cobham Mission Systems. *Cryocoolers 18*, 73-77 (2014).
- [11] Conrad T, Haley D, Lieb T, Grabau M, Miramontes S, Garcia E, et al. FLIR FL-100 miniature linear Stirling cryocooler development summary. *Proc. SPIE 11002, Infrared Technology and Applications XLV, 1100202* (2019).

- [12] Jiang H, Xi Z, Zhang X. Mathematical modeling of a general heat-dynamics active network for free piston Stirling engines. *Applied Thermal Engineering*, 213:118652 (2022).
- [13] Huang BJ, Lu CW. Split-type free-displacer Stirling refrigerator design using linear network analysis. *Cryogenics*; 36:1005-1017 (1996).
- [14] Swift GW. *Thermoacoustics: A Unifying Perspective for Some Engines and Refrigerators*. Springer (2017).
- [15] Ward B, C. J. and S. G. W. Design Environment for Low-Amplitude Thermoacoustic Energy Conversion (DeltaEC software). Version 6.4, Los Alamos National Laboratory. <https://www.lanl.gov/thermoacoustics> (2012).

Third-Order Modelling and Comparison of a Thermal Compressor Versus a Mechanical Compressor in a Heat-actuated Stirling Refrigerator

Zindh Waleed*, Michael Gschwendtner, Danielle Yang

Mechanical Engineering, Auckland University of Technology, 55 Wellesley St E, Auckland, New Zealand

*Corresponding author: zindhwaleed@gmail.com

Keywords: Heat-actuated Stirling refrigerator, Vuilleumier cycle, Duplex Stirling refrigerator, Thermodynamic modelling

Abstract

This paper presents the thermodynamic modelling and comparison of thermal compressors to mechanical compressors in a heat-actuated Stirling refrigerator. Sage, a third-order modelling software used for the design and simulation of Stirling systems is used to compare a Vuilleumier (VM) configuration - which achieves a pressure variation by thermal compression, and a Duplex configuration - which achieves a pressure variation by mechanical compression. Both models were optimized under similar operating parameters to attain and determine the highest possible Coefficient of Performance (COP) and refrigeration capacity for a specified system size.

Based on the results of the simulations, the performance with changes to the frequency in both configurations are presented and discussed to better understand the working characteristics of these configurations. Further investigations were carried out to determine the exact effects of the additional piston mass in the mechanical compressor performance compared to that of the thermal compressor. These findings indicate that for systems of the same size operated under similar conditions (pressure, temperature, and frequency), the mechanical compressor has the potential of achieving a higher COP and higher-pressure amplitudes, but the thermal compressor can go to much higher frequencies, and thus, achieve higher cooling capacity by increasing the frequency without being constrained by resonance.

Introduction

The Free-Piston Stirling Engine (FPSE) was first invented by William T. Beale in 1964. It is a variation of the typical Stirling engine and has no kinematic coupling mechanisms, which means that the motion of the reciprocating elements is governed entirely by their mass (inertia) and the action of gas/spring forces, and in some cases, mechanical springs. Compared to conventional crank mechanisms, the FPSEs do not introduce the issues of side loads, which lead to wear of the piston seals. FPSE systems can be used to replace applications where linear motion is employed, for example, in linear electricity

generation, heat pumping, liquid pumps, and gas compression.

An exciting option is a FPSE coupled to a Stirling refrigerator and incorporated into a single unit to produce a cooling output from heat input. These are generally referred to as heat-actuated refrigerators. The thermal energy supplied to the heat engine can be from any heat source including solar energy, combustion of fossil fuels, or waste heat from industrial power plants. These refrigerators are categorized as follows:

- Vuilleumier refrigerator
- Duplex Stirling refrigerator
- Heat-actuated thermoacoustic refrigerator

In this work, the focus will be on the parametric comparison between the VM (the thermal compressor) and the Duplex Stirling system (the mechanical compressor).

Principle of operation

Thermal compressor

The Vuilleumier cycle (VM) was first patented by Rudolph Vuilleumier in 1918 [1]. The VM configuration is a closed gas cycle which employs two displacers that move the gas between three spaces at different temperatures [2]. The pressure fluctuation in this system is achieved by shuttling the gas from the hot temperature space to the lower temperature space and vice versa using reciprocating displacers. During this process, the overall volume of the system remains constant.

The VM configuration can be either crank-based or free-piston-based as shown in Figure 1. The crank-based configuration consists of displacers mechanically linked to a crankshaft using connecting rods. Compared to the crank mechanism, the free-piston type VM is simpler, lighter, and more compact [3]. However, almost all VM machines that have been developed utilize a sinusoidal displacer motion [3, 4]. Furthermore, the highest cooling capacity and performance of VM are observed when the displacers are linked by a phase angle of 90° [5].

For the theoretical analysis of a VM, both isothermal and adiabatic models have been developed [6]. Whilst the isothermal models provide a simple and easy method of analysis [4], the adiabatic models provide more accuracy in predicting how they would behave in practical scenarios [2].

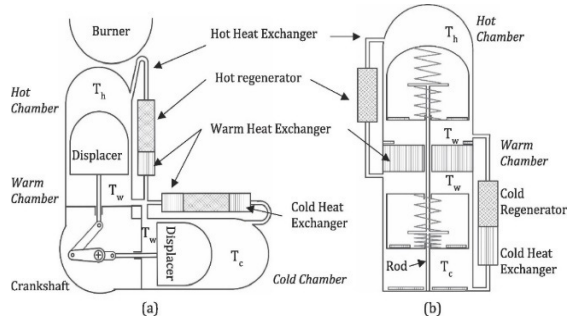


Figure 1. (a) Crankshaft-based VM and (b) Free-Piston VM (Chen et al., 2018, p. 554).

Table 1 summarizes some of the progress made on VM refrigerators over the years [7].

Table 1. The progress of Vuilleumier refrigerators over the years.

Author	T_c (K)	T_w (K)	T_H (K)	COP_{VM}	COP_{ideal}	% Carnot
Kuhl and Schulz (1990) [8]	263	313	773	0.16	3.13	0.05
Thomas (1992) [9]	273	313	773	0.04	4.06	0.01
Carlsen (1994) [10]	285	313	873	0.67	6.53	0.10
Kawajiri, Honda et al. (1997) [4]	285	318	973	<0.7	5.81	<0.12
Pfeffer, Kühl et al. (1999) [11]	273	323	773	0.39	3.18	0.12
Kuehl, Schulz et al. (1999) [12]	262	306	853	0.57	3.82	0.15
Rüther (2004) [13]	273	318	693	0.08	3.28	0.02

Mechanical compressor

The Duplex Stirling System concept was first introduced by SunPower corporation in the 1980s [14], and there have been further reports on this system since then [15, 16]. Figure 2 depicts the initial design of a Duplex Stirling heat pump, which is essentially a heat pump driven by a heat engine using a common power piston.

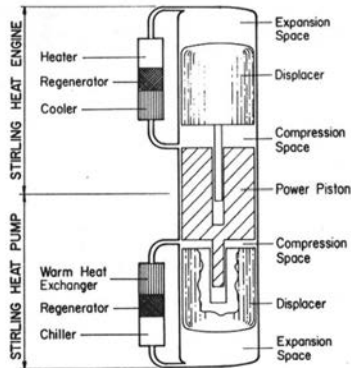


Figure 2. Schematic of a Duplex Stirling refrigerator [14].

In this heat-actuated refrigerator, repeated heating, and cooling cause a pressure variation, which leads to the movement of the power piston. This movement is converted to useful mechanical work which drives the refrigerator part of the system [17]. In a Duplex system, the assumption is that all work produced by the heat engine is consumed by the refrigerator as there is no means to exchange work with the surroundings. Since there would be dissipation losses in a practical application, the work produced by the heat engine has to be larger than the work required by the refrigerator to have a working system.

Hu et al. (2017) attributed the difficulties in having a practical working Duplex Stirling refrigerator to its deviations from the designed models. They determined that even slight variations in parameters such as friction, heat source temperature, and piston diameter have a major effect on the performance of the Duplex system [18]. Doğan, Ozturk et al. (2018) [19] examined the effects of using 9 different pairings of CO₂, He, and H₂ as working fluids on the overall performance of a Duplex Stirling refrigerator. The results from this investigation showed that the highest performance is maintained when using He as both the refrigerant and working fluid of the system.

Erbay et al. (2017) conducted a detailed thermodynamic analysis of the heat engine and refrigerator separately for a Duplex Stirling refrigerator. They took into account the constraint of work equality between the heat engine and the refrigerator, i.e., the equality of work produced by the engine and the work consumed by the refrigerator [20]. Dai et al. conducted a thermodynamic analysis using the finite time thermodynamic

method for a solar-powered Duplex Stirling refrigerator taking into consideration the work equality, power, and cycle time equality as constraints. Their model is presented as a guide for the thermal design of a real solar Duplex Stirling refrigeration system [21]. Over the years, there has been a significant amount of research on Stirling engines and Stirling coolers as individual units. The experimental results show that the thermal-to-mechanical efficiency of Stirling heat engines approaches 60-70% of Carnot efficiency [22], whilst the mechanical-to-thermal COP of Stirling refrigerators can approach 41-46% of Carnot. Therefore, based on the Carnot efficiency of the heat engine and refrigerator, the Duplex system can perform at 28-32% of Carnot efficiency [23].

Methodology

Mechanical configuration and performance indicators of the systems

The configurations of thermal and mechanical compressors displayed in Figure 3 were simulated such that all the components of the systems are the same size and made of the same materials. This was to reduce the number of variables in the modelling of these systems and to isolate the effect of adding just the power piston on the performance of the system. The main focus of this study was to determine the effects of adding a free moving mass, i.e., the connecting piston between a heat-actuated refrigerator and the engine part, on the efficiency of the heat engine, the COP of the refrigerator, the overall COP of the combined system, and the possible cooling capacity as compared to that of a simple thermal compressor of the same size, to determine the optimum operating conditions of such a system.

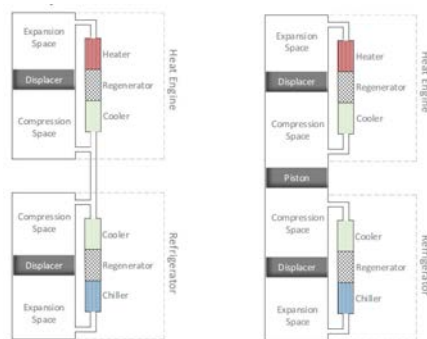


Figure 3. Thermal compressor (on the left) and mechanical compressor (on the right).

The coefficient of performance (COP) is the ratio of ‘desired energy transfer’ to the ‘energy required’. In the case of a heat-actuated refrigerator, the overall COP of the system can be calculated by the following equation:

$$COP_{cooling} = \frac{\dot{Q}_{in,REF}}{\dot{Q}_{in,HE}} \quad [1]$$

Where, $\dot{Q}_{(in,REF)}$ is the heat absorbed by the low-temperature heat exchanger on the refrigerator side. For the VM, Equation [1] is sufficient to calculate the COP of the system. However, for the Duplex system, the work produced by the power piston plays a major role in determining the performance of that system as given by Equation [2].

$$COP_{cooling} = \frac{\dot{Q}_{in,REF}}{\dot{Q}_{in,HE} + \dot{W}_{net,system}} \quad [2]$$

Initial modelling procedure of the heat-actuated refrigerator

Sage is a third-order modelling software developed by David Gedeon [24]. It can be used to simulate one-dimensional models of thermal systems for Stirling machines. Sage is generally used to investigate the thermodynamic behaviour of the working gas, and it also takes into account the interactions of the working gas with the walls of each component, as well as the heat transfer by conduction in the walls of the components in both axial and radial direction. This helps in understanding and determining the losses due to heat conduction, which is a major part in modelling of Stirling systems.

The Sage model can be built up to define important design parameters such as the sizes of the individual components, temperatures, pressure, etc. The most important feature of Sage utilised in this study is the mapping tool - which allows detailed parametric studies of the user-defined variables. The results from the Sage model can be analysed by mapping the Stirling engine performance and determining the predicted heat input, net work, and total COP [25]. At the beginning, this procedure was used to find the optimum dimensions of all components.

The piston diameter, mean pressure, temperatures of the hot, ambient, and cold spaces were the only set variables at the start of this procedure. During this study, the frequency and piston mass were the main parameters varied to determine their impact on the performance of the system. The main operating parameters of this system are highlighted in Table 2.

Table 2. Parameters of the heat-actuated refrigerator for both the mechanical and thermal compressor.

Parameters	Value
Mean Pressure (bar)	30
Heater Temperature (K)	673
Ambient Temperature (K)	298
Refrigeration Temperature (K)	258
Working gas	Helium
Operating frequency (Hz)	10 - 40
Piston diameter (mm)	50
Piston mass (kg)	0.5 - 3

The mapping tool in Sage was used to find the optimum geometric parameters of the heat exchangers (outlined in Table 3) by an iterative process where the lengths, and the number of fins (for the heat absorbers and rejectors) were varied to determine the optimum sizes for a satisfactory cooling capacity.

Table 3. Design parameters of the heat exchangers.

Parameters	Heat Engine	Regenerator	Refrigerator
Number of fins	150	-	200
Length (mm)	15	65	10
Diameter (mm)	-	50	-
Regenerator Matrix	-	Mesh Wire	-
Material	Brass	SS304	Brass

One of the most important factors to understand from this study is how pressure, and thus, the performance of a system is impacted by the change in temperature, or by the change in volume inside a system. This is to recognize whether heat-actuated refrigerators would perform better with thermal compression (where the temperature change is the main driving force) or mechanical compression (where volume variation of the gas is the main driving force). Generally, the performance of a heat-actuated refrigerator driven by a mechanical compressor is affected by the resonant frequency of the compressor (in this case, the connecting piston between the heat engine and refrigerator), the amplitudes of the piston and the displacers, and the phase shift between the piston and displacers.

Results and discussion

This section focuses on the comparison between thermal and mechanical compressors to determine the differences in COP, cooling capacity, and temperatures reached with changing frequencies and heat inputs.

Comparison between thermal and mechanical compressors

Pressure amplitude and COP

The main physical difference between the VM and the Duplex is the addition of the piston as a work transfer unit between the heat engine and the refrigerator. This piston significantly increases the achievable pressure amplitude in the system due to the inertial force of the piston mass. Comparatively, for this geometry, the VM has a much lower pressure amplitude as seen in Figure 4 and is constant even with increases in frequency (pressure amplitude of approximately 3% of mean pressure). Since the working gas in the VM is just shuttled back and forth between the hot and cold spaces, there is a low variation of pressure with a change in frequency inside this system.

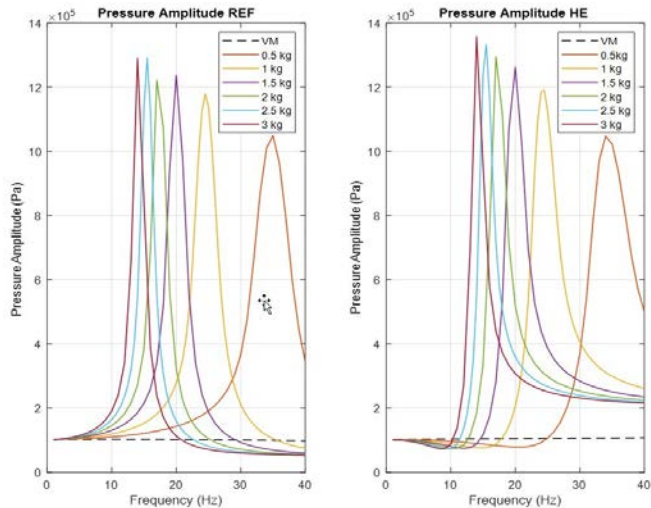


Figure 4. Pressure amplitude of refrigerator (left) and heat engine (right) of both the VM and the Duplex with change in mass and frequency.

The lower pressure variation in the VM is one of the major contributing factors to the overall lower COP compared to the Duplex system as seen in Figure 5. This figure

illustrates the COP change in the mechanical compressor with different masses (0.5 kg – 3 kg) as compared to a thermal compressor (VM). It also shows that with an increase in mass, the COP increases to a certain point, up to 2.5 kg, and then gradually decreases with further increases in mass. There is a very minute difference in the COP with an increase in the mass of the piston beyond 1 kg, indicating that for the given configuration, there is no necessity for masses heavier than 1 kg.

There is a maximum frequency for the mechanical compressor systems until which they operate as a heat-actuated refrigerator. From the graph, it can be identified as the point where COP drops to zero. Thus, mechanical compressors are limited to a specific range where they still function as the specified type of machine, whereas the thermal compressor can continue to operate at higher frequencies. This indicates that whilst the Duplex is capable of achieving higher COP and higher pressure amplitudes, the VM can go up to much higher frequencies, and thus, higher overall cooling capacity. On the one hand, the Duplex achieves higher COP and higher pressure amplitude. On the other hand, the VM can go to much higher frequencies, and thus, higher cooling capacity.

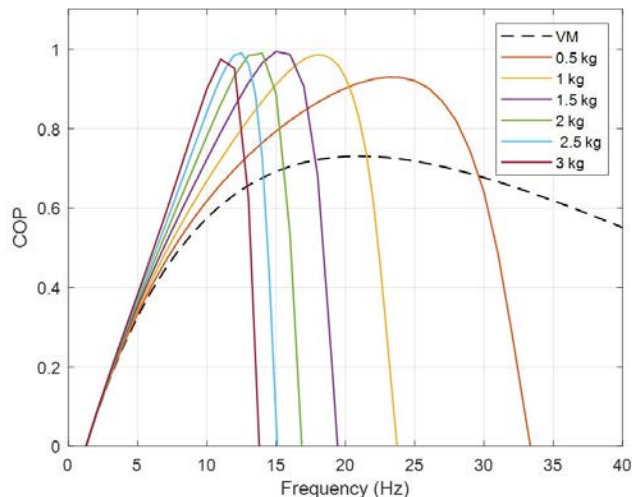


Figure 5. COP of thermal versus mechanical compressor (with varying piston masses) with frequency.

This can be better explained by referring to Figure 6 which shows the average gas temperatures of the absorber and rejector of the refrigerator part of the Duplex and the

VM. Whilst the change in frequency leads to a slight change in the temperature of the VM, there is a very significant switch in the Duplex system. Beyond resonance, instead of absorbing heat, the system is rejecting heat to the cold space specified in the Sage model. This means that the system is no longer capable of producing the work required to generate this level of cooling, and essentially just acts as a heat conduction pathway. Due to the increased pressure amplitude at resonance, it leads to higher temperature swings, to the point where the gas in the absorber is hotter than the cold space and the gas in the rejector is colder than the surroundings.

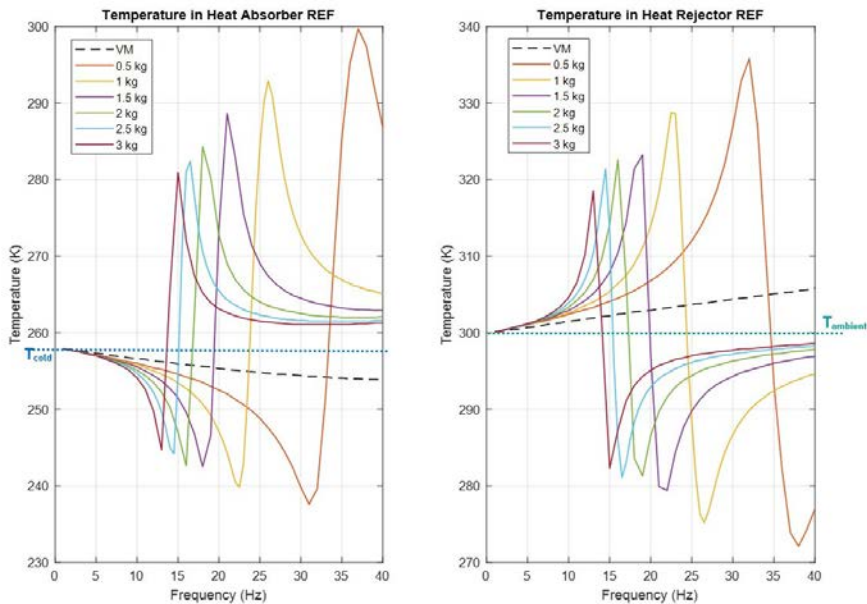


Figure 6. Average gas temperature in the heat exchangers of the refrigerator with change in frequency and mass of the piston.

Another consequence of frequencies above resonance is that the average gas temperatures overshoot the temperatures of the reservoirs as shown in Figure 6. Since the reservoir temperatures are already defined in Sage, which in this case is 258 K, above resonance, the system is no longer capable of producing the level of cooling required by the set conditions.

The flip in the temperatures for the mechanical compressors can be better explained with reference to the phase shift of the displacers in the heat engine and refrigerator relative to the piston compared to the piston amplitude as a function of the operating frequency (Figure 7). In an oscillatory system, at resonance, the phase between the exciting force (i.e., the pressure swing caused by the harmonic motion of the displacers) and the displacement of the work transferring piston jumps by approximately 180° as observed by Figure 8.

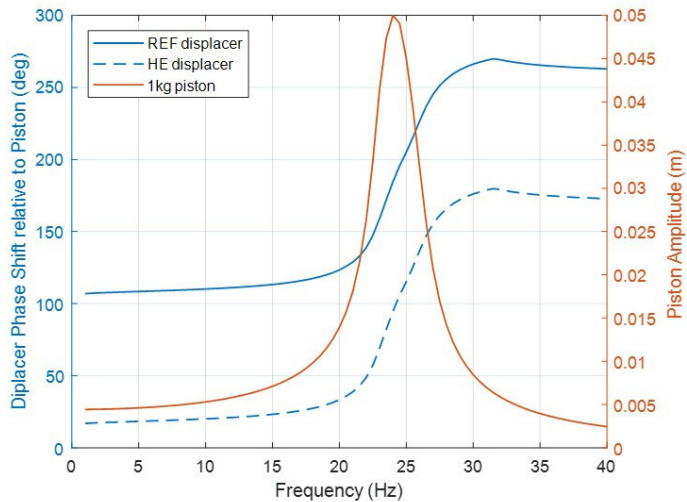


Figure 7. Piston amplitude and phase shift of the displacers with respect to the piston as a function of the operating frequency for the 1 kg piston.

This is one of the main contributing factors to the much lower cooling capacity and heat input of the Vuilleumier configuration of this size. All these factors indicate that for a VM to achieve the same level of performance, the system would need to be drastically larger than a mechanical compressor system, or the system would need to run at a higher frequency.

With the increase in mass, since resonance occurs at lower frequencies (which lead to reduced friction losses), there is a much lighter damping as can be seen by Figure 8. A sharper change in the phase of the piston relative to the displacers at resonance indicates lighter damping.

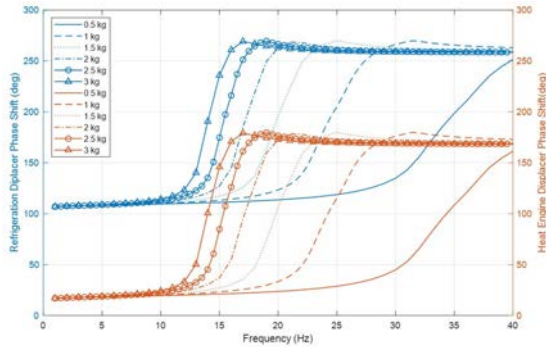


Figure 8. Phase shift of the displacers with respect to the piston as a function of the operating frequency for different masses.

Change in hot space temperature.

To understand the difference in how the mechanical and thermal compressors respond to changes in temperatures supplied to the system, the hot space temperature of the heat engine was varied from 473 K to 873 K.

Figure 9 shows the influence of heat source temperature on the heat input (on the top), and the cooling capacity (on the bottom) on both the thermal and mechanical compressor (with a piston of 1 kg), whilst Figure 10 displays the overall COP of these machines.

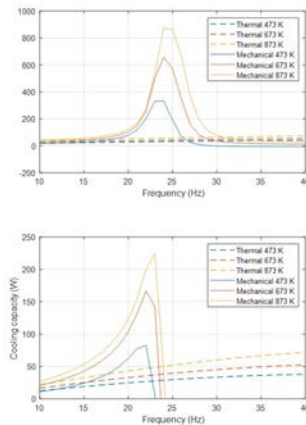


Figure 9. Effect of changing hot space temperature and frequency on the a) heat input, and b) cooling capacity of mechanical and thermal compressors.

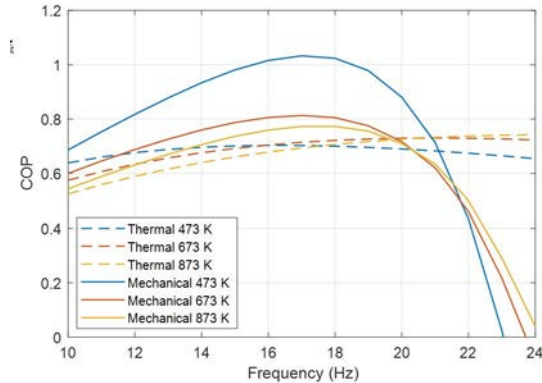


Figure 10. Effect of changing hot space temperature and frequency on the COP of the mechanical and thermal compressors.

According to Figure 9-Figure 10, for the thermal compressor, increases in the heat source temperature from 473 K to 873 K only led to minor increases in the system's heat input and cooling capacity. However, there are significant increases for the mechanical compressor with the higher temperature. When it is operated under its natural frequency at 873 K, the heating input is nearly 15 times larger than the heating input of the thermal compressor. Since the mechanical compressor already has a high temperature swing due to the piston inertia, with increase in the heat source temperature, there is an even larger temperature swing, and thus, higher heat absorption.

For each heating temperature, when operating at approximately their natural frequency, the COP of the mechanical compressor for a smaller system seems to be generally higher than that of the thermal compressor. This is more apparent at lower temperatures (such as 473 K) where the COP of the thermal compressor and mechanical compressor is 0.69 and 1.03, respectively. This is nearly 33% lower than the COP of the mechanical compressor. With the increase in the heater temperatures, the increase in pressure amplitude of the system at higher frequencies (with a maximum at resonance) for the mechanical compressor leads to a much larger cooling capacity. This is at the expense of a reduced COP. Therefore, for a system of this size, a higher heat source temperature is not required to obtain better cooling and COP since a heat source temperature of approximately 673 K is capable of producing a similar performance as that of 873 K.

At a temperature of 673 K, the thermal compressor and the mechanical compressor have

a cooling capacity of 35.5 W and 166 W, respectively. Thus, for a system of this size, when operated at its optimum frequency, the mechanical compressor has the potential of producing nearly five times the cooling output compared to a thermal compressor. Thus, for the overall performance of the system, mechanical compression, i.e., systems that employ volume variation to change the pressure of a system has a higher cooling rate in terms of power density.

Conclusion

This study aimed to use third-order modelling to simulate a mechanical compressor and determine the parametric differences to a thermal compressor of specified size and conditions with the potential application as a heat-actuated refrigerator. The following summarizes the important findings from this analysis:

1. Sage can be used to demonstrate the effects of increase in frequency on the temperature variations and its subsequent effects on the performance of the system.
2. There is a larger impact on the performance in terms of COP and cooling capacity with the introduction of a piston (which leads to volume variations) compared to just running it using temperature variations.
3. For systems of the same size operated under similar conditions (pressure, temperature, and frequency), the mechanical compressor has the potential of producing significantly larger cooling outputs.
4. When the systems approach its resonant frequency, the phase shift of the displacers relative to the piston flips by 180° for each mass. These results also show that with an increase in mass the damping of the system is reduced.
5. The Duplex can achieve higher COP and higher pressure amplitude, but the VM can go to much higher frequencies, and thus, higher cooling capacity by increasing the frequency without being constarined by resonance.

These findings indicate that for this specific purpose of building a four-system heat-actuated prototype capable of producing a cooling of approximately 50 W, it is more feasible to have mechanical compression over thermal compression.

Acknowledgements

This paper would not have been possible without the guidance and expertise of my supervisor, Dr. Michael Gschwendtner. I would also like to thank Dr. Danielle Yang for her support and assistance with writing this paper.

References

- [1] R. Vuilleumier, "Method and apparatus for inducing heat changes," 1918.
- [2] H. Chen, C. Lin, and J. P. Longtin, "Performance analysis of a free-piston Vuilleumier heat pump with dwell-based motion," *Applied Thermal Engineering*, vol. 140, pp. 553-563, 2018, <https://doi.org/10.1016/j.applthermaleng.2018.05.028>
- [3] J. Matsue, T. Nakazato, and H. Shirai, "A Dynamic Analysis of Free Piston Vuilleumier Cycle Heat Pumps," *JSME International Journal Series B*, vol. 43, no. 3, pp. 518-525, 2000, <https://doi.org/10.1299/jsmeb.43.518>
- [4] K. Kawajiri, T. Honda, and T. Sugimoto, "Study of Free Piston Vuilleumier Heat Pump: Basic Performance Analysis," *JSME International Journal Series B*, vol. 40, no. 4, pp. 617-625, 1997, <https://doi.org/10.1299/jsmeb.40.617>
- [5] K. Kawajiri, T. Honda, and T. Sugimoto, "Study of Free Piston Vuilleumier Heat Pump: Performance Characteristics of Prototype Machine during Forced Vibration," *JSME International Journal Series B*, vol. 40, no. 4, pp. 626-634, 1997, <https://doi.org/10.1299/jsmeb.40.626>
- [6] G. Dogkas and E. Rogdakis, "A review on Vuilleumier machines," *Thermal Science and Engineering Progress*, vol. 8, pp. 340-354, 09/17 2018, <https://doi.org/10.1016/j.tsep.2018.09.004>
- [7] S. Schulz and B. Thomas, "A Linear Model of a Free-Piston Vuilleumier Machine Compared to Experimental Results of a Prototype," 1992. [Online]. Available: <https://doi.org/10.4271/929032>
- [8] H. D. Kuhl and S. Shulz, "Measured performance of an experimental Vuilleumier heat pump in comparison to 3rd order theory," 1990 1990, vol. 5: IEEE, pp. 436-441.
- [9] B. Thomas, "Entwicklung und Experimentell Untersuchung einer Freikolben-Vuilleumier-Kaltmaschine," PhD Thesis, Verlag Shaker Aachen, 1992.
- [10] H. Carlsen, "Results from 20 kW Vuilleumier heat pump test program," in *Intersociety*

Energy Conversion Engineering Conference, Lyngby, Denmark, 1994 1994, p. 3837.

- [11] T. Pfeffer, H. D. Kühl, S. Schulz, and C. Walther, "Entwicklung und experimentelle Untersuchung neuer Regeneratorkonzepte für regenerative Gaskreisprozesse am Beispiel einer Vuilleumier-Wärmepumpe," *Forschung im Ingenieurwesen*, vol. 65, no. 7, pp. 257-272, 1999.
- [12] H.-D. Kuehl, S. Schulz, and C. Walther, "Thermodynamic Design and Optimization of a 20 kW Vuilleumier Heat Pump," *SAE Technical Paper*, 0148-7191, 1999.
- [13] J. Rüter, *Anwendungsorientierte Weiterentwicklung des Freikolben-Konzeptes für Vuilleumier-Wärmepumpen*. Shaker, 2004.
- [14] B. Penswick and I. Urieli, "Duplex Stirling machines," United States, 1984-08-01 1984, Research Org.: Sunpower, Inc., Athens, Ohio, Sponsor Org.: [Online]. Available: <https://www.osti.gov/biblio/5854260> [Online]. Available: <https://www.osti.gov/servlets/purl/5854260>
- [15] D. M. Berchowitz and J. Shonder, "Estimated size and performance of a natural gas fired duplex Stirling for domestic refrigeration applications," Oak Ridge National Lab., TN (United States), 1991.
- [16] G. Chen and W. T. Beale, "Thermally actuated duplex free-piston Stirling system for domestic cooling and heating applications," in *Int Conf on CFC's and Halon Alternatives*, Beijing, China, 1993 1993.
- [17] P. Puech and V. Tishkova, "Thermodynamic analysis of a Stirling engine including regenerator dead volume," *Renewable Energy*, vol. 36, no. 2, pp. 872-878, 2011, <https://doi.org/10.1016/j.renene.2010.07.013>
- [18] J. Y. Hu, E. C. Luo, W. Dai, and L. M. Zhang, "Parameter sensitivity analysis of duplex Stirling coolers," *Applied Energy*, vol. 190, pp. 1039-1046, 2017, <https://doi.org/10.1016/j.apenergy.2017.01.022>
- [19] B. Doğan, M. M. Ozturk, and L. B. Erbay, "Effect of working fluid on the performance of the duplex Stirling refrigerator," *Journal of Cleaner Production*, vol. 189, pp. 98-107, 2018/07/10/ 2018, <https://doi.org/10.1016/j.jclepro.2018.04.076>
- [20] L. B. Erbay, M. M. Ozturk, and B. Doğan, "Overall performance of the duplex Stirling refrigerator," *Energy Conversion and Management*, vol. 133, pp. 196-203, 2017, <https://doi.org/10.1016/j.enconman.2016.12.003>

- [21] D. Dai, Z. Liu, F. Yuan, R. Long, and W. Liu, "Finite time thermodynamic analysis of a solar duplex Stirling refrigerator," *Applied thermal engineering*, vol. 156, pp. 597-605, 2019, <https://doi.org/10.1016/j.applthermaleng.2019.04.098>
- [22] M. He, "Stirling Engine for Solar Thermal Electric Generation," 2016.
- [23] B. Luo, P. Zou, T. Jiang, Q. Gao, and J. Liu, "Decoupled duplex Stirling machine: Conceptual design and theoretical analysis," *Energy Conversion and Management*, vol. 210, p. 112704, 2020, <https://doi.org/10.1016/j.enconman.2020.112704>
- [24] D. Gedeon, *Sage User 's Guide.*, 2016.
- [25] S. G. Qiu, Y. Gao, G. Rinker, and K. Yanaga, "Development of an advanced free-piston Stirling engine for micro combined heating and power application," *Applied Energy*, vol. 235, pp. 987-1000, 2019, <https://doi.org/10.1016/j.apenergy.2018.11.036>

Thermodynamic Analysis of a β -Type Stirling Cryocooler at Low Charged Pressures

Duc-Thuan Phung*, Chin-Hsiang Cheng, Stefan Popesku

Department of Aeronautics and Astronautics, National Cheng Kung University, Taiwan

*Corresponding author: thuan.phungduc.0811@gmail.com

Keywords: β -type Stirling cryocooler, Low charged pressure, Thermodynamic performance

Abstract

Stirling cryocoolers have established themselves as commercially successful machines within the realm of Stirling devices, finding applications across diverse fields such as superconducting materials, remote sensing, electronic technology, stored cryogenics, and aerospace. They offer several advantages, including low-noise operation, minimal vibration, extended lifespan, high reliability, and the ability to be miniaturized. However, efforts to reach lower temperatures often involve increasing the number of cooling stages and pressurizing Stirling cryocoolers, leading to increased complexity in structure, operation, and maintenance costs.

Addressing the need for Stirling coolers with fewer stacked-up stages while maintaining the capability to achieve cryogenic temperatures, this study conducts a comprehensive thermodynamic analysis of a prototype rhombic-drive β -type Stirling cryocooler. The primary aim is to evaluate its potential to achieve cryogenic temperatures, particularly at low charged pressures. A second-order thermodynamic model is developed, solving a system of equations encompassing empirical equations for pressure drop, conservation equations for mass and energy, and ideal-gas equations of state. The model also accounts for non-uniform pressure, ensuring constant total mass and direct involvement in the energy equation.

To validate the thermodynamic model, a prototype β -type Stirling cryocooler is manufactured. Results demonstrate close alignment between numerical and experimental data regarding the temperature of the cold head across varying motor speeds (500 to 850 rpm) and charged pressures (1, 1.5, and 2 bar). As motor speed increases from 500 to 850 rpm at 1.5 bar, the numerical cold-head temperature decreases from 176.1 to 149.6 K, closely matching experimental observations. Additionally, increasing charged pressure from 1 to 4 bar at 850 rpm leads to a cold-head temperature decrease from 169.4 to 110.4 K. Further analysis suggests that adjusting operating and geometrical parameters can potentially enable the β -type Stirling cryocooler to achieve cryogenic temperatures.

Introduction

Cryocoolers are devices capable of generating cryogenic temperatures, typically below 120 K, and providing large cooling power. Therefore, cryocoolers are well-suited to a variety of rapidly expanding high-technology applications such as superconducting

materials, electronic technology, cryogen storage, high-speed imaging, infrared detectors, and aerospace equipments. The Atacama Large Millimeter/Submillimeter Array telescope employs a three-stage commercial cryocooler based on the Gifford–McMahon (GM) cooling cycle, which achieves temperatures around 4 K [1]. Additionally, the large superconducting magnet in magnetic resonance imaging equipment is cryogenically cooled by a three-stage closed-cycle refrigeration system [2]. Several NASA's space instruments necessitate cryogenic temperatures to extend the wavelength range and facilitate the use of advanced detectors [3]. Cryocoolers can be broadly categorized into two major types: regenerative cryocoolers, which utilize the back-and-forth motion of working gas between hot and cold zones, encompassing Stirling cryocoolers, pulse-tube cryocoolers, and GM cryocoolers; and recuperative cryocoolers, which utilize continuous gas flow between hot and cold zones, with high-pressure working gas moving towards the cold zone and low-pressure working gas moving towards the hot zone. These include Brayton and Joule-Thomson cryocoolers.

Stirling cryocoolers operate according to the ideal Stirling cycle, where a working gas is cyclically compressed and expanded to achieve cryogenic temperatures. Typically, Stirling cryocoolers consist of one piston exposed to the hot zone and one displacer situated between the cold and hot zones. The working gas absorbs thermal energy from the cold zone and releases it to the hot zone, a process efficiently facilitated by regenerators. Structurally, Stirling cryocoolers can be categorized into alpha-type, beta-type and gamma-type. Beta-type Stirling cryocoolers feature one piston and one displacer inside coaxial cylinders [4], whereas gamma-type Stirling cryocoolers have the piston and displacer separated by different cylinders [5]. Additionally, alpha-type Stirling cryocoolers comprise two pistons in two distinct cylinders [6]. Stirling cryocoolers offer several advantages meeting commercialization requirements, including non-degradable performance over years, maintenance-free operation, substantial cooling capacity, and reliability [7]. Several companies produce commercialized Stirling cryocoolers, such as Sunpower Inc. with its CryoTel line [8] and Honeywell, offering typical cooling capacities up to 5W@80K [7]. By stacking multiple stages, Stirling cryocoolers can achieve lower temperatures and increased cooling power [9, 10]. Xu et al. [11] conducted experiments with a one-stage beta-type Stirling cryocooler under the charged pressure of 1.7 MPa, achieving a pressure ratio of 2.63 and providing the no-load temperature

of 49.1K and 700W@77K. Subsequently, the same team [12] developed a two-stage Stirling cryocooler based on the design of the one-stage version, reaching a no-load temperature of 15.8 K and providing 138W@30K and 47W@20K with a pressure of 2.2 MPa. Similar advancements have been made with pulse-tube cryocoolers. Dang et al. [13] investigated a three-stage pulse tube cryocooler, achieving temperatures as low as 8.8 K. Additionally, they developed a prototype four-stage Stirling pulse tube cryocooler, reaching temperatures around 4 K at the fourth stage cold head [14, 15]. Wang et al. [16, 17] developed a two-stage free-piston Stirling cryocooler, reaching 28 K under no-load conditions and providing 78W@40W with a supplied power of 3.2 kWe.

This research investigates the thermodynamic performance of a one-stage Stirling cryocooler utilizing a rhombic-drive mechanism. The development of the thermodynamic model relies on equations governing local and global mass conservation, energy balance, and momentum considerations in integral form. To validate the numerical model, a prototype Stirling cryocooler is constructed and tested. Additionally, a parametric study is conducted to assess the feasibility of achieving cryogenic temperatures at low charged pressures.

Numerical model

Cryocooler geometry

In this study, a thermodynamic model is developed to analyze the performance of a one-stage beta-type Stirling cryocooler, depicted in Figure 1. The working-gas domain within the cryocooler is divided into the compression chamber, expansion chamber, and moving regenerator. The rhombic-drive mechanism is associated with one piston and one displacer. The displacer comprises a porous zone internally and a shell externally. When the mechanism operates at a fixed motor speed, the temperature of the expansion chamber decreases until achieving stable temperature while a temperature gradient forms along the regenerator.

To develop the thermodynamic model, several assumptions are made:

- (1) Pressure, density, and temperature are governed by the ideal gas equation of state.
- (2) The working gas is considered completely sealed within the system.
- (3) The effects of gravity are neglected for simplicity.

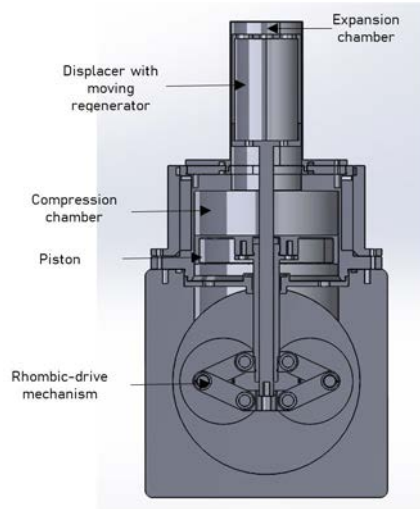


Figure 1. Schematic of a rhombic-drive one-stage beta-type Stirling cryocooler.

In the thermodynamic model, the working-gas domain is partitioned into N chambers. It is noted that while the expansion and compression chambers each consist of only one chamber, the regenerator is divided into several sub-chambers to account for temperature and pressure distribution. The flow and thermodynamic parameters as well as heat and work transfer through the i^{th} chamber walls are detailed in Figure 2.

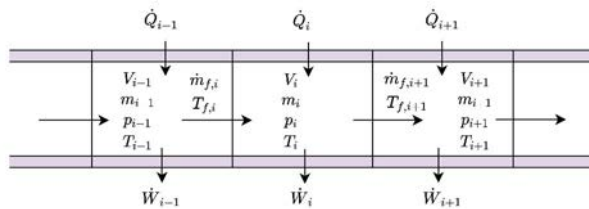


Figure 2. Work and heat transfer for chamber i .

The specifications of the one-stage Stirling cryocooler are outlined in Table 1.

Table 1. Specifications of the Stirling cryocooler.

Motor speed	min 500	max 850	rpm
Charged pressure	min 1.0	max 2.0	bar
Working gas	helium		
Ambient temperature	300		Kelvin
Cryocooler height	250		mm
Piston	bore 100		mm
Displacer	bore 49		mm
Regenerator	diameter 44	length 78	mm
Phase difference	67.750		
Compression ratio	2.6		

Governing equations

As mentioned earlier, the working gas is assumed to adhere to the ideal gas equation of state. Applying this equation to each chamber yields

$$p_i V_i = m_i R T_i, \quad i = 1, \dots, N \quad (1)$$

where p_i , V_i , m_i , T_i are the pressure, volume, mass and temperature of the i^{th} chamber, respectively. R represents the gas constant of the working gas. N is the total number of working-gas chambers.

The working gas in the working space is assumed not to leak, thus maintaining a constant total mass throughout the operation of the Stirling cryocooler.

$$\sum_{i=1}^N m_i = m_t \quad (2)$$

where the total mass m_t is determined based on the charged pressure p_c , the initial volumes of chambers V_i^0 , and the initial temperatures of chambers T_i^0 .

$$m_t = \sum_{i=1}^N p_c V_i^0 / R T_i^0 \quad (3)$$

To calculate the mass flow rate, it is necessary to consider local mass conservation. The formula for the i^{th} chamber is:

$$dm_i/dt = \dot{m}_i - \dot{m}_{i+1}, \quad i = 1, \dots, N \quad (4)$$

where \dot{m}_i and \dot{m}_{i+1} are the mass flow rates entering and existing the i^{th} chamber, as shown in Figure 2. The mass flow rates at two ends of the cryocooler must be equal zero.

$$\dot{m}_1 = 0, \quad \dot{m}_N = 0 \quad (5)$$

where, for the other mass flow rates, they can be estimated as follows:

$$\dot{m}_{i+1} = \dot{m}_i - dm_i/dt, \quad i = 0, \dots, N - 1 \quad (6)$$

To ensure algorithm stability, the mass in each chamber is calculated based on the uniform pressure p_u

$$p_u = m_t / \sum_{i=1}^N \frac{V_i}{RT_i} \quad (7)$$

and the ideal-gas equation of state

$$m_i = P_u V_i / (RT_i), \quad i = 1, \dots, N \quad (8)$$

The temperature can be determined using the energy balance equation

$$\begin{aligned} d[(m_i c_v + m_{s,i} c_s) T_i] / dt = I_{t,i} (T_w - T_i) / R_i + I_{ch,i} (T_{ch} - T_i) / R_{ch,i} + \\ \dot{m}_i c_p T_{f,i} - \dot{m}_{i+1} c_p T_{f,i+1} - p_i dV_i / dt, \quad i = 1, \dots, N \end{aligned} \quad (9)$$

where m_s is the mass of the wire mesh, c_v and c_p are the constant-volume and -pressure heat capacities, respectively, c_s is the heat capacity of the wire mesh, I_t is the indicator for the isothermal boundary condition, and I_{ch} is the indicator for contact between the i^{th} chamber and the cold head. Eqn. (9) raises the problem of how to determine the absolute pressure p_i and enthalpy flow rate $\dot{m}_i c_p T_{(f,i)}$.

The absolute pressure p_i is computed from two parts: (1) one due to friction effect, denoted by p_f , and (2) the other due to the global mass conservation, denoted by p_b . The pressure drop over the i^{th} chamber arises from the momentum equation, which shows its dependence on the dynamic pressure $1/2 \rho_i v_i^2$ and the friction coefficient f .

$$\Delta p_i / L_i = f_i \left(\frac{1}{2} \rho_i v_i^2 \right) / d_{h,i}, \quad i = 1, \dots, N \quad (10)$$

where Δp_i , L_i , $d_{(h,i)}$ are the pressure drop, the length and hydraulic diameter of the the i^{th} chamber, respectively. The density ρ_i and velocity v_i are determined by

$$\rho_i = m_i/V_i, \quad i = 1, \dots, N \quad (11)$$

$$v_i = |\dot{m}_i + \dot{m}_{i+1}|/(2\rho_i A_i), \quad i = 1, \dots, N \quad (12)$$

The pressure variation due to the pressure drop is estimated as follows

$$p_{r,1} = 0 \quad (13)$$

$$p_{r,i+1} = p_{r,i} - \text{sgn}(v_{i+1})(\Delta p_i + \Delta p_{i+1})/2, \quad i = 1, \dots, N - 1 \quad (14)$$

where p_r is the relative pressure due to the pressure drop only, and sgn denotes the signum function.

The base pressure p_b is determined to ensure that the absolute pressure satisfies the total mass conservation

$$p_b = (m_t - \sum_{i=1}^N p_{r,i} V_i / RT_i) / (\sum_{i=1}^N V_i / RT_i) \quad (15)$$

and then the absolute pressure is determined

$$p_i = p_b + p_{r,i}, \quad i = 1, \dots, N \quad (16)$$

The enthalpy flow rate is approximated using the upwind scheme

$$\dot{m}_i c_p T_{f,i} \approx \ll \dot{m}_i \gg c_p T_{i-1} - \ll -\dot{m}_i \gg c_p T_i, \quad i = 2, \dots, N - 1 \quad (17)$$

where

$$\ll \dot{m}_i \gg \equiv \max(\dot{m}_i, 0) \quad (18)$$

The cold-head temperature of the cold head is obtained from its energy balance equation

$$d(m_{ch} c_s T_{ch})/dt = (T_N - T_{ch})/R_{ch,i} + k A_c (T_a - T_{ch})/L_c + \mathbb{P}_{cooling} \quad (19)$$

where $\mathbb{P}_{cooling}$ is the cooling power, A_c is the annular area of the cylinder, L_c is the length of the cold cylinder, and R_{ch} is the thermal resistance of the cold head.

Solution procedure

To solve the above equations, the implicit Euler method is employed for discretizing the first-order derivatives of quantities with respect to time in Eqs. (4, 9, 19). Given temperature, pressure, mass flow rates, and volumes from the previous time level, an iterative procedure is necessary to calculate their values at the new time level due to the nonlinearity of the governing equations. In each time level, the mass, mass flow rate, pressure drop, absolute pressure, and temperature are iteratively solved until their values converge, as illustrated in Figure 3. The cyclic-averaged temperature is accumulated from

one time level to another within a cycle. The entire program terminates when the cyclic-averaged temperature between two adjacent cycles is less than the predefined value.

Results and discussion

The initial-boundary conditions for the baseline case of the thermodynamic model are presented in Table 2. The motor speed is held constant in each simulation case. Additionally, the cold cylinder and cold head are covered by a ceramic fiber heater, leading to the assumption of adiabatic walls for the regenerator and expansion chamber.

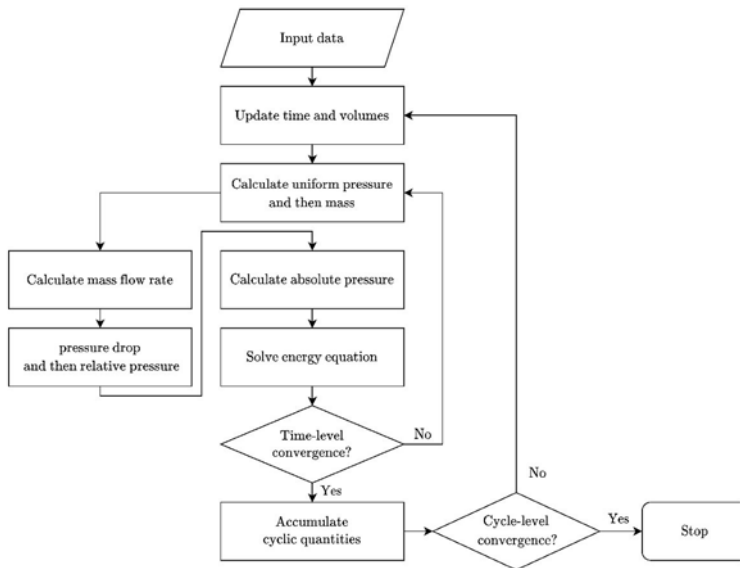


Figure 3. The solution procedure for the thermodynamic model.

Table 2. Initial and boundary conditions for the baseline case.

	Expansion chamber wall	Adiabatic	
Boundary conditions	Regenerator walls	Adiabatic	
	Compression chamber wall	300	K

Initial conditions	Crank angle	0	Rad
	Working-gas temperature	300	K
	Porous solid temperature	300	K
	Cold-head temperature	300	K
	Charged pressure	1.5	bar
	Mass flow rate	0	kg/s

The thermodynamic model of the beta-type Stirling cryocooler is validated by comparing its cold-head temperature with experimental data, as depicted in Figure 4. Both the experiment and thermodynamic model are conducted at three pressures (1.0, 1.5, and 2.0 bar), with the motor speed ranging from 500 to 850 rpm. It is worth noting that, at each charged pressure, the variation trend of the cold-head temperature with the motor speed from the thermodynamic model closely aligns with that of the experiment. At a charged pressure of 1.0 bar, the numerical cold-head temperature decreases from 200 to 169.4 K, while the experimental cold-head temperature ranges from 208.5 to 168.7 K. For the charged pressure of 1.5 bar, the numerical cold-head temperature decreases from 176.1 to 149.6 K, while the experimental counterpart decreases from 181.5 to 148.2 K. At the charged pressure of 2.0 bar, the numerical cold-head temperature drops from 161.1 to 137 K as the motor speed varies from 500 to 800 rpm, whereas the experimental temperature decreases from 173.1 to 151.3 K at motor speeds from 500 to 700 rpm. The maximum differences between the experimental and numerical results at 1.0, 1.5, and 2.0 bar are 8.5, 5.4, and 12 K, respectively.

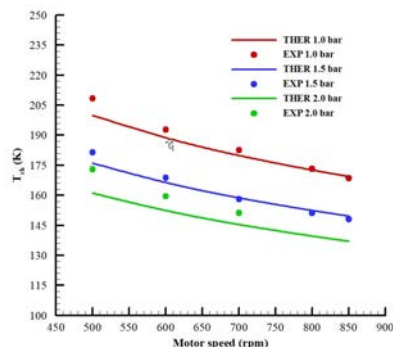


Figure 4. Comparison between the numerical and experimental cold-head temperature.

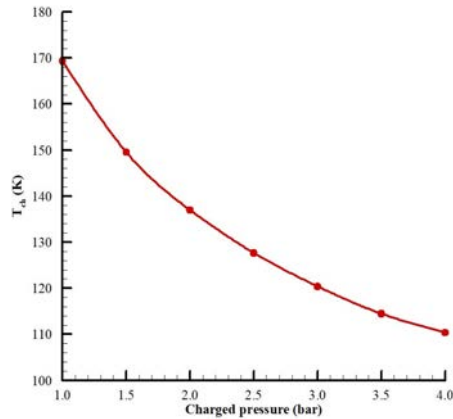


Figure 5. Variation in the numerical cold-head temperature with the charged pressure.

Subsequently, the influence of several geometrical and operating parameters on the cold-head temperature of the beta-type Stirling cryocooler was numerically investigated. Focusing on the effect of charged pressure, at a motor speed of 850 rpm, as the charged pressure increased from 1.0 to 4.0 bar, the numerical cold-head temperature was observed to decrease from 169.4 to 110.4 K. This phenomenon can be attributed to the proportional increase in the mass of the working gas with the charged pressure. Consequently, the mass flow rate and enthalpy flow rate through the chambers are also enhanced, leading to greater energy transport from the expansion chamber to the compression chamber. Thus, the cold-head temperature experiences a decrease with an increase in the charged pressure, as illustrated in Figure 5.

The piston radius is another influential parameter affecting the cold-head temperature, primarily due to its impact on the compression ratio and mass flow rates through the chambers. As previously mentioned, an increase in mass flow rates leads to enhanced energy transfer from the expansion chamber to the compression chamber. Consequently, the cold-head temperature exhibits a decrease with an increase in piston radius, as illustrated in Figure 6. In this study, piston radii ranging from 45 to 60 mm are investigated. At a motor speed of 850 rpm and a charged pressure of 2.0 bar, the cold-head temperature is observed to decrease from 138.6 to 135.6 K with an increase in piston radius.

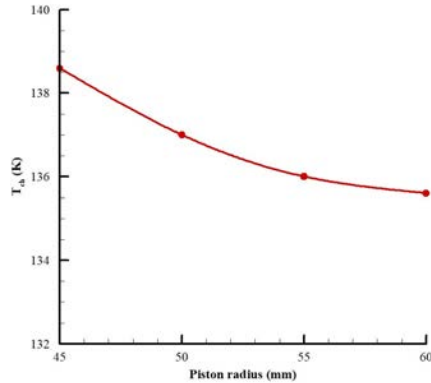


Figure 6. Variation in the numerical cold-head temperature with the piston radius.

The impact of the displacer radius on the cold-head temperature is depicted in Figure 7. As the displacer radius increases from 22.5 to 25 mm at a charged pressure of 2 bar and a motor speed of 850 rpm, a notable decrease in the cold-head temperature is observed, dropping from 220.9 to 80.5 K. This trend of variation can be attributed to the increase in the porous zone with the displacer radius. This enlarged porous zone facilitates higher enthalpy flow rates between the compression and expansion chambers. As a result, more efficient heat transfer occurs, leading to a significant reduction in the cold-head temperature.

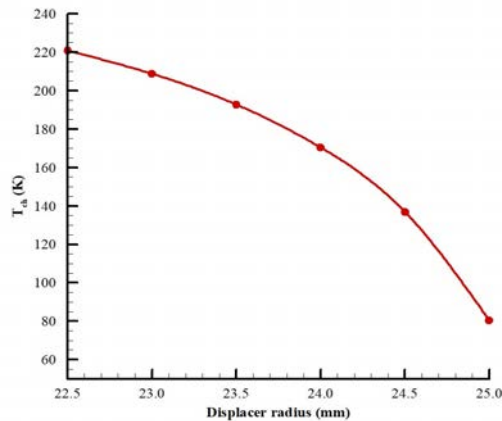


Figure 7. Variation in the numerical cold-head temperature with the displacer radius.

Conclusions

In this study, a thermodynamic model of the rhombic-drive one-stage Stirling cryocooler is developed. The validation of the numerical model was conducted by comparing its simulated cold-head temperature with experimental data. Remarkably, the variation trends of the cold-head temperature with the motor speed at three different charged pressures exhibited good agreement between the numerical model and the experiment. The maximum deviation between the experiment and numerical model at 1.0, 1.5, and 2.0 bar were found to be 8.5, 5.4, and 12 K, respectively.

Furthermore, the parametric study unveiled the positive influence of charged pressure, piston radius, and displacer radius on the cold-head temperatures. Specifically, as the charged pressure increased from 1.0 to 4.0 bar, the cold-head temperature exhibited a notable decrease from 169.4 to 110.4 K. Similarly, variations in piston radius from 45 to 60 mm resulted in a decrease in the numerical cold-head temperature from 138.6 to 135.6 K. Moreover, the numerical cold-head temperature decreased significantly from 220.9 to 80.5 K as the displacer radius increased from 22.5 to 25 mm.

This comprehensive numerical study confirmed that the one-stage Stirling cryocooler could effectively achieve cryogenic temperatures with low charged pressures, demonstrating its potential for practical application.

Acknowledgements

The authors express their gratitude for the financial support provided by the National Science and Technology Council (MOST 111-2221-E-006 -101 -MY3).

References

- [1] Orłowska A, Harman M, Ellison B. Receiver cryogenic system. ALMA project book, 5 (2002).
- [2] Jha AR. Cryogenic technology and applications. Elsevier, (2011).
- [3] Ross Jr RG, Boyle RF. An Overview of NASA Space Cryocooler Programs--2006. In: International Cryocooler Conference, (2007).
- [4] Cheng CH, Huang CY, Yang HS. Development of a 90-K beta type Stirling cooler with rhombic drive mechanism. International Journal of Refrigeration, 98:388-98 (2019).

- [5] Rawlings T. Numerical modelling of Stirling cryocoolers. Doctoral dissertation, University College London (2022).
- [6] Ahmed H, Almajri AK, Mahmoud S, Al-Dadah R, Ahmad A. CFD modelling and parametric study of small scale Alpha type Stirling Cryocooler. *Energy Procedia*, 142:1668-73 (2017).
- [7] Honeywell International Inc.. Stirling Cycle Cryocoolers. <https://aerospace.honeywell.com/us/en/products-and-services/product/hardware-and-systems/air-and-thermal-systems/stirling-cycle-cryocoolers>. (Accessed on March 20, 2024)
- [8] Sunpower Inc.. CryoTel Cryocoolers. <https://www.sunpowerinc.com/products/stirling-cryocoolers/cryotel-cryocoolers>. (Accessed on March 20, 2024)
- [9] Köhler JW. The Stirling refrigeration cycle. *Scientific American*, 212(4):119-27 (1965).
- [10] Prast G. A Philips gas refrigerating machine for 20 K. *Cryogenics*, 3(3):156-60 (1963).
- [11] Xu Y, Sun D, Qiao X, Yan SW, Zhang N, Zhang J, Cai Y. Operating characteristics of a single-stage Stirling cryocooler capable of providing 700 W cooling power at 77 K. *Cryogenics*, 83:78-84 (2017).
- [12] Sun D, Qiao X, Yang D, Shen Q. Experimental study on a two-stage large cooling capacity stirling cryocooler working below 30 K. *Cryogenics*, 129:103619 (2023).
- [13] Dang H, Bao D, Gao Z, Zhang T, Tan J, Zha R, Li J, Li N, Zhao Y, Zhao B. Theoretical modeling and experimental verifications of the single-compressor-driven three-stage Stirling-type pulse tube cryocooler. *Frontiers in Energy*, 13:450-63 (2019).
- [14] Dang H, Zha R, Tan J, Zhang T, Li J, Li N, Zhao B, Zhao Y, Tan H, Xue R. Investigations on a 3.3 K four-stage Stirling-type pulse tube cryocooler. Part A: Theoretical analyses and modeling. *Cryogenics*, 105:103014 (2020).
- [15] Dang H, Zha R, Tan J, Zhang T, Li J, Li N, Zhao B, Zhao Y, Tan H, Xue R. Investigations on a 3.3 K four-stage Stirling-type pulse tube cryocooler. Part B: Experimental verifications. *Cryogenics*, 105:103015 (2020).
- [16] Wang X, Zhu J, Chen S, Dai W, Li K, Pang X, Yu G, Luo E. Study on a high capacity two-stage free piston Stirling cryocooler working around 30 K. *Cryogenics*, 80:193-8 (2016).

- [17] Wang X, Dai W, Zhu J, Chen S, Li H, Luo E. Design of a two-stage high-capacity Stirling cryocooler operating below 30K. *Physics Procedia*, 67:518-23 (2015).

Fluent simulation of a beta Stirling engine for very low temperatures

J.A. Auñón Hidalgo*, D. Núñez Gevorkian

Department of Mechanical, Thermal and Fluid Engineering, Industrial Engineering School, University of Malaga, Malaga (29071), Spain

*Corresponding author: aunon@uma.es

Keywords: ZIFF-1000 Stirling engine, ANSYS-Fluent simulation, Thermodynamic analysis, Heat transfer and fluid dynamics and Energy efficiency and optimization

Abstract

This research article presents an in-depth study of the ZIFF-1000 Stirling engine, focusing on its simulation through ANSYS-Fluent software. The research initiates with a thorough study of the ZIFF-1000 engine, including its unique design features such as the crankshaft mechanism, simplified geometry, and the regenerator, along with the hot and cold heat exchangers. The work emphasizes the significance of these components in enhancing the engine's efficiency and operational reliability.

The main contribution of this study is the advanced simulation of the Stirling engine using ANSYS-Fluent for very low temperatures. This involved intricate processes like the adaptation of the engine's geometry for simulation, meticulous meshing, defining fluid and solid zones, and establishing dynamic meshing and boundary conditions. These simulations aimed to provide a comprehensive understanding of the engine's thermodynamic behavior and performance under various conditions.

The research highlights the simulation's capability to accurately predict the engine's performance, particularly focusing on aspects such as heat transfer, fluid flow dynamics, and energy efficiency. The simulation results are meticulously analyzed, providing critical insights into the engine's operational characteristics, such as temperature distribution, pressure fluctuations, and efficiency under different operating scenarios.

Moreover, the research discusses the challenges encountered during the simulation process, including the complexities associated with accurately replicating the physical phenomena within the engine and the limitations of the simulation tools.

In conclusion, this study not only advances the understanding of Stirling engine simulations but also proposes improvements for future research and practical applications of these engines in various industrial and environmental contexts. The findings of this research have significant implications for the design and optimization of Stirling engines, contributing to the development of more efficient and environmentally friendly energy systems.

Introduction

This research delves into the simulation of the ZIFF-1000 Stirling engine, a beta-type engine designed for cryogenic applications (Figure 1). Triggered by the University of

Málaga's acquisition of this innovative machine, our aim is to contribute to the body of knowledge on cryogenic machinery and its technologies.

This research offers a detailed simulation of the ZIFF-1000 Stirling engine, a Soviet-manufactured beta-type engine designed for air liquefaction. This engine, based on Philips-developed technology, was created to bypass Philips patents, and achieve superior performance. Its modern counterparts are available from the Dutch company “Stirling Cryogenics BV,” specifically the SPC-1 cryo-generator, with some parts being interchangeable with the ZIFF-1000. Before operation, the machine is charged with helium, the working fluid, which will increase in pressure as the engine runs. The cooling circuit is fed with ambient temperature water, which warms up by absorbing the heat removed from the air and the heat generated by the engine's moving parts.

The ZIFF-1000 operates on a Stirling cycle [3] executed by a compressor piston and a displacer piston, driven by a crankshaft using a crank-slider mechanism with a 110° phase shift between pistons to mimic the Stirling cycle's sequential volume changes. The engine's upper part, known as the liquefier, is an isolated volume connected to the thermodynamic cycle through a copper heat exchanger and a column that increases the heat exchange surface with the air to be liquefied. The engine also features a metallic mesh that collects moisture from the air, which freezes and blocks air passage through an upper opening— however, more liquid air generation occurs with this opening left open.

This study focuses on simulating the ZIFF-1000 engine's operation, incorporating its complex geometry, dynamic movement of pistons, and thermal interactions within the engine. By exploring the simplified but accurate representation of the engine's geometry and dynamics, the research aims to contribute to optimizing Stirling engines for cryogenic applications. This involves examining the engine's regenerator, cold and hot focus heat exchangers, and the effects of these components on the engine's efficiency and performance. Through this simulation, we intend to provide insights into improving cryogenic machinery's design and operational strategies, enhancing their application in industrial and environmental settings.

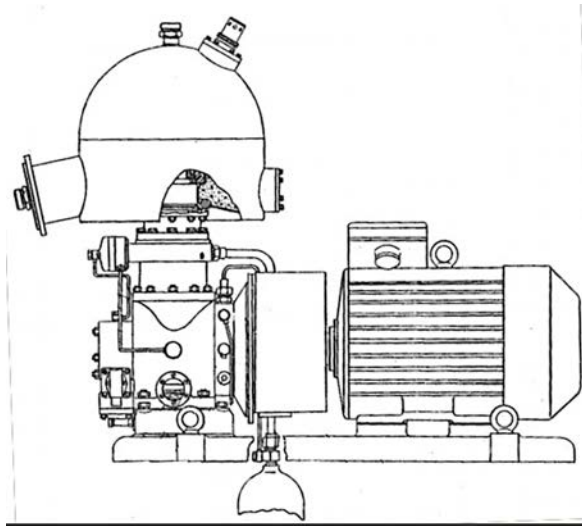


Figure 1. ZIF-100 machine representation.

Literature Review

The Stirling engine, recognized for its unique closed-loop regenerative cycle, adapts to a wide array of heat sources, offering a versatile and sustainable energy solution [1]. Originating in the 19th century by Robert Stirling as a safer alternative to the hazardous steam engines of the time [2], its design and efficiency have significantly evolved, benefiting from advancements in materials science and computational technologies. This evolution enables the engine to exploit diverse energy sources, including renewables like solar and geothermal power [3], making it suitable for a variety of applications from low-temperature operations to power generation in isolated or sensitive environments. Recent studies have aimed at boosting the engine's performance by optimizing its design, selecting superior materials, and incorporating sophisticated regenerative components, with Computational Fluid Dynamics (CFD) simulations providing crucial insights into improving thermodynamic processes and design features [4][5][6][7][8]. Nonetheless, research continues to explore the potential of novel materials for key components like the regenerator and heat exchangers to further enhance the engine's efficiency, especially in low-temperature contexts [9].

ZIFF-1000 Stirling engine description and geometry creation.

The ZIFF-1000 Stirling engine represents a beta-type engine distinguished by its cryogenic functionality. Central to its operation is the helium gas acting as the working fluid, facilitating the refrigeration cycle pivotal to the engine's cryogenic application. The design features a sophisticated crankshaft mechanism that orchestrates the movement of the pistons, thereby driving the cycle.

The motion of the system has been modeled using the crank-slider mechanism (see Figure 2). This motion is employed for contouring, dynamic mesh configuration, and the selection of the time step to be followed.

The geometry to be modeled is complex due to the oil circuits, helium loading, and asymmetrical shapes of the moving parts and machine contours. Therefore, a simpler geometry has been represented while maintaining the volumes of the real geometry (see Figure 3).

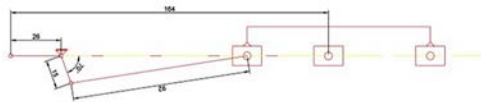


Figure 2. Kinematic diagram, with dimensions, of the crank-slider mechanism.

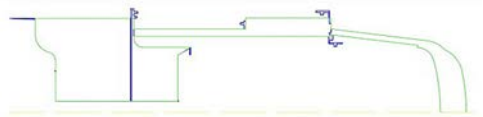


Figure 3. Comparison of simplified geometry (green) with real geometry (blue).

The formula for velocity is as follows:

$$v = r \cdot \omega \cdot \left[-\sin(\theta + \omega \cdot t) - \frac{r \cdot \sin(2 \cdot (\theta + \omega \cdot t))}{2 \cdot \sqrt{l^2 - r^2} \cdot \cos^2(\theta + \omega \cdot t)} \right] \quad (1)$$

Where v is lineal piston velocity in m/s, r is the crank length in m, l is the crank length in m, θ is the phase shift in rad, ω is the angular velocity in rad/s and t is the time in s. If the angular velocity is positive, the cycle operates as a heat pump. If the angular velocity is negative, the cycle operates as a refrigerator. In the simulation, the angular velocity will always be negative.

The simplified engine's model for the simulation can be seen on Figure 4 and Figure 5. Key components of the engine include the regenerator and the hot and cold heat

exchangers, each playing a critical role in the engine's efficiency and overall performance. The regenerator acts as a temporary energy storage unit, recovering heat from the gas as it transitions between the hot and cold zones, thus enhancing the engine's thermal efficiency. Conversely, the heat exchangers facilitate the transfer of heat into and out of the system, crucial for maintaining the temperature gradients essential for the engine's operation.

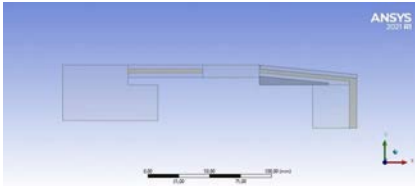


Figure 4. Geometry of the simulation. Design Modeler screenshot.

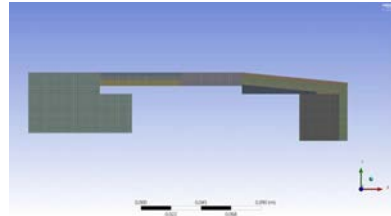


Figure 5. Geometry of the simulation. Mesh screenshot.

The technical specifications of the engine can be seen in the following table. These data have been used for the validation of the results obtained from the simulation.

Table 1. Main technical specifications of the ZIF-1000 Stirling engine.

Rotation frequency	1480		rpm
Working gas	helium		
Initial working gas pressure	19		bar
Mean working gas pressure	min 25	max 26	bar
Cooling Heat	16850		W
Power extracted to Air	895		
Liquid Air flow rate	2.11		g/s
Cold efficiency	4.8		%
Heat efficiency	91.79		%
Total efficiency	96,59		%
Heater temperature	min 60	max 62	°C
Cooler temperature	min -196	max -193	°C
Displacer	bore 70	stroke 30	mm
Working piston	bore 90	stroke 52	mm
Nominal power	18400	electric	W

Simulation Setup in ANSYS-Fluent

The simulation of the ZIFF-1000 engine in ANSYS-Fluent required a series of preparatory steps to ensure the model accurately reflects the engine's physical and operational characteristics.

After adapting the geometry, the next step is meshing. For the meshing process, the dynamic nature of the engine was considered, particularly the movement of the pistons and the helium gas flow through the various engine components. It is crucial to highlight that in dynamic areas, that is, in the expansion and compression chambers, a rectangular mesh had to be adapted, allowing the use of the layering technique for dynamic meshing. A node distance of $\Delta x = 0.5$ mm was selected. These areas can be seen in the following figures.

Regarding the models used, the energy model and the k-omega SST viscous model have been activated. The rest of the configuration has been left as default.

Regarding the "cell zone conditions," the type of fluid in each zone (helium, air, and water) was specified, and the porous model was activated in the cold, hot exchangers, and the regenerator.

The porosities in the three zones (cold exchanger, hot exchanger, and regenerator) were calculated as follows:

$$\gamma_F = \frac{V_f}{V_T} \quad (2)$$

where γ_i is the porosity of the focus, V_i is the fluid volume, and V_T is the total volume.

The porosities were determined as follows:

Table 2. Porosities

Cold focus exchanger	0,385
Hot focus exchanger	0,205
Regenerator	0,732

As for the boundary conditions, they were adapted so that the simulation includes a constant mass flow rate of water and air. All external walls of the simulation, i.e., those not in contact with a fluid on both sides, are adiabatic. Inlet and conditions for air and water have a temperature of 27 °C.

Table 3. Boundary conditions

Water flow rate	0,357	kg/s
Inlet water velocity	0,383512	m/s
Outlet water velocity	0,357100	m/s
Air flow rate	0,002110	kg/s
Inlet air velocity	1,855012	m/s
Outlet air velocity	0,002110	m/s

Regarding dynamic meshing, the layering method was used, taking advantage of the fact that the mesh in the zones with movement is rectangular, a necessary condition for this method of dynamic meshing. The movement of the piston and displacer is imposed by a UDF (User- Defined Function) that calculates the speed from (1).

To reach the steady-state regime of the simulation more quickly, the initial conditions were divided into two stages: a first phase called common initialization and a second phase called helium pressure initialization. In the first stage, the temperatures of the cold focus walls are also fixed at -223 °C. Once the air reaches a temperature below -194 °C, the fixed temperatures of the walls are released to finally achieve the steady state. The initial conditions for the experiment start with helium at a gauge pressure of 4,750,000 Pa, significantly higher than the air and water pressure, which is at atmospheric level (0 Pa). The setup is characterized by an axial velocity of 0 m/s, turbulent kinetic energy set to 1 m²/s², and a specific dissipation rate of 1 s⁽⁻⁴⁾, with an overall temperature maintained at 300 K.

Residual, relaxation factors and numerical methods were left as default.

Finally, a simulation was launched with $\Delta t = 0.00012$ s and 10,000-time steps. The restriction of the maximum time step based on mesh size is given by:

$$\Delta t_{max} < \frac{\Delta x_{max}}{v_{max}}$$

For the case of the simulation, $\Delta x_{max} = 5 \cdot 10^{-4}$ [m] y $\Delta 35 = 4.03$ m/s, therefore $\Delta t_{max} = 1.2408 \cdot 10^{-4}$ s.

Results

In the steady-state regime of our beta Stirling engine simulation for very low temperatures, the validation against the real machine ZIFF-1000 trial was conducted. Figure 6 indicates the achievement of steady state, which allowed for a direct comparison of simulation outcomes with experimental data. Initial conditions for the simulation were set with water and air mass flow rates at 0.3571 kg/s and 0.00211 kg/s, respectively, both at an entry temperature of 300 K, and helium at an initial pressure of 47.5 bar and temperature of 300 K.

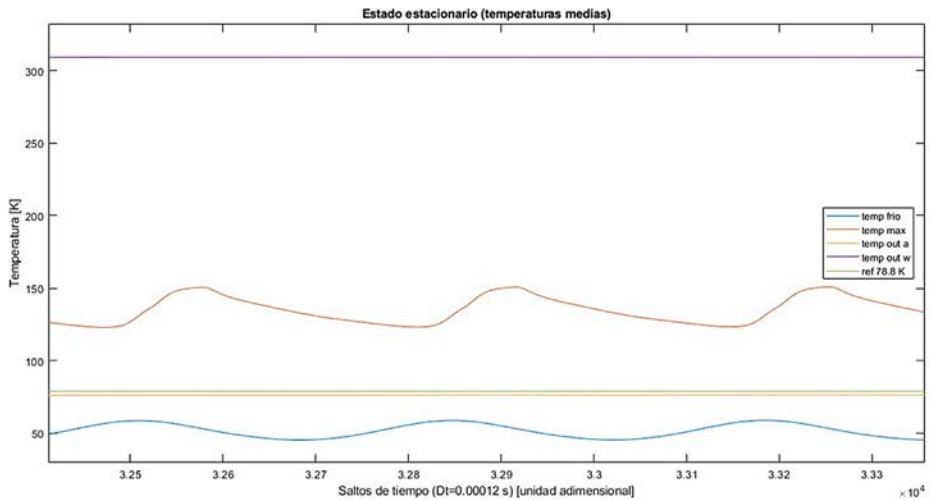


Figure 6. Temperatures distribution of the Stirling engine at the steady state.

Table 4. Comparison between experimental data and simulations.

	Experimental data	Simulation
Mean pressure (bar)	25~26	27.12
Air flow rate (g/s)	2.11	2.11
Cold focus heat (W)	900	910.31
Hot focus heat (W)	16850	14008.3

The simulation results, including mean helium pressure, liquid air generation, and cold focus heat, align closely with the trial data, indicating a high degree of accuracy.

However, a notable discrepancy exists in the hot focus heat. This discrepancy can be justified by several factors:

- In the real machine trial, the cooling water traverses other hot areas of the machine, unlike in the simulation where it is used solely to cool the Stirling cycle.
- The porous media representing heat exchanger slots and the regenerator are idealized in the simulation, leading to an expected higher engine performance and consequently less heat needing to be cooled for the same level of cooling, as observed in the results.
- The simulation does not account for the heat generated by the friction of moving parts, resulting in less heat to be evacuated by water.
- Considering these factors, and comparing the simulation results to the trial data, the simulation within this thesis is deemed coherent with the real experiment outcomes.

Simulation Results Overview

The temperature distribution within the Stirling engine delineates two distinct zones: higher temperatures in the compression chamber and lower temperatures in the expansion chamber, influenced by helium flow and the thermal conductivity of solid copper components. The maximum temperature in the expansion chamber, near 150 K at the regenerator interface, highlights the cooling limit imposed by this peak temperature on the engine's performance.

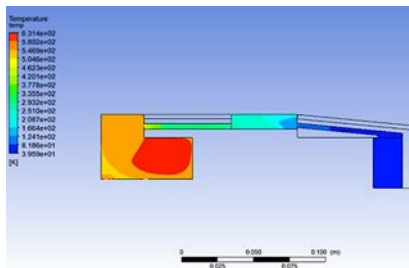


Figure 7. Temperature contour at 0° crankshaft position.

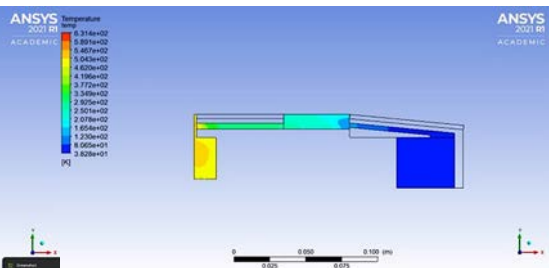


Figure 8. Temperature contour at 90° crankshaft position.

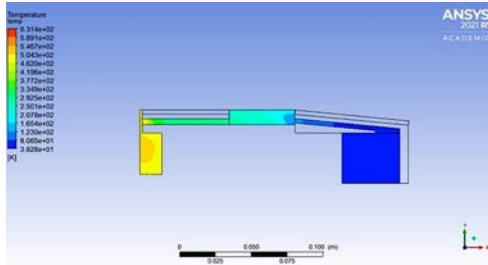


Figure 9. Temperature contour at 180° crankshaft position.

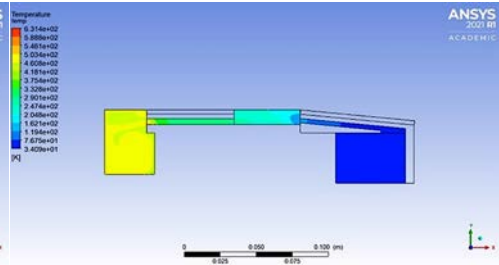


Figure 10. Temperature contour at 270° crankshaft position.

The PV diagram (Figure 11) of the Stirling engine displays an oval shape with a closed cycle indicating the system has reached a steady state. This observation confirms the engine's operation within its intended thermodynamic parameters. The closed cycle in the s-T diagram (Figure 12) shows that the minimum temperature remains well above 78.8 K, attributed to averaging temperatures across the entire cycle. This method of averaging temperatures across the cycle leads to the expansion chamber's specific temperature values being less distinguishable, emphasizing a strategic decision in how temperature data is presented.

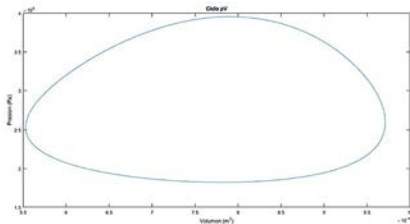


Figure 11. PV diagram of the steady state of the ZIF-1000.

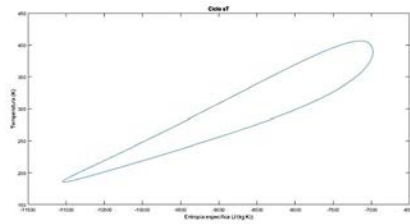


Figure 12. sT diagram of the steady state of the ZIF-1000.

Conclusion and Future Work

This article confirms the coherence between the simulated results and the experimental data of the ZIFF-1000 Stirling engine, particularly in terms of mean working pressure. The simulation demonstrates higher efficiency compared to the actual machine, primarily evidenced by the differences in hot focus heat. The behavior of the regenerator aligns with expectations from other independent studies, supporting the validity of using

constant properties for the working fluid's thermal conductivity, specific heat, and dynamic viscosity.

It has been shown that equivalent heat transfer can be achieved by modifying the fluid properties for simplified analysis. A pseudo-transient regime was effectively employed to expedite the simulation's convergence to a steady state, aligning with the known characteristics of the Stirling engine.

The cryogenic capability of the engine is notably influenced by the temperature rise due to hot helium moving into the expansion chamber, impacting the temperatures of the engine's solid zones.

Future Work

To improve the simulation model's accuracy for Stirling engines under cryogenic conditions, the proposals include developing an advanced User-Defined Function (UDF) for modeling non-equilibrium behavior in porous media, adjusting for volume variations within simulation domains. This enhancement aims to refine heat exchange and fluid dynamics simulations within the engine, especially around gas interactions with porous heat exchangers and regenerators. Additionally, a comprehensive analysis of pressure loss parameters through experimental and simulation studies is suggested to identify accurate correlations for pressure drops across heat exchangers and regenerators, thereby enhancing the model's ability to replicate real-world engine performance, with a focus on minimizing efficiency losses.

References

- [1] Robert Stirling. (1816). Regenerator and Hot Air Engines [Patente No. 4081]. Reported by THE ENGINEER. Retrieved from http://hotairengines.org/patents/stirling-patents/THE%20ENGINEER_Stirling's%201816%20patent.pdf
- [2] Hebert, L. (1827). Air Engines [Patent of 1827]. In Galloway, p. 667. Description from Galloway. Retrieved from http://hotairengines.org/patents/stirling-patents/GALLOWAY_Stirling%20engines%201827.pdf
- [3] West, C. (1986). Principles and applications of Stirling engines. Van Nostrand Reinhold.

- [4] Buliński, Z., Kabaj, A., Krysiński, T., Szczygieł, I., Stanek, W., Rutczyk, B., Gładysz, P. (2019). A Computational Fluid Dynamics analysis of the influence of the regenerator on the performance of the cold Stirling engine at different working conditions. *Energy Conversion and Management*, 195, 125–138. <https://doi.org/10.1016/j.enconman.2019.04.089>
- [5] Jajcevic, D., Almbauer, R., Schmidt, S., & Karl, G. (2009). Simulation Strategy and Analysis of a Two-Cylinder Two Stroke Engine Using CFD Code Fluent. In *Simulation for Innovative Design* (pp. 235-246).
- [6] Costa Pereira, S. (2014). Numerical characterization study of pressure drop and heat transfer phenomena in woven wire matrix of a Stirling engine regenerator [Tesis de doctorado, Universidad de Mondragón].
- [7] Ackermann, R. (1997). *Cryogenic Regenerative Heat Exchangers*. Plenum Publishing Corporation.
- [8] Katooli, M. H., Askari Moghadam, R., & Hajinezhad, A. (2019). Simulation and experimental evaluation of Stirling refrigerator for converting electrical/mechanical energy to cold energy. *Energy Conversion and Management*, 184, 83–90. <https://doi.org/10.1016/j.enconman.2019.01.014>
- [9] Ahmed, F., Hulin, H., & Khan, A. M. (2019). Numerical modeling and optimization of beta- type Stirling engine. *Applied Thermal Engineering*, 149, 385–400. <https://doi.org/10.1016/j.applthermaleng.2018.12.003>

Thermodynamic modelling and CFD simulation

New Analytical Method for Stirling Engine Thermodynamic Cycle Calculation Using Simplified Adiabatic Model

S. P. Stolyarov^{a*}, A. S. Stolyarov^b, Ye Maung^c

a Head of the Department of Ship Internal Combustion Engines and Diesel Engines, State Marine Technical University, St. Petersburg, Lotsmanskaya Street, 3, 190121, Russia

b Senior Lecturer of the Department of Ship Internal Combustion Engines and Diesel Engines, State Marine Technical University, St. Petersburg, Lotsmanskaya Street, 3, 190121, Russia

c PhD student of the Department of Ship Internal Combustion Engines and Diesel Engines, State Marine Technical University, St. Petersburg, Lotsmanskaya Street, 3, 190121, Russia

* Corresponding author: stsp56@yandex.ru

Keywords: Stirling engine, External combustion engine, Isothermal cylinder, Adiabatic cylinder, Calculation method, Thermodynamic process, Working process, Indicator parameters, Indicator diagram

Abstract

This paper uses a simplified adiabatic model to predict the thermodynamics cycle of Stirling engine. A detailed comparison between the present and the existing models are made for an engine with a rhombic mechanism and has a cylinder power of 8 kW. In conclusion, the standard deviation from the reference calculation was 0.19% of the average cycle pressure, the error in determining the cycle power was 0.6%. If the methods are valid, the Stirling thermodynamic cycles predicted can be used as a foundation of developing Stirling engines.

Introduction

The relevance of improving methods for calculating working processes in Stirling engines (SE) is determined by long-term interest in these engines, at different times due to various advantages of SE, currently, mainly, the prospects for use in environmental projects and in special power plants, including underwater vehicles from Sweden, Japan, Singapore and China. The problem of theoretical substantiation of SE is aggravated by their small-scale production and lack of accumulated operating experience, the variety of design solutions used, which shows that SE have not yet received an optimal design. Since the advent of the first method for calculating the working cycle of SE (Schmidt, 1861) [1], there have been fundamental changes in the basic sciences, calculation algorithms and the design of the main elements of the SE. As scientific methods and design solutions developed, the goals and objectives of calculation methods became

more complex. As clarifications, accounting for hydraulic resistance in heat exchangers and connecting ducts of the internal circuit, temperature drops in the processes of heat supply and removal, cyclic processes of energy accumulation in the regenerator matrix, complete or partial adiabaticization of working volumes, thermal flows through structural elements, leakage of working fluid through piston and rod seals were introduced. Taking into account clarifications, methods were created that were called second order design methods; the most famous such method was developed by W.R. Martini [2].

A consequence of the introduced complications, as well as the peculiarity of a closed thermodynamic cycle that requires coordination of parameters at the initial and final points, was a situation in which the calculation of the working process with a high degree of adequacy could only be performed using methods of numerical modelling of thermophysical processes. The first significant works in this direction were published by T. Finkelstein in the 1960s. [3,4], somewhat later, numerous studies by different authors were devoted to the problem of modelling the SE cycle [5, 6, 7]. However, complex mathematical models have not solved the problem of creating an engineering method intended for calculations when designing a SE. As a result, until now, simplified methods based on G. Schmidt's isothermal algorithm are used in design and research work [8].

Problem of Synthesizing Calculation Method

The problem of synthesizing a calculation method at an engineering level consists in dividing step-by-step process modelling algorithms into a set of calculation algorithms for individual physical processes, for which it becomes possible to substantiate integral relations that link the parameters of the thermodynamic cycle with thermophysical processes that determine irreversible losses and reduce the efficiency of the SE cycle.

The basis of the engineering level calculation method is the method of calculating the main indicator parameters: pressure and temperature in the working spaces of the internal circuit of SE. Moreover, in accordance with the principles of organizing the working process, the accuracy of the calculation is determined by the detail of the temperature distribution of the working fluid among the elements of the volume of the internal circuit. According to the results of the analysis of the parameters of various types of Stirling engine cycles, including use of the BS-Stirling software package, the accuracy of the calculation of indicator parameters is significantly influenced by the change in

temperature in the hot and cold cylinders. The main physical phenomena in SE working cylinders: compression or expansion, inlet or outlet of the working fluid, supply or removal of heat into the cylinder and pistons, leakage or return flow of the working fluid through piston and rod seals, dissipation of the energy of convective and mechanical friction. The effect of each of these factors is determined by specific design solutions, the design coordination of which requires engineering methods. In practice, these methods must correspond to the structure of engineering documentation, for example, the content of technical or detailed projects, i.e., they must represent an autonomous algorithm with initial data, calculation scheme, methods and results. The basis for design methods for assembly units and internal circuit parts is the calculation of the thermodynamic cycle, i.e., the indicator parameters of the SE. Thus, it is advisable to separate the method of engineering calculation of the thermodynamic cycle of the SE from the accompanying physical phenomena, and build it with the adoption of appropriate assumptions. Methods in which processes in working spaces are assumed to be adiabatic have been developed since the 1960s. [3,9]. A feature of these algorithms is the presence of logical operations that do not allow the synthesis of an analytical relationship to describe indicator parameters [10]. Despite the repeated appeal of various authors to adiabatic methods, the question of the criteria for the admissibility of this assumption remains practically unexplored. Only G. Walker points out that at a cycle frequency of more than 1000 min⁻¹, the processes in the working spaces “are more adiabatic than isothermal in nature” [3].

Mathematical Model of the New Analytical Method

The mathematical core of the method is built on basic concepts similar to G. Schmidt’s method.

For an external combustion engine with a closed working circuit and a gaseous working fluid, the main equation of the mathematical model of the cycle is the equation of mass balance of the working fluid in the elements of the internal circuit (IC), expressed through the equation of state [3]

$$M = \sum M_i = \sum \frac{P_i V_i}{R \cdot T_i} = \text{const}, \quad (1)$$

where pressure P_i and temperature T_i are distributed over volumes V_i in accordance with the principles of the mathematical model.

SE includes the volumes of expansion space $V_e(\alpha)$ and compression space $V_c(\alpha)$, changing in accordance with the kinematic diagram of the mechanism, the volumes of the heater V_h , regenerator V_r , cooler V_k , as well as “dead volumes” in the hot V_{dh} and cold V_{dc} zones. In the part of the dead volumes adjacent to the heat exchangers of the internal circuit V_{dhex} and cold V_{dcex} , the processes are assumed to be isothermal with a temperature the same as in the adjacent element. Parts of the dead volumes in the working cylinders and adjacent pipes and manifolds V_{dhwc} and cold V_{dhwk} are assumed to be adiabatic with a temperature the same as in adjacent working spaces.

In engineering methods with a step-by-step calculation algorithm, as a rule, gas-dynamic calculations are performed on the basis of thermodynamic ones. In this case, the cycle is calculated under the assumption that the hydraulic resistance during the flow of the working fluid between the elements of the internal circuit can be neglected and the pressure can be assumed to be a concentrated value, depending on the phase of the working process α , $P_i=P(\alpha)$.

In the simplest isothermal methods, the temperature of the working fluid in each of the elements is assumed to be a constant value, independent of the phase of the working process.

The temperature of the working fluid in the heater is set

$$T_h = T_{wh} - \Delta T_h, \quad (2)$$

taking into account the average temperature of the heat exchange surface T_{wh} and the average temperature drop per cycle ΔT_h . The temperature of the working fluid in the cooler is determined accordingly

$$T_k = T_{wk} + \Delta T_k. \quad (3)$$

The temperature of the working fluid in the regenerator is averaged according to the condition of the equivalent mass of the working fluid

$$T_r = \frac{T_h - T_k}{\ln \frac{T_h}{T_k}}. \quad (4)$$

In adiabatic methods, heat transfer in working spaces is neglected, and the temperature in the working spaces is determined by the adiabatic equation for expansion space

$$T_e = T_{e0} \cdot \left(\frac{P}{P_{max}} \right)^{\frac{k-1}{k}}, \quad (5)$$

$$T_c = T_{c0} \cdot \left(\frac{P}{P_{min}} \right)^{\frac{k-1}{k}}, \quad (6)$$

The temperature at the base extreme points is assigned taking into account the adiabatic difference

$$T_{e0} = T_h + \Delta T_e, \quad (7)$$

$$T_{c0} = T_k + \Delta T_c, \quad (8)$$

The magnitudes of the adiabatic differences are determined by the magnitudes of the phase shifts of the extrema of the hot and cold volumes, as well as the amplitude of the cyclic change in pressure.

Taking into account the accepted notation, equation (1) can be transformed to the form

$$\frac{R}{P(\alpha)} \cdot M = \sum \frac{V_i}{T_i} = \frac{V_e(\alpha) + V_{dhwc}}{T_e} + \frac{V_{dhex} + V_h}{T_h} + \frac{V_r}{T_r} + \frac{V_{dcex} + V_k}{T_k} + \frac{V_{dcwc} + V_c(\alpha)}{T_c}, \quad (9)$$

Let us denote the factor of isothermal volumes

$$W = \frac{V_{dhex} + V_h}{T_h} + \frac{V_r}{T_r} + \frac{V_{dcex} + V_k}{T_k}, \quad (10)$$

Now, taking into account the substitution of expressions (5) and (6), the main equation of the mathematical model takes the form

$$\frac{R}{P_{max}} \cdot M = W \cdot \left(\frac{P(\alpha)}{P_{max}} \right) + \left(\frac{P(\alpha)}{P_{max}} \right)^{\frac{1}{k}} \times \left[\frac{V_e(\alpha) + V_{dhwc}}{T_{e0}} + \frac{V_{dcwc} + V_c(\alpha)}{T_{c0}} \cdot \left(\frac{P_{min}}{P_{max}} \right)^{\frac{k-1}{k}} \right], \quad (11)$$

Let us denote a set of parameters depending on the phase of the working process

$$U(\alpha) = \frac{V_e(\alpha) + V_{dhwc}}{T_{e0}} + \frac{V_{dcwc} + V_c(\alpha)}{T_{c0}} \cdot \left(\frac{P_{min}}{P_{max}} \right)^{\frac{k-1}{k}}, \quad (12)$$

To linearize equation (11), we apply the approximation of a power function with the clarifying parameter m

$$\left(\frac{P(\alpha)}{P_{max}} \right)^{\frac{1}{k}} = \left(1 - \left(1 - \frac{P(\alpha)}{P_{max}} \right) \right)^{\frac{1}{k}} \approx 1 - \left(\frac{1}{k} + m \right) \left(1 - \frac{P(\alpha)}{P_{max}} \right), \quad (13)$$

The value of the parameter m is determined so that the approximation error in the central part of the calculated range overestimates the result, and at the left border of the range underestimates it, (see Fig. 1).

For Stirling engine cycles with developed heat exchangers and moderate specific power of the working volume at $1 > P_{min}/P_{max} > 0,6$ with an approximation error of less than 0.6%.

$$m = 0.1251 \cdot \left(\frac{P_{min}}{P_{max}} \right)^2 - 0.3162 \cdot \left(\frac{P_{min}}{P_{max}} \right) + 0.1928, \quad (14-1)$$

For cycles with high specific power of the working volume at $1 > P_{min}/P_{max} > 0.25$ with an approximation error of less than 3.7%

$$m = 0.1587 \cdot \left(\frac{P_{min}}{P_{max}} \right)^2 - 0.3696 \cdot \left(\frac{P_{min}}{P_{max}} \right) + 0.2133, \quad (14-2)$$

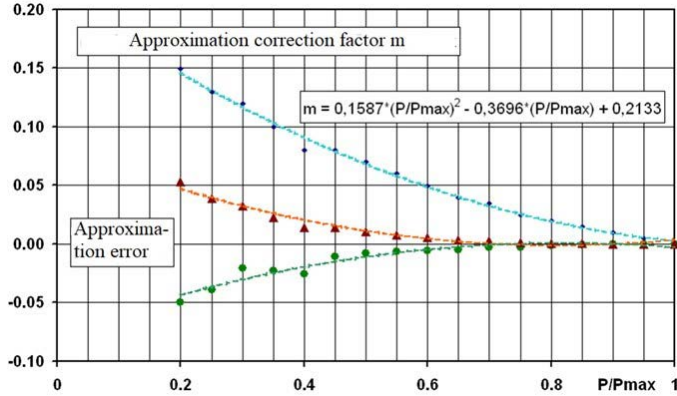


Figure 1. The value of the approximation correction factor m and the approximation accuracy on the calculated interval.

As a result of linearization, equation (11) takes the form

$$\frac{P(\alpha)}{P_{max}} = \frac{\frac{R}{P_{max}} \cdot M - \left(1 - \frac{1}{k} m\right) \cdot U(\alpha)}{W + \left(\frac{1}{k} + m\right) \cdot U(\alpha)}. \quad (15)$$

In order to bring the equation into a form convenient for use as part of engineering methods, we introduce the notation $U(\alpha)_{max} = U_a$, $U(\alpha)_{min} = U_i$ and compose expressions for the maximum and minimum pressure of the cycle, adding the conditions reaching extreme pressure values.

$$\left(\frac{P(\alpha)}{P_{max}}\right)_{max} = \frac{\frac{R}{P_{max}} \cdot M - \left(1 - \frac{1}{k} m\right) \cdot U_i}{W + \left(\frac{1}{k} + m\right) \cdot U_i} = 1. \quad (16)$$

From this equation we express

From this equation we express

$$\frac{R}{P_{max}} \cdot M = W + U_i. \quad (17)$$

From the condition

$$\left(\frac{P(\alpha)}{P_{max}}\right)_{min} = \frac{\frac{R}{P_{max}} \cdot M - \left(1 - \frac{1}{k} m\right) \cdot U_a}{W + \left(\frac{1}{k} + m\right) \cdot U_a} = \frac{P_{min}}{P_{max}} \quad (18)$$

we obtain

$$\frac{P_{min}}{P_{max}} = 1 - \frac{U_a - U_i}{W + \left(\frac{1}{k} + m\right) \cdot U_a}. \quad (19)$$

As a result, the expression for calculating pressure can be represented as

$$\frac{P(\alpha)}{P_{max}} = 1 - \frac{k}{1+k \cdot m} + \frac{k}{1+k \cdot m} \cdot \frac{W + \left(\frac{1}{k} + m\right) \cdot U_i}{W + \left(\frac{1}{k} + m\right) \cdot U(\alpha)} \quad (20)$$

Adequacy of the Developed Method

The adequacy of the developed method was assessed by comparison with other known available methods.

The method implemented in the BS-Stirling software package was chosen as a reference. According to the results of studies using experimental data and published information on more than 60 SEs, the errors of the BS-Stirling software package with a confidence probability of 0.95 were no more than 5% for the power value and no more than 10% for the indicator efficiency value [11].

Comparative calculations were carried out for a Stirling engine with a rhombic mechanism with a cylinder power of 8 kW using the following methods:

- Isothermal, volumes are determined by harmonic functions of the 1st order.
- Isothermal, volumes are determined according to exact formulas for the rhombic mechanism.
- Isothermal, volumes are determined by harmonic functions of the 1st order, with adjustment of the pressure amplitude according to the cycle parameters.
- Adiabatic, volumes are determined according to exact formulas for the rhombic mechanism.
- Adiabatic, volumes are determined according to exact formulas for a rhombic mechanism, with correction of the temperature in the cavities.
- Process modelling, software package “BS-Stirling 4.2”.

The calculation results are illustrated in Table 1, Fig. 2 and Fig 3.

Table 1. Accuracy of various variants of the Stirling engine cycle calculation methods.

No.	Methods	Workdone per cycle, J	Error, %
1	Adiabatic, rhombic mechanism	407.5	-0.6
2	Adiabatic, rhombic mechanism with correction of temperature in working spaces	409.4	-1.1
3	Modelling, BS-Stirling 4.2 program	405.0	0

4	Isothermal, rhombic mechanism	368.4	9.0
5	Isothermal, volumes are harmonics of the 1st order	276.8	31.6
6	Isothermal, volume harmonics of the 1st order. adjustment according to cycle parameters	326.3	19.4

The developed method makes it possible to determine the pressure value in the cycle with an accuracy sufficient for an engineering method - the standard deviation from the reference calculation was 0.19% of the average cycle pressure. In Fig. 2 and Fig 3, the lines of calculations using adiabatic methods and the reference calculation practically merged into one line. The error in determining the cyclic power using the developed method was 0.6% which is clearly less than the probable error in calculating the power of the SE using a known method of any level of complexity.

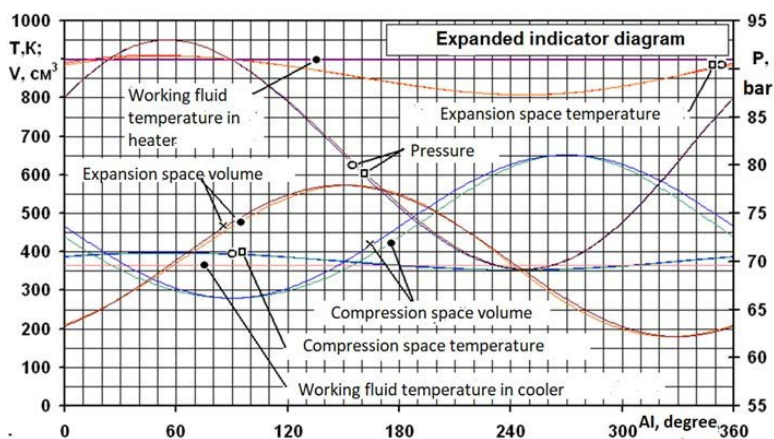


Figure 2. Expanded indicator diagram Pressure and temperature in the expansion and compression spaces: ○—exact solution. □—adiabatic model; volume of the spaces: ●—exact solution. × - 1st order harmonics.

The main tuning parameters in the adiabatic model are the adiabatic difference ΔT_e and ΔT_c , which adjust the temperature level in the expansion and compression spaces (in accordance with the principles of workflow organization, the temperature of the heat supply and removal processes), and thus affect the efficiency of the cycle.

When calculating the temperature in the working spaces in the adiabatic method, not

only heat transfer is neglected, but also, the phenomenon of mixing the working fluid with portions cyclically coming from adjacent heat exchangers. These corrections did not have a significant negative impact on the temperature in the working spaces; the differences between the adiabatic and reference methods were no more than 10 K. (see Fig. 2).

The accuracy of the determination of the volumes of the expansion and compression spaces had a significant impact on the accuracy of calculation of pressure and cyclic workdone. A simplified description of volumes using a one-term harmonic formula for a rhombic mechanism gives a cycle error of more than 15%.

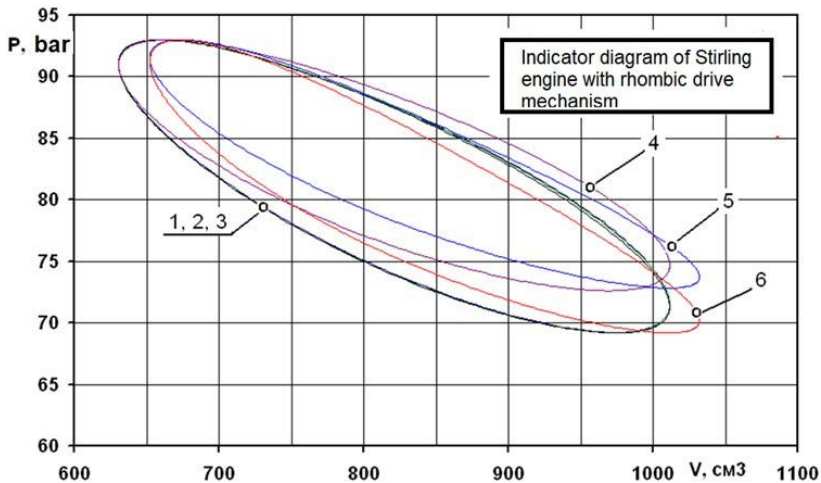


Figure 3. Indicator diagram
 1– developed adiabatic method, 2– adiabatic method with correction of the temperature in the working spaces, 3– modelling using the BS-Stirling 4.2 program; 4 – isothermal method; 5 – isothermal method, working volumes - 1st order harmonics; 6 – isothermal method, working volumes - 1st order harmonics, adjustment according to cycle parameters.

Comparing the results of calculations using various methods, it should be noted that the cycle has a large workdone when calculating using adiabatic methods. This is a consequence of the increased pressure amplitude in the internal circuit, which in processes of cyclic adiabatic compression and expansion is greater than for isothermal compression.

Area of Expedient Application of the Developed Method

The area of expedient application of the developed method is limited to the minimum number of initial and determined parameters.

The method does not consider processes in heat exchangers, does not take into account hydraulic resistance in the elements of the internal circuit, regeneration efficiency, inertial effects, non-stationary and uneven distribution of temperature fields and heat flows and other phenomena that affect the effective performance of the SE.

The main parameter determined in the method is the pressure value. As a correction means, correction of the temperature in the working spaces was introduced. This made it possible to obtain a reliable view of the indicator diagram and determine the cyclic power.

The developed algorithm is intended to create an engineering method for calculating the thermodynamic cycle of a SE. which will ensure the further development of a set of engineering methods for various stages of SE design. In particular, directly on the basis of the calculation of the thermodynamic cycle, methods can be created for calculating the forces acting in the SE mechanism, for the hydraulic calculation of the internal circuit, for calculating heat transfer in the heater, regenerator and cooler.

Conclusion

This article presents mathematical relationships for calculating the parameters of the thermodynamic cycle of an external combustion engine operating under the Stirling cycle with the assumption that heat transfer in the working cylinders can be neglected and the processes in the working spaces are close to adiabatic. The developed method makes it possible to calculate the pressure in the cycle with an accuracy sufficient for engineering calculations: the deviation of the pressure from the reference calculation was 0.19% of the average pressure of the cycle, the error in determining the cycle power was 0.6%. The developed method is intended for use in mechanical engineering, in particular for calculating the thermodynamic Stirling cycle and developing on its basis other engineering methods aimed at supporting the design process of Stirling engines.

References

- [1] Finkelstein T., Organ A.J. Air Engines. The History, Science and Reality of the Perfect Engine. – New York: ASME Press, (2001).

- [2] Martini W.R. Stirling Engine Design Manual. – Cleveland, Ohio: NASA Lewis Research Center, (1978).
- [3] Walker G. Stirling engines. – M.: Mechanical Engineering, (1985). (in Russian)
- [4] Finkelstein T. Thermodynamic analysis of Stirling machines. //Stirling engines. Collection of articles. Edited by V.M. Brodyansky. – M.: Mir, pp. 205-223. (1975). (in Russian)
- [5] Reader G., Hooper Ch. Stirling engines. – M.: Mir, (1986). (in Russian)
- [6] Schock A. Stirling Engine Nodal Analysis Program// J. Energy, Vol. 2, No. 6. – p. 354-362, (1978).
- [7] Berchowicz D.M., Urieli I., Rallis C.J. A Numerical Model for Stirling Cycle Machines. //Trans. ASME Journal of Engineering Power, Vol. 102, No. 4. - p. 756-761, (1980).
- [8] Belozertsev V.N. Calculation methods and experimental studies of Stirling thermal machines: textbook. Handbook / V.N. Belozertsev, A.A. Gorshkalev, S.O. Nekrasova, A.A. Shimanov. – Samara: Publishing House of SSAU, (2015). (in Russian)
- [9] Martini W.R. Validation of Published Stirling Engine Design Methods Using Engine Characteristics from the Literature// Proc. 15th IECEC, pp. 2245-2250, (1980).
- [10] Urieli I., Kushnir M. The Ideal Adiabatic Cycle – A Rational Basis for Stirling Engine Analysis// Proc. 17th IECEC, Vol. 4, pp. 1662-1668, (1982).
- [11] Stolyarov S.P., Stolyarov A.S., Experience in performing computational and experimental studies of Stirling machines using the BS-STIRLING software package. //Actual problems of marine energy: Materials of the fourth All-Russian interdisciplinary Scientific and Technical Conference (February 12-13, 2015). – St. Petersburg: Publishing House of St. Petersburg State Marine Technical University. pp. 40-43, (2015). (in Russian)

Performance of β -type Stirling Engine Under Various Kinematic-drive Mechanisms

A. Abuelyamen*, R. Ben-Mansour

Mechanical Engineering Department, King Fahd University of Petroleum & Minerals, Dhahran 31261, Saudi Arabia

*Corresponding author: ahmedsalih45@yahoo.com

Keywords: Stirling Engine, CFD, Kinematic, Rhombic, Crank, Scotch, Lever-controller

Abstract

In this work, a performance comparison of β -Stirling engine govern by different kinematic-drive mechanisms (rhombic, crank, scotch, and lever-controller) is conducted numerically. The Stirling engine is set to work between temperature limits of 300 K and 800 K. The air is adopted as a working fluid. The radiation heat transfer is included to formulate an accurate CFD model. Furthermore, the thermal properties of the air are taken to be depending on the gas temperature. The model is validated against experimental data from the literature, where the CFD estimation of the power output shows a good estimate with a difference of 8.1% in comparison to experiment results. The results reveal that the kinematic-drive mechanisms have a high impact on the Stirling engine performance because it arranges the location of the gas during compression and expansion processes. Among these mechanisms, rhombic mechanism recorded the highest power output and thermal efficiency. The maximum performance of rhombic mechanism is then followed by scotch, crank, and lever-controller mechanisms, respectively.

Introduction

Nowadays, Stirling engine starts to attract researchers in both academic and industrial fields. It is classified as an external heat engine; therefore, various heat sources can be utilized to run the Stirling engine including combustion of biogas, geothermal, or solar energy. The ideal thermal efficiency of Stirling cycle is high as Carnot cycle. However, the experimental results of Stirling engine are much lower than the ideal performance.

Recently, a tremendous effort has been made by researchers trying to improve the actual performance of the Stirling engine. One of the methods that is used to enhance the performance of Stirling engine is by applying different kinematic-drive mechanisms. The crank mechanism is the most used mechanism with Stirling engine [1]–[3]. It can be applied to the three types of Stirling engine (α , β , and γ). Also, there is the rhombic mechanism which is functional with β -type Stirling engine [4], [5]. The other mechanisms

that can be applied to Stirling engine are ross-yoke mechanism [6], [7], lever-controller mechanism [8], [9] and the free piston motion [10], [11]. The kinematic mechanism of the piston plays a significant role in the heat transfer inside Stirling engine since it controls the movement of the gas inside Stirling chambers. It controls how fast the gas moves from the hot chamber to the cold chamber in order to be compressed or expanded. The importance of the piston motion mechanism becomes clear during the compression and expansion process. For instance, in the compression process, it is preferred to have all of the working fluid in the cold zone, so the energy required to compress the gas would be small. Nevertheless, it is difficult to achieve that because there is always an amount of gas in the other zone (hot zone). As a result, some of the gas would expand during the compression process which increases the required compression power.

The ideal Stirling cycle consists of two isothermal processes, in which the heat is added to the engine at a heat source temperature of T_H and rejected to a heat sink at a temperature of T_C . In addition to the isothermal processes, there are two constant-volume regeneration processes. In fact, to achieve the isothermal process, it requires to provide an infinite large surface area for heat transfer or allowing infinite long time for the process, which neither is practical. Furthermore, the regenerator produces a lot of pressure drop and its effectiveness would not reach 100 percent. Moreover, the regeneration process in a real Stirling engine does not occur at constant-volume as labeled in the ideal Stirling cycle. For instance, in the crank mechanism, the piston motion is controlled by a sinusoidal profile. Thus, the regeneration process takes place at variable engine volume. Due to all these limitations, the actual performance of the Stirling engine is lower than the ideal cycle. Nevertheless, Stirling engine has the potential for high efficiency.

Few of studies were conducted to investigate and compare the performance of Stirling engine with different driving mechanisms [12], [13]. However, these studies were conducted using analytical methods with assumptions of uniform pressure and temperature across the engine. Salazar and Chen [14] stresses the poor assumption of constant heat transfer coefficient in such analysis due to non-uniform temperature distribution. Abuelyamen et al. [4] clarified that not only the gas temperature distribution is non-uniform inside Stirling engine domain, the pressure also varied slightly across the engine domain. Consequently, the power output obtained from the PV-diagram by

taking the average pressure across the engine domain mismatches the power obtained from the net heat transfer through the surface boundaries. Accordingly, the purpose of this study is to compare the performance of β -type Stirling engine with four kinematic-driving mechanisms by using CFD method. This study helps in the understanding of the complex phenomena of heat transfer and fluid flow inside Stirling engines.

Problem formulation

Geometry description

In order to evaluate the influence of the kinematic-drive mechanism, a β -type Stirling engine is tested with four mechanisms of kinematic-driving (rhombic, crank, lever-controller and scotch mechanism). The β -type Stirling engine consists of three zones: compression zone, expansion zone and a narrow channel that connects the expansion and compression zones.

Figure 1 shows the four mechanisms under study, where the movement of the displacer and the piston are governed by these mechanisms. The computational domain includes the compression zone, the expansion zone and the narrow channel as showing in Figure 2. The connecting links (such as the crank and the connecting rod in the crank mechanism) were not included in the computational domain. However, the movement of the displacer and the piston are managed through a user-defined-function (UDF) implemented to the software. Additionally, due to the cylindrical shape of the engine, the computational domain is considered as an axisymmetric domain. The geometrical dimensions of the β -type Stirling engine driven by a rhombic mechanism (Figure 1.a) are represented in Table 1. The dimensions of the connecting links for the other mechanisms (Figure 1.b-d) are summarized in Table 2.

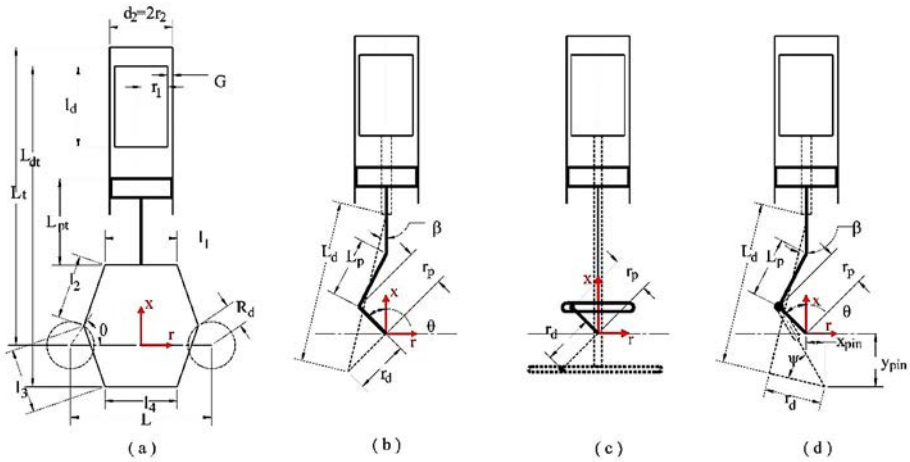


Figure 1. β -type Stirling engine with different piston motion mechanisms: (a) Rhombic, (b) Crank, (c) Scotch, and (d) Lever-controller.

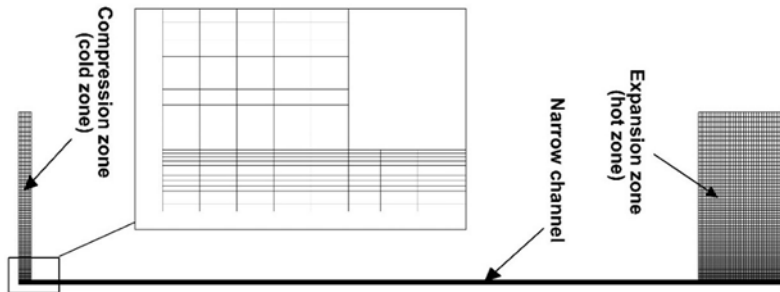


Figure 2. The computational domain of β -type Stirling engine.

Table 1. Dimensions of β -type Stirling engine govern by the rhombic mechanism (mm).

r_1	20	L	42
r_2	20.5	L_{pt}	50.93
G	0.5	L_{dt}	163.74
$l_1 = l_2 = l_3 = l_4$	18	l_d	79.46
L_t	158	R_d	3.5

Table 2. Dimensions summary for the crank, scotch, and lever-controller mechanisms (mm).

	Crank	Scotch	Lever-controller
r_p	5.05	5.05	5.05
r_d	4.975	4.975	18
L_p	14.033	-	14.033
L_d	5.127	-	60
ψ	-	-	70°
x_{pin}	-	-	$r_p/\sqrt{2}$
y_{pin}	-	-	$2.5r_p$

Governing equations

The transport equations describing the flow fields and heat transfer phenomena inside Stirling engine are embodied mathematically by transient axisymmetric compressible Navier-Stokes equations, conservation of energy equation, conservation of mass and the ideal gas equations. Those equations can be written in cylindrical coordinates as:

The continuity:

$$\frac{\partial \rho_f}{\partial t} + \frac{\partial}{\partial x}(\rho_f \tilde{u}) + \frac{1}{r} \frac{\partial}{\partial r}(\rho_f r \tilde{v}) = 0 \quad (1)$$

The momentum:

$$\begin{aligned} \frac{\partial}{\partial t}(\rho_f u) + \frac{\partial}{\partial x}(\rho_f \tilde{u}u) + \frac{1}{r} \frac{\partial}{\partial r}(\rho_f r \tilde{v}u) &= \rho_f g - \frac{\partial p}{\partial x} + \mu \frac{\partial}{\partial x} \left(\frac{\partial u}{\partial x} \right) + \frac{u}{r} \frac{\partial}{\partial r} \left(r \frac{\partial u}{\partial r} \right) + \frac{\mu}{3} \frac{\partial}{\partial x} (\nabla \cdot V) \\ \frac{\partial}{\partial t}(\rho_f v) + \frac{\partial}{\partial x}(\rho_f \tilde{u}v) + \frac{1}{r} \frac{\partial}{\partial r}(\rho_f r \tilde{v}v) &= -\frac{\partial p}{\partial r} + \mu \frac{\partial}{\partial x} \left(\frac{\partial v}{\partial x} \right) + \frac{u}{r} \frac{\partial}{\partial r} \left(r \frac{\partial v}{\partial r} \right) + \frac{\mu}{3} \frac{\partial}{\partial r} (\nabla \cdot V) - \frac{\mu v}{r^2} \end{aligned} \quad (2)$$

The energy:

$$\begin{aligned} \frac{\partial}{\partial t}(\rho_f T_f) + \frac{\partial}{\partial x}(\rho_f \tilde{u}T_f) + \frac{1}{r} \frac{\partial}{\partial r}(\rho_f r \tilde{v}T_f) &= -\frac{1}{c_{pf}} \left[\frac{\partial p}{\partial t} + \nabla \cdot (pV) - p(\nabla \cdot V) \right] + \frac{k_f}{c_{pf}} \left[\frac{\partial}{\partial x} \left(\frac{\partial T_f}{\partial x} \right) + \frac{1}{r} \frac{\partial}{\partial r} \left(r \frac{\partial T_f}{\partial r} \right) \right] \\ &+ \frac{\mu}{c_{pf}} \left\{ 2 \left[\left(\frac{\partial u}{\partial x} \right)^2 + \left(\frac{\partial v}{\partial r} \right)^2 + \left(\frac{v}{r} \right)^2 \right] + \left(\frac{\partial v}{\partial x} + \frac{\partial u}{\partial r} \right)^2 - \frac{2}{3} (\nabla \cdot V)^2 \right\} \end{aligned} \quad (3)$$

Ideal gas equation:

$$pV = \rho_f RT_f \quad (4)$$

Where $\vec{u} = u - u_c$, $\vec{v} = v - v_c$ are the relative velocity components of the fluid and moving frames with velocities of u_c and v_c in the axial direction (x) and the radial direction (r), respectively.

Furthermore, in order to include the internal radiative heat transfer inside Stirling engine, the discrete ordinates (DO) radiation model is adopted. The DO model solves the radiative heat transfer equation (RTE) by taking into account the radiation energy between the wall surfaces as well as the effect of absorption, emission, and scattering of the radiation energy through the gas medium (Air). However, in the present work, the coefficients of absorption, emission, and scattering are set to be zero because the working fluid (air) is not a radiative participating medium (i.e. it does not participate in absorption, emission, and scattering of the radiation energy). Therefore, the radiation heat transfer occurs only between the surfaces, then, it transfers to the air through the convection mode. Setting these coefficients to zero will reduce the computational expense and will not affect the accuracy of the results because the air is not considered as participating medium.

The general form of RTE for an absorbing, emitting, and scattering medium is:

$$\frac{dI(\vec{r}, \vec{s})}{ds} + (a + \sigma_s)I(\vec{r}, \vec{s}) = an^2 \frac{\sigma T^4}{\pi} + \frac{\sigma_s}{4\pi} \int_0^{4\pi} I(\vec{r}, \vec{s}') \Phi(\vec{s} \cdot \vec{s}') d\Omega' \quad (5)$$

For the gray diffuse radiation, the net radiative heat flux leaving the surface is given by:

$$q_{out,rad} = (1 - \epsilon_w)q_{in,rad} + n^2 \epsilon_w \sigma T_w^4 \quad (6)$$

Where q_{in} is the incident radiative heat flux:

$$q_{in} = \int_{\vec{s} \cdot \vec{n} > 0} I_{in} \vec{s} \cdot \vec{n} d\Omega \quad (7)$$

The total supplied and rejected heat transfer were calculated as follows:

$$\begin{aligned} Q_{in} &= \frac{\omega}{2\pi} \sum_{i=1}^N Q_i \Delta t \quad \text{if } q > 0 \\ Q_{out} &= \frac{\omega}{2\pi} \sum_{i=1}^N Q_i \Delta t \quad \text{if } q < 0 \end{aligned} \quad (8)$$

Where Δt is time step. Q_{in} , Q_{out} , and Q_i are the total heat added, total heat rejected and total heat transfer, respectively, during the step (i). Q_i is calculated across the outer surface of the domain. The software gives the value of Q_i in terms of (W) or (J/s). It is multiplied by Δt to obtain the amount of energy transferred during the step (i). Therefore, the summation value for all number of steps (N) of one cycle gives the total energy produced during that cycle in a unit of (J/cycle). Accordingly, it multiplies by $(\omega/2\pi)$, which represents the number of revolutions in each one second. The power output is gotten from equation 9, where the term in the summation represents the average area under the P-V diagram (J/cycle).

$$W_{out} = \frac{\omega}{2\pi} \sum_{i=1}^N 0.5(p_{i-1} + p_i) \cdot (V_i - V_{i-1}) \quad (9)$$

Governing equations

The working fluid of the present work is considered to be air with atmospheric pressure, and it is treated as an ideal gas. In addition, the thermal properties of the air are taken to be depending on the gas temperature. Furthermore, the engine is assumed to be running at a rotational speed of 1800 rpm. The heating and cooling temperatures are set between ($T_H = 800$ K) and ($T_C = 300$ K). Accordingly, the external cylinder of the engine exposes to temperature limits between T_H and T_C , which is a function of axial coordinate (x):

$$T(x) = \begin{cases} T_C \text{ (K)}, & \text{if } x \leq 0.08 \text{ m} \\ T_C + \frac{x-0.08}{0.158-0.08} (T_H - T_C) \text{ (K)}, & \text{if } x > 0.08 \text{ m} \end{cases} \quad (10)$$

Moreover, the movement of the displacer and the piston are governed according to the applied kinematic mechanism. Where their velocities are described as below:

Rhombic mechanism:

$$\begin{aligned} u_p(t) &= R_d \omega \left\{ \cos \theta - \sin \theta \left[l_2^2 - \left(\frac{L}{2} - \frac{l_1}{2} - R_d \cos \theta \right)^2 \right]^{-0.5} \left[\frac{L}{2} - \frac{l_1}{2} - R_d \cos \theta \right] \right\} \\ u_d(t) &= R_d \omega \left\{ \cos \theta + \sin \theta \left[l_3^2 - \left(\frac{L}{2} - \frac{l_4}{2} - R_d \cos \theta \right)^2 \right]^{-0.5} \left[\frac{L}{2} - \frac{l_4}{2} - R_d \cos \theta \right] \right\} \end{aligned} \quad (11)$$

where;

$$\theta = \omega t \quad (12)$$

Crank mechanism:

$$\begin{aligned} u_p(t) &= r_p \omega \cos \theta - \frac{r_p^2 \omega \cos \theta \sin \theta}{\sqrt{L_p^2 - r_p^2 \cos^2 \theta}} \\ u_d(t) &= r_d \omega \cos \beta - \frac{r_d^2 \omega \cos \beta \sin \beta}{\sqrt{L_d^2 - r_d^2 \cos^2 \beta}} \end{aligned} \quad (13)$$

Where;

$$\beta = \theta + \pi/2 \quad (14)$$

Scotch mechanism:

$$\begin{aligned} u_p(t) &= -r_p \omega \sin \theta \\ u_d(t) &= -r_d \omega \sin \beta \end{aligned} \quad (15)$$

Lever-controller:

$$\begin{aligned} u_p(t) &= -r_p \omega \sin \theta - \frac{r_p^2 \omega \sin \theta \cos \theta}{\sqrt{L_p^2 - r_p^2 \sin^2 \theta}} \\ u_d(t) &= \frac{-r_d \cos \xi \cdot \left(\frac{r_p \omega \cos \theta}{\kappa_2} + \frac{r_p \omega \kappa_1 \sin \theta}{\kappa_2^2} \right)}{\left(\frac{\kappa_1}{\kappa_2} \right)^2 + 1} \\ &\quad - \frac{\frac{r_d \sin \xi}{L_d} \cdot \left(x_{\text{pin}} - r_d \cos \xi \right) \cdot \left(\frac{r_p \omega \cos \theta}{y_{\text{pin}} + r_p \omega \cos \theta} + \frac{r_p \omega \kappa_1 \sin \theta}{\kappa_2^2} \right)}{\left[\left(\frac{\kappa_1}{\kappa_2} \right)^2 + 1 \right] \cdot \sqrt{1 - \left(\frac{x_{\text{pin}}}{L_d} - \frac{r_d \cos \xi}{L_d} \right)^2}} \end{aligned} \quad (16)$$

Where:

$$\xi = (\psi - \pi / 2) + \text{atan} \left(\frac{\kappa_1}{\kappa_2} \right) \quad (17)$$

$$\kappa_1 = x_{\text{pin}} + r_p \sin \theta \quad (18)$$

$$\kappa_2 = y_{\text{pin}} + r_p \cos \theta \quad (19)$$

Furthermore, all cases are set to start from the same initial volume, so they will have the same amount of air mass inside Stirling engine. This initial volume is corresponding to the volume in the geometry of Figure 1.a with ($\theta=0^\circ$). Furthermore, they are set to have an approximately similar value of the maximum and minimum total volume. Therefore, the links dimensions in the crank, scotch and lever-controller mechanisms are managed to produce similar values of minimum and maximum volume as indicated in Table 2. Also, the angle θ is shifted by 0.81623487, 0.94252011, and 0.81623487 radians for the crank, scotch and lever-controller mechanism, respectively, in order to achieve a similar value of minimum and maximum volumes for all mechanisms under study. The engine volume is changed only with the movement of the piston. Thus, the displacement of the piston for all mechanism has the same limits (See Figure 3.a). However, the displacer movement is not restricted to having equal displacement in order to avoid interference between the piston and the displacer or between the displacer and the cylinder top.

Solution methodology

In order to solve the continuity, energy and momentum equations (1-3) in addition to radiative heat transfer Equation 5, a general-purpose code of ANSYS fluent was used. The program uses the finite volume method to discretize governing differential equations (1, 2, 3 and 5). The second order upwind finite difference scheme was adopted for continuity, momentum and energy equations. To couple the pressure and velocity, a coupled scheme was utilized because it shows a relatively fast convergence compared with a SIMPLE scheme. The SIMPLE scheme uses a pressure-based segregated algorithm in which the momentum equation and the pressure correction equation are solved separately. This semi-implicit solution method results in slow convergence [15].

Furthermore, variable thermal properties were implemented in the software. An ideal

gas which is represented by equation 4 was used to calculate the density while the kinetic theory was used to identify the heat capacity and the viscosity. In addition, laminar flow is assumed because the maximum Re based on the hydraulic diameter of the narrow channel does not exceed the laminar range for all cases under study. However, in some cases, it becomes in the transitional range (2,000 – 4,000) in part of the cycle, but it does not convert to fully turbulent conditions. The temperature profile (described by equations 10) and movement of the piston and the displacer (equations 11 and 19) are implemented in the software through a user-defined function (UDF).

Independence studies and validation

Mesh and time step

Before starting the simulation of Stirling engine, mesh and time dependence study were carried out. Four different mesh sizes were examined and summarized in Table 3. The aspect ratio for all meshes under study was kept under 11.8. It was found that the mesh size of 6869 cells with 480 step/cycle (which is corresponding to a time step of 6.94444×10^{-05} s) achieves the mesh and time step independent solution with a deviation of 0.6% in generated power compared with the finest mesh size with the smallest time step.

Table 3. Summary values of the mesh and time dependent study.

	No. of cells	No. of interval in the narrow channel	No. of steps per cycle		
Case 1	2,740	10	360	480	720
Case 2	6,869	14			
Case 3	9,600	16			
Case 4	15,020	20			

Then, a sensitivity analysis was conducted for the parameters that affect the solution of discretized RTE of the DO radiation model. These parameters called angular discretization parameters (number of divisions and pixels). Table 4 summarizes the values of the radiation parameters independent study. Judging from the net heat transfer profile, it turns out that the angular discretization values for DO model become independent of

divisions and pixel numbers by values of 4 and 2, respectively. The maximum error in the net heat transfer profile is 0.24%. The error here is calculated under the assumption that the right solution is the solution which has the highest number of divisions and pixel values (case of 8 division and 4 pixels).

Table 4. Summary values of the radiation parameters independent study.

	Divisions number	Pixel number
Case 1	2	1
case 2	4	2
case 3	8	4

Model validation

The accuracy of the CFD results depends highly on the precise description of the thermal boundary conditions along with the full description of the geometrical domain. Because this information is required as inputs for the CFD simulation and any deficiency information means less accuracy of CFD results. The work of Aksoy and Cinar [16] was chosen to validate current work as it gives more details information that are needed for CFD simulation. Comparing with the experimental data in [16], the present numerical model shows an error of 8.1% in the power output. Additionally, the model is also validated against a numerical model of Salazar and Chen [14] and it showed a good matching in the p-V diagrams. More detail about the numerical and experimental validation are available in the authors' previous work [4].

Results and discussion

In this work, the performance of β -type Stirling engine was examined with four kinematic-drive mechanisms (rhombic, crank, scotch, and lever-controller). Table 5 summarizes the performance of these mechanisms. In general, the power output of the four mechanisms is very small. The reason is related to the small geometry size, and also, due to the absence of the regenerator. More importantly, the engine is taken to be run at atmospheric charge pressure of air which has low thermal conductivity. Higher power output can be obtained by increasing the charge pressure or utilizing a gas with high thermal conductivities value [4]. In spite of the low performance, applying different

kinematic mechanisms to control the movement of the piston and the displacer result in different power output and thermal efficiency values as shown in Table 5. It can be noticed from the table that the rhombic mechanism registers the best performance with a power output of 9.9 W and thermal efficiency of 8.5%. Then it followed by scotch mechanism and crank mechanism. While the lever-controller mechanism recorded the lowest power output (8.33 W) and the lowest thermal efficiency (6.8%). It is clear that the type of motion mechanism plays a substantial role in the performance of Stirling engine. It arranges the location of the gas; thus, it would be in the appropriate zone during the compression and expansion processes through the movement of the displacer. Accordingly, in order to understand the influences of the motion mechanism on the Stirling engine performance, the movement of the displacer and the piston are monitored during one complete cycle.

Table 5. The performance of β -type Stirling engine under different piston motion mechanisms.

	Q_{in}	Q_{out}	Q_{net}	Efficiency
Rhombic	116.0	-106.4	9.90	8.5%
Crank	117.0	-108.0	9.31	8.0%
Scotch	118.3	-108.9	9.69	8.2%
Lever-controller	122.1	-114.2	8.33	6.8%

Figure 3.a represents the x-coordinates of the piston and the displacer-bottom surfaces of rhombic and lever-controller mechanisms. The displacement profiles of the piston surface in the two mechanisms (rhombic and lever-controller) are close to each other. Nevertheless, the displacer profile varies widely between the two mechanisms resulting in different power output value. The engine volume changes according to the displacement of the piston surface only, since there is a gap distance between the displacer and the cylinder wall. In Figure 3.a, the highest x-coordinate represents the smallest engine volume where the engine volume is fully compressed and vice versa for fully expansion volume. As represented in Figure 3.a, the expansion process starts from step 420, and it continues until step 180 passing through step 0 (or step 480). At the beginning of the expansion process (step 420 at Figure 3.a), the displacer is positioned much closer to the piston in the case of rhombic mechanism than in the case of the lever-

controller mechanism. Therefore, a small amount of the gas is located in the cold zone in the case of rhombic mechanism than in the case of the lever-controller mechanism. Bearing in mind the fact that if a gas is cooled down during an expansion process its pressure will drop down, and hence, the extracted power would be small. Therefore, it is preferable to have a small amount of gas in the cooling zone during the expansion process. In view of that, the expansion process of rhombic mechanism generates more work than the work produced by the lever-controller mechanism as pointed out by the p-V diagram in Figure 3.b. The rhombic mechanism keeps producing higher work than the work produced by lever-controller mechanism until the displacer reverse its motion direction earlier in the rhombic mechanism (step 75 at Figure 3.a), where the cold zone starts to become larger in the rhombic mechanism. Consequently, the generated power from the rhombic mechanism degraded gradually until it becomes smaller than the value in the lever-controller mechanism (Figure 3.b). Because the gas starts to be cold down as the cold zone is getting enlarge which is not desirable during the expansion process.

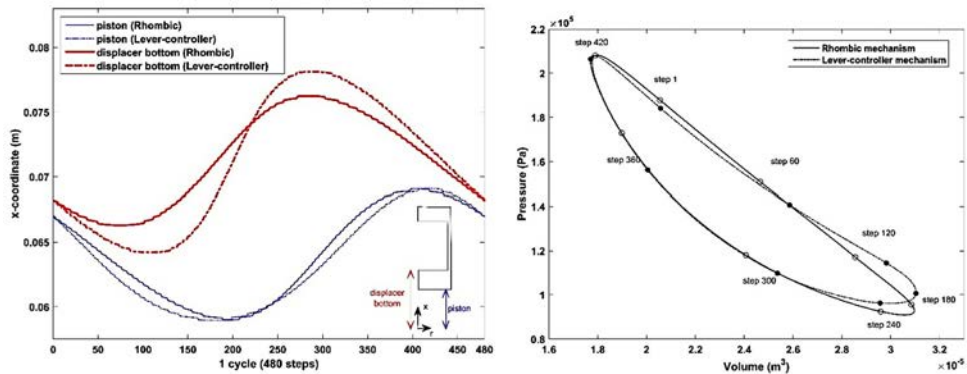


Figure 3. Comparison between rhombic and lever-controller mechanisms a) x-coordinates of the piston and displacer-bottom b) p-V diagrams.

On the other hand, the compression process starts by the end of the expansion process when the piston reaches the bottom dead center “BDC”. It is the point where the engine has the maximum volume. The compression process takes place approximately between the steps of 180 and 420. By referring to Figure 3.b, it easily to note that the lever-controller mechanism consumes higher work at the beginning of the compression

process (step 180) than the consuming work in the case of the rhombic mechanism. The reasons for that might be rationalized to many factors. Firstly, the expansion process of the lever-controller mechanism ends up with a relatively higher-pressure level than the corresponding pressure level in the rhombic mechanism (step 180 in Figure 3.b). Secondly, at the beginning of the compression process, the displacer is much closer to the piston in the lever-controller mechanism which means that the hot zone contains a lot of gas. The existence of the gas in the hot zone during the compression process increases the required power for the compression process because the gas absorbs additional heat, hence, it expands and resists the compression process. Moreover, due to the kinematic of lever-controller mechanism, the displacer accelerates faster in the first half of the compression process in the lever-controller mechanism than in the rhombic mechanism. Thus, the lever-controller mechanism forces the hot gas to move through the narrow channel with very high velocity. Accordingly, the hot gas did not find enough time to cool down as it passes through the narrow channel like what is happening in the rhombic mechanism. Therefore, the gas enters the cold zone at higher temperature level in the case of lever-controller mechanism than in the case of rhombic mechanism as shown in Figure 4. Consequently, the lever-controller mechanism consumes more power than rhombic mechanism during the beginning of the compression process. However, during the second half of the compression process, both mechanisms (rhombic and lever-controller) consume almost the same amount of power to compress the gas. Because in this period of the process the displacer reaches near to its top-dead-center “TDC” where its velocity is very small, hence, no more hot gas is pushed toward the cold zone.

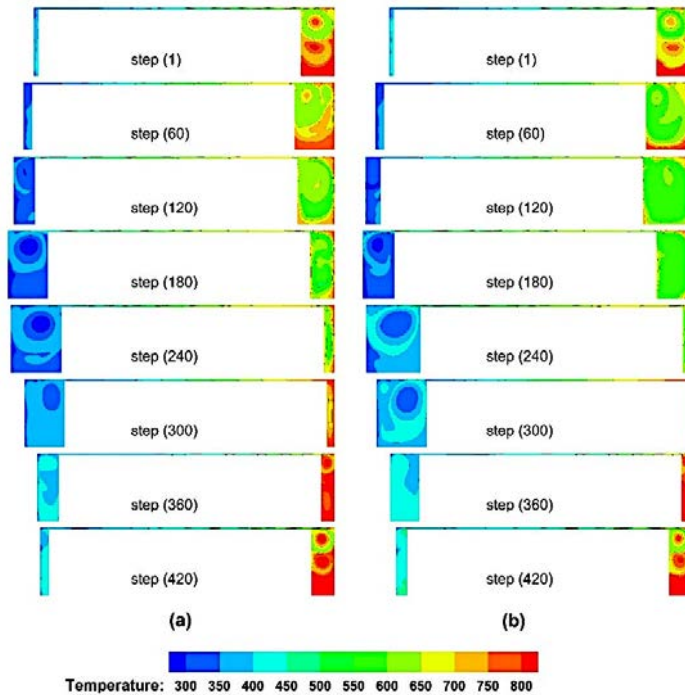


Figure 4. Temperature contours (K) of (a) rhombic and (b) lever-controller.

The scotch mechanism also shows a good performance; however, its performance is lower than the performance of the rhombic mechanism. Figure 5.a compares the p-v diagrams of the scotch and rhombic mechanisms. The scotch mechanism produces less work during the expansion process compared to the work produced by the rhombic mechanism. Nonetheless, the compression process of the scotch mechanism consumes less work than rhombic mechanism, therefore, the overall power output of scotch mechanism is not far off from the power output generated by using rhombic mechanism. Figure 5.b shows the x-coordinates of the piston and displacer-bottom for the scotch and rhombic mechanisms. During the compression process (step 180-420), the distance between the piston and the displacer is larger in the scotch mechanism than in the case of the rhombic mechanism. Hence, the cold zone of scotch mechanism has larger volume than the corresponding volume in rhombic mechanism and vice versa for the hot zone. This situation is desirable for the compression process. Because, as the

hot zone becomes smaller the gas absorbs a small amount of heat, and thus, it would not expand. As a result, the compression resistance becomes lighter. The hot zone volume in scotch mechanism remains smaller than the corresponding volume in rhombic mechanism during the whole compression process, which explains the lower consuming work of scotch mechanism during the complete compression process compared to the consuming work of rhombic mechanism. On the other hand, during the expansion process, the displacer of scotch mechanism reverses its motion direction earlier (at step 47) than in the case of the rhombic mechanism (at step 75). Thus, the cold zone volume starts to grow up earlier in scotch mechanism resulting in a small power output than the extracted power through the rhombic mechanism.

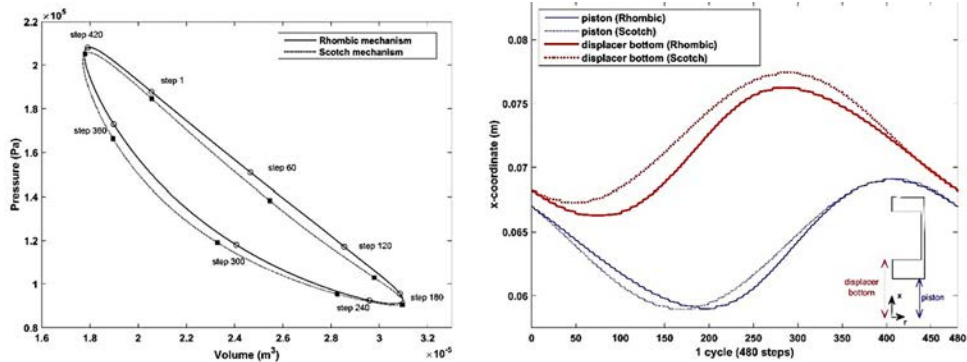


Figure 5. Comparison of rhombic and scotch mechanisms, a) the p-V diagrams b) x-coordinates of the piston and displacer-bottom.

On another hand, the crank mechanism reflects a lower performance than rhombic and scotch mechanisms. However, its p-V diagram is very close to the p-V diagram of scotch mechanism as shown in Figure 6. The crank mechanism shows a lower value of expansion work compared to the scotch mechanism. In addition, it consumes extra work than scotch mechanism at the beginning of the compression process. Nevertheless, it compensates for this extra work in the second half of the compression process. At the beginning of the compression process, the piston of the crank mechanism accelerates faster than the piston of the scotch mechanism, thus, it consumes more power during the first half of the compression process. Then, the piston in the crank mechanism decelerates slower than the piston of the scotch mechanism in the second half of the compression process

which makes the required power to compress the gas to be smaller in crank mechanism than in the scotch mechanism. Regarding the expansion process, the displacer reverses its motion direction earlier in the crank mechanism. Thus, the cold zone of the crank mechanism is getting larger during the expansion process, which is not desirable as explained previously. Hence, the extracted power from the crank mechanism is lower than corresponding power output from the scotch mechanism.

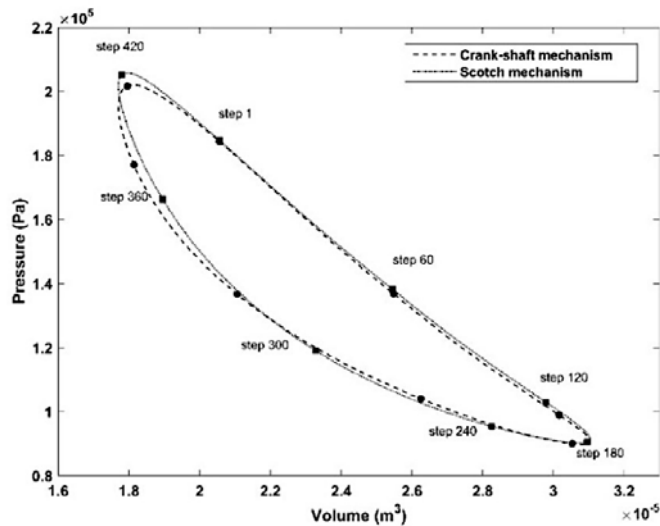


Figure 6. Comparison of PV-diagrams of crank and scotch mechanisms.

Conclusions

In present work, a CFD simulations of four kinematic-drive mechanisms (rhombic, crank, scotch, and lever-controller) were performed for a β -type Stirling engine. The performance of each mechanism is estimated and compared against each other. The four cases are set to work with the same temperature limits, charge pressure, and the same working fluid, as well as, they have equal engine size. Since the air temperature fluctuating between a wide range of temperature level (300 -800 K), thermal properties of air are taken to be depending on the gas temperature which is more realistic than using thermal properties at average temperature. The internal radiation heat transfer inside Stirling engine is considered as well. The results show that the kinematic mechanism of the displacer plays a significant role in maximizing the power output during the expansion process

and minimizing the consuming power during the compression process. Consequently, it affects the power output and the thermal efficiency. The rhombic mechanism recorded the highest power output and thermal efficiency (9.9 W and 8.5%). Then it followed by scotch (9.69 W and 8.2%), crank (9.31 W and 8.0%), and lever-controller (8.33 W and 6.8%) mechanisms.

References

- [1] J. A. Auñón, J. M. Pérez, M. J. Martín, F. Auñón, and D. Nuñez, “Development and validation of a software application to analyze thermal and kinematic multimodels of Stirling engines,” *Heliyon*, vol. 9, no. 9, 2023, <http://doi.org/10.1016/j.heliyon.2023.e18487>.
- [2] E. Öztürk, “Optimization of a novel drive mechanism approaching the ideal cycle for beta type Stirling engines,” *Eng. Sci. Technol. an Int. J.*, vol. 47, no. September, pp. 0–2, 2023, <https://doi.org/10.1016/j.jestch.2023.101555>.
- [3] A. Abuelyamen and R. Ben-mansour, “Energy efficiency comparison of Stirling engine types (α , β , and γ) using detailed CFD modeling,” *Int. J. Therm. Sci.*, vol. 132, no. August 2017, pp. 411–423, 2018, <https://doi.org/10.1016/j.ijthermalsci.2018.06.026>
- [4] A. Abuelyamen, R. Ben-Mansour, H. Abualhamayel, and E. M. A. Mokheimer, “Parametric study on beta-type Stirling engine,” *Energy Convers. Manag.*, vol. 145, pp. 53–63, 2017, <https://doi.org/10.1016/j.enconman.2017.04.098>
- [5] R. Ben-Mansour, A. Abuelyamen, and E. M. A. Mokheimer, “CFD analysis of radiation impact on Stirling engine performance,” *Energy Convers. Manag.*, vol. 152, 2017, <https://doi.org/10.1016/j.enconman.2017.09.056>
- [6] K. Bataineh, “Mathematical formulation of alpha -type Stirling engine with Ross Yoke mechanism,” *Energy*, vol. 164, pp. 1178–1199, 2018, <https://doi.org/10.1016/j.energy.2018.08.134>
- [7] D. Smirnov et al., “Experimental study of a high-tolerance piston-cylinder pair in the alpha Ross-yoke Stirling refrigerator,” *Int. J. Refrig.*, vol. 100, pp. 235–245, 2019, <https://doi.org/10.1016/j.ijrefrig.2019.01.018>
- [8] H. Karabulut, C. Çınar, E. Ozturk, and H. S. Yucesu, “Torque and power characteristics of a helium charged Stirling engine with a lever controlled displacer driving mechanism,” *Renew. Energy*, vol. 35, pp. 138–143, 2010, <https://doi.org/10.1016/j.renene.2009.04.023>

- [9] H. Karabulut, M. Okur, S. Halis, and M. Altin, "Thermodynamic, dynamic and flow friction analysis of a Stirling engine with Scotch yoke piston driving mechanism," *Energy*, vol. 168, pp. 169–181, 2019, <https://doi.org/10.1016/j.energy.2018.11.078>
- [10] W. Ye, W. Wang, J. Zhu, and Y. Liu, "Optimizing design of a free piston Stirling engine using response surface methodology and grey relation analysis," *Case Stud. Therm. Eng.*, vol. 54, no. October 2023, p. 103981, 2024, <https://doi.org/10.1016/j.csite.2024.103981>
- [11] A. P. Masoumi, A. R. Tavakolpour-Saleh, and V. Bagherian, "Performance investigation of an active free-piston Stirling engine using artificial neural network and firefly optimization algorithm," *Heliyon*, vol. 10, no. 7, p. e28387, 2024, <https://doi.org/10.1016/j.heliyon.2024.e28387>
- [12] H. Karabulut and F. Aksoy, "Thermodynamic analysis of a b type Stirling engine with a displacer driving mechanism by means of a lever," *Renew. Energy*, vol. 34, pp. 202–208, 2009, <https://doi.org/10.1016/j.renene.2008.03.011>
- [13] H. Solmaz and H. Karabulut, "Performance comparison of a novel configuration of beta-type Stirling engines with rhombic drive engine," *Energy Convers. Manag.*, vol. 78, pp. 627–633, 2014, <https://doi.org/10.1016/j.enconman.2013.11.028>
- [14] J. L. Salazar and W. L. Chen, "A computational fluid dynamics study on the heat transfer characteristics of the working cycle of a β -type Stirling engine," *Energy Convers. Manag.*, vol. 88, pp. 177–188, 2014.
- [15] "ANSYS Fluent Theory Guide," Release 15.0, 2013.
- [16] F. Aksoy and C. Cinar, "Thermodynamic analysis of a beta-type Stirling engine with rhombic drive mechanism," *Energy Convers. Manag.*, vol. 75, pp. 319–324, 2013, <https://doi.org/10.1016/j.enconman.2013.06.043>

β Stirling-engine for Laboratory and Educational Applications in Heat Engine and Cooling Mode

Norbert Lømmen^{a,*}, Arne Høeg^b

a Department of Mechanical Engineering and Maritime Studies, Western Norway University of Applied Sciences, Inndalsveien 28, 5063 Bergen, Norway

b Enerin AS, Evja Vest, Florø, Norway

*Corresponding author: nlu@hvl.no

Keywords: Heat engine, Cooler, Tests, Modelling, Development

Abstract

A model of a β -Stirling-engine used for laboratory and educational applications has been developed in Sage of Athens. Its output has been compared to data from a series of tests in both heat engine and cooling mode. The main purpose of the model is to support and guide the further development of the engine towards a cryocooler for laboratory-scale liquefaction of technical gases like nitrogen, argon, and carbon dioxide as well as hydrogen. Using the Sage-model as a starting point for the further development of the current cooler design to a two-stage cryo-cooler is another aim of the current investigations.

In this work, the design of the engine is discussed, and the engine is compared to similar ones by means of dimensionless groups. This is followed by a description of the Sage-model, where different paths of energy losses are accounted for. The engine has been used in bachelor thesis projects at Western Norway University of Applied Sciences since 2011. Test data from running the motor in both heat engine and cooling mode with helium as working fluid are available. As the motor is currently converted to a cryocooler, the most recent data is available from test runs in cooling mode. Satisfactory agreement between the Sage-model and experimental data has been achieved.

The motor is usually run at pressures between 20-40 bar (gauge) and between 900-1500 rpm. In heat engine mode, heat is provided by a propane burner at ca. 750°C while cooling water at 10°C-12°C acts as heat sink. Up to 860 W output of electrical energy have been achieved. In cooling mode, temperatures down to -167°C have been achieved with the original heat exchanger as cold head at 1200-1400 rpm. At these conditions, the coefficient of performance and second-law efficiency are 0.0793-0.0767 and 13.6%-13.2%, respectively, according to the Sage-model.

Introduction

In 2010, Bergen University College, now Western Norway University of Applied Sciences (Høgskulen på Vestlandet, HVL), received a disassembled β -Stirling engine from the Norwegian company Sigma Elektroteknisk AS for use in education, research, and development. The engine, a Sigma 1-125A, had been developed and constructed around the years 1999/2000 and was one of two units that had been produced. Since its arrival

at HVL, it has been at the center of several final year projects by bachelor students in mechanical engineering and energy technology [1–3], as well as a testbed for heat pump and cryocooler development in cooperation with Enerin AS. The main aim of the current work with the engine is the development of a cryocooler capable of liquefying technical gases like nitrogen, argon and carbon dioxide [4] and its integration in a future hydrogen technology laboratory at HVL. Recently, the focus has been on the implementation and refinement of a simulation model within the framework of the Sage of Athens software [5] (hereafter only called Sage) that properly represents the existing hardware in order to use it as starting point for finding ways to improve the efficiency of the engine in both heat engine and cooler mode. In the long term, the development of a two-stage cryocooler is aimed at.

This article is structured as follows. At first the main properties of the engine will be given, before it is compared to similar sized engines by means of dimensionless groups. After that, the Sage model is described. Experimental results from operation as both heat engine and cooler are presented. They are thereafter compared to the simulation results and discussed before conclusions are drawn.

Engine properties and instrumentation

Figure 1 a) shows the Stirling-engine on its rigg with the propane-combustor heat source on top and with helium (working fluid) and propane pressure containers on its right side. The main mechanical properties of the engine are listed in Table 1 and Table 2. Figure 1 b) also shows the exposed heat source heat exchanger covered in ice formed from humid air while running the engine in cooling mode (current temperature in the photo is -63°C).

Table 1. Main technical specifications of the β -Stirling engine.

Rotation frequency	min 900	max 1500	rpm
Working gas	helium		
Pressure	min 20	max 80	bar (gauge)
Heater temperature	min 600	max 750	$^{\circ}\text{C}$
Displacer	bore 65	length 125	mm
high ΔT	crank radius 19.05	rod length 85.2	mm
low ΔT	crank radius 10	rod length 44.7	mm

Working piston	bore 65	length 100	mm
high ΔT	crank radius 19	rod length 175	mm
low ΔT	crank radius 10	rod length 175	mm
Phase angle	high ΔT 60	low ΔT 78	°
Nominal power	3000	electric	W

Table 2. Volumes (high ΔT configuration) and heat exchanger properties.

Compression space volume	displaced 123	dead 3.1	cm ³
Expansion space volume	displaced 126	dead 6.8	cm ³
Regenerator porosity	62 and 68		%
Heat sink	number of tubes	230	
	length 76	diameter 1	mm
Heat source	number of finned tubes	50	
	length 200	diameter 2	mm

The engine is equipped with several sensors for temperature, pressure, and crank angle, which are connected to a computer running LabView through a DAC from National Instruments. The 4-5 kW 4-pole electric motor/generator (manufacturer and type unknown) is located inside the crank case and connected to an inverter from ABB (ACS880-11) that either delivers electric power to the grid (heat engine mode) or draws from it (cooling and heat pump mode).

Three K-type temperature sensors are placed at different locations on the engine. One is mounted between the pipes of the heat source heat exchanger in order to measure the temperature on the outside of the heat exchangers pipes. The other two sensors are located at the inlet and outlet of the cooling water loop.

In autumn 2022, the engine was equipped with a crank angle sensor, which is mounted on the crank shaft on the opposite end to the electric motor. It consists of a toothed wheel (one tooth per 6°) and a magnetic sensor, which was fit into the end cap of the crank case. An Arduino unit is programmed to generate six equidistant pulses per tooth based on the current rotational speed of the crank shaft, so that Labview can take a measurement for each degree of a full rotation of the crank shaft. The data points that are finally written to the logfile are averages from 10 rotations. This setup helps in correlating the rotation angle of the crank shaft to the piston positions and the gas

volume in the engine. It is the basis for making P - V diagrams from measured data and compare the shape of these P - V curves and the work per cycle with results from the Sage model (see section Sage model).

Originally, two pressure sensors of type MBS 3100 060G1372 were mounted on the motor and the main part of measurements were made with those. One measures the pressure in the crank case, the other measures the pressure at the transition from the compression space to the regenerator. The latter one was recently replaced by a model 6217AB02000 sensor from Kistler. Its much faster read out frequency compared to the other pressure sensor makes the generation of P - V -diagrams possible.



Figure 1. a) The β -Stirling-engine with connected helium and propane reservoirs and exhaust pipe ready for operation as a heat engine in the engine laboratory at Western Norway University of Applied Sciences; b) The exposed and ice-covered heat exchanger at the top of the engine at -63°C while cooling down in cooling mode.

When used as heat engine, propane consumption by the combustor was measured by weighing the propane bottle with a load cell (HBMU9C/5kN) at two points in time during steady operation. A flow meter (SICK FFUS15-1G1|0) measures the volume flow of cooling water.

Comparison to similar engines

The Sigma 1-125A was a redesign of the TEM 1-130A, that was originally designed by TEM of Malmö with some inspiration from the 1-98 engine from United Stirling and Philips.

The dimensionless numbers compression ratio, Beale number, Mach number and Stirling number, align with those for similar-sized engines from United Stirling Sweden and Inresol. A comparison is shown in Table 3. At the bottom of the table, six dimensionless numbers are given for easier comparison of the four engines. The volumetric compression ratio is the ratio of maximum and minimum volume. The Mach number is calculated by

$$\text{Ma} = \frac{\omega L_{\text{ref}}}{\sqrt{RT_{\text{ref}}}} \quad (1)$$

where ω is the shaft speed in rad/s, L_{ref} is equal to the cubic root of the displaced volume in the first calculation of Ma in Table 3 and equal to the tube length of the compression space heat exchanger in the second calculation. R is the working medium's individual gas constant and T_{ref} is the absolute temperature of the cooler. The Stirling number is given by

$$N_{\text{SG}} = \frac{P_{\text{ref}}}{\omega \mu_{\text{ref}}} \quad (2)$$

where P_{ref} is the charge pressure and μ_{ref} is the dynamic viscosity of the working medium at the temperature of the cooler. The Beale number is calculated with

$$N_{\text{B}} = \frac{\dot{W}}{P_{\text{ref}} V_{\text{sw}} \omega} \quad (3)$$

where \dot{W} is the rated output power and V_{sw} the swept volume.

Table 3. Comparison of the Sigma 1-125A with three other similar sized Stirling engines: the Inresol V2-6, the United Stirling of Sweden (USS) V-160 and the USS P40. Abbreviation: hx - heat exchanger.

Engine	Sigma 1-125A	Inresol V2-6	USS V-160	USS P40
Configuration	beta	gamma	alpha	double-acting alpha
Number of circuits	1	1	1	4
Crankshaft angle / °	60	90	105	90
Cylinder volume / cm ³	126	451	160	95
Circuit swept volume (V_{sw}) / cm ³	122	451	195	134
Displaced volume / cm ³	124	566	160	93
Expansion hx volume / cm ³	61	377	33	33
Regenerator volume / cm ³	145	446	69	155

Compression hx volume / cm ³	14	96	37	28
Dead volume (total) / cm ³	32	181	86	31
Working medium	Helium	Nitrogen	Helium	Hydrogen
Charge pressure (rated; P_{ref}) / MPa	8	2.5	15	15
Heater tube temperature / K	973	1023	973	1023
Cooler tube temperature / K	373	300	330	333
Shaft speed / rpm	1550	600	1500	4000
Rated power (\dot{W}) / W	4000	5000	8000	11000
Volumetric compression ratio	1.39	1.27	1.68	1.49
Mach number	0.009	0.018	0.010	0.016
Mach number	0.014	0.021	0.019	0.032
Stirling number	2.5×10^9	2.2×10^9	4.8×10^9	4.0×10^9
Beale number	4.1	4.4	2.7	5.5
$V_{min} dT^3 / \dot{W} / (m^3 K^3) / W$	17	126	10	8

Sage model

Sage of Athens version 11 [5] has been used to model the Stirling-engine both in heat engine and in cooler mode. The model was created from the bottom up, first with main components (see Figure 2) like power piston, displacer, pressure source and gas circuit with its components on the top row in Figure 3. After the basic model was working stably, several connections for heat conduction between the top of the motor (expansion space) and the bottom (crank case) inspired by the work of Demke and Penswick [6] were added. These include the displacer rod (Figure 2), inner gas volume of the displacer (Figure 3), and heat conduction paths along the cylindrical parts surrounding the gas spaces and the heat exchangers in the gas circuit (Figure 4). This setup is called the main model in Table 4.

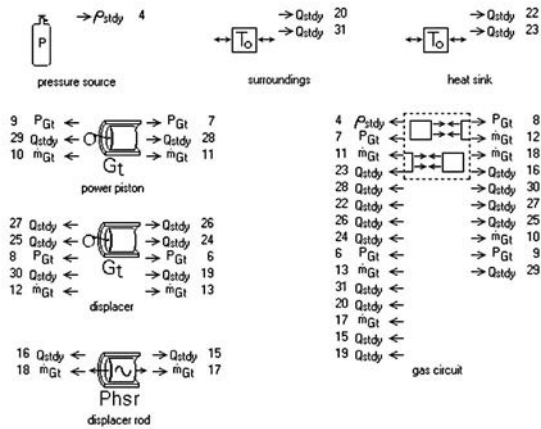


Figure 2. Main components in the Sage of Athens model of the β -Stirling engine.

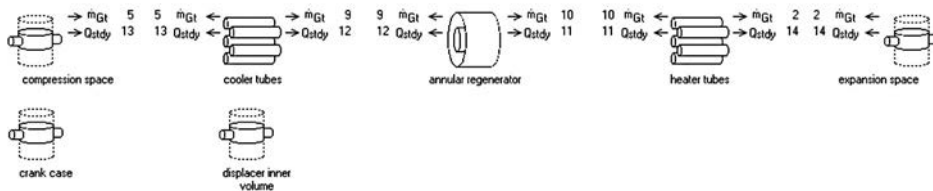


Figure 3. Gas circuit components in the Sage of Athens model of the β -Stirling engine.

The temperature difference between expansion space and the cooler tubes may exceed several hundred kelvin. For an expansion space not fully thermally isolated from the surroundings and the rest of the engine, this means both loss of thermal energy when operated as heat engine or heat leakage into the expansion space when operated as cooler. This is why the thick surface in Figure 4 e) has a connection all along the components to its left side in the gas circuit made up of distributed conductors as well as directly to the parasitic thermal energy reservoir called surroundings in Figure 2. Further loss channels are based on the cylinder-piston gaps and along the displacer rod towards the crank case.

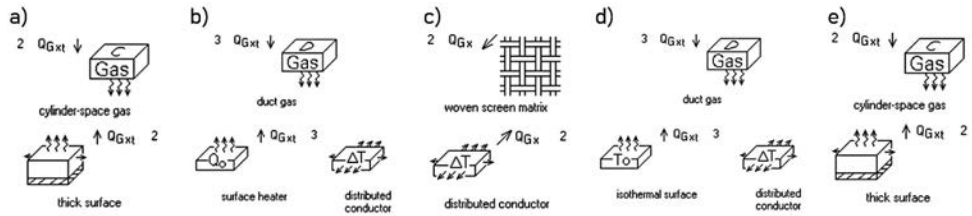


Figure 4. Setup of the main gas circuit components in the Sage of Athens model of the β -Stirling engine. From left to right compression space, cooler tubes, annular regenerator, heater tubes and expansion space.

To simulate a setup with almost perfect thermal insulation of the cold head from the surroundings, connection 3₁ in Figure 2 can be disconnected. This is used to model the cooler's properties in the cases designated 1b and 2b in Table 4.

Earlier versions of this model had isothermal surfaces for both cooler tubes and heater tubes. Since the temperature of the cooling water is measured at both inlet and outlet to the cooler tubes, a surface heater removing the measured thermal power from the working fluid is a better choice (Figure 4 b)). The same can be done to the heater tubes (Figure 4 d)) in case the cooling load in cooling mode is known or the heat input from a burner when the engine is operated in heat engine mode. On the other hand, isothermal surfaces connected to both heater and cooler tubes can help in finding coefficient of performance (COP_R) and second-law efficiency (η_{II}) when the exact cooling load is not known. This model is called the alternate model (alt.) in Table 4.

Calculations

Experimental data and output from the Sage models are used to mainly calculate coefficients of performance (COP_R), second-law efficiencies (η_{II}), the efficiency of the crank mechanism and electric motor/generator ($\eta_{crank-el}$) as well as thermal efficiencies for the heat engine mode (η_{th}).

The coefficient of performance is the ratio of the cooling load $\dot{Q}_{in,source}$ and the necessary input power \dot{W} . In this work, it is distinguished between the mechanical P-V-power W_{PV} (P: pressure; V: volume) and the electrical power \dot{W}_{el} . This gives the two definitions

$$\text{COP}_{R,PV} = \frac{\dot{Q}_{\text{in,source}}}{\dot{W}_{PV}} \quad (4)$$

and

$$\text{COP}_{R,\text{system}} = \frac{\dot{Q}_{\text{in,source}}}{\dot{W}_{\text{el}}} \quad (5)$$

The second law efficiencies for the operation as cooler are based on the coefficient of performance of a reversible cooler operating between the same temperature levels

$$\text{COP}_{R,\text{rev}} = \frac{T_{\text{source}}}{T_{\text{sink}} - T_{\text{source}}} \quad (6)$$

where T_{source} is the absolute temperature of the low-temperature heat source and T_{sink} is the absolute temperature of the high-temperature heat sink. The second-law efficiencies based on mechanical and electrical power input are then simply

$$\eta_{\text{II},PV} = \frac{\text{COP}_{R,PV}}{\text{COP}_{R,\text{rev}}} \quad (7)$$

and

$$\eta_{\text{II},\text{system}} = \frac{\text{COP}_{R,\text{system}}}{\text{COP}_{R,\text{rev}}} \quad (8)$$

respectively. The efficiency of the conversion of electrical input power to P - V -power by the crank mechanism is measured by the ratio

$$\eta_{\text{el-crank}} = \frac{\dot{W}_{PV}}{\dot{W}_{\text{el}}} \quad (9)$$

For the heat engine calculations, the thermal efficiency is calculated as

$$\eta_{\text{th},PV} = \frac{\dot{W}_{PV}}{\dot{Q}_{\text{in,source}}} \quad (10)$$

and

$$\eta_{\text{th},\text{system}} = \frac{\dot{W}_{\text{el}}}{\dot{Q}_{\text{in,source}}} \quad (11)$$

when calculated based on either mechanical or electric output power, respectively. The second-law efficiencies are ratios of these and the thermal efficiency of a reversible heat engine ($\eta_{\text{th,rev}}$) operating between a high-temperature thermal energy source and a low-temperature thermal energy sink with

$$\eta_{\text{th,rev}} = 1 - \frac{T_{\text{sink}}}{T_{\text{source}}} \quad (12)$$

This gives

$$\eta_{II,PV} = \frac{\eta_{th,PV}}{\eta_{th,rev}} \quad (13)$$

and

$$\eta_{II,system} = \frac{\eta_{th,system}}{\eta_{th,rev}} \quad (14)$$

respectively. Since the energy conversion in heat engine mode is from mechanical to electrical, the corresponding efficiency of the crank mechanism and electric motor connection is defined as

$$\eta_{crank-el} = \frac{\dot{W}_{el}}{\dot{W}_{PV}} \quad (15)$$

Test results and comparison to Sage-model

Over the years, tests as both heat engine and cryocooler have been undertaken with the described Stirling-engine, often as part of bachelor thesis work.

The most recent test results with the physical Stirling-engine are from operation in cooler mode from spring and autumn 2023. These will be compared to results obtained with the above-mentioned Sage model before older data from tests in heat engine mode are presented.

Cooler mode

Measured data from two cases can be found in the columns marked 'exp.' in Table 4. Starting with the cooler being at room temperature, it took ca. 20 minutes to cool the cold top down from 24°C to -114°C (159 K) at 21 bar (absolute) helium pressure and 1400 rpm (case 1). A 5 cm thick cylinder made from styrofoam was used as thermal insulation around the cold head. The electric motor was supplied with 3.65 kW while thermal power removed by the cooling water was 2.93 kW. The inlet temperature of the cooling water increased from 11.9°C to 16.6°C. A P-V-diagram was made from crank angle and pressure data logged as described in section Engine properties and instrumentation. The experimentally measured P-V-curves for both case 1 and 2 are shown in Figure 5. The curve for case 2 encloses a slightly smaller area and has a differently rounded left side compared to case 1. This may be explained with the difference in rpm and fill pressures between these two cases (1400 rpm vs. 1308 rpm).

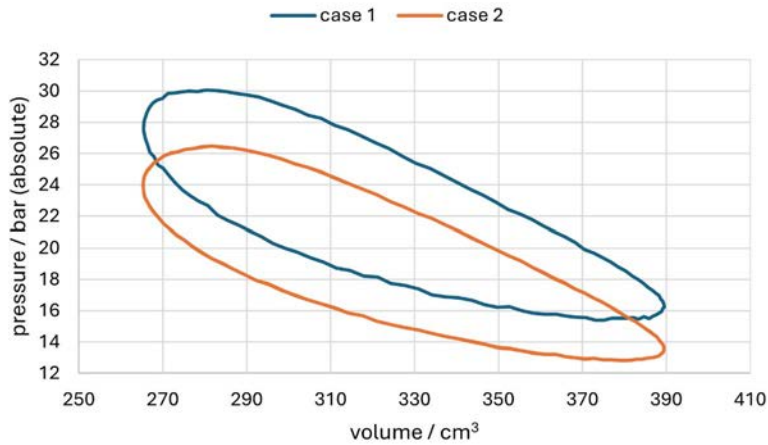


Figure 5. Measured P - V -curves for case 1 and 2 (see also Table 4).

The area surrounded by the experimental cycle curve corresponds to 82.6 J and thereby to a P - V -power of 1.93 kW at 1400 rpm. In comparison, the main Sage model calculated a P - V -power of 1.98 kW (corresponding to 85.0 J per cycle) when the output thermal power is set to the value measured in the experiment and otherwise same values for pressure, rpm and cooling water inlet temperature (heat sink temperature). The average temperature of the heater tubes (cold head, T_{source}) is 155.5 K, which corresponds to -117.7 °C. That means that there is a 2.9% difference in input power and a 2.4% difference in cold head temperature. The cooling load (heat flow from the isothermal surface to the duct gas in the heater tubes; see Figure 4 d)) in this state of operation is 0.939 kW according to the Sage-model. However, there is also a heat flow of 0.208 kW through the solid parts of the cooler from the surroundings to the expansion space while 0.202 kW are lost from the crank case to the surroundings. At these conditions the cooler has a COP_R of 0.473 and a second-law efficiency of 40.0%.

The ratio between calculated input power and measured input power to the electric motor of the physical cooler ($\eta_{el-crank}$) is 52.8%. This means, that the actual cooler has a $COP_{R,system}$ of 0.250, corresponding to 21.1% second-law efficiency for the whole system. When applying the alternate model (isothermal surfaces for both heater and cooler tubes), the cooling load decreases by 4%, while the thermal power transferred to the heat sink decreases by 2.8%. The heat loss from the crank case increases by 60% in

comparison and the calculated P - V -power is 4% higher compared to the main model. Coefficient of performance and second-law efficiency based on P - V -power are 0.437 and 36.8%, respectively. They decrease to 0.231 and 19.4% when taking the losses in electric motor and crank mechanism into account.

Table 4. Details of the two experimental cases that were studied with Sage models. The measured data (pressure, rpm, heat power to sink, source and sink temperature, P - V - and electric input power) except for P - V - and electric power were used as input data in the Sage models.

	Case 1	Sage 1a		Sage 1b		Case 2	Sage 2a		Sage 2b		
	exp.	main	alt.	main	alt.	exp.	main	alt.	main	alt.	
pressure	21 bar (absolute)					18.5 bar (absolute)					
rpm	1400					1308					
$Q_{in,source} / W$	2930	939	902	1122	1094	2419	742	704	929	899	
$Q_{out,sink} / W$		2930	2849	2930	2874		2419	2419	2323	2419	2348
$Q_{out,creep} / W$		202	324	239	327		166	302	203	306	
$Q_{in,ambient} / W$		208	206	10	8		229	227	28	26	
$W_{PV,cycle} / J$	82.6	85.0	88.5	87.3	90.0	76.6	74.0	77.7	76.4	79.3	
W_{pv} / W	1927	1984	2065	2038	2099	1670	1614	1694	1666	1729	
W_{el} / W	3650	3757	3911	3860	3975	3279	3169	3326	3271	3395	
$\eta_{el,crank}$	52.8%	52.8%	52.8%	52.8%	52.8%	50.9%	50.9%	50.9%	50.9%	50.9%	
T_{sink} / K	285	285	285	285	285	279	279	279	279	279	
T_{source} / K	159	155	155	153	154	153	150	151	148	150	
$COP_{R,PV}$		0.473	0.437	0.551	0.521		0.460	0.416	0.557	0.520	
$\eta_{II,PV}$		40.0%	36.8%	47.2%	44.6%		39.8%	35.2%	49.1%	44.7%	
$COP_{R,system}$		0.250	0.231	0.291	0.275		0.234	0.212	0.284	0.265	
$\eta_{II,system}$		21.1%	19.4%	24.9%	23.5%		20.3%	17.9%	25.0%	22.7%	

When the thermal connection between surroundings and expansion volume is disconnected in both main and alternate model, the cooling load increases by 19.5% in the main model and 21.3% in the alternate model in case 1. The increase is even larger in case 2 (25.2% and 27.7%), which otherwise shows similar trends compared with case 1, but a slightly lower value for $\eta_{el,crank}$. The heat flow from the surroundings to the expansion space decreases considerably to only a few watt (Sage case 1b) and few tens of watt (Sage case 2b), respectively, and is likely to be the reason for the increased cooling load.

Averages of the values for coefficient of performance based on P - V -power ($COP_{R,PV}$) for each case based on both main and alternate model and both variant a and b of each case were used to estimate the cooling load ($\dot{Q}_{in,source}$) in each of the two experiments. For case 1, the average $COP_{R,PV}$ from the different variants of Sage-models was 0.469, giving a cooling load ($\dot{Q}_{in,source}$) of 0.955 kW. For case 2, the experimental cooling load has been estimated to be 0.815 kW, based on an average $COP_{R,PV}$ of 0.488 from the different Sage models.

For estimating the cooling load and necessary input power for the lowest measured temperature of -167°C (106 K), the alternate Sage model with isothermal surfaces at both heater and cooler tubes was used as data for the removed thermal power to the heat sink was not available. The initial temperature of the heater tubes was set to 106 K. All other initial and fixed values were unchanged. The cooling load is calculated to be 0.419 kW at 2.88 kW input power. This gives a coefficient of performance of 0.146 and a second-law efficiency of 25%. With the observed discrepancy between simulated and measured input power, the actual input power might be correspondingly higher and equal 5.34 kW. A coefficient of performance of 0.0784 and 13.5% second-law efficiency would be the result.

Heat engine mode

Shortly after its construction, the Sigma 1-125A was tested extensively as both ultra-high temperature heat pump (20°C source, 650°C heat sink) and as heat engine at rated capacity in the years from 2000 to 2002. Unfortunately, most of the test data has been lost, but the team recalls that the testing was typically performed with 3 kW electric output power, and that the engine needed ball bearing replacement every 2000 hours. Table 5 shows data from two test points for Sigma 1-125A and two test points for intermediate prototypes between TEM 1-130A and Sigma 1-125A. Values in black are from test notes, values in gray are estimates and interpolated values from the time of writing this paper.

Table 5. Test data from the original tests in heat engine mode of both the Sigma 1-125A and 1-130B-L3 and -L4 from autumn 1999 and early 2000. Values in black are from test notes, values in gray are estimates and interpolated.

Motor		1-125A	1-125A	1-130B-L4	1-130B-L3
Date		03.02.2000	16.02.2000	08.11.1999	30.09.1999
Time		19:24	20:14	16:43	14:43
Fuel		Commercial propane/butane fuel (LPG)			
Fuel flow rate	l/min	10.7	9,9	11.3	9.93
Air flow rate	l/min	22.1	22	24.2	23.8
Air temp	°C	30	34	28	27
Exhaust temp	°C	239	237	244	181
Heater tube temp	°C	726	674	697	743
Gas consumption	kW	15.80	14.62	16.68	14.66
Exhaust losses	kW	1.69	1.63	1.91	1.34
Other heat loss estimate	kW	1.7	1.7	1.7	1.7
Heat to helium	kW	12.41	11.29	13.07	11.62
Burner efficiency	η_{burner}	79%	77%	78%	79%
Cooling water flow	l/min	21.8	16	25	
Cooling water temp	°C	10.9	56.75	25.45	
Heat to cooling water	kW	9.16	5.71	8.93	8.02
Charge pressure	bar (g)	74.8	80	80	80
Indicated power (measured)	kW	7	6	5.31	4.28
Displacer power (simulated)	kW	0.7	0.7	0.7	0.68
Thermal efficiency	η_{thermal}	51%	47%	35%	31%
Friction estimate	kW	0.1	0.1	0.1	0.1
Shaft power	kW	4.8	5.2	4.53	3.5
Mechanical efficiency	$\eta_{\text{mechanical}}$	98%	98%	98%	97%
Generator cooling	kW	1.0	1.2	0.7	0.95
Generator heat to crankcase (estimate)	kW	0.8	1.0	0.87	0.46
Electric power (measured)	kW	2.93	3.073	2.96	2.09
Generator efficiency	$\eta_{\text{generator}}$	61%	59%	65%	60%
Engine/generator efficiency	η_{engine}	19%	21%	18%	14%

The most recent measured data from operation in heat engine mode are from 2020 and were reported in the bachelor thesis by Fonnes and Storsve [3]. A selection of those will

be compared to data produced with the main Sage model. As these data are from before the time crank angle sensor and the faster pressure sensor were mounted on the engine, there are no P - V -diagrams and loss factors between P - V -power and electric output power available.

The original propane burner was used as a heat source and propane consumption was measured in intervals of steady operation with a stopwatch and a scale. Unfortunately, only the heat source temperature is available from these measurements. The temperature of the exhaust gases leaving the hot side heat exchanger to the working fluid were not recorded. The temperature of the heat source was set at values around 750°C (1023 K), revolutions were set to 1500 rpm and measurements were carried out at 31.5 , 36.5 , and 41.5 bar (absolute) pressure helium, respectively. Since the outlet temperature from the hot side heat exchanger could not be measured, it was not possible to calculate the thermal input power and estimate thermal losses between heat source and sink. Table 6 shows measured cooling power and electric power output along with results from the main Sage model, which was set to the same cooling power.

The results based on the main Sage model show, that there is a large loss of useful energy between the power piston and the electric power output. Only between 13.5% and 18.8% of the P - V -power are converted to electric power ($\eta_{\text{crank-el}}$), resulting in very low thermal efficiencies for the whole system ($\eta_{\text{th,system}}$) of 6.5% - 9.2% and correspondingly low second-law-efficiencies ($\eta_{\text{II,system}}$) of 9% - 12.6% .

Table 6. Experimental results from heat engine operation [3] and Sage-model.

	Experimental			Sage (main)		
$P / \text{bar (absolute)}$	31.5	36.5	41.5	31.5	36.5	41.5
$T_{\text{sink}} / \text{K}$	285	285	285	285	285	285
$T_{\text{source}} / \text{K}$	1022	1035	1030	1022	1035	1030
$\dot{Q}_{\text{out,sink}} / \text{W}$	3848	4334	5224	3848	4334	5224
$\dot{Q}_{\text{in,source}} / \text{W}$				8201	9380	10910
$\dot{W}_{\text{PV}} / \text{W}$				3937	4566	5604
$\eta_{\text{th,PV}}$				48.0%	48.7%	51.4%
$\dot{W}_{\text{el}} / \text{W}$	532	859	850	532	859	850
$\eta_{\text{crank-el}}$				13.5%	18.8%	15.2%
$\eta_{\text{th,system}}$				6.5%	9.2%	7.8%
$\eta_{\text{II,system}}$				9.0%	12.6%	10.8%

Discussion

In 2011, Ladner [7] published correlations for, amongst others, coefficient of performance and second-law efficiency for Stirling-cryocoolers based on temperatures in heat source and heat sink (set to $T_H = 300$ K). Even though the heat sink temperature differs by 15 K between Ladner's study and this work, the temperatures are close enough for the correlations to be used for a comparison. These give a $COP_{R,system}$ of 0.294 ($T_C = T_{source} = 159$ K) and 0.271 ($T_C = T_{source} = 153$ K), respectively. The ones obtained with the Sage model and corrected for the losses in electric motor and crank mechanism are 0.250 and 0.234. The picture is similar for the second-law efficiency, where Ladner's correlations give 25.9% and 26.0%, respectively. The loss-corrected Sage-results are 21.1% and 20.3%, respectively. For the lowest temperature measured, Ladner's correlations give a coefficient of performance of 0.130, while the Sage model gives a value of 0.0784 for $T_C = T_{source} = 106$ K. The second-law efficiency values differ accordingly with 23.4% and 13.5%, respectively. These values are for a fill pressure of 20 bar (gauge). Increasing the fill pressure in the main Sage-model to 40 bar (gauge) yields improvements with 0.110 for the coefficient of performance and 20.8% for the second-law efficiency at 106 K (corrected for electrical-mechanical losses).

In 2014, Xu et al. [8] reported a β -Stirling-cryocooler capable of 640.5 W of cooling power at 77 K, 1450 rpm and 11 kW of input power at 26.5 bar. This corresponds to a COP_R of 0.0582 and second-law efficiency of 15.9%. This is much better than the coefficient of performance of 0.0457 and second-law efficiency of 13.2% that would be possible with the Stirling-cooler reported in this work. However, the input power to the Sigma 1-125A is currently limited to 5 kW. This would result in a possible cooling load of 229 W. Xu et al. later improved their cryocooler to 700 W cooling load at 77 K and 10.9 kW input power [9].

These comparisons and the fact that the measured P - V -diagrams and results from the Sage model show good agreement make it clear that there is room for improvement in the electrical-mechanical part of the crank-mechanism. As per today, it suffers mainly from friction in bearings and some crank-shaft vibrations. Work on moving the electromotor outside of the crank casing [8] and development of a better-balanced crankshaft is under way in spring 2024 [10]. Another aim is to measure the thermal energy generated by friction in the crank-casing by measuring the temperature increase in an extra cooling

water loop through this part of the engine as it was done in the first experiments in 2000. The performance and engine efficiency of the Sigma 1-125A in heat engine mode are not very good compared to industrial Stirling engines from United Stirling Sweden, for example. The thermal efficiency and the overall engine efficiency seem to have deteriorated since it was originally built in 1999 although it has been operated very little since 2010. Three main issues have been identified. The first one is the propane burner, which was not designed for the engine. The engine used a modified burner from a salvaged V-160, with operating parameters set by trial and error. The V-160 was a higher-capacity engine, and the burner was operated off-design. Next, the shaft speed was continuously varying due to the torque amplitude. The pressurized crankcase did not allow for a large flywheel. Hence, the induction motor used as generator experienced high losses due to accelerating magnetic fields. Finally, the friction estimate may be slightly optimistic, as the engine uses grease lubricated roller bearings.

Mechanical losses of about 50% have been reported before for β -Stirling engines [11], but the over 80% that are estimated for operation as heat engine are a reason to redo the heat engine measurements from 2020 after the above-mentioned modifications have been implemented. The available experimental data is not sufficient to explain these losses. Measuring the temperature of the exhaust from the propane burner in addition to the temperature of the combustion chamber in order to estimate the available heat input to the Stirling-engine working fluid along with measuring P - V -diagrams should help to clear the picture.

Conclusion

There is good agreement between the developed Sage model and operation of the Stirling-engine in cooling mode. The inclusion of thermal loss channels has been important to achieve this. Comparison to other Stirling-coolers shows that improvements on cooling load and coefficient of performance should be possible. However, unusually large mechanical losses have been observed for operation in heat engine mode that are difficult to explain with the available experimental data.

Ongoing work on a better-balanced crank mechanism and external placement of the electric motor/generator are expected to reduce mechanical losses and lead to a better agreement between experiments and model. Other improvements can be made with

respect to better thermal isolation of the cold head from the rest of the machine's body and a corresponding reduction in heat conduction to the expansion volume.

A systematic mapping of the mechanical losses as function of rpm and fill pressure will also be conducted for further refinement of the model for both cooling and heat engine mode. The improved model is then to be used in the design and development of a new cold head and a two-stage version of the Sigma 1-125A as the focus will be on applications for cryo-cooling in the future.

Acknowledgements

This work was in part financed by Western Norway University of Applied Sciences, by Regional Forskningsfond Vestland through the StirLH₂-project and through a scholarship by FRAMO-stiftelse Høgskulen på Vestlandet for Norbert Lümme. The authors would like to thank lab engineers Harald Moen, Frode Wessel Janssen, Kjetil Gravelseter and Nafez Ardestani for their help and expertise with operating and maintaining the Stirling-engine in the engine laboratory at Western Norway University of Applied Sciences.

References

- [1] Thorsen HM, Reve M, Nesse K. Design, build and setup of test jig for Stirling engine & Investigation of feasibility for a standalone inert gas system including Stirling engine and cargo pumps. Bachelor thesis, Bergen University College (2011).
- [2] Dahle Sivertsen I, Sagafos Andersen S. Preparation and Testing of a Stirling Engine. Bachelor thesis, Bergen University College (2013).
- [3] Bakke Fonnes S, Storsve AM. Developing a β -Stirling engine for running on low temperature difference. Bachelor thesis, Western Norway University of Applied Sciences (2020).
- [4] Pedersen Tjøsvoll K, Issa Rashdan KJ, Haugland Lie E. Development of a cooling head for a Stirling cryocooler. Bachelor thesis, Western Norway University of Applied Sciences (2023).
- [5] Gedeon D. Sage of Athens, www.sageofathens.com (2016).
- [6] Demko R, Penswick LB. Sage Simulation Model for Technology Demonstration Convertor by a Step-by-Step Approach, in: Third International Energy Conversion Engineering Conference, San Francisco, CA (2005).

- [7] Ladner DR. Performance and Mass vs. Operating Temperature for Pulse Tube and Stirling Cryocoolers, in: International Cryocoolers Conference, 633–644 (2010).
- [8] Xu Y, Cai YC, Sun DM, Shen Q, Zhao X, Zhang J, Cheng ZZ. Study on a High-Power Stirling Cryocooler. in: International Cryocoolers Conference, 163–168 (2014).
- [9] Xu Y, Sun D, Qiao X, Yu YSW, Zhang N, Zhang J, Cai Y. Operating characteristics of a single-stage Stirling cryocooler capable of providing 700 W cooling power at 77 K. *Cryogenics* 83, 78–84 (2017).
- [10] Beck Nikolaisen MR, Skjæveland Nesse J. Development of IMM's β -Stirling engine. Bachelor thesis, Western Norway University of Applied Sciences (2024).
- [11] Makhkamov KhKh, Ingham DB. Analysis of the Working Process and Mechanical Losses in a Stirling Engine for a Solar Power Unit. *Journal of Solar Energy Engineering* 121, 121–127 (1999).

Quantifying Hysteresis Loss in a Stirling Refrigerator using Sage

Danielle Yang^{a,*}, Michael Gschwendtner^a, Zindh Waleed^a, Michael Protheroe^a

a Department of Mechanical Engineering, Auckland University of Technology, New Zealand

*Corresponding author. danielle.yang@aut.ac.nz

Keyword: Sage, p-V work, Hysteresis, Refrigeration, Losses

Abstract

Stirling coolers consist of several spaces in which a volume of gas undergoes expansion and compression. In such a space, heat transfer occurs due to the cyclic temperature difference between the working gas and the adjacent walls. This cyclic heat dissipation is known as hysteresis loss. Hysteresis loss is one of the many losses within Stirling machines that are not completely understood, let alone quantified. This project used Sage, a numerical software package for Stirling machines, to model both a single space piston cylinder model and an alpha Stirling refrigerator to quantify hysteresis loss. Schematics of heat transfer between different components of the models are produced using MATLAB. A discussion of hysteresis as a loss or mechanism of work-to-heat transfer is presented, and it is found that for the modelled alpha Stirling refrigerator operating within the ambient temperature regime, the maximum hysteresis loss is less than 2% of the total work input.

Introduction

Stirling machines harness the interactions between compression and expansion of a gas to perform various cooling and power generation tasks. Due to the cyclic nature of Stirling operation, hysteresis loss remains a significant issue. Despite this, hysteresis loss lacks consistent quantification within the existing literature. In an effort to contribute to further understanding of this phenomenon, this paper presents a study on a single-cylinder with regenerator material Sage model and a complete Stirling refrigerator model. The inter-component net heat transfer is discussed, as well as the relationship between net P-V work and the pressure phase shift in a refrigeration model. Discussions are presented on the suitability of the Peclet number in predicting hysteresis loss, and the implications of hysteresis being classified as a loss rather than an inherent heat transfer mechanism. Through this discussion, we seek to contribute to the understanding of hysteresis and its implications for Stirling machine design and optimisation.

Background

The existing literature provides some insights into the characteristics of heat transfer within a cyclically compressed volume of gas, but also shows the large discrepancies in the understanding of what hysteresis loss is, and how large it is in terms of Stirling refrigerators.

Most studies conclude that this heat transfer loss is the difference between compression and expansion work when looking at a simple single space system, but do not go further into its definition [1-5]. Others have slightly different definitions or methods of measurement, such as the net P-V work when no refrigeration work is being performed [6].

Hysteresis loss seems to have a peak in between two distinct operating conditions, the most common being isothermal and adiabatic [1-3, 5, 7], but parameters such as cavity gap length [8] and non-dimensional hydraulic radius [9] are also presented. Instead of the loss peaking between two operating conditions, Pourmovahed and Otis [10] found that the pressure amplitude has a peak. However, this is most likely due to the system being analysed as a resonant system with the pressure amplitude modelled as the output over a range of operating frequencies. Other insights such as the fact that hysteresis loss is dependent in some way on heat transfer and its phase difference with the bulk gas temperature [9], that the heat transfer is more affected by the gas properties and not the cylinder properties [3], and that the heat flux increases substantially at the end of the compression stroke [11] are important to consider.

Most significantly, there seems to be no consensus on the magnitude of hysteresis loss and its overall effect on the efficiency or Coefficient of Performance of Stirling engines and refrigerators. The literature concludes hysteresis loss in a Stirling engine ranges from a loss of a maximum of 10% [12] or is typically 5%, but can get up to 25% of the power output [2]. Some do not quantify it, but rather state that it is a large or important thermal loss [1], and do not offer a conclusion on its effect, but conclude that existing methods are either sufficient [4, 5, 10, 13, 14] or insufficient [7, 15] at determining its magnitude. Furthermore, yet another study concludes that hysteresis loss is negligible [16]. In addition, most of the conclusions are made specifically for the configuration, dimensions, and temperature regime of interest of each study, and the effect of hysteresis loss in a Stirling refrigerator and its similarities or differences between a Stirling engine are not discussed.

The literature shows that hysteresis is a poorly understood heat transfer phenomenon in Stirling machines. Many have attempted to explain and quantify hysteresis loss, but modelling has only been done for simple single or double space models, with no analysis of hysteresis loss as it appears in an actual Stirling refrigerator. When refrigerator models are considered, they are usually very simplified models with no regenerator included. Furthermore, the conclusions from these studies also vary, leading to inconclusive interpretations on the magnitude and effects of hysteresis loss in Stirling applications. More work must be done on understanding the underlying mechanism of hysteresis loss to truly quantify it and make a statement on the magnitude of its effect on the performance of Stirling machines. While Wang [7] and Park and Chang [16] do apply heat transfer models to ideal adiabatic analyses of Stirling refrigerators, these models are highly idealised second order models at best, so do not account for the interaction between different losses, nor are they experimentally validated. The only third order model attempt at modelling hysteresis loss [15] was basic in the fact it only modelled a single cylinder with an internal grid, not a complete Stirling refrigerator. In addition, some recent studies simply use Urieli and Berchowitz' 1980 equation to predict hysteresis loss [17-19].

Building upon these foundations, this study seeks to provide clarity on the correlations between hysteresis loss, net heat transfer, and P-V work in a cylinder as well as a full Stirling refrigerator model. Sage is used due to its suitability as a robust numerical software package tailored specifically for modeling Stirling machines. It includes sophisticated models that consider the interplay between various components, which is important when modelling the heat and work-transfer interactions in a multiple space Stirling refrigeration system. The following section details the Sage models produced in this study.

Cylinder with Regenerator Sage Model

The Sage model for the regenerator test rig consisted of two main spaces – the cylinder space and a canister space filled with regenerator material. The cylinder wall was modelled as a 'thick surface', and the wall was held constant at a temperature $T_w = 300$ K to simulate room temperature surroundings, using a line heat source.

The schematic of this Sage model is shown in Figure 1. The average gas volume was kept

as close as possible to the first single-cylinder experiment, which meant that the zero position of the piston needed to be shifted to make up for the volume occupied by the solid regenerator material.

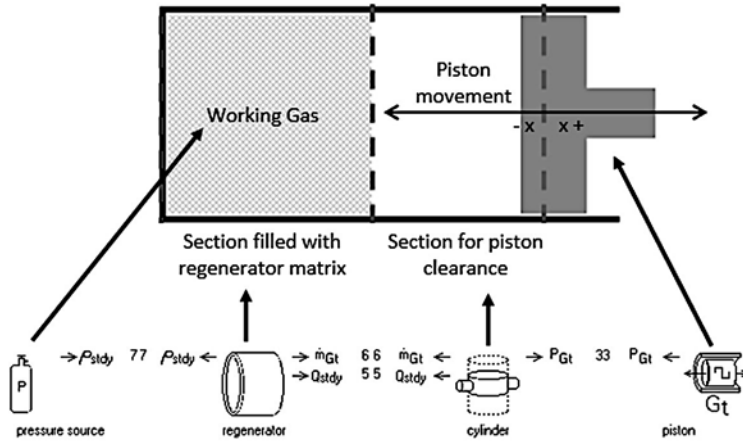


Figure 1. Schematic and Sage model of single cylinder with regenerator material.

The regenerator was modelled as a woven screen matrix with a wire diameter of 0.1 mm, with a porosity of 0.626. This was to model an existing test rig of the same configuration, which was used to experimentally validate the model [20]. The dimensions of the model are given in Table 1. The magnitude and phase data for gas pressure, volume, and temperature were recorded with the working gas as air.

Table 1. Dimensions of the single cylinder with regenerator Sage model.

Parameter	Value	Unit
Diameter	0.05	m
Stroke	0.01	m
Stroke Volume	1.9634×10^{-5}	m^3
Volume Ratio (Compression Ratio)	1.5178	
Average Volume	3.980×10^{-5}	m^3
Piston Face Area	7.854×10^{-3}	m^2
Regenerator Length	0.0236	m
Regenerator Porosity	0.626	

Alpha Stirling Sage Model

An alpha Stirling configuration was chosen to be the configuration analysed, as shown in Figure 2. The reason for choosing an alpha configuration as opposed to a free displacer beta configuration was the simplicity of design, and the control of both piston and displacer. The motion of a beta configuration Stirling refrigerator is dependent on gas forces and gas-spring resonance, which changes the operating parameters of the system, and the frequency ranges in which the refrigerator could physically operate. As both piston and displacer motion are controlled in an alpha configuration, the effects of hysteresis loss can be more easily identified as this control removes the resonant system considerations of the free displacer when analysing the system. The Sage model of the alpha Stirling refrigerator can be seen in Figure 3.

The operating parameters of the alpha Sage model are shown in Table 2. The working gas input was helium, and the mean pressure input to Sage was 2 MPa. The regenerator was set to replicate the wire mesh available in the lab, which was a woven screen matrix of with a wire diameter of 0.1 mm and a porosity of 0.7. The model was mapped from 0.1 to 160 Hz. The temperature range of interest was the near-ambient range, with an absorber temperature of 20 °C and a rejector temperature of 50 °C, but further studies should be done over a wider range of operating temperatures.

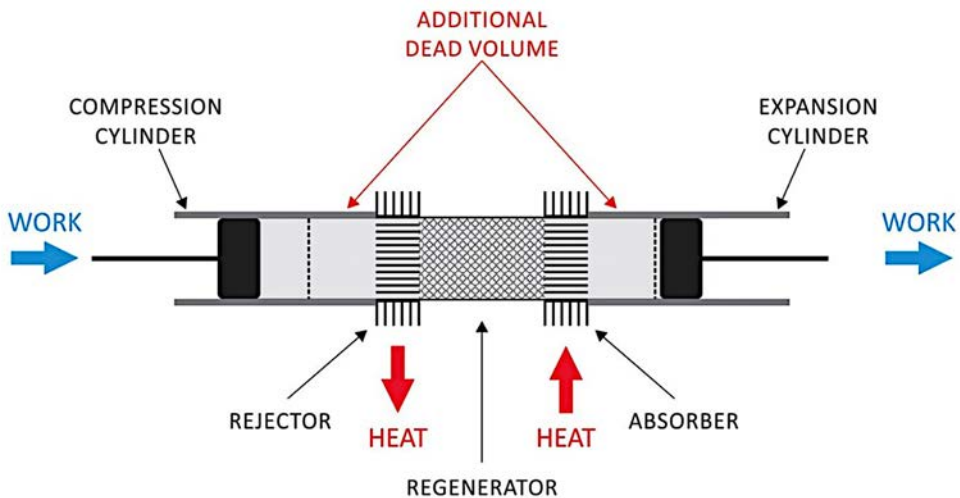


Figure 2. Schematic of an alpha Sage refrigerator.

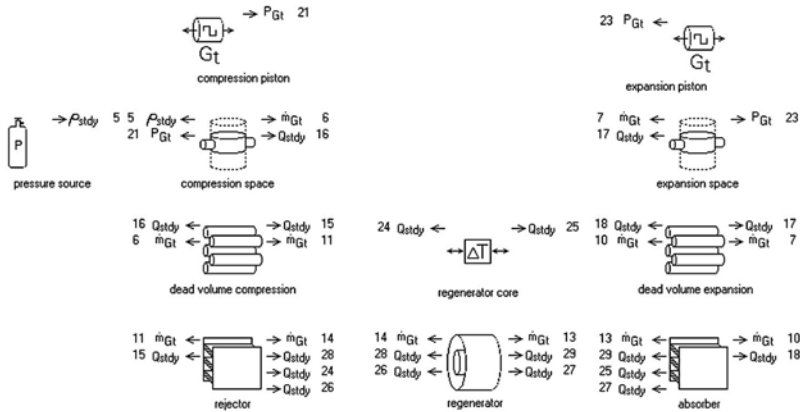


Figure 3. Sage model of the alpha Stirling refrigerator.

Table 2. Dimensions of the alpha Stirling refrigerator Sage model.

Item	Specification
Working gas	Helium
Mean pressure	2 MPa
Total mean volume	0.016294 L
Absorber temperature	293 K, 20 °C
Rejector temperature	323 K, 50 °C
Piston diameter	19.5 mm
Piston stroke	6 mm
Mean volumes of the compression and the expansion spaces	$3.196 \times 10^{-6} \text{ m}^3$
Dead volumes of the compression and the expansion spaces	$1.404 \times 10^{-6} \text{ m}^3$
Rejector volume	$1.55 \times 10^{-6} \text{ m}^3$
Absorber volume	$1.388 \times 10^{-6} \text{ m}^3$
Regenerator void volume	$4.156 \times 10^{-6} \text{ m}^3$
Regenerator porosity	0.7
Regenerator material	SS304
Phase shift between expansion and compression piston	90 °
Mapped frequency range	0.1 – 160 Hz
Operating frequency range (approx.)	1 – 160 Hz

The Peclet Number in Stirling Refrigerators

As previous literature [4, 5] found that the non-dimensional loss for a single cylinder system peaked at a Peclet number of approximately 10, better design practices might be established by understanding the Peclet numbers around which Stirling refrigerators typically operate. However, Stirling machines consist of more complex geometry than a simple piston-cylinder experiment. The question arises of how to quantify the Peclet number of a Stirling machine – would it be an overall value, or would each component have a different Peclet number?

Given that the temperature, pressure, and other properties within Stirling machines vary throughout each component, the first approach taken was to quantify the Peclet number within each space. As the Peclet number is based on the hydraulic diameter in the form of the ratio of volume to wetted surface area, each component in a Stirling machine has a different Peclet number. The problem with this approach is that the non-dimensional loss cannot be calculated in constant-volume spaces as the loss calculation requires a variation of volume in the form of adiabatic compression and expansion to give a non-zero result [5]. However, the Peclet number may still be quantified and, assuming the critical Peclet number of 10 is still valid, it can be used to identify the high loss spaces and which spaces are closer to isothermal or adiabatic.

As an example, the Peclet numbers were calculated for the alpha Stirling Sage model. This model has a COP of 1.67 when running with the temperature limits of $T_{cold} = 243$ K and $T_{hot} = 303$ K. The volume, wetted area, and respective Peclet numbers for each component are listed in Table 3. The operating frequency was set to 60 Hz, which is approximately the frequency for which the largest cooling effect is achieved.

Table 3. Dimensions and local Peclet number for each space in the alpha Stirling Sage model.

Component	Volume [m ³]	Wetted Area [m ²]	Hydraulic Diameter [m]	Local Peclet Number Pe_w
Compression	3.196×10^{-6}	0.001253	0.0102	25.36
Expansion	3.196×10^{-6}	0.001253	0.0102	44.42
Rejector	1.55×10^{-6}	0.01095	0.000566	0.0802
Absorber	1.388×10^{-6}	0.009807	0.000566	0.1264
Regenerator	4.156×10^{-6}	0.07125	0.0002333	0.0167

The local Peclet numbers in Table 3 all fall either well below or well above $Pe_{\omega} = 10$, with the highest local Peclet numbers being those within the expansion and compression spaces of 44.42 and 25.35, respectively. The local Peclet numbers within all the heat exchangers are very low, all being well under 1. With the ability to quantify local Peclet numbers, the question that arose was: if one was able to change the local Peclet number, would this minimise hysteresis loss and increase the overall COP?

The Peclet number in each space was calculated over the range of operating frequencies, from 1 to 100 Hz. The net heat transfer in each space as well as the overall COP is plotted vs the local Peclet number in Figure 4 a-e. The COP also does not appear to have a correlation with heat transfer in any separate space, which means that a combination of other phenomena has a larger effect on the COP than the Peclet number or heat transfer within separate components.

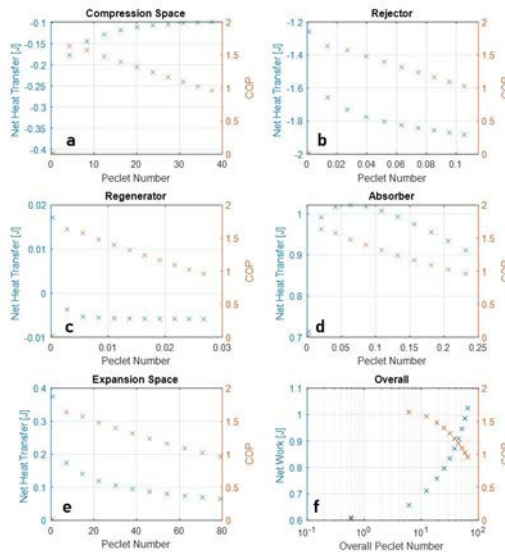


Figure 4. Heat transfer and COP vs Peclet number in the alpha Sage model.

The overall Peclet number of the system was also calculated by using the overall hydraulic diameter and a mass-weighted thermal diffusivity to account for the variation in thermal diffusivity and amount of gas in each space. The net P-V work input to the system and COP is plotted against the overall Peclet number in Figure 4f.

There does not appear to be a relationship between the net P-V work and COP when compared to the mass weighted overall Peclet number. This, along with the previous insights regarding net heat transfer and local Peclet numbers, shows that while spaces can be identified which operate in the isothermal or adiabatic regions with the Peclet number, the Peclet number alone is not a sufficient quantity to use as a design tool to minimise hysteresis loss to increase the COP of a Stirling refrigerator.

Quantifying Hysteresis Loss

Figure 5 shows a schematic of net heat transfer over one cycle for the single cylinder regenerator model obtained in Sage. This schematic allows a more complete understanding of the magnitudes and directions of heat flows within the system. It separates the system into its three levels: the gas level, the fin/matrix level, and the wall level. To be consistent with the first law, the net heat transfer in between each level must equal the net P-V work in. Likewise, the sum of heat flow in and out of each individual block must be zero.

It can be seen from Figure 5 that the piston inputs P-V work into the cylinder and adjacent regenerator gas. The heat then transfers through the matrix, the wall, and then to the ‘temperature source’, which is the Sage terminology for a heat source or sink at a set temperature; in this case, an ambient temperature of 27 °C. The cylinder wall conducts a small amount of heat back into the cylinder gas, but overall, there is a net P V work input that is equal to the sum of the heat transferred from the walls into the surroundings.

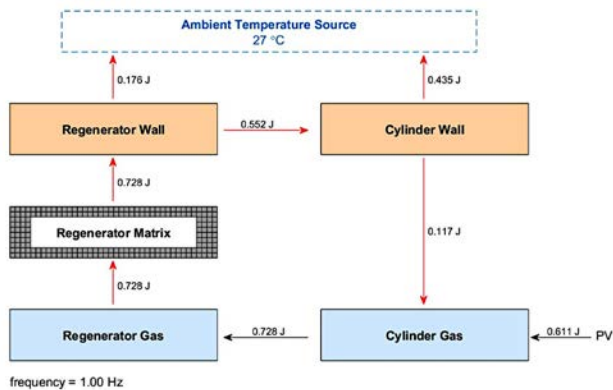


Figure 5. Local net heat transfer and overall COP vs Peclet number in the alpha Sage model.

Figure 6 shows a schematic of net heat transfer over one cycle for the alpha Stirling Sage model. As expected, the compression space has an overall work input while the expansion space has work output, as seen from the blue arrows. The work is transferred through the walls or through the gas in the form of heat. Heat is transferred through both the gas and walls in from the hot side (compression space) to the cold side (expansion space). The refrigeration effect comes from the heat transfer between the walls, fins, and gas.

Looking at each system and considering the first law for closed cycles reveals that no matter how many spaces there are, the net P-V work into the system will still equal the net heat out. In the case of the single cylinder experiment, the net heat out is simply the sum of heat lost and recovered during one cycle between the gas and the wall. In the case of a refrigeration system, the net heat out is the sum of the heat rejected into the hot space, and the heat absorbed from the cold space. No matter where the heat flows go within the system, the pressure phase is simply affected by the net heat flow between the system and the environment.

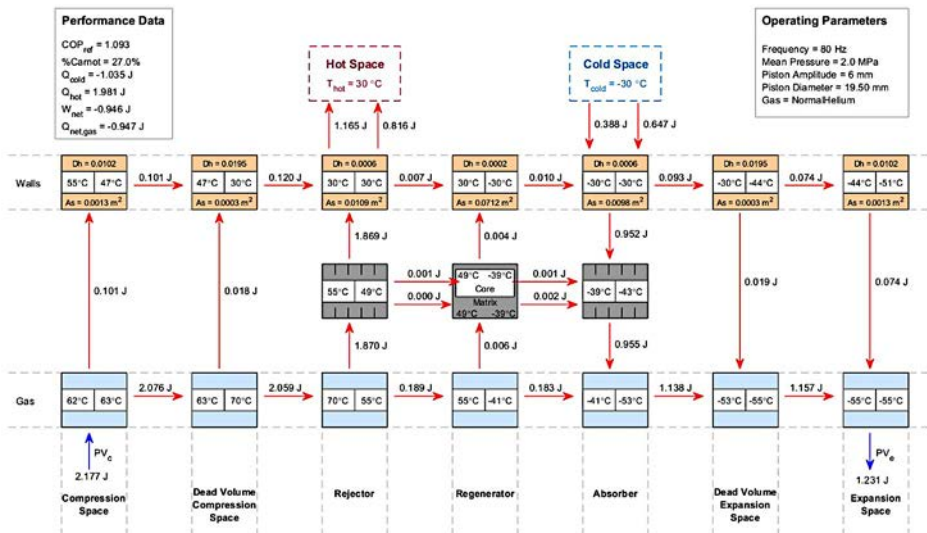


Figure 6. Schematic of net heat flow within the alpha Stirling refrigerator Sage model.

The effect of an ‘isothermal’ or ‘adiabatic’ gas was explored, by attempting to create an idealised working gas within Sage by setting the conductivity of the gas to either be extremely high or extremely low. The reason for this was to try to see the effect of the regenerator if the heat transfer was ‘ideal’. However, this resulted in inconsequential findings due to the cold and hot temperatures being fixed inputs in Sage, which always lead to heat conduction from the hot to the cold space, either through the wall or through the gas.

As in a real refrigerator, identifying and quantifying ‘hysteresis loss’ in this alpha Stirling Sage model is challenging. It cannot be assumed that the net heat transfer out of the gas is hysteresis loss, because the net heat transfer out of the gas is equal to the net P V work input. It is possible to accidentally account for a heat flow twice as two different losses, therefore over-quantifying the loss. For example, if the compression space and its dead volume has a net heat transfer into the walls from the gas, how much of that heat is being rejected into the hot space, and how much of that is being conducted through the walls as axial heat conduction loss to the cold space?

In an attempt to quantify hysteresis loss from the data given in Sage, it can be theorised that hysteresis loss can be attributed to the spaces in which net heat transfer is not beneficial, such as the regenerator, the compression space, and its respective dead volume. If this is the case, the hysteresis loss would be the sum of the net heat out (compression and its dead volume, and the regenerator) minus the net heat into the gas (expansion and its dead volume). In the case of Figure 5-31, the hysteresis loss could be quantified as follows:

$$Q_{\text{hysteresis}} = 0.101 + 0.018 + 0.006 - 0.019 - 0.074 = 0.032 \text{ J}$$

This means that out of the total 1.981 J of heat rejected into the hot space, 0.032 J of this is due to hysteresis, which is less than 2%. The hysteresis loss quantified in this way is plotted versus operating frequency in Figure 7. At some frequencies (10 and 20 Hz), the hysteresis loss is not a loss at all – there is a net heat flow into the gas. Interestingly, these correspond to the points of maximum COP, as seen in Figure 8. While the Sage data does not show much in terms of net heat transfer changing in each space for that range, the rejector heat transfer amplitude peaks between 10 and 20 Hz, which could influence the COP. Further study into this net heat gain by the gas should be carried out.

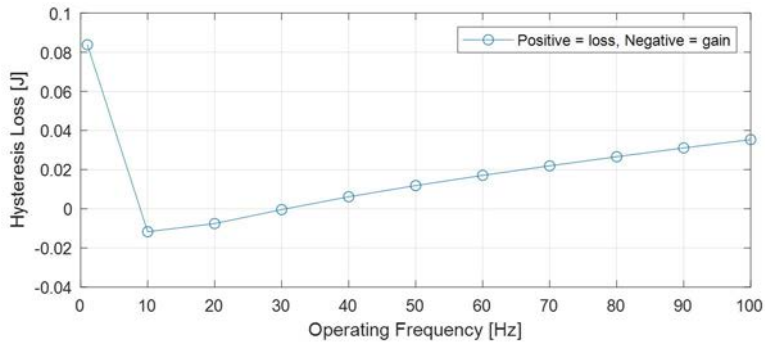


Figure 7. Hysteresis loss vs operating frequency.

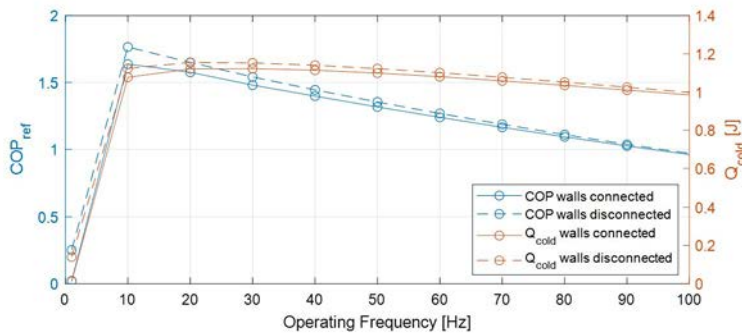


Figure 8. COPref and Qcold for alpha Stirling Sage model, with and without hysteresis loss.

Figure 8 also shows that, if there is no heat flow between the gas and the walls of the compression/expansion spaces and the dead volumes, both COP and heat absorbed from the cold space increase. This was done by removing the heat flow connections between the walls and the working gas within those spaces. It can be noted that as the operating frequency increases, the hysteresis loss decreases to negligible values due to the system behaving more adiabatically. At 10 Hz, where the COP is largest, there is only a 7.3% increase if the heat flow connections are removed.

Conclusion

Through Sage modelling of a Stirling refrigerator, it was found that the relationship between the pressure phase shift and net P-V work is the same as that of a single space

model, and is therefore not indicative of hysteresis loss alone, and reinforces that the pressure phase shift is an inherent first-law phenomenon.

The Peclet number was calculated for each space using their respective hydraulic diameters and evaluated in terms of its suitability in predicting hysteresis loss. In addition, hysteresis loss was theorised to be the net heat transfer from spaces which do not require net heat transfer, such as dead volume and the expansion and compression spaces. It was found that if hysteresis loss is quantified in this way, it only contributes to a small difference in COP when an alpha Stirling refrigerator is simulated running within the near-ambient temperature limits. The reason for hysteresis loss being negligible in Stirling refrigerators could be due to the isothermally present presence of the regenerator, which has a large surface area and high heat capacity.

References

- [1] Lee, K.P., J.L. Smith, and H.B. Faulkner. Performance loss due to transient heat transfer in the cylinders of Stirling engines. in 15th Intersociety Energy Conversion Engineering Conference. 1980. Seattle, Washington: The American Institute of Aeronautics and Astronautics.
- [2] Scheck, C.G., Thermal Hysteresis Loss in Gas Springs, in Engineering and Technology. 1988, Ohio University: Ohio, USA.
- [3] Chafe, J.N., A Study of Gas Spring Heat Transfer in Reciprocating Cryogenic Machinery, in Dept. of Mechanical Engineering. 1988, Massachusetts Institute of Technology: Massachusetts, USA.
- [4] Kornhauser, A.A., Gas-Wall Heat Transfer During Compression and Expansion, in Dept. of Mechanical Engineering. 1989, Massachusetts Institute of Technology: Massachusetts, USA.
- [5] Kornhauser, A.A. and J.L. Smith, The Effects of Heat Transfer on Gas Spring Performance. *Journal of Energy Resources Technology*, 1993. 115: p. 70-75.
- [6] Orłowska, A.H. and G. Davey, Measurement of losses in a Stirling cycle cooler. *Cryogenics*, 1987. 27: p. 645-651.
- [7] Wang, A.C.-M., Evaluation of gas spring hysteresis losses in Stirling cryocoolers, in Department of Mechanical Engineering. 1988, Massachusetts Institute of Technology.

- [8] Cooke-Yarborough, E.H. and D.J. Ryden, Mechanical Power Losses Caused by Imperfect Heat Transfer in a Nearly-Isothermal Stirling Engine, in 20th Intersociety Energy Conversion Engineering Conference. 1985. p. 3.307-3.312.
- [9] Lee, K.P., A Simplistic Model of Cyclic Heat Transfer Phenomena in Closed Spaces. Proceedings of the 18th IECEC, 1983: p. 720-723.
- [10] Pourmovahed, A. and D.R. Otis, Effects of Thermal Damping on the Dynamic Response of a Hydraulic Motor-Accumulator System. Journal of Dynamic Systems, Measurement, and Control, 1984. 106: p. 21-26.
- [11] Nikanjam, M. and R. Greif, Heat transfer during piston compression. Journal of Heat Transfer, 1978. 100: p. 527-530.
- [12] Foster-Miller Associates, I., Design and development of Stirling engines for stationary power generation applications in the 500 to 3000 horsepower range. 1980: United States.
- [13] Kornhauser, A.A. and J.L. Smith, A Comparison of Cylinder Heat Transfer Expressions Based on Prediction of Gas Spring Hysteresis Loss. Fluid Flow and Heat Transfer in Reciprocating Machinery, ASME, 1987.
- [14] Bailey, P., et al., Gas Spring Losses in Linear Clearance-Seal Compressors. 2007.
- [15] Willich, C., C.N. Markides, and A. White, J., An investigation of heat transfer losses in reciprocating devices. Applied Thermal Engineering, 2017. 111: p. 903-913.
- [16] Park, J.S. and H.-M. Chang, A Stirling Cycle Analysis with Gas-Wall Heat Transfer in Compressor and Expander, in Cryocoolers 9, R.G. Ross, Editor. 1997, Springer US: Boston, MA. p. 147-156.
- [17] Getie, M., et al., Investigation of thermal and fluidic losses and their effect on the performances of a Stirling refrigerator. 2021. 2.
- [18] Getie, M., et al., A non-ideal second order thermal model with effects of losses for simulating beta-type Stirling refrigerating machine. International Journal of Refrigeration, 2021. 130: p. 413-423.
- [19]. Wang, S., et al., A Potential Method to Predict Performance of Positive Stirling Cycles Based on Reverse Ones. Energies, 2021. 14(21): p. 7040.

[20] Yang, D., The pressure-volume relationship and hysteresis loss in Stirling refrigerators, in Department of Mechanical Engineering. 2023, Auckland University of Technology: Auckland, New Zealand.

Simple Prediction method of Gas Temperature for Stirling Engine

Fujio Toda^{a,*}, Mari Matsubar^{a,b} Takasi Ishijima^c

a Utsunomiya University 350 Minemachi Utsunomiya,321-8505, Japan, Fomer Professor,
ftodafujio@outlook.jp

b Japan, Professor

c Japan, Assistant Professor

*Corresponding author: ftodafujio@outlook.jp

Keywords: Gas tmperature, Engine performance Analysis, Thermodynamic modelling and simulation

Abstract

In this paper propose new simple prediction method in cylinder gas temperature which allow the rapid and accurate calculation of boundary surface gas temperature in to the heat exchanger (expansion space, heater, regenerator, cooler and compression space) in crank-driven Stirling engine, basis of temperature effectiveness. These model Equation can be calculated only main dimension of Stirling engine. In these equations main necessary factor the compression ratio ϵ and heat transfer unit number NTU , overall heat transfer coefficient K and mean mass flow rate \bar{m} , Reynolds number Re, Nusselt number Nu, Prandtl number Pr [1].

It is possible that this analytical method quickly calculates gas temperature by giving the engine speed. It does not diverge like the quasi-steady flow model [2]. Moreover, it is possible to obtain the value which is approximate to the measured value[3].

Stirling engine can be operated relatively by many kinds of low temperature heat sources as energy of fossil fuel, solar radiation, biogas, geothermal and exhaust heat sources [4]. The authors first designed and developed low temperature difference Stirling engine for global environment which can generate 100W of shaft power with heat source 130 °C. And temperature ratio is 0.8 [5]. Therefore, we conducted an experiment to demonstrate a simple method for predicting gas temperature using a Stirling engine that can be operated at low-level heat source temperatures such as geothermal heat and exhaust heat [6].

Introduction

Isothermal analysis models and adiabatic analysis models based are used as performance analysis methods for Stirling engines. Research to date has shown that relatively effective performance analysis is possible with this model. However, the isothermal analysis model and the adiabatic analysis model [7], [8] require an expansion space, a compression space, and the temperature of the working gas in the heater and cooler. In design, it is virtually impossible to accurately predict the internal gas temperature, the

effect of regenerator efficiency, or the effect of temperature drop on the working gas when changing the compression ratio. As an analysis method that takes these effects into consideration, analysis using a quasi-steady flow analysis model is required. However, the quasi-steady flow analysis model is an analysis method based on numerical integration, and the analysis requires time, and if reliable initial calculation conditions are not provided, the analysis is likely to diverge. Furthermore, it is not suitable for predicting performance in the early stages of design or considering the effects of heat exchanger settings.

Analysis method

Figure 1 shows the analytical model. Changes in estimated gas temperature at each element within the engine are also shown. The change in working gas temperature of each heat exchanger is expressed by equation (1) using temperature efficiency E [9].

$$T_{out} = E \cdot (T_w - T_{in}) \quad (1)$$

Here, T_{in} : heat exchanger inlet temperature, T_{out} : heat exchanger outlet temperature, T_w : heat exchanger wall temperature, E : temperature efficiency.

Furthermore, when using the assumption that the working gas temperature changes adiabatically in high-temperature and low-temperature spaces, the temperature change is expressed by the following equation using the engine's compression ratio ϵ .

$$T_{out} = \epsilon^{1-\kappa} \cdot T_{in} \quad (2)$$

$$T_{out} = \epsilon^{\kappa-1} \cdot T_{in} \quad (3)$$

Equation (2) represents the case of adiabatic compression, and Equation (3) represents the case of adiabatic expansion. Here, T_{in} : high and low temperature space inlet temperature, T_{out} : high/low temperature space exit temperature, κ : specific heat ratio. Using these relational expressions, determine the gas temperature at each interface

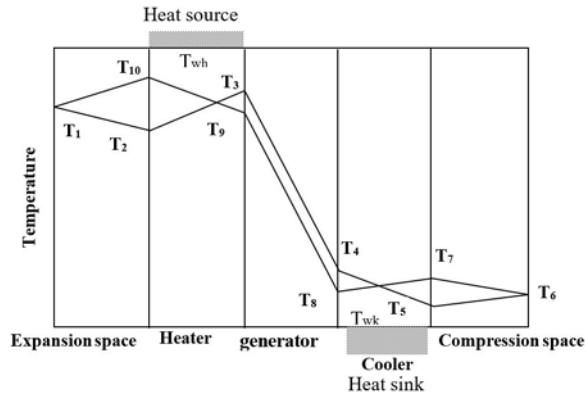


Figure 1. Estimated temperature distribution of each space gas.

Figure 1 shows T_1 is the representative gas temperature in the expansion space. The working gas passes through the heater at $T_2 \rightarrow T_3$ and is heated, passes through the regenerator at $T_3 \rightarrow T_4$ and stores heat in the regenerator wire mesh, and then passes through the cooler at $T_4 \rightarrow T_5$ to be cooled. This is the flow of working gas in the iso volume cooling stroke. Next, the working gas will be compressed in the adiabatic compression stroke, but it is assumed that the working gas in the compression space changes adiabatically without exchanging heat with the outside. Also, temperature changes of the working gas existing in each heat exchanger are not particularly considered. Next, the working gas passes through a cooler and is cooled in the heating stroke from T_7 to T_8 , receives the stored heat as it passes through the regenerator at T_8 to T_9 , and is heated by a heater at T_9 to T_{10} . The heated working gas undergoes an adiabatic change within the expansion space. The relationship between gas temperature changes inside the heat exchanger is shown below using temperature efficiency.

$$T_1 = (T_2 + T_{10})/2 \quad (4)$$

$$T_3 = T_2 + (T_{wh} - T_2) \cdot E_h \quad (5)$$

$$T_4 = T_3 - (T_3 - T_{wr2}) \cdot E_r \quad (6)$$

$$T_5 = T_4 - (T_4 - T_{wk}) \cdot E_k \quad (7)$$

$$T_6 = (T_5 + T_7)/2 \quad (8)$$

$$T_8 = T_7 - (T_7 - T_{wk}) \cdot E_k \quad (9)$$

$$T_9 = T_8 + (T_{wr1} - T_8) \cdot E_r \quad (10)$$

$$T_{10} = T_9 + (T_{wh} - T_9) \cdot E_h \quad (11)$$

$$T_{wr1} = (T_3 + T_9)/2 \quad (12)$$

$$T_{wr2} = (T_4 + T_8)/2 \quad (13)$$

Here,

Eh: temperature efficiency of the heater,

Er: temperature efficiency of the regenerator,

Ek: temperature efficiency of the cooler,

Twr1: average temperature of the regenerator on the heater side,

Twr2: average temperature of the regenerator on the cooler side,

Twh : Wall temperature of heater,

Twk: Wall temperature of cooler.

Furthermore, assuming that the gas temperature in the expansion space and compression space changes adiabatically, it can be expressed by the following equation using the compression ratio ε of the engine.

$$T_1 = T_{10}(1 + \varepsilon^{1-\kappa})/2 \quad (14)$$

$$T_6 = T_5(1 + \varepsilon^{\kappa-1})/2 \quad (15)$$

By solving these simultaneous equations, the working gas temperature T_1 in the expansion space is given by the following equation.

$$T_1 = \frac{\alpha_{wh} \cdot T_{wh} + \alpha_{wk} \cdot T_{wk}}{\alpha_1} \quad (16)$$

here,

$$\alpha_1 = 2 \cdot [(1 + z_r^2) + \varepsilon_1 \cdot z_h^2 \cdot (1 + z_r) \cdot E_r - \varepsilon_2 \cdot E_r \cdot (1 + z_r) \cdot z_k^2 + \varepsilon_1 \cdot \varepsilon_2 \cdot (4 \cdot z_r^2 - E_r^2) \cdot z_h^2 \cdot z_k^2] + \varepsilon_2 \{4 \cdot z_h \cdot z_r^2 - E_r^2 \cdot z_h - E_r \cdot (1 + z_r)\} \cdot E_h \cdot z_k^2$$

$$\alpha_{wk} = 2 \cdot \varepsilon_1 \cdot E_k \cdot z_h \cdot z_r \cdot (1 + z_r) (1 + \varepsilon_2 \cdot z_k)$$

however,

$$\varepsilon_1 = \varepsilon^{1-\kappa}, \quad \varepsilon_2 = \varepsilon^{\kappa-1},$$

$$Z_h = 1 - E_h, \quad Z_r = 1 - E_r, \quad Z_k = 1 - E_k$$

In this way, the average gas temperature within the expansion space can be determined. By finding one of the temperatures T_1 to T_{10} , the gas temperature at the interface can be calculated at any time using equations (3) to (15). After determining the expansion space temperature and compression space temperature, it can be used for the 2nd-order

isothermal analysis model [10,11] and the adiabatic analysis model by providing the gas temperature obtained by analysis.

Temperature efficiency of heaters and coolers

The temperature efficiency E of heaters and coolers is simply expressed by the following formula using the heat unit transfer number NTU (number of units) [12].

Heater, cooler:

$$E_{h,k} = 1 - e^{-NTU_{h,k}} \quad (17)$$

$$NTU_{h,k} = \frac{h_{h,k} \cdot S_{h,k}}{\dot{m}_{h,k} \cdot c_p} \quad (18)$$

$$h_{h,k} = Nu \frac{\lambda_{h,k}}{d_{h,k}} \quad (19)$$

Here, $h_{h,k}$ is the turbulent heat transfer coefficient in the circular tube of the heater and cooler (the heat transfer rate is used from the outer wall of the tube), $S_{h,k}$ is the surface area. of the heater and cooler in contact with the working gas is the average mass flow rate per unit time passing through the heater or cooler, c_p is the specific heat at constant pressure, and Nu is the Nusselt number (a dimensionless number expressing the magnitude of the heat transfer coefficient). NTU is a dimensionless number that indicates the heat exchange capacity of the heat exchanger, and the larger the value, the better the performance.

The heat transfer rate of the heater and cooler is calculated based on the difference between the surface temperature of the heater and the internal wall temperature of the engine.

Regenerator temperature efficiency

The temperature efficiency E_r of the regenerator is given by the following equation.

$$E_r = \frac{NTU_r}{NTU_r + 1} \quad (20)$$

In addition, NTU_r is derived by the following formula.

$$NTU_r = \frac{h_r \cdot S_r}{c_p \cdot \frac{\bar{m}_r}{2} \cdot \frac{N}{60} \cdot 2} \quad (21)$$

When calculating the heat transfer coefficient h_r , it is common to convert it to the Nusselt number Nu and express it as a function of the Reynolds number Re.

NTU uses the average value of one cycle for mass flow rate. The gas flow rate is also the average gas flow rate for one cycle.

Evaluation equation for heat transfer coefficient using wire mesh

i) The formulas for defining the Nusselt number and Reynolds number when the wire diameter of the wire mesh is the representative length of the laminated wire mesh are shown below.

$$h_r = Nu_r \cdot \frac{\lambda}{d_r} \quad (22)$$

$$Re = \frac{\bar{u}_r \cdot d_r}{\nu} \quad (23)$$

Here h_r is the heat transfer coefficient in the regenerator, d_r is the diameter of the wire mesh, λ is the thermal conductivity of the working gas, and is the average value of the gas flow rate in the regenerator during one cycle. The experimental evaluation formula for Tanaka's Nusselt number is shown below.

ii) Empirical formula for unsteady reciprocating flow

Tanaka et al.'s experimental formula [13].

$$Nu_r = 0.24 \cdot Re^{0.67} \quad (5 < Re < 120) \quad (24)$$

This experiment uses three types of wire mesh of 50, 100, and 200 mesh, and the variation in each experimental value of this experimental formula is -13 to +20%.

iii) Mass flow rate

The average mass flow rate in each heat exchanger can be determined using the following relational expression.

$$\bar{m} = \rho \cdot F_A \cdot \bar{u} \quad (25)$$

Here, ρ is the density of the working gas, F_A is the gas passage area of each element of the heat exchanger, and \bar{u} is the average flow rate of the working gas.

iv) Working gas density

The working gas density ρ can be calculated using the following formula.

$$\rho = p / (R \cdot T) \quad (26)$$

Here, p : pressure inside the cylinder, R : gas constant [for air; 286.84J/kg·K], T : gas temperature inside the cylinder.

v) Gas passage area of each heat exchanger element

Since heaters and coolers often use pipes, the cross-sectional area is the total number of pipes.

vi) Working gas flow rate

For the working gas flow rate, use the gas flow rate given in Reference [14],[15].

(a) Flow loss work in heater $W_{\text{loss.h}}$

$$\begin{aligned} W_{\text{loss.h}} = C_h S_{DP} r_{DP} \left[\frac{\pi A_h (1 - \lambda)^2}{\lambda D} \sin(\phi + \Delta\theta) + \frac{2\pi \lambda B_h \sin \Delta\theta}{A + D} \right. \\ \left. + \pi D_h \left\{ \frac{(D - A)(\lambda - 1)^2}{D^2} \sin(2\phi - \phi_h - \pi + \Delta\theta) \right\} \right. \\ \left. + \frac{2\lambda \sin \phi}{A + D} \cos(\phi - \phi_h - \pi + \Delta\theta) \right] \quad (27) \end{aligned}$$

$$\text{However } \lambda^2 = \frac{A + D}{A - D}$$

(b) Flow losses in the regenerator $W_{\text{Floss.r}}$

$$\begin{aligned} W_{\text{Floss.r}} = C_{r1} S_{DP} r_{DP} \int_0^{2\pi} G_{r1}(\theta) \sin(\theta + \Delta\theta) d\theta \\ + C_{r2} S_{DP} r_{DP} \int_{\phi_1}^{\phi_2} G_{r2}(\theta) \sin(\theta + \Delta\theta) d\theta \quad (28) \end{aligned}$$

(c) Flow losses in the cooler $W_{loss,k}$

$$\begin{aligned}
W_{loss,k} = C_k \cdot S_{DP} \cdot r_{DP} & \left[\frac{\pi A_k (1-\lambda)^2}{\lambda D} \sin(\phi + \Delta\theta) + \frac{2\pi\lambda B_k \sin \Delta\theta}{A+D} \right. \\
& + \pi D_k \left\{ \frac{(D-A)(\lambda-1)^2}{D^2} \sin(2\phi - \phi_k - \pi + \Delta\theta) \right. \\
& \left. \left. + \frac{2\lambda \sin \phi}{A+D} \cos(\phi - \phi_k - \pi + \Delta\theta) \right\} \right] \quad (29)
\end{aligned}$$

(d) Analysis method of flow loss work

$$\begin{aligned}
W_i &= \int_0^{2\pi} (p - \Delta p) dv \\
&= \int_0^{2\pi} p dv - \int_0^{2\pi} \Delta p dv \\
&= W_{is} - W_{Floss} \quad (30)
\end{aligned}$$

(e) Total flow loss

$$W_{loss} = W_{loss,h} + W_{loss,r} + W_{loss,k} \quad (31)$$

Plot type Low Temperature Difference Stirling Engine

Structure of Engine

Figure 2 shows 100W class low temperature difference Stirling engine, and table 1 shows the specifications[3],[15],[16]. This engine is γ type engine composed of power piston, displacer and flywheel [2]. The bore of the displacer piston is 800mm, and stroke is 80mm. Considering adiabaticity, the material was made to be the foamed polyurethane. The experimental conditions are shown at table 2. It is features to apply the pressure to the engine inside in the low temperature difference Stirling engine as first trial. By this system, it is possible that the performance of the low temperature difference Stirling engine is improved epoch-making. Figure 3 shows the experimental equipment system.

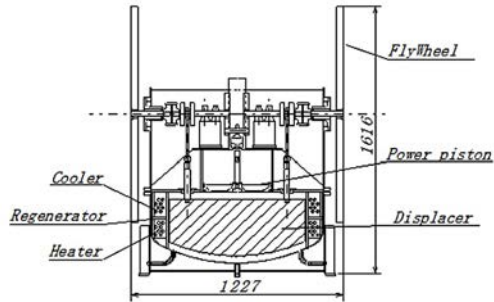


Figure 2. 100W Class Low Temperature Difference Stirling Engine.

Table 1 Engine specifications.

Power piston	Bore mm Stroke mm Swept volume cc Drive mechanism	400 100 12566 Scotch Yoke
Displacer piston	Bore mm Stroke mm Swept volume cc	800 80 40212.4
Heater and Cooler	Type Material Number of tubes Pitch of Fin mm	Fin tube Copper 8 3.2
Regenerator	Material Mesh	Brass wire cloth 50

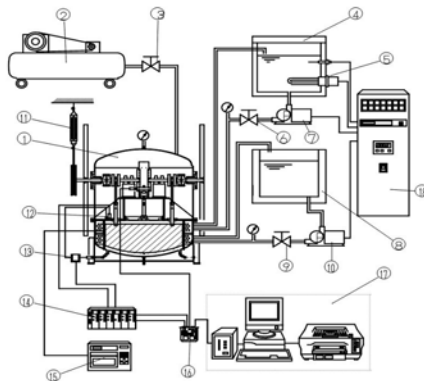


Figure 3. Configuration of the experimental setup.

Table 2. Experimental Conditions.

Heat source:	Fluid material Temperature Flow volume	Ethren glycol 130 °C 20 l/min
Heat sink:	Fluid material Temperature Flow volume	Water 15 °C 20 l/min
Buffer pressure	kPa	101.3

Table 3. Experimental equipment system.

1) Test engine 2) Air compressor 3) Pressure control valve 4) Constant temperature water bat 5) Heater for heat source 6) Flow control valve 7) Pump for heat source 8) Water Bath 9) Flow control valve	10) Pump for coolant Water 11) Spring balancer 12) Pressure transducer of cold 13) Differential pressure gauge 14) Strain amplifier 15) Hybrid recorder 16) A/D converter 17) Personal computer 18) Central control panel
--	---

Calculation results and discussion

The calculations were performed on a prototype 100W class low-temperature difference Stirling engine.

Figure 4 shows the calculations were performed on a prototype. This is the change in each space gas temperature calculated using this analysis method. Since almost the same results as in Figure 1 were obtained, this analysis method is considered to be an effective simulation method. It can be seen that the insulation changes between the heating space and the compression space.

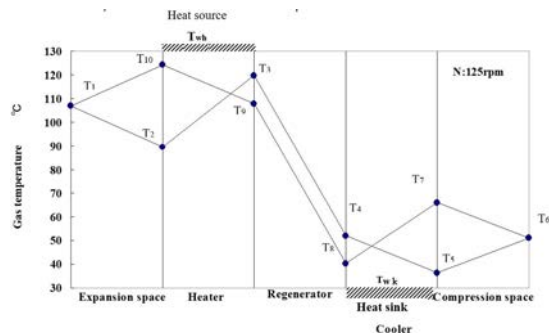


Figure 4 Results of simple gas temperature estimation method.

Figure 5 shows a comparison of the calculated and measured values of the expansion chamber gas temperature and compression chamber gas temperature using a test engine. In the experiment, hot water with a temperature of 127 °C was used as the high heat source temperature, and cold water with a temperature of 35 °C was used as the low-temperature heat source. Calculations were made using both heat source temperatures. The high temperature side gas temperature is calculated to be slightly lower. Also, the gas temperature on the low-temperature side is calculated to be slightly higher. However, the calculated results and the measured values show almost the same changes, indicating that the present analysis method simulates the measured values well even when the engine speed changes.

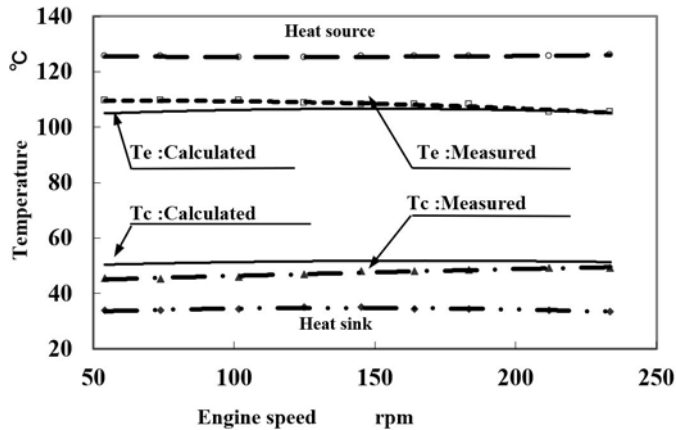


Figure 5 Comparison with analysis value and measured value of gas temperature.

Original Shaft power analysis model

Figure 6 shows the shaft power analysis model using the original isothermal model and mechanism efficiency. High heat sources are represented as heat sources, and low heat sources are represented as heat sinks. The thermal inner wall temperature is expressed as T_{wh} , and the low thermal inner wall temperature is expressed as T_{wc} . From the inner wall temperature (T_{wh}), the amount of heat Q_1 is supplied into the engine. The working gas is affected by the heat transfer coefficient, and the working gas temperature decreases to T_h and T_c . This calculation method is widely known as the Schmidt cycle.

This analytical model uses the second method analytical formula [18] that takes gas flow into account for this Schmidt cycle. This analytical method can usually be calculated using thermodynamic methods. This analysis method uses the mechanism effectiveness proposed by J.R. Senft, [19, 22], which can calculate shaft power. Details were announced at the 16th ISEC Conference in Bilbao, Spain.

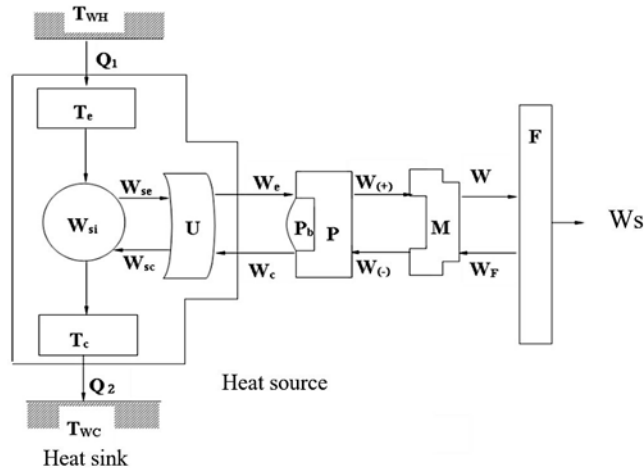


Figure 6 Analysis model of Shaft power.

Comparison of simple gas temperature analysis method and actual measurements

Figure 7 shows calculated values calculated using the simple gas temperature analysis method and actual measured values. If you look closely, you can see some differences between the low rotation speed range and the high rotation speed range. It does not take into account anything other than flow losses. The temperature on the expansion side and the temperature on the compression side show an adiabatic change [23]. Therefore, this analysis method is one of the effective analysis methods for Stirling engine simulation.

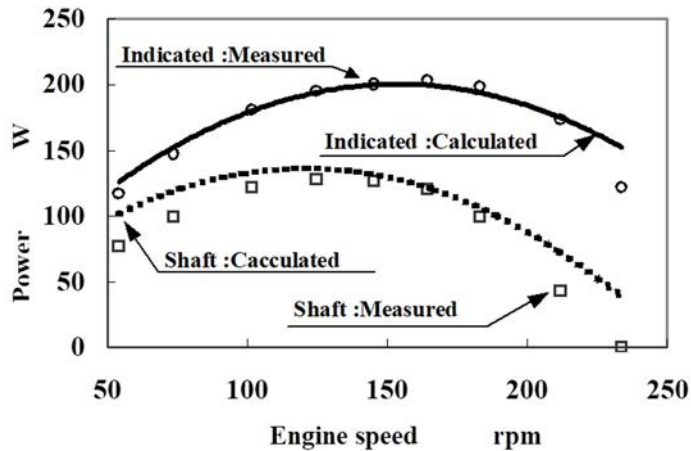


Figure 7 Comparison of calculated value and measured value of shaft power.

Conclusion

We devised an original simple gas temperature estimation method and clarified the following.

1. This analysis method is one of the new analysis methods for Stirling engine.
2. We were able to represent the gas temperature at each interface within the engine, including the regenerator, as a distribution temperature.
3. The analytical distribution method using temperature efficiency can almost accurately predict the expanding gas temperature and the compressed space gas temperature.
4. As a result of a comparative study with a 100W class low temperature difference Stirling engine, we were able to express the actual measured values almost accurately.

References

- [1] F.Toda, et al., "Heat transfer and balance on a small Stirling Engine", 5th ISEC, pp.335-340 1991.
- [2] Israel Urieli, David M Berchowitz, "Stirling Cycle Engine Analysis", JW Arrowsmith LTD, pp.102-167, (1984).
- [3] Shoichi Iwamoto, Fujio Toda, Shinji Suzuki, Dynamic characteristics of 100W class low temperature difference Stirling engine, Japan Society of Marine Engineers, 56th Academic Conference pp.118 122, 1996.

- [4] F.Toda, et al., "Development of Low Temperature Difference Stirling Engine" 17th ISEC pp.286-292, 2016.
- [5] F.Toda, et al., "Development of 300W Class Low Temperature Difference Stirling Engine" IAEC'95, 7th pp.437-442, 1995.
- [6] F.Toda, et al., "Development of Low Temperature Difference Stirling Engine" 6th ISEC pp.471-476, 1993.
- [7] Israel Urieli, David M Berchowitz, Stirling Cycle Engine Analysis, JW Arrowsmith LTD, pp.20-49, (1984)
- [8] Israel Urieli, David M Berchowitz, Stirling Cycle Engine Analysis, JW Arrowsmith LTD, pp.87-97, (1984).
- [9] Kaneyasu Nishikawa, Yasunobu Fujita, Heat transfer, Rikogakusha Publishing p.369-377 (1989).
- [10] F.Toda, et al., "Development of 300W class Low Temperature Difference Stirling Engine" 7th ICSC, pp.437-442, 1995.
- [11] F.Toda, et al., "Performance Characteristics for Experimental Small Stirling Engine" M.E.S.J., Vol.18, No.1, p.25-30, (1990).
- [12] A.J Organ, Thermodynamic Design of Stirling Cycle Machines, Proc Instn. Mech Engrs., Vol.201, No.C2, pp.107-131, (1987) of Philosophy at the Massachusetts Institute of Technology, June, pp.287-292, (1981).
- [13] RC110 Research on optimal element design method of Stirling equipment suitable for global environment and various calorific values, Japan Society of Mechanical Engineers Research Cooperation Subcommittee Research Results Report, 36-50, (1994).
- [14] F. Toda, Shoichi Iwamoto, Proposal of the Performance analysis Stirling Engine, ISEC16, Bilbao-Spain, p.42, (2014).
- [15] F.Toda, et al., "Development of 300W class Low Temperature Difference Stirling Engine" 7th ICSC, pp.437-448 (1995).
- [16] F.Toda, et al., "Performance Characteristics for Experimental Small Stirling Engine" M.E.S.J., Vol.18, No.1, (1990), p.25.

- [17] J.R.Senft, "Buffer Pressure Effects in Stirling engines", 5th ICSE, pp.1-8, (1988).
- [18] J.R.Senft, "An Ultra Low Temperature Differential Stirling Engine", 5th, International Stirling Engine Conference,), p.1, (1991).
- [19] J.R.Senft, "Limits on the mechanical efficiency of heat engine", 22nd ,Intersociety energy Conversion Engineering Conference, Paper#879071,Philadelphia, (1987).
- [20] Hiroshi Sekiya, Numerical analysis and mechanism of Stirling engine Part B 56-527 p.2121, (1990).
- [21] Akihiko Hakuzu and (2 others), "Characteristic analysis of Stirling engine (first report)" Part B 48-428 pp.1753-1760, (1982).
- [22] J.R.Senft, "Buffer Pressure Effects in Stirling engines", 4th ICSE, pp.20-50, (1988).
- [23] Theodor Finkelstein, "Thermodynamic Analysis of Stirling Engines", J.SPACECRAFT, pp. 4-9, (1967).

Artificial Intelligence Applications for Stirling Engines Development: a mini-review

F.S. Marra^{a,*}, L. Acampora^b

a Istituto di Scienze e Tecnologie per l'Energia e la Mobilità Sostenibili, CNR, Italy

b Energy Technologies and Renewable Sources Department (TERIN) - ICT Division, ENEA, Portici, Italy

***Corresponding author:** francescosaverio.marra@stems.cnr.it

Keywords: Artificial intelligence, Machine learning, Neural networks, Deep learning, Model reduction

Abstract

The Stirling engine continues to be developed, and numerous advanced variants have been proposed since its introduction. These variants are specifically developed to be used in diverse applications, from electrical or mechanical power generation to heating and cooling, and to be used with different energy sources. To correctly design all these variants and determine the optimal configuration several theoretical and modeling approaches have been developed. However, accurate performance prediction of a Stirling engine is challenging because sophisticated modeling approaches that balance accuracy with computational efficiency are required.

Recently, Artificial Intelligence (AI) models have emerged as promising tools for performance prediction and optimization of Stirling engines. This mini-review synthesizes the existing literature on AI applications in Stirling engine development and optimization. It starts with an overview of relevant AI methodologies, followed by a detailed survey of AI-based modeling efforts categorized by their objectives. Implementation details of these AI methods are discussed to provide insights into their application processes.

Introduction

Despite the so many years passed since the appearance of the Stirling machine, its technological progress is still far from being exhausted. Numerous variants have been suggested, and the categorization into alpha, beta, and gamma types fails to encompass all the additional variations inspired by the fundamental operating principle of the original Stirling engine. Moreover, this machine can be used to realize, with a proper combination of primary energy source and engine components, different applications. These applications primarily involve converting thermal energy into mechanical energy and transforming mechanical energy into cooling, spanning a range of energy qualities from high-temperature sources to waste heat sources, and from refreshing to deep

cooling processes.

Several approaches have been developed to predict the performances of all these possible applications. With this respect, a further classification arose which distinguishes the modelling approaches based on the level of detail adopted in the description of the spatial and temporal evolution of the state of the engine [1].

The common task of these models is always to predict the main performances that can be obtained in a specific application characterized by design variables, energy source parameters, operating and environmental conditions, and ageing of the engine components.

Obtaining accurate predictive modeling of the engine capable of taking into account all these variables is a very difficult task. This task is further complicated by the contrasting needs of achieving high accuracy while simultaneously requiring low computation (or simulation) times for design optimization and real-time control. A Stirling engine (SE) is inherently complex in structure and in the manufacturing process. Several coupled non-linear processes, including thermal, mechanical, and electromagnetic interactions, as well as several nonlinear losses, contribute all together to establish real performances. Engineering technical problems such as thermal and mechanical losses, gas leakage, and lubrication add further uncertainties to the prediction. As a result, the model predictions depend on many factors, such as the operating conditions, structural parameters, thermos-physical properties of the working fluid, and the forms of the energy sources. Therefore, while complete and accurate models are very complex and difficult to solve, the simplest ones result in poor predictive capabilities [2].

In recent years, a new class of models is emerging, which derive from the application of Artificial Intelligence (AI) approaches to the modeling of SEs. The use of Neural Network modelling of SE in comparison or hybridized with other soft computing methods like Genetic algorithm, Particle Swarm Optimization, and Fuzzy Logic, has also been recently reviewed [3].

Being the AI-based models not yet very common in the community of SE developers, this work intends to review the main contributions proposed in the literature. To facilitate the lecture and to introduce the commonly adopted nomenclature and terminology, a brief description of the main branches of the AI approaches is first exposed. Readers already familiar with the AI methods could immediately skip this section. Then the

survey of the published literature reporting applications of AI methods to the Stirling engine technology is presented by attempting to organize the various contributions following the main task pursued. Then, some details on the implementation of the AI methods adopted in these contributions will be presented to illustrate the development procedure for applying these methods.

Description of AI methods

The discipline of Artificial Intelligence is nowadays very broad and includes a variety of approaches and techniques with different tasks.

This discipline encompasses all methods and algorithms that can learn from data and generalize to unseen data in order to replace classical modeling, which relies on developing a set of governing equations describing physical processes and then solving them using mathematical methods, often involving numerical solutions. More specifically the focus will be limited to the field of study in artificial intelligence known as Machine Learning (ML). The most well-known and widespread ML methods employ a model based on a pre-established set of universal equations that mimic the behavior of a network of neurons (Neural Network, NN) with “learning” capability. This model contains numerous parameters that enable the entire set of equations to adapt until it effectively transforms the input signal, representing the known (or measurable) parameters of the Stirling system, into the correct unknown variables.

As illustrated in Figure 1, any artificial neural network (ANN) consists of a network of simple mathematical relations called artificial neurons (or simply neurons) because they are based on the behavior of biological neurons [4]. The first model of neurons, called perceptron, was introduced theoretically in 1943 by McCulloch and Pitts and implemented about 15 years after by Rosenblatt [4].

Each neuron takes multiple inputs (e.g. $x = [x_1; x_2; \dots; x_m]$). These inputs are linearly combined by using some adjustable parameters (called weights $w = [w_1; w_2; \dots; w_m]$) and a bias b . Finally, this sum is passed through a nonlinear function f (called activation function) that generates the output of the neuron y . Mathematically, this process can be described by the relation:

$$y = f(w^T x + b)$$

In the original perceptron, the activation function proposed was a step function.

However, the derivatives of this function are 0 almost everywhere, limiting the capability of the perceptron to adapt to different situations and applications. Therefore, this function is not used anymore in practical applications but is replaced by other nonlinear smooth functions such as the sigmoid function, the hyperbolic tangent function, and the rectified linear (ReLU) function.

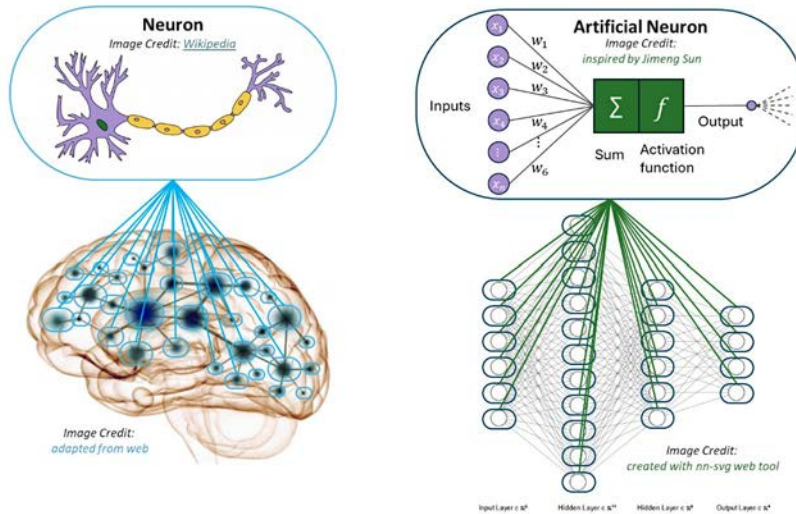


Figure 1. Illustration of the inspiring model of the Artificial Intelligence: on the left, a single neuron structure and the human brain formed by many interconnected neurons; on the right, a single artificial neuron and an Artificial Neural Network formed by many interconnected artificial neurons.

The modeling power of a single perceptron is very limited; it can work only for simple cases. Already in the 1960s, it was known that this simple model could be significantly enhanced by combining multiple perceptrons in certain ways. However, the lack of suitable computer resources and effective learning algorithms (the algorithms used to identify the weights of the neural network) have limited the development of AI algorithms for nearly three decades. Only in 1986, Rumelhart et al. [5] proposed a learning procedure for a network of neurons using the back-propagation algorithm. Under simple conditions, it has been proved that a well-structured and sufficiently large neural network can approximate, up to any arbitrary precision, any function [6]. A peculiar property of the ML approach, as previously anticipated, is represented by the

possibility to derive a model of the system analyzed without any knowledge about the physical processes acting in the system, by collecting info directly from experimental observations. The large number of observations to be collected in the whole span of range for each parameter of interest to develop a reliable ML model can represent a very demanding task.

In terms of required computational resources, not so many differences arise between ML approaches and classical modeling approaches. In classical modeling, the computational effort is spent to obtain the model's solution, and this effort must be repeated for any single realization of the simulations. It increases with the accuracy desired and the detail in the virtual representation of the Stirling engine. With the ML approaches, the computational effort is concentrated on the training of the Neural Network by processing the data collected from a large number of realizations (that could be obtained from experiments or again by means of numerical simulations). The advantage is gained in the retrieval stage of known input-output relations and the ability to correctly predict, with a further minimal computational effort, the input-output relationship for never seen input (a property called generalization). In unsupervised training, the network is structured with inputs only while both input and output data are provided in the supervised training technique. A concise but very effective overview of the terminology adopted and the different approaches available in applications related to energy engineering problems is available in [7].

For the purposes of the present review, only two general methods are recalled, both belonging to the more general class of Machine Learning, as they represent those most largely adopted in the application to the SEs' technology.

Regression. In this case, the neural network must produce, similarly to classical physics-based approaches, a continuous function of the continuous input parameters. The aim is, therefore, to represent the model of the engine as a black-box whose inner structure does not inform about the physical processes involved.

Classification. In this case, the neural network must produce the most appropriate selection, among a discrete set of possible alternatives, given the input data. The aim is therefore to recognize within a single system, structural properties or the "best" combination of its components or determine into which of a set of classes the single system is to be classified.

These methods are both part of the so-called Machine Learning method, which when involving multiple layers of neurons between the input and output layers, becomes Deep Learning methods implemented with the so-called Deep Neural Networks (DNN).

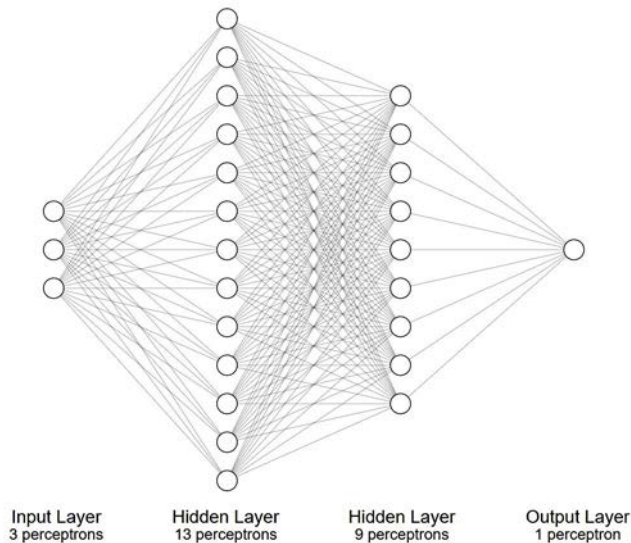


Figure 2. A DNN structure (3-13-9-1) adopted for the modelling of a single feature of a Stirling engine.

Review of existing literature

Design and operation optimization based on published data

Most of the applications concern the use of Machine Learning approaches to model the Stirling machines. Neural networks (NN), after their training phase has been completed, can be used as a tool to predict the output power of the Stirling engine with high precision and reduced computational effort and thus they can be efficiently adopted alongside genetic optimization algorithms, which require a large number of evaluations at different values of the parameters.

Adopting the data published in a previous work [8], which correlated the power output to both design (radius of stroke, piston diameter, volume of heat buffer chamber, and the volume of the gas chamber) and operation parameters (angular velocity, wall

temperature of gas chamber, thermal resistance), a black-box model of a thermal-lag Stirling engine was built [9]. The optimum value of the design and operating parameters was then efficiently obtained adopting a genetic optimization algorithm leveraged by the inexpensive evaluations of the ML black-box model for any desired input.

The optimization of design and operating parameters of a natural gas fueled alpha-type Stirling engine, adopted as an alternative to domestic UPS, was achieved by determining the Pareto frontier of a power and efficiency multi-optimization formulation which considered engine operating speed, charge pressure, temperatures of hot and cold cylinders, swept volume and gas constants as the main nonlinear parameters [10]. Again, published literature data were used [11],[12] for the training of the DNN, complemented by a simplified analytical model for the many missed values of efficiency. To assess the error introduced, the prediction performances of the DNN were then validated against a physical model.

Design and operation optimization based on experimental data

The seek for the optimal operational conditions for a given engine has promoted several investigations to assess the capability of a NN trained on experimental data to accurately predict their performances. The approach has shown to be effective for almost all types of SEs.

The terms of a global energy balance equation determined at steady state conditions from experimental measurements were collected during 500 runs of a prototype gamma-type Stirling engine by changing the conditions of the cold source and the angular velocity of the engine [13]. This data was adopted to train a DNN with 90 neurons distributed in 6 layers, to predict the efficiency of the engine as a function of cold side temperature and the engine rotation speed. The DNN was then adopted in a genetic optimization algorithm to find the optimal operating conditions.

An alpha-type SE fueled with LPG (Liquefied Petroleum Gas) was investigated to relate the output power to the working fluid adopted [14]. Four different gases were used: Argon, Nitrogen, Helium, and Air. 530 samples (350 for training and 180 for testing) were adopted to develop a NN with a single hidden layer with up to 10 neurons, which results sufficient to reproduce the output power within 10% of error, with the maximum error arising in the case of Helium.

A sensitivity analysis on the performance of an ANN, adopted for reproducing the performances of the Philips M102C beta-type SE, was proposed in [15]. In this study, the number of hidden layers of the NN, with 4 input neurons (temperature of heat source, rotation speed, working fluid, pressure) as input variables and 2 output (power and torque), was fixed to 1. The results show a non-linear and even non-monotonic trend of the Mean Square Error with the number of neurons. A similar analysis was reported in [16], but limiting the input to 3 operational parameters (pressure, hot end temperatures, and rotation speed) to predict uniquely the torque of the beta-type SE.

The performances, measured by power and torque, of a beta-type SE with the heat source provided with an electrical furnace, were experimentally studied by Özgören et al. [17]. The experimental results were used to train an ANN with five input parameters namely, hot source temperature, piston coating, compression ratio, charge pressure, and engine speed. Then, the dependence on both design (piston coating) and operational parameters were included. 608 experimental samples were determined and used to train two separated NNs with structure 5–13–9–1 and 5–13–7–1, for torque and power respectively, furnished estimates on the testing data with Medium Error Percent lower than 5%.

The control of the flywheel rotation speed of a Low Temperature Differential (LTD) gamma-type SE to achieve the desired speed at varying hot sink temperatures was pursued in [18]. The structure of the NN was composed of 3 input neurons (cold sink, ambient air temperatures, and flywheel rotation speed), one hidden layer with 50 neurons, and a single output neuron (hot sink temperature). 650 recorded engine operating points were used for the training. The trained network has been then adopted by fixing the rotation speed at the desired value and obtaining the hot sink temperature for the actual cold sink and ambient air temperature.

A NN model for a beta-type SE correlating pressure and engine speed with power and torque was developed in [19]. The NN adopted was a single hidden layer with 10 neurons trained on 48 datasets which resulted sufficient to predict the performances with a regression coefficient of 0.05.

The use of the Support Vector Machine (SVM) with a Least Square error estimation was also proposed as an alternative to ANN models for the Particle Swarm optimization approach to obtain the estimate of power and torque output not only as function of

operation parameters (temperature of heat source and rotation speed) but also with respect to different type of SEs (alpha-beta- and gamma- types), using data collected from the literature [20]. SVM is another ML methodology that differs from NN, being based on the algebraic combination of different kernel functions than perceptrons. SVM generally performs well for not too large and not noisy training data and in some classification problems, an aspect involved when distinguishing among different SE types. For the problem at hand, which includes the classification of the engine type, it showed superior performances than the NN approach.

The SVM has been adopted also to build a model capable of describing the multivariate output of SE (specific fuel consumption, torque, and power) as a function of multiple inputs (rotation speed, temperature of heat source, pressure, and fuel) [21]. In this work, the authors focused on the detection of outliers (experimental data points whose values are not in line with the majority of other values, for instance, due to reading errors, false registrations, unusual conditions, etc.) which could lead to poorly performing NN.

Then, such an approach proves to be effective in elaborating a black-box model giving a fast and accurate prediction of the engine performances.

Design and operation optimization based on simulation data

When experimental data were not available, or to avoid the expensive realization of multiple prototypes, also modeling data from numerical simulations were used to build the data set for the training.

Four design parameters (phase angle, displacer stroke, piston diameter, and regenerator matrix porosity) and a single operational parameter (rotation speed) were optimized with respect to the power output and the thermal efficiency of a low temperature gamma-type SE adopting a NN as evaluator function of an improved Conjugate Gradient method [22]. The NN was composed of 25 neurons in a single hidden layer, trained adopting the results of 55 different CFD simulations of the engine (training data were enlarged to 3168 sets by adopting a triangulation-based interpolation method). The NN demonstrated to adequately substitute the CFD evaluations required for each optimization step, leading to obtain an optimized configuration of the engine increasing the output power by 102% and the thermal efficiency by 5%.

A third order model for the SE simulation was adopted in [23] to derive the dataset for the training of a NN with one hidden layer, and subsequently perform the optimization of two design (displacer stroke and phase angle) and one operational (engine frequency) parameters of a gamma-type SE, with respect to power output and efficiency. The code adopted for simulations was validated with comparisons to experimental data. The maximum estimation error for the original configuration was about 11% for the power and about 18% for the rejected heat rate. The dataset was formed adopting a grid of 5 values for each parameter, leading to a total of 125 samples. A number of 10 neurons was found to give the best overall performances in terms of accuracy and computational efficiency. A single optimal point was defined by weighting the two different outcomes (0.7 for power, and 0.3 for efficiency). No comparison of the theoretical optimal point with experimental results was performed.

The free piston SE poses further challenges to its optimization, being characterized by more dynamic output parameters such as operating frequency, piston amplitude ratio, and phase angle, depending on design parameters. The ability of a NN to predict the FPSE's dynamic output parameters, taking into consideration the six dynamic input parameters, including the damping coefficients of load and displacer, spring stiffness, masses of power piston, and displacer, was investigated in [24]. The dataset for the training of the NN was obtained using a modeling approach. Interestingly, the authors observed that, despite some large prediction errors contained in the model prediction, especially about the phase angle, due to simplifications adopted in the model development and the lack of info about physical parameters, the ability of the model to correctly catch the trends with change on the parameters' values was sufficient for a successful reproduction of the engine dynamic output. A dataset consisting of 55 steady states was adopted to train the NN. A large number of NN configurations were tested, with both one and two hidden layers, showing that non necessarily those with the largest number of neurons give the best performances, a result probably connected to the not large number of samples in the dataset.

Energy system operation

Another possible application of ML having a more practical emphasis and borrowed from other renewable energy technologies regards the operation control to increase the

efficiency of installations of a full system where the Stirling engine is one of the several components assembled together.

A hybrid Genetic Algorithm – Particle Swarm Optimization [25], was employed to optimize the convergence rate of the Particle Swarm Optimization, where a NN was used to model a solar powered SE, to find the optimal values of the regenerator effectiveness, absorber temperature, and high temperature of working fluid, to maximize power output and efficiency. The training data set was based on simulation data.

An interesting application was proposed for the regulation of the rotation speed of a solar Stirling water pump [26]. The complexity of this configuration comes from the different power inputs, the solar thermal input for the heating of the hot side of the SE, and the photovoltaic input required to power the electric motor. The existence of an optimal rotation speed depending on the environmental conditions (affecting the hot side temperature, the cold sink temperature, and the photovoltaic power produced), and on the water head to win was demonstrated by adopting a third order mathematical model, whose numerical integration is too complex and with slow convergence to be adopted for real-time control. Therefore, a NN having the water head and the absorber and sink temperatures as the inputs and the optimum speed of the DC motor as the output was considered as the model engine of the controller. A total of 1029 samples, obtained by the integration of the model, were used to train the NN composed of a single hidden layer with 10 neurons. The optimum rotation speed determined by the NN model was finally compared to the optimum rotation speed obtained in an experimental realization of the system having the same characteristics, a rare case of a complete validation cycle. This approach was validated with small differences attributed to the adoption of training data from the model which do not consider several losses.

Unmeasurable parameters reconstruction

Another interesting application of NNs, based on their ability to learn and generalize, regards the possibility of deriving critical unmeasurable parameters of SEs. This approach has been applied to derive the damping coefficients of power and displacer pistons, the damping coefficient between displacer rod and power piston, and the gas temperature within the compression and expansion spaces of a Free Piston SE [27]. To obtain this result, a relatively complex NN architecture was required, composed of 9 input parameters (mass of the power piston, the mass of the displacer piston, the stiffness of the power

piston, the stiffness of the displacer piston, the oscillator frequency, the phase angle, the minimum and maximum gas pressures, and the ideal gas constant), two hidden layers of 40 and 20 neurons respectively, and 5 output neurons for the corresponding 5 desired unmeasurable parameters. The required input/output data for the supervised training of the NN were acquired from simulations of the associated dynamic model over a wide range of input parameters and the desired output variables. The trained NN was then adopted to predict the desired parameters of two real SEs, for which these parameters were available. In all cases, the predicted values resulted in very good agreement with the experimental one, showing the effectiveness of this approach.

AI implementation

As already observed, in several studies the topology and dimension of the NN were subject to investigations. Unfortunately, no deterministic rules exist to forecast the best combination of the hyperparameters of the NN, only the number of neurons in the input layer (equal to the number of input parameters) and of the output layer (equal to the number of values that must be determined) are fixed. The hyperparameters include the number of hidden layers, the number of neurons in each layer, the activation function, the selection of repartition of data in training, validation and test sets, and even the training algorithm.

Because the success of an NN model is highly dependent on the quality of the training data, special care must be devoted also to the treatment of the dataset: commonly adopted strategies include the filtering of inconsistent data, the scaling of variables, and techniques to enlarge the experimental dataset with simulation results to increase the range of parameter values where the NN performs accurately.

Some published investigations detail the adopted strategies.

Published data [11] were used to develop a NN, with a single hidden layer, correlating heat source temperature, engine speed, and charging pressure to the output power of an alpha-type Stirling [28]. The number of neurons in the hidden layer of the NN was optimized leading to the conclusion that a single hidden layer of 10 neurons, a very simple architecture, is sufficient to reproduce the data with a deviation within 1.53%.

The correct selection of the hyper-parameters of the NN (type of perceptron, number of neurons, and their distribution in the different layers) is one of the aspects to face when developing an NN model of the Stirling Engine.

In order to determine an optimal topology of the NN for the prediction of power and torque of SEs, assuming as input variables the temperature of the hot working fluid, the pressure, and the fuel flow rate, the adoption of the group method of data handling was proposed [29]. With this approach, a quadratic function is built to recognize the performance of the NN by varying the connection of the single neurons with those of the previous layer. This function is composed of polynomials pairing the neurons in successive layers. Adopting a genetic algorithm, it is then possible to generate an optimal network topology. As a consequence, an explicit polynomial formulation of the NN input-output function is determined. This approach has been used assuming as input experimental data published in previous works.

The adoption of hybrid analytical-NN models has proved to be a viable alternative to pure NN models to increase the accuracy of the prediction of SE performances [30]. The NN model for two four cylinders SE (the Ford 4-215 and the General Motors 4L23) was first determined, with charge pressure, hot side temperature, and engine speed as input parameters, to model the power output based on experimental datasets with a single hidden layer of 10 neurons. The isothermal model by Urieli and Berchowitz [31] was then adopted to enlarge the available dataset for the Ford SE, but corrected following [32], while the isothermal model proposed by Martini [1] was adopted for the GM's SE. The results showed that not only the accuracy of the hybrid model is superior, but also its robustness with respect to outliers in the experimental datasets.

Three different ML approaches were compared in application to Stirling Cryocoolers (SC) in [33]: backpropagation NN, support vector regression, and random forest regression. The results of one-dimensional simulations formed the initial dataset composed of 6000 samples, to investigate the effect of phase shift, expander stroke, and compressor stroke on photovoltaic power and cooling capacity, two outputs that are shown to have a high correlation degree. This circumstance negatively affects the capability of other multivariable regression techniques, an issue further complicated by the non-uniqueness of the output values on the parameter space. A high degree of correlation also exists among the input parameters which are therefore preprocessed not only for normalization but also for finding, by means of Principal Component Analysis, an orthogonal basis to use as input. All approaches resulted effective to produce a surrogate model of the SC to use in Particle Swarm Optimization.

The performances of three different algorithms to build a NN to predict power and torque at varying engine speeds and charge pressures have been compared in terms of accuracy and computational cost of the training stage [34]: Artificial Neural Network (ANN), Artificial Neural Network trained with Particle Swarm Optimization (PSO) and Adaptive Neuro-Fuzzy Inference System (ANFIS) models. The results obtained considering a dataset of 48 experimental samples from the literature showed that the best model was achieved with the ANFIS approach, followed by the PSO method. The comparison of the time required to train these two models was however largely in favor of the ANFIS one: 3.15 seconds for the ANFIS and 129.94 seconds for the PSO.

Sophisticated techniques have been also developed to increase the accuracy of the NN. A hybrid Taguchi Method (TM) - Adaptive Neuro-Fuzzy Inference System (ANFIS) - Teaching-Learning Based Optimization (TLBO) approach [35] was developed to optimize the design parameters of the jet pump in a jet pump-based thermoacoustic-Stirling heat engine. The procedure combines the Taguchi method to optimize the selection of the data set and optimization trials, with an optimization method based on a teaching-learning paradigm to obtain the best values for the main 4 geometric parameters of the jet pump. The ANFIS algorithm was adopted to perform the system performance evaluations required in the optimization step. Experimental data were used to train the NN.

Conclusion

The review of existing literature and methodologies used for the optimization of Stirling engine design and operation highlights the wide range of approaches adopted and the challenges faced by researchers. Furthermore, the review shows that through the application of Artificial Intelligence (AI) techniques, it is possible to accurately predict Stirling engine performances and optimize both design and operational parameters.

Specifically, the use of NNs trained on published experimental data has proven to be effective in predicting Stirling engine performances, enabling rapid and accurate assessment of the best design configurations and operational parameters.

Even when experimental data were not available, the use of numerical simulation data allowed for training NN models for Stirling engine modeling. These models, although based on simulated data, have been effective in predicting Stirling engine performances and identifying the best design configurations and operational parameters.

Furthermore, the application of ML techniques for energy management has shown promising results in regulating the operation of energy systems that include Stirling engines as a main component. This approach enables the overall efficiency of the system to be optimized and maximizes the utilization of available energy resources.

Finally, research results show that the estimation assessment of unmeasurable parameters (i.e. inaccessible through direct measurements) using NNs has opened new perspectives for the characterization and optimization of Stirling engines.

In conclusion, the implementation of Artificial Intelligence techniques in Stirling engine optimization represents a rapidly evolving field that holds great potential for advancing the efficiency and performance of these engines across various applications.

References

- [1] Martini W.R. 1983. Stirling Engine Design Manual, 2nd Ed. NASA CR-168088. DOE/NASA, Washington D.C.
- [2] Hachem H, Gheith R, Aloui F, Ben Nasrallah S. Technological challenges and optimization efforts of the Stirling machine: A review. *Energy Conversion and Management* 2018;171:1365–87.
- [3] Zare S, Tavakolpour-saleh AR, Aghahosseini A, Sangdani MH, Mirshekari R. Design and optimization of Stirling engines using soft computing methods: A review. *Applied Energy* 2021;283:116258.
- [4] Jiang H. *Machine learning fundamentals: A concise introduction*. Cambridge University Press, 2021.
- [5] Rumelhart, D. E., Hinton G. E., Williams R. J. Learning representations by back-propagating errors. *nature* 1986; 323.6088: 533-536.
- [6] Cybenko, G. Approximation by superpositions of a sigmoidal function. *Mathematics of control, signals and systems* 1989; 2: 303-314.
- [7] Ihme M, Chung WT, Mishra AA. Combustion machine learning: Principles, progress and prospects. *Progress in Energy and Combustion Science* 2022;91:101010.
- [8] Cheng C-H, Yang H-S, Jhou B-Y, Chen Y-C, Wang Y-J. Dynamic simulation of thermal-lag Stirling engines. *Applied Energy* 2013;108:466–76.

- [9] Alborzi M, Sarhaddi F, Sobhnamayan F. Optimization of the thermal lag Stirling engine performance. *Energy & Environment* 2019;30:156–75.
- [10] Yildiz C, Bayata F, Mugan A. Multi-objective optimum design of an alpha type Stirling engine using meta-models and co-simulation approach. *Energy Conversion and Management* 2021;232:113878.
- [11] Çınar C, Aksoy F, Solmaz H, Yılmaz E, Uyumaz A. Manufacturing and testing of an α -type Stirling engine. *Applied Thermal Engineering* 2018;130:1373–9.
- [12] Karabulut H, Cesu HSY, Koca A. Manufacturing and Testing of a V-Type Stirling Engine. *Turk J Engin Environ Sci* 2000;24:71–80.
- [13] Sobhnamayan F, Sarhaddi F, Behzadmehr A. A Trained Neural Network for the Prediction of Optimum Operation Mode of a Stirling Engine. *International Journal of Mechanical and Production Engineering Research and Development* 2019;9:293–306.
- [14] Chmielewski A, Mozaryn J, Krzeminski M. Theoretical and experimental background for artificial neural network modeling of alpha type Stirling engine. 2017 22nd International Conference on Methods and Models in Automation and Robotics (MMAR), Miedzyzdroje, Poland: IEEE; 2017, p. 570–5.
- [15] Sadatsakkak SA, Ahmadi MH, Ahmadi MA. Implementation of artificial neural-networks to model the performance parameters of Stirling engine. *Mechanics & Industry* 2016;17:307.
- [16] Ahmadi MH, Mehrpooya M, Khalilpoor N. Artificial neural networks modelling of the performance parameters of the Stirling engine. *International Journal of Ambient Energy* 2016;37:341–7.
- [17] Özgören YÖ, Çetinkaya S, Sarıdemir S, Çiçek A, Kara F. Artificial neural network based modelling of performance of a beta-type Stirling engine. *Proceedings of the Institution of Mechanical Engineers, Part E: Journal of Process Mechanical Engineering* 2013;227:166–77.
- [18] Hojati M, Mansouri E, Moradzadeh H. Stirling engine parameters prediction to control its rotation speed using artificial neural network. *J Braz Soc Mech Sci Eng* 2022;44:72.
- [19] Machesa M, Tartibu L, Tekweme F, Okwu M, Ighravwe D. Performance Prediction of a Stirling heat engine using Artificial Neural Network model. 2020 International

Conference on Artificial Intelligence, Big Data, Computing and Data Communication Systems (icABCD), Durban, South Africa: IEEE; 2020, p. 1–6.

- [20] Ahmadi MH, Ahmadi MA, Sadatsakkak SA, Feidt M. Connectionist intelligent model estimates output power and torque of stirling engine. *Renewable and Sustainable Energy Reviews* 2015;50:871–83.
- [21] Ahmadi MH, Ahmadi MA, Ashouri M, Razie Astaraei F, Ghasempour R, Aloui F. Prediction of performance of Stirling engine using least squares support machine technique. *Mechanics & Industry* 2016;17:506.
- [22] Cheng C-H, Lin Y-T. Optimization of a Stirling Engine by Variable-Step Simplified Conjugate-Gradient Method and Neural Network Training Algorithm. *Energies* 2020;13:5164.
- [23] Hooshang M, Askari Moghadam R, Alizadeh Nia S, Masouleh MT. Optimization of Stirling engine design parameters using neural networks. *Renewable Energy* 2015;74:855–66.
- [24] Ye W, Wang X, Liu Y. Application of artificial neural network for predicting the dynamic performance of a free piston Stirling engine. *Energy* 2020;194:116912.
- [25] Ahmadi MH, Sorouri Ghare Aghaj S, Nazeri A. Prediction of power in solar stirling heat engine by using neural network based on hybrid genetic algorithm and particle swarm optimization. *Neural Comput & Applic* 2013;22:1141–50.
- [26] Tavakolpour-Saleh AR, Jokar H. Neural network-based control of an intelligent solar Stirling pump. *Energy* 2016;94:508–23.
- [27] Shourangiz-Haghighi A, Tavakolpour-Saleh AR. A neural network-based scheme for predicting critical unmeasurable parameters of a free piston Stirling oscillator. *Energy Conversion and Management* 2019;196:623–39.
- [28] Jiang H, Rahman A, Zhang X. Prediction of the Performance for Alpha-type Stirling Engine Through Artificial Neural Network Technique, Västerås, Sweden: Volume 5: Innovative Solutions for Energy Transitions: Part IV; 2019, p. Paper ID:786.
- [29] Ahmadi M, Ahmadi M-A, Mehrpooya M, Rosen M. Using GMDH Neural Networks to Model the Power and Torque of a Stirling Engine. *Sustainability* 2015;7:2243–55.

- [30] Jiang H, Xi Z, A. Rahman A, Zhang X. Prediction of output power with artificial neural network using extended datasets for Stirling engines. *Applied Energy* 2020;271:115123.
- [31] Urieli I, Berchowitz DM. *Stirling cycle engine analysis*. Taylor & Francis (1984).
- [32] Shoureshi R. *Analysis and design of Stirling engines for waste-heat recovery [dissertation]*. Cambridge: Massachusetts Institute of Technology; 1981
- [33] Yang Z, Liu S, Li Z, Jiang Z, Dong C. Application of machine learning techniques in operating parameters prediction of Stirling cryocooler. *Cryogenics* 2021;113:103213.
- [34] Machesa MGK, Tartibu LK, Tekweme FK, Okwu MO. Evaluation of the Stirling Heat Engine Performance Prediction Using ANN-PSO and ANFIS Models. 2019 6th International Conference on Soft Computing & Machine Intelligence (ISCMI), Johannesburg, South Africa: IEEE; 2019, p. 217–22.
- [35] Le Chau N, Dao T-P, Dang VA. An efficient hybrid approach of improved adaptive neural fuzzy inference system and teaching learning-based optimization for design optimization of a jet pump-based thermoacoustic-Stirling heat engine. *Neural Comput & Applic* 2020;32:7259–73.
- [36] Machesa MGK, Tartibu LK, Okwu MO. Performance analysis of stirling engine using computational intelligence techniques (ANN & Fuzzy Mamdani Model) and hybrid algorithms (ANN-PSO & ANFIS). *Neural Comput & Applic* 2023;35:1225–45.
- [37] Taki O, Senhaji Rhazi K, Mejdoub Y. Stirling engine optimization using artificial neural networks algorithm. *ITM Web Conf* 2023;52:02010.
- [38] González-Plaza E, García D, Prieto J-I. A Revision of Empirical Models of Stirling Engine Performance Using Simple Artificial Neural Networks. *Inventions* 2023;8:88.
- [39] Domenikos G-R, Koronaki I, Papingiotis T, Bitsikas P. Parametric Numerical Analysis of β -Type Stirling Engine. *Energies* 2023;16:6518.
- [40] Kraitong K, Mahkamov K. Optimisation of Low Temperature Difference Solar Stirling Engines using Genetic Algorithm, 2011, p. 3945–52.
- [41] Suleiman OME, Adam A, Hassan T. Performance and Design Optimization of Solar Powered Stirling Engine Using Genetic Algorithm. *Academic Journal of Engineering Sciences* 2018;1:AJES.MS.ID.000501.

- [42] Abdullah AS, Manoj A, Selvakumar S. A Hybrid Data Analytic Approach to Evaluate the Performance of Stirling Engine using Machine Learning Techniques. 2021 IEEE Bombay Section Signature Conference (IBSSC), Gwalior, India: IEEE; 2021, p. 1–4.
- [43] Taki O, Rhazi KS, Mejdoub Y. Stirling engine multi-objective optimization using a genetic algorithm. *IJPEDS* 2024;15:623.
- [44] Chen P, Deng C, Luo X, Ye W, Hu L, Wang X, et al. Performance optimization of a free piston Stirling engine using the self-directed online machine learning optimization approach. *Applied Thermal Engineering* 2024;236:121482.
- [45] Islas S, Beltran-Chacon R, Velázquez N, Leal-Chávez D, López-Zavala R, Aguilar-Jiménez JA. A numerical study of the influence of design variable interactions on the performance of a Stirling engine System. *Applied Thermal Engineering* 2020;170:115039.
- [46] Masoumi AP, Tavakolpour-Saleh AR. Experimental assessment of damping and heat transfer coefficients in an active free piston Stirling engine using genetic algorithm. *Energy* 2020;195:117064.
- [47] Zare Sh, Tavakolpour-Saleh AR. Frequency-based design of a free piston Stirling engine using genetic algorithm. *Energy* 2016;109:466–80.
- [48] Boretti A. α -Stirling hydrogen engines for concentrated solar power. *International Journal of Hydrogen Energy* 2021;46:16241–7.
- [49] Masoumi AP, Tavakolpour-Saleh AR, Rahideh A. Applying a genetic-fuzzy control scheme to an active free piston Stirling engine: Design and experiment. *Applied Energy* 2020;268:115045.
- [50] Eser S, Yuce BE. A metaheuristic approach for multi-objective optimization of the Stirling cycle with internal irreversibilities and regenerative losses using artificial bee colony algorithm. *Energy Conversion and Management* 2023;292:117372.
- [51] Qiu H, Wang K, Yu P, Ni M, Xiao G. A third-order numerical model and transient characterization of a β -type Stirling engine. *Energy* 2021;222:119973.
- [52] Hojati M, Mansouri E. Intelligent speed control of a Stirling engine using artificial neural network. In Review; 2021.
- [53] Tavakolpour-Saleh AR, Zare Sh, Bahreman H. A novel active free piston Stirling engine: Modeling, development, and experiment. *Applied Energy* 2017;199:400–15.

Heat transfer / fluid flow analysis

A Straight-tube Type Thermoacoustic Engine designed as a Heat Transfer Device

Akitsugu Watanabe^{a, *}, Kazuyuki Yoshioka^b, Yuki Ueda^c

a Tokyo University of Agriculture and Technology, Japan

b Shoden-Kogyo co., Ltd., Japan

c Tokyo University of Agriculture and Technology, Japan

Corresponding author: s236195y@st.go.tuat.ac.jp

Keywords: Thermoacoustic oscillation, Dream pipe, Heat transfer enhancement

Abstract

In this study, we propose a straight-tube type thermoacoustic engine that functions as a heat transfer device transferring heat from hot to cold interfaces. The engine consists of a straight tube and a stack sandwiched between hot and cold heat exchangers as like as well-known standing-wave thermoacoustic engines. The engine generates self-excited sound in it. The engine utilizes this sound to transfer heat using the dream pipe effect. The proposed engine uses only gas as a working fluid and hence, the phase change between liquid and gas does not occur in it. This allows us to use the proposed engine safely to transfer heat from high-temperature sources, such as inside of industrial furnaces. One of the most important parameters to control the amount of heat transfer is the stack position in the straight tube. The stack position is numerically optimized to maximize heat transfer from the hot to cold heat exchangers. For numerical optimization, the numerical integration data were calculated with the DeltaEC provided by the Los Alamos National Laboratory. The transferred heat amount is obtained as a function of the stack position. It was found that the optimized stack position is different from the well-known optimized one for an efficient straight-tube type thermoacoustic engine. With the present optimized position, the amount of heat transferred turned out to exceed 1,000W. Because the diameter of the used tube is 60mm, the power density exceeds 354 [kW/m²]. This means that the effective thermal conductivity is 229 [W/(m K)]. This value is equivalent to the thermal conductivity of aluminum (235 [W/(m K)]).

Introduction

With the Sustainable Development Goals (SDGs) as a backdrop, there is an increasing demand for improvements in energy efficiency across various industrial processes, including the cooling processes of industrial furnaces. Therefore, heat pipes, commonly used in these cooling processes, are facing demands for improved controllability of heat transfer, enhanced safety, and simpler designs. Heat pipes have limited control over heat transfer because they utilize the hard-to-control phase-changing properties of the

working fluid. They pose a risk of accidents due to the sudden boiling of the working fluid. Additionally, the design of cooling systems utilizing heat pipes can be constrained by limitations in their positioning.

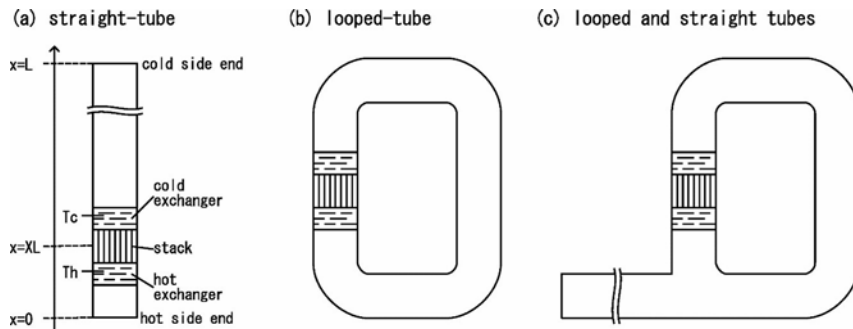


Figure 1. Various thermoacoustic engines: (a) standing-wave thermoacoustic engine with a straight tube, (b) traveling-wave thermoacoustic engine with a looped tube, (c) traveling-wave thermoacoustic engine with looped and straight tubes.

To improve the cooling system as an alternative to the commonly used heat pipes, we turned our attention to the dream pipe proposed by Kurzweg, utilizing forced working-fluid-oscillation [1]. In dream pipes, narrow tubes are placed between high-temperature and low-temperature sources, the working fluid, which is liquid, is inserted in the tubes, and the oscillator causes the working fluid to move between the sources. As a result of the oscillation of the working fluid, heat flow from the high temperature source to the low one is generated. The generated heat flow is significantly larger than that caused by normal heat conduction of the working fluid. The dream pipes have advantages compared with conventional heat pipes; there is no restriction on the position of use and high controllability of heat transfer amount [2][3].

When applying dream pipes to high-temperature areas, such as industrial furnaces, there are still some challenges that need to be addressed. One challenge is the risk of accidents caused by the sudden boiling of the working fluid. This risk remains because liquids, even when not employed as phase-changing working fluids for heat transfer, continue to pose such hazards. Another challenge is reducing energy consumption in the cooling process. Generating forced oscillation still requires energy, even if its efficiency is improved.

Changing the working fluid from liquid to gas can prevent the risk of accidents caused by sudden boiling, but it increases energy consumption in the cooling process due to changes in physical attributes of the working fluid. To reduce energy consumption of generating forced oscillation, we use a thermoacoustic-spontaneous gas oscillation. This gas oscillation is generated when a temperature gradient along the longitudinal direction of a narrow tube exceeds a critical value and is utilized in thermoacoustic engines to generate acoustic power flow. Utilizing this self-generated acoustic power flow as the acoustic power flow for the dream pipe effect makes it possible to reduce the energy consumption related to the generation of forced acoustic power flow and improve energy efficiency.

As providers of acoustic power sourced from thermal energy, three types of thermoacoustic engines have been developed: (a) straight-tube, (b) looped-tube, and (c) looped and straight tubes thermoacoustic engines (Figure 1).

For improving energy efficiency, traveling-wave thermoacoustic engines, including (b) looped-tube and (c) looped and straight tubes thermoacoustic engines may seem better. Because traveling-wave thermoacoustic engines have achieved conversion efficiency over 30%, and configurations of thermoacoustic engines that operate at lower temperatures have also been proposed [4].

In designing cooling system, standing-wave thermoacoustic engines like (a) straight-tube thermoacoustic engines are better. This is because a hot-heat exchanger of straight-tube engines can be easily insert in or set near the heat source within industrial furnaces compared with a hot-heat exchanger of traveling-wave thermoacoustic engines. Thus, we consider that standing-wave thermoacoustic engines are suitable for transporting heat from heat sources inside industrial furnaces. Regarding their efficiency, a straight-tube type thermoacoustic engine proposed by Swift achieves a conversion efficiency of 9% by setting the relative stack position X to 11%, where X is defined as the ratio of the position of the stack center from the hot side end of the straight tube (see Fig. 1(a)) and the length of the tube [5].

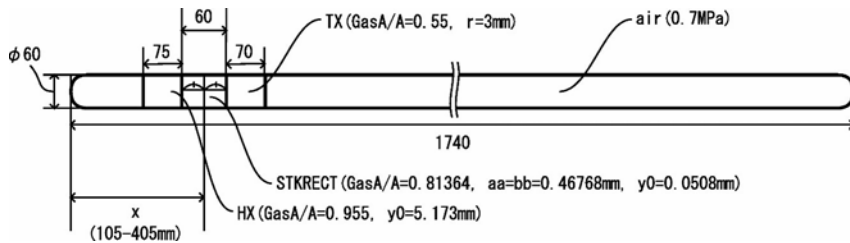


Figure 2. The straight-tube type thermoacoustic engine for calculation.

The optimal configuration of the straight-tube thermoacoustic engines for heat transfer has not been studied. In the engine design optimization of this study, the most important value that we want to maximize is the amount of the heat transfer from a hot heat source, Q_{H1} . On the other hand, in conventional studies as mentioned above, the important values are the output power W and the efficiency W/Q_{H1} . This difference can make the optimal configuration of a thermoacoustic engine for heat transfer differ from that of the engines of conventional studies. This is because heat transfer Q_{H1} is affected not only by the output power W but also by the effective thermal conductivity resulting from the dream pipe effect.

The effective thermal conductivity resulting from the dream pipe effect is known to increase significantly with the displacement amplitude in the narrow tube section. In standing-wave thermoacoustic engines such as the straight-tube type, the displacement amplitude is zero at the closed end and increases as it moves away from the closed end. Therefore, these studies on the dream pipe effect suggest that the optimal configuration of thermoacoustic engines used as heat transfer means might differ from those optimized as means of generating acoustic power flow.

Based on the new perspective of using the straight-tube type thermoacoustic engine as a heat transfer means, this study discusses the initial considerations regarding the optimal configuration of thermoacoustic engines when it is used as a heat transfer means. The relative stack position X has been selected as a parameter and numerically optimized to increase the heat amount transferred from the high-temperature heat exchanger to the low-temperature heat exchanger. For this numerical optimization, numerical integration data were calculated using DeltaEC, determining the heat transfer amount. The details of this optimization are described later.

The effective thermal conductivity also is calculated from the heat amount and gas temperature of the heat exchangers. To examine the feasibility of the proposed engine for practical applications like transferring heat from high-temperature to low-temperature interfaces in some industrial applications such as cooling industrial furnaces with low-energy consumption, the calculated effective thermal conductivity is compared with the thermal conductivity of some metals like aluminum. The details of this comparison are described later.

Calculation model

For the calculation to determine the optimal X of the proposed engine for maximizing heat transfer, the DeltaEC of the Los Alamos National Laboratory was selected due to its longstanding reputation for stability and reliability in thermoacoustic studying. A model for numerical integration using the DeltaEC was designed. This model replicates the straight-tube type thermoacoustic engine shown in Figure 2. As described earlier, the straight-tube thermoacoustic engine consists of a straight tube and a stack sandwiched between high and low-temperature heat exchangers.

The straight tube is made of “stainless” steel (a preset material in DeltaEC) with a length of 1740 mm. Both the high and low-temperature heat exchangers are positioned adjacent to the stack, meaning their positions vary depending on the stack position.

The high-temperature heat exchanger having parallel plates (HX), made of “stainless” steel, has a length of 75 mm, an openness ratio ($GasA/A$) of 95.5%, and parallel plates spaced 10 mm apart (indicated by the parameter y_0 (=5.2 mm) for half distance).

The low-temperature heat exchanger having a shell and tubes (TX) is made of “stainless” steel with a length of 70 mm, an openness ratio of 55%, and tubes with a diameter of 3 mm.

The stack with rectangular holes (STKRECT), made by “celcor” (a ceramic material preset in DeltaEC), is 60 mm in length, where the side lengths of the square holes is 0.47 mm, the half-thickness (y_0) of walls separating holes is 0.051 mm, and an openness ratio ($GasA/A$) is 82%. This model simulates a commercially available ceramic honeycomb with a wall thickness of 4 milli-inches, having 600 square cells per square inch (4/600 ceramic honeycomb).

The internal radius of all components is set to 30 mm, resulting in a total diameter of 60 mm and a cross-sectional area of approximately 2800 mm². The temperature of the high-temperature heat exchanger is set to 500 °C, and the low-temperature heat exchanger to 15°C. This scenario assumes the cooling target is an industrial furnace at 500 °C, and the heat is transferred to cooling water at 15 °C. The working fluid used is dry air pressurized up to 0.7 MPa, equivalent to dry air at a gauge pressure of 0.6 MPaG, which is approximately 7 times the atmospheric pressure at ground level.

In this configuration, the dimensionless number $\omega\tau_a$, related to angular frequency ω and thermal relaxation time τ_a , becomes around 13.

Numerical Optimization

In the calculation using DeltaEC, the center position of the stack was varied as the critical parameter, ranging from 105 mm to 405 mm from the high-temperature heat exchanger, in 5 mm increments. This is for determining the optimal X , which relates to the center position of the stack, of the proposed engine for maximizing heat transfer. The 105 mm parameter corresponds to the closest position of the stack to the high-temperature heat exchanger without any gap from the high-temperature side end at the model described above. The 405 mm parameter corresponds to a configuration with the center position reaching 1/4 of the tube of the model, which is the ideal position for the dream pipe effect where the displacement amplitude is maximized for any given acoustic powers. This numerical integration calculated the heat transfer amount, the temperature difference across the stack, and the average temperature of the stack.

For each parameter adjustment, some errors indicating inaccurate results were observed as the nature of the numerical integration of DeltaEC. Thus, the calculations were repeated until no errors were observed, and the results for each parameter without errors were considered the numerical integration data.

Upon observing peaks in the heat transfer amount for the above parameters, the numerical integration was concluded.

Results

Figure 3 displays the amount of heat transferred [W] for the relative stack position X in the calculation. The horizontal axis represents the relative stack position X [%], which is the value obtained by dividing the distance x of the stack center from the high-

temperature side end by the length L of the tube. The vertical axis shows the amount of heat transferred Q_H [W].

In Figure 3, Q_H takes the largest value of 1,214 W at the relative stack position X of 18-19%. It indicates that the optimized parameter for heat transfer is within 18-19%. This optimized parameter for heat transfer will be discussed with a comparison to the well-known parameter X for the known straight-tube type thermoacoustic engine for generating sound power [2]. At the optimized parameter, the temperature difference across the ends of the stack is 138.2 K, and the average temperature of the stack is 419.8 K. These measurements will be utilized in the Discussion section to calculate the stack's effective thermal conductivity.

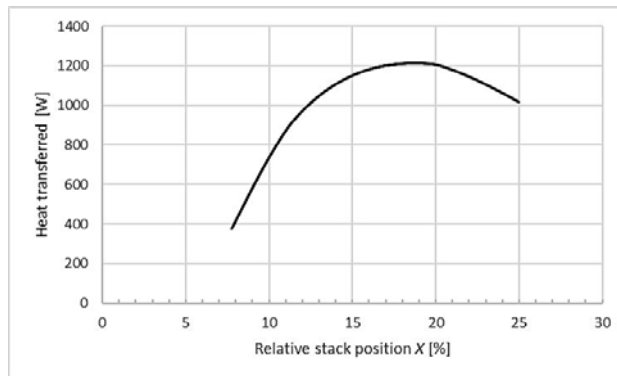


Figure 3. The heat transferred for relative stack position X .

Discussion

As mentioned above, Figure 3 shows the optimized value of X for transferring heat in the proposed engine (18-19%) is different from the well-known optimized X (about 11%) for generating sound power. This difference is derived by the difference in objectives. This difference is examined using known equations for viscous fluids. The work source w for viscous fluids, proposed by Tominaga, can be divided into four components: energy dissipation due to viscosity W_v , energy dissipation due to thermal conduction W_p , work source from the traveling wave component W_{prog} , and work source from the standing wave component W_{stand} as shown in equations (1) to (5) [6],

$$w = W_v + W_p + W_{prog} + W_{stand} \quad (1)$$

$$W_v = \frac{1}{2} \omega \rho_m \text{Im} \left[\frac{1}{1 - \chi_v} \right] |u_{1r}|^2 \quad (2)$$

$$W_p = \frac{\omega}{2} \left(\frac{\gamma - 1}{\gamma p_m} \right) \chi_\alpha'' |p_1|^2 \quad (3)$$

$$W_{prog} = \frac{\omega}{2T_m} \frac{dT_m}{dx} (\text{Re}(b)_r) |p_1| |\xi_{1r}| \sin \theta \quad (4)$$

$$W_{stand} = -\frac{\omega}{2T_m} \frac{dT_m}{dx} (\text{Im}(b)_r) |p_1| |\xi_{1r}| \cos \theta \quad (5)$$

where ρ_m and γ are the mean density and the heat capacity ratio of the working gas, respectively, p_m and T_m are the mean pressure and the mean temperature of the working gas, respectively, ω and θ are the angular frequency and the relative phase of pressure fluctuation against displacement fluctuation of the gas-oscillation, respectively, $|u_{1r}|$ is the amplitude of cross-sectional mean flow velocity, $|p_1|$ is the amplitude of pressure variation, $|\xi_{1r}|$ is the displacement amplitude, r is the characteristic length of the regenerator, τ_v is the viscous relaxation time expressed by r and the kinetic viscosity of the working gas, τ_α is the thermal relaxation time expressed by r and the thermal diffusivity of the working gas, χ_v is the complex function that depends on $\omega\tau_v$, χ_α is the complex function that depends on $\omega\tau_\alpha$, and b_r is a function defined by $(b_r = (\chi_\alpha - \chi_v)) / ((1 - \chi_v)(1 - p))$. Since θ is almost zero in the straight-tube thermoacoustic engine, the traveling wave component W_{prog} is almost zero, and the standing wave component W_{stand} is represented by equation (6),

$$W_{stand} = -\frac{1}{2T_m} \frac{dT_m}{dx} (\text{Im}(b)_r) |p_1| |u_{1r}| \sin \varphi \quad (6)$$

where relative phase φ of u_{1r} against p_1 is defined as $\varphi = \pi/2 - \theta$. Parameters such as b_r , χ_α , and $1/((1 - \chi_v))$ depend on the dimensionless number $\omega\tau_\alpha$, thus they can be considered nearly constant under the present calculation. Therefore, the acoustic energy generated by the work source w is the result of subtracting W_v (proportional to $|u_{1r}|^2$) and W_p (proportional to $|p_1|^2$) from W_{stand} (proportional to $|p_1| |u_{1r}|$).

As an initial consideration, we explored the pressure amplitude and the velocity amplitude of standing waves in a uniform air column assuming no energy dissipation. Under this assumption, the complex pressure amplitude $p_1(x)$ and the complex velocity

amplitude $u_1(x)$ at a position x from the end of a tube of total length L satisfy equations (7) and (8), respectively,

$$p_1(x) = -iz_s \frac{\cos\{k_s(L-x)\}}{\sin k_s L} U_0 \quad (7)$$

$$u_1(x) = \frac{\sin\{k_s(L-x)\}}{\sin k_s L} U_0 \quad (8)$$

where z_s is the characteristic impedance of the working gas, k_s and U_0 are the wavenumber and the velocity amplitude of the standing waves, respectively. In a fundamental mode of standing waves in the above-mentioned model, a straight-tube thermoacoustic engine, $k_s L$ is approximately equal to π . Under this condition, $p_1(x)$ and $u_1(x)$ can be represented as equations (9) and (10) with the relative stack position X that has been defined as $X=x/L$.

$$p_1(x) = iz_s \frac{\cos \pi X}{\sin k_s L} U_0 \quad (9)$$

$$u_1(x) = \frac{\sin \pi X}{\sin k_s L} U_0 \quad (10)$$

From equations (9) and (10), the product of the complex pressure amplitude $p_1(x)$ and the complex velocity amplitude $u_1(x)$ reaches its maximum when the relative stack position X is 25%. From this consideration, the relative stack position X that maximize the product of the amplitude of pressure variation $|p_1|$ and the amplitude of mean flow velocity $|u_{1r}|$ is also expected to reach its maximum near $X = 25\%$.

Thus, it can be stated that the calculated optimized value of X for the proposed engine (18-19%) is approximately the midpoint between 25% and the well-known optimized X (about 11%) for an efficient straight-tube type thermoacoustic engine. In other words, the calculated optimized value of X is approximately the midpoint between the optimized value for dream pipe effect and the optimized value for the efficiency W/Q_{in} . This vital consideration is expected to contribute to the future design and optimization of actual devices, enhancing the performance and efficiency of the proposed thermoacoustic engine.

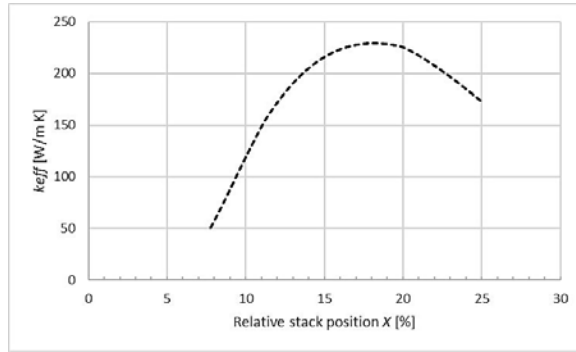


Figure 4. The effective thermal conductivity for relative stack position X

Because the diameter of the used tube is 60mm, the power density is about 429 [kW/m²] at the optimized parameter. To examine the feasibility of the proposed engine for practical applications like transferring heat from high-temperature to low-temperature interfaces in some industrial applications such as cooling industrial furnaces with low-energy consumption, the effective thermal conductivity k_{eff} [W/(m K)] is calculated by Equation (11),

$$k_{eff} = \frac{Q_H}{A_{gas}} \frac{L_{st}}{T_H - T_C} \quad (11)$$

where A_{gas} and L_{st} are the cross-sectional area available to the working gas in the stack and the length of the stack, respectively, T_H and T_C are the temperatures of the high-temperature and the low-temperature interfaces, respectively.

Figure 4 displays the effective thermal conductivity k_{eff} [W/(m K)] for the relative stack position X [%]. The horizontal axis represents the relative stack position X [%]. The vertical axis represents the effective thermal conductivity k_{eff} [W/(m K)]. The largest value of k_{eff} at relative stack position X of 18-19% is 229 [W/(m K)]. Hence, from this comparison, it is evident that the effective thermal conductivity of the stack in the optimized straight-tube type thermoacoustic engine exceeds that of iron (80 [W/(mK)]), brass (130 [W/(m K)]) and tungsten (173 [W/(m K)]), and is approximately the same as that of aluminum (235 [W/(m K)]).

These examinations suggest that the proposed straight-tube type thermoacoustic engine possesses the functionality of a heat pipe for transferring heat from high-temperature interfaces to low-temperature ones. This thermoacoustic engine, which solely uses gas as the working fluid, reduces the risk of sudden boiling at high temperatures inherent in heat pipes that use phase change, allowing for safe application in high-temperature interfaces such as industrial furnaces. Furthermore, since it utilizes acoustic power flow converted from heat flow, this gas-only thermoacoustic engine can achieve higher energy efficiency than other cooling methods that do not involve phase change, such as forced convection cooling.

Conclusion

In this study, we proposed a straight-tube type thermoacoustic engine functioning as a heat pipe for transferring heat from high-temperature to low-temperature interfaces. The numerical integration data of DeltaEC suggests that the proposed engine has the potential of utilizing as a heat pipe for transferring heat from high-temperature to low-temperature interfaces with less energy consumption.

To investigate the optimal configuration and effectiveness of the proposed straight-tube thermoacoustic engine, numerical integration data were calculated using DeltaEC from the Los Alamos National Laboratory, determining the heat transfer amount and the effective thermal conductivity. From the numerical integration data, it was found that the optimized heat transfer parameter is between 18-19% for the relative stack position X . This significantly differs from the optimized sound generation parameter (10-11%) for the same thermoacoustic engine. An examination based on Biwa's discussion on the dream pipe effect and the relationship between $\omega\tau_a$ and the heat transfer amount revealed a potential discrepancy between the optimization for sound generation and the optimization for the dream pipe effect.

The effective thermal conductivity was calculated from the amount of heat transferred and the gas temperature of the heat and cold exchangers. The calculated effective thermal conductivity (229 [W/(m K)]) was compared with the thermal conductivity of various metals. This comparison showed that the effective thermal conductivity of the stack in the optimized straight-tube thermoacoustic engine proposed is approximately the same as that of aluminum. This suggests that the straight-tube thermoacoustic

engine proposed in this study could be utilized as a heat pipe for transferring heat from high-temperature to low-temperature interfaces with less energy consumption if the working fluid is optimized to increase the heat transfer amount and means to control the effective thermal conductivity are implemented. We leave the studies for the working fluid optimization and the controlling means as future works.

Acknowledgments

This research is a part of a joint research project between Tokyo University of Agriculture and Technology, and Shoden-Kogyo co., Ltd.

References

- [1] U. H. Kurzweg, Ling de Zhao; “Heat transfer by high-frequency oscillations: A new hydrodynamic technique for achieving large effective thermal conductivities”. *Phys. Fluids*; 27 (11): 2624–2627 (1984). <https://doi.org/10.1063/1.864563>
- [2] Nishio, S., Nagata, S., Numata, S. and Shirakashi, R., “Study of thermal characteristics of bubble-driven heat-transport device”, *Heat Trans. Asian Res.*, 32: 167-177 (2003). <https://doi.org/10.1002/htj.10082>
- [3] Nishio S. and Tanaka H., “Performance Comparison of Single-Phase Forced-Oscillating-Flow Heat-Pipes”, *JSME International Journal Series B Fluids and Thermal Engineering*, 46(3): 392-398 (2003), <https://cir.nii.ac.jp/crid/1390282679652718080>
- [4] S. Backhaus, G. W. Swift, “A thermoacoustic-Stirling heat engine: Detailed study”, *J. Acoust. Soc. Am.*; 107 (6): 3148–3166 (2000). <https://doi.org/10.1121/1.429343>
- [5] G. W. Swift; “Analysis and performance of a large thermoacoustic engine”. *J. Acoust. Soc. Am.*; 92 (3): 1551–1563 (1992). <https://doi.org/10.1121/1.403896>
- [6] Tominaga, A., “Thermoacoustic Theory of Viscous Fluids”, *Journal of Cryogenics and Superconductivity Society of Japan*, 27(7): 549-554 (1992), <https://doi.org/10.2221/jcsj.27.549>

Study on Internal Cooling of a High-temperature Linear Alternator for Free-piston Stirling Generators

Jing Luo^{a,b,c}, Yanlei Sun^{a,b}, Yanyan Chen^{a,b,*}, Qingyue Jin^{a,b,c}, Xinyu Zhu^{a,b,c}, Limin Zhang^{a,b}, Jianying Hu^{a,b}, Ercang Luo^{a,b,c,*}

a Key Laboratory of Cryogenics, Technical Institute of Physics and Chemistry, Chinese Academy of Sciences, Beijing, China

b Key Laboratory of Cryogenic Science and Technology, Beijing, China

c University of Chinese Academy of Sciences, Beijing, China

Corresponding author: yychen@mail.ipc.ac.cn (Y. Chen); ecluo@mail.ipc.ac.cn (E. Luo)

Keywords: Free-piston Stirling generator, High-temperature linear alternator, Internal cooling, Oscillating flow, Steady flow

Abstract

Linear alternators play a pivotal role in the acoustic-to-electrical conversion of free-piston Stirling generators (FPSGs). However, space applications demand an elevated heat dissipation temperature of FPSGs to minimize radiator size, necessitating linear alternators to operate at exceptionally high temperatures. High temperature operation imposes restrictions on permissible temperature rises within the alternator, while crucial components like permanent magnets and non-metallic skeletons undergo transformative changes, resulting in heightened electromagnetic losses and exacerbating alternator heating. To mitigate the temperature rise of vulnerable components such as permanent magnets and coils, ensuring prolonged stable operation in high-temperature environments, this paper conducts a numerical study on internal cooling using quasi-one-dimensional software SAGE and Computational Fluid Dynamics (CFD) analysis methods for a high-temperature linear alternator with a power generation of a dozen kilowatts and a heat dissipation temperature of 523 K. The results indicate that optimizing the internal flow field by adding baffles to enhance the heat transfer effect of the alternating flow can reduce the average temperature of permanent magnets from 609 K to 537 K, and the average temperature of coils from 578 K to 533 K. Furthermore, the maximum gas temperature in the flow channels near the permanent magnets decreases from 715 K to 545 K, with a corresponding increase in flow friction loss only rising from 70 W to 139 W. Significantly, the addition of baffles leads to the formation of multiple topological loops within the internal flow channels of the alternator. Introducing asymmetric flow control structures such as gas diodes on this basis allows for further enhancement of heat transfer using the steady flow generated in the loops. With an asymmetric differential pressure reaches 1000 Pa, corresponding to a volumetric flow rate of 0.0066 m³/s for the steady flow, the maximum gas temperature in channels near the permanent magnets can be further reduced to 529 K, with a theoretical power consumption of 6.6 W. Last but not least, a comparison between SAGE and CFD simulation results is presented, demonstrating that SAGE is suitable for rapidly simulating the flow and heat transfer in multi-dimensional internal flow fields of the alternator, providing valuable insights. This research offers guidance for the design of linear alternators, especially high-temperature linear alternators, in FPSGs.

Introduction

The free-piston Stirling generator (FPSG), with its advantages of high efficiency, high reliability, and high specific power, has emerged as one of the most promising space thermal-to-electric conversion technologies within the hundred-kilowatt power range [1,2]. A typical FPSG comprises a free-piston Stirling engine unit and a linear alternator (LA) unit, in which the LA plays a pivotal role in the acoustic-to-electrical conversion [3]. The linear motion characteristics of LAs enable them to be directly coupled with the reciprocating oscillating pressure waves in Stirling systems, eliminating the need for kinematic conversion structures such as magnetic gears, thus offering advantages of simplicity and efficiency. The electromagnetic losses in LAs are ultimately dissipated in the form of heat, making thermal management a crucial consideration in the design of LAs. In conventional FPSGs deployed on the ground, LAs operate in ambient temperature environments, typically utilizing cooling water flowing through the casing or internal fins for heat dissipation [4]. In this scenario, heat within the LA primarily relies on convective heat transfer induced by gas oscillations to exhaust heat to cooling walls. When the power level and heat dissipation temperature of the LA are both relatively low, this cooling scheme is sufficient to meet the heat dissipation requirements.

However, in the harsh environment of space, heat dissipation can only be achieved through radiative heat transfer, with the required surface area inversely proportional to the fourth power of its absolute temperature [5,6]. To minimize the radiator size, it is necessary to increase the heat dissipation temperature of the FPSG as much as possible, which results in the LA also having to operate at exceptionally high temperatures [7]. Considering the temperature limitations of existing alternator materials, a feasible choice for the heat dissipation temperature is approximately 523 K [8,9]. High temperature operation not only reduces the allowable temperature rise of the LA but also demands corresponding changes in the materials of the permanent magnets and some non-metallic structural components. This inevitably leads to an increase in electromagnetic losses, exacerbating the temperature rise issue within the LA. If only the above cooling scheme is employed, most of the working gas will just flow and transfer heat in the wider peripheral channels of the outer stators (on the order of 10 mm in width), where sufficient space needs to be reserved for the coil leads. In contrast, the channels near the permanent magnets and coils are much narrower, typically around 1 mm in width. The

narrower width and corresponding higher flow resistance result in less gas flow through these channels, leading to poorer convective heat transfer effects. More importantly, since the losses from the permanent magnets and coils constitute the largest proportion, the temperature rise issue in this vicinity is particularly severe. Therefore, a more effective cooling scheme must be implemented to prevent serious safety concerns such as demagnetization of permanent magnets or melting of coil insulation.

In this context, the paper conducts a numerical study on internal cooling using quasi-one-dimensional software SAGE and Computational Fluid Dynamics (CFD) analysis methods for a high-temperature linear alternator (HTLA) with a power generation of a dozen kilowatts and a heat dissipation temperature of 523 K. According to the available electromagnetic calculations, the HTLA can output an electric power of 17914 W under the rated conditions with an operating frequency of 70 Hz and a piston stroke of 15 mm, achieving an efficiency of 83.6%. Among the total heat generated, the losses from the permanent magnets contribute 1479 W, from the coils contribute 485 W, from the outer stators contribute 100 W, and from the inner stators contribute 17 W. Using this heat generation as a reference, the paper analyzes the internal temperature field of the HTLA and optimizes the internal flow field to address the localized high-temperature issues near the permanent magnets and coils, ensuring the long-term stable operation of the HTLA in high-temperature environments. The findings of this study hold significant guidance for the cooling design of LAs used in FPSGs.

Model description

The calculation models for the internal temperature field of the HTLA are introduced in this section. Based on the actual magnetic circuit structure, a CFD model and a SAGE model of the HTLA are established. The schematics and boundary conditions of these two models are described in the following, and finally the independence analysis is carried out.

CFD model

Although the outer stators exhibit gaps in the outer periphery after segmentation, resulting in a lack of complete axial symmetry, the main body of the HTLA remains axially symmetrical. Therefore, to capture the primary contradictions and simplify calculations, a two-dimensional axisymmetric simplified model is still chosen, in which the outer

stators are equivalent to an irregular structure based on the surface area and the gas flow area, as shown in Figure 1. In the HTLA, there is significant obstruction among the components, and the interior primarily relies on the alternating flow in the bounce space for convective heat transfer, so the radiation heat transfer inside the HTLA is not considered in the model. The whole model represents a high-pressure closed system, with helium as the internal working gas and a mean pressure set to 15 MPa. A single-piston dynamic mesh boundary is utilized in the model to simulate the compressive and expansive effects of the power piston on the bounce space. The velocity of the dynamic mesh is defined through UDF programming to match the rated conditions of the HTLA, i.e., an operating frequency of 70 Hz and a piston stroke of 15 mm, defined as $v=6.597 \cdot \cos(2\pi ft)$ m/s.

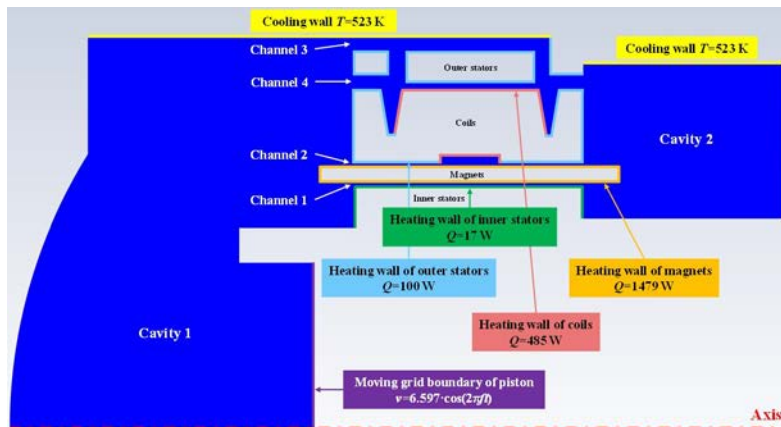


Figure 1. CFD model for temperature field simulation of the HTLA.

For ease of description in subsequent analysis, the flow structure within the HTLA is divided into several main parts, including cavity 1, cavity 2, channel 1, channel 2, channel 3, and channel 4. As for the heat transfer boundaries, the model applies fixed heat flux boundaries to the surfaces of the permanent magnets, coils, inner stators, and outer stators. The heat flux densities are determined based on their respective electromagnetic losses and heat transfer surface areas. The cooling wall of the HTLA casing adopts a fixed wall temperature boundary, disregarding the heat transfer temperature difference from the external cooling fluid to the helium side wall, with a set wall temperature of

523 K. Additionally, all other boundaries are adiabatic. In the computational process, the turbulence model employs the standard k-omega model based on experience with alternating flow calculations. The pressure-velocity coupling is conducted using the SIMPLE algorithm, and momentum and energy discretization adopt second-order upwind schemes. With this setup, transient calculations are performed until the transient energy is stable and conserved, enabling analysis of the flow and heat transfer conditions within the HTLA.

SAGE model

Due to the need for extremely small time steps in transient CFD calculations involving alternating flow to accurately capture parameters such as time-averaged acoustic power and heat transfer, it takes at least one month of computation time to obtain steady-state results of time-averaged energy conservation when using CFD models for temperature field analysis, which consumes a significant amount of computational resources and time. Therefore, it is considered prudent to simultaneously employ the quasi-one-dimensional SAGE software for fast calculation. SAGE is a commercial software developed for alternating flow systems and is now widely used in the engineering design of thermoacoustic engines [10,11] and Stirling engines [12,13]. By comparing its results with CFD calculations, the feasibility of using SAGE for rapid simulation of internal flow and heat transfer within the HTLA can be verified. Based on the equivalent flow area and heat transfer area, a SAGE model for temperature field simulation of the HTLA is established, as shown in Figure 2. The SAGE model also employs helium as the working gas, with a mean pressure of 15 MPa. Additionally, the boundary conditions for piston motion and component heat transfer within the model are the same as those in the CFD model.

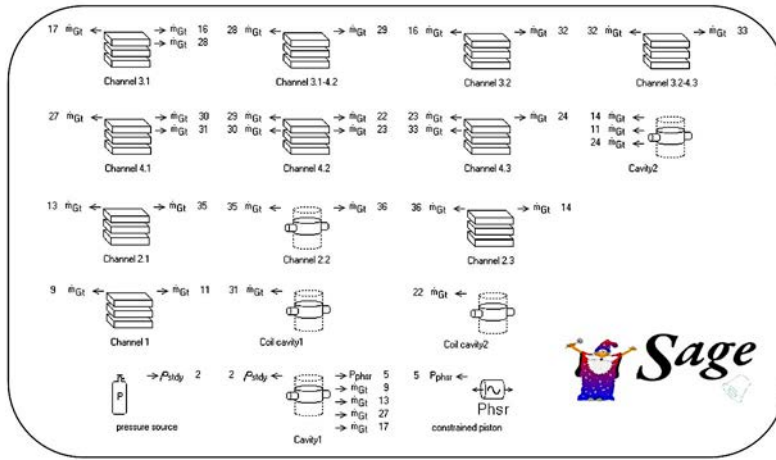


Figure 2. SAGE model for temperature field simulation of the HTLA.

Independence analysis

The quality of meshing significantly influences the accuracy and precision of CFD calculations. In the CFD model of the HTLA, channel 1 and channel 2 near the permanent magnets are the narrowest, with a width of only 1 mm. Consequently, the mesh size in these areas is set to the smallest across the entire domain, reaching 0.2 mm, while the mesh sizes in other fluid domains range from 0.5 to 2 mm. The meshing results are illustrated in Figure 3, and the total number of mesh cells is close to 20000, with an excellent mesh quality of 0.96. Based on previous computational experience, for transient CFD simulations involving alternating flows, the time step has a much greater impact on the calculation results compared to the number of mesh cells. Therefore, it can be considered that the current mesh quality meets the requirements, and the subsequent analysis will primarily focus on the independence of the time step.

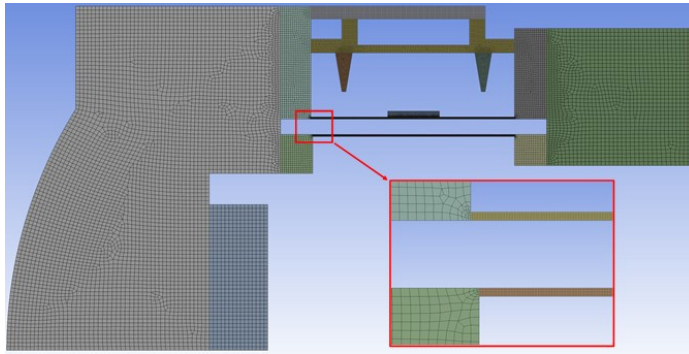


Figure 3. Meshing of the CFD model.

In systems with alternating flows, the time-averaged energy is very sensitive to phase differences between parameters. In CFD simulations, the accurate capture of phase primarily relies on extremely small time steps. Therefore, it is necessary to investigate the independence of the time step. For the HTLA studied in this paper, which oscillates at a frequency of 70 Hz, i.e., one cycle lasts about 1.43×10^{-2} s. Figure 4 investigates the effect of different calculation steps per cycle on the final energy conservation results. It can be observed that as the number of calculation steps increases (corresponding to a decrease in time step), the difference in energy conservation becomes smaller, indicating a reduction in computational error. However, this also leads to longer computation times. Considering both computational accuracy and time cost, the number of calculation steps per cycle is set to 2000, corresponding to a time step of 7.14×10^{-6} s. At this setting, the difference in energy conservation accounts for less than 3% of the total energy, falling within an acceptable range. Therefore, the subsequent calculations and analyses are carried out with this time step.

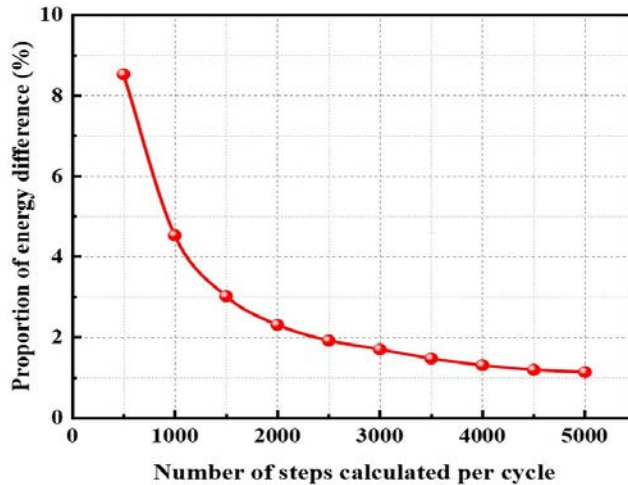


Figure 4. Validation of time step independence for the CFD model.

Results and discussions

Based on the above CFD and SAGE models, this section first simulates and analyzes the initial temperature field inside the HTLA to ascertain the severity of the temperature rise issue. Subsequently, study on the internal cooling techniques are conducted to address the localized high-temperature issues affecting vulnerable components. The improvement measures taken include the addition of flow baffles and asymmetric flow control structures.

Initial temperature field analysis

Figure 5 illustrates the distribution of the time-averaged temperature field inside the HTLA when no enhanced cooling measures are employed. It can be observed that due to the narrow width of the channels near the permanent magnets, there is significant flow resistance, resulting in the maximum local gas temperature in that region, exceeding 700 K. Additionally, because the coils and outer stators form enclosed narrow gaps, the gas temperature in those areas is also elevated. This implies that the wall temperatures of the permanent magnets and coils, which come into contact with these gases, are also very high.

Table 1 presents the time-averaged computational results obtained from the two-dimensional CFD simulation. In the analysis, it is assumed that the solid components have good thermal uniformity, and the average wall temperatures are taken for components such as the permanent magnets, coils, outer stators, and inner stators. It can be observed that without any enhanced cooling measures, the maximum wall temperature inside the HTLA is recorded in the permanent magnets, reaching 609 K, which is close to the demagnetization temperature of 623 K. Following this, the inner stators exhibit an average temperature of 586 K, while the average temperature of the coils is 578 K. In contrast, the outer stator, due to its lower losses and proximity to the cooling wall, registers the lowest average temperature at 550 K. By comparing the volumetric flow rate amplitudes at the inlet of each channel within the bounce space, it is found that the channel 3 and channel 4, located near the periphery of the outer stators, have significantly larger flow areas, resulting in lower flow resistance. As a result, the majority of the gas flows through these two channels, with their volumetric flow rates exceeding five times that of the channels near the permanent magnets. This phenomenon constitutes a core reason for the poorer heat dissipation and higher temperature rise in the vicinity of the permanent magnets and coils.

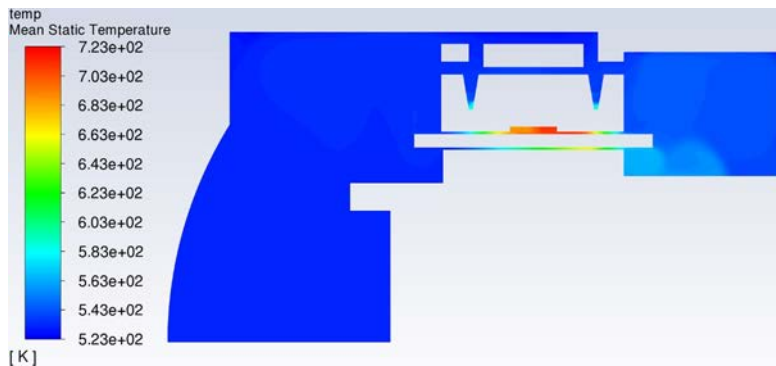


Figure 5. Initial time-averaged temperature field of the HTLA.

Additionally, Table 1 provides the results obtained from a simplified quasi-one-dimensional SAGE model. By comparing these results with those from the CFD simulations, the feasibility of using SAGE for rapid analysis of the internal flow and temperature fields in LAs is verified. The comparison reveals that the results obtained

from SAGE have high reference value. Taking the CFD calculation results as a benchmark, the deviations in average temperatures calculated by SAGE are within 5%, with a power consumption deviation of 11.4%, and a maximum deviation of 13.3% in volumetric flow rate amplitude. Furthermore, Figure 6 compares the axial distribution of the average gas temperature within the narrow channels between the SAGE and CFD simulation results. It can be observed that both in trend and numerical values, the results obtained from SAGE align well with those from CFD, which indicates that SAGE can effectively simplify the calculation of flow and temperature field within the HTLA while maintaining high accuracy. This facilitates the rapid assessment of the overall effects resulting from structural adjustments, thereby saving significant computational resources and time.

Table 1. Comparison of initial calculation results between SAGE and CFD.

Calculation model	SAGE	CFD
Average temperature of magnets (K)	626	609
Average temperature of coils (K)	595	578
Average temperature of inner stators (K)	609	586
Average temperature of outer stators (K)	550	550
Volumetric flow rate amplitude of channel 1 (m ³ /s)	2.6e-3	3.0e-3
Volumetric flow rate amplitude of channel 2 (m ³ /s)	3.5e-3	3.9e-3
Volumetric flow rate amplitude of channel 3 (m ³ /s)	1.7e-2	1.7e-2
Volumetric flow rate amplitude of channel 4 (m ³ /s)	2.0e-2	1.9e-2
Heat dissipation of cooling wall (W)	2143	2095
Heat productivity of electromagnetic components (W)	2081	2081
Power consumption of flow friction (W)	62	70
Proportion of differences in energy conservation (%)	0	2.6

Although the average temperatures of the components in Table 1 do not exceed the temperature limit of 623 K, it's important to note that the magnetic performance of the permanent magnets and the service life of the insulation materials decrease with increasing temperature. Moreover, as shown in Figure 6, the gas temperature in channel 2 near the permanent magnets and coils may reach up to 715 K. In reality, due to the presence of thermal resistance, components cannot achieve an ideal uniform temperature distribution. Therefore, it is necessary to take corresponding measures to

enhance the cooling effect inside the HTLA, suppress the temperature rise of components such as the permanent magnets and coils, thus ensuring the high performance and long lifespan of the HTLA.

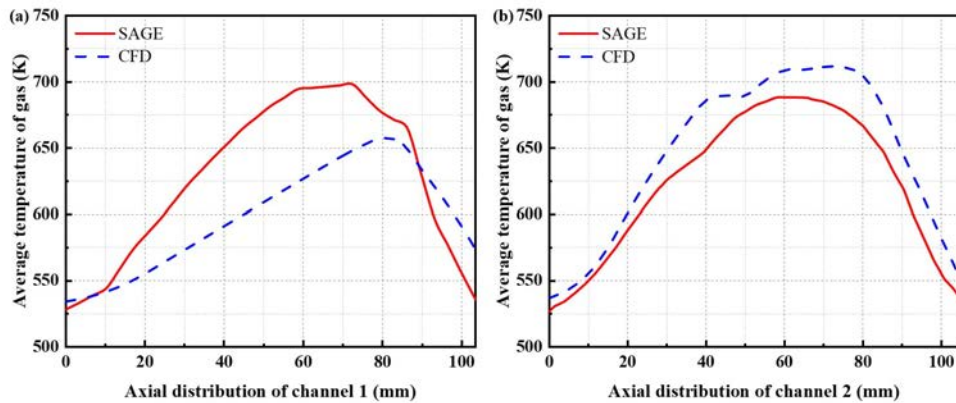


Figure 6. Comparison of initial gas temperature distribution in channels between SAGE and CFD.

Enhancing heat transfer effect of alternating flow

Due to the significant alternating flow characteristics of the working gas within the HTLA, it is considered to enhance local heat transfer effects by adjusting the flow structure. The improved structure, as shown in Figure 7, involves sealing off the side channels adjacent to chamber 1 and adding baffles extending towards the casing wall. This configuration creates an elongated channel with a length of 100 mm and a gap width of 2 mm between the outer stator periphery and the casing wall, thereby matching the flow resistance of the peripheral channel with that of the narrow channels near the permanent magnets, facilitating increased gas velocity for enhanced convective heat transfer. Additionally, an annular groove with a width of 0.4 mm has been added to the side of the baffles to enhance local heat dissipation of the coils, which can be equated to 17 circular through-holes with a diameter of 5 mm evenly distributed along the circumference in the actual baffles.

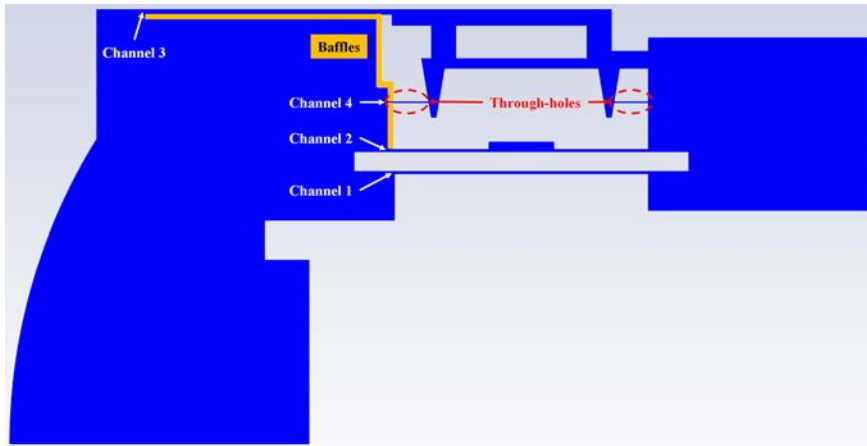


Figure 7. Schematic of the fluid domain in the HTLA after adding baffles.

Figure 8 illustrates the time-averaged temperature field distribution obtained from CFD simulations after adding the flow-blocking baffles. The introduction of baffles significantly increases the velocity amplitudes of oscillating flow in channel 1, channel 2, and channel 3. This not only enhances the convective heat transfer coefficients between the gas and the surfaces of the permanent magnets and coils, but also strengthens the heat transfer between the gas and the cooling walls, leading to a noticeable improvement in the local high temperatures of the gas in the channels adjacent to the permanent magnets. In addition, the design of through-holes also results in better cooling of the coils, with the global maximum gas temperature of 545 K.

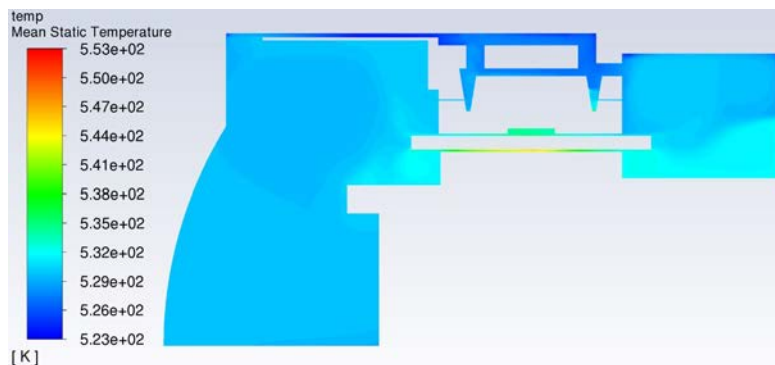


Figure 8. Time-averaged temperature field in the HTLA after adding baffles.

Table 2 quantifies the impact of adding baffles on the flow and heat transfer characteristics within the HTLA. From the CFD simulation results, it is observed that after optimizing the internal flow field with the addition of baffles, the average temperature of the permanent magnets decreases from 609 K to 537 K, the average temperature of the inner stators decreases from 586 K to 538 K, the average temperature of the coils decreases from 578 K to 533 K, and the average temperature of the outer stators decreases from 550 K to 529 K. By comparing the volume flow rate amplitudes at the inlet of each channel, it is evident that the volumetric flow rate amplitudes in channel 1 and channel 2 significantly increase to a level close to that of channel 3, which is the core reason for the improved heat dissipation effect. However, the introduction of flow-blocking baffles inevitably increases the flow friction losses inside the bounce space, resulting in an increase in power consumption from the initial 70 W to 139 W, which is within the acceptable range compared to the power generation of more than ten kilowatts.

Table 2. Comparison of calculation results between SAGE and CFD after adding baffles.

Calculation model	SAGE	CFD
Average temperature of magnets (K)	540	537
Average temperature of coils (K)	560	533
Average temperature of inner stators (K)	539	538
Average temperature of outer stators (K)	539	529
Volumetric flow rate amplitude of channel 1 (m ³ /s)	6.0e-3	8.1e-3
Volumetric flow rate amplitude of channel 2 (m ³ /s)	7.7e-3	9.7e-3
Volumetric flow rate amplitude of channel 3 (m ³ /s)	2.6e-2	2.3e-2
Volumetric flow rate amplitude of channel 4 (m ³ /s)	6.2e-3	7.1e-3
Heat dissipation of cooling wall (W)	2211	2161
Heat productivity of electromagnetic components (W)	2081	2081
Power consumption of flow friction (W)	130	139
Proportion of differences in energy conservation (%)	0	2.7

Both SAGE and CFD calculations confirm the effectiveness of adding flow-blocking baffles in improving the high-temperature issues of the HTLA. For the flow channel 3 formed by the baffles and casing wall, further enhancement of cooling effect can be achieved by increasing the axial length of the channel or reducing the gap width. However, this would

lead to increased flow friction losses, necessitating a comprehensive consideration. As the axial length of the baffles is constrained by the casing size and cannot be adjusted arbitrarily, the adjustment of the installation height of the baffles is primarily used to control the gap width of channel 3. Considering the long computational time required for CFD simulations and the previously validated reliability and accuracy of SAGE for rapid analysis of internal flow and temperature fields in LAs, SAGE is used to simulate the flow and heat transfer characteristics under different widths of channel 3. The results are shown in Figure 9. As the width of channel 3 decreases, the velocity amplitude of oscillating flow in channel 1 and channel 2 increases, and the maximum temperature of gas decreases significantly accordingly. However, when the width of channel 3 falls below 2 mm, the power consumption caused by the flow friction losses of the narrow channel increases exponentially, reaching the order of hundreds of watts, so it is sufficient to select a gap width of 2 mm for the channel 3 after comprehensive consideration.

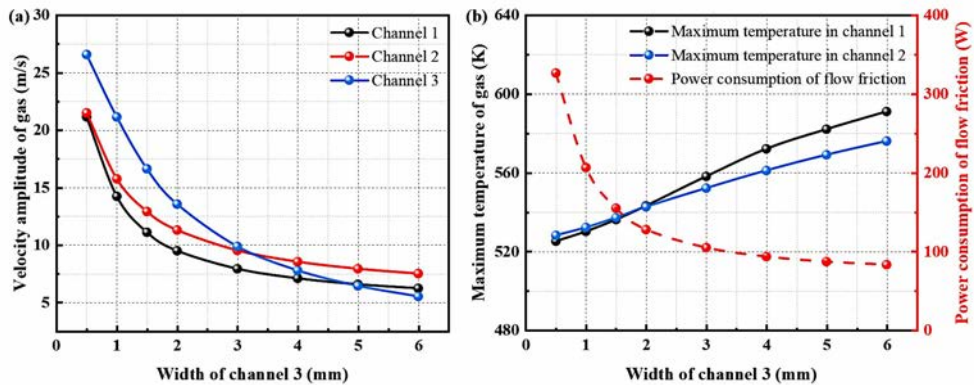


Figure 9. Flow and heat transfer characteristics with different widths of channel 3.

Enhancing heat transfer effect of time-averaged steady flow

With the aforementioned addition of flow-blocking baffles and through-holes to optimize the flow field, multiple topological loops are formed among channels 1, 2, 3, and 4 in the HTLA. Consequently, the internal working gas exhibits not only alternating oscillations but also some time-averaged steady flows passing through each channel. These steady flows also contribute to enhancing heat transfer. On the basis of the above structure, the

introduction of asymmetric flow control structures, such as gas diodes or check valves depicted in Figure 10, is beneficial for increasing the steady flows in the loops, thereby further improving the cooling effect of the HTLA.

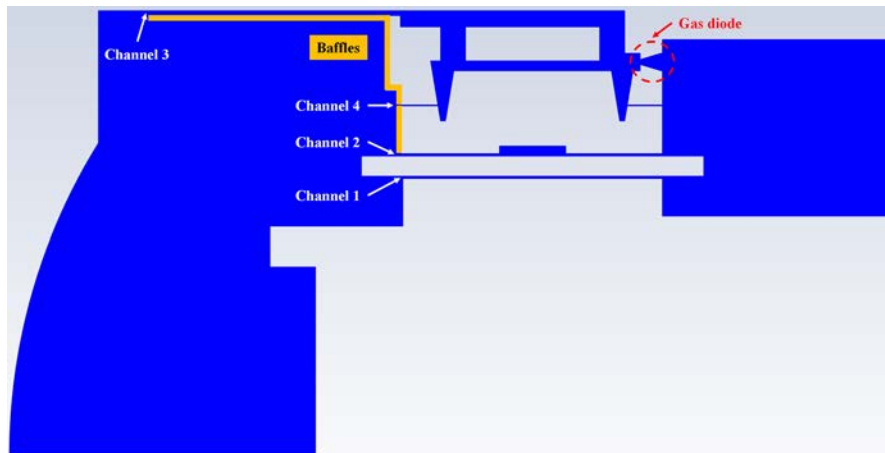


Figure 10. Schematic of the fluid domain in the HTLA after adding asymmetric flow control structures.

In systems with alternating flows, the generation of time-averaged steady flows primarily relies on the unidirectional differential pressure due to the asymmetry of flow structures. However, the influence of structural parameters on the steady flows is highly complex. Therefore, conducting CFD simulations under different magnitudes of steady flows by manually adjusting the gas diode structure would demand significant computational resources and time. To efficiently obtain instructive results, simplified calculations are also conducted using SAGE, where a differential-pressure-regulating pump module is employed to provide the required differential pressure, and thus adjust the magnitudes of the steady flows. Figure 11 shows the flow and heat transfer characteristics within the HTLA with different asymmetric differential pressure. As the differential pressure increases, the volumetric flow rate of the time-averaged steady flow and the power consumption of the pump increase accordingly, while the gas temperature near the permanent magnets further decreases. Beyond an asymmetric differential pressure exceeding 1000 Pa, the temperature variation tends to stabilize, albeit with a significant increase in power consumption of the pump. Therefore, the unidirectional differential

pressure provided by the asymmetric flow control structures should ideally be around 1000 Pa. At this point, the volumetric flow rate of the steady flow is 0.0066 m³/s, and the maximum gas temperature in channels near the permanent magnets is decreased to 529 K

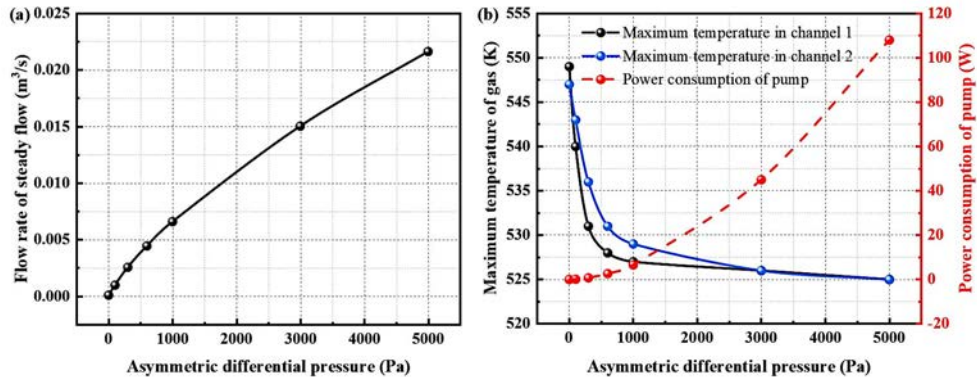


Figure 11. Flow and heat transfer characteristics with different asymmetric differential pressure.

Conclusion

This paper presents a numerical study on internal cooling techniques for a high-temperature linear alternator used in free-piston Stirling generators, addressing the demands of high heat dissipation temperature in space applications. The main conclusions are as follows:

- (1) Through comparisons of the average temperatures of components, volumetric flow rates of gas in the channels, power consumption of flow friction, and axial distribution of gas temperatures, it is found that the results obtained from SAGE are in good agreement with those from CFD both in trend and numerical values, which indicates that SAGE can simplify the calculation of flow and heat transfer characteristics within the alternator while maintaining high accuracy, thus saving significant computational resources and time.
- (2) The two-dimensional CFD simulation results indicate that without implementing any enhanced cooling measures, the average temperature within the alternator will reach 609 K for the permanent magnets, 586 K for the inner stators, 578 K for the coils, and 550

K for the outer stators. Moreover, the gas temperature near the permanent magnets and coils may reach up to 715 K. Therefore, appropriate measures must be taken to enhance the internal cooling effect of the alternator.

(3) By reasonably arranging the flow-blocking baffles, a narrow flow channel with a axial length of 100 mm and a gap width of 2 mm is formed between the outer stator periphery and the casing wall. Additionally, through-holes are incorporated on the side of the baffles. This configuration allows for a significant reduction in the average temperature of the permanent magnets to 537 K, the coils to 533 K, the inner stators to 538 K, and the outer stators to 529 K. Moreover, the global maximum gas temperature is reduced to 545 K. At this point, the increase in power consumption due to gas flow friction is only 69 W.

(4) By increasing the time-averaged steady flows in the various loops, the cooling effect of the alternator can be further enhanced, effectively reducing the localized temperature rise of vulnerable components such as the permanent magnets and coils. Results from SAGE simulations indicate that with an asymmetric differential pressure of 1000 Pa, corresponding to a volumetric flow rate of 0.0066 m³/s for the steady flow, the maximum gas temperature in channels near the permanent magnets can be further decreased to 529 K, with a theoretical power consumption of the pump is only 6.6 W.

Acknowledgements

This work was financially supported by the National Key Research and Development Program of China (No. 2021YFC28026003).

References

- [1] Luo J, Zhang L M, Chen Y Y, et al. Numerical study on a free-piston Stirling electric generator with a gas-spring-postpositioned displacer for high power applications. *Energy*, 271: 127023 (2023).
- [2] Ye W L, Wang X J, Liu Y W, et al. Analysis and prediction of the performance of free-piston Stirling engine using response surface methodology and artificial neural network. *Applied Thermal Engineering*, 188: 116557 (2021).
- [3] Jia Z L, Wang R Y, Hu J Y, et al. Study on the coupling between engine and alternator in a free-piston Stirling generator. *Applied Thermal Engineering*, 217: 119222 (2022).

- [4] Chen Y H, Yu G Y, Chen Y Y, et al. Post-positioned gas spring enables ultra-high output power of hybrid thermoacoustic electric generators. *Cell Reports Physical Science*, 5: 101835 (2024).
- [5] Li Z, Zhang H, Huang Z, et al. Characteristics and optimization of heat pipe radiator for space nuclear propulsion spacecraft. *Progress in Nuclear Energy*, 150: 104307 (2022).
- [6] Chiranjeevi P B, Krishnaraj K, Vinod K G, et al. Numerical simulations, experimental investigation and optimization of hybrid space thermal radiators. *Applied Thermal Engineering*, 234: 121275 (2023).
- [7] Geng S. Overview of NASA magnet and linear alternator research efforts. In: *AIP Conference Proceedings* (2005).
- [8] Dhar M. Stirling space engine program, Volume 1-Final report. New York, Mechanical Technology Incorporated (1999).
- [9] Dhar M. Stirling space engine program, Volume 2-Appendixes A, B, C, and D. New York, Mechanical Technology Incorporated (1999).
- [10] Wang X T, Wu Z H, Zhang L M, et al. Traveling-wave thermoacoustic refrigerator for room temperature application. *International Journal of Refrigeration*, 120: 90–96 (2020).
- [11] Xu JY, Hu JY, Luo EC, et al. A cascade-looped thermoacoustic driven cryocooler with different- diameter resonance tubes. Part I: Theoretical analysis of thermodynamic performance and characteristics. *Energy*, 181: 943–953 (2019).
- [12] Park J, Ko J, Kim H, et al. The design and testing of a kW-class free-piston Stirling engine for micro-combined heat and power applications. *Applied Thermal Engineering*, 164: 114504 (2020).
- [13] Chang D P, Hu J Y, Sun Y L, et al. Numerical investigation on key parameters of a double-acting free piston Stirling generator. *Energy*, 278: 128003 (2023).

Novel designs of drive mechanisms and configurations

A Novel Cam-Drive Mechanism for Non-Sinusoidal Motion in a Stirling Engine

Wong HM

*Department of Mechanical and Materials Engineering, Lee Kong Chian Faculty of Engineering and Science, Universiti Tunku Abdul Rahman, Sungai Long, Selangor, Malaysia
Center for Sustainable Mobility Technologies, Universiti Tunku Abdul Rahman, Sungai Long, Selangor, Malaysia*

Corresponding author: wonghm@utar.edu.my

Keywords: Cam, Dwell, Non-sinusoidal, Kinematic

Abstract

The ideal Stirling cycle have two constant volume processes for heat regeneration and two constant temperature processes for heat addition and removal. These processes are sequenced and timed to create mechanical work. The main components responsible for these time-based processes are the working piston and displacer. Therefore, their position, motion and timing are vital for the engine's operation and its output performance. The drive mechanism of a Stirling engine is responsible for the working piston and displacer's motion, timing and extracting mechanical work. A crank-slider mechanism is commonly used as the drive mechanism but it provides near sinusoidal motion to the components. This limits net heat transfer to the internal working fluid and consequently limits mechanical work. To increase net heat transfer and mechanical work of a Stirling engine, the use of non-sinusoidal working piston and displacer motion was proposed through the use of a novel cam-drive mechanism. A cam is a classical, simple and proven technology as it has been used in many applications and machines. As a cam-drive mechanism to extract mechanical work, it can be designed for various types of working piston and displacer non-sinusoidal motion as well as integrating dwell. An experimental approach was used to assess the capability of the cam-drive mechanism. A gamma configuration medium temperature difference Stirling engine was developed with a cam-drive mechanism which has a two-sided face grooved radial cam flywheel operating with roller oscillating cam followers. Various motions for the working piston and displacer was designed and tested. Kinematic analysis for this mechanism ensures smooth, low noise and low vibrations operation during the design stage. Through the use of a data acquisition system, thermal efficiency was found to improve 36% in comparison with the benchmarked sinusoidal working piston and displacer motion. This paper documents the design, fabrication and experience in using a cam-drive mechanism in a Stirling engine.

Introduction

Kinematic Stirling engine uses a drive system that comprise of a slider-crank mechanism and other similar derivatives such as the crank rocker, wobble yoke, rhombic drive, swash plate, Scotch yoke, and the Ross yoke [1]. These drive mechanisms time the processes

or events of the Stirling engine cycle as well as to extract mechanical work [2, 3]. These mechanisms also are simple, balanced, robust, well used and time proven technologies, dated back since the inception of the Stirling engine. This is the reason for 60% of the industrial Stirling engine uses kinematic drive system [3].

There are other drive mechanisms created over time, offering simplicity, robustness, and efficiency than a crank-slider based drive mechanisms. Van de Ven [4] suggested the use of hydraulics in a liquid piston Stirling engine. Cullen and McGovern [5] suggested the use of motor / generator coupled with rack and pinion gearing in an alpha Stirling engine configuration. Nico-Seto and Nobes [6] uses a set of oval elliptical gears in their Stirling engine research.

Inclusion of dwell had agreed that it improves heat transfer, especially in the displacer motion. Gopal [7] investigated the inclusion of dwell in the displacer motion. When compared with the benchmarked sinusoidal motion, he found the thermal efficiency increased by 15%. Briggs [8] manipulated the displacer motion electronically in a free piston Stirling engine by altering the displacer's duration at each of the hot and cold end. As much as 14% improvement in thermal power was found. Nicol-Seto and Nobes [6] altered the displacer motion from sinusoidal to non-sinusoidal through the use of oval elliptical gears and able to obtained 3% increase in power. The simulation investigation of Craun and Bemiah [9] regarding the use of non-sinusoidal motion of displacer found 40% increase in the engine performance when compared with sinusoidal displacer motion. Improved transfer of heat leads to increase of power output via the implementation of dwell in the displacer motion. Kolin realizes the significance of dwell and implemented this in his low temperature difference Stirling engine [10]. Wong and Goh [11] implement dwell in their Stirling engine prototype and found an increase of 36% increase in thermal efficiency.

Implementing dwell is challenging and best outcome can be achieved through good control of the motion and timing [7, 11]. According to Rothbart [12], motion control can be achieved by using linkage mechanism, servo valve-controlled hydraulic cylinder, stepper motor and controller, industrial adjustable mechanism, and cam and follower. The cam and follower mechanism are known for its good dynamic properties, low cost, high load capability, and able to be used for high power operations. This mechanism itself is a well proven technology and used in many machines that provides high power

and accurate motion control such as packaging machines, shoe making machines and even in internal combustion engines (cam shaft operating the valvetrain). Therefore, the cam and follower mechanism may be a solution for such a demand of accurate implementation of dwell and high torque transfer as a drive mechanism.

This paper documents the development of the cam-drive mechanism and the gamma type Stirling engine test rig used for the cam-drive early testing as well as the experiences of using such mechanisms. Performance improvement from implementing dwell in motion of both displacer and piston was done [11] and reported. This is an early development stage of the cam-drive mechanism, in search for better thermal efficiency. The vibration and mechanical efficiency of the cam-drive mechanism usage in a Stirling engine however was not investigated at this stage.

Stirling engine test rig

The Stirling engine test rig was developed to prove the usage of the proposed novel cam-drive mechanism. The test rig comprises of a Stirling engine prototype that incorporates a novel cam-drive mechanism, an engine loading mechanism and a data acquisition system.

Stirling engine prototype

A gamma type Stirling engine prototype was designed, as shown in Figure 1. This configuration was chosen for its suitability for low and medium temperature difference operation [13]. Moreover, any changes made to the motion of displacer and the working piston, the engine would not change its compression and expansion ratio, as long as the stroke of the working piston remained unchanged. There were some mass minimizing efforts for all of its reciprocating components to minimize vibration and noise. This will be discussed in later section. The specifications of the Stirling engine are listed in Table 1.

Cam-drive mechanism

The development of this cam-drive mechanism was to control motion and the implementation of dwell. The targeted displacement for the drive mechanism was include rise-dwell-fall-dwell (RDFD). Cycloidal motion was chosen for its suitability at high speed application [9]. This motion gives finite value of jerk (rate change of acceleration) while compromising all other basic cam requirements. Finite value of jerk means finite change

of forces onto the reciprocating components (the working piston and the displacer). Requiring the whole cycle of RFD motion to complete within one revolution or 360° of a cam further stresses the importance to control jerk as lesser time is available for each segment of rise and fall from dwells. The increase of engine speed further increases jerk. In other words, usage of cycloidal motion would reduce operational stress of the reciprocating components and therefore minimizing mechanical noise and vibration.

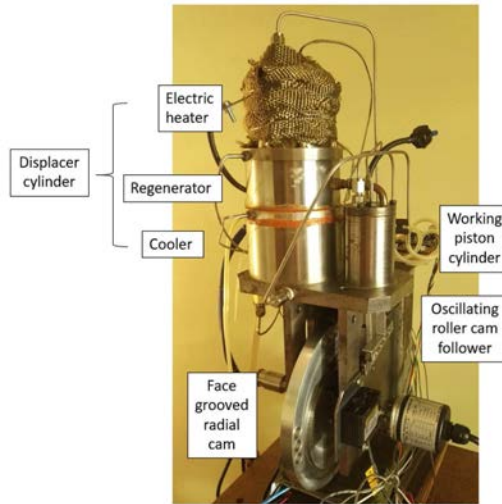


Figure 1. Stirling engine with cam-drive mechanism.

Table 1. Specifications of the Stirling engine.

Engine capacity	267 cc
Displacer cylinder bore / stroke	60 mm / 35 mm
Displacer cylinder construction	Stainless steel hot end, aluminum cold end
Displacer	Thin walled stainless steel, mild steel cap with stainless steel shaft
Regenerator	Coiled stainless steel dimpled sheet
Working piston bore / stroke	40 mm / 35 mm
Working piston cylinder	Mild steel
Working piston	Graphite with aluminum center.
Linkages	Aluminum
Heater	Insulated, adjustable DC power supply with NiChrome wire
Cooler	Water cooling

The cam drive mechanism had a flywheel with two face grooved closed radial cams on either side of the flywheel face. An oscillating roller cam follower at each side of the flywheel had its roller fit into the face groove and follows the grooved cam profile. This setup gives low frictional loss as it doesn't need of a return spring to ensure contact with the cam profile [14]. A connecting rod links the reciprocating components on one end while the other end links to the oscillating roller cam follower. Each set of the cam, cam follower, and connecting rod is responsible for the motion of either the working piston or the displacer, hence the need for the face grooved cam on either side of the flywheel. Figure 2 showed the schematic diagram of one side of the face grooved closed radial cam and its associated oscillating roller cam follower.

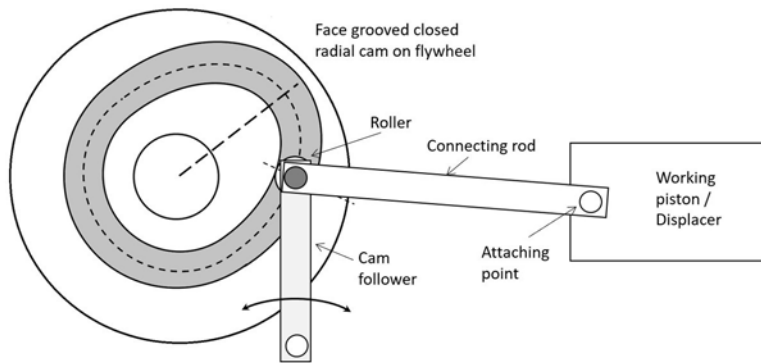


Figure 2. Schematic diagram of the cam-drive mechanism.

The process of designing the motion of working piston and displacer began from determining the displacement of the reciprocating components relative to the cam angle. The RDFD motion of the reciprocating components were separated into four segments, namely the rise, dwell, fall, and dwell. Each of the segments corresponds to a range of angles the cam operates where the summation of all the segments would be a full rotation of the cam. The rising cycloidal displacement function [14] can be rewritten as:

$$s_R = h \left[\frac{\theta_R}{\beta_R} - \frac{1}{2\pi} \sin \left(2\pi \frac{\theta_R}{\beta_R} \right) \right] \quad (1)$$

where, s_R is the cam rising displacement (mm), h is the stroke (mm), θ_R is the relative cam angle starting from beginning of rise segment ($^\circ$), and β_R is the total cam angle in rise segment to complete ($^\circ$). The value would start from zero (0) to the maximum stroke of 35 mm. The reciprocating component would now be at top dead center (TDC) where it dwells and remained there until the next segment. The fall segment displacement can be rewritten as:

$$s_F = h \left\{ 1 - \left[\frac{\theta_F}{\beta_F} - \frac{1}{2\pi} \sin \left(2\pi \frac{\theta_F}{\beta_F} \right) \right] \right\} \quad (2)$$

where, s_F is the cam fall displacement (mm), θ_F is the relative cam angle starting from beginning of fall segment ($^\circ$), and β_F is the total cam angle in fall segment to complete ($^\circ$). This segment would have its displacement to fall from dwell at 35 mm to bottom dead center at zero (0). These equations were applied into a spread sheet to calculate the displacement (s) of working piston and displacer respected to the cam angle, across all four segments of RDFD. A small interval of 0.05° was used. Analysis of svaj was done in the same spreadsheet to assess values of velocity, acceleration and jerk.

Next is to determine the cam follower's roller position. Figure 3 highlighted the lengths, distances and angles made by the linkages, influenced by displacement of the reciprocating components. As shown in the figure, the connecting rod would tilt as the reciprocating components change its displacement from TDC to BDC. This tilting would create lateral force onto the reciprocating components (increase frictional losses). To minimize these unwanted lateral forces, tilting was restrained by sizing the length of the cam follower that would only give a small 2 mm vertical distance change. With the same spreadsheet, the position of the roller (R_x , R_y) can be found with the equations below:

$$A_x = A_{x, fixed} - (h - s) \quad (3)$$

$$A = \sqrt{(A_x)^2 + (A_{y, fixed})^2} \quad (4)$$

$$\beta_1 = \tan^{-1} \left(\frac{A_{y, fixed}}{A_x} \right) \quad (5)$$

$$\beta_2 = \cos^{-1} \left(\frac{R_f^2 + A^2 - L^2}{2R_f A} \right) \quad (6)$$

$$\beta_3 = 90^\circ - \beta_1 - \beta_2 \quad (7)$$

$$R_f = \frac{1}{4} \left[\left(\frac{h}{2} \right)^2 - 4 \right] \quad (8)$$

$$R_x = R_f (\sin \beta_3) \quad (9)$$

$$R_y = R_f (\cos \beta_3) \quad (10)$$

where, $A_{x, \text{fixed}}$ is horizontal distance measured from the cam follower pivot to the working piston / displacer attaching point while at TDC, $A_{y, \text{fixed}}$ is the vertical distance from the cam follower pivot to the center of the cylinders, A_x is the current x-distance between the cam follower pivot to the attaching point (mm), A is the current distance between follower pivot to the attaching point (mm), β_1 is the angle between horizontal axis to A line ($^\circ$), β_2 is the angle between A line to R_f line ($^\circ$), β_3 is the angle between vertical axis to R_f line ($^\circ$), R_f is the cam follower's length, R_x is the current x-distance of follower arm (mm), and R_y is the current y-distance of follower arm (mm).

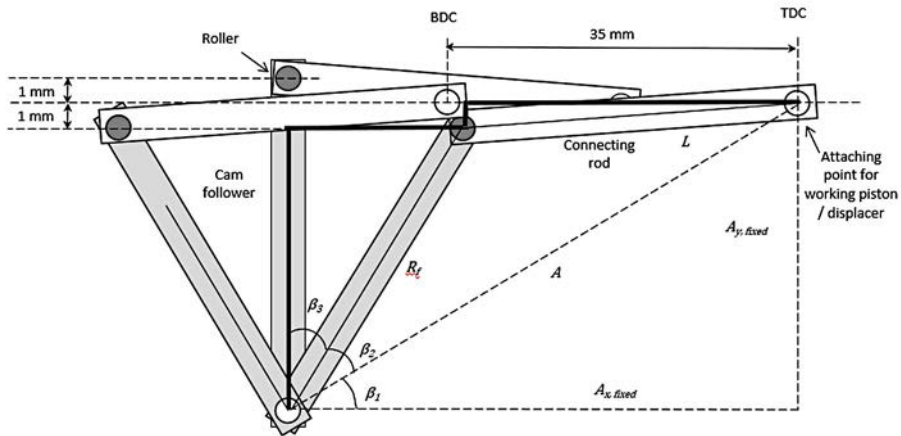


Figure 3. Schematic diagram of the oscillating roller cam follower and the connecting rod.

The current position of the cam follower's roller (R_x , R_y) at its associated cam angle could not directly used to produce the cam profile. The follower not only creates radial distance changes relative to a cam's center point, it also changes the contact angle as well. Thus, the final calculation for the cam profile needed to be compensated for this angle of contact. Figure 4 showed the relationship between the cam's center to the roller contact. From Figure 4, compensating angle, α was introduced for this need. Cam profile was obtained from the value of R_{cam} (the radial distance of the cam's pitch curve to the center of the cam) and compensating angle, α relative to the cam angle. Information from CAD data was used to determine the exact location of the cam to find the required parameters. Related equations are found below:

$$(R_{cam})_x = 67.508 + R_x \quad (11)$$

$$(R_{cam})_y = A_{y, fixed} - R_y \quad (12)$$

$$R_{cam} = \sqrt{[(R_{cam})_x]^2 + [(R_{cam})_y]^2} \quad (13)$$

$$\alpha = \tan^{-1} \left(\frac{(R_{cam})_y}{(R_{cam})_x} \right) \quad (14)$$

$$\theta_{compensated} = \theta - \alpha \quad (15)$$

where $(R_{cam})_x$ is the current distance R_{cam} in x-direction, $(R_{cam})_y$ is the current distance R_{cam} in y-direction, θ is the current cam angle, and $\theta_{compensated}$ is the corrected current cam angle. Each of the current coordinates at this point becomes polar coordinates of $(R_{cam}, \theta_{compensated})$. Plotting of all these coordinates would give the cam's pitch curve (center line for the cam profile) for each the working piston side and displacer side. The rotational direction of flywheel cam was set clockwise for the working piston (same positive direction of the calculation) while the displacer side to set counterclockwise direction (the negative direction of the calculation), as they are both on the same flywheel. The small interval of 0.05° used to define the displacement gave refined coordinates in order to produce a high resolution milling during prototyping stage on a CNC mill.

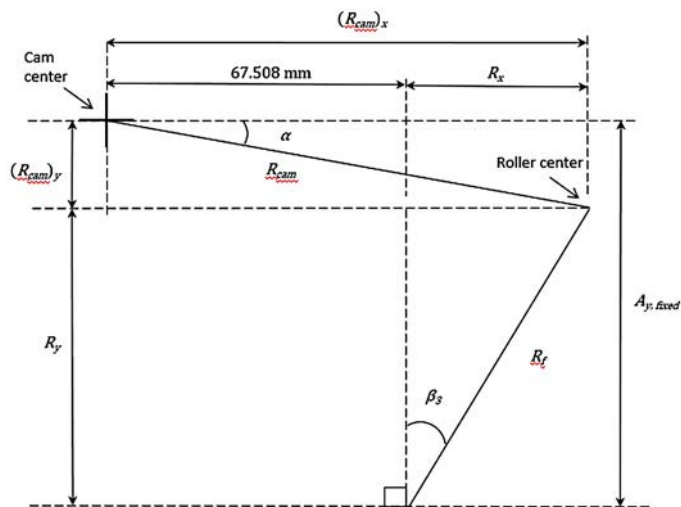


Figure 4. Relationship of cam follower position to cam center.

These coordinates were then transferred and drawn in a 3D computer aided design software. Once the both the groove has been formed in a 3D model, the flywheel cam would be naturally imbalanced. Therefore, lightening holes were created to balance the flywheel in order that the center of gravity of the flywheel cam is located at the center. These additional steps were taken to minimize the vibration caused by the rotation of the flywheel cam. Figure 5 shows the samples of the flywheel cams produced.



Figure 5. Samples of the flywheel with the grooved radial cam. [11]

Engine loading mechanism

The test rig was equipped with a mechanical prony-brake. It provides loading to Stirling engine, enabling engine speed control. This type of engine loading was deemed adequate for its task as the engine was low powered. However, engine brake torque was not measured at the time of conducting the experiment and could not investigate on the mechanical efficiency of the cam-drive mechanism.

Data acquisition system

The test rig data acquisition system comprised of a laptop to collect data from PicoLog and Thermocouple Data Logger, both from PicoTech. The measured parameters were summarized in Table 2. Temperature measurement was used to monitor the operation of the engine. The schematic diagram of the data acquisition system can be found in Figure 6.

Table 2. Measuring parameters of the data acquisition system.

Pressure	Working power cylinder, hot end of the displacer cylinder, and cold end of the displacer cylinder
Temperature	Working power cylinder, hot end of the displacer cylinder, hot end of the regenerator, cold end of the regenerator, cold end of the displacer, cooling water inlet, and cooling water outlet.
Cam	Cam angle and marker.
Displacement	Working power piston, and displacer.

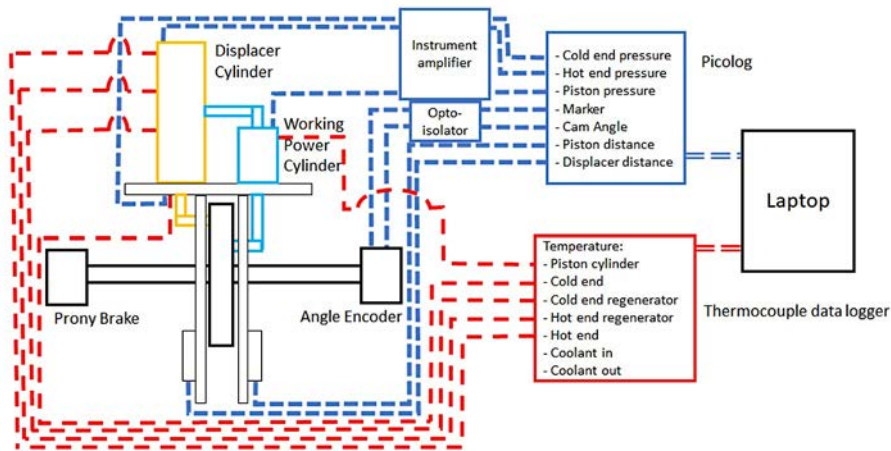


Figure 6. Schematic diagram of the data acquisition system.

Test procedure

The test was to evaluate the usage of different RFD settings and compares them with a benchmark sinusoidal motion. Achieving this would prove that the cam-drive mechanism is able to be used as defined or intended. There were four tested cams altogether where three of the cams had RFD motion settings and one sinusoidal motion, as shown in Figure 5. The description of the cams can be found in Table 3. The cam labeled as “crank” was designed to provide sinusoidal motion, emulating a crank-slider motion. “90_90” flywheel cam provided ideal motion of the displacer and working piston. Shortcomings found in the “90_90” cam was learnt and improved, became the “90_90 Ovrp” cam. This cam lengthened the working piston rise and fall duration to 150° while shortens its

dwelt to only 30° and the displacer motion remained the same. This allowed a before and after 30° overlap in the two transitions of displacer dwell, as shown in Table 3. Motivated with the new-found improvement of the “90_90 Ovr1p” cam, the “135_45 Ovr1p” cam further lengthened the displacer dwell to 135° while reduced the overlap to 15°.

Table 3. Description of the tested cams.

Cam	Motion type	Description	Displacer	Working Piston
Crank	Sinusoidal	Benchmark	Sinusoidal	Sinusoidal with 90° phase lagging
90_90	RDFD	Ideal cycle	0° - 90° (Rise), 90° - 180° (Dwell), 180° - 270° (Fall), 270° - 360° (Dwell)	0° - 90° (Dwell), 90° - 180° (Rise), 180° - 270° (Dwell), 270° - 360° (Fall)
90_90 Ovr1p	RDFD	Overlap motions, reduced working piston dwell	0° - 90° (Rise), 90° - 180° (Dwell), 180° - 270° (Fall), 270° - 360° (Dwell)	30° - 60° (Dwell), 60° - 210° (Rise), 210° - 240° (Dwell), 240° - 390° (Fall)
135_45 Ovr1p	RDFD	Increased displacer dwell, reduced piston dwell, overlap motions	0° - 45° (Rise), 45° - 180° (Dwell), 180° - 225° (Fall), 225° - 360° (Dwell)	15° - 30° (Dwell), 30° - 195° (Rise), 195° - 210° (Dwell), 210° - 375° (Fall)

Tests were conducted with 350W heating power. The engine was to warmed up until the cold end temperature reached 40 ±0.5 °C. This cold end temperature was maintained with the adjustment of cooling water flow throughout the experiment. Engine speed was adjusted with the prony brake. The data acquisition system was used to collect the data of pressures, positions of the displacer and working piston, and the encoder pulses. Ten consecutive cycles were recorded and analyzed via a spreadsheet. The raw data was filtered, processed to obtain pressure and volume which was then used to calculate the indicated work output, indicated mean effective pressure, power and also thermal efficiency.

Results

Results of the tests conducted by Wong and Goh [11] were found to be positive. Figure 7 showed the PV diagram of the four tested cams. The “crank” cam operates with a classical ellipsoidal shaped PV diagram. The usage of a cam-drive mechanism was able to replicate sinusoidal motion, similar to a crank-slider mechanism, hence the similar outcome. This outcome served as the benchmark for the rest of the cams.

The three non-sinusoidal RDFD motion however produced unique shaped PV diagrams. First observation was that they all produced constant volume processes, similar to an ideal Stirling cycle. Next, the 90_90 cam performed poorly compared to the benchmark sinusoidal motion. PV diagram of the 90_90 cam had a “bowtie” shape where it narrowed in the middle section. Due to this shape, work (the area under the curve) by the expansion process was slightly larger than the work by the compression process, leading to a small production of net work. Also to note that the “bowtie” peaks (at both BDC and TDC) did not produce any work as they occur when there were no change in volume, rendering it unwelcomed. Wong and Goh had analyzed the performances in detail [11].

The shortcoming of the 90_90 cam was addressed and improved upon to become the 90_90 Ovr1p. The 90_90 Ovr1p was found able to reduce the effect of the vertical pressure change with no volume change. This created additional work in the cycle and widened the “bowtie” shape, as shown in Figure 7. It is important to note that the displacer dwell was maintained (the exact of 90_90 cam) and the overlap was designed into the working piston during the displacer dwell. With this encouraging outcome, the 135_45 Ovr1p cam was designed to further extend the displacer dwell for improved heat transfer. With this extra duration of displacer dwell, the performance was raised further. Summary of the performance of all the cams can be found in Table 4.

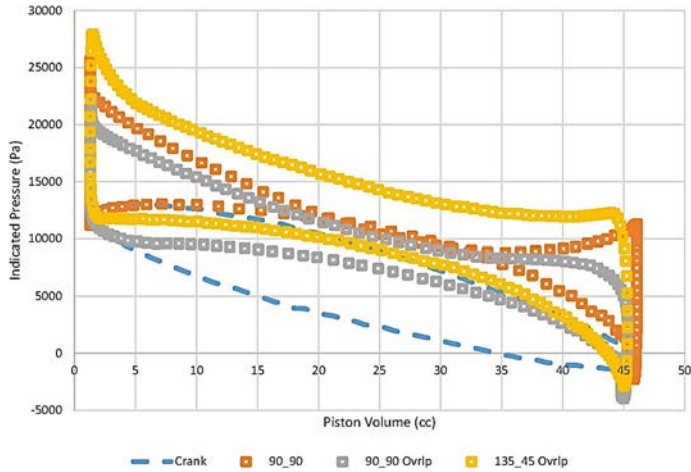


Figure 7. PV diagram for the four tested cams [11].

Table 4. Performance outcome of the four tested cams [11].

Cam	IMEP (Pa)	Power (W)	Thermal Efficiency ($\times 10^{-4}$)
Crank	5300.82	0.448	12.81
90_90	2896.50	0.224	6.38
90_90 OvrIp	4721.80	0.380	10.79
135_45 OvrIp	7534.59	0.613	17.43

Table 4 showed the use of ideal Stirling cycle motion of 90_90 cam reduced power output by 50% compared to the crank cam. This was expected as similar observation were found by other researchers [15, 16]. Use of motion overlapping in 90_90 OvrIp enabled power to improve 69% over the 90_90 cam. Overlapping of working piston into the displacer dwell made better use of the pressure change during the constant volume regeneration heat addition and removal. The displacer dwell period was further extended in the 135_45 OvrIp cam and the output was found better. With this new setting, performance was up 36% when compared against the baseline crank cam.

Throughout the experiment and running of the Stirling engine, the test rig produced slight vibration and engine noise. The flywheel cam was balanced in design and in prototyping (produced by using CNC milling), these vibrations may come from the

reciprocating displacer and working piston as well as the oscillating roller cam follower. Efforts of lightening had been made but its existence of reciprocating mass were still evident in the operation. It was noted that these vibration and noises would contribute to low mechanical efficiency. As mentioned prior, mechanical efficiency was not found as a proper dynamometer was not available.

Conclusion

A novel cam-drive mechanism was developed. It is capable of generating both sinusoidal and non-sinusoidal motions for the displacer and the working piston. Steps needed to create such motions were disclosed. Four types of different motions were developed. From the developed cam, tests confirmed that the cam-drive mechanism able to perform as intended. Performance of the tested Stirling engine had strong relationship with the motions of displacer and working piston. The ideal Stirling cycle motion performed worst comparing with the traditional sinusoidal drive. It was found that inclusive of overlaps allow the work and power to be generated effectively. The duration of displacer dwell also has a strong connection to the performance of the engine. To date, the best performing cam has a long displacer dwell duration of 135°. This cam managed to improve as much as 36% in thermal efficiency. Vibration and noise of the cam-drive mechanism was slight but evident, indicating the need to counter the effect of the reciprocating mass of the displacer and working piston.

Acknowledgements

The author would like to thank Universiti Tunku Abdul Rahman for the support given to enable this research to be conducted through the UTAR Research Fund (Project no.: IPSR/RMC/UTARRF/2015-C2/W03). Much appreciation to Prof. Ir. Dr. Goh Sing Yau for his guidance in the project.

References

- [1] Erol D, Yaman H, Doğan B. A Review Development of Rhombic Drive Mechanism Used in the Stirling Engines. *Renewable and Sustainable Energy Reviews*, vol. 78. (2017). <https://doi.org/10.1016/j.rser.2017.05.025>
- [2] Arslan TA, Kocakulak T. A Comprehensive Review on Stirling Engines. *Engineering Perspective*, vol. 3, no. 3. (2023) <https://doi.org/10.29228/eng.pers.66847>

- [3] Stirling Engine Assessment. The Electric Power Research Institute, Inc. (2002)
- [4] Van de Ven JD. Mobile Hydraulic Power Supply: Liquid Piston Stirling Engine Pump. *Renewable Energy*, vol. 34, no. 11. (2009). <https://doi.org/10.1016/j.renene.2009.01.020>
- [5] Cullen B, McGovern J. Development of a Theoretical Decoupled Stirling Cycle Engine. *Simulation Modelling Practice and Theory*, vol. 19, no. 4 (2011). <https://doi.org/10.1016/j.simpat.2010.06.011>
- [6] Nicol-Seto M, Nobes D. Experimental Evaluation of Piston Motion Modification to Improve the Thermodynamic Power Output of a Low Temperature Gamma Stirling Engine. 19th International Stirling Engine Conference (2021). <https://doi.org/10.1051/e3sconf/202131304002>
- [7] Gopal VK. Active Stirling Engine. University of Canterbury. (2012).
- [8] Briggs M. Improving Free-Piston Stirling Engine Power Density. Case Western Reserve University. (2015).
- [9] Craun M, Bemiah B. Optical Periodic Control of an Ideal Stirling Engine Model. *Journal of Dynamic Systems, Measurement, and Control*, 137, 071002-1 (2015). <https://doi.org/10.1115/1.4029682>
- [10] Kolin I, Koscak-Kolin S, Golub M. Geothermal electricity production by means of the low temperature difference Stirling Engine. World Geothermal Congress 2000 (2000).
- [11] Wong HM and Goh SY. Experimental comparison of sinusoidal motion and non-sinusoidal motion of rise-dwell-fall-dwell in a Stirling engine. *Journal of Mechanical Engineering and Sciences*, vol. 14, no. 3, Pg 6971 – 6981, (2020). <https://doi.org/10.15282/jmes.14.3.2020.01.0546>
- [12] Rothbart HA. *Cam Design Handbook*. New York: McGraw-Hills. (2004).
- [13] Egas J and Clucas DM. Stirling engine configuration selection. *Energies*. Pg 1-22, (2018). <https://doi.org/10.3390/en11030584>
- [14] Norton RL. *Design of Machinery: an Introduction to the Synthesis and Analysis of Mechanisms and Machines*. McGraw-Hill (2012).

- [15] Ranieri S, Prado GAO, MacDonald BD. Efficiency reduction in Stirling engines resulting from sinusoidal motion. *Energies*, vol. 11, no. 11, (2018). <https://doi.org/10.3390/en11112887>
- [16] Červenka L. Idealization of the real Stirling cycle. *J. Middle Eur. Constr. Des. Cars.*, Vol. 14, No. 3, (2017). <https://doi.org/10.1515/mecdc-2016-0011>

Direct Generation of Compressed Air by Cascaded Overdriven Free Displacer Thermocompressors

H.-D. Kühl^{a,*}, F. Fischer^a

a Laboratory of Thermodynamics, TU Dortmund University, Emil-Figge-Str. 70, 44227 Dortmund, Germany

Corresponding author: hans-detlev.kuehl@tu-dortmund.de

Keywords: Thermocompressor, Thermal compressor, Compressed air, Stirling cycle, Waste heat utilization

Abstract

As conventional generation of compressed air is costly and inefficient, reciprocating thermocompressors have been proposed as an alternative technique to generate it directly from waste heat without any detour via mechanical power. The compression ratio of a single stage is limited by the temperature ratio and dead volume effects. So, cascades of several stages are required to reach relevant pressure levels. Due to the low power density, economic competitiveness forces a low-cost, large-scale series production and hence an identical design of all stages. According to recent proposals, this can favorably be realized by so-called overdriven free displacers, which run self-sustained at variable frequencies without a crank mechanism. Theoretical models and design conceptions for such systems are briefly summarized and supplemented by experimental results from a first single-stage prototype, which largely confirm theoretical predictions regarding stationary and dynamic operating characteristics, particularly including favorable self-starting capabilities. However, leakage effects at the bushings of the displacer rod deteriorated the performance particularly at higher pressure levels, and the concept of water lubrication proved to be impractical. The consequences of these findings for future cascade designs are discussed, and an outlook is provided.

Introduction

Compressed air is an important industrial energy source, but its production is costly and primary energy-intensive. At the same time, most industrial processes generate waste heat, the potential of which is rarely exploited at present. One potential way of utilizing such waste heat is to generate compressed air by so-called reciprocating thermocompressors, which are comparable to the displacer - heat exchanger system of a β - or γ -Stirling engine, but feature check valves instead of a compression piston. Thus, the air to be compressed simultaneously acts as the working fluid of the cycle, and the supplied heat flow is directly converted to a compressed air flow, without any detour via mechanical power.

Such a thermocompressor was first proposed in a patent granted to Vannevar Bush in 1935 [1]. A disadvantage of this system clearly is its low power density due to the almost ambient operating pressure. Furthermore, the pressure ratio is thermodynamically limited by the temperature ratio and dead volume effects. To achieve typical industrial pressure levels of 6-10 bar and thus supplement or replace the conventional generation of compressed air, a cascade of multiple stages is therefore required. Bush already proposes a two-stage system in his patent, suggesting a smaller stroke volume of the second stage to maintain an even load distribution despite the higher pressure level. However, this concept would result in the need for an individual design of each stage in a larger cascade, and each of these would require a drive mechanism and auxiliary mechanical power to operate the displacer.

To reduce the constructional complexity and thus increase the economic competitiveness of such systems, Thomas and Barth [2] suggest using identical stages regardless of the rising pressure levels and to actuate them synchronously by a common crank shaft. However, the constraint of equal mass flows in all stages entails unfavorable operating conditions with an additionally reduced power density for most of these. To resolve this issue, Fischer and Kühn [3] propose to additionally omit the entire crank mechanism as a further simplification and to apply the concept of an overdriven free displacer instead, which is particularly well known from Ringbom-Stirling engines [4]. Thus, the operating frequencies are decoupled and may adapt automatically, so that the power density of every stage is maintained close to optimum conditions. Furthermore, a self-sustained operation even including self-starting capabilities can thus be realized, since the required p,V -work may be generated internally via the cross section of the displacer rod plunging into the cold cylinder volume more or less deeply.

Theoretical models for such systems including an analysis of stability issues have been developed at various levels of idealization and were reported in previous publications [3,5,6]. These will be briefly reviewed in the following and supplemented by recent experimental results obtained from a first single-stage prototype featuring a further simplified design as already outlined in [5]. Finally, an outlook regarding the realization of a cascade is given.

Summary of Fundamentals and Previously Reported Work

Operation of the Idealized Isothermal Cycle

Figure 1 a illustrates the basic layout of a single thermocompressor stage as discussed in detail previously [3,5]. Additional heat exchangers are provided to transfer the net heat flows at the hot and the cold temperature level, T_h and T_c , as the cylinder volumes typically do not provide sufficient heat transfer surfaces. Similarly to the Stirling cycle, a regenerator is recommendable to improve the performance, and the assumption of isothermal cylinder volumes and a perfect regeneration is required for an ideal cycle. In this case, the amounts of heat exchanged as well as the work done per cycle can be visualized as loop areas for the hot, the cold and the overall cycle volume in the p, V plane, as illustrated in Figure 1 b.

The most essential operating parameter of such systems is the pressure ratio $\Pi = p_i/p_o$, i.e. the ratio of the outlet pressure p_i to the inlet pressure p_o as indicated in Figure 1b. Evidently, there is a maximum, which never exceeds the inverse of the temperature ratio, $\tau = T_c/T_h$ and is additionally reduced by dead volume effects. It can be evaluated as

$$\Pi_{max} = \frac{B+D}{B-D} = \frac{1+D/B}{1-D/B} \quad (1),$$

where B and D denote the average and the amplitude of the sum of the temperature-related volumes in the cycle. These determine the current cycle pressure as a function of the displacer position and the enclosed mass m of the working fluid (air), which may of course vary between m_{min} and m_{max} in this case due to the opening of the inlet and outlet valves. Designating the stroke volume amplitude in the hot cylinder as \hat{V} and $\rho = A_R/A_D \ll 1$ as the ratio of the cross sections of the displacer A_D and its rod A_R , B and D may be obtained as

$$B = \frac{\hat{V}}{T_c} (1 - \rho + \theta) + \sum \frac{V_{d,i}}{T_{d,i}} \quad (2)$$

$$\text{and } D = \frac{\hat{V}}{T_c} (1 - \rho - \theta) \quad (3).$$

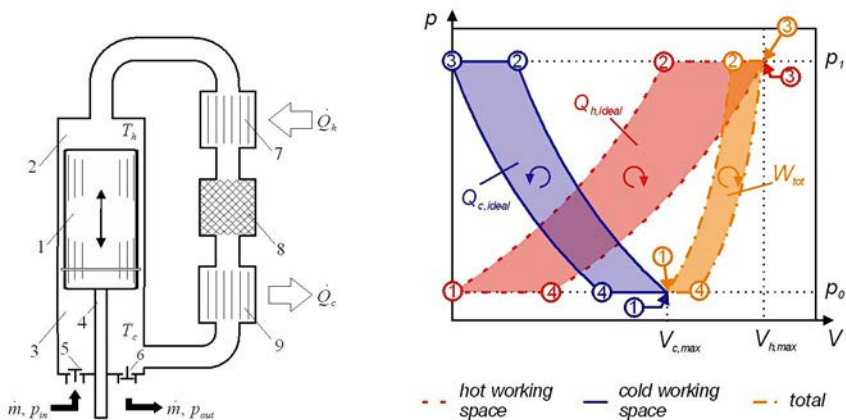
As eq. (2) also includes the sum of any dead volumes $V_{d,i}$ related to their corresponding mean temperatures $T_{d,i}$, we definitely always have $D \ll B$. Particularly in the case of waste heat utilization at $T_h \approx 300^\circ\text{C}$, we therefore typically obtain values of $\Pi_{max} \approx 1.4 \dots 1.6$ only. Evidently, $\Pi = \Pi_{max}$ is the limiting case, when the valves do not open anymore and thus, the

p, V loop areas in Figure 1 b are zero, i.e. no heat is exchanged, no work is generated, and the stage will therefore stop operating, since no auxiliary power input is assumed. The same obviously applies to the limiting case $\Pi=1$, and therefore, a maximum heat input Q_h and work output W occurs at medium values of Π . The plots of the corresponding functions,

$$Q_h = p_0 \cdot 2\hat{V} \cdot \frac{\Pi_{max}-\Pi}{\Pi_{max}-1} \cdot \ln \Pi \quad ; \quad W = \rho Q_h \quad (4),$$

are similar to inverted parabolas. Their maximum is found to be at $\Pi_{opt} \approx \sqrt{\Pi_{max}}$, which will be referred to as the optimum pressure ratio in the following. Introducing the specific gas constant R , the mass of air conveyed per cycle is found to decrease linearly with Π [3]:

$$\Delta m = p_0 \cdot (\Pi_{max} - \Pi) \frac{B-D}{R} \quad (5)$$



(a) Layout of a thermocompressor: (1) displacer, (b) p, V -diagram for an ideal thermocompressor cycle including process states and curves for the two working spaces and the total volume cycle including process states and curves for the two working spaces and the total volume cycle

Figure 1. Simplified schematic drawing of the single—stage thermocompressor and visualization of the amounts of heat exchanged and the work done by the idealized cycle in a p, V -diagram [3].

Overdriven Mode Operation of the Displacer

The work generated according to eq. (4) adds to the kinetic energy of the displacer. Contrarily to Ringbom-Stirling engines, there is no need to stop the displacer by viscous damping at the ends of stroke, since it need not be synchronized with a crank-coupled piston. Instead, the displacer is intended to bounce back after an ideally elastic impact, thus preserving its kinetic energy. So, its operating frequency N will gradually increase, until the work generated via its rod is entirely dissipated by speed-dependent fluid friction effects. Applying some simplifying assumptions, such as linearly speed-dependent friction forces, its equation of motion was solved analytically by Fischer and Kühl [3], and it was found that the stroke function vs. time may be well approximated by a triangular function, if the displacer mass is sufficiently high, and that this case also yields the highest operating frequencies. This result is contrary to the situation in Ringbom-Stirling engines, where the displacer mass should be as low as possible to minimize the loss of kinetic energy at the ends of stroke.

Furthermore, it is important to suspend the displacer in a medium stroke position by a weak mechanical spring during standstill to improve its self-starting capabilities. According to eq. (1) to (3), $\Pi_{\max} > 1$ is only possible if we have $D > 0$, i.e. for $\theta < 1 - \rho$. Assuming a constant, near-ambient value of T_c , this happens as soon as the hot cylinder is heated beyond a design-dependent threshold value of T_h . Above this value and as long as the valves are closed, a deflection of the displacer towards the “hot” end of stroke results in a decrease of the cycle pressure and vice versa. If a constant pressure – possibly close to the average cycle pressure – acts on the reverse side of the rod, this results in an accelerating force in the direction of the initial deflection, i.e. the displacer is unstable. This instability is a mandatory precondition for any kind of overdriven mode operation [4], which may in this case favorably enable a spontaneous self-starting of a stage, e.g. by minor fluctuations of a buffer pressure due to leakage effects or unsteady operation of other stages in a cascade.

Design Considerations Regarding a Thermocompressor Cascade

As already mentioned in the introduction, Fischer and Kühl [3] propose to arrange several identical overdriven free-displacer thermocompressors in a cascade to thus generate compressed air at typical industrial pressure level of approximately 6-10 bar. Of course, it is by no means clear that a particular stage design is equally operational

at any location in such a cascade, since particularly the density of the air changes by one order of magnitude, and this will presumably affect the optimum design of the heat exchangers, the regenerator, connecting ducts, gas springs etc. Furthermore, it is important to operate any stage close to the optimum pressure ratio Π_{opt} to maintain an acceptable power density, as it is low anyway.

If all stages operate at the same frequency N as in the crank-driven design by Thomas and Barth [2], this is evidently not possible. Numbering the stages by an index $k=1, \dots, n$ in the direction of flow, the inlet pressure p_0 must be substituted by p_{k-1} in eq. (4) and (5). Since every stage must inevitably convey the same mass flow in steady-state operation, the mass Δm according to eq. (5) must also be the same in this case. Since it is evidently proportional to the inlet pressure p_{k-1} , this is only possible if every stage adopts an individual pressure ratio $\Pi_k > \Pi_{k-1}$. Depending on the target pressure p_n and the number of stages provided, the pressure ratios will therefore spread rather evenly over the entire range from $\Pi=1$ to Π_{max} , i. e. Π_1 will be close to unity, and Π_n close to Π_{max} . Therefore, only very few stages in the medium pressure range will operate near Π_{opt} , i. e. at an acceptable power density.

This is why Fischer and Kühl [3] suggested decoupling the frequencies of the stages by the concept of overdriven free displacers and varying the frequencies inversely with the inlet pressures, i.e. selecting $N_2 = N_1 / \Pi_1$ and so on. If the design and the operating conditions of all stages are the same and thus, the same constants B and D according to eq. (2) and (3) and the same pressure ratio Π apply, it is easy to derive from eq. (4) that the heat flows $\dot{Q}_{h,k} = N_k \times Q_{h,k}$ and the generated power $P_k = N_k \times W_k$ are also the same. Furthermore, the Reynolds numbers in any flow channel are the same, too, since their pressure- and speed-dependences cancel out. So, the Nusselt numbers and the heat transfer coefficients are also the same in every stage, i.e. we have complete similarity regarding any heat transfer in the stages, and a given heat exchanger design will therefore be equally operational throughout the cascade. If the number of stages is chosen appropriately, so that the pressure ratio is

$$\Pi = \sqrt[n]{p_n/p_0} \approx \Pi_{opt} \approx \sqrt{\Pi_{max}} = \sqrt{(B+D)/(B-D)} \quad (6),$$

all stages can be operated close to the maximum possible power density of their design. However, the described similarity does unfortunately not apply to flow losses, and these

are the main reason for the dissipation of the generated mechanical power P_k , which is the same in all stages under the above assumptions. A frictional pressure drop may be evaluated as

$$\Delta p_k = \zeta (Re) \frac{l}{d_h} \frac{\rho_k}{2} u_k^2 \quad (7).$$

In this equation, the Darcy friction factor ζ as well as the length l and the hydraulic diameter d_h of the considered flow passage are the same in any stage, the density ρ_k increases linearly with the inlet pressure, and the flow velocity u_k is proportional to the frequency N_k and thus varies inversely. So, the same finally applies to the pressure drop Δp_k , too. Considering that the dissipated power equals the product of Δp_k and the volume flow, which features the same dependence once again, the power loss even decreases with the square of the inlet pressure, and therefore, the frequencies will not vary inversely with the inlet pressure in practice.

To demonstrate the consequences of this finding, it is assumed that two consecutive stages 1 and 2 initially operate according to the above conditions, i.e. at $\Pi_1 = \Pi_2 \approx \Pi_{opt}$ and so that there is an equilibrium between the generated and the dissipated work per cycle in stage 1 at the frequency N_1 . In the second stage, the generated work is $W_2 = W_1 \times \Pi_1$, whereas the dissipated work is a linear function of the frictional pressure drop, since the volumetric displacement is the same. In case of laminar flow, the pressure drop is independent of the density and a linear function of the flow velocity and thus the frequency. So, a frequency $N_2 = N_1 \times \Pi_1$ instead of $N_2 = N_1 / \Pi_1$ is required to dissipate the generated work in stage 2.

In the case of fully turbulent flow, i.e. if $\zeta(Re) \sim Re^{-1/4}$ or even $\zeta \approx const.$ may be assumed, this discrepancy is less severe, since we have an almost linear dependence on the pressure via the density in eq. (7), which contributes a major share to the required increase of W_2 . As we furthermore have an almost square dependence on the velocity in this case, a marginal increase of the frequency would be sufficient to fulfill the condition $W_2 = W_1 \times \Pi_1$. In any case, stage 2 will convey a larger mass flow than stage 1, since we have $N_2 > N_1$ and, in addition, $\Delta m_2 = \Delta m_1 \times \Pi_1$ because of eq. (5). So, the pressure difference $p_2 - p_1$ between the adjacent buffer volumes will increase, and Π_2 will thus be shifted to values above Π_{opt} . As a consequence, Δm_2 is linearly reduced according to eq. (5). Furthermore, there also is a decrease of W_2 , which is, however, less than linear due to the effect of $\ln(\Pi)$ in eq. (4).

The decrease of N_2 will therefore be far less than that of Δm_2 , depending on the prevailing flow conditions. In any case, Π_2 will increase until the mass flow $\dot{m}_2 = N_2 \times \Delta m_2$ recedes to the value provided by stage 1. Due to the differently intense dependences on Π_2 , this value can only be matched by a combination of $N_2 > N_1$ and $\Delta m_2 < \Delta m_1$ particularly in case of laminar flow. So, the operating frequencies must be expected to increase along the cascade rather than to decrease. Any subsequent stage will run at a somewhat higher pressure ratio than the preceding one, and a similarity regarding the heat transfer is not maintained anymore.

However, the exergy flow supplied to the air as an ideal gas by an isothermal compression in stage k can generally be evaluated for a given ambient temperature T_{amb} according to

$$\Delta \dot{E}_k = \dot{m} R T_{amb} \ln \Pi_k \quad (8).$$

Since the mass flow is the same throughout the cascade and we generally have $\Pi_{k+1} > \Pi_k$, any subsequent stage will transfer a higher exergy flow than the preceding one and hence perform better – regardless of any similarity considerations. So, the evidence that the design and the operating conditions of the first stage are most crucial for the performance of the entire cascade [3] is once again confirmed. The exergy flow $\Delta \dot{E}_1$ provided by this stage should therefore be maximized by all means. In fact, this maximum is not precisely at $\Pi = \Pi_{opt}$ but somewhat below, because a minor decrease of heat input per cycle according to eq. (4) – which is marginal in the vicinity of Π_{opt} – is overcompensated by an increased mass flow.

Stability Issues Concerning Cascade Operation

In the above example of two consecutive stages, it was assumed that the temporarily increased mass flow conveyed by stage 2 only affects the pressure ratio Π_2 . However, this mass flow will not only increase the pressure p_2 in its outlet buffer, but also decrease p_1 in its inlet buffer, which simultaneously is the outlet buffer of stage 1. So, the pressure ratio of this stage is also affected, and the same will apply to a subsequent stage 3. So, the above discussion is actually somewhat simplified, and the question arises whether the described interactions may cause instability in the anticipated operation of cascade consisting of n stages. Applying some simplifying assumptions again, this issue was investigated analytically by Fischer et al. [6]. Summarizing the results, which cannot be reproduced here for reasons of conciseness, it was found that there is a lower

stability limit for the operating pressure ratio of any stage k , which can be proven to be considerably lower than Π_{opt} . It can therefore be concluded that the anticipated optimum operation of a cascade with the first stage running at or marginally below Π_{opt} and any subsequent stages at pressure ratios further above is generally stable. Fischer et al. [6] were furthermore able to confirm this analytical prediction by an advanced numerical model of a three-stage cascade accounting for the major loss mechanisms. Similarly, they could also confirm the predicted instability of the overdriven displacers at standstill and the consecutive self-starting of the stages due to a gradual decrease of the target pressure p_n , as e.g. caused by an assumed air consumption.

Experimental Investigation of a Single-Stage Prototype

Development of a Simplified Design

As mentioned above, the condition $\theta < 1 - \rho$ must be fulfilled for overdriven mode operation of a displacer, since otherwise, no acceleration and thus no gain of kinetic energy is possible. However, this condition does not ensure an operation at an acceptable power density. As derived in [3], the maximum heat input per cycle at $\Pi_{opt} \approx \sqrt{\Pi_{max}}$ may be

approximated as

$$Q_{h,opt} \approx p_0 \hat{V} (\sqrt{\Pi_{max}} - 1) \quad (9)$$

and is thus directly dependent on Π_{max} , which in turn depends on the ratio D/B according to eq. (1). So, it is essential to maximize D and to minimize B as far as possible. Assuming that θ is preset by the temperature of the available heat source, maximizing D is equivalent to minimizing ρ . However, ρ also directly affects the magnitude of the generated p,V work W . In order to maximize the power density in terms of exergy supplied to the compressed air, it is therefore essential to minimize any frictional pressure drop as well as any mechanical friction losses, e.g. at the guide bushings of the displacer rod or possibly not ideally elastic limit stops. Furthermore, minimizing B is equivalent to minimizing the dead volumes.

To meet all these requirements simultaneously, it was therefore decided to simplify the design of the first single-stage prototype according to a recommendation by Walker [7] for Stirling engines designed for low pressures and thus low power densities, namely to

reduce the heat exchangers and the regenerator, which were designated as separate components according to Figure 1a, to a plain annular gap between the displacer and the cylinder wall. Despite presumably increased thermal losses, such a design offers a variety of advantages:

- Minimum dead volume, yielding a low value for B
- Minimum flow losses, allowing a small value of ρ and thus a large value of D
- Maximum constructional simplicity, reducing the manufacturing effort
- Minimum susceptibility to fouling

The resulting design is schematically illustrated in Figure 2a. To accommodate as many check valves in parallel as possible and thus minimize the associated flow losses, the cold cylinder bottom was exclusively reserved for the inlet valves. The outlet valves were instead incorporated in the bottom plate of the displacer. Thus, its interior forms a part of the outlet buffer space, which is connected to the main part at the bottom end of the assembly via the hollow displacer rod. This volume accommodates any auxiliary equipment, e.g. a mechanical spring suspending the displacer in a medium position at standstill, the springs forming the elastic limit stops, any required mounting and adjusting screws and furthermore an LVDT displacement transducer to monitor and record the displacer motion, which is not shown in Figure 2a for transparency reasons. The large external surface of this volume additionally helps to reject heat to the ambience and thus reduce the load on the cooler, which consists of the lower section of the annular gap and a surrounding water-cooled jacket. Hence, the compressed air will expectedly reach its lowest temperature in this volume, and it is therefore anticipated that any condensation of air moisture, which is inevitable in the higher stages of a cascade due to the almost isothermal compression, will primarily occur here.

The handling of this condensing water is another issue to be discussed. In the present design, it was decided to make use of this phenomenon and to utilize this water, which will primarily accumulate in the sump of the outlet buffer space, for lubrication and sealing in the water-resistant polymer bushings guiding the displacer rod. It is hence channeled into the gaps of these bushings via capillaries, which are not shown in Figure 2 a, either. The existing pressure differences are sufficient for this purpose, since these bushings are located in the bottom plate of the cold cylinder and the plate between the inlet and the outlet buffer.

As further illustrated in Figure 2a, the cross section of the displacer rod is reduced to one half by a step located in the range of the inlet buffer space. The overall force acting on the reverse side of the rod is therefore the same as the force exerted on the entire cross section by an average pressure, which would be hard to control in a separate, third buffer volume.

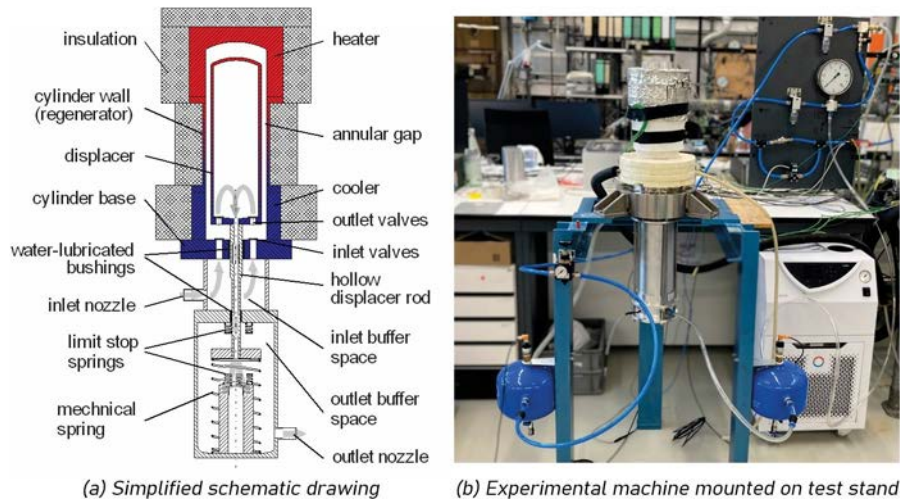


Figure 2. Single-stage prototype thermocompressor [8].

Experimental Results for Single-Stage Operation

As depicted in Figure 2b, the experimental prototype according to the described design was realized and mounted on a test stand providing the required auxiliary equipment, such as additional, larger inlet and outlet buffers including a pressure control, a mass flow meter to measure the conveyed flow of compressed air, a controlled water supply to the outlet buffer space simulating the moisture condensation, a cooling water supply and an electric heater including the corresponding temperature controls. The data acquisition system used to view, monitor and record the experimental data and to provide the master control functions is not shown. In operation, any relevant stationary quantities, such as temperatures, flow rates, buffer pressures etc. are continuously displayed and recorded. Furthermore, the thermo compressor cycle is monitored via the displacement

transducer and a high-speed pressure transducer providing the instantaneous cycle pressure in the cold cylinder.

To record a particular operating state, these data are stored at a sufficiently high temporal resolution together with the aforementioned stationary data. Figure 3a shows an exemplary plot of these cyclic data including the pressure values in the buffer volumes, which evidently are not entirely constant despite the installed control systems, but are subject to minor fluctuations due to the periodic opening and closing of the inlet and outlet valves. During the opening of the inlet valves, a minor oscillation of the cycle pressure is observed, which is attributed to a fluttering of the valve reeds made from silicon rubber. This material was found to yield the best performance regarding flow losses as well as reliable opening and closing.

The data reflecting the instantaneous displacer position can of course be used to evaluate the size of the cylinder volumes and thus generate experimental p,V diagrams as shown in Figure 3b. Evidently, the predicted shape of the loops according to Figure 1b is qualitatively well reproduced, although the design and operating data are of course different. However, please note that the loop for the hot cylinder volume was generated using the pressure in the cold cylinder. It is therefore not quantitatively correct, since flow losses are neglected.

During the experimental investigations, various operating states at different inlet pressures and pressure ratios were recorded, so that experimental operating curves showing the dependence of various stationary data, such as the heat input, the exergy gain of the compressed air, the frequency or the mass flow, on the preset experimental parameters, particularly the pressure ratio, could be generated. A selection of these was presented by Fischer and Kühl already [8] and is not fully reproduced here for reasons of conciseness. In addition, all relevant experimental data collected in the experiments as well as detailed information about the machine design are accessible via the Zenodo repository [9].

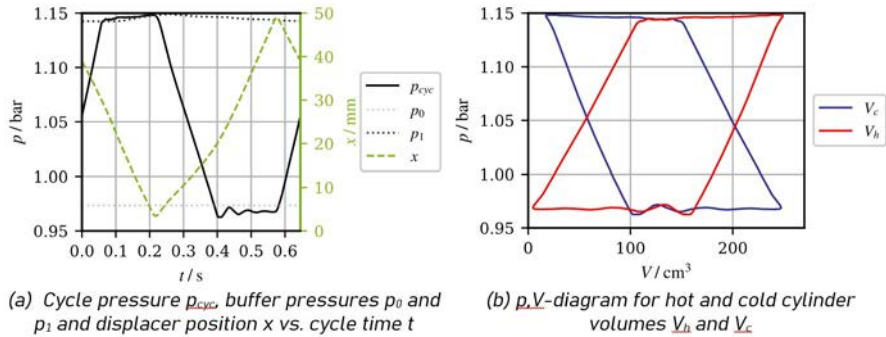


Figure 3. Cyclic measurement results for pressure ratio $\Pi = 1.18$ and ambient inlet pressure at heater temperature $T_h = 295$ °C cooler temperature $T_c = 8$ °C [8].

In general, deviations between the experimental results and the theoretical predictions were observed regarding the maximum achievable pressure ratio. These must be attributed to leakage effects at the guide bushings of the displacer rod, which were of course not included in the model of the idealized cycle as reproduced above. Despite the described water feed into the bushing gap, noticeable leakage flows of air into the inlet buffer space were detected from both the outlet buffer space and the active cycle volume. As a result, the theoretically predicted maximum pressure ratio Π_{\max} was never reached experimentally. Instead, the measured net flow of the compressed air dropped to zero at a lower pressure ratio, although the compressor was still running and non-zero p,V loop areas indicated that the inlet and outlet valves did still open periodically. However, the entire mass flow primarily conveyed via these valves was evidently used up by the aforementioned leakage flows. Contrarily to the ideal cycle, which of course stops when approaching Π_{\max} , since Q_h , W and Δm drop to zero according to eq. (4) and (5), it was found to be virtually impossible to stop a real thermocompressor featuring such leakage losses by increasing Π towards Π_{\max} . Instead, the only safe way to stop the running experimental machine was to discharge the compressed air in the outlet buffer by opening a valve and thus enforce $\Pi=1$.

Experimental Emulation of a Four-Stage Cascade

Of course, such leakage effects also affect the operation of a thermocompressor cascade, since they become increasingly important in the upper stages due to the higher density

of the air and the increasing absolute pressure differences acting along the bushings. They are therefore essential for the explanation of the operating curves displayed in Figure 4, which show the exergy gain ΔE of the air flow, the operating frequency N and the mass flow \dot{m} vs. the pressure ratio and for various inlet pressures as listed in the textbox in Figure 4b.

Evidently, the curves for ΔE and \dot{m} drop to zero at pressure ratios considerably below the theoretical maximum, which is $\Pi_{\max}=1.41$ for the given design and operating conditions. The higher the inlet pressure is chosen, the lower is this practical upper limit, which will be denoted by Π_{\lim} in the following. As mentioned above, the machine is still running when it is reached, and therefore the operating curves of the frequency do not drop to zero at the corresponding value of Π_{\lim} . However, the location of their maximum, which can be identified as the practical optimum pressure ratio, also decreases when the inlet pressure is raised.

Furthermore, a stable operation is evidently possible even at pressure ratios considerably below this practical optimum. This confirms the results of the aforementioned theoretical stability considerations [6], which predict a lower stability limit in this range. Applying the derived analytical stability criteria to the special case of the first stage of a cascade, where – just as in the present case – the inlet pressure may be assumed to be constant, the lower stability limit equals the zero of an analytical function $K_3(\Pi)$ and may be approximated as

$$\Pi_{0,K3} \approx (\sqrt{5 + 4 \Pi_{\max}} - 1)/2 \quad (10).$$

Applying the values of Π_{\lim} instead of Π_{\max} , the actual lower limits are well reproduced. The indicated values for the inlet pressure have actually been chosen on purpose, and the intention was to emulate the operation of a four-stage cascade experimentally, although just one prototype stage was available. Following the theoretical considerations presented above, it is recommendable to operate the first stage at maximum exergy gain to achieve an optimum performance of the cascade. According to Figure 4a this corresponds to a pressure ratio $\Pi_1 \approx 1.17$ and thus an outlet pressure $p_1 = 1.18$ bar, since the inlet pressure is $p_0 = 1.01$ bar. So, the second set of operating curves was recorded using p_1 as the preset inlet pressure. Now, it is essential to consider that the mass flow must be the same in all stages of the cascade and that this mass flow is imposed by the chosen

operating point of stage 1 in this case. Evaluation of the corresponding curve in Figure 4c at the chosen pressure ratio $\Pi_1 \approx 1.17$ (vertical dotted line) therefore yields a value of $\dot{m} \approx 0.104$ g/s, as indicated by the horizontal dotted line. The intersection of this line and the operating curve recorded at an inlet pressure of $p_1 = 1.18$ bar yields a value of $\Pi_2 \approx 1.19$ as the correct steady-state operating pressure ratio of the second stage in the emulated cascade. Thus, the inlet pressure of stage 3 can be evaluated as $p_2 = 1.18 \text{ bar} \times 1.19 \approx 1.40$ bar, and this value was hence preset as the inlet pressure for the recording of the third set of curves, and so on.

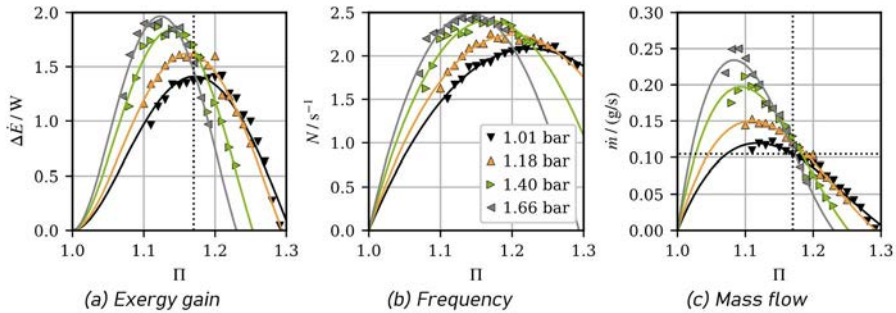


Figure 4. Measurement results for various inlet pressures p_k and $T_h = 295$ °C and $T_c = 8$ °C including fitted functions and dotted lines, which represent the optimum operating point of the “first” stage at ambient inlet pressure [8].

The operating pressure ratio of any subsequent stage is always found at the intersection of the corresponding curve in Figure 4c and the mass flow imposed by stage 1. Thus, the inlet pressure of the next stage may be evaluated. Table 1 summarizes the operating data of the emulated cascade including the corresponding exergy gains and frequencies, which may be determined by Figure 4a and b, respectively.

Table 1. Operating data of an experimentally emulated four-stage cascade for $\dot{m} \approx 0.104$ g/s.

Number of Stage	k	1	2	3	4
Inlet pressure	p_{k-1} / bar	1.01	1.18	1.40	1.66
Operating pressure ratio	Π_k	1.17	1.19	1.18	1.17
Operating frequency	N_k / s ⁻¹	1.92	2.21	2.37	2.40
Exergy gain	ΔE_k / W	1,42	1,53	1,52	1,43

Evidently, the predicted increase of the latter can be confirmed despite the leakage effects, which obviously become more dominant when the inlet pressure is raised. This is indicated by the decreasing values of Π_{lim} as well as by the general shift of the curves and particularly their maxima to lower pressure ratios. As a consequence, the predicted increase of the operating pressure ratios along the cascade cannot be fully confirmed. Instead, there is a maximum at stage 2, and lower values are found for the higher stages due to the increased leakage. The same of course applies to the exergy gain, which is directly linked to the pressure ratio according to eq.(8), since the mass flow is the same in all stages.

Anyway, the experimental results confirm that a thermocompressor cascade may operate at an acceptable overall power density and that an almost even load distribution throughout all stages is possible. Of course, instability problems due to potential interactions between the stages via pressure changes in the intermediate buffer spaces could not be investigated.

Conclusion and Outlook

By the realization and experimental investigation of this first prototype of an overdriven free-displacer thermocompressor, the theoretically predicted operating characteristics and performance could be largely confirmed. In particular, the overdriven mode operation of the displacer including the anticipated self-starting capabilities could be well reproduced. The design of the displacer rod plunging into both the inlet and the outlet buffer with one half of its cross section proved to be a very practical and simple way to maintain an even force balance under varying operating conditions and can definitely be recommended for future designs. However, the concept of lubricating and sealing the guide bushings with condensing water must be revised, as the leakage problem could not be solved this way, but turned out to be comparatively severe. This is most likely due to the required polymer material and the entailed tolerance issues, which can presumably be better handled if metallic materials, such as sintered bronze, are used. This approach is therefore meanwhile tested experimentally.

The simplified design, which was primarily developed to reduce the manufacturing effort for this first prototype, proved to be fully operational. It was therefore decided to maintain this design concept, i.e. realizing the heat exchangers and the regenerator

by a plain annular gap around the displacer instead of the originally envisaged separate and comparatively complex components, for the realization of an experimental cascade of three identical stages as the next investigation step, which has already been realized. Experimental data are available [10], and a presentation of the results is expected to be published soon [11].

In the revised design, which was applied for the experimental cascade, the goal of reducing the manufacturing effort was further pursued. Although the components had to be machined individually once again, the number of components was reduced, their shape was simplified and the design was adapted to facilitate a potential future series production. On a theoretical level, these design simplifications were meanwhile even further developed. The displacer and the cylinder are e.g. envisaged to be produced by deep drawing, the housing of the buffer spaces may essentially consist of an aluminum tube produced by extrusion molding, and its surface is expected to be sufficiently large to reject the waste heat if it is e.g. exposed to a cooling water flow. The heat input at the hot temperature level is assumed to be provided by a flue gas stream passing through fins that are pressed or possibly brazed onto the hot section of the cylinder, whereas the regenerator section is surrounded by a block of ceramic insulation material. Envisaging a rectangular flow channel for the cooling water featuring a square pitch of cylindrical bores in the top and the bottom sheet that match the diameter of the buffer space housing, it is conceivable to virtually “plug” multiple stages into these bores and thus arrange them both in series and in parallel. If the external shape of the fins and the insulation around the upper section of the units is rectangular or even square, the required flow channel for the flue gas stream may thus be created automatically without much further constructional effort, and any single stage may easily be “unplugged” and replaced in case of a failure or potential maintenance, which is, however, expected to be hardly required. Figure 5 visualizes this concept schematically. Evidently, the basic idea is to provide larger capacities by arranging the required number of units in parallel, whereas the desired target pressure determines the number of units in series. Thus, a large-scale series production of just one particular compressor unit could be set up, which could be produced at very low cost. Its size should of course be further optimized under various aspects including manufacturing issues as well as theoretical constraints. However, scaling and similarity considerations indicate that current size is rather close

to the thermodynamic optimum, if the present, simple design based on an annular gap around the displacer shall be maintained.

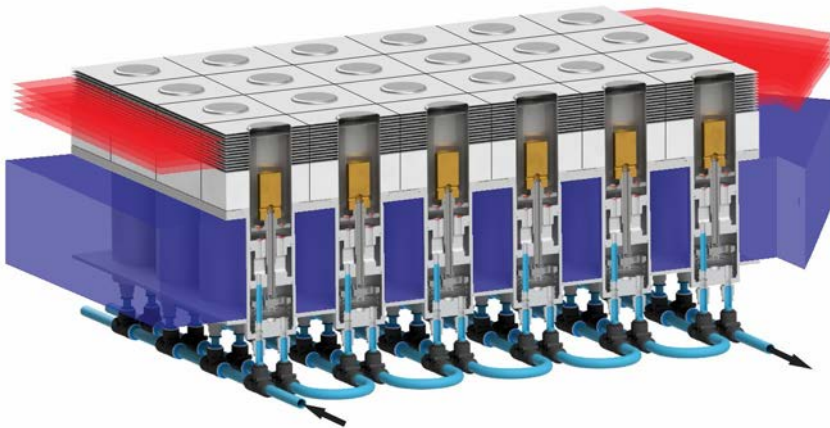


Figure 5. Illustration of an array of parallel thermocompressor cascades with finned heater heads inserted in a common cooling water channel, including a visualization of the hot and cold fluid flows.

Acknowledgements

This research was funded by the German Research Foundation (DFG), grant # KU 755/5-1.

References

- [1] V. Bush, Apparatus for Compressing Gases US Patent 2,157,229 (1935).
- [2] S. Thomas, E.J. Barth, Multi-Stage Modeling of a Stirling Thermocompressor, in: ASME, Proceedings of the ASME/BATH 2017 Symposium on Fluid Power and Motion Control (FPMC2017), Sarasota, FL, USA (2017), <https://doi.org/10.1115/FPMC2017-4320>
- [3] F. Fischer, H.-D. Kühl, Analytical model for an overdriven free-displacer thermocompressor, Appl. Therm. Eng 185 (2021), <https://doi.org/10.1016/j.applthermaleng.2020.116251>
- [4] G. Walker, J.R. Senft, Free Piston Stirling Engines, Springer, Berlin, 1985.

- [5] F. Fischer, H.-D. Kühl, Generation of compressed air by cascaded thermocompressors–project status, E3S Web Conf. 313 (2021), <https://doi.org/10.1051/e3sconf/202131304003>
- [6] F. Fischer, S. Peveling, H.-D. Kühl, Simulation and stability analysis of a thermocompressor cascade with overdriven free displacers, Therm. Sci. Eng. Prog. 44 (2023), <https://doi.org/10.1016/j.tsep.2023.102037>
- [7] G. Walker, Stirling-cycle machines, Clarendon Press, Oxford, 1973.
- [8] F. Fischer, H.-D. Kühl, Generation of compressed air by overdriven free-displacer thermocompressors – Experimental investigation of a single stage, Appl. Therm. Eng 244 (2024), <https://doi.org/10.1016/j.applthermaleng.2024.122712>
- [9] F. Fischer, H.-D. Kühl, Experimental data for a single-stage overdriven free-displacer thermocompressor, [Data Set], Zenodo (2023), <https://doi.org/10.5281/ZENODO.8289373>
- [10] F. Fischer, H.-D. Kühl, Experimental data for a three-stage overdriven free-displacer thermocompressor cascade, [Data Set], Zenodo (2024), <https://doi.org/10.5281/zenodo.10726185>
- [11] F. Fischer, H.-D. Kühl, Generation of Compressed Air by Overdriven Free-Displacer Thermocompressors – Experimental Investigation of a Three-Stage Cascade, Appl. Therm. Eng (2024, under review)

Study on Stable Operation of Displacer with Low Damping

Yuanhang Chen^{a,b}, Yanyan Chen^{a,*}, Guoyao Yu^{a,c,*}, Yiwei Hu^{a,b}, Jing Luo^{a,b}, Yanlei Sun^a, Ercang Luo^{a,b}

a Key Laboratory of Cryogenic Science and Technology, Technical Institute of Physics and Chemistry, Chinese Academy of Sciences, Beijing 100190, China

b University of Chinese Academy Sciences, Beijing 100049, China

c Institute of Optical Physics and Engineering Technology, Qilu Zhongke, Jinan 251000, China

Corresponding author: yychen@mail.ipc.ac.cn; gyyu@mail.ipc.ac.cn

Keywords: Free piston Stirling engine, Displacer, Gas spring, Low damping, Stable operation

Abstract

Free piston Stirling engine heavily relies on the internal acoustic field to realize ideal thermoacoustic effect in the regenerator. The displacer serves as a critical component, acting as a phase shifter that orchestrates the thermoacoustic conversion process. The functionality of the displacer directly correlates with the engine's overall efficiency and reliability.

Research highlights that the bulk of failures in free piston Stirling engines are linked to displacer-related issues. These range from mechanical spring breakdowns to friction-induced debris, which can clog the regenerator or disrupt piston action. Hence, the importance of a displacer's low damping and stable performance won't be overstated.

Ensuring the displacer's motion requires a specific stiffness, conventionally provided by gas or mechanical springs. Gas springs, as opposed to mechanical ones, are less prone to fatigue and are unaffected by pressure changes, yet they demand centering devices that offer adequate radial stiffness and enable a frictionless operation through gas bearings.

This paper introduces a novel approach to secure the displacer's low damping and stability by using centering magnets. These magnets maintain the displacer's position both circumferentially and axially, supplemented by balanced magnets and gas bearings for stability during operation. By utilizing the commercial software MAGNET, we designed magnets of various structures to attain low damping and stability, with theoretical and experimental results validating this method. The experimental data confirms that the displacer, under the support of gas bearings and at optimal displacement, operates within the desired conditions, exhibiting a damping coefficient under 10 Ns/m.

Furthermore, experiments showed that while multi-stage magnet configurations improve magnetic stiffness, they also limit the maximum displacement. We've deduced a universal relationship between magnetic stiffness and displacement, facilitating the design of magnets tailored to specific operational requirements. Our research offers a reliable design framework, promising to enhance the efficiency and lifespan of free piston Stirling engine by improving the performance of displacer assembly.

Introduction

It is imperative to develop or enhance energy utilization devices in order to alleviate global energy and derivative challenges. Mitigating carbon emissions and achieving carbon neutrality are critical challenges in the energy sector, requiring innovative solutions and collaborative efforts from all stakeholders. The Free Piston Stirling Generator (FPSG), proposed and developed over the past half-century, has been extensively researched and applied, demonstrating remarkable advantages and immense potential for practical implementation [1]. Due to the elimination of the crank mechanism in FPSG, its unique features include high reliability, oil-free operation, maintenance-free design, and high efficiency. From the perspective of thermoacoustics, FPSG can be regarded as a resonant system characterized by mass-spring-damping effect. First and foremost, stable and low damping operations of the two movers (i.e., displacer and power piston) are crucial. On account of its multiple roles of acoustic field tuning, acoustic work recovery and acoustic resonance, displacer has been mostly concerned. Its operational state significantly impacts the efficiency, lifespan, and dynamic processes such as onset and transient adjustment. Xiao et.al indicated that motion damping especially on the displacer has a serious influence on the system performance [2]. The research done by Jia et.al shows that the reduction of the damping coefficient is an effective method to improve FPSG's performance [3]. Zhu et.al proposed that the damping coefficient would affect the performance of FPSG, the heating temperature, the operating stroke, and other parameters [4]. Zare et.al unveiled that the accurate characterization of the equivalent damping coefficient is the key to the model calculation [5]. Notably, research indicates an increased occurrence of failure modes in free piston Stirling generators attributed to displacer issues, such as mechanical spring fractures or friction debris leading to regenerator blockages or piston malfunctions [6]. Therefore, ensuring minimal damping and stable operation of the displacer becomes crucial for the engine's efficient and reliable functioning.

In contrary to damping, spring is somewhat overlooked due to its simple role of providing requisite axial stiffness. However, spring and bearing are highly intertwined in FPSG, which in turn affects the damping and stable operation. Based on the arrangement of springs, FPSG can be mainly categorized into gas spring type and mechanical spring type. Mechanical springs have been widely employed in prototypes to support the displacer,

primarily utilized by Qnergy Inc. in developing combined heat and power systems. This mechanical spring also functions as a bearing, known as ultra-high radial stiffness flexure, offering exceptional rigidity. In some prototypes, gas bearings are employed to provide radial stiffness for wear elimination [7]. While in demanding circumstances such as space application, gas spring is favored to rebound the displacer. On the other hand, for both mechanical and gas springs, the positioning of the spring varies depending on custom types, such as being located in bounce space or compression space, and being sprung to ground or power piston. Each type of spring can adopt these location schemes with their respective advantages and disadvantages [8]. Fig. 1 illustrates four classical schemes. The mechanical flexure springs are strategically positioned in either the bounce or compression space, effectively regulating the frequency and stroke for desired output power. Moreover, the gas spring, located within the compression space, leading to a complex structure and large dead volume, with ultimately decreased efficiency [9]. The post-positioned gas spring has been proposed and validated, demonstrating significant potential for enhancing power density and scaling up output power [10]. So far, the static stiffness required to constrain the displacer, the pneumatic connection of the centering mechanism, as well as anti-rotation measures have yet to be addressed, let alone the lateral force and gravity offset effect pertaining to the equilibrium positioning of the displacer. In this paper, we propose a centering and balance magnet scheme to ensure low damping and stable operation of the displacer. The proposed scheme was firstly investigated through commercial software MAGNET in terms of magnet field and force calculation. Subsequently, experimental results verified that our proposed scheme effectively enables stable operation with a reduced damping coefficient by an order of one compared with traditional design. Finally, a conclusion was drawn.

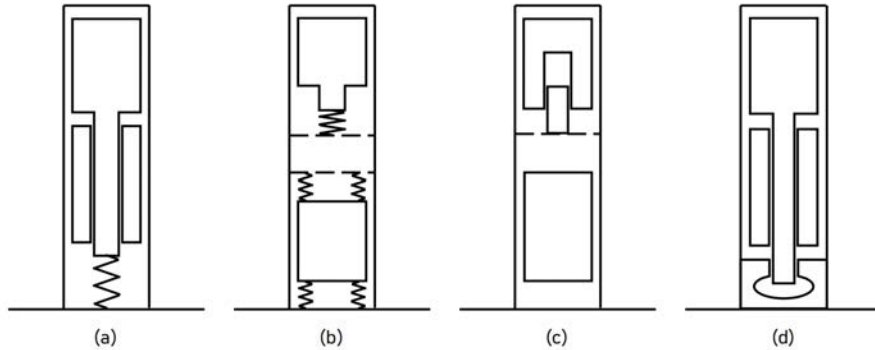


Figure 1. Common configurations of the FPSGs: (a) Flexure spring in bounce space, (b) Flexure spring in compression space, (c) Gas spring in compression space, (d) Gas spring in bounce space.

Theoretical Analysis

As discussed in the previous section, adopting a post-positioned gas spring presents three challenges as illustrated in Fig. 2: offset, rotation, and tilt. Firstly, a simple gas spring fails to provide static stiffness, resulting in drifting of the equilibrium position during both static and dynamic stages. Secondly, although the centering magnet has been considered as an optimal solution and implemented in some prototypes, displacer rotation looms. Additionally, a practical issue arises when a dual-opposed configuration is adopted – i.e., inevitable lateral force induced by gravity center offset.

There are two approaches to mitigate offset: one involves enhancing static stiffness through a multi-stage centering magnet, while the other focuses on suppressing pressure differences via a centering hole. Given the presence of the centering hole, anti-rotation becomes crucial in this scheme, and cogging force facilitates anti-rotation. If a balancing force can be applied to the displacer to eliminate tilt torque, it would promote gas-bearing lubrication without any wear.

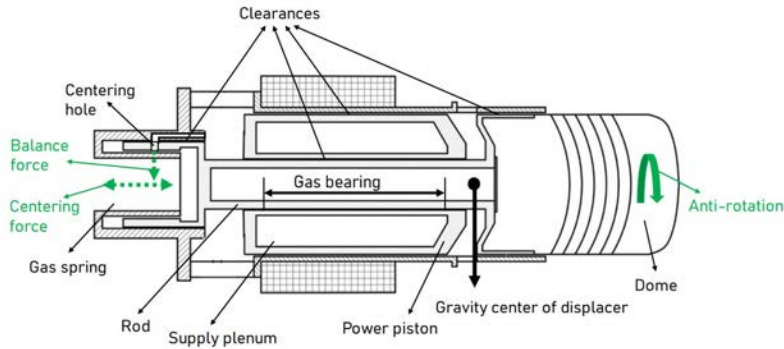


Figure 2. The arrangement of the displacer and power piston within the cylinders.

Fig. 3 shows the schematic drawing of the centering magnet assembly, which mainly comprises static and moving parts. The magnets on the moving part are magnetized in a direction that aligns with the counterpart on the static one, but opposite to the adjoining stage with respect to the multi-stage layout. When the moving part oscillates along the axis direction, a magnetic force is generated accordingly to restore it to its equilibrium position. As the number of stages increases, the interaction between each stage could enhance the centering force.

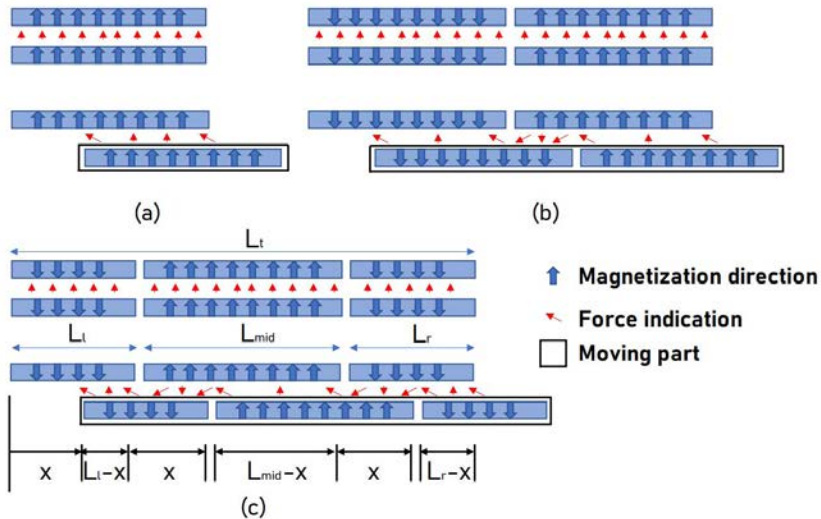


Figure 3. Schematic diagram of the principle of centering magnet.

According to Fig. 3, the axial stiffness of a single-stage structure is denoted as k_1 , while the axial stiffness with n -stage magnets (k_n) can be derived using the following equation.

$$k_n = k_1 \times (2n - 1) \quad (1)$$

The anti-rotation strength arises from the cogging force, which diminishes as the moving part deviates from its equilibrium position due to a gradual decrease in the area of attraction and an increase in the area of repulsion. The force indication in Fig. 3 can describe how the action area transforms with changes in position. If the local repulsion exceeds attraction, the moving part might rotate due to its circumferential freedom. From this perspective, there is a critical position to avoid rotation, where the offset distance x_n from the equilibrium position is determined as follows:

$$x_n = L_t / (2n - 1) \quad (2)$$

The variable L_t represents the total length of magnets.

Besides the multi-stage magnet assembly, another important contraption is the balance magnet. The balance magnet configuration involves the installation of a magnet on the displacer and a magnetic conductive silicon steel on the stator. During its movement, the balance magnet ensures a quasi-constant magnitude of normal force on the displacer. Fig. 4 illustrates the layout of this novel structure, indicating that a length constraint is required to maintain stability. The balance magnet length L_m satisfies the following inequality.

$$L_m < L_t - 2x \quad (3)$$

The maximum displacement amplitude of the displacer is denoted as x .

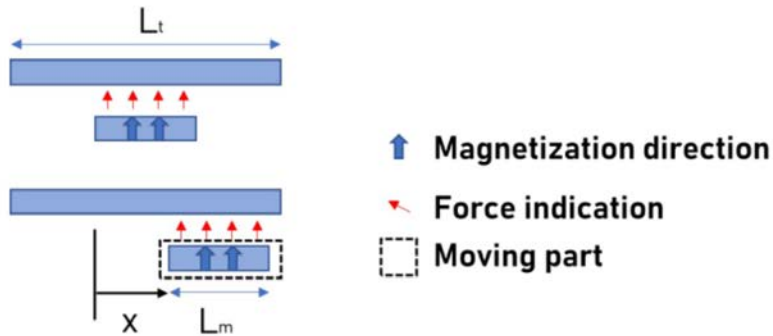


Figure 4. Schematic diagram of the principle of balance magnet.

With the preliminary introduction of multi-stage centering magnet assembly and balance magnet, numerical simulations were firstly conducted by employing the commercially-available software MAGNET. The L_t is 54 mm, with a maximum displacement amplitude of 20 mm for the displacer. The length of the balance magnet is either 10 mm or 20 mm. Fig. 5 illustrates the magnetic field distributions under different stage designs. It can be observed that the magnetic induction intensity is enhanced and the interaction between stages results in a higher restoration force.

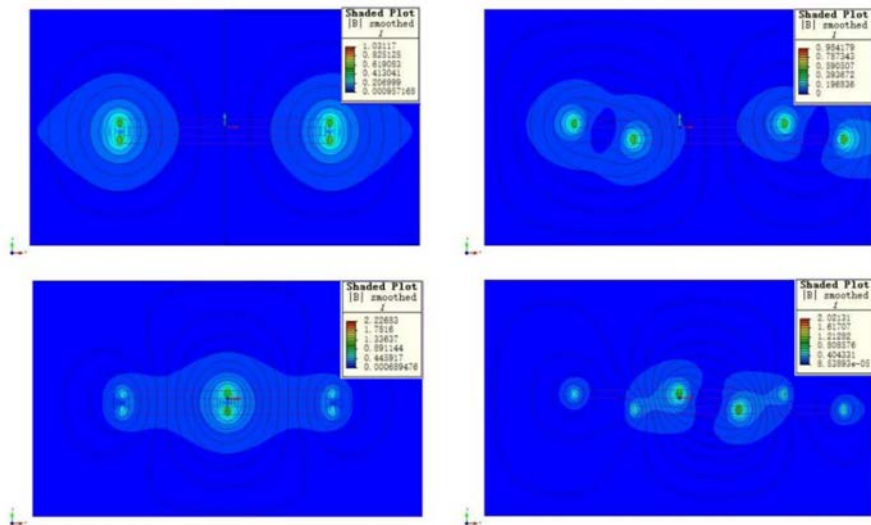


Figure 5. Magnet field distribution with 1 and 2 stages centering magnets.

The magnetic field of the balance magnet structure, as illustrated in Fig. 6, demonstrates its potential to provide a stable equilibrium force.

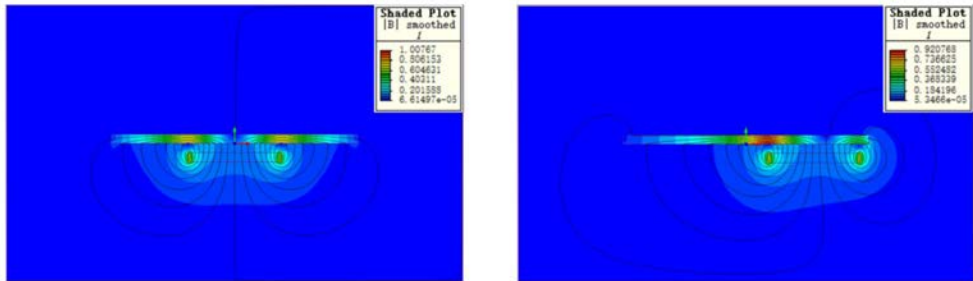


Figure 6. Magnet field distribution of the balance magnet.

The force results obtained from the dynamic simulation have been plotted in Fig. 7, quantitatively validating Equation (1). It's obvious that the axial stiffness of 3-stage and 2-stage structures is approximately five and three times as high as that of a single-stage, respectively. The critical displacement amplitude predicted by Equation (2) for zero anti-rotation torque (as well as zero normal force) closely aligns with the simulation results, the differences primarily arising from end effects. These end effects stem from the finite length of both the mover and stator along the longitudinal direction [12]. According to Fig. 7 (b), the length of the balance magnet would impact the magnitude of force along its trajectory.

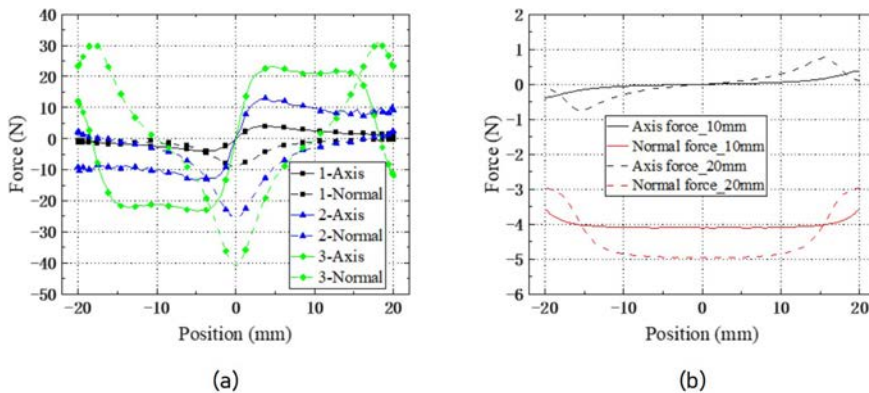


Figure 7. Simulation results of the models: (a) Centering magnets, (b) Balance magnet.

Design and simulation

With the fundamental simulation and verification, a specific design was implemented to take into consideration the practical layout and further experimental validation. In this design, the centering magnets are divided into eight groups and evenly distributed circumferentially, with an exclusion of the top and bottom positions in the gravitational direction for the sake of accommodating the balance magnet. Fig. 8 illustrates the layout. It is worth noting that by incorporating gaskets with varying thicknesses, it becomes possible to adjust the gap between the balance magnet and the silicon steel counterpart. The permanent magnet is N45H, while the silicon steel grade is M300-35A [13].

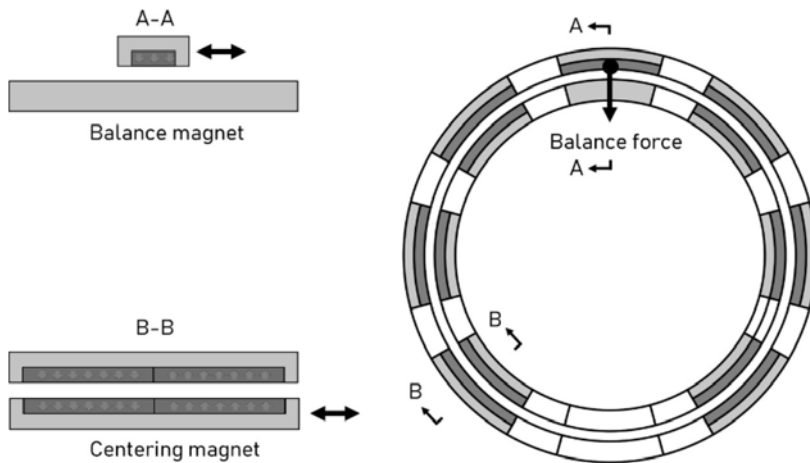


Figure 8. The layout of magnets in the prototype.

Design parameters, such as the total length of the magnets, diameter, and operational displacement amplitude are determined not only for optimal restoring force and balance force, but also catering to thermodynamic and mechanical requirements. Taking the displacer's maximum displacement amplitude of 18 mm for instance.

Two-dimensional (2D) and three-dimensional (3D) models were both developed and simulated. Fig. 9 illustrates the geometric models, wherein explicit indications of 15-degree gaps can be observed in the 3D model to prevent interaction between adjacent magnets and potential interference with the balance magnet. However, 2D simulation was still carried out to facilitate calculation, overlooks characteristics in the third

dimension, which may result in an accelerated computed velocity but fails to account for interactions occurring in this direction.

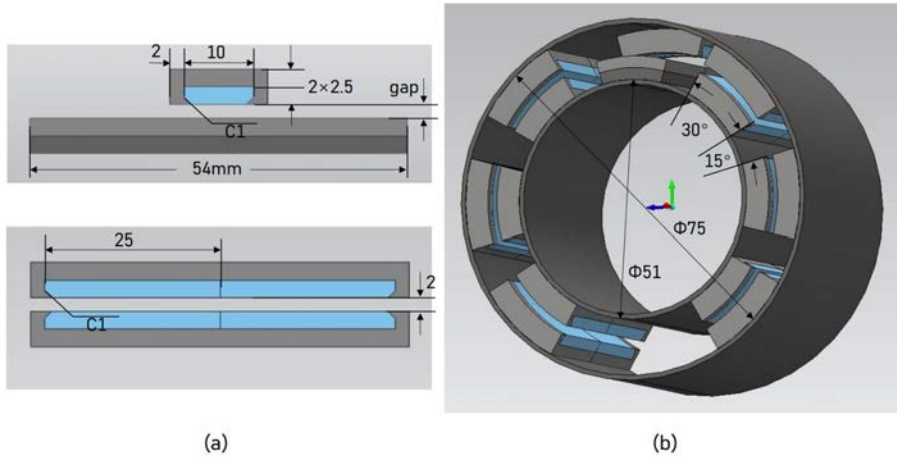


Figure 9. The (a) 2D and (b) 3D models of the assembly.

The simulation results are presented in Fig. 10. The lower values obtained in the 3D simulation compared to the 2D simulation may be attributed to end effects and the equivalent length (17 mm of balance magnet, 100mm of centering magnet on the circumference direction) longer along the 3D model. Notably, the maximum restoration force exceeds 200N. Additionally, a quasi-constant balancing force within the gravity range can be achieved through variable gaps.

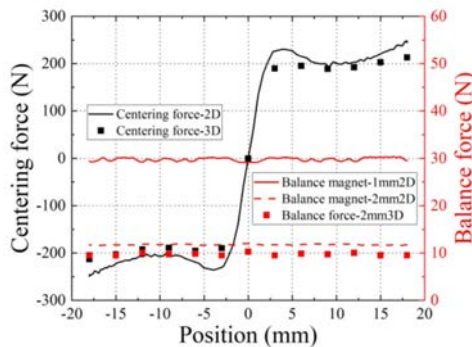


Figure 10. Simulation results of the prototype.

Experiments and discussions

A test rig was manufactured based on the design parameters to gauge axial stiffness and damping coefficient. The test rig includes the cylinders, power piston, displacer, and magnet assembly. Besides the parts, the test rig comprises a laser displacement sensor (Keyence G80) with a range of $\pm 15\text{mm}$ and an accuracy of $\pm 0.2\ \mu\text{m}$, a force sensor (Forsentek FSSM-500N) with an accuracy class of 0.1, an electric moving stage (SC300 provided by Zolix Inc., driven by servomotor for rectilinear motion), a data acquisition system, and mounting fixtures components such as mechanical and gas tube connections, as shown in Fig. 11. The balance weight is used to adjust the gravity center of displacer to simulate the serious offset case which. Laser measuring point 1 is utilized for assessing axial position during axial stiffness test while points 2 and 3 are deployed to measure displacement.

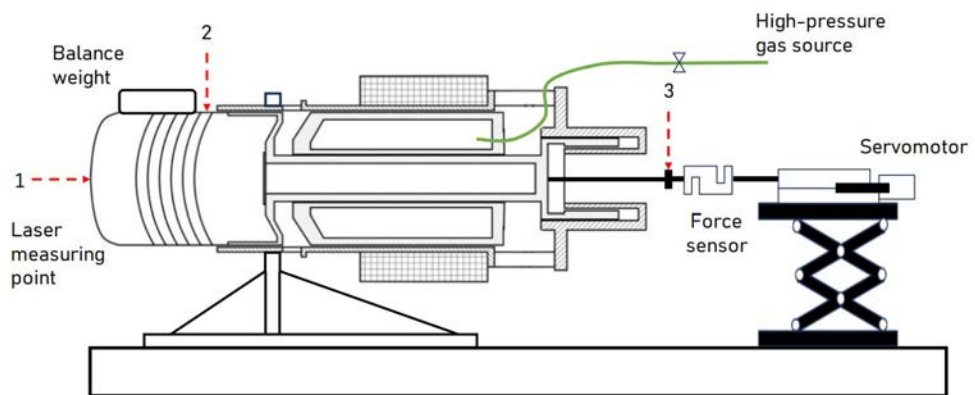


Figure 11. Experiment layout of the prototype.

The axial centering force, damping coefficient, and floating distance were acquired based on the test devices. The damping coefficient is estimated from a free vibration of a single degree of freedom [14]. Fig. 12 presents the test results for axial force, which exhibit similar values and trends to the simulations. However, the experimental results are slightly lower than the 3D results, possibly due to variations in the properties of magnets. Throughout the push and drag process, no rotation phenomenon was detected.

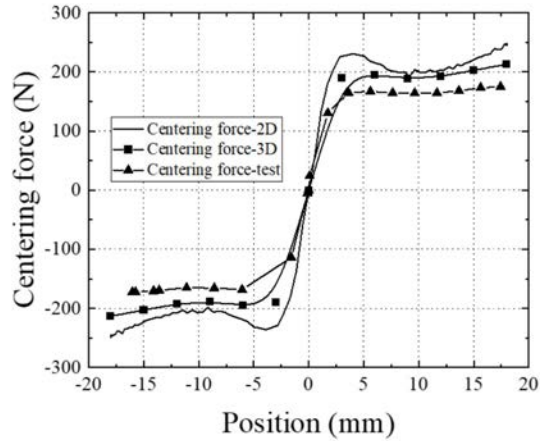


Figure 12. Comparison of the simulation results and test results of centering magnets.

The lateral drift of the displacer at measuring points 2 and 3 is depicted in Fig. 13. Fig. 13 (a) illustrates the drift curve of the displacer with a balance weight of 0.88 kg, after supplying air under varying balance magnet gaps. The left side represents the dome side (measure point 2), while the right side corresponds to the gas spring side (measure point 3). It can be observed that the drift on the left side is smaller than that on the right side, indicating an inclination of the displacer towards its left side. For instance, in the absence of a balance magnet, the air supply pressure is set at 3 bar, resulting in a lateral displacement of 7.5 μm on the dome side and an upward displacement of 56 μm on the gas spring side due to the counterweight effect. The increase in air supply pressure leads to an improvement in the tilt degree on the dome side and reduces the slope of the curve depicted in Fig. 13 (a). The tilt of curves in Fig. 13 indicates the tilt of the displacer directly. As the gap between balance magnets decreases, there is initially a gradual decrease in the inclination degree of the displacer followed by tilting towards the gas spring side (point 3 from higher than point 2 to lower it), while the distance of the two points is near means the tilt has been suppressed.

The drift curve of both ends with a 1.23 kg balance weight displacer after supplying air at different balance magnet gaps is depicted in Fig. 13 (b), exhibiting a similar trend to that of the 0.88 kg balance weight. The drift curve with a 0.4 mm gap indicates that the tilt is worse with the gas pressure increasing. Therefore, if the point of action of the resultant

force deviates significantly from the center of the gas-bearing force, it might hamper its capability and even exacerbate the displacer tilt.

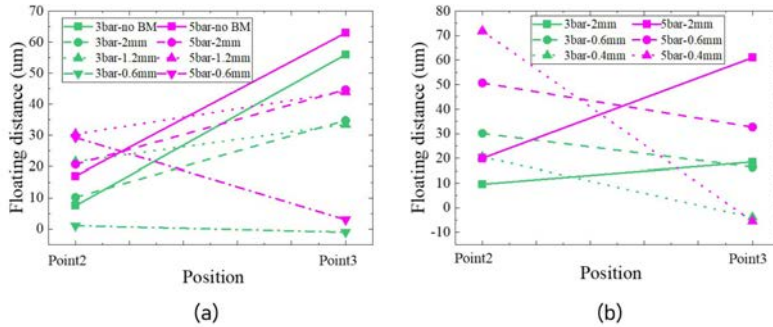


Figure 13. The floating distance curve, (a) 0.88 kg (BM is the abbreviation of balance magnet), (b) 1.23 kg.

The test results in Fig. 14 depict the variation of the damping coefficient of the displacer with different balance weights and magnet gaps, meanwhile maintaining a constant air supply pressure of 5 bar. These results demonstrate that the tilt torque induced by using a balance magnet is indeed conducive to achieving a low damping coefficient. Especially, with the effect of the balance magnet, the damping coefficient is improved from 13.4 Ns/m to 5.9 Ns/m for the case of 0.88 kg balance weight, and correspondingly from 46.9 Ns/m to 8.8 Ns/m for the case of 1.23 kg balance weight.

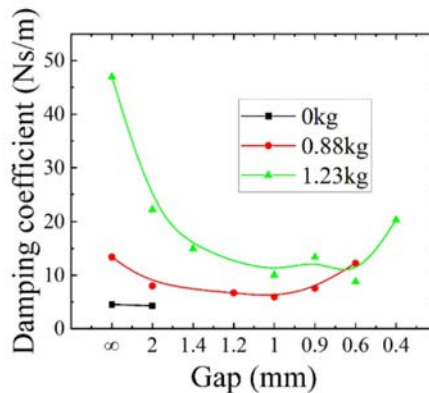


Figure 14. Operation damping coefficient Versus the gap (∞ means no balance magnet).

Conclusions

In this study, we proposed and tested a scheme for ensuring low damping and stable displacer operation by utilizing centering magnets for circumferential clamping and desired axial static stiffness. Meanwhile, the stability of both circumferential and axial positions during operation is further guaranteed through balanced magnets and gas bearings. A general correlation between magnetic stiffness and maximum operational displacement adaptive for various configurations was developed. Theoretical calculations combined with experimental results corroborate that this approach enables low-damping operation of the displacer. Specifically, with gas-bearing support at the designated displacement, the displacer compound stably poises with a damping coefficient below 10 Ns/m. Future work will concentrate on system-level tests to verify the role of multi-stage centering magnets and balanced magnets in achieving high efficiency and long lifetime.

Acknowledgements

This research was financially supported by the National Key Research and Development Program of China (No. 2021YFC28026003). The authors greatly thank Mr. Zhen Wang, Mr. Ruifeng An, Mr. Ying Ma, Mr. Bin Liu, Mr. Jianmin Fang, Mr. Yangbin Cheng, et al. for their invaluable engineering support in prototype manufacturing and experiments.

References

- [1] Zare, S., and Tavakolpour-Saleh, A. (2020). Free piston Stirling engines: A review. *Int. J. Energy Res.* 44, 5039–5070. <https://doi.org/10.1002/er.4533>
- [2] Xiao, L. et al. Transient and steady performance analysis of a free-piston Stirling generator. *Energy* 273, 127184 (2023).
- [3] Jia, Z. et al. Study on the coupling between engine and alternator in a free-piston Stirling generator. *Applied Thermal Engineering* 217, 119222 (2022).
- [4] Zhu, K., Wei, Z., Xia, Y. Effect of damping coefficients on a free-piston Stirling engine under a constant power condition based on a thermodynamic-dynamic coupled model. *Applied Thermal Engineering* 232, 121027 (2023).
- [5] Zare, S., Tavakolpour-Saleh, A. R. Predicting onset conditions of a free piston Stirling engine. *Applied Energy* 262, 114488 (2020).

- [6] Liu, X., Wu, Y. & Lu, G. Failure analysis of the space Stirling cryocoolers. in The Proceedings of 2011 9th International Conference on Reliability, Maintainability and Safety 986–991 (2011). <https://doi.org/10.1109/ICRMS.2011.5979409>
- [7] Gaines, G. C. & Sickenberger, R. ASC and TDC Stirling Converter and Control Testing. in AIAA Propulsion and Energy 2019 Forum (American Institute of Aeronautics and Astronautics, Indianapolis, IN, 2019). <https://doi.org/10.2514/6.2019-4062>
- [8] Walker, G. & Senft, J. R. Free Piston Stirling Engines. vol. 12 (Springer Berlin Heidelberg, Berlin, Heidelberg, 1985).
- [9] Luo, J. et al. Numerical study on a free-piston Stirling electric generator with a gas-spring- postpositioned displacer for high-power applications. Energy 271, 127023 (2023).
- [10] Chen, Y. et al. Post-positioned gas spring enables ultra-high output power of hybrid thermoacoustic electric generators. Cell Reports Physical Science 101835 (2024) <https://doi.org/10.1016/j.xcrp.2024.101835>
- [11] Dhar, M. Stirling Space Engine Program. <https://ntrs.nasa.gov/citations/19990097555> (1999). [12] Boff, B. H. B., Eckert, P. R. & Amara, Y. A Comprehensive Review on the End Effects of Linear Permanent Magnet Machines. IEEE Trans. on Ind. Applicat. 59, 1728–1741 (2023).
- [13] Simcenter Magnet, 2020.2. Available: <https://plm.sw.siemens.com/en-US/simcenter/electro-magnetics-simulation/magnet/>
- [14] Feeny, B. F. & Liang, J. W. A DECREMENT METHOD FOR THE SIMULTANEOUS ESTIMATION OF COULOMB AND VISCOUS FRICTION. Journal of Sound and Vibration 195, 149–154 (1996).

Stirling heat pumps

Experimental Study of an Efficient Low-temperature Free-piston Stirling Heat Pump

Riyang Wang, Jianying Hu^{*}, Zhanghua Wu, Ercang Luo, Yanlei Sun

Key Laboratory of Cryogenics, Technical Institute of Physics and Chemistry, Chinese Academy of Sciences, Beijing, China

Corresponding author: jyhu@mail.ipc.ac.cn

Keywords: Free-piston, Stirling heat pump, Low-temperature, Building heating

Abstract

Heat pump technology has the potential to significantly reduce the energy consumption and environmental pollution caused by coal-fired and gas-fired heating systems. However, conventional heat pump systems often struggle to operate in low-temperature environments, posing a challenge in meeting the heating demands of cold regions. In light of the wide range of available temperatures offered by free-piston Stirling heat pump technology, this study designed and tested an electrically-driven free-piston Stirling heat pump for building heating. In experimental trials, the prototype demonstrated promising performance. When circulating water is heated from 41 °C to 46 °C, the overall coefficient of performance reaches 1.78 at an ambient temperature of -28 °C. Notably, the relative Carnot efficiency increases as the ambient temperature decreases or the heating temperature rises, standing in stark contrast to the behavior of the vapor compression heat pump cycle. Even at an ambient temperature as low as -40 °C, the heat pump operates reliably, achieving a coefficient of performance of 1.57. These experimental performances show a promising prospect for building heating in cold regions.

Introduction

The widespread use of energy has played a crucial role in advancing civilization and promoting prosperity for humanity. However, it has also posed a significant challenge to achieving sustainable development [1]. The architectural field ranks among the three principal sectors of energy consumption and is a significant contributor to both direct and indirect carbon discharges [2,3]. Efficient heating systems in buildings are vital for achieving energy savings and reducing emissions [4]. Heat pumps are capable of extracting heat from a variety of low-grade sources such as air [5], water [6] and soil [7], and converting it into high-temperature heat, which offers substantial advantages compared to coal-fired and gas-fired heating systems, owing to its exceptional efficiency and environmentally friendly.

Conventional vapor compression heat pumps are not applicable for low ambient temperatures [8], primarily due to restrictions in the physical properties of refrigerants. In order to fulfil the heating needs of cold regions, it is imperative to develop new technologies. The Stirling heat pump operates based on the reverse Stirling cycle, which has a theoretical efficiency equal to that of the Carnot cycle [9]. It typically employs helium as the internal working gas, with zero ozone depletion potential and global warming potential. Notably, helium does not undergo phase change during operation, allowing for a wide accessible temperature range.

The electrically-driven free-piston Stirling heat pump is an emerging technology with limited literature, particularly in terms of experimental reports. In 2011, Bassem et al. built a thermoacoustic Stirling heat pump with a heating temperature as high as 370 °C and a temperature lift of 340 °C [10]. Widyaparaga et al. demonstrated a coaxial travelling-wave thermoacoustic Stirling heat pump with an annular regenerator [11]. They discovered that altering the operating frequency can change the direction of heat transfer within the regenerator. Since 2014, Tveit and colleagues have constructed multiple four-cylinder double-acting Stirling heat pumps to provide high-temperature steam for milk sterilization [12-15]. At a heat supply temperature of 183 °C and a heat source temperature of 85 °C, the coefficient of performance reached 2.1. The above-mentioned researches have focused on the design of Stirling heat pumps aiming to generate high-temperature heat. In addition, building heating is also a potential application field for Stirling heat pumps. In 2015, Li et al. developed an electrically-driven free-piston Stirling heat pump, where the heat pump unit is arranged in reverse to prevent the heating heat exchanger from adversely impacting the linear compressor [16]. The overall coefficient of performance was 1.4 with an ambient temperature of -20 °C and a heating temperature of 50 °C. Sun et al. built an opposed linear compressor-driven free-piston Stirling heat pump. It was capable of generating 2253 W heat at 45 °C with an ambient temperature of 0 °C. However, the overall performance was only 1.48 due to the inadequate compatibility between the linear compressor and the heat pump unit [17].

An electrically-driven free-piston Stirling heat pump is composed of a linear compressor and a heat pump unit, and the degree to which these two parts are matched influences the system's performance significantly. However, in the existing Stirling heat pumps

for building heating, the match between the linear compressor and heat pump unit is poor, leaving considerable potential to improve overall heating efficiency. Therefore, this paper first designed and optimized an electrically-driven free-piston Stirling heat pump utilizing the principle of impedance matching between the linear compressor and the heat pump unit. Subsequently, an experimental prototype based on the optimized results was constructed, aiming at exploring the performance of the heat pump under various conditions.

System description

This section introduces the structure of an electrically-driven free-piston Stirling heat pump, followed by the simulation model and design process.

System configuration

Fig. 1 presents the schematic diagram of an electrically-driven free-piston Stirling heat pump. In this figure, HHX refers to heating heat exchanger and AHX refers to ambient heat exchanger. This heat pump system consists of two parts: the linear compressor and the heat pump unit. The linear compressor mainly comprises a power piston and an electromagnetic conversion unit, while the heat pump unit is composed of a heating heat exchanger, a regenerator, an ambient heat exchanger, and a displacer. The displacer is arranged coaxially with the power piston.

In this system, the input electric power is first converted into acoustic power by the linear compressor, and then consumed by the heat pump unit. The heat pump unit pumps the heat absorbed from the environment by the ambient heat exchanger to the heating heat exchanger, and then releases it into the room.

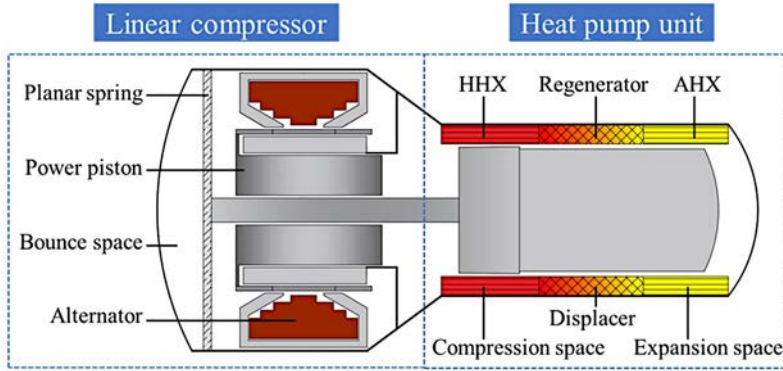


Figure 1. Schematic diagram of the electrically-driven free-piston Stirling heat pump.

Simulation model and design process

In this paper, the commercial software SAGE [18] is employed for the numerical simulation and design of the free-piston Stirling heat pump. SAGE has a graphical interface and is commonly used to simulate the steady state of thermoacoustic heat engines [19] and Stirling machines [20,21]. The evaluation of the heat pump system performance is based on the following defined parameters.

The input electric power W_e is calculated as

$$W_e = \frac{1}{2} \text{Re}(\tilde{V}\tilde{I}^*) \quad (1)$$

The acoustic power input to the heat pump unit W_a is the sum of the acoustic power W_{a-com} at the power piston's surface facing the compression space and the acoustic power W_{a-b} that faces the bounce space.

$$W_a = W_{a-com} + W_{a-b} = \frac{1}{2} \text{Re}(\tilde{P}_{com}\tilde{U}_{pis}^*) + \frac{1}{2} \text{Re}(\tilde{P}_b\tilde{U}_{pis}^*) \quad (2)$$

The efficiency of the linear compressor η_e is calculated as

$$\eta_e = \frac{W_a}{W_e} \quad (3)$$

The coefficient of performance of the heat pump unit COP_h is calculated as

$$COP_h = \frac{Q_h}{W_a} \quad (4)$$

The overall heating performance COP is calculated as

$$COP = \frac{Q_h}{W_e} \quad (5)$$

The relative Carnot efficiency of the whole system η_{re} is calculated as

$$\eta_{re} = COP \frac{T_H - T_C}{T_H + 273.15} \quad (6)$$

where \sim indicates an oscillating parameter. $*$ indicates conjugate. Re indicates taking the real part. V and I denote the voltage and current. P_{com} and P_b refer to the pressure fluctuations in the compression space and the bounce space, respectively. U_{pis} is the power piston's sweep volume. W_e is the input electric power. Q_h is the heating capacity provided by the heat pump. T_H is the heating temperature and T_c is the ambient temperature.

A simplified analysis of the linear compressor is performed using the lumped parameter method. Its operating process fulfils the electrical balance equation and the force balance equation.

$$\tilde{V} = Z_{\text{elec}} \tilde{I} + BL \tilde{v}_{\text{pis}} \quad (7)$$

$$(\tilde{P}_{\text{com}} - \tilde{P}_b) A_{\text{pis}} = BL \tilde{I} - Z_{\text{mech}} \tilde{v}_{\text{pis}} \quad (8)$$

where Z_{elec} is the electrical impedance, BL is the electromechanical constant, v_{pis} is the power piston's velocity, A_{pis} is power piston's area and Z_{mech} is the mechanical impedance. The impedance Z_{com} at the surface of the power piston facing the compression space is

$$Z_{\text{com}} = \frac{\tilde{P}_{\text{com}}}{\tilde{U}_{\text{pis}}} \quad (9)$$

The impedance Z_b at the surface of the power piston facing the bounce space is

$$Z_b = \frac{\tilde{P}_b}{\tilde{U}_{\text{pis}}} \quad (10)$$

Bringing Eqs.(1), (2), (7), (8), (9) and (10) into Eq.(3), the linear compressor efficiency can be further expressed as

$$\frac{1}{\eta_e} = \frac{R_{\text{com}} - R_b + \frac{R_{\text{mech}}}{A_{\text{pis}}^2} + \frac{R_{\text{elec}} A_{\text{pis}}^2}{(BL)^2} \left[\left(R_{\text{com}} - R_b + \frac{R_{\text{mech}}}{A_{\text{pis}}^2} \right)^2 + \left(X_{\text{com}} - X_b + \frac{X_{\text{mech}}}{A_{\text{pis}}^2} \right)^2 \right]}{R_{\text{com}} + R_b} \quad (11)$$

where R_{com} and X_{com} are the real and imaginary parts of Z_{com} , respectively. R_b and X_b are the real and imaginary parts of Z_b , respectively. R_{mech} and X_{mech} are the real and imaginary parts of Z_{mech} , respectively. R_{elec} is the real part of Z_{elec} .

The acoustic impedance should be co-resonant with the mechanical impedance for the compressor to be efficient. When the power piston's area is

$$A_{pis,best} = \sqrt[4]{\frac{R_{mech}^2}{(R_{com}-R_b)^2} \left(\frac{(BL)^2}{R_{elec}R_{mech}} + 1 \right)} \quad (12)$$

the maximum linear compressor efficiency can be achieved.

$$\eta_{e-max} = \left(\sqrt{\frac{(BL)^2}{R_{elec}R_{mech}} + 1} - 1 \right) / \left(\sqrt{\frac{(BL)^2}{R_{elec}R_{mech}} + 1} + 1 \right) \quad (13)$$

This maximum efficiency depends only on the compressor's parameters. Bigger BL , smaller internal electrical resistance and mechanical damping contribute to a higher compressor efficiency. Since the pressure fluctuation in the bounce space is much smaller than that in the compression space, the R_b can be neglected compared with R_{com} . From Eq. (12), it can be seen that the R_{com} is the key parameter to achieve an efficient match between the linear compressor and the heat pump unit.

Based on the above analysis, to make both the linear compressor and the heat pump unit perform efficiently, the structural parameters of the heat pump unit are optimized first, and then the compressor parameters are designed based on the principle of impedance matching. The design process is shown in Fig. 2. Firstly, determine the diameter of the displacer. Secondly, optimize the dimensions of the heat pump unit's core components, including the length, the equivalent diameter, the porosity and the wire diameter of the regenerator, as well as the length and the porosity of the heating and ambient heat exchangers. The required heating capacity is used as the constraint, and the maximum COP_h is the optimization objective. In addition, it is imperative to adjust the mass of the displacer and the diameter of the displacer's rod when optimizing the above parameters since the displacer plays a crucial role in regulating the acoustic field. The nonlinear optimizer in SAGE is based on Powell's Sequential Quadratic Programming. This approach breaks down the problem into a series of quadratic programming sub-problems with quadratic objective functions and linear constraints. From the optimized structural parameters of the heat pump unit, the impedance at the compression space R_{com} can be obtained. According to Eq. (13), to make η_e as high as possible, it should be better to select a bigger BL , a smaller R_{elec} and a smaller R_{mech} . Then, the optimum power piston area corresponding to the highest linear compressor efficiency can be calculated based on Eq. (12). In this way, a high-performance electrically-driven free-piston Stirling heat pump is obtained.

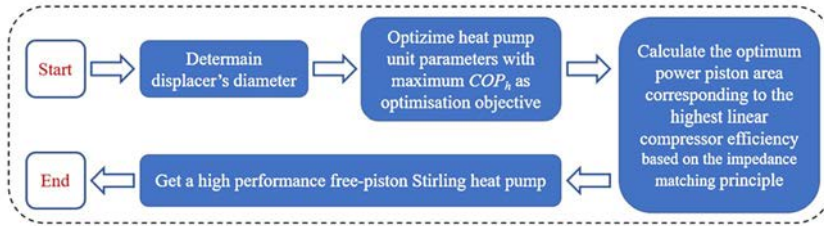


Figure 2. The design process of an electrically-driven free-piston Stirling heat pump.

Experimental apparatus

As shown in Fig. 3, an electrically-driven free-piston Stirling heat pump is constructed based on the above design process. Fig. 4 shows the schematic diagram of the experimental test platform, which is composed of a heat pump prototype, a power supply, an electric heating module, a circulating water system and a parameter measurement system. The structural parameters of each component of the heat pump prototype are shown in Table 1. The power supply provides electric power to the linear compressor. The electric heating module inputs heat to the ambient heat exchanger through heating rods to simulate heat absorption from the environment. The circulating water system continuously takes away the heat generated by the heating heat exchanger. Through the equation $Q_h = c m (T_{out} - T_{in})$, the provided heating capacity can be calculated. Where c is the specific heat capacity of water, m is the circulating water flow rate, T_{in} and T_{out} are temperatures when circulating water flows into and flows out of the heating heat exchanger, respectively.

Table 1. Main structural parameters of a free-piston Stirling heat pump.

	Components	Details
Linear compressor	Bounce space	Void volume 758 cc
	Power piston	Diameter 45 mm, moving mass 0.75 kg, damping coefficient 20 N·s/m
	Alternator	Motor constant 90 N·A ⁻¹ , coil resistance 2.76 Ω
Heat pump unit	Compression space	Void volume 34 cc
	Heating heat exchanger (annular fins)	Length 32 mm, porosity 20.19%
	Regenerator (wire mesh)	Length 23 mm, equivalent diameter 53 mm, wire diameter 0.05 mm, porosity 77.75%
	Ambient heat exchanger (annular fins)	Length 30 mm, porosity 16.40%
	Displacer	Diameter 60 mm, rod diameter 15 mm, moving mass 0.45 kg
	Expansion space	Void volume 23 cc

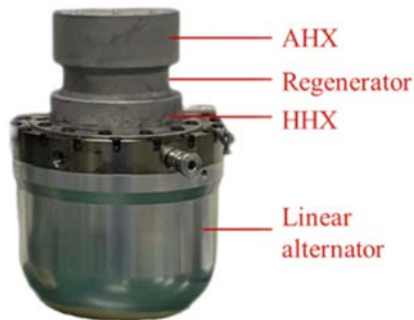


Figure 3. The electrically-driven free-piston Stirling heat pump prototype.

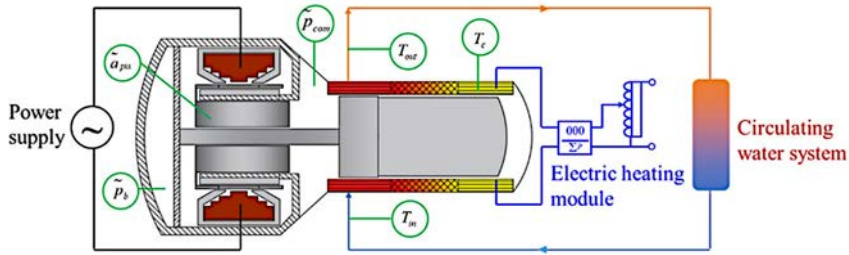


Figure 4. The schematic diagram of experimental test platform.

Results and discussion

In this section, a series of experimental studies are carried out on the above heat pump prototype. Firstly, the matching between the linear compressor and the heat pump unit is examined. Then, the effects of ambient and heating temperatures on system performance are investigated.

Match between linear compressor and heat pump unit

Table 2 presents system performance with an ambient temperature of $-28\text{ }^{\circ}\text{C}$ and the circulating water is heated from $41\text{ }^{\circ}\text{C}$ to $46\text{ }^{\circ}\text{C}$. When 698 W of electric power is input, the linear compressor transfers 602 W of acoustic power to the heat pump unit, and the heating capacity of 1180 W is obtained. The linear compressor efficiency reaches 86.2% and the overall coefficient of performance is 1.69 , achieving an efficient match between the linear compressor and the heat pump unit.

Table 2. Performance parameters of heat pump system.

W_e (W)	W_a (W)	Q_h (W)	η_e	COP_h	COP
698	602	1180	86.2%	1.96	1.69

Different ambient temperatures

Ambient temperature has a significant effect on the operating status of the heat pump. The heating performances under various ambient temperatures are tested. T_{in} and T_{out} are $41\text{ }^{\circ}\text{C}$ and $46\text{ }^{\circ}\text{C}$, respectively.

The variations of acoustic powers in the compression space W_{a-com} and bounce space W_{a-b} and the phase difference between pressure and volumetric flow rate in the compression space θ_{PU-com} are shown in Fig. 5 (a). A large part of the acoustic power generated by the linear compressor is transferred to the heat pump unit through the compression space, while the acoustic power in the bounce space accounts for a small percentage. In this set of experiments, the power piston's displacement is the same for each condition, so the amplitudes of pressure and volumetric flow rate in the compression space are almost constant. In this way, it can be seen from Eq. (2) that the variation of W_{a-com} mainly depends on θ_{PU-com} . With increasing ambient temperatures, θ_{PU-com} gradually declines, leading to a decrease in W_{a-com} . Fig. 5(b) presents the compressor efficiency η_e and coefficient of performance of the heat pump unit COP_h . The higher the ambient temperature, the greater the COP_h . However, the change in ambient temperature has little effect on η_e . When the ambient temperature increases from $-28\text{ }^\circ\text{C}$ to $0\text{ }^\circ\text{C}$, η_e is maintained between 86% and 87%. Fig. 5 (c) gives the heating capacity Q_h , overall COP and relative Carnot efficiency η_{re} . Q_h changes slightly and remains around 1200 W. The combined change in η_e and COP_h causes the overall COP to decrease with the reduction of the ambient temperature. It is noteworthy that the relative Carnot efficiency η_{re} gradually increases. When the ambient temperature decreases from $0\text{ }^\circ\text{C}$ to $-28\text{ }^\circ\text{C}$, η_{re} changes from 32.1% to 39.2%. The free-piston Stirling heat pump is much more efficient under larger heat-pumping temperature differences.

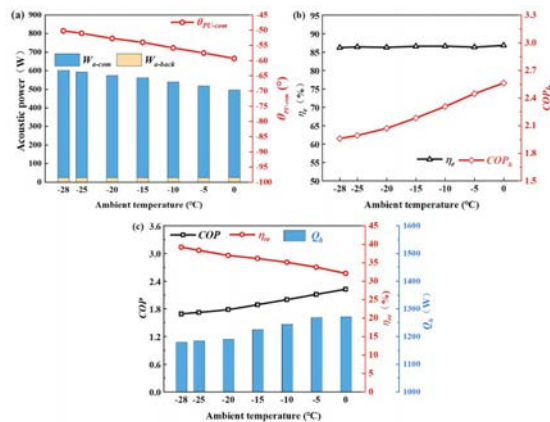


Figure 5. (a) Acoustic power and phase difference between pressure and volumetric flow rate in the compression space θ_{PU-com} (b) compressor efficiency η_e and COP_h (c) overall COP, relative Carnot efficiency η_{re} and heating capacity Q_h under different ambient temperatures.

In the heat exchanger, the external fluid flows unidirectionally on the outside and the internal working gas flows alternately on the inside. The temperature difference between the internal gas and external fluid needs to be focused. For ambient heat exchanger (Hereafter referred to as AHX), an electric heating module is used to simulate heat absorption from the environment. The heat-transfer temperature difference ΔT_{AHX} is defined as

$$\Delta T_{AHX} = T_c - T_{gas-AHX} \quad (14)$$

The heat-transfer temperature difference in the heating heat exchanger (Hereafter referred to as HHX) ΔT_{HHX} is defined as

$$\Delta T_{HHX} = T_{out} - T_{gas-HHX} \quad (15)$$

where $T_{gas-AHX}$ and $T_{gas-HHX}$ are the internal gas's average temperatures in the AHX and HHX, respectively. In the experiment, ΔT_{AHX} is around 7 °C and ΔT_{HHX} is around 11 °C.

The extent to which the heat-transfer temperature difference affects the system performance can be roughly evaluated by $\eta_{\Delta T}$.

$$\eta_{\Delta T} = 1 - \frac{T_H + \Delta T_{HHX} + 273.15}{(T_H + \Delta T_{HHX}) - (T_c - \Delta T_{AHX})} / \frac{T_H + 273.15}{T_H - T_c} \quad (16)$$

The numerator of the second term represents the Carnot efficiency of the heat pump cycle taking into account the heat-transfer temperature difference, while the denominator represents that without heat-transfer temperature difference. The larger the $\eta_{\Delta T}$, the bigger the adverse effect on the system performance. For example, with an ambient temperature of -28 °C and a required heating temperature of 46 °C, if there are no heat-transfer temperature differences, the heat source and heat sink temperatures are respectively -28 °C and 46 °C for the internal gas undergoing the heat pump cycle. Under this situation, the Carnot efficiency is 4.31. However, with a ΔT_{AHX} of 7 °C and a ΔT_{HHX} of 11 °C, heat source and heat sink temperatures are respectively -35 °C and 57 °C and the Carnot efficiency is 3.59. The system performance is reduced by 16.7% due to the heat-transfer temperature difference.

Fig. 6 gives $\eta_{\Delta T}$ under different ambient temperatures. It can be seen that $\eta_{\Delta T}$ tends to increase with a rising ambient temperature. $\eta_{\Delta T}$ is 16.7 % with an ambient temperature of -28 °C. However, when the ambient temperature increases to 0 °C, the system performance is reduced by 25.6% due to the presence of the heat-transfer temperature difference. The large heat-transfer temperature difference in the heat exchanger is an important reason for the relatively poor performance of the free-piston Stirling heat pump with a small heat-pumping temperature difference.

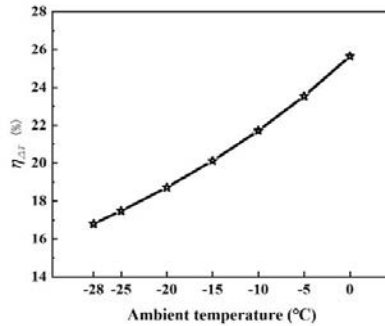


Figure 6. The extent to which heat-transfer temperature difference affects system performance.

Different heating temperatures

The heating temperature is a crucial parameter determined by consumer requirements. The performance at various heating temperatures T_{out} is investigated, maintaining an ambient temperature of -28 °C. The difference between T_{in} and T_{out} is set at 5 °C and T_{out} varies within the range of 40 °C to 49 °C.

The impacts on W_{a-com} , W_{a-b} , ϑ_{PU-com} , η_e , COP_h , COP , η_{re} and Q_h are illustrated in Fig. 7. As T_{out} goes up, ϑ_{PU-com} increases slightly. According to Eq. (2), such a change in ϑ_{PU-com} leads to a small increase in acoustic power. In addition, from Eq. (11), it can be seen that during the operation of this heat pump, η_e mainly depends on the acoustic impedance in the compression space, which is determined by ϑ_{PU-com} . The nearly constant ϑ_{PU-com} maintains η_e at 87.5%. With T_{out} rising, Q_h is around 940 W, the COP_h and overall COP decrease, but the relative Carnot efficiency is on the upward trend. These results indicate that the larger the difference between heating temperature and ambient temperature, the higher the thermodynamic perfection of the Stirling heat pump.

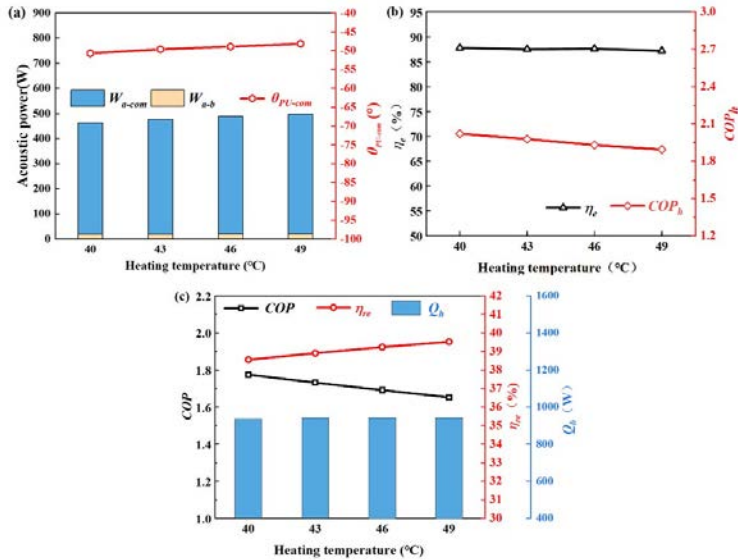


Figure 7. (a) Acoustic power and phase difference between pressure and volumetric flow rate in the compression space θ_{PU-com} (b) compressor efficiency η_c and COP_h (c) overall COP, relative Carnot efficiency η_{re} and heating capacity Q_h under different heating temperatures.

Recovery of heat from compressor

In the linear compressor, the damping loss caused by the power piston and the Joule heat loss in the electromagnetic conversion unit are ultimately dissipated as heat. If this heat is captured, more heating capacity can be provided. Therefore, a water jacket is added to the compressor's back cover to carry away the heat from the compressor. As shown in Fig. 8, the circulating water flows first into the water jacket and then through the heating heat exchanger.

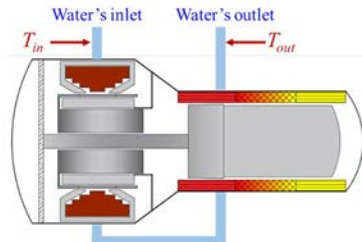


Figure 8. Schematic diagram of a Stirling heat pump with a water jacket added to the back cover.

Fig. 9 shows the overall COP with and without water jacket at different ambient temperatures, with T_{in} of 41 °C and T_{out} of 46 °C. It can be seen that employing a water jacket can indeed increase the heating capacity and thus improve the performance. When the ambient temperature is -28 °C and -15 °C, the overall COP increases from 1.69 to 1.78 and 1.89 to 1.97, respectively. In addition, it is worth noting that this heat pump prototype is able to operate even at an ambient temperature as low as -40 °C and the overall COP reaches 1.57.

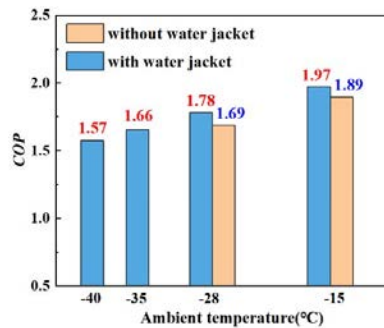


Figure 9. COP with and without water jacket at different ambient temperatures.

The performances of this free-piston Stirling heat pump are compared with those of low-temperature vapor compression heat pumps, which can be roughly classified into three types: improved compressor systems [22-25], quasi-two-stage systems [26-29] and cascade systems [30-33]. As shown in Fig. 10, the COPs of the Stirling heat pump are close to or even higher than those of vapor compression heat pumps at ambient temperatures between -30 °C and -10 °C. Few vapor compression heat pumps are capable of operating in environments below -30 °C. However, the free-piston Stirling heat pump can perform efficiently with an ambient temperature as low as -40 °C. It has a very broad application prospect for building heating in cold regions.

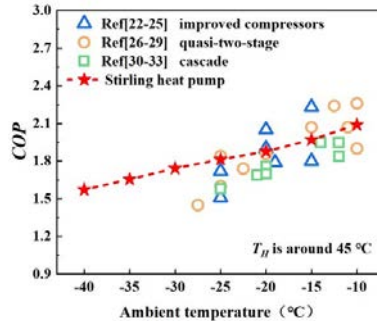


Figure 10. Performance comparison of this Stirling heat pump and vapor compression heat pumps.

Conclusion

In this paper, an electrically-driven free-piston Stirling heat pump is designed and tested. Based on the impedance mating principle, a design method capable of efficiently matching the linear compressor and the heat pump unit is provided, thus improving the compressor efficiency and the overall coefficient of performance. When circulating water is heated from 41 °C to 46 °C, the linear compressor efficiency is 86.2% and the overall COP reaches 1.78 at an ambient temperature of -28 °C. In addition, experimental studies are conducted to investigate the heating performance at different ambient and heating temperatures. The following conclusions can be drawn:

1. There is an optimal surface area of the power piston corresponding to the highest linear compressor efficiency, independently of the heat pump unit. Bigger BL, smaller internal electrical resistance and mechanical damping contribute to a higher compressor efficiency.
2. Ambient and heating temperatures have a small impact on compressor efficiency, but influence the performance of the heat pump unit significantly. As the ambient temperature declines or the heating temperature rises, the overall COP decreases, but the relative Carnot efficiency increases. The free-piston Stirling heat pump is much more efficient under larger heat-pumping temperature differences.

With an ambient temperature as low as 40 °C, the heat pump can operate reliably, and an overall COP of 1.57 is obtained. The free-piston Stirling heat pump has a promising

prospect for building heating in cold regions. In addition, to further improve the system performance at smaller heat-pumping temperature differences, it is necessary to take measures to reduce the heat-transfer temperature difference in the heat exchanger. Using shell and tube heat exchangers instead of finned heat exchangers and reducing operating frequency may be effective.

Acknowledgements

This work is financially supported by the National Nature Science Foundation of China (No. 51876213 and 51976230).

References

- [1] BP. BP statistical review of world energy 2022, 2022.
- [2] Ü V Diana, F C Luisa, S Susana, B Camila, P Ksenia. Heating and cooling energy trends and drivers in buildings. *Renewable and Sustainable Energy Reviews*, 2015, 41.
- [3] Ü V Diana, P Ksenia, S Maja, E Jiyong. Energy use in buildings in a long-term perspective. *Current Opinion in Environmental Sustainability*, 2013, 5(2).
- [4] H Zhang, S Wang, J Hao, X Wang, S Wang, F Chai, et al. Air pollution and control action in Beijing. *Journal of Cleaner Production*, 2016, 112: 1519-1527.
- [5] J Emhofer, K Marx, A Sporr, T Barz, B Nitsch, M Wiesflecker, et al. Experimental demonstration of an air-source heat pump application using an integrated phase change material storage as a desuperheater for domestic hot water generation. *Applied Energy*, 2023, 336, 120784.
- [6] N Liu, L Shi, L Han, M Zhu. Moderately high temperature water source heat-pumps using a near-azeotropic refrigerant mixture. *Applied Energy*, 2004, 80(4): 435-447.
- [7] S J Self, B V Reddy, M A Rosen. Geothermal heat pump systems: Status review and comparison with other heating options. *Applied Energy*, 2013, 101: 341-348.
- [8] S. S. Bertsch, E. A. Groll. Two-stage air-source heat pump for residential heating and cooling applications in northern U.S. climates. *International Journal of Refrigeration*, 2008, 31(7):1282-1292.
- [9] G Walker, J Senft. *Free piston Stirling engines*. Berlin, Heidelberg: Springer-Verlag; 1985.

- [10] M M Bassem, Y Ueda, A Akisawa. Thermoacoustic Stirling Heat Pump Working as a Heater. *Applied Physics Express*, 2011, 4(10).
- [11] A Widyaparaga, T Koshimizu, E Noda, et al. The frequency dependent regenerator cold section and hot section positional reversal in a coaxial type thermoacoustic Stirling heat pump. *Cryogenics*, 2011, 51(10): 591-597.
- [12] T M Tveit, H Arne. Performance analysis and verification of a novel high temperature difference heat pump. 11th International Energy Agency Heat Pump Conference, 2014.
- [13] T M Tveit. Application of an industrial heat pump for steam generation using district heating as heat source. 12th International Energy Agency Heat Pump Conference, 2017.
- [14] T M Tveit, M Johansson, C A P. Zevenhoven. Environmentally friendly steam generation using VHTHPs at a pharmaceutical research facility. 13th International Energy Agency Heat Pump Conference, 2020.
- [15] C Haikarainen, T M Tveit, H Saxén, et al. Simulation of pressure imbalance phenomena in a double-acting α -cycle Stirling engine. *Energy Conversion and Management*, 2020, 221.
- [16] K Li, G Yu, Y Zhang, et al. Theoretical and experimental study of free piston Stirling heat pump. *Journal of Engineering Thermophysics*, 2015, 36(01): 41-45.
- [17] Y Sun. Theoretical and experimental study of a novel free-piston thermally driven thermoacoustic-thermal (cold) combined supply system. Institute of Physical and Chemical Technology, Chinese Academy of Sciences, 2021.
- [18] D Gedeon. Sage user's guide. Gedeon Associates, 2014.
- [19] J Xu, J Hu, E Luo, L Zhang, W Dai. A cascade-looped thermoacoustic driven cryocooler with different-diameter resonance tubes. Part I: Theoretical analysis of thermodynamic performance and characteristics. *Energy*, 2019, 181:943-53.
- [20] L Samuel, G Michael, N Martin. A novel solar-powered liquid piston Stirling refrigerator. *Applied Energy*, 2018, 229.

- [21] Z Jia, R Wang, J Hu, L Zhang, Z Wu, Y Chen, et al. Study on the coupling between engine and alternator in a free-piston Stirling generator. *Applied Thermal Engineering*, 2022, 217.
- [22] A A Safa, S A Fung, R Kumar R. Comparative thermal performances of a ground source heat pump and a variable capacity air source heat pump systems for sustainable houses. *Applied Thermal Engineering*, 2015, 81, 279-287.
- [23] G Ma, Q Chai. Characteristics of an improved heat-pump cycle for cold regions. *Applied Energy*, 2004, 77(3): 235-247.
- [24] S Xu, G Ma. Research on air-source heat pump coupled with economized vapor injection scroll compressor and ejector. *International journal of refrigeration*, 2011, 34(7): 1587-1595.
- [25] D H Kim, H S Park, M S Kim. The effect of the refrigerant charge amount on single and cascade cycle heat pump systems. *International journal of refrigeration*, 2014, 40: 254-268.
- [26] S Fan, Q Liu, S He. Scroll compressor development for air-source heat pump water heater applications. In: *Proceeding of international refrigerant and air conditioning conference*, 2008.
- [27] W Wei, L Ni, C Zhou, et al. Performance analysis of a quasi-two stage compression air source heat pump in severe cold region with a new control strategy. *Applied Thermal Engineering*, 2020, 174: 115317.
- [28] C Lin, T Ouyang, H Chen, et al. Application of low-temperature air-source heat pump technology. *Refrigeration and Air Conditioning*, 2014, 14(08): 119-122.
- [29] H Li, Z Su, C Jian, et al. Study on quasi two-stage compression cycle characteristics of air source heat pump water heater in cold area. *Thermal Science and Technology*, 2020, 19(04): 313-319.
- [30] Y Xu, Y Huang, N Jiang, et al. Experimental and theoretical study on an air-source heat pump water heater for northern China in cold winter: Effects of environment temperature and switch of operating modes. *Energy and Buildings*, 2019, 191: 164-173.

- [31] S S Bertsch, E A Groll. Two-stage air-source heat pump for residential heating and cooling applications in northern US climates. *International journal of refrigeration*, 2008, 31(7): 1282-1292.
- [32] Y Yang, R Li, Y Zhu, et al. Experimental and simulation study of air source heat pump for residential applications in northern China. *Energy and Buildings*, 2020, 224: 110278.
- [33] J Kim, J Lee, H Choi, et al. Experimental study of R134a/R410A cascade cycle for variable refrigerant flow heat pump systems. *Journal of Mechanical Science and Technology*, 2015, 29(12): 5447-5458.

Numerical Investigation on Ultra-High- Temperature Thermoacoustic Stirling Heat Pump

K.Q. Luo^a, L.R. Dai^{b,c}, Y.L. Sun^b, Z.H. Wu^b, J.Y. Hu^{b,c}, Y. Huang^a, E.C. Luo^{b,c,*}

a State Key Laboratory of Mesoscience and Engineering, Institute of Process Engineering, Chinese Academy of Sciences, Beijing, China

b CAS Key Laboratory of Cryogenics, Technical Institute of Physics and Chemistry, Chinese Academy of Sciences, Beijing, China

c University of Chinese Academy of Sciences, Beijing, China

* Corresponding author: ecluo@mail.ipc.ac.cn

Keywords: Thermoacoustic Stirling technology, Heat pump, Ultra-high-temperature zone

Abstract

Cooling/heating have caused large amount of energy consumption and carbon emission, thus it is necessary and urgent to develop high efficiency, low-carbon and high reliable cooling/heating technologies. The mechanically-driven thermoacoustic Stirling heat pump is an emerging energy conversion technology with significant advantages of high potential efficiency and environmental-friendly working medium. According to the previous literature, it is found that there are few researches focusing on the ultra-high-temperature zone. Therefore, this paper aims to investigate the operating performance, thermoacoustic characteristic and the distribution of exergy loss of the mechanically-driven thermoacoustic Stirling heat pump under ultra-high-temperature zone, as well as exploring its application possibility in the industrial field. Firstly, the system performance of thermoacoustic Stirling heat pump unit under ultra-high-temperature condition is analyzed. Then, the influences of heat-supply temperature and temperature lift on the coefficient of performance and the relative Carnot efficiency of thermoacoustic Stirling heat pump unit are given, while the distributions of exergy losses and heat transfer temperature differences under different temperature lifts are also presented. Finally, its application prospect in the hydrogen metallurgy and ammonia synthesis industrial processes is carried out. It can be concluded that the mechanically-driven thermoacoustic Stirling ultra-high-temperature heat pump technology will show positive function on the industrial decarbonization.

Introduction

Energy and environment are not only the core issues of the rapid social economy developments, but also the basic material guarantee of national production and life. According to the statistical review of world energy published by the Energy Institute (EI) [1], the global primary energy consumption in 2022 reached the highest level in history (more than 600EJ), while the global primary energy demand increased by about 1%;

and the record breaking growth of renewable energy did not change the dominance of fossil fuels, which still accounted for 82% of global energy supply. Besides, with the rapid development of social economy and the continuous improvement of human production and quality of life, the field of cooling/heating has been widely utilized in various cases, such as household air-conditioning and refrigerator [2], district heating [3], cold-chain transportation [4], food and tobacco drying [5] and so on. According to the statistic data reported by the International Energy Agency (IEA), the energy consumption required for cooling/heating accounts for about 50% of the total global energy consumption, and the corresponding carbon emissions can reach more than 40% of the total global carbon emissions [6]. Therefore, it is essential and urgent to promote energy saving and emission reduction of cooling/heating technology.

Heat pump technology is a kind of effective energy utilization devices that can transfer thermal energy from low-grade heat source to high-grade heat source, which only requires a small amount of mechanical energy. Mechanically-driven thermoacoustic Stirling heat pump is an emerging cooling/heating technology based on the reverse thermoacoustic effect, which shows great advantages of environmental-friendly working medium and high potential efficiency. Due to the resonant and phase adjustment components, it can be mainly classified into two types, including the crank-connecting-rod type and the free-piston type, as is shown in Figure 1. These two types of heat pump systems both consist of a pressure wave generator and a Stirling heat pump. The relevant researches on the mechanically-driven thermoacoustic Stirling heat pumps are summarized in Table 1. It can be found that there are quite few researches focusing on the ultra-high-temperature zone, especially with the heat-supply temperature over 500°. Besides, the existing theoretical investigations on the thermodynamic characteristics are generally based on the view of traditional Stirling cycle, which lacks the deep analysis of internal thermoacoustic characteristics, matching mechanism of acoustic impedance and the distribution of exergy loss, etc.

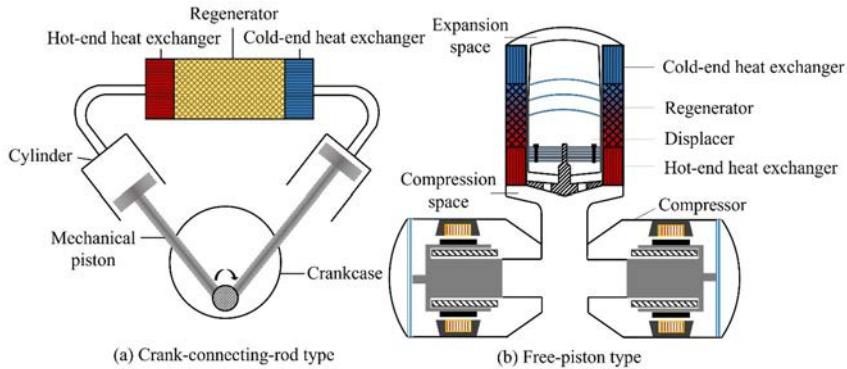


Figure 1. Classification of mechanically-driven thermoacoustic Stirling heat pump.

Table 1. Review on the mechanically-driven thermoacoustic Stirling heat pump.

References	Methods of Research	Type of Heat Pump	Findings
[7]	Experimental	Crank-connecting-rod	The prototype showed poor performance resulting from excessive piston ring friction and poor heat transfer between the oils and heat exchanger tubes.
[8]	Experimental	Free-piston	Reverse arrangement structure was proposed for the first time. The prototype obtained an entire COP of 1.4 under a temperature difference of -20/50°C.
[9]	Experimental	Crank-connecting-rod	A series of experimental measurements and comparisons were conducted for validating present model. The results showed that the prototype could produce 904W of heating power and 38°C of hot water under 5bar helium at 1000rpm.
[10]	Theoretical	Free-piston	A calculated model was established by Sage and its temperature adaptability was analyzed. The COP was about 2.6 when the cold-end temperature was 40 °C and the heating temperature was 100°C.

[11]	Theoretical	Crank-connecting-rod	The performance of a 10 kW (34,000 Btu/hr) heat pump has been modeled using Schmidt's method. With the range of source temperatures from 15 °C to 35 °C and sink temperatures from 45 °C to 90 °C, the COP varies from 3.96 to 6.69.
[12]	Theoretical	Free-piston	It simulated the operating performances under different pressures, frequencies and temperature differences. Under the ambient temperature of 20 °C, heating temperature of 120 °C, working frequency of 45 Hz and mean pressure of 8 MPa, the COP of the whole system reached 2.5, and the relative Carnot efficiency was 63.6%.
[13]	Experimental	Free-piston	A prototype was designed and built, and the distributions of acoustic field and exergy loss were analyzed. Under the hot-end temperature of 45 °C and 0 °C of the ambient temperature, the heating capacity and COP were 2253 W and 2.76, with the relative Carnot efficiency of 39.1%.

To sum up, this paper aims to investigate the thermoacoustic Stirling heat pump unit operating at ultra-high-temperature zone (especially with the heat-supply temperature reaches more than 500 °C and explore its application prospects in the industrial field. In this paper, the background and research progress of the mechanically-driven thermoacoustic Stirling heat pump is firstly presented in Section 1; then the operating performance, thermoacoustic characteristics and the distributions of exergy loss of thermoacoustic Stirling heat pump unit under ultra-high-temperature zone are systematically analyzed in Section 2; and the outlook of mechanically-driven ultra-high-temperature thermoacoustic Stirling heat pump utilizing in the industrial field is carried out in Section 3; finally the main conclusions are given in Section 4.

Numerical Analysis of Thermoacoustic Stirling Heat Pump Unit Under Ultra-High-Temperature Zone

In this section, the configuration and calculated model of the thermoacoustic heat pump unit are introduced at first, and then its operating performances, thermoacoustic

characteristics and the distributions of exergy losses under different heat-supply temperatures and temperature lifts are analyzed and discussed.

Model description

As can be seen from Figure 1, these two types of mechanically-driven thermoacoustic Stirling heat pump systems both include the thermoacoustic Stirling heat pump unit (TASHP unit), which is the key unit for energy conversion. It consists of a hot-end heat exchanger with the isothermal wall at the heat-supply temperature of T_{hp} , a regenerator filled with porous materials and a cold-end heat exchanger with the isothermal wall at the heat-source temperature of T_{source} , as is shown in Figure 2. And the main structural parameters are listed in Table 2.

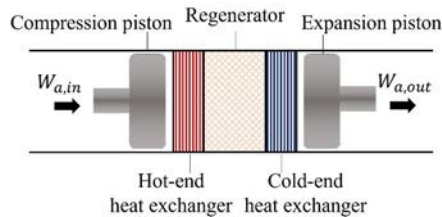


Figure 2. The configuration and Sage model of TASHP unit.

Table 2. The main structural parameters of TASHP unit.

Hot-end heat exchanger	Shell-and-tube type, tube inner-diameter 1 mm, porosity 0.15
Regenerator	Diameter 100mm, filled with stainless steel wire mesh, porosity 0.8, wire diameter 50 μ m
Cold-end heat exchanger	Shell-and-tube type, tube inner-diameter 1 mm, porosity 0.15

The simulated model of TASHP unit is established through the commercial software Sage [14]. It is a one-dimensional calculating software, which is widely used in the simulation and optimization of various thermoacoustic systems. Each component is connected continuously by mass flow, pressure wave and energy flow. The one-dimensional governing equations of continuity, momentum and energy for the gas domain are the basis of simulation, which are given as follows:

$$\frac{\partial \rho A}{\partial t} + \frac{\partial \rho u A}{\partial x} = 0 \quad (1)$$

$$\frac{\partial \rho u A}{\partial t} + \frac{\partial u \rho u A}{\partial x} + \frac{\partial P}{\partial x} A - F A = 0 \quad (2)$$

$$\frac{\partial \rho e A}{\partial t} + P \frac{\partial A}{\partial t} + \frac{\partial}{\partial x} (u \rho e A + u P A + q) - Q_w = 0 \quad (3)$$

Where P , u , ρ , A and e refer to the pressure, velocity, area and total energy per unit mass, respectively; t and x represent the time and direction of x -axis, respectively. Besides, the term F in the momentum equation is viscous pressure gradient; the term Q_w in the energy equation refers to the heat flow; the term q in the energy equation is instantaneous axial heat flux.

In the simulation, the displacement of compression piston, the displacement and phase of expansion piston, the lengths of regenerator and two heat exchangers are all chose as optimized parameters. Besides, the coefficient of performance (COP_h), relative Carnot efficiency (η_h) and heating capacity are used for estimating the operating performance of the TASHP unit, which are expressed as follow:

$$COP_h = \frac{Q_{hp}}{\Delta W_a} = \frac{Q_{hp}}{W_{a,in} - W_{a,out}} \quad (4)$$

$$\eta_h = COP_h \cdot \frac{T_{hp} - T_{source}}{T_{hp}} = \frac{Q_{hp}}{W_{a,in} - W_{a,out}} \cdot \frac{T_{hp} - T_{source}}{T_{hp}} \quad (5)$$

where Q_{hp} and ΔW_a refer to the heating capacity and consumption of acoustic power, respectively; $W_{a,in}$ and $W_{a,out}$ are the inlet and outlet acoustic power of the TASHP unit.

Results and discussion

System performance under ultra-high-temperature condition

Table 3 and Figure 3 show the system performance of TASHP unit under the mean pressure of 5 MPa, the working frequency of 50Hz, the working medium of helium, the standard temperature of 30 °C, as well as the heat-supply temperature T_{hp} of 650 °C and temperature lift of 150 K (ΔT_{lift} , the temperature difference between T_{hp} and T_{source}), including the operating performance and the distribution of total exergy loss. The TASHP unit shows great performance with the COP_h and η_h of 3.79 and 61.57%, respectively. According to the simulated results from Figure 3, it can be found that the

energy dissipation in the TASHP unit is mainly contributed to the flow friction, heat transfer between gas and solid and axial heat conduction. The vast majority of the exergy losses occurred in the heat exchangers are due to the non-ideal heat transfer between gas and solid; while the exergy losses caused by flow friction and axial heat conduction are mainly happened in the regenerator, because of the filled porous material and the temperature gradient inside the regenerator.

Table 3. The operating performance of TASHP unit under ultra-high-temperature zone.

Heating capacity	2092 W
Acoustic power consumption	552.1 W
Coefficient of performance	3.79
The relative Carnot efficiency	61.57%
Inlet pressure ratio	1.16

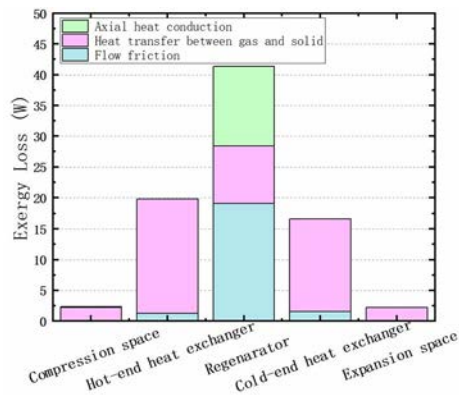


Figure 3. The distribution of total exergy loss happened in the TASHP unit.

The distributions of acoustic power and enthalpy flows, as well as the mean gas and solid temperatures are shown in Figure 4. The variations of enthalpy flows in these two heat exchangers refer to the heat absorbing or releasing, and the declining trend of acoustic power along the regenerator represents the energy conversion process. Besides, the thermodynamic processes of the working medium happened in the TASHP unit are without phase-change, resulting in the heat transfer temperature differences between the gas domain and solid wall inside the two heat exchangers, which ultimately lead to the large amount of exergy losses.

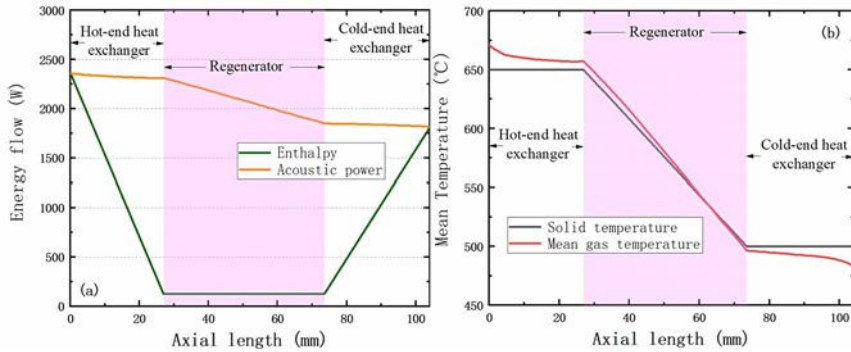


Figure 4. The distributions of energy flows (a) and mean temperatures (b).

Influences of heat-supply temperature and temperature lift

Figure 5 depicts the COP_h and η_h under the heat-supply temperature of 500~800 °C and temperature lift of 100~200 K. The COP_h of TASHP unit ranges from 2.7 to 5.5 and the η_h varies from 51.3% to 69.7%. The highest COP_h is achieved at the heat-supply temperature of 800 °C and the temperature lift of 100 K, while the highest η_h reaches at the heat-supply temperature of 500 °C and the temperature lift of 200 K. It can be concluded that mechanically-driven thermoacoustic Stirling technology shows outstanding performance at the working conditions of high heat-supply temperature and large temperature lift.

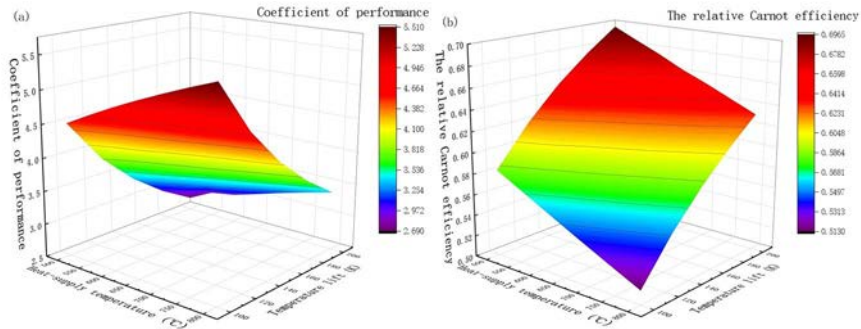


Figure 5. COP_h (a) and η_h (b) under different heat-supply temperatures and temperature lifts.

In order to deeply analyze the influence of temperature lift on the TASHP unit, the exergy losses occurred in these three key thermoacoustic components and their ratios to the total acoustic power consumption are given in Figure 6, with the heat-supply temperature fixed at 650 °C. With the increasing of temperature lift, the exergy loss occurred in the regenerator gradually comes to dominate, while the energy dissipations in the two heat exchangers are not the main reason for restricting the working performance of TASHP unit under larger-temperature-lift condition. When the temperature lift is relatively small, the exergy loss in heat exchanger caused by non-ideal heat transfer is comparatively large, exchangers gradually diminish. The reason is that the effect of temperature lift on the heat transfer temperature difference is relatively low (as is shown in Figure 7, the variation of heat transfer temperature difference is no more than 4 K with T_{hp} fixed at 650 °C). Besides, the ratios of exergy losses all present the decreasing tendencies, which means that mechanically-driven thermoacoustic Stirling heat pump technology is suitable for operating at larger-temperature-lift condition.

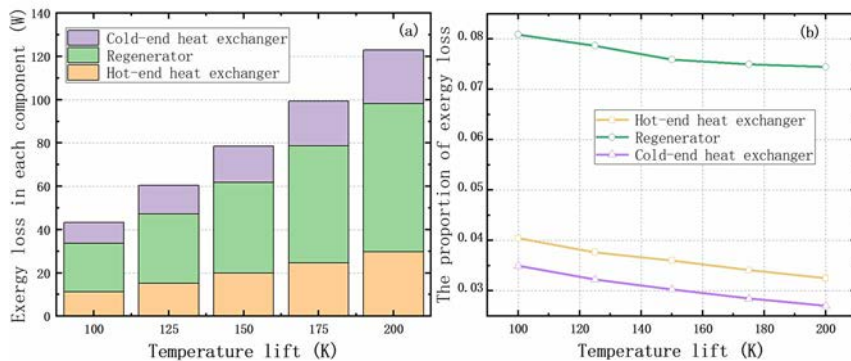


Figure 6. Exergy losses (a) and their proportions to the total acoustic power consumption (b) in each component under different temperature lifts.

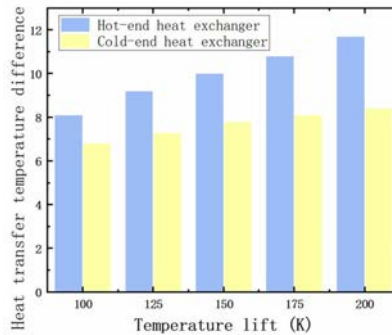


Figure 7. The influence of temperature lift on heat transfer temperature difference.

Application prospect in industrial field

As is well known, industrial heating supply is one of the main fields of heat consumption. For instance, the steel industry is a kind of energy-intensive industry, which can produce large amounts of carbon emissions. The iron and steel production mainly relies on the blast furnace converter process at present; while the hydrogen-based direct-reduced iron process will become one of the main routes of iron and steel production in the future. Hydrogen metallurgy iron producing technology uses hydrogen instead of traditional carbon reducing agent, which shows huge carbon emission reduction potential [15, 16]. Its chemical reaction belongs to an endothermic reaction and its reaction temperature is quite high (the temperature will reach more than 600 °C). Therefore, this metallurgical process has a large amount of high-temperature heat demand. However, if these high-temperature heats are obtained through direct combustion of traditional industrial boilers, it will not only have low energy utilization efficiency, but also cause environmental pollution and other problems.

Hence, it is urgent to explore high-efficient and low-carbon industrial high-temperature heating supply technology.

On the other hand, the potential for energy conservation in the industrial field is huge, due to the larger amount of waste heat is directly discharged during many industrial production processes [17]. Taking the synthetic ammonia industry as an example, the relevant chemical reaction occurred in the ammonia synthesis process is an exothermic reaction (the reaction temperature is around 400 °C ~500 °C) and high-temperature

heat will be continuously generated during the producing process, its direct emission will cause substantial energy dissipation [18]. If the industrial waste heat resources (such as the heat release of synthetic ammonia reaction) are recycled and the heat demands with higher temperature grade (such as the heat absorption of hydrogen metallurgy reaction) are obtained by quality improvement technology, it can not only reduce energy consumption and save primary energy, but also avoid the environmental pollution caused by the discharge processes of waste gas or waste liquid.

As is mentioned in Section 2, the mechanically-driven thermoacoustic Stirling technology shows great working performance under ultra-high-temperature zone especially with large temperature lift. It has broad application prospect in the industrial waste heat recovery and high-temperature heating supply. The prospective application scheme is as follow: utilizing the industrial waste heat generated by the chemical reaction in the ammonia synthesis industry as the low-temperature heat source, and providing high-temperature heat required by the hydrogen metallurgy process in the steel industry through the mechanically-drive thermoacoustic Stirling ultra-high-temperature heat pump technology. In addition, the hydrogen used for the hydrogen metallurgy process can be electrolytic hydrogen production through green electricity such as photoelectric technology. It is an effective and low-carbon heating method for not only meeting the demand of high-temperature industrial heating supply, but also achieving the recovery of industrial waste heat, which is an important technical route for energy saving and emission reduction in ammonia synthesis and hydrogen metallurgy industry.

Conclusion

In summary, a numerical investigation on the mechanically-driven thermoacoustic Stirling ultra-high-temperature heat pump technology is carried out, and its application prospect in industrial field is also introduced. The main conclusions can be summarized as follow:

- (1) The TASHP unit can achieve the COP_h and η_h of 3.79 and 61.57% respectively at the heat-supply temperature of 650 °C and temperature lift of 150K, with the heating capacity of 2092W.
- (2) The ranges of COP_h and η_h of TASHP unit are 2.7~5.5 and 51.3%~69.7% respectively, with the heat-supply temperature of 500~800 °C and temperature lift of 100~200 K.

- (3) The temperature lift shows small effect on the heat transfer temperature differences in the two heat exchangers and the exergy losses caused by non-ideal heat transfers inside the heat exchangers vary slightly, ultimately leading to the outstanding operating performance of TASHP unit at larger temperature lift.
- (4) The mechanically-driven thermoacoustic Stirling ultra-high-temperature heat pump technology can absorb the waste heat from the synthetic ammonia industry as low-temperature heat source and elevate its temperature grade, providing the high-field.

Acknowledgements

This work was financially supported by the Key Research and Development Projects of the Ministry Science and Technology No.2022YFF0712600.

References

- [1] Statistical Review of World Energy 2023(72nd edition). Energy Institute (2023).
- [2] Xiaohui She, Lin Cong, Binjian Nie, et al. Energy-efficient and -economic technologies for air conditioning with vapor compression refrigeration: A comprehensive review. *Applied Energy*, 232: 157-186 (2018).
- [3] Kristian Gjoka, Behzad Rismanchi, Robert H. Crawford. Fifth-generation district heating and cooling systems: A review of recent advancements and implementation barriers. *Renewable and Sustainable Energy Reviews*, 171: 112997 (2023).
- [4] Enyuan Gao, Qi Cui, Huaqian Jing, et al. A review of application status and replacement progress of refrigerants in the Chinese cold chain industry. *International Journal of Refrigeration*, 128: 104-117 (2021).
- [5] Li Jin Goh, Mohd Yusof Othman, Sohif Mat, et al. Review of heat pump systems for drying application. *Renewable and Sustainable Energy Reviews*, 15(9): 4788-4796 (2011).
- [6] Renewable Energy Policies in a Time of Transition. International Energy Agency (2018).
- [7] DH Rix. The design and initial testing of a prototype stirling cycle heat pump. *Proceedings of the Institution of Mechanical Engineers, Part C: Journal of Mechanical Engineering Science*, 202(6): 431-438 (1988).

- [8] Li Ke, Yu Guoyao, Zhang Yibing, et al. Theoretical and experimental research on free piston Stirling heat pump(in Chinese). *Journal of Engineering Thermophysics*, 36(1): 41-45 (2015).
- [9] Chin-Hsiang Cheng, Hang-SuinYang, and Hong-Xin Chen. Development of a beta-type stirling heat pump with rhombic drive mechanism by a modified non-ideal adiabatic model. *International Journal of Energy Research*, 44(7): 5197–5208 (2020).
- [10] Riyong Wang, Jianying Hu, Zilong Jia, et al. Study on the temperature adaptability of free-piston Stirling heat pump. *Energy Conversion and Management*, 249: 114864 (2021).
- [11] Steve Kowalski, Ahmad Abuheiba, Rusty Jewett, et al. Efficiency and capacity performance of a stirling cycle water-to-water heat pump. Technical report, Oak Ridge National Lab.(ORNL), Oak Ridge, TN (United States) (2022).
- [12] Chang Depeng, Wang Riyong, Sun Yanlei, et al. Study on Performance of Ultra-High Temperature Air Source Free Piston Stirling Heat Pump for Producing 120~150 °C. Steam (in Chinese). *Journal of Engineering Thermophysics*, 44 (11): 2967-2973 (2023).
- [13] Longran Dai, Kaiqi Luo, Yanlei Sun, et al. A 2 kW-class free-piston Stirling heat pump prototype suitable for coldregions for domestic heating. *International Journal of Refrigeration*, 159: 112-123 (2024).
- [14] Gedeon D. Sage user's guide, Stirling, pulse-tube and low-T cooler model classes. Athens, OH (2014).
- [15] Zhiyuan Fan and S. Julio Friedmann. Low-carbon production of iron and steel: Technology options, economic assessment, and policy. *Joule*, 5(4): 829-862 (2021).
- [16] Jude A. Okolie, Biswa R. Patra, Alivia Mukherjee, et al. Futuristic applications of hydrogen in energy, biorefining, aerospace, pharmaceuticals and metallurgy. *International Journal of Hydrogen Energy*, 46(13): 8885-8905 (2021).
- [17] Ao Luo, Hao Fang, Jianjun Xia, et al. Mapping potentials of low-grade industrial waste heat in Northern China. *Resources, Conservation & Recycling*, 125: 335-348 (2017).

- [18] Daniel Florez-Orrego, Meire Ellen Ribeiro Domingos, François Marechal. Techno-economic and environmental analysis of high temperature heat pumps integration into industrial processes: the ammonia plant and pulpmill cases. *Sustainable Energy Technologies and Assessments*, 60: 103560 (2023).

Stress analysis/noise and vibration

Vibration Analysis of a V6 Double-acting Gamma Stirling Heat Pump

Arne Høeg^{a,*}, Sindre Abrahamsen^a, Gunnar Vartdal^a, Tobias Dahl^a, Norbert Lümmen^b

a Enerin AS, Evja Vest, Florø, Norway

b Department of Mechanical Engineering and Maritime Studies, Western Norway University of Applied Sciences, Inn-dalsveien 28, 5063 Bergen

* Corresponding author: arne@enerin.no

Keywords: Heat pump, Vibration, Simulation, Gamma, Double-acting

Abstract

The Enerin HoegTemp industrial heat pump is a 4-circuit double-acting gamma configuration 6-cylinder stirling machine, designed for medium temperatures in the range $-100\text{ }^{\circ}\text{C}$ to $+250\text{ }^{\circ}\text{C}$. The rated heating capacity is $400\text{ kW}_{\text{th}}$, and the maximum heating capacity is above $500\text{ kW}_{\text{th}}$. It has been designed to have small vibrations generally, but specifically to not have first-order or second-order mass moments or mass forces in the vertical direction.

This paper presents the heat pump configuration, dimensions, and inertial properties of the Enerin HoegTemp heat pump. In addition to basic information regarding the heat pump, this includes information on simulated eigenfrequencies, effects of the coupling between the electric motor and the heat pump, as well as the engine mounts and connected dampers. A vibration analysis is presented based on the simulated performance, torque curve, and inertial forces of the heat pump. The simulated performance and torque curves are based on simulations using the Sage of Athens stirling machine simulation software, while simple vibration simulations based on the simulated torque curves and moments of inertia have been performed using custom Julia code. The simulated data are compared to measured vibrations from a SICK MPB10 condition monitoring sensor mounted on the heat pump, allowing comparison between simulated and measured vibrations along the vertical and the two horizontal axes.

The presented data can serve as a reference for vibrations for similar stirling machines, but also as a solid basis on which to design engine room floors and dampers for stirling machines of similar sizes and configurations.

Enerin HoegTemp heat pump

The Enerin HoegTemp industrial heat pump is a 4-circuit double-acting gamma configuration 6-cylinder stirling machine, designed for medium temperatures in the range $-100\text{ }^{\circ}\text{C}$ to $+250\text{ }^{\circ}\text{C}$. The rated heating capacity is $400\text{ kW}_{\text{th}}$, and the maximum heating capacity is above $500\text{ kW}_{\text{th}}$. It has been designed to have small vibrations generally, but specifically to not have first-order or second-order mass moments or mass forces in the vertical direction.

The heat pump uses pressurized helium (refrigerant R-704) as working medium and has a non-pressurized crankcase with oil-lubricated mechanicals, separated from the process by proprietary piston rod seals. The heat pump complies with EU's Machinery Directive and Pressure Equipment Directive, as well as other relevant directives and standards, such as EN 13345-3.



Figure 1. HoegTemp heat pump installed at IVAR biogas facility, Stavanger, Norway.

Three heat pumps have been installed so far: The first (shown) at the IVAR biogas facility near Stavanger, Norway. Two other heat pumps at GE Healthcare, Lindesnes, Norway and Pelagia, Måløy, Norway. The first installation is described by Høeg et al [1-2]. The heat pump is similar to the HighLift 4-106 series heat pump from Single-Phase Power, described by Høeg et al [3-5], but differs in that it is a double-acting gamma configuration, while the former was a double-acting alpha configuration of the Franchot type. The main advantages being that the gamma configuration allows higher sink temperatures, and higher COP.

Configuration and properties

The HoegTemp heat pump is a 90° V6, where each cylinder bank is an independent pair of stirling circuits in the double-acting gamma configuration. Each circuit consists of a displacer cylinder with 2 parallel heat exchanger modules, connected to one end of a common power cylinder, and separated by the power piston. The displacer pistons are 180° phase shifted. With 90° between the two cylinder banks, the four circuits are 90°

apart.

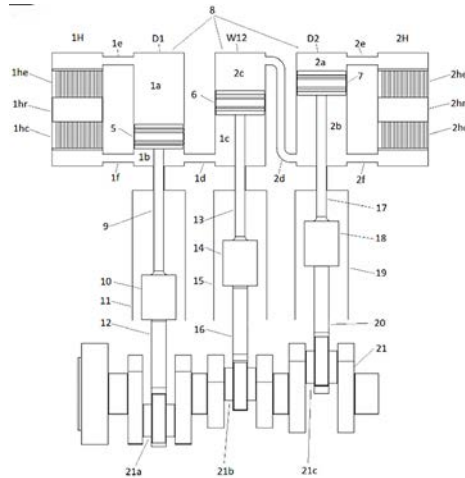


Figure 2. Principal sketch of one cylinder bank of the HoegTemp heat pump. From the left: heat exchanger, displacer cylinder, power cylinder, displacer cylinder, heat exchanger. Crankshaft with flywheel on the left and 4 main bearings.

The main advantages of this configuration compared to double-acting alpha configurations, lie in the process design freedom, but there are some balancing benefits too. The 90° V block allows first order inertial forces to be completely balanced, except for production tolerances. The $90^\circ/90^\circ$ crankshaft allows balancing of $2/3$ of second-order inertial forces and moments. The second and fourth order inertial forces are almost symmetrical, which means that the inertial moments are very low. The configuration could in theory be perfectly balanced, except for the fourth order mass forces, with forked connecting rods and light displacer components with half the oscillating mass of the power pistons.

Another interesting feature is that the inertial forces on the power piston are counter acting the gas forces, thereby reducing the combined loads on the mechanicals.

Table 1. Inertial forces and moments at 800 RPM.

Inertial force	Value	Direction
First order inertial force	158 N	Undefined (prod. Tol.)
First order inertial moment	722 Nm	Counter-rotating
Second order inertial force	6722 N	Horizontal
Second order inertial moment	188 Nm	Horizontal
Fourth order inertial force	3715 N	Vertical
Fourth order inertial moment	104 Nm	Vertical

Compared to the similar capacity heat pump SPP HighLift 4-106A [3-5], the horizontal forces are 66% lower while the vertical fourth-order forces are 25% higher. The inertial moments are 75% - 97% lower.

The main design loads on the engine mounts are second-order horizontal forces from 400 N @ 6.7 Hz to 15 kN @ 40 Hz, and fourth-order vertical forces from 200 N @ 13.4 Hz to 8 kN @ 80 Hz. In addition, the uneven torque adds first and third order moments on the heat pump skid.

The engine mounts have eigenfrequencies at 2 Hz vertical and 1 Hz horizontal, corresponding to 30 RPM. The skid with engine mounts is then supercritical at all normal operating points.

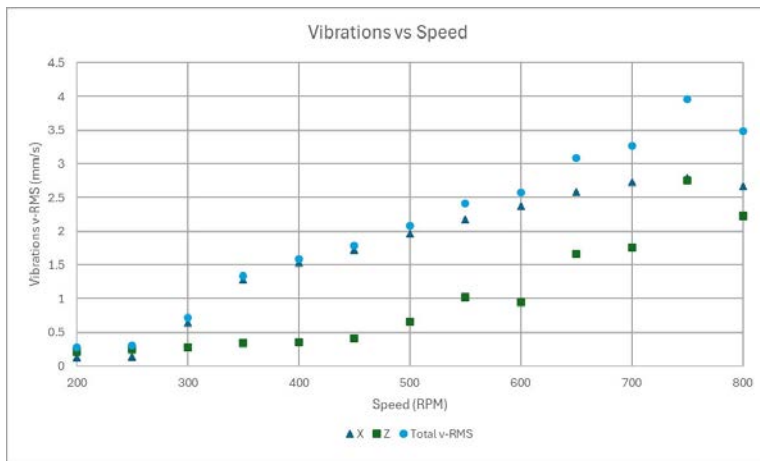


Figure 3. Vertical (z) and horizontal (x) and total vibrations as function of shaft speed.

Operation and loads

The HoegTemp is designed to be operated between 200 and 1200 RPM, at max charge pressure. Peak COP is at 500 RPM and peak heating capacity is at 950 RPM. Heat delivery can be controlled between 50% and 100% by varying the shaft speed at max charge pressure, and from 10% and 100% by varying both charge pressure and shaft speed. Generally, a 2x change in power consumption is achieved in less than 1 second, while the heat delivery will lag up to 1 minute.

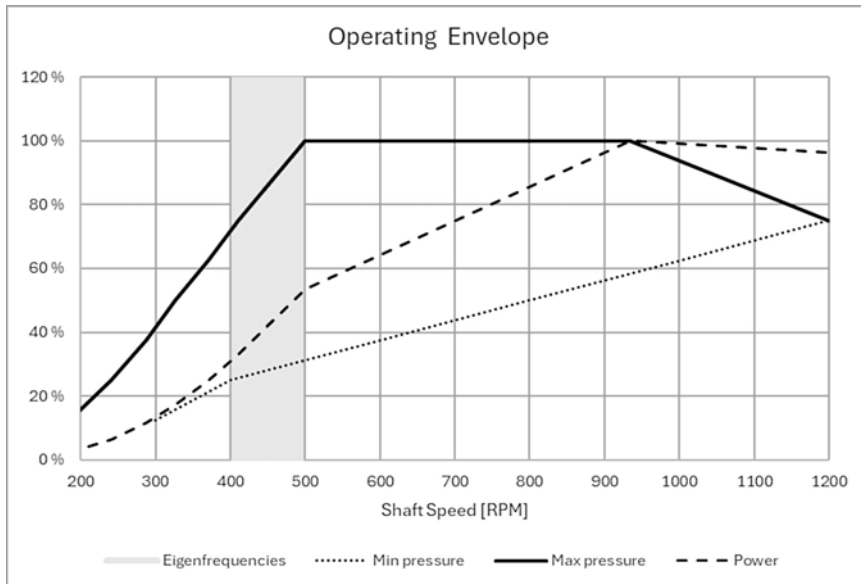


Figure 4. Operating envelope for the HoegTemp heat pump.

The two circuits of a circuit pair are different in that the power piston separates the hot volume of one circuit and the cold volume of the other circuit. The consequence of this difference is that the two circuits have different pressure amplitudes and slightly different COPs. The process will be very similar at other temperatures than at the simulated temperatures for the diagram. If the operating conditions change, the process will adapt to the new temperatures quickly, without any transient losses. Høeg et al [5] showed that the average COP with varying sink temperature was a function of the average temperature only.

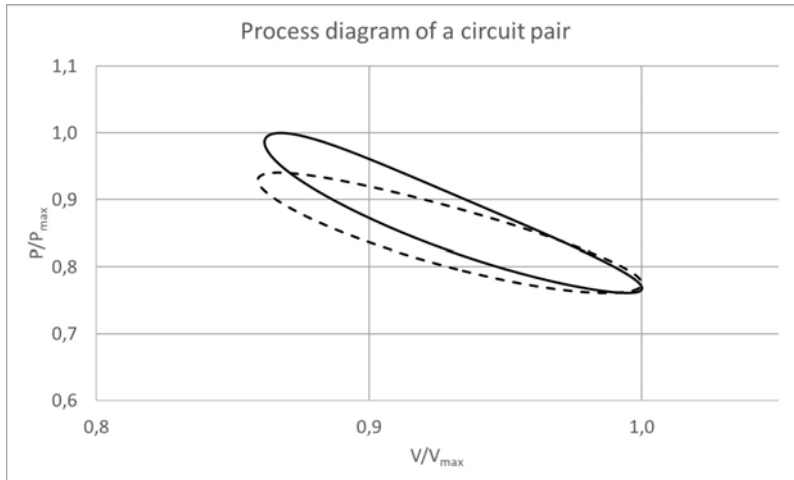


Figure 5. Process diagram for one pair of circuits in the HoegTemp heat pump.

With very similar process diagrams for each circuit in a pair, and 4 circuits 90° apart, it would be assumed that the torque would be nearly constant, as shown for siemens-type double acting alpha stirling engines [6]. As can be seen in the chart below, the torque from the 4 displacers adds up to a constant torque, while the torque from the two power pistons have strong first order and third order torque amplitudes. The reason for this is the cross-sectional area of the piston rods, acting as gas springs with the average charge pressure.

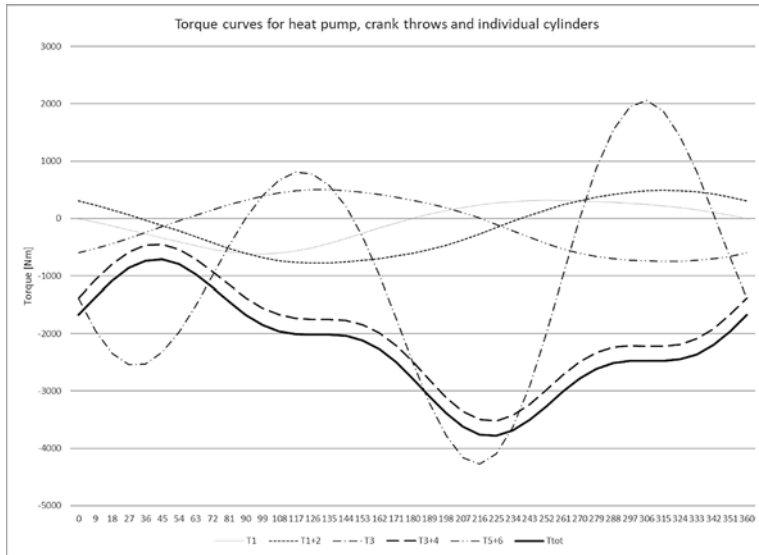


Figure 6. Torque from one displacer (T_1), 2 displacers connected to one crank throw (T_{1+2}), one power piston (T_3), 2 power pistons connected to one crank throw (T_{3+4}), the other two displacers (T_{5+6}) and from all 6 pistons (T_{tot}) in the HoegTemp heat pump.

Dynamic model and simulation

A vibration analysis is presented based on the simulated performance, torque curve, and inertial forces of the heat pump. The simulated performance and torque curves are based on simulations using the Sage of Athens stirling machine simulation software, while simple vibration simulations based on the simulated torque curves and moments of inertia have been performed using the Julia programming language. The system was modelled as five rotating masses, all connected in series with a torsion spring and damper between each mass [7] and a schematic can be seen in Figure 7.

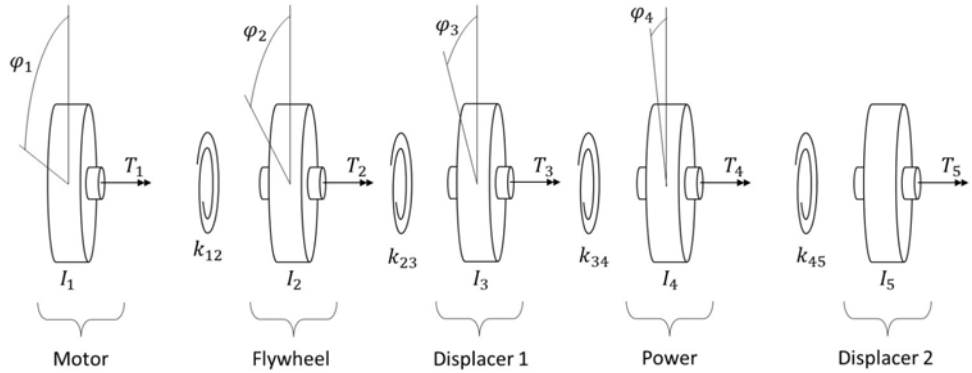


Figure 7. Simulation model for dynamic simulation of the HoegTemp heat pump.

Each mass is excited by a torque $T(\varphi)$. The equations of motion were derived from newtons second law in rotational form:

$$\Sigma T = I\dot{\varphi} \quad (1)$$

When applied to all the masses, this leads to five coupled equations that can be written in matrix form. As an example, with four masses:

$$\begin{bmatrix} I_1 & 0 & 0 & 0 \\ 0 & I_2 & 0 & 0 \\ 0 & 0 & I_3 & 0 \\ 0 & 0 & 0 & I_4 \end{bmatrix} \begin{bmatrix} \varphi_1 \\ \varphi_2 \\ \varphi_3 \\ \varphi_4 \end{bmatrix} + \begin{bmatrix} d_{12} & -d_{12} & 0 & 0 \\ -d_{12} & d_{12} + d_{23} & -d_{23} & 0 \\ 0 & 0 & -d_{23} & -d_{34} \\ 0 & 0 & d_{23} + d_{34} & -d_{34} \end{bmatrix} \begin{bmatrix} \dot{\varphi}_1 \\ \dot{\varphi}_2 \\ \dot{\varphi}_3 \\ \dot{\varphi}_4 \end{bmatrix} + \begin{bmatrix} k_{12} & -k_{12} & 0 & 0 \\ -k_{12} & k_{12} + k_{23} & -k_{23} & 0 \\ 0 & -k_{23} & k_{23} + k_{34} & -k_{34} \\ 0 & 0 & -k_{34} & k_{34} \end{bmatrix} \begin{bmatrix} \varphi_1 \\ \varphi_2 \\ \varphi_3 \\ \varphi_4 \end{bmatrix} = \begin{bmatrix} T_1 \\ T_2 \\ T_3 \\ T_4 \end{bmatrix} \quad (2)$$

Or using matrix notation

$$\mathbf{I}\ddot{\varphi} + \mathbf{D}\dot{\varphi} + \mathbf{K}\varphi = T \quad (3)$$

Where \mathbf{I} is a diagonal inertia matrix, \mathbf{D} and \mathbf{K} are tridiagonal damping and stiffness matrices and T is a vector containing the torques, as a function of angle φ , from the Sage simulation.

This second order equation has to be rewritten as a system of first order equations for numeric integration. Using $x = [\varphi_1 \ \varphi_2 \ \varphi_3 \ \varphi_4 \ \omega_1 \ \omega_2 \ \omega_3 \ \omega_4]^T$, we can move the terms over and invert the mass matrix to arrive at

$$\dot{x} = \left[\mathbf{I}^{-1}(T(\varphi) - \mathbf{D}\omega - \mathbf{K}\varphi) \right] \quad (4)$$

Data used in the simulation:

- Crankshaft inertia 6.2 kgm² (1.4 kgm² for each of the 3 crank throws, 1 kgm² for each shaft end)
- Flywheel inertia 25 kgm²
- Motor rotor inertia 12.7 kgm²
- Crankshaft torsional stiffness between crank throws 4.85 MNm/rad
- Crankshaft torsional stiffness from flywheel flange to first crank throw 5.66 MNm/rad
- Coupling torsional stiffness 19.5 kNm/rad
- Coupling damping factor 0.7
- Crankshaft damping factor 0.4 Nms/rad
- Rotor damping factor 2.0 Nms/rad

Both the Jacobian of \dot{x} and the system dynamics showed both very low and very high eigenfrequencies, hinting that the system is stiff and places high requirements on the integrator [8]. We had particular interest in the slower system dynamics, but the faster dynamics introduced a lot of noise and instability. The Julia package DifferentialEquations [9] has many solvers suitable for stiff systems, for example the Rodas5() showed a tenfold speed increase, but in the end, the automatic solver selection had better overall results.

The torsion angle between all elements are calculated at all running speeds from 100 rpm to 1000 rpm. The first resonant frequency can be seen in the vibration damper in figure 8.

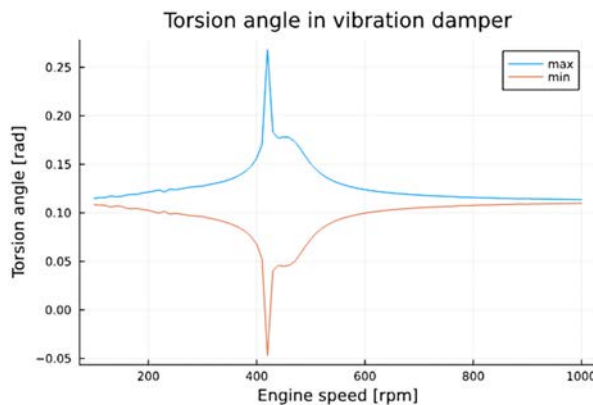


Figure 8. Chart showing torsion in the damper and the two highest-loaded crankshaft elements, as function of shaft speed.

The source of the trailing hump after the resonant peak is unknown. The two most important eigenfrequencies of the HoegTemp heat pump in this installation, are 7.5 Hz and 133 Hz, corresponding to 450 RPM and 8000 RPM. Within the operating envelope between 500 RPM and 1000 RPM, the excitation torques from the pistons have a frequency of 8.33 Hz and 66 Hz, which is sufficiently far from the system eigenfrequencies. A simplified analysis of the coupling eigenfrequency would be to use the equation for a shaft with two flywheels:

$$f = \frac{1}{2\pi} \sqrt{k_{coupling} \cdot \frac{I_{p,flywheel} + I_{p,rotor}}{I_{p,flywheel} I_{p,rotor}}} \quad (5)$$

Equation 5 gives an eigenfrequency of 7.56 Hz or 453 RPM. Quite similar to the simulated results, but not quite. As a first approximation in design of a heat pump, the textbook equation is a good starting point.

The torsion amplitudes in the crankshaft are shown in figure 9. There is a small hump at the first resonance frequency, but overall, the torsion angle is increasing in the whole sub-critical area and reaches a peak at the second eigenfrequency of 133 Hz, or 8000 RPM. This resonance peak is not shown in any plot here due to the long simulation times needed. Within the operating envelope, the highest torsion amplitude is then at 1000 RPM, as shown in figure 9. The torque found from the dynamic simulation at 1000 RPM is still slightly lower than the applied max torque at 1000 RPM.

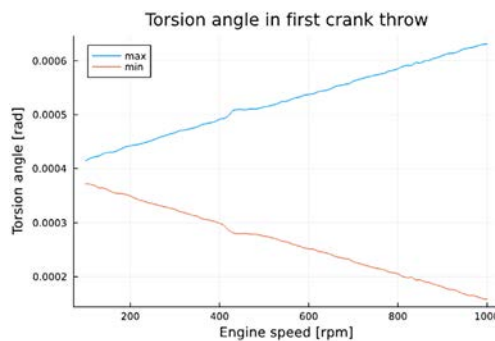


Figure 9. Chart showing torsion in the first crank throw (between the flywheel and the displacer), as function of shaft speed.

The electric motor and its control system tries to keep a constant running speed.

However, this speed will be influenced by torques from the stirling process and the dynamics between the motor and the stirling machine. This dynamic results in a motor speed variation at different target speeds. This was simulated by a constant motor torque which resulted in an average motor speed plotted on the x-axis of figure 10. The speed variation is then a function of the average running speed. It may be of interest to avoid the lower end of the running envelope to attain a smoother running motor [10].

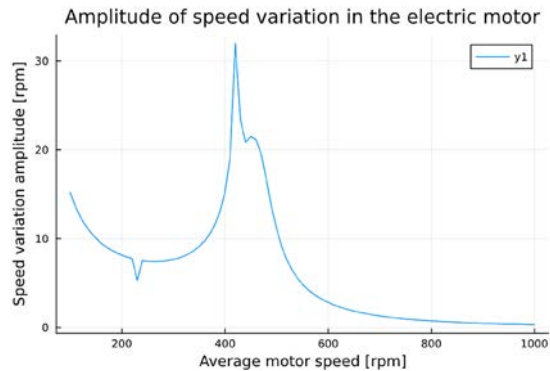


Figure 10. Plot showing the speed variation in the motor due to the dynamical behavior of the oscillatory system.

Conclusion

The vibration measurements indicate that the heat pump is free of problematic eigenfrequencies in the normal operating range, and the measurements confirm the subjective observation that the heat pump has low vibrations. The accelerometer measures only 3 axes (vertical, horizontal and axial), and may not register torsional vibrations.

The simulation and textbook calculations both show eigenfrequencies outside the normal operating range. To reduce the first eigenfrequency just above 400 RPM, a softer coupling and/or a flywheel with higher inertia could be applied, but a softer coupling with similar torque capability is not available off the shelf, and a flywheel with higher inertia would reduce the eigenfrequencies of the crankshaft so that the margin between the fourth order applied torque from the process and the first crankshaft eigenfrequency would become an issue.

The simulation model may be used to estimate dynamic properties of later installations with different capacities, motors and equipment. Especially if the heat pump is tuned for higher capacity and hence higher power consumption and higher average torque, selecting the right combination of coupling, flywheel and possibly a torsional damper, may be aided by the model.

Acknowledgements

The installation at IVAR biogas facility has been partly funded by Innovation Norway, and by IVAR of Norway. The research has been funded by the EU Horizons project SUSHEAT and the Research Council of Norway.

References

- [1] Høeg A, Løver K, Asphjell, TA. Performance of a new ultra-high temperature industrial heat pump. 14th IEA Heat Pump Conference, USA, (2023).
- [2] Høeg A, Løver K, Vartdal G. Performance of a High-Temperature Industrial Heat Pump, using Helium as Refrigerant. High-Temperature Heat Pump Symposium 2024, Denmark, (2024).
- [3] Høeg A, Tveit TM, Asphjell, TA. Mechanical Design of the 4-500 kWth Stirling Cycle Heat Pump SPP 4-106. 17th International Stirling Engine Conference, UK, (2016).
- [4] Høeg A, Tveit TM. Process design for a 4 x 10.6 litre low-temperature Stirling engine. 18th International Stirling Engine Conference, Taiwan, (2018).
- [5] Høeg A, Tveit TM. Low to very high temperature thermal energy recycling – 3 case studies. 19th International Stirling Engine Conference, Italy, (2021).
- [6] Jet Propulsion Laboratory publication 78-71, 2 (1978).
- [7] van Basshuysen, Schäfer, Handbuch Verbrennungsmotor, 3. Auflage, chapter 6.2 Drehschwingungen, Vieweg Verlag, Germany, (2005).
- [8] Butcher. Numerical Methods for Ordinary Differential Equations. 3rd ed, Wiley, (2016).

- [9] Rackauckas et al. DifferentialEquations.jl-a performant and feature-rich ecosystem for solving differential equations in Julia. Journal of Open Research Software, Vol 5, (2017).
- [10] Sikora M, Vlach R. Dynamic Model of Stirling Engine Crank Mechanism with Connected Electric Generator. Applied and Computational Mechanics 3, (2009).

Regenerator and porous medium

Determination of the Regenerator Loss in a Stirling Engine by Gas Temperature Measurements

S. Peveling^a, F. Kusche, H.-D. Kühl^{b*}

a,b Laboratory of Thermodynamics, TU Dortmund University, Dortmund, Germany,

* Corresponding author: hans-detlev.kuehl@tu-dortmund.de

Keywords: Regenerator loss, Gas temperature measurement, Fluid flow analysis, Stirling cycle

Abstract

The regenerator is the most critical part of a Stirling engine, and its losses may significantly reduce the thermal efficiency. For the improvement of regenerators in a convertible Stirling-Vuilleumier experimental machine, these losses need to be quantified, whereas their determination in a running machine cannot be performed by energy balances, as heat flows are subject to a variety of different loss mechanisms occurring in such an engine. An alternative method is the evaluation of the closed-loop integral of the enthalpy flow, for which the gas temperatures and the mass flows must be known. Therefore, fine-wire thermocouples were produced with a welding setup developed for this purpose, and gas temperature probes equipped with these were inserted in the regenerator housing to perform high-speed gas temperature measurements. A procedure for processing the measured temperatures is shown, and the obtained temperatures and the calculated regenerator losses are compared to a third-order numerical model. Arising deviations are discussed with respect to the assumptions of the numerical model and are partially clarified within this contribution. As differences between simulated and measured regenerator losses remain, suggestions for further improvements of the presented method are made.

Introduction

The optimal design of regenerators is a major focus of research in the field of Stirling technology, as it is indispensable for high efficiencies [1]. There are various approaches to increase the efficiency of regenerators, such as the optimization of geometrical parameters or the development of new regenerator designs [2,3]. Another approach is the axial variation of the matrix parameters [4,5] to adjust them to the changing flow conditions and gas properties. As those matrices are to be investigated in an experimental Stirling engine in the future, a method for the determination of the regenerator performance within an engine needs to be developed. The thermal regenerator loss can be used to characterize the quality of a regenerator, but is often determined by

energy balances in specially designed test rigs [6]. As the overall energy balance of a Stirling engine is affected by various loss mechanisms, the regenerator loss needs to be determined in a different way.

In this work, the regenerator loss in an experimental machine already investigated intensively in previous works [7,8] is determined via high-speed gas temperature measurements performed with fine-wire thermocouples. Therefore, a setup for the manufacturing of those fine-wire couples and the modification of the regenerator housing is presented. A procedure for the adjustment of the measured gas temperatures is introduced, and first results regarding the gas temperature course and thermal regenerator loss are shown and compared to simulations using a third-order numerical model [9]. Deviations between measured and simulated values and open issues resulting from these are discussed.

Thermal Regenerator Losses

Influence of the Thermal Regenerator Loss on the Thermal Efficiency

The importance of the regenerator loss for the thermal efficiency of the Stirling cycle can be illustrated by a simplified consideration of its influence on the latter. An ideal Stirling cycle operating with a mass m of an ideal gas at a compression ratio $\Psi = V_{\max}/V_{\min}$ without any dead volumes absorbs a heat amount $Q_{h,id} = m R T_h \ln \Psi$ by isothermal expansion at a hot temperature level T_h and rejects a heat amount $Q_{c,id} = m R T_c \ln \Psi$ at a cold temperature level T_c . The thermal efficiency is defined as the ratio of the work output W and the heat input $Q_{h,id}$, and is known to yield the Carnot value in this case:

$$\eta_{th} = \frac{W}{Q_{h,id}} = \frac{Q_{h,id} - Q_{c,id}}{Q_{h,id}} = \frac{T_h - T_c}{T_h} = 1 - \frac{T_c}{T_h} = \eta_C \quad (1)$$

Assuming a constant isobaric heat capacity c_p and once again neglecting the buffer effect of its volume, an ideal regenerator in such an ideal cycle periodically exchanges a heat amount

$$Q_{R,id} = m c_p (T_h - T_c) \quad (2).$$

For a non-ideal regenerator, the non-regenerated heat amount equals the thermal regenerator loss ΔH_{RL} , i.e. the net amount of enthalpy per cycle that is conveyed from the hot to the cold cylinder volume. It can be expressed as the difference between the ideally and the actually regenerated amounts of heat, $Q_{R,id}$ and Q_R , respectively:

$$\Delta H_{RL} = Q_{R,id} - Q_R = (1 - \eta_R)Q_{R,id} \quad (3)$$

It can also be written in terms of the regenerator efficiency η_R , which is the ratio of these two heat amounts. For energy conservation reasons, the regenerator loss is equal to an additional heat amount that needs to be supplied to the cycle at the hot temperature level. The thermal efficiency of an otherwise ideal Stirling cycle with no dead volume and a given compression ratio Ψ thus reduces to

$$\eta_{th} = \frac{W}{Q_{h,id} + \Delta H_{RL}} = \frac{m R (T_h - T_c) \ln \Psi}{m R T_h \ln \Psi + (1 - \eta_R) m c_p (T_h - T_c)} = \frac{T_h - T_c}{T_h + \frac{c_p}{R} \frac{(1 - \eta_R)}{\ln(\Psi)} (T_h - T_c)} \quad (4).$$

Figure 1 visualizes Eq. (4) as a function of the regenerator efficiency assuming helium as the working fluid and thus $c_p/R \approx 2.5$, a hot temperature level $T_h = 500^\circ\text{C} \approx 773\text{ K}$, a cold temperature level $T_c = 30^\circ\text{C} \approx 303\text{ K}$, and a compression ratio $\Psi = 1.4$.

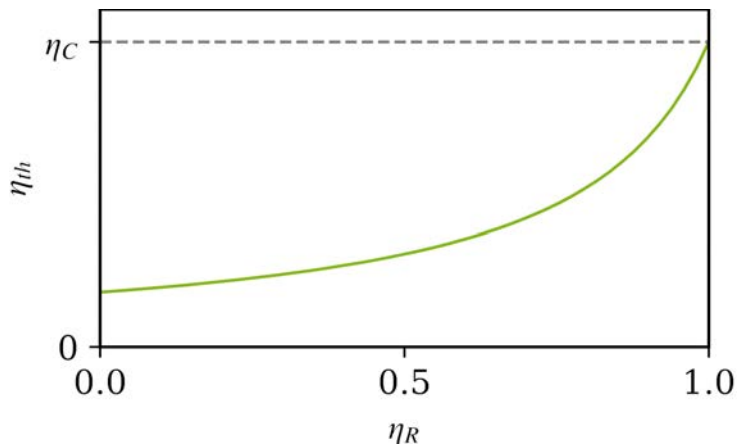


Figure 1. Thermal efficiency as a function of the regenerator efficiency for helium, $T_h = 500^\circ\text{C}$, $T_c = 30^\circ\text{C}$, $\Psi = 1.4$.

It is clear that the regenerator efficiency is critical to the thermal efficiency of a Stirling engine, and that the thermal efficiency increases disproportionately with increasing regenerator efficiency. As many regenerators typically have efficiencies above 95%, small improvements can have a large impact on thermal efficiency.

Loss Mechanisms

The thermal regenerator loss can be attributed to several loss mechanisms, which are of varying importance in a Stirling engine compared to other regenerative machines [10]. The heat transfer loss results from the temperature difference between the gas and the regenerator matrix due to limited heat transfer and is usually most important in a Stirling engine. The temperature swing loss is caused by the limited heat capacity of the matrix causing the matrix temperature to fluctuate. However, this is a small loss compared to the heat transfer loss. As the axial temperature gradient is very large, there is a constant heat flow through the solid material, both the regenerator matrix and its housing, which has a significant influence on the total loss. In addition, the flow through a porous medium deviates from a pure plug flow, resulting in increased energy transport and ultimately increased losses. This phenomenon is often referred to as the dispersion loss. Furthermore, the flow through the matrix also causes a pressure drop, of course. However, such dissipative flow losses are not in the focus of this work.

Experimental Determination Based on Gas Temperatures

The thermal regenerator loss can be determined by calculating the closed-loop integral of the enthalpy flow \dot{H} at the cold end of the regenerator, assuming that the heat flow due to thermal conduction is completely transferred to the gas:

$$\Delta H_{RL} = \oint \dot{H} dt = \oint \dot{m} h(T_G, p) dt \quad (5)$$

The experimental determination of the enthalpy flow requires the mass flow \dot{m} and a representative temperature T_c of the gas flow. As the regenerator loss is to be determined in an existing experimental machine, the construction space for modifications of the machine is limited. Therefore, the mass flow cannot be measured, but is taken from a third-order simulation model, since the calculation of mass flows with such models is reliable. As has been done in numerous works [11, 12], the gas temperature could be

determined experimentally using fine-wire thermocouples, if a probe with a thermocouple can be inserted into the machine.

Experimental setup

Welding setup

To record the cyclic gas temperature profile with sufficient temporal resolution, fine-wire thermocouples with low thermal inertia are required to minimize the difference between the measured temperature and the gas temperature. In contrast to previous works, the smallest commercially available wire diameter for thermocouples is now 50.8 μm , with the typical diameter of the welding spot being approximately 2.5 times the wire diameter, resulting in a welding spot diameter of 125 μm . Test measurements with these have revealed that their thermal inertia is too large to use the recorded temperatures for the calculation of the regenerator loss.

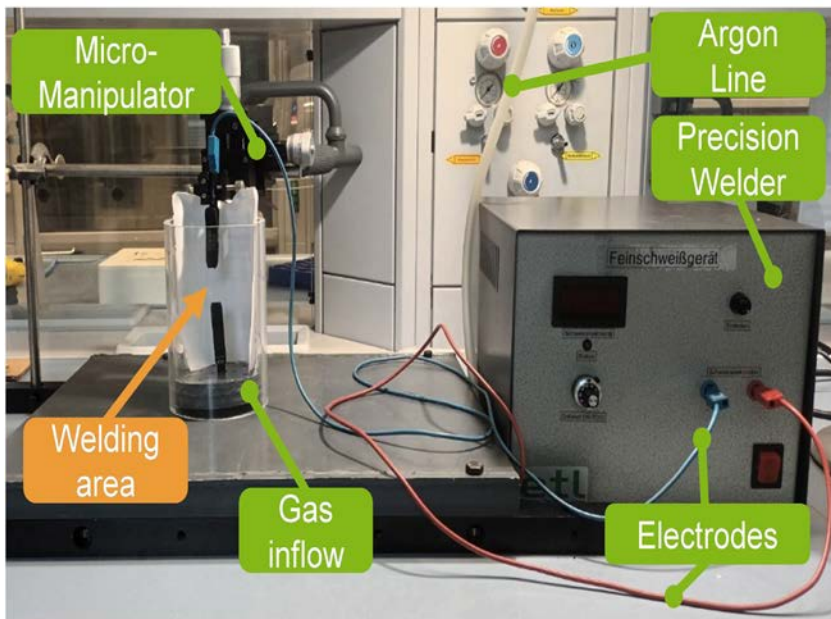


Figure 2. Welding setup for manufacturing of fine-wire thermocouples.

As the individual wires of Chromel and Alumel, the alloys of which the type K thermocouples are made, can still be obtained with a wire diameter of $25.4\ \mu\text{m}$, a welding setup (Figure 2) has been created for the production of fine-wire thermocouples with smaller diameters. The wires are each clamped in a crocodile clip, one of which is firmly positioned at the bottom of a transparent cylinder and one of which is mounted on a micromanipulator, which allows positioning with an accuracy of $10\ \mu\text{m}$. The cylinder is flooded with argon so that the welding process can be carried out under inert gas, which greatly improves the quality and stability of the welding spot. The precision welding machine charges an exchangeable capacitor with a defined voltage, adjustable between 10 and 20 volts. It also detects the electrical contact between the two wires and automatically discharges after a few seconds of delay.

Figure 3 shows a microscope image of an exemplary welding spot of a manufactured thermocouple. The diameter of the welding spot of this particular thermocouple is about $44\ \mu\text{m}$, whereas it is normally in the range of 35 to $50\ \mu\text{m}$. In previous works, the welding spot of commercially acquired thermocouples was in the same range for wire diameters of $12.7\ \mu\text{m}$. This means that it is now possible to produce thermocouples with the same thermal inertia as in previous works, which was proven in response tests. As an additional advantage, the thicker wires increase the mechanical stability of the thermocouple.

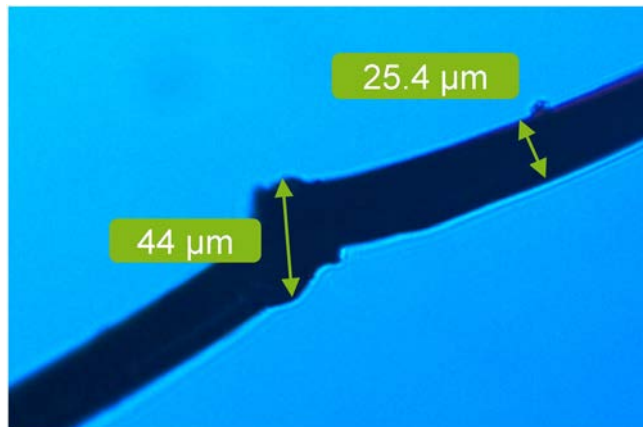


Figure 3. Microscope image of a manufactured welding spot.

Modification of the experimental machine

The experimental machine shown in Figure 4 has been designed for combined heat and power generation and can operate as a Stirling engine, a Vuilleumier heat pump, and in a hybrid mode combining the aforementioned processes. It has been investigated and well documented in numerous works [7,13]. The regenerator to be investigated is located between the heater and a shell-and-tube heat exchanger and is the regenerator between the hot and cold temperature level of the machine when operating as a Stirling engine. The temperature probes are placed at the cold end of the regenerator in the gap between the regenerator matrix and the heat exchanger, as this simplifies the construction and sealing of the temperature probes.

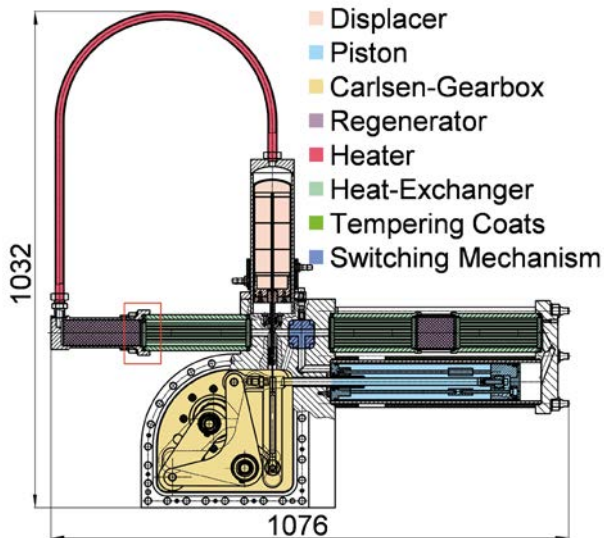


Figure 4. Technical drawing of the experimental machine.

Since the gap between the regenerator matrix and the shell-and-tube heat exchanger is only 4 mm wide, the space for modifications is limited. As illustrated in Figure 5, a threaded bore was drilled into the regenerator housing, in which a mounting fixture for the temperature probe was inserted and permanently sealed with epoxy glue. The temperature probe can be screwed into the fixture and is sealed with an o-ring, so that a repeated insertion is possible. The probe consists of a screw with two lengthwise

bores, in which the 0.5 mm support wires made from the respective thermocouple alloys are imbedded, and a guiding tongue for the wires to extend and adjust the length of the probe. The support wires are first coated with a thin layer of epoxy glue to ensure electrical insulation and then sealed in the bores and sidewise attached to the tongue using the same glue. Their ends protrude a few millimeters beyond the tip of the tongue, and the fine-wire thermocouple was soldered around them.

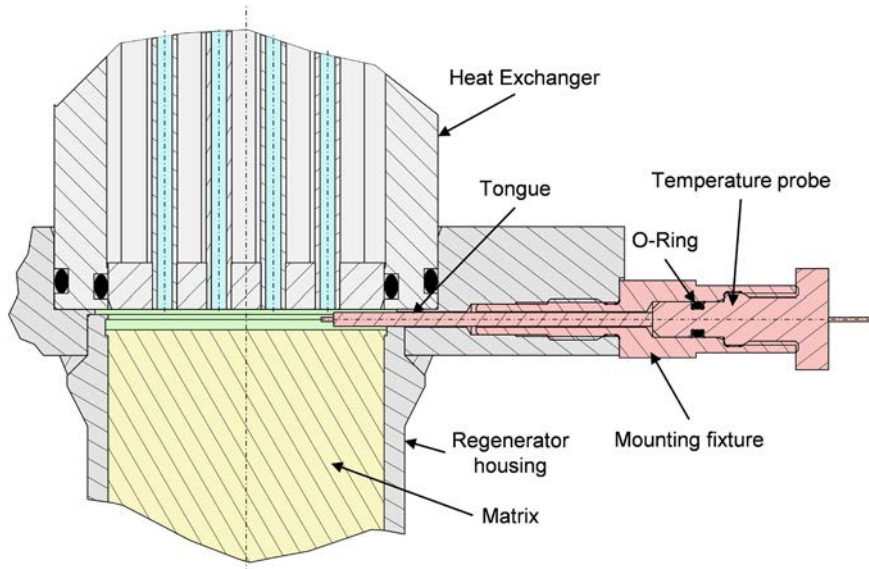


Figure 5. Modification of the regenerator housing with the inserted temperature probe.

As illustrated in Figure 6, the shell-and-tube heat exchanger features a square pitch, which is oriented at a particular circumferential angle, so that the temperature probe can be positioned centrally in front of two different tubes. Thus, the thermocouple wire is directly exposed to the core flow into or out of the tube, and an optimum heat transfer between the gas and the probe is ensured. All measurements shown in this work have been carried out in the configuration shown.

Determination of the Regenerator Loss

Correction of the Gas Temperature and the Energy Balance of the Dead Volume

In order to use the measured gas temperatures for the calculation of the regenerator loss, two adjustments have to be made. Firstly, the thermal inertia and therefore the lag between the gas temperature and the measured temperature, which is the temperature of the solid body, is small, but never zero. This is especially true during flow reversal phases, as a small mass flow leads to poor heat transfer conditions.

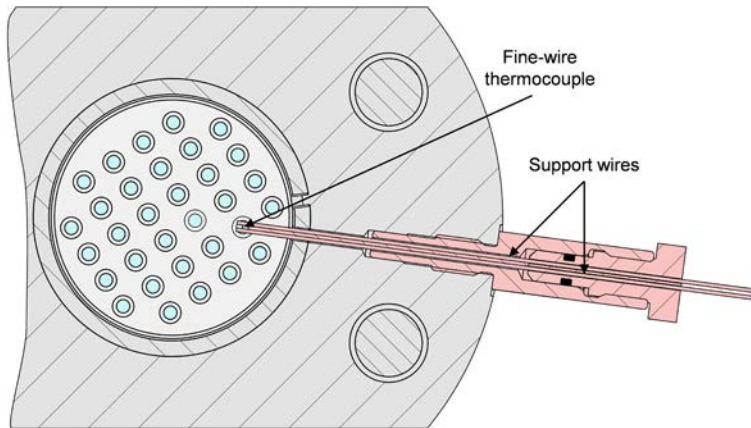


Figure 6. Front view of the heat exchanger and the inserted temperature probe.

Therefore, a method for the correction of the gas temperature is derived. Since the penetration depth of the temperature swings is much larger than the radius of the thermocouple, its temperature can be assumed to be uniform and the temperature change of the thermocouple is only limited by convection. The energy balance for the thermocouple, assumed to be a sphere, is as follows:

$$m_{tc}c_{p,tc} \frac{dT_{tc}}{dt} = \alpha(t)A_{tc}(T_G(t) - T_{tc}(t)) \quad (6)$$

In this equation, m_{tc} denotes the mass, $c_{p,tc}$ the isobaric heat capacity, A_{tc} the surface area and T_{tc} the temperature of the thermocouple, T_G the temperature of the gas and α the heat transfer coefficient. Introducing the angular frequency ω to substitute the time t

by the crank angle φ , Eq. (6) can be easily resolved for the gas temperature, since the temperature of the thermocouple is known and its derivative vs. t or φ , respectively, is readily determinable:

$$T_G(\varphi) = T_{tc}(\varphi) + \frac{m_{tc}c_{p,tc}}{\alpha(\varphi)A_{tc}} \omega \frac{dT_{tc}}{d\varphi} \quad (7)$$

The heat transfer coefficient is calculated using a Nusselt correlation for a stationary flow [14] around a sphere as a first approximation, which can be justified by the small Valensi numbers resulting from the small sphere diameters. The crank angle-dependent Reynolds number

$$Re(\varphi) = \frac{\dot{m}(\varphi)d_{tc}}{A_f(\varphi)\eta} \quad (8)$$

is evaluated using the mass flow obtained from the aforementioned third-order simulation, the thermocouple diameter d_{tc} , the dynamic viscosity η , and the free flow area A_f . The latter is also a function of the crank angle, since it is equal to the cross section of the gap, when the gas flows from the matrix into the heat exchanger, and equal to the cross section of the heat exchanger tubes during a flow in the opposite direction.

The second adjustment concerns the energy balance of the gap, where the temperature probe is located. Figure 7 shows the modelling of the considered section of the experimental machine in the one-dimensional third-order simulation program kpsim. Evidently, the gap is modelled as a simple dead volume between the heat exchanger and the regenerator.

As the temperature probe is located directly in front of a heat exchanger tube, the probe is exposed to the free jet exiting the tube, when the flow is directed from the heat exchanger to the regenerator. So, the exit temperature of the heat exchanger is measured, and mixing effects of the free jets with the gas in the dead volume are not captured. In the opposite flow direction, the gas enters the dead volume as a plug flow over the full cross section, so the measured gas temperature is equal to that of the gas leaving the dead volume.

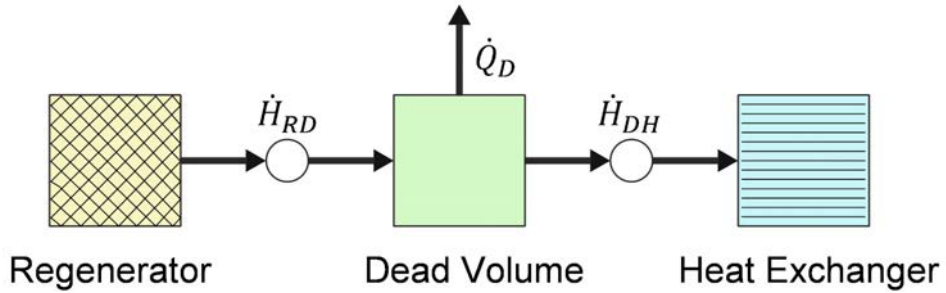


Figure 7. Energy balance in the gap (colors correspond to Figure 5 and Figure 6).

According to this consideration, the temperature of the enthalpy flow \dot{H}_{DH} is measured, but the regenerator loss equals the closed-loop integral of \dot{H}_{RD} . These two enthalpy flows are not identical due to heat transfer in the dead volume, which features a large surface relative to its volume. Since the heat exchanger is intensively cooled with water, the heat flow from the dead volume to the heat exchanger via the front of its tube plate must be considered. Hence, the corrected energy balance for the determination of the regenerator loss is

$$\Delta H_{RL} = \oint \dot{H}_{RD} dt = \oint (\dot{H}_{DH} + \dot{Q}_D) dt = \Delta H_{DH} + Q_D \quad (9).$$

The transferred heat Q_D can be estimated with the numerical model, although the modelling of a dead volume in the third-order simulation program requires specification of constant values for the wall temperature and the heat transfer coefficient. Due to the high thermal inertia of the wall, it appears acceptable to assume its temperature as constant and possibly adapt it to the wall temperature of the heat exchanger tubes. Assuming a constant heat transfer coefficient is more questionable, as it is highly dependent on the flow state. In addition, it cannot be derived from standard Nusselt correlations, as there is no standard flow situation that can be applied to the volume under consideration. Hence, a mean heat transfer coefficient α_m is derived from an additionally created CFD simulation of the considered section including the heat exchanger and part of the regenerator. It is evaluated by dividing the heat transferred per cycle Q_D by the

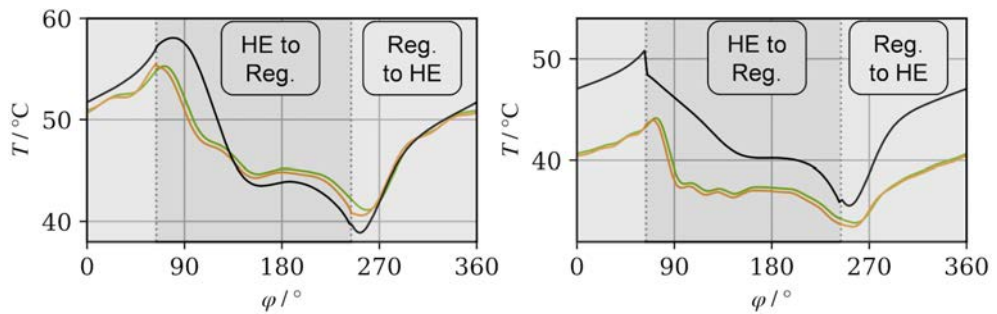
heat transfer area A and the integral of the temperature difference $\Delta T(t)$ between the gas in the dead volume and the tube plate:

$$\alpha_m = \frac{Q_D}{A \oint \Delta T(t) dt} \quad (10)$$

Comparison with the third-order Numerical Model

Figure 8 shows plots of the gas temperature vs. the crank angle at two operating points corresponding to a high (a) and a reduced power level (b). The black curves are predictions by the third-order numerical model, the green curves are the measured courses, and the orange curves are the corrected courses according to Eq. (7), assuming a welding spot diameter of 45 μm . The gas is flowing from the heat exchanger to the regenerator between crank angles of 64° and 244° ("HE to Reg.", dark shaded in Figure 8) and in the opposite direction between 0° and 64° and 244° and 360° ("Reg. to HE", light shaded).

First of all, the difference between the measurement with and without correction is evidently very small, as expected because of the low thermal inertia of the thermocouple. Moreover, there is a good qualitative agreement of the courses between the simulated and measured temperatures, but there is a quantitative deviation, which increases for operating points with low power density. At both operating points, the simulation predicts higher steady-state regenerator temperatures as indicated by the higher gas temperatures in the respective flow phase. The measured outlet temperature from the heat exchanger is higher than the simulated temperature in Figure 8a) but lower in Figure 8b), which can be partly explained by the experimental setup of the machine. The cold cycle temperature $T_c=30^\circ\text{C}$ is set as the mean temperature of the water cycle feeding two heat exchangers and two tempering jackets around the cylinders, so that the inlet and outlet temperature of one heat exchanger can vary slightly depending on the heat rejected by the cycle at different operating points.



a) $p = 36 \text{ bar}$, $n = 383 \text{ min}^{-1}$, $T_h = 500 \text{ }^\circ\text{C}$

b) $p = 20 \text{ bar}$, $n = 200 \text{ min}^{-1}$, $T_h = 400 \text{ }^\circ\text{C}$

Figure 8. Comparison of measured temperatures with (orange) and without correction (green) with simulated temperatures from third order model (black).

The regenerator loss for a constant mean pressure and heater temperature but for four different speeds is shown in Figure 9, with the colors of the bars corresponding to Figure 8. Although the presented correction has only a small effect on the temperature courses, the effect on the closed-loop integral of the enthalpy flow and hence the regenerator loss is more significant, with the difference between the loss with and without the correction increasing with increasing speed. This is because of the linear effect of the angular frequency and the additional non-linear increase of the heat transfer coefficient in Eq. (7). Since the enthalpy flow is calculated as the product of the measured temperature and the simulated mass flow and the enthalpy loss per cycle is only a small fraction of the enthalpy amplitude, the phase shift between these quantities is critical. As the correction also affects the phase of the gas temperature, its significant influence on the enthalpy loss can be explained.

Furthermore, the measured enthalpy loss increases with speed, whereas the simulated loss decreases. This trend reveals a significant difference between the measured and simulated regenerator losses. The simulation code only allows modelling of thermal conduction effects within a cycle component such as the regenerator, but no thermal bridges between adjacent components, i.e. the regenerator, the dead volume, and the heat exchanger in this case. At the ends of the regenerator, the heat flow due to thermal conduction is hence transferred to the gas. Thermal conduction causes a speed-

independent heat flow \dot{Q}_{hc} , and therefore the heat amount per cycle increases as the speed decreases:

$$Q_{hc} = \frac{2\pi}{\omega} \dot{Q}_{hc} \quad (11)$$

In the experimental machine, there is a large thermal bridge between the housing of the regenerator and the heat exchanger via their flanges, so most of the thermal losses caused by thermal conduction in the regenerator housing are directly transferred to the heat exchanger and thus do not affect the gas temperature and the enthalpy flow at the cold end.

To test this hypothesis, the heat conduction in the regenerator housing is set to zero in the numerical model, which is obviously an unrealistic borderline case. The results of this simulation are shown in Figure 10. As assumed, the thermal conduction in the regenerator housing has a large effect on the simulated regenerator loss, and the large deviations between the measured and the simulated enthalpy loss can partly explain the deviations of the simulated gas temperatures especially at low speeds. Nevertheless, the measured regenerator loss increases while the simulated regenerator loss decreases slightly at higher speeds. There may be several reasons for this, which require further investigations. To give a few examples, these may be uncertainties in the heat transfer coefficient used to simulate the heat flow transferred in the dead volume, which is only implemented as a temporal mean value and not a function of the operating conditions, the heat transfer coefficient at the thermocouple, the phasing of the mass flow and the temperature, and the diameter of the matrix fibers used for the simulation.

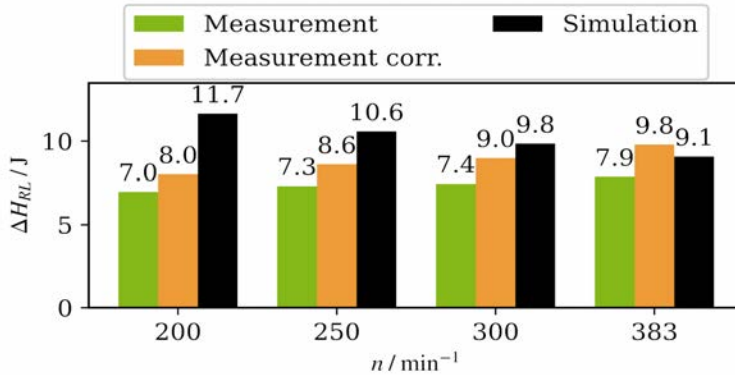


Figure 9. Measured and simulated regenerator loss for $p = 31,2$ bar and $T_h = 400$ °C.

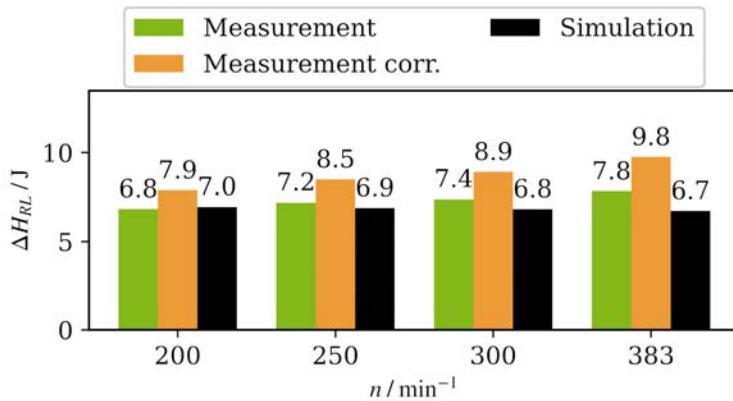


Figure 10. Measured and simulated (without heat conduction in the regenerator housing) regenerator loss for $p = 31,2$ bar and $T_h = 400$ °C.

Conclusion and Outlook

The cyclic gas temperatures between a heat exchanger and a regenerator in an experimental machine were successfully measured, and a determination method for the regenerator loss was presented. These measurements were made after modification of the regenerator housing to insert a temperature probe with self-fabricated fine-wire thermocouples, for which the welding setup was presented. For the evaluation

of the measured regenerator loss, a procedure for the further processing of these temperatures based on heat transfer equations and energy balances was introduced, and a comparison with a third-order numerical model was carried out.

One major deviation has been resolved, but there are still smaller deviations that require further investigation. On the one hand, this may be done by improving the third-order numerical model kpsim or by further extending the CFD simulation mentioned above, and on the other hand, more experimental results may be generated and analyzed by utilizing the ability of the experimental machine to provide a wide range of operating conditions and to operate as a Vuilleumier heat pump.

Acknowledgements

This research was funded by the German Research Foundation (DFG), grant # KU 755/7-1.

References

- [1] G. Walker, Stirling-cycle machines, Clarendon Press, Oxford 1973
- [2] R.C. Tew Jr., M.B. Ibrahim, D. Danila, T.W. Simon, S. Mantell, L. Sun, D. Gedeon, K. Kelly, J. McLean, J.G. Wood, S. Qiu, A Microfabricated Involute-Foil Regenerator for Stirling Engines, in: AIAA, Proceedings 5th IECEC, St. Louis, MO, USA, 25 (2007).
- [3] I. Rühlich, H. Quack, New Regenerator Design for Cryocoolers, in: Proc. International Cryogenic Engineering Conference No. 17, Bournemouth, GB, 291–294 (1998).
- [4] D. Bao, J. Tan, L. Zhang, Z. Gao, Y. Zhao, H. Dang, A two-dimensional model of regenerator with mixed matrices and experimental verifications for improving the single-stage Stirling-type pulse tube cryocooler, Applied Thermal Engineering 123 (2017), <https://doi.org/10.1016/j.applthermaleng.2017.05.152>
- [5] V.V. Kishor Kumar, B.T. Kuzhiveli, Performance Enhancement of a Miniature Stirling Cryocooler with a Multi Mesh Regenerator Design, Journal of Engineering Science and Technology 12 (2017). [6] D. Gedeon, J.G. Wood, Oscillating-Flow Regenerator Test Rig: Hardware and Theory with Derived Correlations for Screens and Felts, NASA CR 198442 (1996).
- [7] I. Geue, J. Pfeiffer, H.-D. Kühl, Laboratory-Scale Stirling-Vuilleumier Hybrid System Part II: Experimental Results, J Propul Power 29 (2013), <https://doi.org/10.2514/1.B34726>
- [8] J. Sauer, H.-D. Kühl, Analysis of unsteady gas temperature measurements

in the appendix gap of a stirling engine, *J Propul Power* 34 (2018), <https://doi.org/10.2514/6.2017-4795>

- [9] J. Sauer, H.-D. Kühl, Numerical model for Stirling cycle machines including a differential simulation of the appendix gap, *Applied Thermal Engineering* 111 (2017), <https://doi.org/10.1016/j.applthermaleng.2016.09.176>
- [10] W.R. Martini, *Stirling Engine Design Manual*, DOE\NASA\3152-78\1, NASA CR 135382, US Department of Energy (1978).
- [11] J. Sauer, H.-D. Kühl, Preliminary Results of Unsteady Gas Temperature Measurements in the Appendix Gap Section of an Experimental Stirling Engine, in: *International Stirling Association, Proceedings 17th ISEC, Newcastle upon Tyne*, 589–597 (2016).
- [12] H.-D. Kühl, T. Pfeffer, S. Schulz, C. Walther, High speed gas temperature measurements in a Vuilleumier heat pump and their reproduction by differential computer simulation, in: *International Stirling Association, Proceedings 8th ISEC, Ancona*, 257–266 (1997).
- [13] H.-D. Kühl, J. Pfeiffer, J. Sauer, Operating Characteristics of a Laboratory-Scale, Convertible Stirling-Vuilleumier-Hybrid CHP System Including a Reversed-Rotation Stirling Mode, in: *International Stirling Association, Proceedings 16th ISEC, Bilbao, Spain*, 294–304 (2014).
- [14] VDI-Gesellschaft Verfahrenstechnik und Chemieingenieurwesen, *VDI Heat Atlas*, VDI-Gesellschaft Verfahrenstechnik und Chemieingenieurwesen, Springer, Berlin, New York 2010.

Thermal receivers, combustors and heat exchangers

Cyclone Nozzle Structure Optimization for Combustor Performance Enhancement in a Stirling Engine fueled by Reformed Gas and Diesel Fuel

J. Lan^{a,b,*}, X. Liang^a, T. Lyu^b, G.T. Lin^b, X. Yang^b, G.X. Gu^b, D. Han^a

a Key Laboratory for Power Machinery and Engineering, Ministry of Education, Shanghai Jiao Tong University, Shanghai 200240, China

b Shanghai Marine Diesel Engine Research Institute, Shanghai, 201108, China

* Corresponding author: lanjian@sjtu.edu.cn

Keywords: Stirling engine, Fuel reforming, Synthetic gas, Oxy-combustion, External combustion efficiency

Abstract

Thermochemical recovery is an advanced waste heat utilization technology that effectively recovers waste heat from oxy-fuel Stirling engines. A Stirling engine combustor with thermochemical recovery heat system can utilize both diesel reforming gas and diesel fuel as combustion sources. In this study, a heat transfer model of the Stirling engine was established, and the high-pressure oxy-fuel combustion of multicomponent fuels was investigated by numerical simulation. The results showed that as the exit diameter of the conical nozzle was reduced from $\varphi 30$ mm to $\varphi 19$ mm, the flame deflection was eliminated and a stable flame was formed. In addition, the direct-blowing cyclone nozzle has the most uniform temperature distribution inside the combustion chamber, and the formation of the return zone avoids the flame from directly rushing to the bottom of the combustion chamber. The optimization of the cyclone nozzle structure improves the total heat transfer capacity, and the heat transfer capacity of the straight cyclone nozzle is 13.9 kW higher than that of the conical nozzle. The heat distribution shows that the heat transfer in the front row is less than that in the rear row, with 37.5%, 38.0%, 28.3%, and 40.9% of the heat absorbed in the front row of heater tubes, respectively. Further, the front row's heat transfer coefficient surpasses that of the back row. The average heat transfer coefficients for the front and rear rows of heating tubes in the tapering nozzle are 738 W/(m²·K) and 703 W/(m²·K) respectively, while those in the straight blowing nozzle are 1093 W/(m²·K) and 1089 W/(m²·K). This disparity is attributed to the well-matched temperature field, flow field, and heater formation in the straight blowing nozzle, resulting in more uniform heating and superior heat transfer performance. The direct blowing type cyclone nozzle exhibits front heating tube heat flow density distribution in the range of 170 kW/m² to 806 kW/m², and back heating tube distribution in the range of 274 kW/m² to 1600 kW/m², surpassing the heat flow density of air combustion type heating tubes. Further analysis recommends optimizing the utilization of heating tubes, particularly improving the performance of the front row, where heat exchange is primarily determined by radiation. Controlling the flame position in the center effectively enhances front-row heating tube heat exchange through radiation. The experimental results show that the temperature uniformity of the heating tube is improved and the efficiency of the external combustion system is increased.

Introduction

Thermochemical recovery is an advanced waste heat utilization technology that effectively captures waste heat from oxy-fuel Stirling engines. Combustion chambers equipped with thermochemical recovery systems in Stirling engines need to be able to efficiently utilize a blend of reformed gas and diesel fuel [1,2]. Research on combustion involving multiple fuel compositions is currently focused on gas turbines, combustors and internal combustion engines [3,4]. Lyu et al. [5] studied a Stirling engine's MILD combustion chamber using diesel fuel and pure oxygen at high backpressure. Simulations showed adding more oxygen-enriched gases improved MILD combustion and made the chamber's temperature more even. This led to an increase in engine efficiency from 31.2% to 32.3%. Lan et al. [6] studied the combustion of diesel fuel and pure oxygen in a Stirling engine, observing the difference between the usual yellow flame and the blue flame of MILD combustion. The effect of the amount of fuel injected, initial temperature and pressure on MILD combustion was investigated. It was found that more fuel and higher temperatures helped to achieve MILD combustion, but higher pressures required higher temperatures or fuels.

Nakagaki et al. [7] investigated the performance of a burner fueled by natural gas and hydrogen-rich gas. Stable and efficient combustion was observed and it was noted that the combustion of hydrogen produced a lighter colored flame compared to natural gas. Additionally, the natural gas was successfully transitioned to hydrogen-rich gas during the system's startup phase without extinguishing the flame, demonstrating seamless fuel switching. In a separate study, Seibert et al. [8] investigated the behavior of a dual-fuel combustor powered by JP-8 and hydrogen. The findings showed that introducing 26% hydrogen by energy reduced the flame float distance by half, indicating significant improvements in combustion efficiency. Pashchenko et al. [9,10] conducted simulations on syngas combustion in a swirl flame. It was found that NO_x emissions for syngas with hydrogen molar fractions ranging from 0.4 to 0.8 were significantly lower, between 88.9 ppm and 93.1 ppm, compared to conventional fuels. This indicates a potential for reducing environmental impact.

The combustion process of liquid fuel reforming is inherently more complex than that of gaseous fuel reforming [11,12]. Zheng et al. [13] conducted simulations to evaluate the impact of various dual-fuel nozzle configurations on the combustion characteristics

of a chemically recovered gas turbine. The findings indicate that combustors equipped with an external swirl nozzle exhibit superior temperature distribution. Liu et al. [14] analyzed the combustion performance of diesel and reformed gas. It was indicated that the temperature in the main combustion zone decreased from 2280 K to 1910 K, aiding in emission reduction. The use of reformed gas resulted in a stable flame and lower wall temperatures, reducing the thermal load on the flame tube. Kumar et al. [15] optimized the parameters of a DI diesel engine fueled by a 40% v/v mixture of isobutanol/diesel through experimentation. The verification of the predicted combinations through testing revealed a prediction error within 4%. Ilbas et al. [16] conducted experimental investigations and numerical simulations on a novel oxyfuel burner, demonstrating its effectiveness. The design of the combustor is crucial for ensuring the efficiency and reliability of Stirling engines. Therefore, extensive research has been conducted to optimize their performance. Koseki et al. [17] investigated the impact of various factors, such as combustion location, cyclone intensity, and throat size affect NO_x emissions in a Stirling engine running on natural gas, without using flue gas recirculation. Optimal settings for reducing NO_x and CO emissions were found and it was shown that by changing the cyclone blade angle from 60° to 80°, more cyclones could reduce NO_x emissions by 20% without increasing CO emissions. Gao et al. [18] developed a novel gas combustor for Stirling engines, incorporating plate heat exchanger and low-swirl combustion technologies to facilitate exhaust gas heat recovery. The numerical analyses indicated that the combustor's maximum temperature reached approximately 2200 K, with a waste heat recovery efficiency exceeding 65.8%.

The efficiency of the Stirling engine's external combustion system is significantly impacted by the compatibility between the burner and heater. Solomon et al. [19] developed a new burner-heater deflector plate that improves how gases move across the heater tube, shown by numerical analysis. This is important for managing high temperatures in the combustion chamber and improving heat transfer. The deflector plate guides the gas flow around the heat exchanger tube better, enhancing heat transfer. Using diffuser plates with different sizes of openings also increases the efficiency of gas flow and heat transfer. Jin et al. [20] created a combustion chamber design that preheats air with exhaust gas. The study modelled and tested the combustion of diesel with air, examining various parts of the system such as burner position and piping configuration. The results

demonstrated that this method can achieve a combustion efficiency of up to 86%.

This study aims to enhance the performance of a Stirling engine combustor by optimizing the structure of the cyclone nozzle. The effects of different nozzles on the combustion performance of the Stirling engine are explored through multicomponent combustion modelling, and the impact of cyclone angle on the engine's combustion performance is experimentally investigated.

Methodology

Numerical methods

Numerical simulations were conducted using Ansys Fluent [21] employing the finite volume method [22]. The governing mass conservation equation is presented as Eq. (1):

$$\frac{\partial \rho}{\partial t} + (\rho v_i) / \partial x_i = Q \quad (1)$$

where ρ is the density of matter; v_i is the velocity in the direction of scale i ; Q is the mass source term; t is time;

The governing equations of conservation of momentum is given as Eq.(2):

$$\frac{\partial}{\partial t} (\rho v_i) + \frac{\partial}{\partial x_j} (\rho v_j v_i) = -\frac{\partial p}{\partial x_i} + \frac{\partial \tau_{ij}}{\partial x_j} + \rho g_i + \sum_k \frac{\rho_k}{\tau_{rk}} (v_{ki} - v_i) + v_i G + F_i \quad (2)$$

where p is the static pressure; ρ is the density of the mixture; G is the mass source term; and ρg_i denotes the buoyancy-affected gravitational term. $\sum_k \frac{\rho_k}{\tau_{rk}} (v_{ki} - v_i) + v_i G + F_i$ denotes the interacting force source term, where v_{ki} represents the i^{th} velocity component of the k component, τ_{rk} is the viscosity of the k^{th} component. τ_{ij} denotes the stress tensor.

The governing equation for energy conservation is equation (3):

$$\frac{\partial(\rho T)}{\partial t} + \text{div}(\rho v T) = \text{div} \left(\frac{k}{c_p} \text{grad } T \right) + \frac{S_T}{c_p} \quad (3)$$

Where $\frac{\partial(\rho T)}{\partial t}$ is the time rate of change of internal temperature of a fluid. $\text{div}(\rho v T)$ represents the divergence of the temperature flux due to fluid motion, where v is the velocity of the fluid, ρ is the fluid density. $\text{div} \left(\frac{k}{c_p} \text{grad } T \right)$ describes the divergence of the conducted heat flux due to a temperature gradient, where k is the coefficient of heat conduction and c_p is the specific heat capacity at constant pressure. In a multi-component system, the specific heat cannot simply be assumed to be constant. The

specific heat c_p may be a function of temperature T and other variables such as pressure P or mole fraction x_i of the component. Therefore, a more general expression is: $c_p = c(T, P, x_1, x_2 \dots x_n)$. $S_T = S_h + \varphi$, $S_h = \rho q$ is the heat contribution per unit volume from the heat source or due to radiation or other physical and chemical causes. φ is the portion of mechanical energy converted to thermal energy due to viscous action, called the dissipation function.

In engineering applications, turbulence numerical simulation predominantly falls into three categories: Direct Numerical Simulation (DNS), Large Eddy Simulation (LES), and models based on the Reynolds-Averaged Navier-Stokes (RANS) equations. Due to the computational limitations associated with LES and DNS, this study employs a model based on the RANS equations [23]. Specifically, the turbulence submodel utilized is the widely adopted Realizable k- ϵ model, a variant of the standard k- ϵ model. Mathematical constraints enhance the model's performance, enabling more precise predictions of cyclonic flow. The governing equation is as follows:

$$\frac{\partial}{\partial t}(\rho k) + \frac{\partial}{\partial x_i}(\rho k u_i) = \frac{\partial}{\partial x_j}[(\mu + \frac{\mu_t}{\sigma_k}) \frac{\partial k}{\partial x_j}] + G_k + G_b - \rho \epsilon - Y_M + S_k \quad (4)$$

$$\frac{\partial}{\partial t}(\rho \epsilon) + \frac{\partial}{\partial x_i}(\rho \epsilon u_i) = \frac{\partial}{\partial x_j}[(\mu + \frac{\mu_t}{\sigma_\epsilon}) \frac{\partial \epsilon}{\partial x_j}] + C_{1\epsilon} \frac{\epsilon}{k} (G_k + C_{3\epsilon} G_b) - C_{2\epsilon} \rho \frac{\epsilon^2}{k} + S_\epsilon \quad (5)$$

$C_{3\epsilon}$ denotes the effect of buoyancy on the rate of dissipation of the turbulent energy, which is expressed as:

$$C_{3\epsilon} = \tanh\left(\frac{u_e}{u_n}\right) \quad (6)$$

where G_k denotes the turbulent kinetic energy induced by the mean velocity gradient, G_b denotes the turbulent kinetic energy induced by the buoyancy effect, and Y_M is the effect of fluctuating expansion on the turbulent dissipation rate in compressible turbulence. S_k and S_ϵ denote the source term [24]. The equation includes the following constants: $C_{1\epsilon} = 1.44$, $C_{2\epsilon} = 1.92$, $\sigma_k = 1.0$, $\sigma_\epsilon = 1.3$ [25].

Given the elevated temperature within the engine combustion chamber, radiation effects are accounted for and modeled utilizing the surface-to-surface radiation model, which incorporates view factors for relevant surfaces. View factors are accounted for to encompass all radiation heat transfer occurring within the combustion chamber. Material

properties governing radiation heat transfer include specific heat, thermal conductivity, viscosity, and molecular weight of the reaction component. The radiation energy flux ($q_{out,y}$) for the combustion chamber, internal surfaces (x) are modeled as a function of emissivity (ϵ_x), Boltzmann's constant (σ), surface temperature (T_x) and reflectivity (ρ_x) as follows:

$$q_{out,x} = \epsilon_x \sigma (T_x^4 - T_w^4) + \rho_x q_{in,x} \quad (7)$$

The incident energy flux ($q_{in,x}$) on the internal surfaces of the combustion chamber is the function of view factors (F_{xy}) for surface (x)-to surface (y) and energy flux ($q_{out,y}$) leaving the surface (y) as follows:

$$q_{in,x} = \sum_{y=1}^N F_{xy} q_{out,y} \quad (8)$$

The following convection-diffusion governing equation for all the species is solved for evaluating the mass fraction of each species (Y_i) in the computational domain.

$$\frac{\partial}{\partial t} (\rho Y_i) + \nabla \cdot (\rho \vec{v} Y_i) = -\nabla \cdot \vec{J}_i + R_i + S_i \quad (9)$$

Here, R_i represents the rate of chemical species i development from the chemical reaction, and S_i defines the rate of source species addition from the dispersed phase or any user-defined sources. The diffusion flux (\vec{J}_i) for the non-premixed turbulent flow combustion process is defined as follows:

$$\vec{J}_i = - \left(\rho D_{i,m} + \frac{\mu_t}{S_{ct,i}} \right) \nabla Y_i - D_{T,i} \frac{\nabla T}{T} \quad (10)$$

where $D_{i,m}$ and $D_{T,i}$ are the mass diffusion and thermal diffusion coefficients for species i . S_{ct} is the turbulent Schmidt number.

The synthetic gas and diesel stabilization combustion process involves several stages. Initially, the Stirling engine is started with diesel fuel, the combustor is diesel fuel combustion and the reaction (11) occurs in the combustor. Subsequently, the water in the evaporator absorbs the waste heat of the exhaust gas and becomes water vapor. The water vapor is then injected back into the combustor, as described by reaction equation (12). Finally, reformed gas is injected, and the reactions in the combustor involve equations (11)-(14). Table 1 summaries the kinetic parameters of the global reactions.

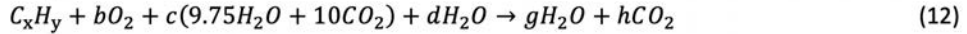
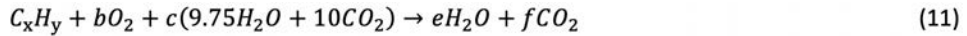


Table 1. The kinetic parameters of the global reactions.

Index: reactions	A [kmol/m ³ s]	E(J/kmol)	Ref.
$C_xH_y + bO_2 + c(9.75H_2O + 10CO_2) \rightarrow eH_2O + fCO_2$	5.1×10^8	2.26×10^8	[26,27]
$CO + 0.5O_2 \rightarrow CO_2$	2.239×10^{12}	1.7×10^8	[28]
$H_2 + 0.5O_2 \rightarrow H_2O$	3.9×10^{17}	1.7×10^8	[29]

Figure 1 depicts the structural design of the combustion chamber in a Stirling engine. The primary role of the multi-component burner is to facilitate stable combustion and efficient heat transfer across various components without necessitating modifications to the Stirling engine's combustion chamber architecture. To achieve this, the fuel and reforming gas nozzles are designed as coaxial units.

During the start-up phase, the system uses diesel and pure oxygen combustion. In the reforming stage, it transitions to gaseous multi-component fuel and diesel with pure oxygen combustion. The transition to a reformed combustion system necessitates the Stirling engine's capability to efficiently combust reformed gas, which exhibits a notable variance in calorific value and composition from the liquid fuel used in the original combustion chamber. To maintain equivalent total fuel heat entering the combustion chamber, a significant increase in the mass flow rate of reformed gas is required. However, this increase can have a negative impact on the flow field organization and combustion efficiency of the combustion chamber. Therefore, optimizing the flow field organization of the reformed gas combustion through strategic planning of the gas injection scheme is crucial, especially considering the requirement for nozzle in situ replacement. In addition, in order to simplify the calculation, the temperature of the inner wall of the heating tube is set to a constant temperature [30].

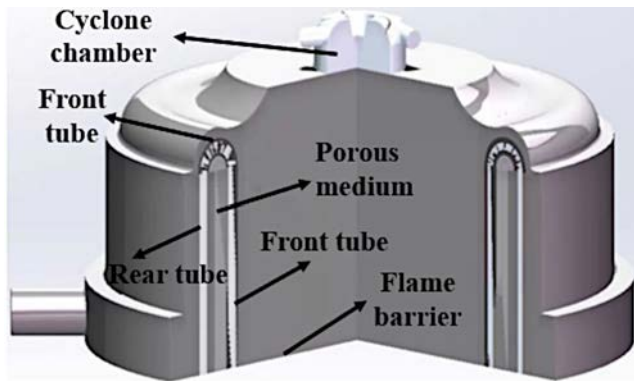


Figure 1. Multi-component fuel burner construction.

The previous section explains that although the porous nozzle design is simple, it results in flames hitting the bottom of the combustion chamber, which prevents an optimal synergy between the combustion chamber and the heater. In contrast, the swirl nozzle emerges as a superior solution for flow field enhancement and flame length reduction, necessitating precise coordination with the fuel nozzle and ejector for peak performance. The efficacy of the combustion chamber depends on the design of the nozzle outlet and its surface area. Figure 2 delineates the configurations of swirl nozzles with varying designs: Swirl nozzle 1 features a reduction type with a diameter of $\varphi 28$ mm and a swirl blade angle of 30° . Swirl nozzle 2, with a scaling structure, maintains the same diameter and blade angle. Swirl nozzle 3, another reduction type, has a reduced diameter of $\varphi 19$ mm and a consistent blade angle. Lastly, swirl nozzle 4, adopting a direct blowing approach, also has a diameter of $\varphi 19$ mm and a swirl blade angle of 30° .

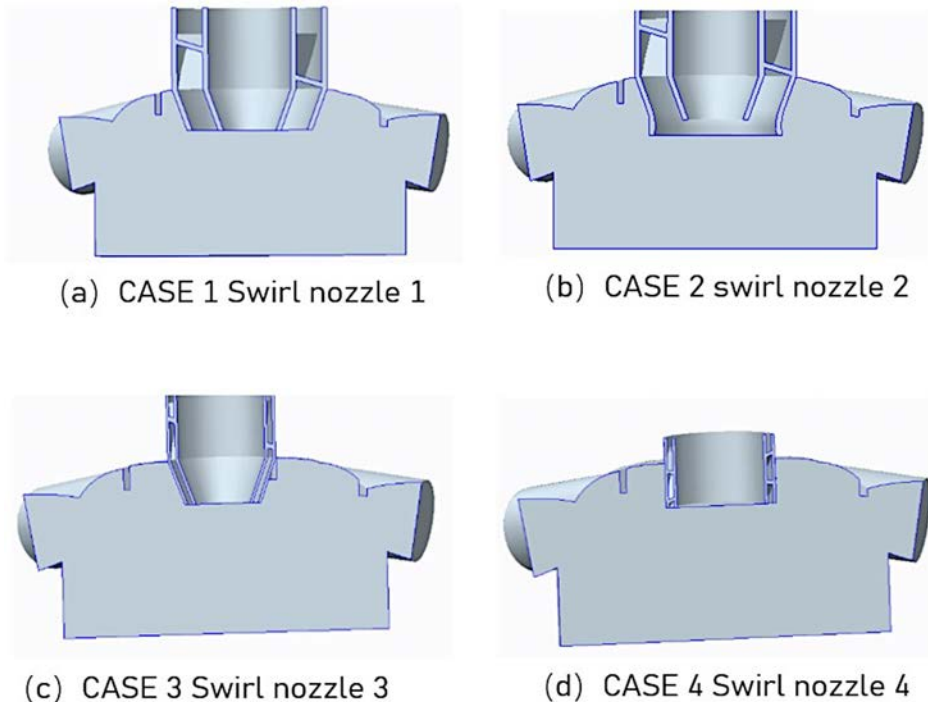


Figure 2. Cyclone multi-component fuel burners.

Experimental setup

Figure 3 illustrates a schematic diagram of an oxy-fuel combustion Stirling engine test facility, incorporating a multi-component fuel supply system, a reformed gas heating system, a Stirling engine, and a test system. The external combustion efficiency of the Stirling engine is determined using the inverse equilibrium method. The circulating gas and oxygen enter the combustion chamber in two ways to accurately control the ejection ratio (The ejection ratio is the ratio of the recirculated exhaust gas to the intake air). Four thermocouples are evenly positioned at the exhaust outlet of the combustion chamber to measure the exhaust temperature. To assess the temperature distribution uniformity of the heater tube, eight thermocouples were mounted around the circumference of the tube wall. Furthermore, the exhaust composition was analyzed using an AVL emissions analyzer.

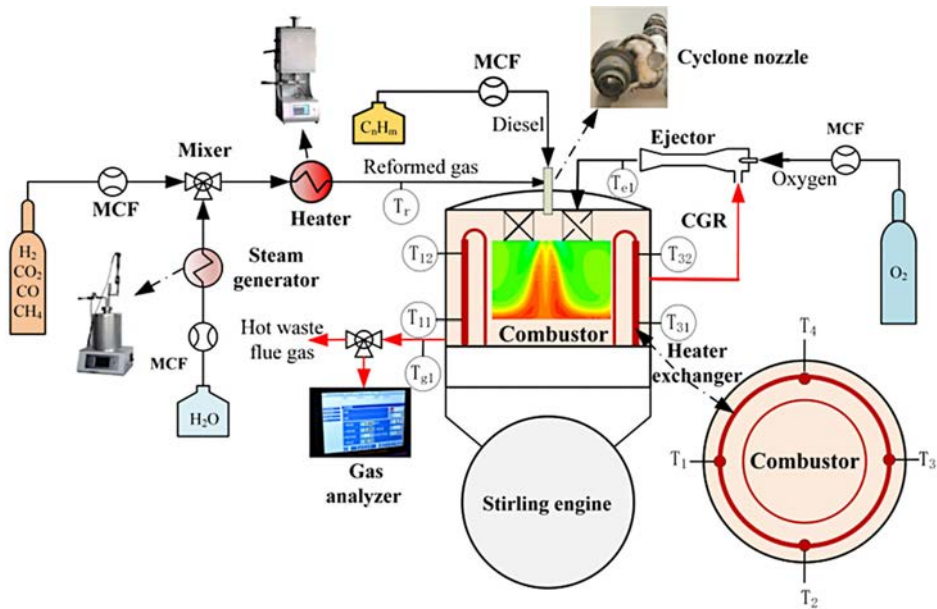


Figure 3. Schematic view of reformed gas and diesel in a Stirling engines combustor test facility.

Figure 3 illustrates the division of the total diesel fuel supply into two streams. One flow is directed towards the reformer, while the other is directed towards the combustor. The fuel distribution ratio can be expressed by the following equation:

$$FDR(\%) = \frac{G_r}{G_f} \times 100 = \frac{G_r}{G_r + G_d} \times 100$$

where G_r is the fuel mass flow rate delivered to the reformer, G_d is the fuel mass flow rate delivered to the combustor, and G_f is the total fuel mass flow rate.

Q_H is heat flow from the combustor to the heater, shown in the following equation:

$$Q_H = h_f(T_f - T_w) + Q_{rad}$$

where Q_{rad} is heat radiation, h_f is convection heat transfer coefficient, T_w is the heating tube temperature, and T_f is the initial combustion gas temperature.

The fuel combustion efficiency in the combustor is indirect combustor efficiency:

$$\eta_H(\%) = \frac{Q_H}{Q} \times 100 = \left(1 - \frac{T_g G_g c_p}{G_f \cdot LHV_{fuel}} \right) \times 100$$

where Q is fuel combustion heat, T_g is the combustion gas temperature after heat exchange with the heater, G_g is the mass flow rate of combustion gas, c_p is the heat capacity of combustion gas, G_f is the fuel mass flow rate, and LHV_{fuel} is the fuel lower heat value.

In order to describe the homogeneity of temperature distribution, the fluctuation temperature of the heating tube wall is defined as follows:

$$\delta T_w = \sqrt{\frac{1}{N} \sum (T_{ij} - \bar{T}_w)^2}$$

where T_{ij} is the temperature of heating tube at each of the N measurement points, \bar{T}_w the average temperature of N heating tubes.

Results and discussion

Distribution of temperature

Figure 4 compares the temperature fields of nozzles with different cyclone configurations for reformed gas under operating conditions of a combustion pressure of 2.2 MPa, an excess oxygen coefficient of 1.06, and an ejection ratio of 7. Cyclone nozzles 1 and 2, which were designed to have reformed gas exit velocities comparable to the pilot exit velocity, exhibit skewed and unstable temperature fields as shown in Figs. 4(a) and (b). The instability of combustion is attributed to the asymmetrical exhaust outlet of the combustion chamber, which reduces the axial velocity of the reformed gas, making it more susceptible to the asymmetrical structure. The mismatch among the velocities of oil, reformed gas, and oxidizer leads to the skewing of the temperature field. The transition from a tapering nozzle to a scaling nozzle not only fails to mitigate this issue but exacerbates the instability of combustion. To address this challenge, it is important to match the oxidizer and fuel velocities. The skewing of the flame can be eliminated by reducing the exit diameter of tapering nozzle 1 from $\varphi=30$ mm to $\varphi=19$ mm, as shown in Figs. 4(c). This results in a stable temperature field concentrated near the central axis, with flames impinging on the bottom of the combustion chamber. Altering the scaling nozzle 3 to a direct blowing nozzle 4 expands the high-temperature distribution area in the combustion chamber and eliminates direct flame impingement on the chamber's bottom.

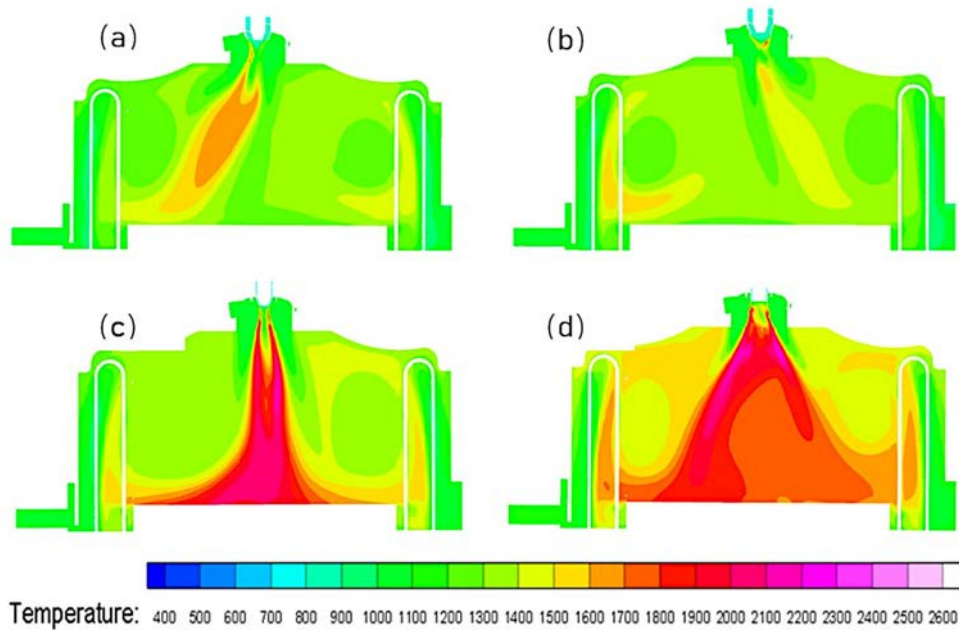


Figure 4. Effect of different structures on the combustion field (T).

Figure 5 illustrates the impact of various cyclone nozzle designs on the axial combustion temperature distribution. The results indicate that cyclone nozzles 1 and 2 exhibit lower axial temperatures due to flame skewing. In contrast, nozzles 3 and 4, which enable stable symmetric combustion, show distinct temperature profiles. Specifically, the axial temperature of nozzle 3 increases progressively, reaching a peak of 2052 K at the bottom of the combustion chamber. The temperature profile of Nozzle 4 initially increases and then decreases, with the highest temperature of 1935 K occurring at $Y=0.21$ m. Notably, the bottom temperature of the combustion chamber for nozzle 4, at 1342K, is significantly lower than that of nozzle 3, which is 2012 K. This discrepancy is attributed to the direct cyclone reforming gas nozzle's ability to enhance the mixing of reforming gas, oxidizer, and diesel fuel, facilitating better fuel diffusion and concentrating combustion in the chamber's center. This design effectively prevents the scouring of the combustion chamber's bottom.

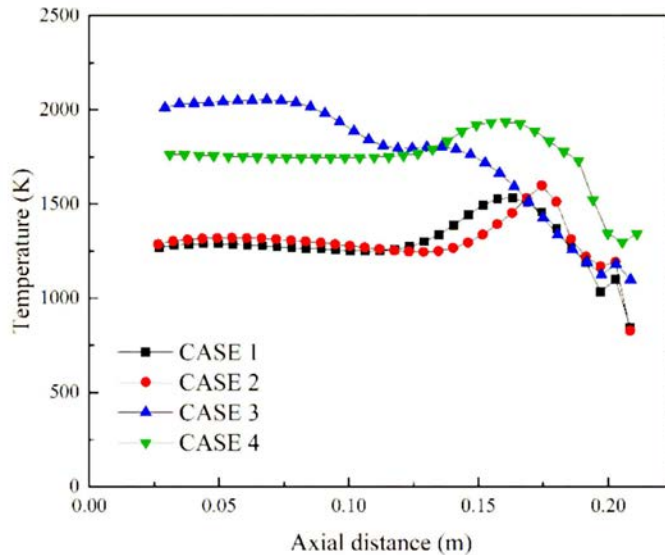


Figure 5. Effect of ejection ratio on axial section of combustion temperature .

Figure 6 reveals that at various heights, under conditions of stable combustion, the temperature distributions are essentially symmetrical in the radial direction. Specifically, Figure 6(a) indicates that due to incomplete combustion by cyclone nozzles 1 and 2, lower temperatures prevail at the bottom. In contrast, cyclone nozzle 3 exhibits a distinct peak temperature of around 2000 K, which tapers to approximately 1500 K towards the edges. The temperature profile for cyclone nozzle 4 varies between 1473 K and 1854 K, with noticeably less fluctuation. Figure 6(b) illustrates the radial temperature distribution at the $Y=80$ mm cross-section, where irregular high temperature peaks indicate unstable combustion. The temperature profiles of cyclone nozzles 3 and 4 are essentially symmetrical, but compared to the $Y=25$ mm section, the high-temperature zone for nozzle 3 narrows, and nozzle 4 exhibits slight temperature fluctuations. At the $Y=130$ mm level, the temperature peaks predominantly in the center and tapers off towards the edges, which is consistent across the sections. Figure 6(d) presents the temperature distribution at the burner outlet, characterized by lower central temperatures. The direct flow nozzle has a higher temperature than the reduction nozzle, attributed to its minimal impact on fuel injection, facilitating an earlier and better mix of fuel and oxidizer.

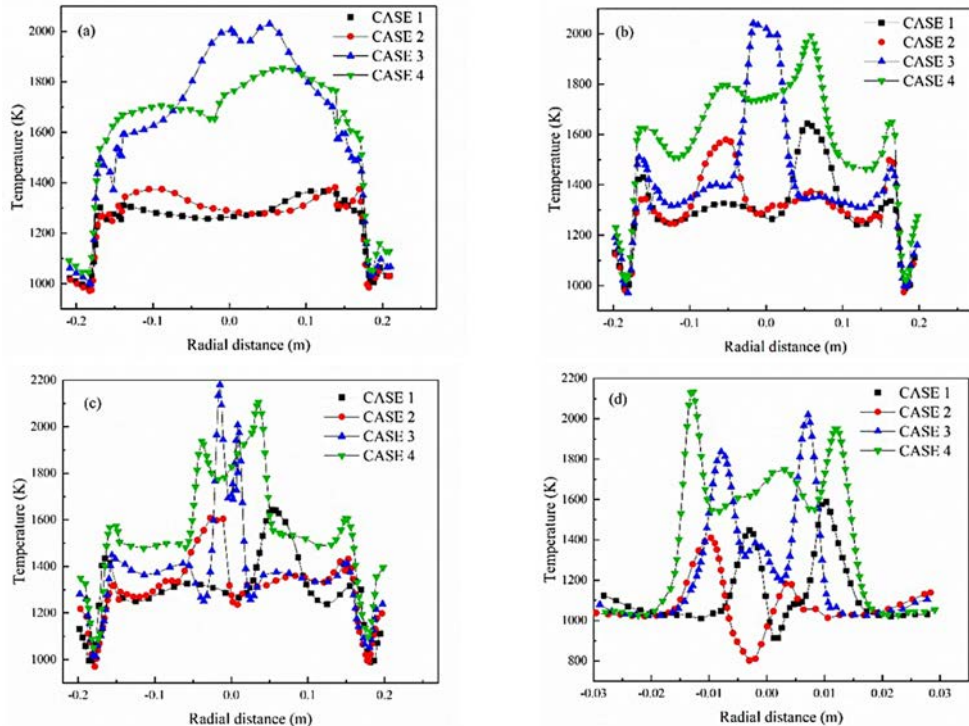


Figure 6. Effect on radial distribution of combustion temperature.

Distribution of velocity

Figs. 7 and 8 illustrate the velocity field and axial velocity quantitative distribution for various reformed gas cyclone nozzles. Figs. 7(a)-(c) and 8 depict that the velocity distributions across the three cyclone nozzle types are largely consistent, with high-velocity flows concentrated near the axis, gradually increasing and then diminishing without creating a reflux zone. The occurrence of flow field displacement, a primary contributor to temperature deviation and incomplete combustion, is observed when the exit velocity of the reformed gas from the cyclone nozzle matches that of the pilot. To enhance the axial flow velocity with diminished perturbation effects, the cyclone nozzle's area can be reduced, resulting in a symmetrically arranged velocity field. Fig. 7(d) presents an 'eight' shaped velocity field, suggesting optimal compatibility between the straight cyclone nozzle and the fuel type. This configuration leads to a

reduction and subsequent increase in axial velocity, resulting in a low-speed reflux zone that aids in flame stabilization.

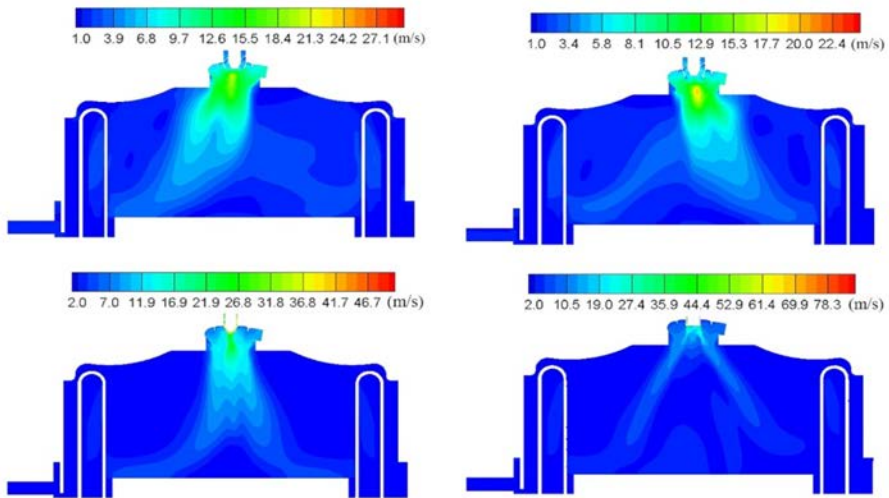


Figure 7. Effect of back pressure on combustion velocity field (m/s).

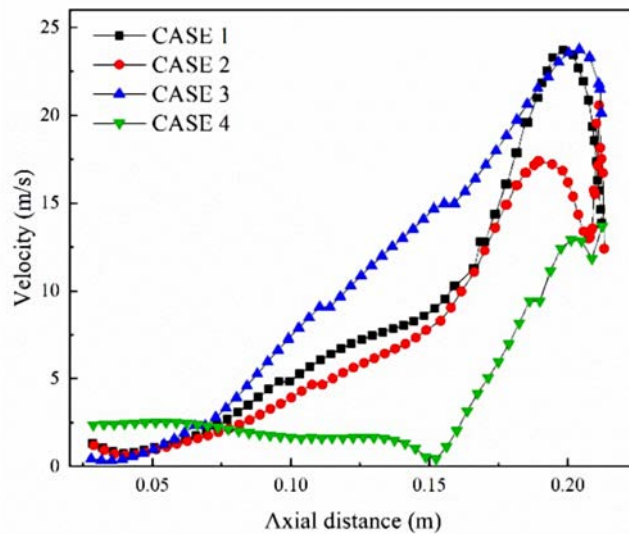
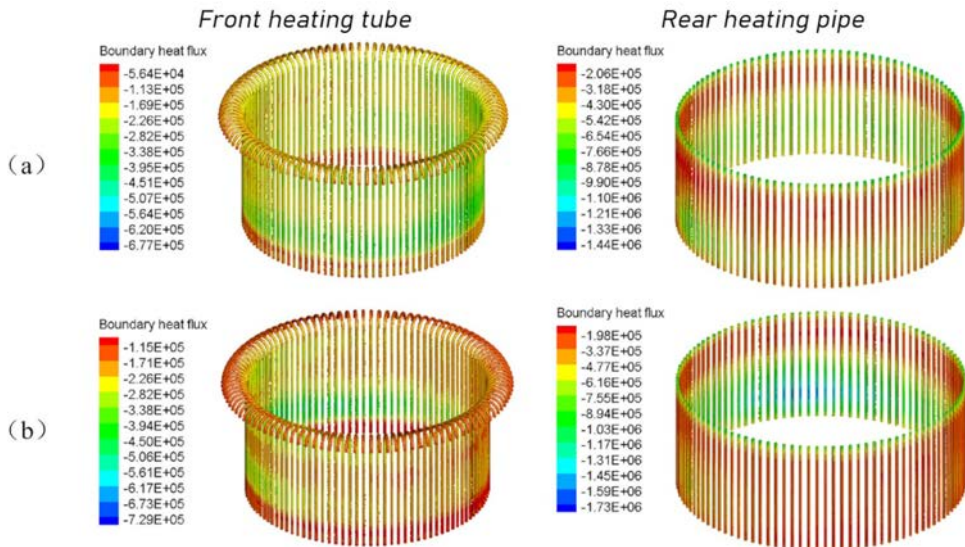


Figure 8. Effect of ejection ratio on axial section of combustion velocity.

Heat transfer characteristics

Figure 9 illustrates the heat flux density distribution across the heating tube under various cyclone nozzle conditions, highlighting a pattern where the lower end of the heating tube experiences higher heat flux density compared to its upper end, and the front of the tube exhibits lower heat flux density than the rear. A comparison between Figs. 9(a) and (b) reveals that the distribution of heat flux density is closely coupled with the temperature field. This coupling results in an uneven distribution of heat flux density across the heating tube, primarily due to flame skewing. A notable increase in heat flux density is observed when the temperature field is optimally aligned with the heater, specifically with a higher flow rate from the reforming gas nozzle. Literature comparisons reveal that the heat flux density in high-pressure oxyfuel combustion exceeds that of atmospheric pressure oxyfuel combustion [31]. For cyclone nozzle 3, the heat flux density at the front-row heater ranges from 110 kW/m² to 540 kW/m², while at the rear-row heater, it spans from 200 kW/m² to 1060 kW/m². In the case of cyclone nozzle 4, the front-row heater shows a heat flux density ranging from 170 kW/m² to 806 kW/m², with the rear-row heater distributing between 274 kW/m² and 1600 kW/m².



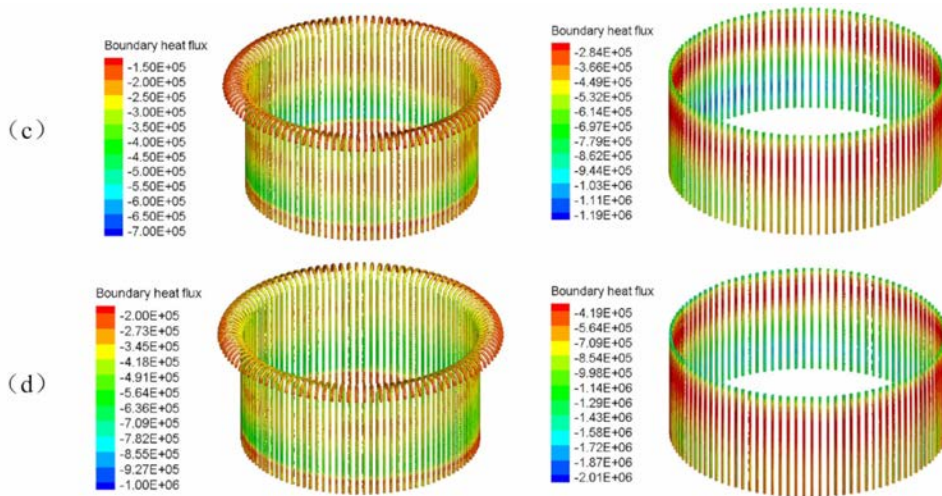


Figure 9. Heat transfer capacity of heater tubes (W/m^2).

Figure 10 presents a comparison of heat distribution and average heat transfer coefficients across various cyclone nozzles, indicating significant increases in total heat transfer capacity through structural optimization of the cyclone nozzle. Specifically, the capacities are 136.5 kW, 138.1 kW, 237.4 kW, and 251.3 kW, with the straight cyclone nozzle exhibiting an increase of 13.9 kW over the tapered nozzle. Regarding heat distribution, similar to porous nozzles, the heat exchange capacity of the heater's front row is consistently lower than that of the back row. However, the proportion of heat absorbed by the front row tubes accounts for 37.5%, 38.0%, 28.3%, and 40.9% of the total, reflecting improved uniformity in heat transfer between the front and back rows following flow field optimization. Notably, under stable combustion conditions, the heat transfer coefficient of the front row surpasses that of the rear row. The average heat transfer coefficients for the front and rear rows of heating tubes with the reduction nozzle are $738 \text{ W}/(\text{m}^2\cdot\text{K})$ and $703 \text{ W}/(\text{m}^2\cdot\text{K})$, respectively. In contrast, for the direct blowing nozzle, these coefficients are significantly higher, at $1093 \text{ W}/(\text{m}^2\cdot\text{K})$ and $1089 \text{ W}/(\text{m}^2\cdot\text{K})$ for the front and rear rows, respectively. This enhancement in heat transfer performance is attributed to the effective synergy between the temperature field and flow field of the direct blowing nozzle, resulting in a more uniform heating of the heater

and, consequently, superior heat transfer efficiency.

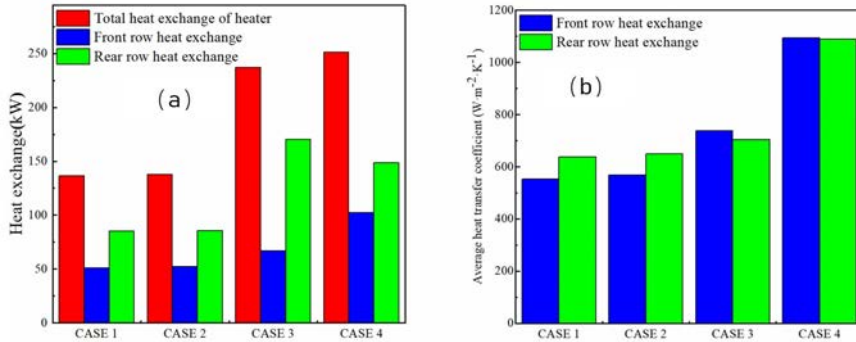


Figure 10. Heat transfer characteristics of combustion chambers with different nozzles: (a) heating tube heat distribution and (b) average heat transfer coefficient.

Figure 11 illustrates the heat transfer characteristics within the combustion chamber using different cyclone nozzles, encompassing total heat transfer, radiant heat transfer, convective heat transfer of the heaters, and the respective contributions of convective and radiant heat transfer. Fig. 11(a) reveals that under varied cyclone nozzle conditions, the radiant heat transfer for the front-row heater registers at 21.4 kW, 26.2 kW, 33.3 kW, and 51.0 kW, while convective heat transfer measures 29.7 kW, 26.3 kW, 33.9 kW, and 51.7 kW, respectively. Notably, both radiant and convective heat transfer rates for the front-row heater of the direct blowing cyclone nozzle substantially exceed those of the other nozzles. The optimization of temperature and flow fields has resulted in an improvement in the efficiency of both radiation and convection heat transfer.

Figure 11(b) illustrates the radiant and convective heat exchange of the rear-row heater under various cyclone nozzle conditions, with radiant heat exchange values of 5.7 kW, 7.0 kW, 8.8 kW, and 13.5 kW, and convective heat exchange values of 79.6 kW, 78.6 kW, 161.5 kW, and 135.1 kW, respectively. The proportion of convective heat transfer to total heat transfer is 93%, 92%, 95%, and 91%, respectively. Similar to observations with porous nozzles, the convective heat transfer significantly exceeds radiant heat transfer, more than tenfold, attributed to the substantial temperature decrease of the gas after front-row heat transfer, thereby reducing radiant heat transfer. With the straight blowing cyclone nozzle, an enhancement in front-row heat transfer performance, and a fixed total heat transfer capacity, results in a decreased convective heat transfer in the rear

row, which is lower than that observed with the reduction nozzle.

Figure 11(c) illustrates the distribution of overall radiation and convection heat transfer across the heating tube, with radiation heat transfer values of 27.2 kW, 33.2 kW, 42.0 kW, and 64.5 kW, and convection heat transfer values of 109.3 kW, 104.9 kW, 195.3 kW, and 186.8 kW, respectively. The ratios of radiation heat transfer are 20%, 24%, 18%, and 26%, respectively. Further analysis indicates that maximizing the overall heat absorption of the heating tube necessitates the optimal utilization of both front and rear heat transfer tubes, particularly enhancing the front row's performance. The efficiency of the front heating tube, predominantly influenced by radiation, suggests that strategically positioning the flame at the center can significantly enhance the front tube's radiation heat exchange.

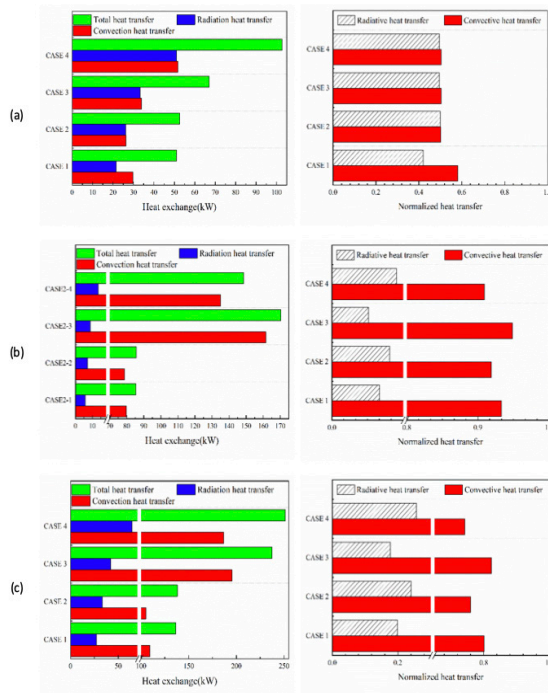


Figure 11. Heat transfer characteristics of combustion chambers with different cyclone nozzles: (a) front heater, (b) rear heater and (c) heater.

Distribution of cyclone structure

Based on the aforementioned analysis, it is evident that nozzle 4 demonstrates superior combustion performance compared to other nozzles in the engine. Consequently, to comprehensively examine the precise influence of cyclone angle on engine combustion performance, this section concentrates on experimental investigations concerning nozzle 4. Figure 12 meticulously illustrates the notable impact of the cyclone structure on the temperature distribution of the heating tube. Specifically, as the cyclone angle gradually increases, a substantial decrease in the average temperature of the lower heating tube is observed, while the temperature of the upper heating tube gradually increases. Additionally, upon thorough analysis of the data retrieved from the four temperature probes (T1, T2, T3, and T4), it was observed that the upper wall temperatures of T1, T3, and T4 consistently surpassed the lower wall temperatures, indicating a distinct disparity in temperature distribution between the upper and lower walls within these regions. Nevertheless, it is noteworthy that at cyclone angles of $\theta = 30^\circ$ and $\theta = 40^\circ$, the lower wall temperature at the T2 probe point exceeds the upper wall temperature, possibly attributable to the proximity of this region to the flame, leading to a diminished temperature differential between the upper and lower walls. Conversely, points T3 and T4 consistently exhibit a substantial temperature differential between the upper and lower walls, thereby elucidating the intricate impact of the cyclone structure on the temperature distribution of the heating tube. Furthermore, the temperature differential between the upper and lower walls of the heater tube increases with the cyclone angle. This occurrence stems from heightened mixing resulting from the intensified cyclone and the upward movement of the flame in the return zone, consequently shortening the flame. Consequently, the temperature of the upper heater rises while that of the lower heater tube declines due to the shortened flame and the migration of combustion intensity towards the upper section of the combustion chamber. Under similar total heat conditions, the temperatures of the upper and lower heaters exhibit inverse trends.

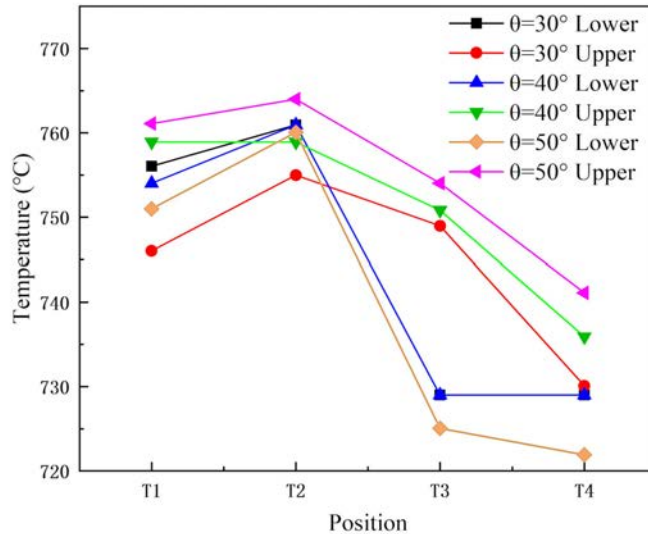


Figure 12. Effects of cyclone structure on the temperature of the heating tube.

Figure 13 elaborates on the precise impact of the cyclone structure on the uniform temperature distribution within the heater tube. Observation of the data reveals a decreasing trend in temperature fluctuations at the upper end of the heater with a gradual increase in cyclone angle, whereas fluctuations at the lower end gradually rise. Generally, elevating the cyclone angle results in an overall increase in temperature fluctuations within the combustion chamber. Specifically, the temperature fluctuation of the heater tube measured 12 °C at a cyclone angle of 30°, escalating to 19 °C at a 50° cyclone angle. Based on the aforementioned findings, it is recommended set the angle of the reformed gas nozzle to less than 30° to reduce the temperature difference between the upper and lower tube walls of the diesel and reformed gas combustion heaters, and minimize temperature fluctuation. This conclusion holds significance in optimizing the combustion process, enhancing heating efficiency, and ensuring the stable operation of combustion equipment.

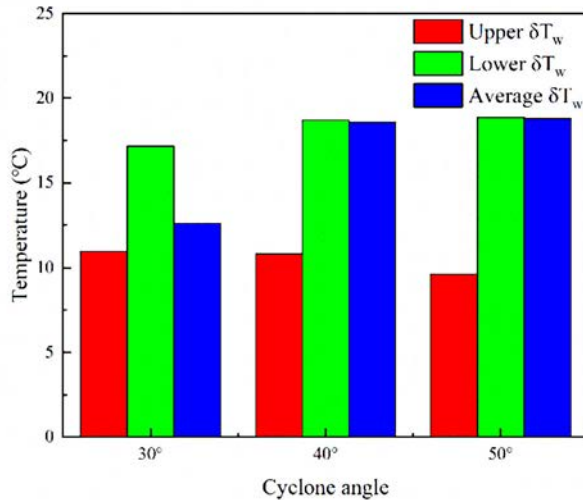


Figure 13. Effects of cyclone structure on the uniformity of temperature distribution of heating tube.

Figure 14 illustrates the impact of cyclone structure on emission characteristics. Experimental results indicate an increasing trend in the content of CO and HC in the exhaust gas with an elevation of the cyclone angle. In detail, CO emission concentrations were recorded at 0.004%, 0.006%, and 0.01% for cyclone angles of 30°, 40°, and 50°, respectively. Similarly, the HC content in the exhaust gas at these angles measured 3 ppm, 6 ppm, and 8.7 ppm, respectively. This phenomenon primarily stems from the elevated cyclone angle, resulting in diminished mixing between oxygen, reformat, and diesel fuel, thereby fostering incomplete combustion and ultimately escalating CO and HC emissions. This discovery holds significance in optimizing combustion system design, mitigating pollutant emissions, and enhancing energy efficiency.

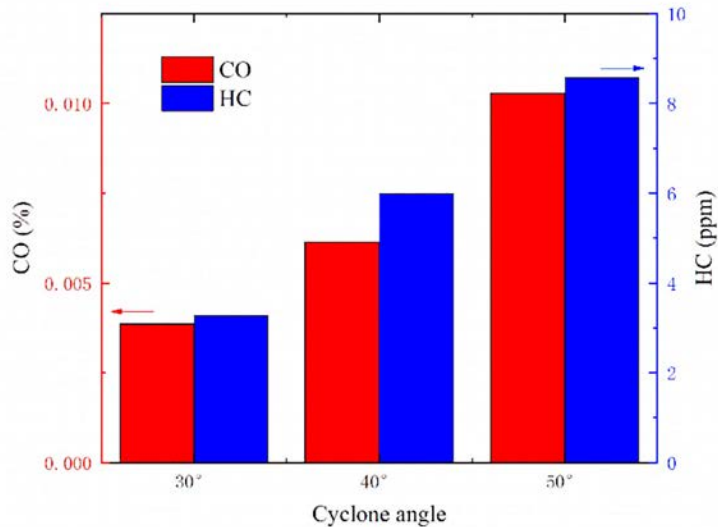


Figure 14. Effect of cyclone structure on emissions.

Table 2 illustrates the detailed impact of cyclone structure on external combustion efficiency. Upon thorough analysis, it is evident that the external combustion efficiency exhibits a pronounced decreasing trend with the gradual increase in cyclone angle. In particular, under experimental conditions with a fuel distribution ratio of 24%, the external combustion efficiency declined from 88.1% to 87.4% as the cyclone angle increased from 30° to 50°. Likewise, with the fuel distribution ratio raised to 38%, the external combustion efficiency decreased from 92.7% to 92.2% with an increase in cyclone angle from 30° to 50°. This phenomenon is primarily ascribed to the shortened flame length resulting from increased cyclone angle, leading to widened temperature disparity between the upper and lower ends of the heater, heightened overall temperature fluctuation, and diminished average temperature. Collectively, these alterations influence the heat absorption capacity of the heater, consequently reducing the external combustion efficiency. The findings of this study offer a crucial theoretical foundation for optimizing burner design, enhancing combustion efficiency, and mitigating energy wastage.

Table 2. Effect of cyclone structure on external combustion efficiency.

Fuel distribution ratio	Combustor efficiency (%)		
	$\theta=30^\circ$	$\theta=40^\circ$	$\theta=50^\circ$
24%	88.1	87.8	87.4
38%	92.7	92.4	92.2

Conclusion

This study presents a method for enhancing combustor performance through optimization of the cyclone nozzle structure in a Stirling engine. Furthermore, a multicomponent fuel combustion model is developed for the Stirling engine, facilitating investigation into the impact of various nozzles on its combustion performance. Additionally, experimental research is conducted to explore the influence of cyclone angle on engine combustion performance.

It was found that there were distortions and instabilities in the temperature field at Nozzles 1 and 2. This instability originated from a velocity mismatch between the fuel, reformat and oxidizer streams, and the solution to this challenge was to match the velocities between the oxidizer and the fuel. Subsequently, Nozzle 3 was replaced by Direct Blow Nozzle 4, thereby enlarging the area of high temperature distribution within the combustion chamber and eliminating direct flame impingement at the bottom. The direct cyclonic reforming gas nozzle (nozzle 4) improves the mixing of reforming gas, oxidizer and diesel fuel, enhancing fuel diffusion and concentrated combustion in the center of the combustion chamber, thereby improving the overall performance of the Stirling engine. In addition, it is advisable to set the reforming gas nozzle angle within 30° to minimize temperature fluctuations by reducing the temperature difference between the diesel fuel and the upper and lower pipe walls of the reforming gas combustion heater.

References

- [1] Damodharan D, Sathiyagnanam AP, Rana D, Saravanan S, Kumar BR, Sethuramasamyraja B. Effective utilization of waste plastic oil in a direct injection diesel engine using high carbon alcohols as oxygenated additives for cleaner emissions . *Energy Conversion and Management*, 2018, 166:81-97.

- [2] Poures MVD, Gopal K, Sathiyagnanam AP, Kumarc BR, Ranad D, Saravanane S, Damodharan D. Comparative account of the effects of two high carbon alcohols (C5 & C6) on combustion, performance and emission characteristics of a DI diesel engine. *Energy Sources, Part A: Recovery, Utilization, and Environmental Effects*, 2020 (14): 1772-1784.
- [3] Gang P, Zheng H. Combustion of reformed gas and liquid fuel in CRGT combustor. *Tehnički Vjesnik*, 2014, 21 (4):715-722.
- [4] Long YX, Li GS, Zhang ZH, Wei WW, Liang JJ. Hydrogen-rich gas generation via the exhaust gas-fuel reformer for the marine LNG engine. *International Journal of Hydrogen Energy*, 2022, 47 (32): 14674-14686.
- [5] Tian Lu, Zhao Liu, Yongxing Jing, Numerical and Experimental Investigation of a MILD Combustion Burner for Stirling Engines. *Proc. 16th Int. Stirling Engine Conf.* 2014.
- [6] Lan J, Gu G, Lu T, et al. Effects of initial conditions on MILD combustion for diesel in a constant pressure combustion bomb. *Energy Reports*, 2021, 7: 1015-1024.
- [7] Nakagaki, Takao, et al. "Development of chemically recuperated micro gas turbine." *J. Eng. Gas Turbines Power* 125.1 (2003): 391-397.
- [8] Seibert M, Nieh S. Measurements of hydrogen-enriched combustion of JP-8 in open flame. *Journal of Energy Resources Technology*, 2017, 139 (1): 012205.
- [9] Pashchenko D. Hydrogen-rich fuel combustion in a swirling flame: CFD-modeling with experimental verification. *International Journal of Hydrogen Energy*, 2020, 45 (38): 19996-20003.
- [10] Karpilov I, Pashchenko D. Effect of methane reforming before combustion on emission and calorimetric characteristics of its combustion process. *International Journal of Hydrogen Energy*, 2021, 46 (76): 38106-38118.
- [11] Gopal K, Sathiyagnanam AP, Kumar BR, Damodharan D, Poures MVD, Saravanan S, Rana D, Sethuramasamyraja B. Prediction and optimization of engine characteristics of a DI diesel engine fueled with cyclohexanol/diesel blends. *Energy Sources Part A Recovery Utilization and Environmental Effects*, 2019, 42 (16):1-12.

- [12] Scenna R, Gupta AK. The Influence of the Distributed Reaction Regime on Fuel Reforming Conditions. *Journal of Energy Resources Technology*, 2018, 140 (12): 122002.
- [13] Zheng HT, Pan G, Chen X, Hu XM. Effect of dual fuel nozzle Structures on Combustion Flow Field in CRGT Combustor. *Mathematical Problems in Engineering*, 2013: 913837.
- [14] Liu X, Zheng HT, Yang R, Li ZM. Fuel pre-reforming and combustion characteristics study of chemically recuperated gas turbine. *Proceedings of the Institution of Mechanical Engineers Part C: Journal of Mechanical Engineering Science*, 2014, 228 (15): 2750-2764.
- [15] Saravanan S, Kumar B R, Varadharajan A, Rana D, Sethuramasamyraja B Rao GLN. Optimization of DI diesel engine parameters fueled with iso -butanol/diesel blends – Response surface methodology approach. *Fuel*, 2017, 203:658-670.
- [16] Ilbas M, Bektas A, Karyeyen S. A new burner for oxy-fuel combustion of hydrogen containing low-calorific value syngases: An experimental and numerical study. *Fuel*, 2019, 256:115990.
- [17] Koseki H, Fujiwara M, Sigimoto T. Study on Stirling Engine Combustor. *SAE Technical Paper*, 1992.
- [18] Gao G, Huang H, Yang Y, et al. Performance simulation of a low-swirl burner for a Stirling engine. *International Journal of Energy Research*, 2019.
- [19] Solomon L, Qiu S. Computational analysis of external heat transfer for a tubular Stirling convertor. *Applied Thermal Engineering*, 2018, 137: 134-141.
- [20] Jin XD, Lü T, Yu GY, Liu JW, Huang XY. Design and Combustion Characteristic Analysis of Free Piston Stirling Engine External Combustion System. *Journal of Shanghai Jiaotong University (Science)*, 2018, 23: 50-55.
- [21] H. Kazemi, M.M. Doustdar, A. Najafi, H. Nowruzzi, M.J. Ameri, Hydrodynamic Performance Prediction of Stepped Planing Craft Using CFD and ANNs, *Journal of Marine Science and Application*, 20 (2021) 67-84.
- [22] S. Li, Y. Ju, Review of the LNG intermediate fluid vaporizer and its heat transfer characteristics, *Frontiers in Energy*, 16 (2022) 429-444.

- [23] M.A. Rizk, S.E. Belhenniche, O. Imine, O.K. Kinaci, Cavitation Predictions of E779A Propeller by a RANSE-based CFD and Its Performance Behind a Generic Hull, *Journal of Marine Science and Application*, 22 (2023) 273-283.
- [24] R. Aoki, H. Mamori, T. Miyazaki, Heat transfer enhancement by feedback blowing and suction based on vortical structure in turbulent channel flow at low Reynolds number, *Journal of Thermal Science and Technology*, 17 (2022).
- [25] J. Nagao, A.L. Pillai, R. Kurose, Investigation of temporal variation of combustion instability intensity in a back step combustor using LES, *Journal of Thermal Science and Technology*, 15 (2020) JTST0036 (0012 pp.)-JTST0036 (0012 pp.).
- [26] Jun-xia Ding, Guo-zhong He, Liang Zhang; Detailed Temperature-dependent Study of n-Heptane Pyrolysis at High Temperature. *Chin. J. Chem. Phys.* 1 June 2013; 26 (3): 329–336.
- [27] Juan-qin Li, Fan Wang, Xue-ming Cheng, Xiang-yuan Li; Reactive Molecular Dynamics Simulation on Thermal Decomposition of n-Heptane. *Chin. J. Chem. Phys.* 1 April 2013; 26 (2): 211–219.
- [28] Laura Solomon, Songgang Qiu, Computational analysis of external heat transfer for a tubular Stirling convertor, *Applied Thermal Engineering*, 2018, 134-141.
- [29] J. Howard, G. Williams, D. Fine, Kinetics of carbon monoxide oxidation in postflame gases, *Symposium (International) on Combustion*, Elsevier, 1973, pp.975–986.
- [30] W. Jones, R. Lindstedt, Global reaction schemes for hydrocarbon combustion, *Combust. Flame* 73 (1988) 233–249.
- [31] Zhang ZW, Li XS, Zhang LQ, Cong Luo, Bowen Lu, Yongqing Xu, Ji Liu, Ailing Chen, Chuguang Zheng, Effect of H₂O/CO₂ mixture on heat transfer characteristics of pulverized coal MILD-oxy combustion. *Fuel Processing Technology*, 2019, 184, 27-35.

Renewable applications of Stirling engines

Optimization of Hybrid Solar-Syngas Power System Using Response Surface Methodology

Shang-Ting Huang*, Chin-Hsiang Cheng

Institution of Aeronautics and Astronautics, National Cheng Kung University, Taiwan (R.O.C.)

*Corresponding author: P48031014@mail.ncku.edu.tw

Keywords: Hybrid power system, Beta-type Stirling engine, Response surface methodology, Integrated system model, Electromagnetic torque control

Abstract

This study presents a pioneering approach to optimizing a micro-combined heat and power (micro-CHP) system that integrates solar energy with syngas combustion, utilizing Response Surface Methodology (RSM) for enhanced system efficiency and electrical power output. The system comprises a dual-reflection solar collector, Stirling engine, fluidized-bed gasifier using wood pellets as fuel, syngas combustor, and a Permanent Magnet Synchronous Generator (PMSG) with a Zero d-Axis Controller, epitomizes innovation in Stirling systems. The research is distinctive in its methodical optimization of two key operational variables - the feeding rate of syngas (0-7 kg/hr) and the loaded torque of the generator (5-35 N-m). Additionally, the study acknowledges the intensity of solar irradiance (0-1000 W/m²) as a significant environmental variable. These variables were meticulously analyzed using RSM to ascertain their optimal levels that maximize the overall efficiency of the system and the electrical power output, ensuring a robust and efficient micro-CHP system.

Unlike conventional modeling, RSM provides a comprehensive understanding of the complex relationships between these variables, offering a detailed exploration of the operational space. This methodical approach ensures that the system's performance is optimized under varying conditions, particularly focusing on the system's ability to provide not just electricity but also heat, thereby enhancing its utility and efficiency.

The incorporation of the PMSG with the controller stands as a pivotal aspect of this study. This integration is crucial for the accurate control of the loaded torque of the generator, aligning with the RSM's findings to ensure that the system operates at its optimal operation condition, particularly in scenarios with fluctuating solar irradiance.

Moreover, this research contributes profoundly to the field, offering insights that could shape future designs and operational strategies. This is especially relevant for settings that demand high efficiency and reliability in both power and heat generation, making the most of the available resources and reducing dependence on non-renewable energy sources.

Introduction

Due to the COVID-19 pandemic and the international conflict in certain area, the world experienced a severe global energy crisis and inflation. The surge in energy costs

had profound inflationary effects on various sectors reliant on energy consumption, exacerbating financial hardships for families and necessitating production cutbacks in factories, thereby impeding economic growth across multiple industries [1-2]. The adoption of renewable energy plays a pivotal role in mitigating the carbon-intensive consequences associated with inflation and interest rate hikes [3]. The utilization of a Stirling engine powered by solar energy stands out as a persuasive solution within the realm of renewable energy [4-5]. However, the intermittent nature of solar radiation poses a challenge to the reliability of solar energy systems. In response to the uncertainties associated with weather conditions, this paper proposes a hybrid solar-syngas power system. The objective is to establish a seamlessly operating system that ensures continuous power generation, overcoming the limitations of solar intermittency. Currently, noteworthy research is being conducted in the field of such systems, as exemplified in the work reported by Boretti [6]. A hybrid concentrated solar/combustion system is proposed for Mauritius, featuring an 8 kW system with a concentrator, molten salt thermal energy storage, biomass combustion heater, Stirling engine, and generator. The hybrid system achieves an 88% reduction in CO₂ emissions compared to a reference oil combustion plant, utilizing solar energy for 41% of thermal energy supply and combustion fuel for the remaining 59%. Angrisani et al. [7] delivered a system concept, employing a Stirling engine for combined heat and electric power production. The system makes use of two sustainable energy sources – direct solar and biomass. It incorporates a fluidized bed combustor for biomass combustion and integrates a Scheffler type mirror into the same system, serving as a solar receiver for the fluidized bed, and facilitating concentrated solar radiation. Hussain et al. [8] discussed the suitability of the concentrated solar power system for hybridization with biomass. The hybrid solar-biomass power plant presents a renewable technology for dispatchable power production across various climate zones. Biomass combustion stands out as the most economically viable supplementary heat technology. However, a key technical challenge for solar-biomass plants lies in designing and implementing effective system control mechanisms.

This paper delves into the critical components and design intricacies of a hybrid solar-syngas power system, providing comprehensive details on simulations. Additionally, to enhance system efficiency, the study employs response surface methodology to optimize

performance under varying operating conditions, with an aim towards achieving real-time control capabilities in the future.

Modeling of hybrid solar-syngas power system

The present investigation explores the impact of different parameters on the performance of a solar-syngas powered Stirling engine. The system under consideration integrates dual-reflection collector, a fluidized-bed gasifier, a hybrid energy receiver, an electrical generator with a controller in conjunction with the Stirling engine. The interaction relationship between each components is showing at Figure 1.

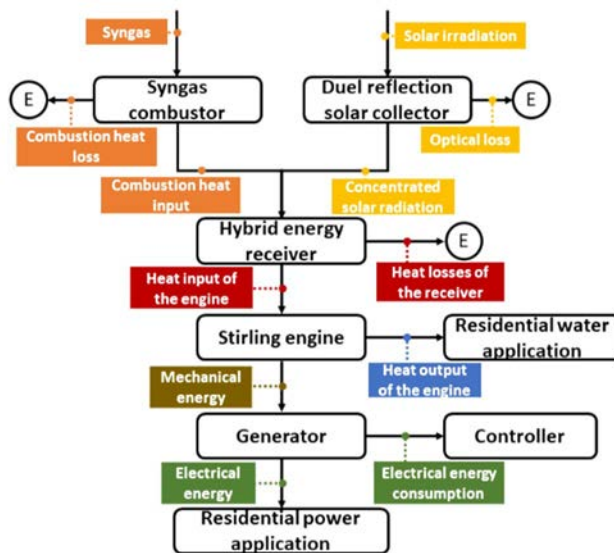


Figure 1. Schematic of hybrid solar-syngas power system.

Beta-type Stirling engine

In this paper, the Stirling engine is a beta-type Stirling engine with rhombic drive mechanism. The rhombic drive mechanism offers the distinct advantage of dynamic balance [9]. Comparative analysis against alternative drive mechanisms consistently demonstrates the superior suitability of the rhombic drive for beta-type Stirling engines [10]. A key issue in designing and optimizing Stirling engines is to build a precise

model to predict output power, thermal efficiency and provide useful information for further improvement. In this paper, a second-order analysis approach to carefully obtain performance and other pertinent details of the Stirling engine, facilitating a comprehensive understanding and offering pathways for refinement. The model utilized in this study builds upon the framework proposed by Yang and Cheng [11], incorporating additional modifications. The model comprises both a thermodynamic model and a dynamic model. These models simulate the pressure variation of working spaces and the velocity profile of all links and joints simultaneously. In a detailed explanation, factors such as inertia of links, gravitational effects, pressure exerted on the piston and displacer, friction forces and the loaded torque from the generator are all taken into considered. The performance of the Stirling engine is determined by the following equations:

$$\dot{W}_i = \frac{\bar{\omega}_{ms}}{60} (\oint p_e dV_e + \oint p_c dV_c) \quad (1)$$

$$\dot{W}_s = \bar{\omega}_{ms} \oint \tau_g d\phi_{ms} / 2\pi \quad (2)$$

$$\dot{Q}_{in.s} = \frac{\bar{\omega}_{ms}}{60} \left(\oint \frac{T_{wh} - T_e}{R_e} + \frac{T_{wh} - T_h}{R_h} \right) \quad (3)$$

$$\dot{Q}_{out.s} = \frac{\bar{\omega}_{ms}}{60} \left(\oint \frac{T_{wj.c} - T_c}{R_c} + \frac{T_{wj.k} - T_k}{R_k} \right) \quad (4)$$

where \dot{W}_p , \dot{W}_s , $\dot{Q}_{in.s}$ and $\dot{Q}_{out.s}$ represent the indicated power, shaft power, absorbed heat and ejected heat of the Stirling engine, respectively; T_{wh} , $T_{wj.c}$, $T_{wj.k}$, T_e , T_h , T_c and T_k denote the temperature of metallic wall at heater, water in water jacket around the compression space, water in water jacket around the cooler, working gas in expansion space, working gas in heater, working gas in compression space and cooler, respectively; p_e and p_c are pressure in the expansion space and the compression space; V_e and V_c are volume in the expansion space and the compression space; τ_g indicates the loaded torque from generator.

Dual-reflection solar collector

The concentrated solar power system in this paper, convert solar radiation from the sun into thermal energy, which is then utilized as concentrating solar thermal power. This power can be converted into mechanical energy and further converted into electrical energy. The system features a 5 m diameter parabolic dish comprised of thin polymer

films with coated aluminum, arranged within a supporting structure. The parabolic dish reflects and concentrates solar radiation onto a secondary elliptic dish with a diameter of 0.6 m, made of stainless steel with mirror-like surface, located in front of the 5 m parabolic dish. After undergoing two reflections and concentrations, solar radiation is focused onto the focal point of the dish's receiver. Here, the required temperatures are achieved. Due to this geometrical design, the receiver and the Stirling engine are mounted in a nacelle behind the parabolic dish, which provides protection from direct exposure of the sun and rain. To maximize system efficiency, solar irradiation is continually directed towards the focal point, where the receiver is positioned. Thus, solar parabolic dishes automatically track the sun's movement using a tracking control system. The solar tracking system in this paper, is Azimuth-Elevation tracking system. The geometrical design of the duel-reflection solar concentrator is listed in Table 1. Additionally, the geometrical design is validated by ray tracing simulation software (SolTrace), which is open-source. Fig.2 represents the simulation result of ray tracing.

Table 1. Dimensions and parameters of the duel-reflection solar collector.

Diameter of parabolic dish	5 m
Diameter of elliptic dish	0.6 m
Focal length of parabolic dish	1.66 m
Rim angle	36.971°
Reflectance	0.9

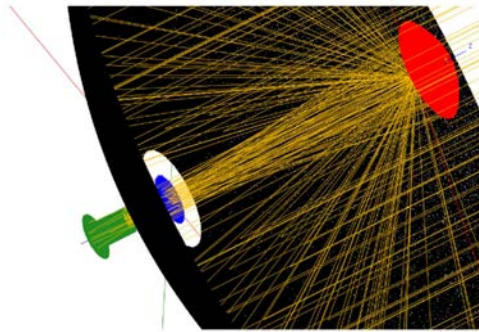


Figure 2. Ray tracing simulation of the duel-reflection solar concentrator.

Hybrid energy receiver

A hybrid energy receiver has been designed to provide continuous heat sources for the Stirling engine. This receiver operates as a directly illuminated type, where heating tubes are directly exposed to concentrated solar radiation. Its aperture is covered with a quartz glass, creating a closed chamber to minimize thermal losses. Hybridization is achieved by enclosing the heating tubes of the Stirling engine with a set of flue tube and installing a series of annular fins on the external surface. During the period of insufficient solar irradiance, high-temperature flue gases emitted by the combustor are directed through the flue tubes to provide combustion energy for the Stirling engine. During operation, the Stirling engine receives either solar radiation or combustion energy. Consequently, in the energy analysis of the Stirling engine, concentrated solar radiation, combustion energy, energy absorbed by the heating tubes of the Stirling engine, and thermal losses via the receiver are all taken into account. Additionally, insulation materials are used to effectively isolate the chamber, minimizing heat loss from the hybrid energy receiver. The energy conservation with the hybrid energy receiver is expressed as follows:

$$m_{hw}c_{p,hw} \frac{dT_{hw}}{dt} = \dot{Q}_{ir} + \dot{Q}_{syn} - \dot{Q}_{in.s} - \dot{Q}_{loss.rec} \quad (5)$$

where m_{hw} and $c_{p,hw}$ denote the mass and specific heat of array of heating tubes, respectively; \dot{Q}_{ir} , \dot{Q}_{syn} and $\dot{Q}_{loss.rec}$ represent solar radiation, combustion energy from syngas and thermal losses of the receiver, respectively. The geometrical design of the hybrid energy receiver is listed in Table 2.

Table 2. Dimensions and parameters of the hybrid energy receiver.

Diameter of aperture	0.3 m
Diameter of receiver	0.44 m
Thickness of insulation	0.04 m
Thermal conductivity of insulation	0.04 W/(m K)

Fluidized-bed gasifier

A capacity of 20 kW and comprised a bubbling fluidized bed, a wood pellet feeder, a syngas storage tank, a cyclone, and a tar remover. Due to the consistent availability of wood pellets in Taiwan, they were chosen as the biomass material for synthesizing gases. Typically, a reactor's temperature must exceed 800 °C for effective gasification, wherein wood pellets are converted into a gaseous mixture consisting of CO, H₂, CH₄, CO₂, and other gases. Table 2 provides the chemical compositions of the synthesized gases and their low heating value (LHV). Gas composition was determined using a gas analyzer. Combustion energy was subsequently calculated based on the LHV and feeding rate of the gaseous mixture, as detailed in Table 3. The feeding rate of the synthesis gas mixture was ranged at 0 to 7.0 kg/h. Fluidized beds, characterized by their geometry and excellent mixing properties, are ideally suited for producing clean synthesis gases. The calculation of the combustion energy term in Equation (5) is as follows:

$$\dot{Q}_{syn} = \dot{m}_{syn} LHV_{syn} \quad (6)$$

where \dot{m}_{syn} and LHV_{syn} represent feeding rate and low heating value of syngas, respectively.

Table 3. Chemical composition (wt. % dry basis) of syngas.

Carbon monoxide	19.46±0.71
Hydrogen	5.78±0.21
Oxygen	0.48±0.42
Carbon dioxide	11.68±0.35
Methane	3.06±0.13

Generator and controller

A permanent magnet synchronous generator (PMSG) is directly driven by the Stirling engine without a gearbox and is subsequently connected to the battery via a three-phase PWM rectifier. The PMSG is then regulated to produce maximum electromagnetic torque with minimum stator current by implementing Zero d-Axis current control. Additionally, optimal torque control ensures the extraction of maximum mechanical power from the Stirling engine. To attain the highest mechanical power transmitted to the generator,

the reference torque required by the control technology is provided by the RSM, which will be discussed in a subsequent section. The momentum equation of the drive train is as follows:

$$I_g \frac{d\omega_{ms}}{dt} = \tau_{pre} - \tau_g - \tau_{mf} \quad (7)$$

where I_g denotes the inertia of drive train, τ_{pre} represents the torque generated by the pressure of working gas in the Stirling engine and τ_{mf} indicates the friction torque generated by the mechanisms of the engine. In steady state the electromagnetic torque will be equal to the minus of the applied load torque.

The electrical model of the PMSG is expressed by the follow equations set in the rotor d-q reference frame.

$$\frac{di_d}{dt} = -\frac{R_s}{L_d} i_d + \frac{N\omega_{ms}L_q}{L_d} i_q + \frac{V_d}{L_d} \quad (8)$$

$$\frac{di_q}{dt} = -\frac{R_s}{L_q} i_q - \frac{N\omega_{ms}L_d}{L_q} i_d - \frac{f_{PM}N\omega_{ms} + V_q}{L_q} \quad (9)$$

$$\tau_e = \frac{3}{2} N [(L_d - L_q) i_d i_q + f_{PM} i_q] \quad (10)$$

where i_d and i_q are current in the stator, N is pole pair number, L_d and L_q are the generator inductance, R_s is the generator resistance and f_{PM} is the permanent magnet flux. Equation (10) shows the electromagnetic torque.

In the context of zero d-axis control, where i_d is constrained to zero, the electromagnetic torque of the generator is proportional to $i_{q,ref}$. The equation (10) can be expressed as follows:

$$i_{q,ref} = \frac{2\tau_e}{3Nf_{PM}} \quad (11)$$

In the control process, the error from i_d , i_q , $i_{d,ref}$ and $i_{q,ref}$ injected into the PI regulator to generate V_d' and V_q' voltages. Subsequently, through Park transformation, pulse width modulation (PWM) receives V_a , V_b and V_c as input signals. Finally, The PWM module

triggers the switching of the Insulated-Gate Bipolar Transistor (IGBT) rectifier, regulating the power flow accordingly.

Response surface methodology

In this study, we utilize Response Surface Methodology (RSM) to establish the functional relationship between design variables and objective responses, as well as to analyze the interactive effects of different variables on the responses. The data utilized for this analysis is derived from a set of numerical simulations. Notably, the primary operational parameters of the hybrid solar-syngas power system, including the intensity of solar irradiance, the feeding rate of syngas, and the loaded torque of the generator, are chosen as input variables. The overall efficiency of the system and the electrical power output are selected as the output responses. To design the numerical experiment, we employ the Central Composite Design (CCD), with each variable assumed to have five levels. The input variables and their corresponding levels are summarized in Table 4. In response surface analysis, the quadratic polynomial regression model is commonly employed to approximate the functional relationship between variables.

Table 4. Input variables and their five levels.

Variable	Level				
	- α	-1	0	+1	+ α
Solar irradiance	0	146.4	500	853.5	1000
Feeding rate of syngas	0	1.03	3.5	5.97	7
Loaded torque of generator	5	9.39	20	30.61	35

The definition of the efficiency of system in this paper can be expressed as follows:

$$\eta_s = \frac{P_e + \dot{Q}_{out,s}}{\dot{Q}_{ir} + \dot{Q}_{syn}} \quad (12)$$

where P_e denotes the electrical power output.

Results and discussion

The interactive effects of operational parameters on Stirling engine performance are analyzed through 2-D and 3-D response surface plots, depicted in Figures 3–6. Figures 3 and 4 illustrate the combined impacts of solar irradiance and syngas feeding rate on

system efficiency and electrical power output. It is observed that both efficiency and electrical power output increase with higher solar irradiance and syngas feeding rate. This trend can be attributed to the role of solar irradiance and syngas feeding rate as external heat input sources for the Stirling engine. As external heat input increases, the temperature of heating tubes rises, resulting in increased absorbed heat by the Stirling engine and subsequently higher electrical power output. However, a decreasing trend is observed near the maximum points of these parameters on system efficiency. This decrease can be attributed to excessively high temperatures of the heating tubes, leading to increased thermal losses from the receiver, thereby reducing system efficiency

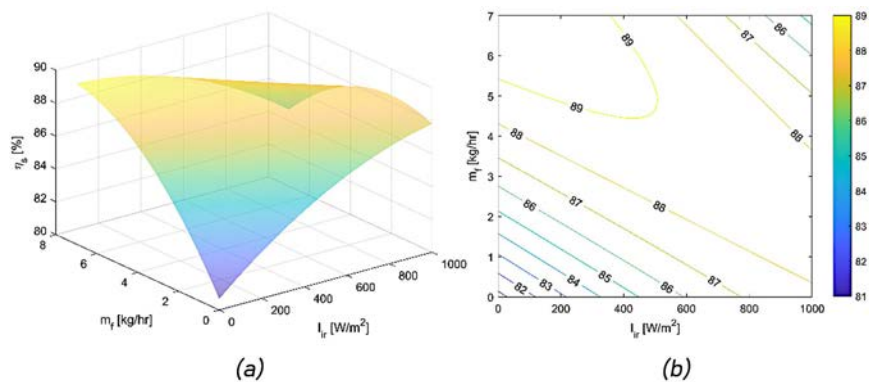


Figure 3. Interactive effects of the solar irradiance and feeding rate of syngas on the system efficiency: (a) 3-D surface plot and (b) 2-D contour plot.

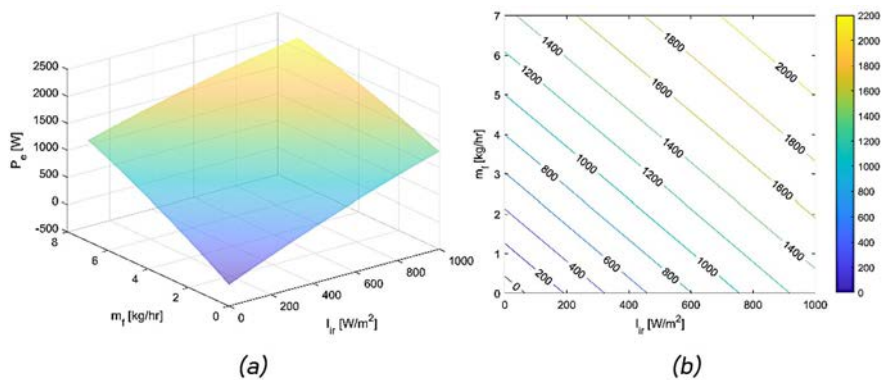


Figure 4. Interactive effects of the solar irradiance and feeding rate of syngas on the electrical power output: (a) 3-D surface plot and (b) 2-D contour plot.

Figures 5 and 6 depict the combined effects of solar irradiance and loaded torque of the generator on system efficiency and electrical power output. In Figure 5(a), presented as a 3-D surface plot, it is observed that as solar irradiance increases, the system efficiency slightly decreases. Notably, an optimal value of loaded torque of the generator is observed within the variation of solar irradiance, contributing to the optimization of system efficiency. The variation in loaded torque of the generator influences the rotation speed of the Stirling engine. As shown in Figures 5(b), with a loaded torque of 21.5 and solar irradiance of 650, the predicted optimal efficiency is 88.77%. Figure 6 illustrates the impact of the loaded torque of the generator on electrical power output, demonstrating an optimal value that corresponds to different levels of solar irradiance. However, due to torque limitations of the generator, only a positive correlation between loaded torque and electrical power output is observed at high levels of solar irradiance.

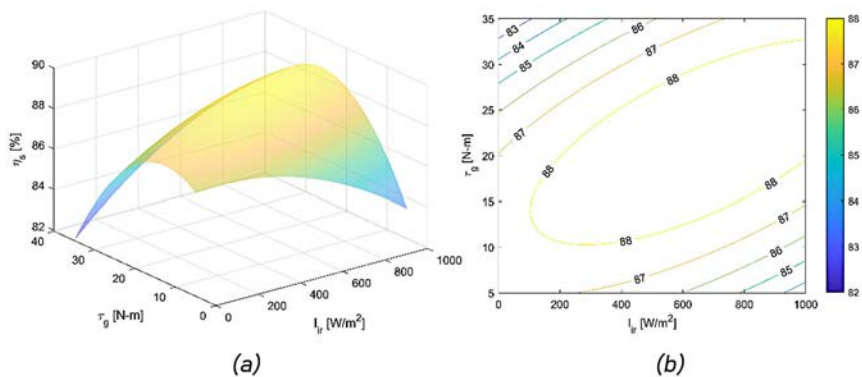


Figure 5. Interactive effects of the solar irradiance and loaded torque of generator on the system efficiency: (a) 3-D surface plot and (b) 2-D contour plot.

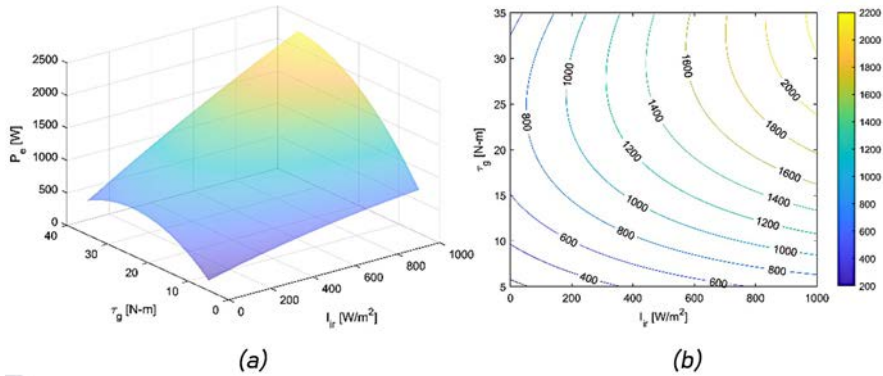


Figure 6. Interactive effects of the solar irradiance and loaded torque of generator on the electrical power output: (a) 3-D surface plot and (b) 2-D contour plot.

In an ideal hybrid solar-syngas power system, optimal efficiency and maximum electrical power output are desirable. However, based on the response surface analysis presented above, an optimal configuration involving solar irradiance, syngas feeding rate, and loaded torque exists. To achieve this optimal combination of objectives, the optimization process incorporates the following objective function:

$$f = \frac{1}{\eta_s} + \frac{1}{P_e} \quad (13)$$

In this paper, the operating variables, including the feeding rate of syngas and the loaded torque of the generator, are optimized at various levels of solar irradiance to minimize the objective function. Figure 7 shows the system efficiency after optimization ($\eta_{s,o}$) and electrical power output after optimization ($P_{e,o}$), both of which have been enhanced at each level of solar irradiance. Specifically, the electrical power output has significantly increased from less than 1000 W to at least 1600 W in the absence of solar irradiance. Additionally, the highest electrical power output observed is 2585 W, with an average system efficiency of 89%.

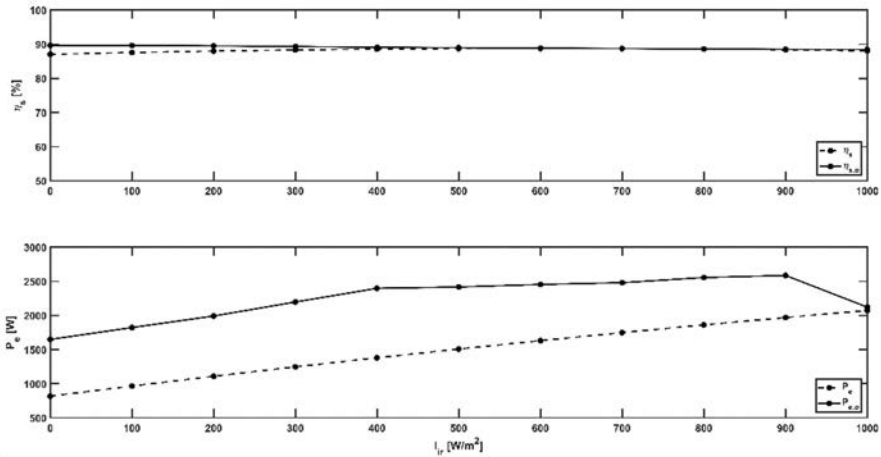


Figure 7. System performance of optimization at different each levels of solar irradiance.

Conclusion

In this study, we have developed a novel model of a hybrid solar-syngas power system, incorporating a dual-reflection solar collector, Stirling engine, fluidized-bed gasifier fueled by wood pellets, syngas combustor, and a Permanent Magnet Synchronous Generator (PMSG) with a Controller. By employing Response Surface Methodology (RSM), we have analyzed the interactive effects of solar irradiance, syngas feeding rate, and generator loaded torque on system efficiency and electrical power output. Through optimization of operating variables at each level of solar irradiance, we have achieved a maximum electrical power output of 2585 W and an average system efficiency of 89%.

References

- [1] Ozili PK, Ozen E. Global energy crisis: impact on the global economy. The Impact of Climate Change and Sustainability Standards on the Insurance Market, 439-454 (2023).
- [2] Hu Z. A study of how soaring energy prices affect the economy. 7th International Conference on Economy, Management, Law and Education (EMLE 2021), Atlantis Press (2022).
- [3] Akan T. Can renewable energy mitigate the impacts of inflation and policy interest on climate change? Renewable Energy, 214 (2023).

- [4] Ferruzzi G, Delcea C, Barberi A, Di Dio V, Di Somma M, Catrini P, Guarino S, Rossi F, Parisi ML, Sinicropi A, Longo S. Concentrating Solar Power: The State of the Art, Research Gaps and Future Perspectives. *energies*, 16.24 (2023).
- [5] Buscemi A, Guarino S, Ciulla G, Brano VL. A methodology for optimisation of solar dish-Stirling systems size, based on the local frequency distribution of direct normal irradiance. *Applied Energy*, 303 (2021).
- [6] Boretti A. A hybrid concentrated solar/biomass combustion system with internal thermal energy storage for fully dispatchable renewable electricity production in Mauritius. *Energy Storage*, 5.1 (2023).
- [7] Angrisani G, Bizon K, Chirone R, Continillo G, Fusso G, Lombardi S, Marra F.S, Miccio F, Roselli C, Sasso M, Solimene R, Tariello F, Urciuolo M. Development of a new concept solar-biomass cogeneration system. *Energy Conversion and Management*, 75 (2013).
- [8] Hussain CMI, Norton B, Duffy A. Technological assessment of different solar-biomass systems for hybrid power generation in Europe. *Renewable and Sustainable Energy Reviews*, 68 (2017).
- [9] Cheng CH, Yu YJ. Dynamic simulation of a beta-type Stirling engine with cam-drive mechanism via the combination of the thermodynamic and dynamic models. *Renewable energy*, 36.2 (2011).
- [10] Erol D, Yaman H, Doğan B. A review development of rhombic drive mechanism used in the Stirling engines. *Renewable and Sustainable Energy Reviews*, 78 (2017).
- [11] Yang HS, Cheng CH, Huang ST. A complete model for dynamic simulation of a 1-kW class beta-type Stirling engine with rhombic-drive mechanism. *Energy*, 161 (2018).
- [12] Cheng CH, Huang ST. Modeling of a hybrid power system integrating solar radiation and syngas combustion energy. *Energy Science & Engineering*, 11.10 (2023).

Authors Index

Abrahamsen S.	435	Ma Z.	66, 109
Abuelyamen A.	231	Marra F. S.	299
Acampora L.	299	Matsubar M.	284
Auñón Hidalgo J. A.	206	Maung Y.	219
Ben-Mansour R.	231	Murti P.	29
Biwa T.	29, 40	Núñez Gevorkian D.	206
Chen YH.	385	Okuhara S.	29
Chen YY.	331, 385	Peveling S.	449
Cheng Y.	109	Phung D. T.	192
Cheng Y. C.	84	Popesku S.	192
Cheng C. H.	125, 192, 495	Protheroe M.	269
Chouder R.	48	Sangdani M. H.	96
Chun Y.	84	Sato T.	17
Dahl T.	435	Sekimoto S.	141
Dai L. R.	420	Shoji E.	29, 40
Dhanasekaran S.	125	Stolyarov A. S.	219
Fischer F.	366	Stolyarov S. P.	219
Gevorkian D. N.	206	Stouffs P.	48
Gschwendtner M.	175, 269	Sun H.	66
Gu G. X.	467	Sun Y.	331, 385, 401
Han D.	467	Sun Y. L.	420
HM W.	350	Takao M.	29
Høeg A.	250, 435	Tavakolpour-Saleh A. R.	96
Hu J.	331, 401, 420	Tetsuka K.	40
Hu Y.	385	Toda F.	284
Huang J. S.	150	Tomihira J.	29
Huang Y.	420	Ueda Y.	141, 319
Huang S. T.	495	Vartdal G.	435
Ishijima T.	284	Waleed Z.	175, 269
Jiang S.	109	Wang R.	401
Jin Q.	66, 331	Watanabe A.	319
Kitahara T.	17	Wu Z. H.	401, 420
Kühl H. D.	366, 449	Xi Z.	158
Kurai Y.	141	Xiao W.	109
Kusche F.	449	Xiao X.	158
Lan J.	467	Xue J.	66
Liang X.	467	Yang H. S.	84
Lin G. T.	467	Yang D.	175, 269
Lümmen N.	250, 435	Yang X.	467
Luo E.	12, 66, 109, 331, 385, 401, 420	Yin C. S.	84
Luo J.	66, 331, 385	Yoshioka K.	319
Luo K. Q.	420	Yu G.	66, 109, 385
Lyu T.	467	Yu Z.	404
Ma Y.	66, 109	Zhang L.	331
		Zhang X.	158
		Zhu X.	331

